

Metals

3.1. Metals

Whereas the fundamental properties of all metallic elements are covered systematically and comprehensively in Chapt. 2.1, this section chapter treats those metals that are applied as base and alloying elements of metallic materials. According to common usage, the section is subdivided into treatments of metallic materials based on a single elements (Mg, Al, Ti, Zr, Fe, Co, Ni, Cu, Pb), and treatments of groups of metals with common dominating features (refractory metals, noble metals). The term metal is used indiscriminately for pure metals and for multicomponent metallic materials, i. e., alloys.

The properties of metallic materials depend sensitively not only on their chemical composition and on the electronic and crystal structure of the phases formed, but also to a large degree on their microstructure including the kind and distribution of lattice defects. The phase composition and microstructure of metallic materials are strongly dependent, in turn, on the thermal and mechanical treatments, which are applied under well-controlled conditions to achieve the desired properties. Accordingly, the production of metallic semifinished products and final parts on one hand, and the properties in the final state on the other hand, are usually intricately linked. This also applies to metallic materials treated in other chapters (Chapt. 4.2 on superconductors and Chapt. 4.3 on magnetic materials), as well as to the majority of other inorganic and organic materials.

According to the complexity of the interrelations between fundamental (intrinsic) and microstructure-dependent (extrinsic) properties of metallic materials, this section provides a substantial amount of explanatory text. By the same token, the data given are mostly typical examples indicating characteristic ranges of properties achievable rather than providing complete listings. More comprehensive databases are indicated by way of reference.

| | |
|---|-----|
| 3.1.1 Magnesium and Magnesium Alloys | 162 |
| 3.1.1.1 Magnesium Alloys | 163 |
| 3.1.1.2 Melting and Casting Practices, Heat Treatment..... | 168 |
| 3.1.1.3 Joining | 169 |
| 3.1.1.4 Corrosion Behavior | 169 |
| 3.1.1.5 Recent Developments | 170 |
| 3.1.2 Aluminium and Aluminium Alloys | 171 |
| 3.1.2.1 Introduction | 171 |
| 3.1.2.2 Production of Aluminium | 171 |
| 3.1.2.3 Properties of Pure Al | 172 |
| 3.1.2.4 Aluminium Alloy Phase Diagrams | 174 |
| 3.1.2.5 Classification of Aluminium Alloys | 179 |
| 3.1.2.6 Structure and Basic Mechanical Properties of Wrought Work- Hardenable Aluminium Alloys... | 180 |
| 3.1.2.7 Structure and Basic Mechanical Properties of Wrought Age- Hardenable Aluminium Alloys... | 182 |
| 3.1.2.8 Structure and Basic Mechanical Properties of Aluminium Casting Alloys | 184 |
| 3.1.2.9 Technical Properties of Aluminium Alloys | 186 |
| 3.1.2.10 Thermal and Mechanical Treatment | 194 |
| 3.1.2.11 Corrosion Behavior of Aluminium | 202 |
| 3.1.3 Titanium and Titanium Alloys | 206 |
| 3.1.3.1 Commercially Pure Grades of Ti and Low-Alloy Ti Materials | 207 |
| 3.1.3.2 Ti-Based Alloys | 208 |
| 3.1.3.3 Intermetallic Ti-Al Materials.... | 209 |
| 3.1.3.4 TiNi Shape-Memory Alloys | 216 |
| 3.1.4 Zirconium and Zirconium Alloys | 217 |
| 3.1.4.1 Technically-Pure and Low-Alloy Zirconium Materials..... | 217 |
| 3.1.4.2 Zirconium Alloys in Nuclear Applications | 218 |
| 3.1.4.3 Zirconium-Based Bulk Glassy Alloys | 218 |

| | | | |
|--|-----|---|-----|
| 3.1.5 Iron and Steels | 221 | 3.1.8.3 Brasses | 298 |
| 3.1.5.1 Phase Relations and Phase Transformations..... | 222 | 3.1.8.4 Bronzes..... | 298 |
| 3.1.5.2 Carbon and Low-Alloy Steels | 227 | 3.1.8.5 Copper–Nickel and Copper–Nickel–Zinc Alloys | 300 |
| 3.1.5.3 High-Strength Low-Alloy Steels | 240 | 3.1.9 Refractory Metals and Alloys | 303 |
| 3.1.5.4 Stainless Steels | 240 | 3.1.9.1 Physical Properties | 306 |
| 3.1.5.5 Heat-Resistant Steels..... | 257 | 3.1.9.2 Chemical Properties | 308 |
| 3.1.5.6 Tool Steels | 262 | 3.1.9.3 Recrystallization Behavior | 311 |
| 3.1.5.7 Cast Irons | 268 | 3.1.9.4 Mechanical Properties..... | 314 |
| 3.1.6 Cobalt and Cobalt Alloys | 272 | 3.1.10 Noble Metals and Noble Metal Alloys | 329 |
| 3.1.6.1 Co-Based Alloys | 272 | 3.1.10.1 Silver and Silver Alloys | 330 |
| 3.1.6.2 Co-Based Hard-Facing Alloys and Related Materials..... | 274 | 3.1.10.2 Gold and Gold Alloys | 347 |
| 3.1.6.3 Co-Based Heat-Resistant Alloys, Superalloys..... | 274 | 3.1.10.3 Platinum Group Metals and Alloys | 363 |
| 3.1.6.4 Co-Based Corrosion-Resistant Alloys | 276 | 3.1.10.4 Rhodium, Iridium, Rhutenum, Osmium, and their Alloys | 386 |
| 3.1.6.5 Co-Based Surgical Implant Alloys..... | 277 | 3.1.11 Lead and Lead Alloys | 407 |
| 3.1.6.6 Cemented Carbides..... | 277 | 3.1.11.1 Pure Grades of Lead | 407 |
| 3.1.7 Nickel and Nickel Alloys | 279 | 3.1.11.2 Pb–Sb Alloys..... | 411 |
| 3.1.7.1 Commercially Pure and Low-Alloy Nickels | 279 | 3.1.11.3 Pb–Sn Alloys..... | 414 |
| 3.1.7.2 Highly Alloyed Ni-Based Materials..... | 279 | 3.1.11.4 Pb–Ca Alloys..... | 416 |
| 3.1.7.3 Ni-Based Superalloys..... | 284 | 3.1.11.5 Pb–Bi Alloys | 419 |
| 3.1.7.4 Ni Plating..... | 288 | 3.1.11.6 Pb–Ag Alloys..... | 420 |
| 3.1.8 Copper and Copper Alloys | 296 | 3.1.11.7 Pb–Cu, Pb–Te, and Pb–Cu–Te Alloys | 421 |
| 3.1.8.1 Unalloyed Coppers..... | 296 | 3.1.11.8 Pb–As Alloys | 421 |
| 3.1.8.2 High Copper Alloys..... | 297 | 3.1.11.9 Lead Cable Sheathing Alloys | 421 |
| | | 3.1.11.10 Other Lead Alloys | 421 |
| | | References | 422 |

3.1.1 Magnesium and Magnesium Alloys

Magnesium is the lightest structural metal with a density of 1.74 g cm^{-3} . It is produced by two basic processes. One is the electrolysis of fused anhydrous magnesium chloride (MgCl_2) derived from magnesite, brine, or seawater, and recently from serpentine ores. The other one is the thermal reduction of magnesium oxide (MgO) by ferrosilicon derived from carbonate ores [1.1]. The use of primary Mg is shown in Fig. 3.1-1. Only one third is used for structural parts, mainly for castings, while the major amount of Mg is still used as an alloying element in Al alloys.

Pure Mg is rarely used for structural applications due to its poor mechanical properties. Therefore, Al and Zn have been introduced as major alloying elements for high-pressure die casting alloys. The main reason

for using magnesium alloys is to lower the weight load, predominantly in transportation industries. The weight reduction amounts to about 30% compared to Al alloys and to about 75% compared to steel. Magnesium has a hexagonal close-packed crystal structure (hcp). Therefore its deformation properties are poor. At room temperature slip occurs on the basal plane $\{0001\}$ in the $\langle 11\bar{2}0 \rangle$ direction only. In addition to slip on basal planes the deformation by twinning is also possible, the twinning system is $\{10\bar{1}2\}\langle 10\bar{1}1 \rangle$. Twin formation leads to different behavior of Mg alloys under tensile and compressive load. With increasing temperature above $200\text{--}225^\circ\text{C}$, prismatic slip planes are activated in addition. This is of main importance for the processing wrought magnesium alloys.

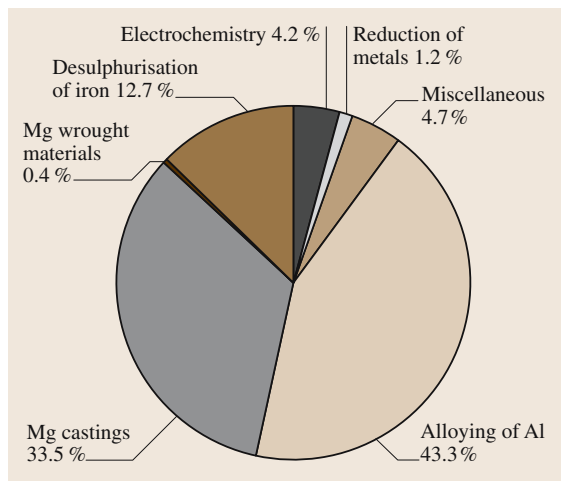


Fig. 3.1-1 World consumption of Mg in 2001 (329 480 t) [1.2]

Alloying elements used in Mg alloys and their abbreviations applied in the designation of Mg materials are listed in Table 3.1-1. General data, maximum solubility data, and compounds formed in major binary magnesium alloy systems are given in Table 3.1-2 [1.4]. Since Al is one of the most important alloying elements, Fig. 3.1-2 [1.3] shows an example of an Al–Mg binary alloy system. The effect of alloying elements in Mg materials is given in Table 3.1-3 [1.3, 4].

3.1.1.1 Magnesium Alloys

The major alloying elements are manganese, aluminium, zinc, zirconium, silicon, thorium, and rare earth metals (E). At present E elements are the most promising candidates for magnesium alloys, with high temperature stability as well as improved corrosion behavior. E metals are forming stable intermetallic compounds at high temperature and therefore they decrease castability. Aluminium and zinc are introduced mainly to

Table 3.1-1 Alloying elements and abbreviations used for Mg materials [1.3]

| A | C | E | K | L | M | Q | S | W | Z |
|----|----|------------|----|----|----|----|----|---|----|
| Al | Cu | Rare earth | Zr | Li | Mn | Ag | Si | Y | Zn |

Table 3.1-2 Solubility data and intermetallic phases in binary magnesium alloys [1.4]

| Solute element | Maximum solubility (wt%) | Maximum solubility (at%) | Adjacent intermetallic phase | Melting point of intermetallic phase (°C) | Type of equilibrium |
|----------------|-----------------------------|-----------------------------|-----------------------------------|--|---------------------|
| Lithium | 5.5 | 17.0 | — | — | Eutectic |
| Aluminium | 12.7 | 11.8 | Mg ₁₇ Al ₁₂ | 402 | Eutectic |
| Silver | 15.0 | 3.8 | Mg ₃ Ag | 492 | Eutectic |
| Yttrium | 12.5 | 3.75 | Mg ₂₄ Y ₅ | 620 | Eutectic |
| Zinc | 6.2 | 2.4 | MgZn | 347 | Eutectic |
| Neodymium | ≈ 3 | ≈ 1 | Mg ₄₁ Nd ₅ | 560 | Eutectic |
| Zirconium | 3.8 | 1.0 | Zr | 1855 | Peritectic |
| Manganese | 2.2 | 1.0 | Mn | 1245 | Peritectic |
| Thorium | 4.75 | 0.52 | Mg ₂₃ Th ₆ | 772 | Eutectic |
| Cerium | 0.5 | 0.1 | Mg ₁₂ Ge | 611 | Eutectic |
| Indium | 53.2 | 19.4 | Mg ₃ In | 484 | Peritectic |
| Thallium | 60.5 | 15.4 | Mg ₅ Tl ₂ | 413 | Eutectic |
| Scandium | ≈ 24.5 | ≈ 15 | MgSc | — | Peritectic |
| Lead | 41.9 | 7.75 | Mg ₂ Pb | 538 | Eutectic |
| Thulium | 31.8 | 6.3 | Mg ₂₄ Tm ₆ | 645 | Eutectic |
| Terbium | 24.0 | 4.6 | Mg ₂₄ Tb ₅ | — | Eutectic |
| Tin | 14.5 | 3.35 | Mg ₂ Sn | 770 | Eutectic |
| Gallium | 8.4 | 3.1 | Mg ₅ Ga ₂ | 456 | Eutectic |
| Bismuth | 8.9 | 1.1 | Mg ₃ Bi ₂ | 821 | Eutectic |
| Calcium | 1.35 | 0.82 | Mg ₂ Ca | 714 | Eutectic |
| Samarium | ≈ 6.4 | ≈ 1.0 | Mg _{6.2} Sm | — | Eutectic |

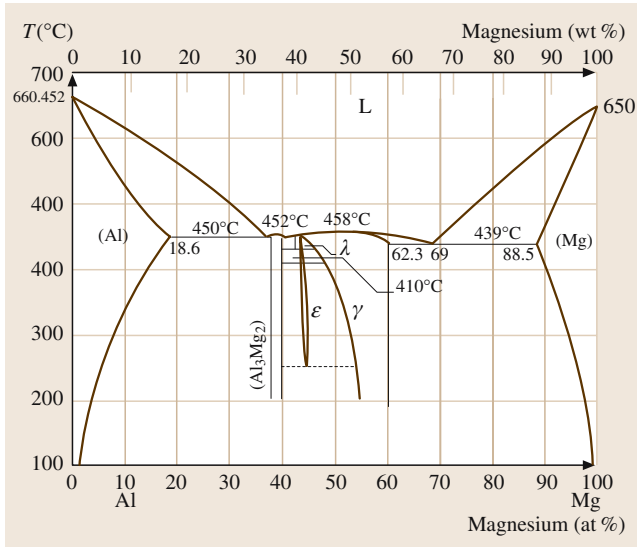


Fig. 3.1-2 Al–Mg phase equilibria [1.3]

Table 3.1-3 General effects of alloying elements in magnesium materials [1.3–5]

| Series | Alloying elements | Melting and casting behavior | Mechanical and technological properties |
|--------|-------------------|---|--|
| AZ | Al, Zn | Improve castability; tendency to microporosity; increase fluidity of the melt; refine weak grain | Solid solution hardener; precipitation hardening at low temperatures ($< 120^\circ\text{C}$); improve strength at ambient temperatures; tendency to brittleness and hot shortness unless Zr is refined |
| QE | Ag, rare earths | Improve castability; reduce microporosity | Solid solution and precipitation hardening at ambient and elevated temperatures; improve elevated temperature tensile and creep properties in the presence of rare earth metals |
| AM | Al, Mn | Improve castability; tendency to microporosity; control of Fe content by precipitating Fe–Mn compound; refinement of precipitates | Solid solution hardener; precipitation hardening at low temperatures ($< 120^\circ\text{C}$); increase creep resistivity |
| AE | Al, rare earth | Improve castability; reduce microporosity | Solid solution and precipitation hardening at ambient and elevated temperatures; improve elevated temperature tensile and creep properties; increase creep resistivity |
| AS | Al, Si | Tendency to microporosity; decreased castability; formation of stable silicide alloying elements; compatible with Al, Zn, and Ag; refine weak grain | Solid solution hardener, precipitation hardening at low temperatures ($< 120^\circ\text{C}$); improved creep properties |
| WE | Y, rare earths | Grain refining effect; reduce microporosity | Improve elevated temperature tensile and creep properties; solid solution and precipitation hardening at ambient and elevated temperatures; improve elevated temperature tensile and creep properties |

increase castability. However, Al forms an intermetallic phase $\text{Mg}_{17}\text{Al}_{12}$ which is brittle and limits ductility and, thus, the use of Al-containing alloys such as AZ91 above 120°C . Manganese has been introduced to increase ductility. It is replacing Zn in several cast alloys. Moreover, Mn is binding Fe in intermetallic phases. These can be separated before casting and therefore Mn can be used to purify the alloys. Silicon was also thought to increase high temperature stability by forming the intermetallic compound Mg_2Si . Due to the typical needle shape of this precipitate (so-called Chinese script microstructure) it has only limited use because it acts like a notch, leading to crack formation at higher stress levels. Zirconium is not used in Al-containing alloys but it is added to other alloys acting as grain refiner.

Wrought magnesium alloys are not used widely. The application of AZ31 is most common for forgings, extrusions, as well as for sheetmetal. There is an increasing demand for the use of wrought magnesium alloys, especially in the automotive industries, in the form of sheet

material. Therefore, a number of processes, which are introduced for the processing of aluminium and steel are under research to find out the economic boundary conditions for the processing of magnesium alloys. Beside the investigations on processing routes, there is ongoing research on alloy development since AZ31 does not meet the given aims in most requirements. The compositions of selected cast and wrought magnesium alloys are given in Tables 3.1-4 and 3.1-5. The mechanical proper-

ties of the cast and wrought magnesium alloys are listed in Tables 3.1-6 and 3.1-7 [1.3, 4].

The system to denote Mg alloys is generally showing major alloying elements and their content in wt%. The first two letters are key letters and are used for the major alloying elements (Table 3.1-1). The two letters are followed by a number, which represents the nominal composition of the major alloying elements in wt%. The number indicates the content rounded to

Table 3.1-4 Nominal composition of selected cast Mg alloys [1.3, 4]

| ASTM designation | Nominal composition (wt%) | | | | | | | | | | |
|------------------|---------------------------|-----|-----|----|----|-----|---------|---------|-----|-----|-----|
| | Al | Zn | Mn | Si | Cu | Zr | RE (MM) | RE (Nd) | Th | Y | Ag |
| AZ63 | 6 | 3 | 0.3 | | | | | | | | |
| AZ81 | 8 | 0.5 | 0.3 | | | | | | | | |
| AZ91 | 9.5 | 0.5 | 0.3 | | | | | | | | |
| AM50 | 5 | | 0.3 | | | | | | | | |
| AM20 | 2 | | 0.5 | | | | | | | | |
| AS41 | 4 | | 0.3 | 1 | | | | | | | |
| AS21 | 2 | | 0.4 | 1 | | | | | | | |
| ZK51 | | 4.5 | | | | 0.7 | | | | | |
| ZK61 | | 6 | | | | 0.7 | | | | | |
| ZE41 | | 4.2 | | | | 0.7 | 1.3 | | | | |
| ZC63 | | 6 | 0.5 | | 3 | | | | | | |
| EZ33 | | 2.7 | | | | 0.7 | 3.2 | | | | |
| HK31 | | | | | | 0.7 | | | 3.2 | | |
| HZ32 | | 2.2 | | | | 0.7 | | | 3.2 | | |
| QE22 | | | | | | 0.7 | | 2.5 | | | 2.5 |
| QH21 | | | | | | 0.7 | | 1 | 1 | | 2.5 |
| WE54 | | | | | | 0.5 | | 3.25 | | 5.1 | |
| WE43 | | | | | | 0.5 | | 3.25 | | 4 | |

Table 3.1-5 Nominal composition of selected wrought Mg alloys [1.3, 4]

| ASTM designation | Nominal composition (wt%) | | | | | | |
|------------------|---------------------------|-----|-----------------|-----|-----|------|----|
| | Al | Zn | Mn | Zr | Th | Cu | Li |
| M1 | | | | 1.5 | | | |
| AZ31 | 3 | 1 | 0.3 (0.20 min.) | | | | |
| AZ61 | 6.5 | 1 | 0.3 (0.15 min.) | | | | |
| AZ80 | 8.5 | 0.5 | 0.2 (0.12 min.) | | | | |
| ZM 21 | | 2 | 1 | | | | |
| ZMC711 | | 6.5 | 0.75 | | | 1.25 | |
| LA141 | 1.2 | | 0.15 (min.) | | | | 14 |
| ZK61 | | 6 | | 0.8 | | | |
| HK31 | | | | | 0.7 | 3.2 | |
| HM21 | | | 0.8 | | 2 | | |
| HZ11 | | 0.6 | | 0.6 | 0.8 | | |

Table 3.1-6 Typical tensile properties and characteristics of selected cast Mg alloys [1.3-5]

| ASTM designation | Condition | Tensile properties | | | Characteristics |
|------------------|-----------------------|------------------------|------------------------|----------------------------|--|
| | | 0.2%proof stress (MPa) | Tensile strength (MPa) | Elongation to fracture (%) | |
| AZ63 | As-sand cast | 75 | 180 | 4 | Good room-temperature strength and ductility |
| | T6 | 110 | 230 | 3 | |
| AZ81 | As-sand cast | 80 | 140 | 3 | Tough, leak-tight casting with 0.0015 Be, used for pressure die casting |
| | T4 | 80 | 220 | 5 | |
| AZ91 | As-sand cast | 95 | 135 | 2 | General-purpose alloy used for sand and die casting |
| | T4 | 80 | 230 | 4 | |
| | T6 | 120 | 200 | 3 | |
| | As-chill cast | 100 | 170 | 2 | |
| | T4 | 80 | 215 | 5 | |
| | T6 | 120 | 215 | 2 | |
| AM50 | As-die cast | 125 | 200 | 7 | High-pressure die casting |
| AM20 | As-die cast | 105 | 135 | 10 | Good ductility and impact strength |
| AS41 | As-die cast | 135 | 225 | 4.5 | Good creep properties up to 150 °C |
| AS21 | As-die cast | 110 | 170 | 4 | Good creep properties up to 150 °C |
| ZK51 | T5 | 140 | 253 | 5 | Sand casting, good room-temperature strength and ductility |
| ZK61 | T5 | 175 | 275 | 5 | As for ZK51 |
| ZE41 | T5 | 135 | 180 | 2 | Sand casting, good room-temperature strength, improved castability |
| ZC 63 | T6 | 145 | 240 | 5 | Pressure-tight casting, good elevated temperature strength, weldable |
| EZ33 | Sand cast T5 | 95 | 140 | 3 | Good castability, pressure tight, weldable, creep resistant up to 250 °C |
| HK31 | Chill cast T5 | 100 | 155 | 3 | Sand casting, good castability, weldable, creep resistant up to 350 °C |
| | Sand cast T6 | 90 | 185 | 4 | |
| HZ32 | Sand or chill cast T5 | 90 | 185 | 4 | As for HK31 |
| QE22 | Sand or chill cast T6 | 185 | 240 | 2 | Pressure tight and weldable, high proof stress up to 250 °C |
| QH21 | As-sand cast T6 | 185 | 240 | 2 | Pressure tight, weldable, good creep resistance and stress-proof to 300 °C |
| WE54 | T6 | 200 | 285 | 4 | High strength at room and elevated temperatures, good corrosion resistance |
| WE43 | T6 | 190 | 250 | 7 | Weldable |

the nearest digit for the range of that element. For variation within this range suffix letters A, B, C, etc., are used to indicate the stage of development of the alloy, and X is used for alloys which are still experimental. For example, AZ91D indicates that the two

major alloying elements are 9 wt% Al and 1 wt% Zn. The letter D signifies that it is the fourth stage in development. The designations of the tempers are identical to those used for Al alloys and are given in Table 3.1-8 [1.3].

Table 3.1-7 Typical tensile properties and characteristics of selected wrought Mg alloys [1.3–5]. (For temper designations see Table 3.1-8)

| ASTM designation | Condition | Tensile properties | | | Characteristics |
|------------------|------------------|-------------------------|------------------------|----------------------------|---|
| | | 0.2% proof stress (MPa) | Tensile strength (MPa) | Elongation to fracture (%) | |
| M1 | Sheet, plate F | 70 | 200 | 4 | Low to medium strength alloy, weldable, corrosion-resistant |
| | Extrusion F | 130 | 230 | 4 | |
| | Forgings F | 105 | 200 | 4 | |
| AZ31 | Sheet, plate O | 120 | 240 | 11 | Medium-strength alloy weldable, good formability |
| | H24 | 160 | 250 | 6 | |
| | Extrusion F | 130 | 230 | 4 | |
| | Forging F | 105 | 200 | 4 | |
| AZ61 | Extrusion F | 105 | 260 | 7 | High-strength alloy, weldable |
| | Forging F | 160 | 275 | 7 | |
| AZ80 | Forging T6 | 200 | 290 | 6 | High-strength alloy |
| ZM 21 | Sheet, plate O | 120 | 240 | 11 | Medium-strength alloy, good formability, good damping capacity |
| | H24 | 165 | 250 | 6 | |
| | Extrusions | 155 | 235 | 8 | |
| | Forgings | 125 | 200 | 9 | |
| ZMC711 | Extrusions T6 | 300 | 325 | 3 | High-strength alloy |
| LA141 | Sheet, plate T7 | 95 | 115 | 10 | Ultra-light weight (S.G. 1.35) |
| ZK61 | Extrusion F | 210 | 185 | 6 | High strength alloy |
| | T5 | 240 | 305 | 4 | |
| | Forging T5 | 160 | 275 | 7 | |
| HK31 | Sheet, plate H24 | 170 | 230 | 4 | High-creep resistance to 350 °C, weldable |
| | Extrusion T5 | 180 | 255 | 4 | |
| HM21 | Sheet, plate T8 | 135 | 215 | 6 | High-creep resistance to 350 °C, weldable after short time exposure to 425 °C |
| | T81 | 180 | 255 | 4 | |
| | Forging T5 | 175 | 225 | 3 | |
| HZ11 | Extrusion F | 120 | 215 | 7 | Creep resistance to 350 °C, weldable |

Table 3.1-8 Temper designations [1.3]

| General Designations | | | |
|-----------------------------|--|-------------------|---|
| F | As fabricated. | | |
| O | Annealed, recrystallized (Wrought products only). | | |
| H | Strain-hardened. | | |
| T | Thermally treated to produce stable tempers other than F, O, or H. | | |
| W | Solution heat-treated (unstable temper). | | |
| Subdivisions of H | | Subdivisions of T | |
| H1, Plus one or more digits | Strained only | T2 | Annealed (Cast products only) |
| H2, Plus one or more digits | Strain-hardened and then partially annealed. | T3 | Solution heat-treated and cold-worked |
| H3, Plus one or more digits | Strain-hardened and then stabilized. | T4 | Solution heat-treated |
| | | T5 | Artificially aged only |
| | | T6 | Solution heat-treated and artificially aged |
| | | T7 | Solution heat-treated and stabilized |
| | | T8 | Solution heat-treated, cold-worked and artificially aged |
| | | T9 | Solution heat-treated, artificially aged, and cold-worked |
| | | T10 | Artificially aged and cold-worked |

3.1.1.2 Melting and Casting Practices, Heat Treatment

Due to the relatively low melting temperature of Mg, casting is the preferred processing route of Mg materials.

The addition of Al and Zn are known to improve castability. All processing operations such as melting, alloying, refining, and the cleaning of melts can be carried out in plain carbon steel crucibles. The use of protective gases or fluxes is a recommended practice during melting. Fluxes consist of salts such as KCl, MgCl₂, BaCl₂, and CaCl₂ [1.6]. Gases are used in different combinations, also forming a stable film during melting. Combinations of argon and/or nitrogen with additions of SF₆ or SO₂ are in use. The application of vacuum during melting cannot be recommended due to the high vapor pressure of liquid Mg at low pressure.

During melting, a control of impurities is also necessary. The elements Fe, Ni, Co, and Cu are critical due to their effect of decreasing the corrosion resistance. The Fe content can be controlled by adding Mn, forming intermetallic compounds which are settling at the bottom of the melting crucible. But in general the amount of these critical elements has to be controlled during the primary production of Mg itself. Fortunately Cu is not part of any feedstock material used for primary

production. Therefore only master alloys or alloying elements for producing the diverse alloys have to be controlled for Co and also for Fe, which is a major impurity in a number of master alloys and alloying elements.

Any casting process can be used to manufacture parts from Mg alloys. But in view of the low liquidus temperatures, the broad melting ranges, and the excellent fluidity of Mg casting alloys, high-pressure die casting (HPDC) is used most frequently at present. Mainly alloys from the AZ or AM series are used in HPDC but alloys from the AS or AE series are also useable when cast with cold chamber HPDC machines. Alloys from the QE or WE series are not suitable for HPDC but for sand casting or permanent mold casting.

The mechanical properties of the Mg alloys can be improved by heat treatment. Mainly T4, T5, and T6 heat treatments are in use. A T4 treatment means dissolution of precipitates. In general, a T4 treatment is followed by an artificial aging (T6). Stress relieving can also be applied to the cast alloys. Major variables which affect the heat-treatments are section size and heating time, annealing time and temperature, and the protective atmosphere. Welded parts made of Mg alloys can be stress relieved. In general, the heat treatments can be applied to castings with the exception of HPDCs. It is not rec-

ommended to heat-treat HPDCs materials because of the entrapment of gases during casting. The absorption of gases can be avoided by applying vacuum during casting. In this case all heat treatments can be applied as well. Table 3.1-9 shows Mg alloys with their respective useful heat treatments.

3.1.1.3 Joining

Brazing and soldering are not practicable due to corrosion problems and the formation of brittle phases. Similar problems occur during welding processes such as metal inert gas welding, laser welding, or even electron beam welding. As with brazing or soldering, the formation of brittle phases leads to failures, drastically decreasing the reliability of welded joints. Riveting and mechanical joining using screws are well introduced. Especially when the joint is supported with adhesives for sealing and for adding additional forces for bonding, riveting and screwing can still be viewed as state of the art in the joining of Mg alloys. Mg alloys are seldom used as rivets or screws due to their limited mechanical properties. But it was proven that Al alloys (5052, 5056, or 6061) for rivets and surface coated steel for screws can be used to fasten Mg alloys due to similarity in corrosion

potentials. Moreover, the use of inert washers or layers to minimize contact between different materials is recommended [1.3, 7]. Due to the increasing demand for Mg wrought materials, especially in sheet form, new joining processes are under investigation. These processes are friction stir welding or clinching, often combined with the use of adhesives. While a certain degree of ductility ($A > 12\%$) is necessary in clinching processes, friction stir welding appears to be independent of that requirement. Experiments have shown that even cast magnesium alloys can be joined using this process.

3.1.1.4 Corrosion Behavior

In general only poor corrosion behavior is attributed to Mg and its alloys. This is mainly true when Mg is in contact with other metals and alloys in accordance with the electrochemical potential series of metals. Therefore, special care has to be taken to avoid conductive contact between Mg alloys and other metals with different electrochemical potentials. When joining Mg parts with other materials, insulating washers, surface-coated screws or nonconducting films and surface coatings can be applied. When investigating a Mg

Table 3.1-9 Heat treatments applied to magnesium alloys [1.3]

| Alloy Cast Alloy | Heat Treatment | | | |
|-----------------------|----------------|----|----|----|
| | F | T4 | T5 | T6 |
| AM100A | | × | × | × |
| AZ63A | | × | × | × |
| AZ81A | | × | | |
| AZ91C | | × | | × |
| AZ92A | | × | | × |
| EZ33A | | | × | |
| EQ21A | | | | × |
| QE22A | | | | × |
| WE43A | | | | × |
| WE54A | | | | × |
| ZC63A | | | | × |
| ZE41A | | | × | |
| ZE63A | | | | × |
| ZK51A | | | × | |
| ZK61A | | × | | × |
| Wrought Alloys | | | | |
| AZ80A | | | × | |
| ZC71A | × | | × | × |
| ZK60A | | | × | |

alloy by itself the material shows similar behavior as plain carbon steels, even in different environments. The main reason for an increase in corrosion rate could be found in the presence of impurities such as Fe, Ni, Co, and Cu. In order to improve the stand-alone corrosion properties these impurities have to be controlled regarding their content. While Co will normally not pose a problem since it is not part of any material used for the primary production of Mg, the content of the other elements needs to be controlled from the beginning in the production of primary Mg. According to the influence of Fe, Ni, and Cu, limits have been defined for high purity alloys which are mainly used today in the production of Mg parts ($\text{Fe}/\text{Mn} < 0.0232$, $\text{Cu} < 0.04 \text{ wt\%}$, $\text{Ni} < 0.005 \text{ wt\%}$ for AZ91 hp). But it should be mentioned that these limits depend on the contents of other alloying elements as well as the casting processes applied [1.3, 8]. Figure 3.1-3 shows the influence of alloying elements on the rate of corrosion [1.7].

3.1.1.5 Recent Developments

Squeeze casting and semi-solid metal processing (SSMP) are recent developments in casting technology by which high quality castings can be produced. Almost all Mg alloys can be subjected to SSMP if they have a broad melting interval [1.3]. First trials using AZ91 led also to the development of different processes which are making use of processing in the semi-solid state. Recently Thixomolding® was introduced, a technique similar to processing techniques for polymers. Thixomolding is in use mainly for the production of housings for handheld devices such as laptops or cameras. It is under research to investigate the capability of this technology for processing alloys which are showing limited castability mainly in HPDC. Another process using the semi-solid behavior of some magnesium alloys is thixocasting which is still a topic of research, not of production. The New RheoCast process (NRC) which is well introduced in Al industries can, also, be applied to casting semi-solid materials based on Mg.

Beyond monolithic alloys the investigation of Mg matrix composites is still in progress. They can be processed using either the ingot metallurgy

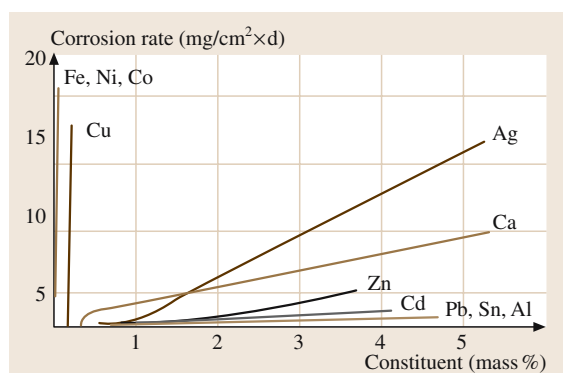


Fig. 3.1-3 Influence of alloying elements on the corrosion rate of Mg [1.7]

route or the powder metallurgy route. There are promising candidates that may be introduced to applications but the production routes are quite expensive and, moreover, the corrosion behavior is not well known.

Apart from cast or powder metallurgical products, the use of wrought Mg materials is thought to increase in the future. To support the demands stemming mainly from the automotive industry the total production route is under investigation right now. This means that the developments of new wrought magnesium alloys as well as the development of suitable deformation processes in combination with appropriate joining techniques are underway. These studies are accompanied by developing modeling and simulation tools to ensure high quality and accurate prediction of properties and lifetime behavior of magnesium-based materials.

Controlling corrosion is the most pressing problem under research at the moment. Since Mg alloys are about to be widely used in several applications, the corrosion problem, i. e., mainly contact corrosion in combination with other metals and alloys is receiving more and more attention. Therefore, the influence of alloying elements, mainly in combination with each other, is investigated intensively. Aside from alloying, different kinds of surface protection such as surface layers and coatings are under investigation. While castings are normally showing sufficient volume to withstand corrosion attack, this is not the case for magnesium sheet materials even for a long time.

3.1.2 Aluminium and Aluminium Alloys

3.1.2.1 Introduction

Aluminium alloys are the second most widely used metallic materials after steels. Comprehensive treatments and data of Al-based materials are given in [1.9, 10]. Their most important properties are: *low density* (2.7 g/cm^{-3}); alloying can result in significant further density reductions in Al-Li alloys; the low density can lead to significant energy savings, especially in applications in transportation; *good mechanical properties* offering optimum tensile strength ranging from 60 to 530 MPa; *good workability* permitting most varied shapes to be produced; *good castability* with a variety of casting techniques: sand, mould, die-casting; *good machinability*; *ease of joining* using all commonly applied techniques; *comparatively high corrosion resistance* thanks to the spontaneous formation of a strongly-adherent passivating surface film in air; *different surface treatments* are applicable; *high electrical and thermal conductivity*, especially of unalloyed aluminium; *good optical properties* depending on the degree of purity; *non-magnetic*; *low absorption cross section* for thermal neutrons; *non-combustible*, not causing sparking; *no health risk* is associated with the use of aluminium and its alloys; excellent *recycling properties*.

3.1.2.2 Production of Aluminium

The production of aluminium is based on the electrolysis of molten alumina Al_2O_3 using the Hall-Herault process. Alumina is extracted in the Bayer process from the bauxite ore which contains 20 to 30 wt% Al. In 2002 the main producers of the ore are Australia (28%), Guinea (20%), Brazil (14%), Jamaica (7%), India (4%), and Guyana (3%) [1.9].

After milling, the ore is first broken down using an Al-containing NaOH solution which is seeded to precipitate aluminium hydroxide $\text{Al}(\text{OH})_3$. This is dehydrated at about 1100°C according to $2\text{Al}(\text{OH})_3 \rightarrow \text{Al}_2\text{O}_3 + 3\text{H}_2\text{O}$.

An electrolytic reduction is carried out in a cell as shown in Fig. 3.1-4. Cryolite Na_3AlF_6 is used as an additive to decrease the high melting point of pure Al_2O_3 (about 2050°C) since the two compounds form a eutectic near 10 wt% of Al_2O_3 in Na_3AlF_6 , Fig. 3.1-5 [1.11, 12]. The electrolysis is carried out in a cell lined with carbon, which serves as the cathode. Carbon anodes are suspended from above the cell into the electrolyte. Two main reactions occur:

$2\text{Al}^{3+} + 6\text{e}^- \rightarrow 2\text{Al}$, and oxygen ions react with the carbon of the cathode to form CO_2 (consumption of the cathode). A primary aluminium smelter requires on average 13 to 14 kW h per kg of Al. The main power used is hydro-electric (52.5% in 2001 [1.13]). In recent decades

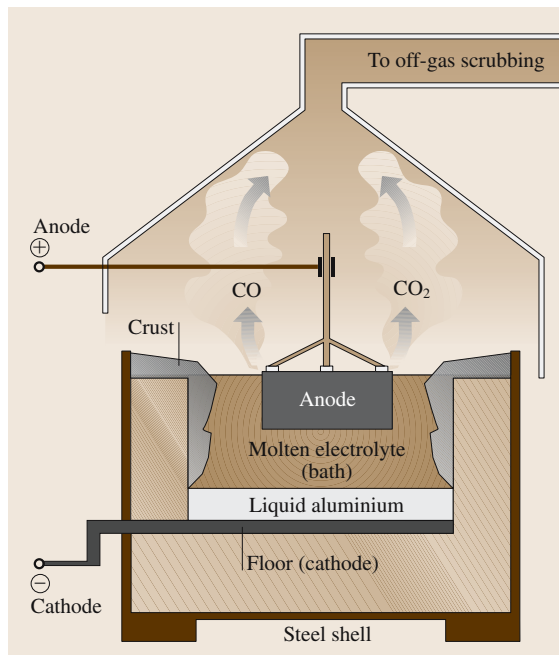


Fig. 3.1-4 Schematic representation of an electrolytic cell for Al winning [1.9]

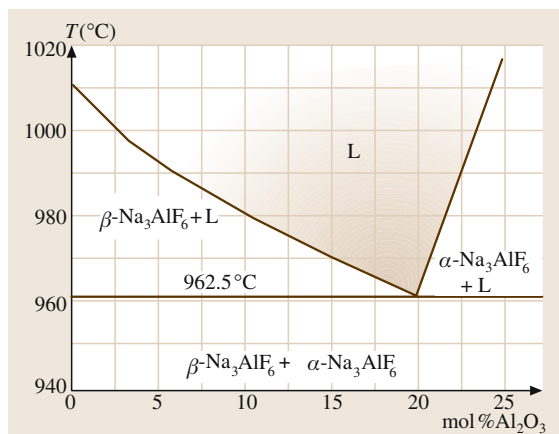


Fig. 3.1-5 Phase diagram of cryolite Na_3AlF_6 -alumina Al_2O_3 [1.9]

secondary production, i. e., recycling of scrap and waste material, has reached 30% of the total production, with high regional variations. Up to 95% less energy is needed to produce Al via secondary production.

3.1.2.3 Properties of Pure Al

Aluminium can be classified as “unalloyed,” “pure,” or “refined,” depending on its degree of purity. The Al from conventional electrolysis is 99.5 to 99.9 wt% pure. Higher purity is produced by “triple-layer refining electrolysis” that can reach ≥ 99.99 wt% purity. The latter grade is used, for example, in the electronics sector.

Physical Properties

The physical properties of pure Al are given in Chapt. 2.1, Table 2.1-11. The temperature dependence of its density is shown in Fig. 3.1-6. The contraction of 6.5% upon solidification corresponds to an increase in density from 2.37 g cm^{-3} in the liquid state to 2.55 g cm^{-3} in the solid state. The temperature depen-

dence of the coefficient of thermal expansion is given in Table 3.1-10.

The specific heat in the solid state increases with temperature from 720 kJ at -100°C , to 900 at 20°C , and 1110 at 500°C . At its melting point Al has a specific heat of 1220 (solid) and 1040 (liquid). In the liquid state the specific heat rises further, e.g., to 1060 kJ at 800°C . Aluminium has a high reflectivity for light, heat, and for electromagnetic radiation. The Young's modulus E of aluminium materials is usually taken to be 70 GPa; it varies between 60 and 78 GPa depending on alloy composition. The shear modulus G varies between 22 and 28 GPa, the value for refined aluminium is 25.0 GPa. Poisson's ratio ν varies between 0.32 and 0.40 (0.35 for refined aluminium).

Unalloyed aluminium has an electrical conductivity of 34 to $38 \text{ m}\Omega^{-1} \text{ mm}^{-2}$. Due to this relatively high conductivity, a large fraction of unalloyed Al and Al–Mg–Si alloys are used for electrical conductors. The temperature dependence of the electrical conductivity depends on alloying additions, impurities, and microstructure (Figs. 3.1-7–3.1-9). Superconductivity occurs at $T_c = 1.2 \text{ K}$ in refined grades of aluminium (≥ 99.99 wt% Al). The electrical conductivity of high-purity aluminium is still high at 4.2 K .

Mechanical Properties

The ultimate tensile strength of pure aluminium increases markedly with increasing amounts of alloying or impurity additions, as shown in Fig. 3.1-10. Unalloyed aluminium is soft (tensile strength 10–30 MPa, Table 3.1-11) and, like all fcc metals, shows a low rate of work hardening.

Chemical Properties

Aluminium, as a relatively reactive element, is a very strong base, as shown by its position in the electrochemical series and its low standard potential ($V_H = -1.66 \text{ V}$). Therefore, it is not possible to obtain the element from aqueous solutions by electrolysis. Similarly, it is not possible to obtain aluminium by a carbother-

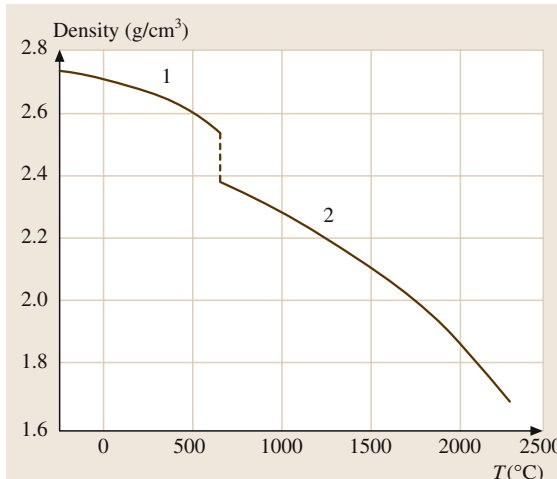


Fig. 3.1-6 Density of solid and liquid aluminium as a function of temperature [1.9]

Table 3.1-10 Coefficient of thermal expansion of Al 99.99 as a function of temperature [1.9]

| Temperature range (°C) | Average linear coefficient of thermal expansion ($10^{-6}/\text{K}^{-1}$) |
|------------------------|---|
| (−200)–20 | 18.0 |
| (−200)–20 | 21.0 |
| 20–100 | 23.6 |
| 20–200 | 24.5 |
| 20–400 | 26.4 |
| 20–600 | 28.5 |

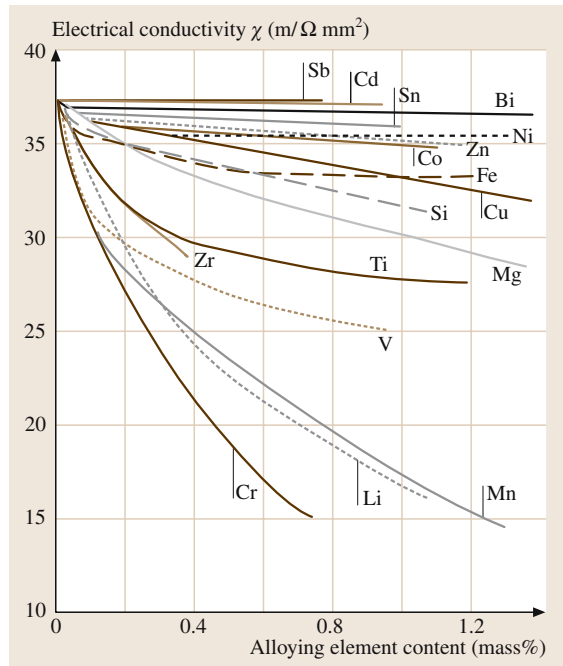


Fig. 3.1-7 Electrical conductivity of as-cast binary alloys based on high-purity aluminium as a function of the alloying element concentration [1.14, 15]

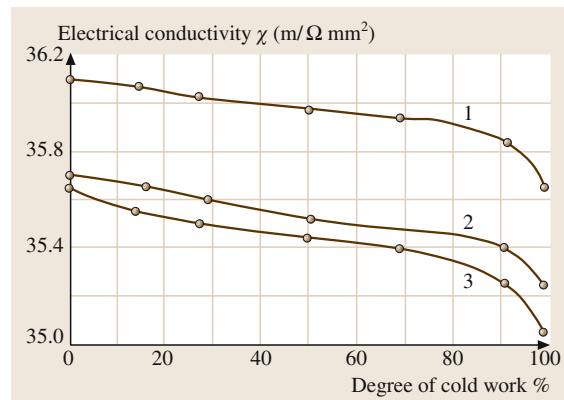


Fig. 3.1-9 Electrical conductivity of unalloyed Al (0.21 wt% Fe; 0.11 wt% Si) as a function of the degree of cold work and the degree of supersaturation and/or intermediate annealing temperature [1.14]; (1) intermediate annealing temperature 350 °C; (2) intermediate annealing temperature 500 °C; (3) as extruded

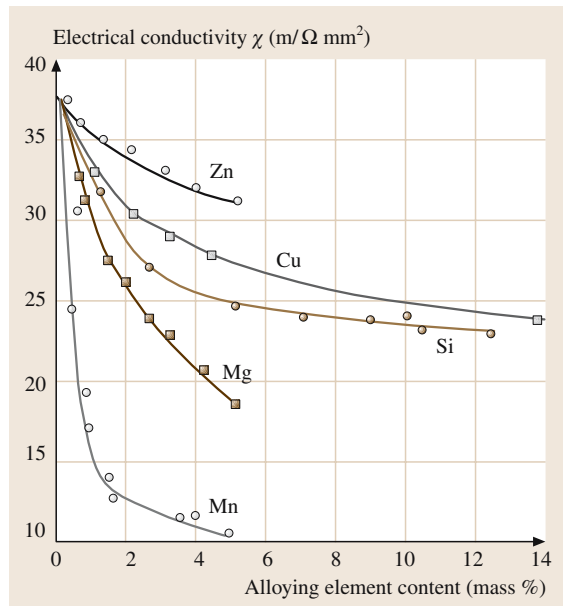


Fig. 3.1-8 Electrical conductivity of as-cast binary aluminium alloys (containing larger amounts of the alloying additions) as a function of concentration of the alloying element [1.14, 15]

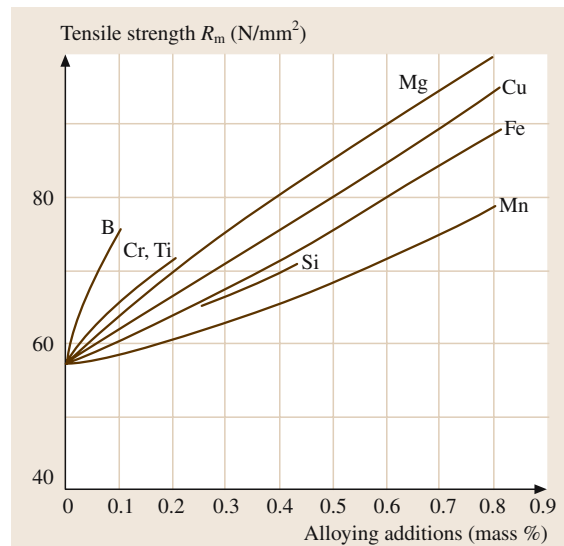


Fig. 3.1-10 Effect of small additions of alloying elements or impurities on the ultimate tensile strength of aluminium of high-purity (99.98 wt% Al, soft condition, 5 h, 360 °C) [1.14]

Table 3.1-11 Typical mechanical properties of refined aluminium (Al 99.98) [1.9]

| Condition | Proof stress $R_{p0.2}$ (MPa) | Ultimate tensile strength R_m (MPa) | Elongation at fracture A_{10} (%) | Brinell hardness number HB |
|-----------|----------------------------------|--|--|-------------------------------|
| Soft | 10–25 | 39–49 | 30–45 | 15 |
| Hard | 69–98 | 88–118 | 1–3 | 25 |

mic reaction. In chemical compounds, aluminium is positively charged and trivalent (Al^{3+}). It reacts readily with hydrochloric acid and caustic soda, but less readily with sulfuric acid; dilute sulfuric acid does not attack aluminium. It is not attacked by cold nitric acid at any concentration, and hardly so when heated. The reaction with sodium hydroxide is given by: $2\text{Al} + 2\text{NaOH} + 3\text{H}_2\text{O} \rightarrow 2\text{Na}[\text{Al}(\text{OH})_4] + 3\text{H}_2$.

Aluminium-based materials are non-flammable. Even turnings and chippings do not ignite. Extremely fine aluminium particles can undergo spontaneous combustion and thus cause explosions. The heat of formation of the aluminium oxide Al_2O_3 is about 1590 kJ mol^{-1} , making aluminium a very effective deoxidiser for the steel industry and in metalothermic metal reduction processes (aluminothermy; e.g., $3\text{V}_2\text{O}_5 + 10\text{Al} \rightarrow 6\text{V} + 5\text{Al}_2\text{O}_3$ and aluminothermic welding, “thermit process” $3\text{Fe}_3\text{O}_4 + 8\text{Al} \rightarrow 9\text{Fe} + 4\text{Al}_2\text{O}_3$).

Important aluminium compounds include aluminium oxide Al_2O_3 , which is commonly called alumina (in powder form) or corundum (in coarse crystalline structure), and aluminium hydroxide $\text{Al}(\text{OH})_3$ (“hydrated alumina,” usually extracted from bauxite in the Bayer process).

3.1.2.4 Aluminium Alloy Phase Diagrams

The properties of aluminium strongly depend on the concentration of alloying additions and impurities. Even the low residual contents of Fe and Si in unalloyed aluminium (Al99 to Al99.9) have a marked effect.

The main alloying elements of Al materials are Cu, Si, Mg, and Zn while Mn, Fe, Cr, and Ti are frequently present in small quantities, either as impurities or additives. Ni, Co, Ag, Li, Sn, Pb, and Bi are added to produce special alloys. Be, B, Na, Sr, and Sb may be added as important trace elements. All of these elements affect the structure and thus the properties of an alloy. The compositions of the more important aluminium materials are discussed below, using the relevant phase diagram. All alloying components are completely soluble in liquid aluminium if the temperature is sufficiently high. However, these elements have only limited solubility in solid solution. Continuous solid solubil-

ity does not occur in any of the alloy systems of Al.

Aluminium-rich solid solutions are often formed and are referred to as α -phase, α_{Al} -phase, or α -Al solid solution. Most of the phases occurring in equilibrium with α -Al are hard. They consist of elements or intermetallic compounds such as Al_2Cu , Al_8Mg_5 , Al_6Mn , Al_3Fe , and AlLi .

Binary Al-Based Systems

Aluminium–Copper. Al–Cu forms a simple eutectic system in the range from 0 to 53 wt% Cu, as shown in Fig. 3.1-11. The α -Al solid solution and the intermetallic compound Al_2Cu (θ phase) are in equilibrium. At intermediate temperatures, metastable transition phases may form and precipitate from the supersaturated solid solution. These metastable phases may be characterised according to their crystal structure, the nature of the phase boundary they form, and their size:

- From room temperature up to $\approx 150^\circ\text{C}$ the coherent Cu-rich Guinier-Preston zones I (GP I phase) form; they are only one to two {001} layers thick and have a highly strained, coherent phase boundary with the α -Al matrix phase.

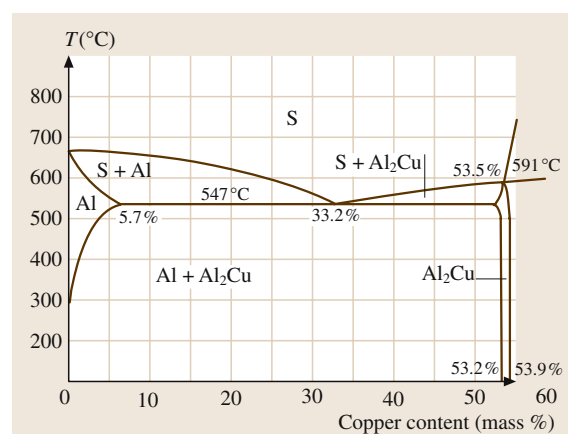


Fig. 3.1-11 Al– Al_2Cu section of the Al–Cu system [1.16]

- At ≈ 80 to ≈ 200 °C the GP II phase, also called θ'' phase, forms; it has a superlattice structure of the Al fcc lattice and has a coherent interface also, but the particle size grows larger than that of GP I.
- Above ≈ 150 °C the θ' phase forms; it is only partially coherent.
- Above ≈ 300 °C the incoherent, stable θ -phase Al_2Cu is formed (over-ageing).

These phase transformations are decisive for the precipitation-hardening behavior of Al–Cu-based technical Al alloys.

Aluminium–Silicon. Al–Si forms a simple eutectic system (Fig. 3.1-12). At room temperature the solubility of Si in Al is negligible. Thanks to the good casting properties of the Al–Si eutectic, this alloy system is the basis of a major part of the Al-based casting alloys. However, when slowly cooled (e.g., in sand casting), a degenerate form of eutectic, microstructure may occur. Instead of the desired fine eutectic array, the alloy develops a structure that is characterised by larger, plate-like primary Si crystals, leading to very brittle behavior. This degenerate behavior can be suppressed by the addition of small amounts of Na, Sb, or Sr to the melt at about 720 to 780 °C. This “modification” causes a lowering of the eutectic temperature and a shift in concentration of the

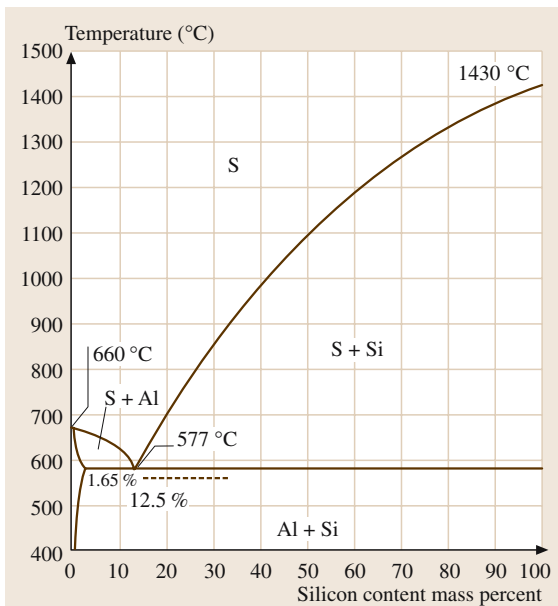


Fig. 3.1-12 Al–Si system; the dotted line shows the extent to which alloys can be supercooled

eutectic point, as indicated in Fig. 3.1-12; the extent of the shift is dependent on the rate of solidification.

Aluminium–Iron. Figure 3.1-13 shows the Al-rich part of this system. The solubility of Fe in Al is very low. In the range shown Al_3Fe is formed by a peritectic reaction at 1160 °C. The eutectic between the Al phase and Al_3Fe crystallises in a degenerate manner to form brittle needles of Al_3Fe . The formation of Al_3Fe needles is also occurring in Al–Fe–Si alloys such as commercially (available) pure aluminium (Fig. 3.1-14).

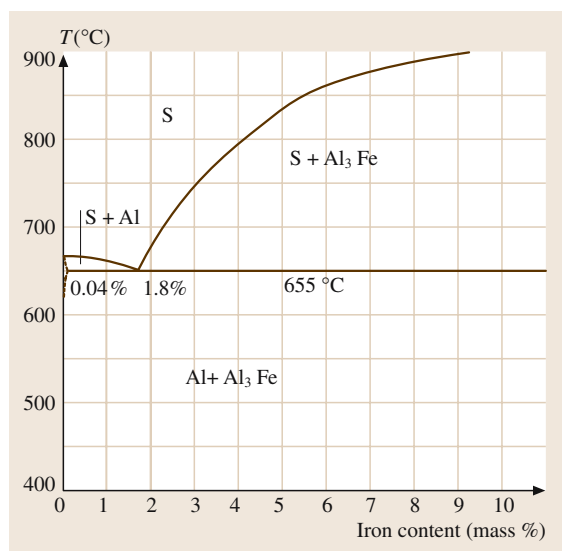


Fig. 3.1-13 Al–Fe system up to 10 wt% Fe

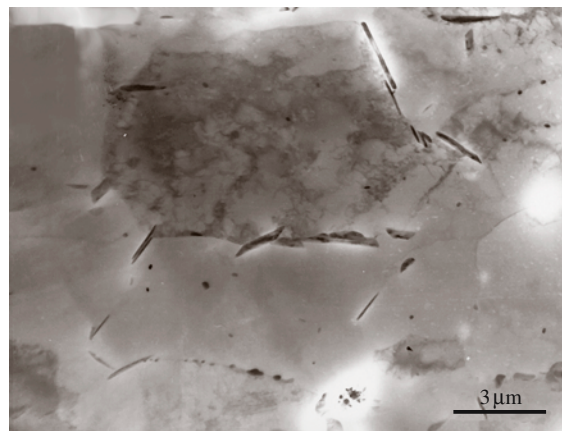


Fig. 3.1-14 Al_3Fe needles formed after annealing commercially pure aluminium sheet (Al99.5) for 65 h at 590 °C, 800X [1.17]

Table 3.1-12 Solubility of some elements in aluminium solid solutions [1.16, 18]

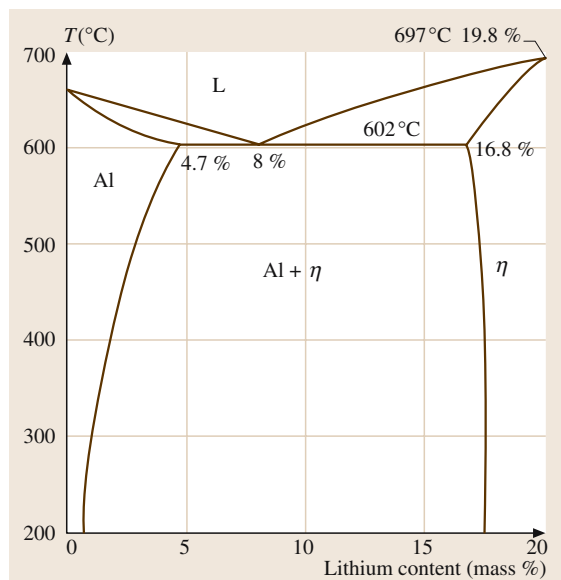
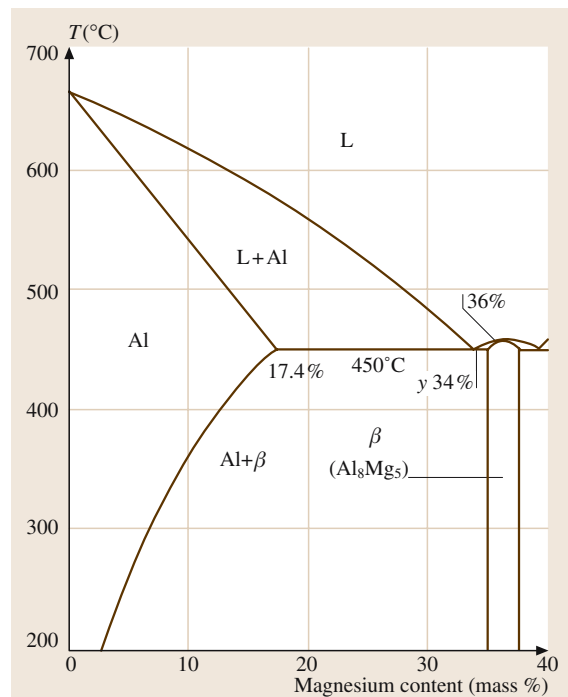
| Element | Temperature of eutectic (E) or peritectic (P) equilibrium °C | Phase in equilibrium with Al solid solution | T_E or T_P (wt%) | 500 °C | 400 °C | Solubility (wt%) 300 °C | 200 °C |
|---------|--|---|----------------------|--------|---------|-------------------------|--------|
| Cu | 547 (E) | Al ₂ Cu | 5.7 | 4.4 | 1.6 | 0.6 | 0.2 |
| Fe | 655 (E) | Al ₃ Fe | ~0.04 | 0.005 | < 0.001 | | |
| Li | 602 (E) | AlLi | 4.7 | 2.8 | 2.0 | 1.5 | 1.0 |
| Mg | 450 (E) | Al ₈ Mg ₅ | 17.4 | ~12.0 | 12.2 | 6.6 | 3.5 |
| Mn | 657 (E) | Al ₆ Mn | 1.82 | 0.36 | 0.17 | 0.02 | |
| Si | 577 (E) | Si | 1.65 | 0.8 | 0.3 | 0.07 | 0.01 |
| Zn | 275 Eutectoid equilibrium | Zn | 31.6 | | | | 14.5 |

Aluminium–Lithium. The Al-rich part of this system is shown in Fig. 3.1-15. The Al(Li) solid solution and the η (Al_3Li) phase are in equilibrium. Al–Li-based alloys are used for their low density.

Aluminium–Magnesium. This system is shown in Fig. 3.1-16. The solid phases are the α -Al solid solution and the β - Al_8Mg_5 intermetallic compound. The high solubility of Mg in Al can be put to practical use for solid solution hardening. The β phase precipitates preferentially at grain boundaries, forming a continuous network at the grain boundaries of the Al-rich α solid solution, e.g., after slow cooling from temperatures above 400 °C, especially in alloys containing more than 3 wt% Mg. Precipitates of the β phase are less noble

electrochemically than the α phase and are thus subject to preferential attack by corrosive media. Accordingly the disadvantage of Al–Mg alloys is their potentially high susceptibility to intergranular corrosion.

Aluminium–Manganese. The Al-rich part of this system includes the intermetallic phases Al_4Mn (above 710 °C) and Al_6Mn (Fig. 3.1-17). The α -Al solid solution and the Al_6Mn phase form a eutectic (Fig. 3.1-17). The solubility of Mn in Al at room temperature is negligibly small. In hypereutectic Al–Mn alloys, pre-

**Fig. 3.1-15** Al–Li system for up to 20 wt% Li [1.18]**Fig. 3.1-16** Al–Al₈Mg₅ section of Al–Mg system

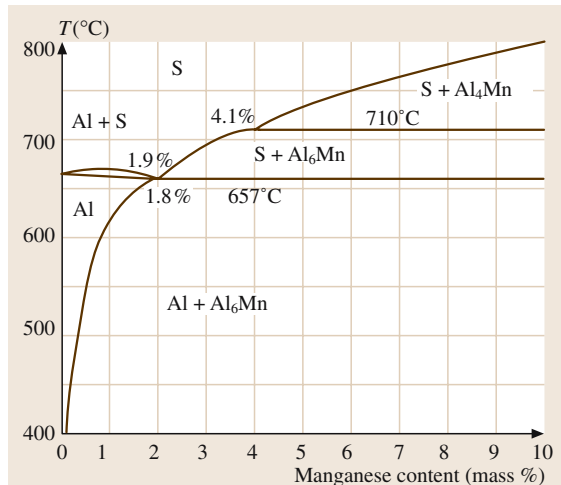


Fig. 3.1-17 (a) Al–Mn equilibrium system up to 10 wt% Mn. (b) Microstructure of an as-cast Al-1 wt% Mn alloy (TEM micrograph, 7000X) [1.17]

cipitation of primary, bar-shaped Al_2Mn crystals occurs in the eutectic structure. These have a marked embrittling effect. Therefore, the maximum Mn content is limited to 2 wt% in commercial Al–Mn alloys.

Aluminium–Titanium. Intermetallic phases with a significantly higher melting point (dissociation tempera-

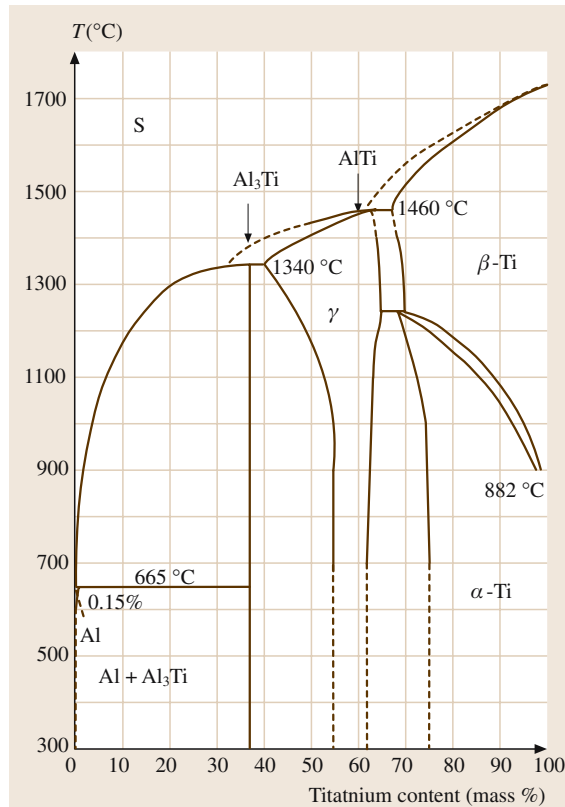


Fig. 3.1-18 Al–Ti system

ture) than Al exist in this system: Al_3Ti (1340°C) and AlTi (1460°C) (Fig. 3.1-18). The structure of Al-rich Al–Ti alloys consists of Al_3Ti and an Al-rich solid solution.

Aluminium–Zinc. Zn is highly soluble in Al. The eutectic point occurs at Zn-rich concentration (Fig. 3.1-19). The liquidus and solidus temperatures depend markedly on temperature.

Ternary Al-Based Systems

Most technical Al alloys contain more than two components because of the presence of impurity and alloying elements.

Aluminium–Iron–Silicon. Figure 3.1-20 shows the Al-rich corner as a section for 0.5 wt% Fe. This concentration range is of particular interest for commercially pure, unalloyed Al. Apart from the solid solution and the AlFe and Si phases there are two ternary phases, i.e., $\alpha\text{-Al}_2\text{Fe}_3\text{Si}$ and $\beta\text{-Al}_9\text{Fe}_2\text{Si}_2$. The exact

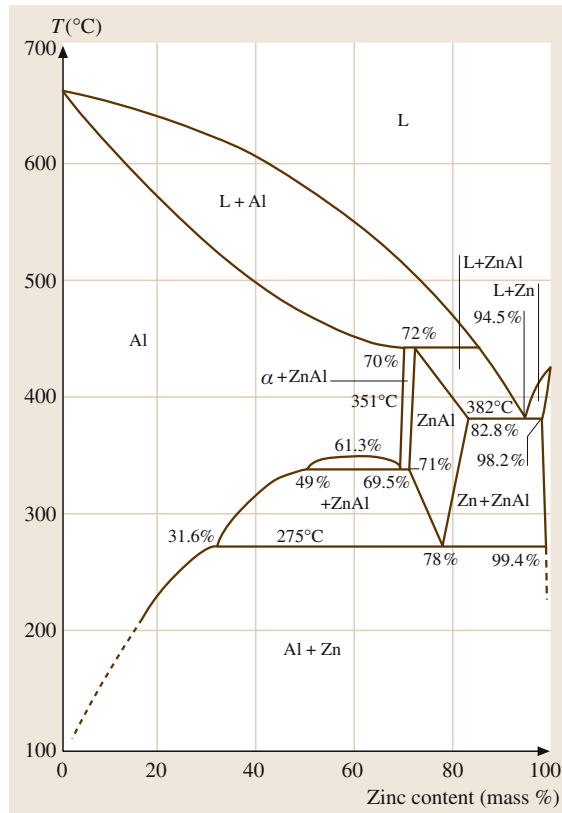


Fig. 3.1-19 Al–Zn system

compositions are subject to discussion and there are corresponding differences in the description of the solidification and precipitation processes. At the level of Fe and Si contents found in commercially pure aluminium ($Al + Si \leq 1$ wt%), α - $Al_{12}Fe_3Si$ will form as a result of the transformation of the α -solid solution and $AlFe$ with decreasing temperature, as shown in Fig. 3.1-14. If the temperature further decreases, precipitation of β - $Al_9Fe_2Si_2$ and even Si will occur. Due to the low rate of diffusion at low temperatures it is possible that all four phases coexist with the Al-rich solid solution phase. The solid solution becomes supersaturated in Fe and Si at the cooling rates used in industrial practice. Moreover, non-equilibrium ternary phases form, often locally at the grain boundaries of the as-cast microstructure. Fe and Si are in solution inside the grains. For a given cooling rate, the maximum Fe solubility decreases with increasing Si content of the alloy, whereas the Si solubility is independent of Fe content [1.19–21]. Thermodynamically, such non-equilibrium microstructures are very stable. The primary

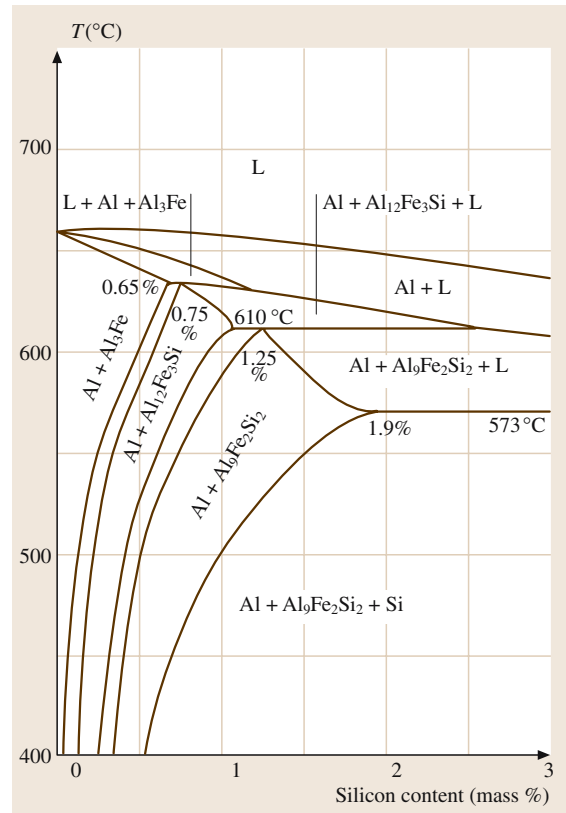


Fig. 3.1-20 Section through the Al–Fe–Si phase diagram at 0.5 wt% Fe [1.11]

non-equilibrium ternary phases only decompose to the secondary equilibrium phases Al_3Fe and Si at about 600 °C [1.22].

Aluminium–Magnesium–Silicon. Figures 3.1-21a and 3.1-21b show the Al-rich corner as a quasi-binary section Al – Mg_2Si (Mg/Si ratio 1:0.58). It divides the system into the two simple ternary eutectic systems shown. The fine-grained microstructure of Al–Mg–Si alloys consists of α - $Al(Mg, Si)$ and numerous intermetallic compounds, such as Mg_2Si (forming a characteristic particle shape called “Chinese script”), Al_6Mn , and Al_3Fe . Mg_2Si has an important effect on properties. Its solid solubility in the aluminium matrix is temperature-dependent and, thus, leads to hardening effects, which are exploited in technical alloys. A coarse network of intermetallic phases impairs forming behavior, but annealing before further processing produces finely-dispersed precipitates. These improve workability but are, also, effective in retarding recrystallization.

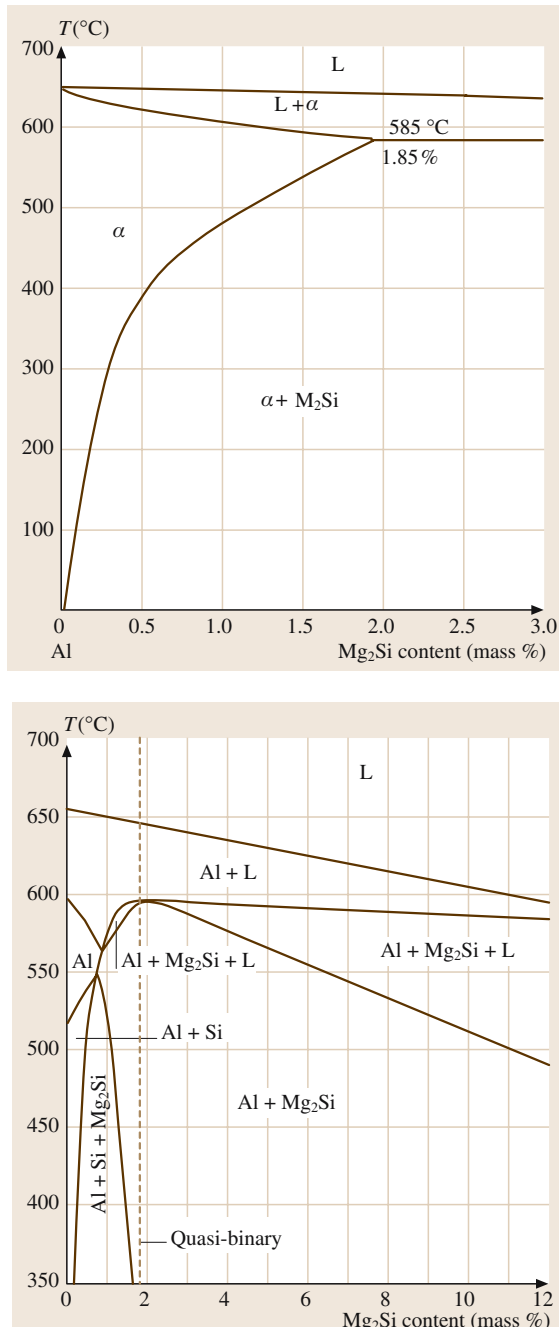


Fig. 3.1-21a,b Al–Mg–Si system (a) Quasi-binary section Al–Mg₂Si; (b) Section at a constant Si content of 1 wt% [1.11]

Aluminium–Copper–Magnesium. In addition to the two binary phases, Al₈Mg₅ (β) and Al₂Cu (θ), there are two ternary phases, Al₂CuMg (S) and Al₆Mg₄Cu (T), in equilibrium with the Al-rich solid solution. The microstructure of castings shows various ternary eutectics which, in addition to Al₂Cu, also contain Mg₂Si, resulting from Si as an impurity, and AlCuMg [1.9].

Aluminium–Copper–Lithium. In addition to binary phases between all three elements, three ternary phases, Al₇Cu₄Li, Al₂CuLi, and Al₅Li₃Cu, occur in equilibrium with the Al-rich solid solution in the aluminium-rich corner of this system.

Aluminium–Zinc–Magnesium. The Al-rich corner consists of two binary phases, Al₈Mg₅ and MgZn₂, and a ternary phase T with a nominal composition Al₂Mg₂Zn₃ having a wide range of homogeneity. The Al–MgZn₂ and Al–T sections may be regarded as quasi-binary systems with eutectic temperatures at 475 and 489 °C, respectively. The Al–Al₈Mg₅–T range constitutes a ternary eutectic, $T_E = 450$ °C. In the Al–T–Zn range there is a four-phase reaction in which the T phase transforms to Mg₂Zn. At high Zn contents, Mg₂Zn₁₁ transforms to MgZn₂ in another four-phase reaction at 365 °C. MgZn₂ subsequently solidifies eutectically at 343 °C together with Al and Zn. There is evidence of eutectic solidification in the as-cast structure of these alloys. If ternary Al–Zn–Mg alloys are solution-treated at temperatures above 450 °C they, consist of a homogeneous α phase solid solution which is supersaturated with respect to one phase at least, corresponding to its composition [1.9].

3.1.2.5 Classification of Aluminium Alloys

Technical aluminium alloys are subdivided first into the two main groups of cast and wrought alloys (Fig. 3.1-22). Typically, the alloying content of casting alloys is 10 to 12 wt%. This is significantly higher than the value for wrought alloys, most of which contain only a total of 1 to 2 wt% alloying elements; their content may be as high as 6 or even 8 wt% in individual cases.

Aluminium alloys are further subdivided, depending on whether or not an alloy can be hardened by the addition of alloying elements, as is the case with

- Precipitation-hardenable alloys which can be strengthened by aging and
- Non-precipitation-hardenable alloys which can be strengthened by work-hardening only.

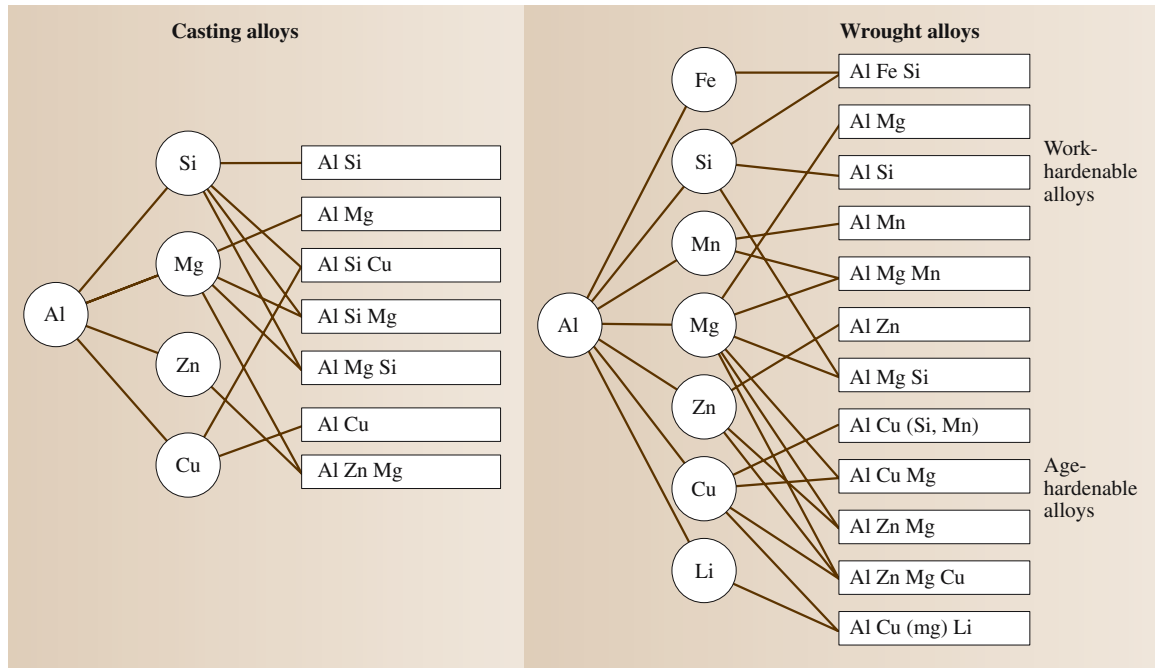


Fig. 3.1-22 Schematic array of cast and wrought aluminium alloys. The numbers are given according to European standardization. In the case of wrought alloys the numbers are the same as those used in North-American standardization

The addition of further alloying elements will always cause hardening, but not all elements have the same hardening effect. Hardening will also depend on whether the solute atoms are present in solid solution or as particles. Alloy hardening can be divided into

- Solid-solution hardening (as with non-precipitation hardening, work-hardenable alloys) and
- Hardening due to elements that are initially in solid solution and are precipitating as second phases (as is the case with age-hardenable alloys).

It should be noted that age-hardenable alloys can be strengthened by the use of a suitable heat treatment whereas the same heat treatment of alloys which are not age-hardenable leads to a loss in strength.

3.1.2.6 Structure and Basic Mechanical Properties of Wrought Work-Hardenable Aluminium Alloys

Al–Fe–Si and Unalloyed Aluminium (1xxx)
Al–Fe–Si contains about 0.6 wt% Fe and 0.8 wt% Si that has been added deliberately. The properties of

Al–Fe–Si alloys, and of unalloyed aluminium, are strongly influenced by the elements which are in solid solution and the binary and higher phases that form. Increasing amounts of alloying additions lead to a marked increase in strength but there is a decrease in electrical conductivity since transition elements have a high effective scattering power for electrons.

Wrought Al–Mn (3xxx)

Manganese additions increase the strength of unalloyed aluminium (Fig. 3.1-23). The chemical resistance is not impaired. These alloys have very good forming properties, when the Mn content is below the maximum solubility of Mn in the Al-rich α -phase, i.e., practically below 1.5 wt%. At higher Mn content, brittle Al_6Mn crystals form and impair workability.

If Al–Mn alloys are rapidly solidified as in continuous casting, considerable supersaturation of Mn occurs. Fe reduces the solubility for Mn and promotes its precipitation in the form of multicomponent phases. Fe is often added to counteract supersaturation and for an increase of the tensile strength (Fig. 3.1-24). Depending on the amount of precipitation, Mn can inhibit recrystallization.

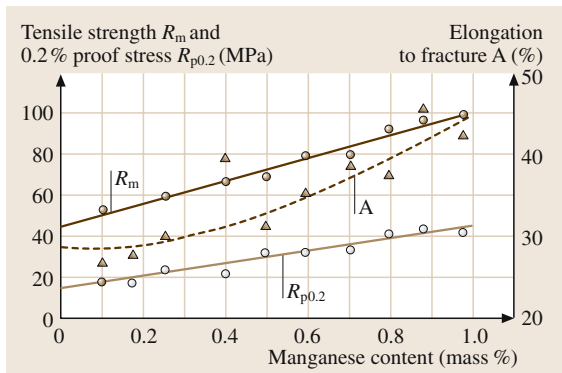


Fig. 3.1-23 Effect of manganese additions on the strength of aluminium; alloys based on 99.5 wt% Al, quenched from 565 °C, sheet samples, 1.6 mm thick [1.23]

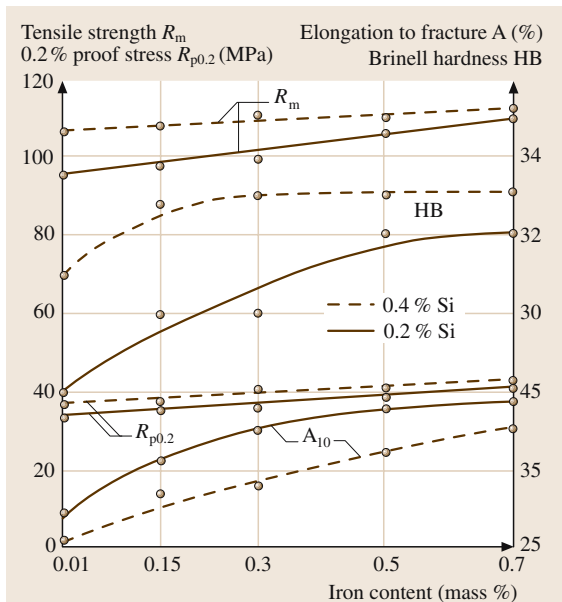


Fig. 3.1-24 Effect of iron and silicon on the strength of an Al–Mn alloy containing 1.2 wt% Mn; soft condition, sheet sample [1.24]

Wrought Al–Si (4xxx)

Aside from 1 to 12.5 wt% Si, wrought Al–Si alloys contain other elements such as Mg, Fe, Mn or Cu.

Wrought Al–Mg and Al–Mg–Mn (5xxx)

The two non-age-hardening alloy systems Al–Mg and Al–Mg–Mn cover the entire compositional range from 0.5 to 5.5 wt% Mg, 0 to 1.1 wt% Mg, and 0 to 0.35 wt% Cr. Alloys with more than 5.6 wt% Mg are of no significance as wrought alloys.

In Al–Mg alloys both tensile strength and 0.2% proof stress increase with increasing Mg content,

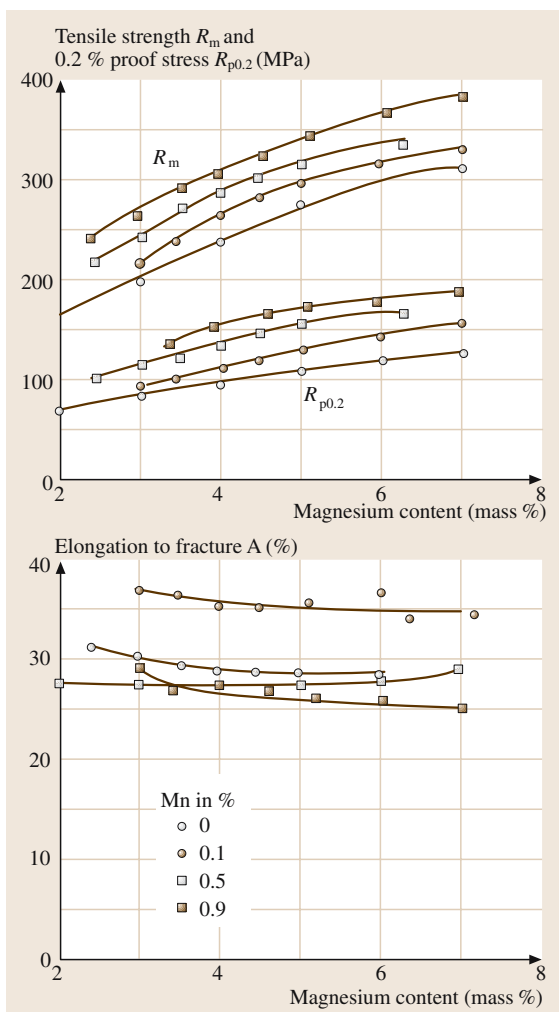
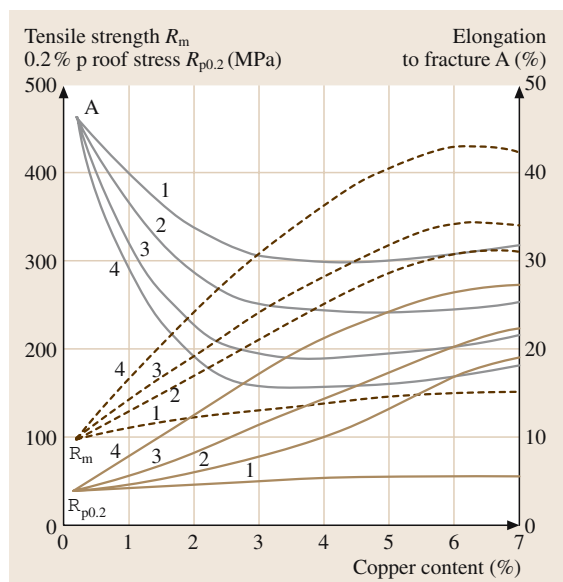


Fig. 3.1-25 Effect of Mn content on the mechanical properties of Al–Mg alloys [1.23]

whereas elongation shows a steady decrease up to about 3 wt% Mg, beyond which it increases again slightly. Embrittlement does not occur at low temperatures. The solubility of Mg in the Al-rich solid solution decreases rapidly with decreasing temperature. Thus most Al–Mg alloys are effectively supersaturated at room temperature. This is of practical significance in alloys containing more than 3 wt% Mg, where precipitation of the β -Al₈Mg₅ can occur, especially after prior

cold working. This is not associated with any beneficial increases in strength but leads to deterioration in the corrosion resistance by intergranular corrosion (Fig. 3.1-16). It is necessary to avoid the formation of continuous networks of β particles at the grain boundaries. Individual β particles can be obtained by a globulization treatment ($200\text{--}250^\circ\text{C}$), followed by slow cooling.

Another means to increase strength is the addition of Mn. Al–Mn–Mg alloys show an additional increase in tensile strength, which is significantly higher than for binary Al–Mn alloys (Fig. 3.1-26). The alloys show good toughness and can be used at low temperatures. If the Mn content exceeds 0.6 wt%, the recrystallization temperature can be increased to such an extent that recrystallization does not occur during extrusion. With extruded sections, there is an increase in tensile strength and proof stress in the longitudinal direction termed “press effect.”



3.1.2.7 Structure and Basic Mechanical Properties of Wrought Age-Hardenable Aluminium Alloys

Wrought Al–Cu–Mg and Al–Cu–Si–Mn (2xxx) Alloys

The 2xxx series alloys usually contain 3.5 to 5.5 wt% Cu and additions of Mg, Si and Mn and residual Fe. They show a significant increase in tensile strength by aging (310 to 440 MPa). Natural (room temperature) or artificial aging (at elevated temperature) may be preferable, depending on the alloy composition (Fig. 3.1-26). Additions of up to 1.5 wt% Mg increase both tensile strength and proof stress. At these Mg contents, the Al-rich solid solution is in equilibrium with the ternary Al_2CuMg phase which, together with the θ phase (Al_2Cu), is responsible for hardening. Mn additions increase the strength (Fig. 3.1-27) and can also cause a press effect. For achieving good ductility, the Mn content is limited to ≈ 1 wt%.

Wrought Al–Mg–Si (6xxx)

Al–Mg–Si alloys are the most widely used wrought age-hardenable alloys. Hardening is attributable to the formation of the Mg_2Si phase. The compositional range of interest is 0.30 to 1.5 wt% Mg, 0.20 to 1.6 wt% Si, up to 1.0 wt% Mn, and up to 0.35 wt% Cr. This is equivalent to about 0.40 to 1.6 vol% Mg_2Si and varying amounts of free Si and/or Mg. Some alloys are close to the pseudo-binary section Al– Mg_2Si , in others there is a significant excess of Si. This affects the maximum

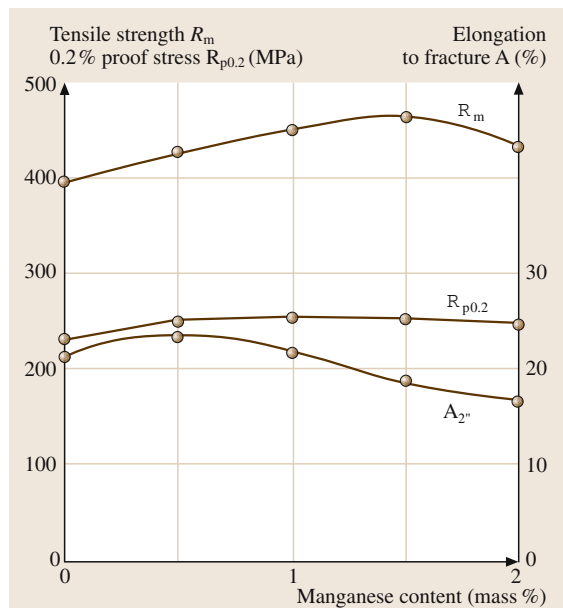


Fig. 3.1-26a,b Behavior of wrought Al–Cu-alloys (a) Effect of copper on the strength of binary Al–Cu alloys; base material 99.95 wt% Al, 1.6 mm thick sheet [1.23]. (1) Soft annealed; (2) Solution annealed and quenched; (3) Naturally aged; (4) Artificially aged. (b) Effect of Mn on the strength of an Al–Cu–Mg alloy with approx. 4 wt% Cu and 0.5 wt% Mg; naturally aged [1.23]

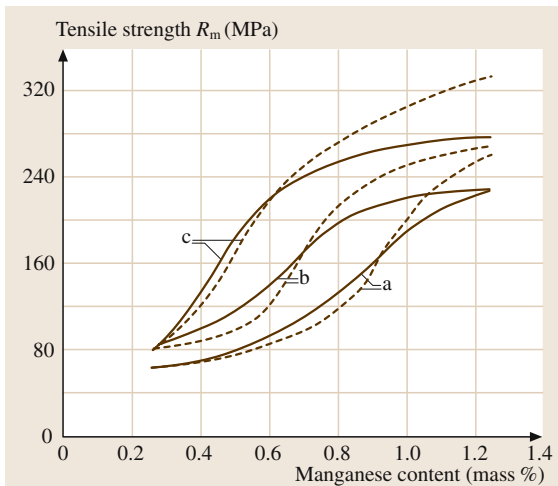


Fig. 3.1-27 Effect of Mg_2Si on tensile strength [1.9]
 (1) stoichiometric composition, (2) 0.3 wt% excess Mg,
 (3) 0.3 wt% excess Si. The solid line refers to alloys that
 were quenched + immediate ageing at 160°C , the dotted line
 represents data for alloys that were quenched +
 intermediate ageing for 24 h at 20°C + ageing at 160°C

attainable strength values because of the resulting variations in the amount of Mg_2Si , as shown in Fig. 3.1-28 for the quenched and artificially aged condition. Additions of 0.2 to 1.0 wt% Mn lead to an increase in the notch impact toughness of Al–Mg–Si alloys (Fig. 3.1-29), and affect the recrystallization behavior. Additions of Cr cause similar effects.

Wrought Al–Zn–Mg- and Al–Zn–Mg–Cu Alloys (7xx)

Additions of Zn to Al lead to an insignificant increase in strength. Combined additions of Zn and Mg cause age hardening and thus an increase in strength (Fig. 3.1-28). The sum of the Zn and Mg contents is limited to about 6–7% because of the risk of stress corrosion cracking at higher levels in Cu-free Al–Zn–Mg alloys; this results in medium strength. Zr, Mn, and Cr are added to reduce the tendency to recrystallize. If suitably heat-treated, such alloys have adequate corrosion resistance. It is important that cooling after solution treatment is not too rapid and that the proper precipitation treatment, usually step ageing, should be used. The alloys are of interest for welded structures because of their low quench

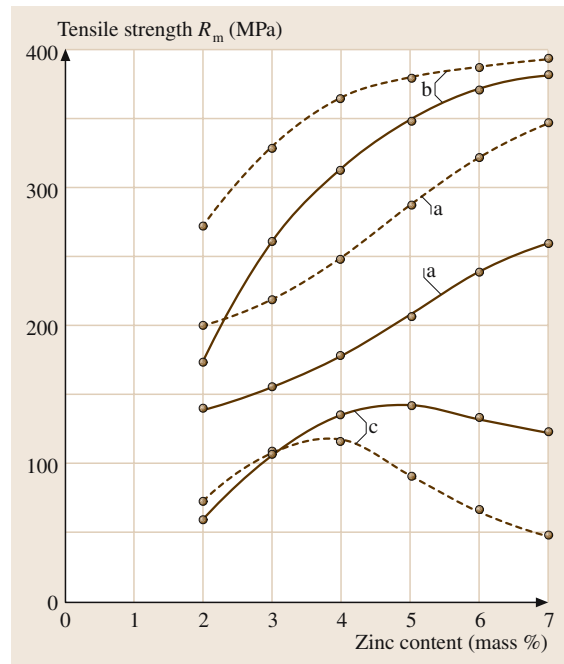


Fig. 3.1-28 Effect of Zn and Mg on the strength and aging effect of Al–Zn–Mg alloys [1.24]
 (1) Solution treatment at 450°C and quenching. (2) Solution treatment at 450°C and quenching plus natural aging for 3 months. (3) Ageing effect i.e., the increase in strength attributable to natural ageing; difference between (1) and (2)

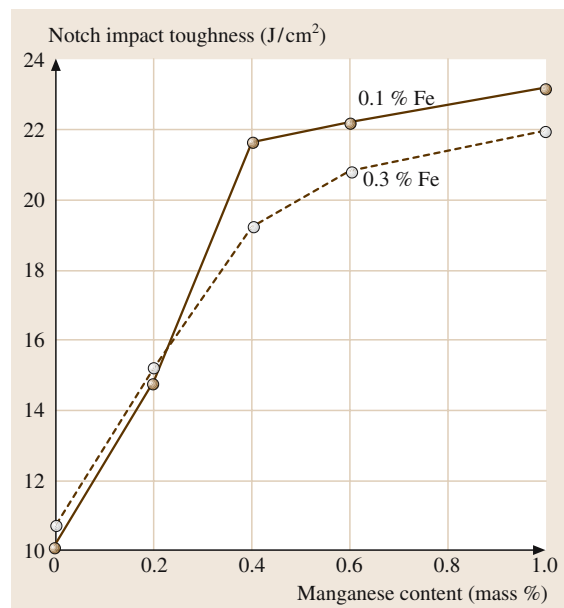


Fig. 3.1-29 Effect of Mn and Fe on the notch impact toughness of AlMgSi1 alloy 1 wt% Si and 0.75 wt% Mg; artificially aged, flat bars, $60 \times 10 \text{ mm}^2$ [1.24]

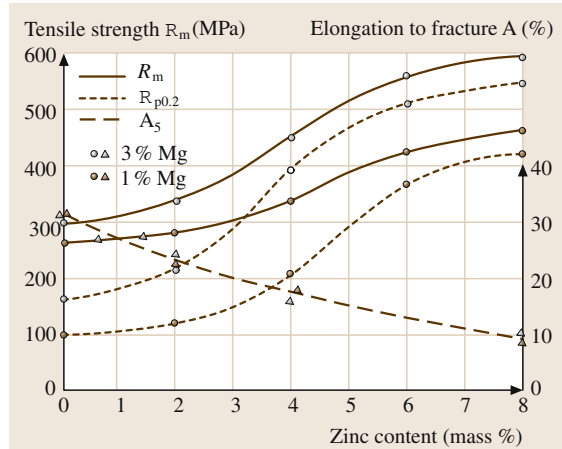


Fig. 3.1-30 Effect of zinc on the tensile properties of Al-Zn-Mg-Cu alloys; solution treated at 460 °C, quenched, aged for 12 h at 135 °C, 1.5 wt% Cu [1.23]

sensitivity. The low-strength heat-affected zone formed during welding is restored to full hardness without the need for renewed solution treatment. Al-Zn-Mg alloys usually contain 0.1 to 0.2 wt% Zr and some Ti in order to improve their weldability and resistance to stress corrosion cracking. Cu additions are avoided, despite their favourable effect on stress corrosion cracking, because they increase susceptibility to weld cracking.

Al-Zn-Mg-Cu Alloys

The addition of 0.5 to 2.0 wt% Cu strengthens Al-Zn-Mg alloys. Cu also reduces the tendency for stress corrosion cracking so that the upper limit for (Zn + Mg) can be increased to 9 wt%, provided additions of Cr are also made. The Zn/Mg ratio should preferably lie between 2 and 3. Al-Zn-Mg-Cu alloys can be aged both naturally and artificially. They attain the highest strength levels of all aluminium alloys. The actual hardening mechanism is attributable to Mg and Zn. Cu increases the rate of aging and acts as a nucleus for the hardening phases. Figure 3.1-30 shows some properties as a function of the Zn content at constant Cu content and two different Mg contents.

3.1.2.8 Structure and Basic Mechanical Properties of Aluminium Casting Alloys

Al-Si Casting Alloys

Due to the Al-Si eutectic (Fig. 3.1-12), these alloys, containing 5 to ≤ 20 wt% Si, have good casting

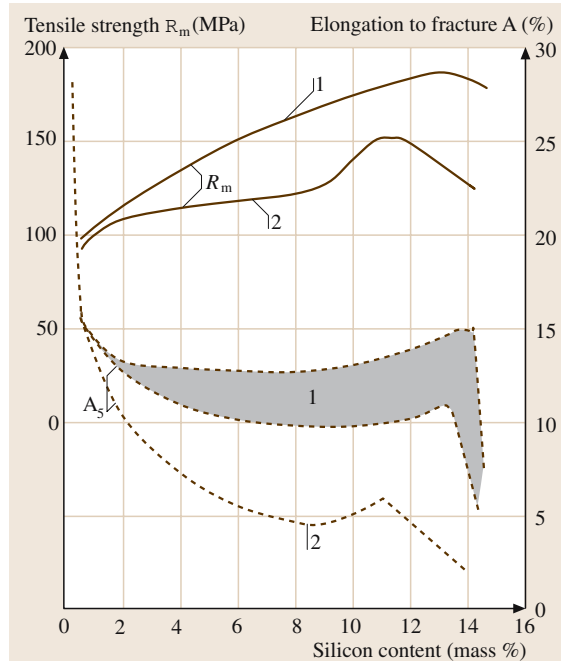


Fig. 3.1-31 Effect of Si on the strength and ductility of Al-Si casting alloys; modified and unmodified sand castings. [1.9] (1) modified; (2) unmodified

properties. The tensile strength increases with the Si content (Fig. 3.1-31). Apart from Si other elements may be added, e.g., for the modification of the eutectic. Cu is present in residual amounts and impairs chemical resistance if levels exceed 0.05 wt%. Additions of about 1 wt% Cu yield an increase in solid solution hardening and thus reduce the tendency for smearing during machining. Residual Fe reduces sticking tendency, but leads to the formation of β -AlFeSi needles which reduce strength and ductility. Therefore the Fe content must be limited. An addition of Mn has a favorable effect on the sticking tendency. Mn leads to the formation of a quaternary phase; but it poses no problem because of its globular shape. “Piston alloys” have hypereutectic compositions of up to 25 wt% Si. During solidification, primary Si crystals are formed which increase wear strength and reduce thermal expansion.

Al-Si-Mg Casting Alloys

These alloys contain about 5 wt%, 7 wt%, or 10 wt% Si and between 0.3 and 0.5 wt% Mg. The optimum amount of Mg decreases with increasing Si content. Mg causes high strength and a moderate ductility depending on the

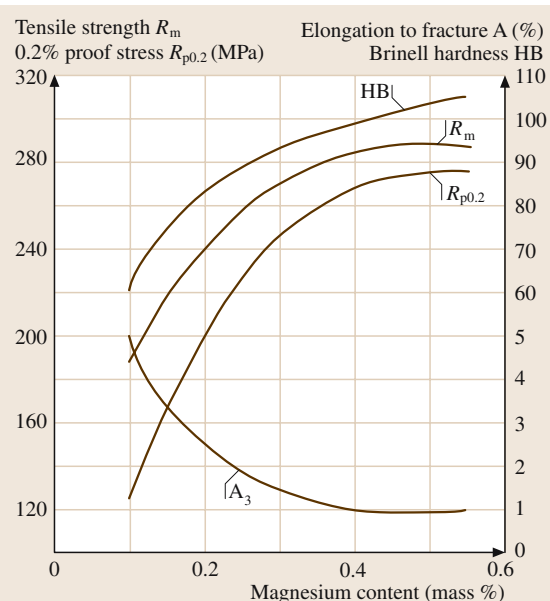


Fig. 3.1-32 Effect of Mg on the mechanical properties of G-AlSi10Mg casting alloy (with 9.5 wt% Si, 0.45 wt% Fe and 0.3 wt% Mn), sand cast and artificially aged [1.25–27]

temper (Fig. 3.1-32). The alloys can be age hardened both naturally and artificially. Fe leads to a reduction in sticking tendency, but also to a drastic reduction in ductility.

Al-Mg Casting Alloys

These alloys contain 3–12 wt% Mg. Strength increases with increasing Mg content (Fig. 3.1-33). Above about 7 wt% Mg, the alloy has to be heat-treated to homogenise the structure and thus obtain good tensile properties. With Mg contents of up to 5 wt%, Si additions of up to 1 wt% are possible, and these lead mainly to improvements in the casting properties. The addition of Si causes hardening due to the formation of Mg_2Si .

Al-Zn-Mg Casting Alloys

They contain 4 to 7 wt% Zn and 0.3 to 0.7 wt% Mg. They can be naturally or artificially age hardened in the as-cast condition, without the need for prior solution treatment. Mg has a significant effect on the mechanical properties in the aged condition (Fig. 3.1-34). If the Mg content is limited, Al-Zn-Mg casting alloys can exhibit particularly good elongation to fracture.

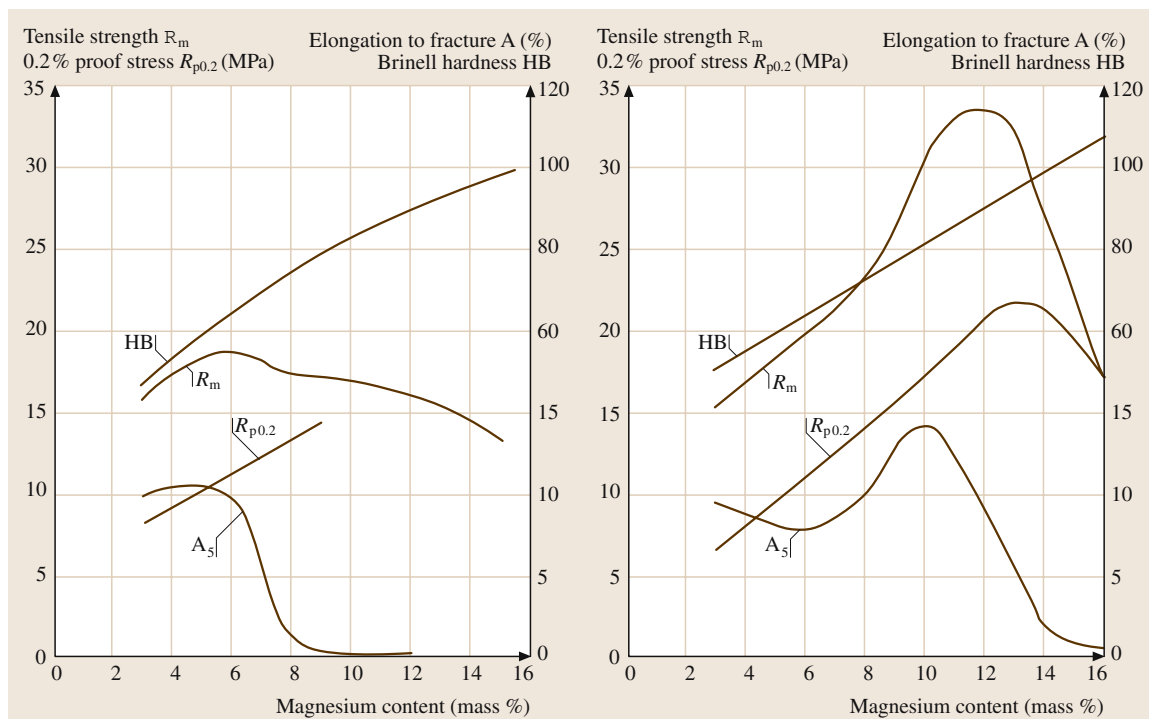


Fig. 3.1-33a,b Effect of Mg on the mechanical properties of Al-Mg casting alloys, sand cast, untreated and homogenised [1.9]. (a) As-cast condition. (b) Homogenized

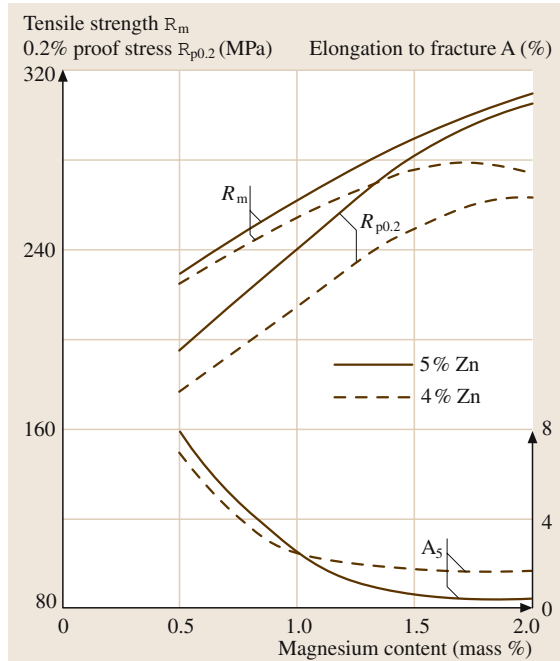


Fig. 3.1-34 Effect of Mg on the strength of cast Al-Zn-Mg alloys; sand casting, artificially aged [1.9]

3.1.2.9 Technical Properties of Aluminium Alloys

The applications of aluminium and its alloys are depending on the properties. In most cases, mechanical properties are an important criterion for assessing the suitability of an Al alloy for a specific application. Other properties, such as electrical conductivity or corrosion resistance, may also be included in the assessment process.

Mechanical Properties

Hardness. The Brinell hardness number HB ranges from 15 for unalloyed Al in the soft temper to about 140 for an artificially aged Al-Zn-Mg-1.5 wt%Cu alloy.

Tensile Strength. Figures 3.1-35 and 3.1-36 indicate the typical levels of strength attainable with wrought and cast aluminium alloys, respectively. There will be a range of tensile strengths in specific alloying systems because of possible additional increases in strength due to hardening by cold work or precipitation. The different alloying elements cause differing degrees of strengthening.

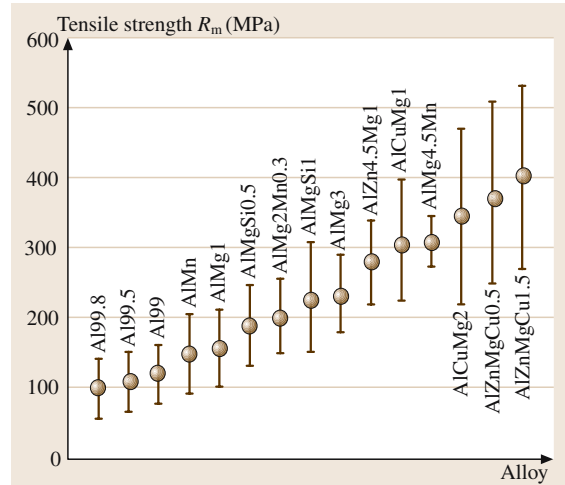


Fig. 3.1-35 Ranges of tensile strength for some important wrought aluminium alloys [1.9]

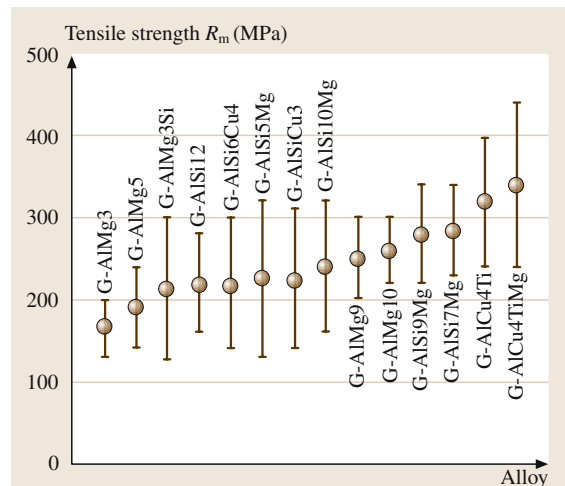


Fig. 3.1-36 Ranges of tensile strength for some important aluminium casting alloys [1.9]

Strength at Elevated Temperatures. An example of the temperature and time dependence of the different mechanical properties is given in Fig. 3.1-37. With regard to the resistance to softening the materials can be classified as follows, depending on their temper:

- Wrought alloys in the soft temper and as-cast non-age-hardenable casting alloys are all practically thermally stable.
- For cold worked wrought alloys, partially annealed to obtain an intermediate temper, the increase in

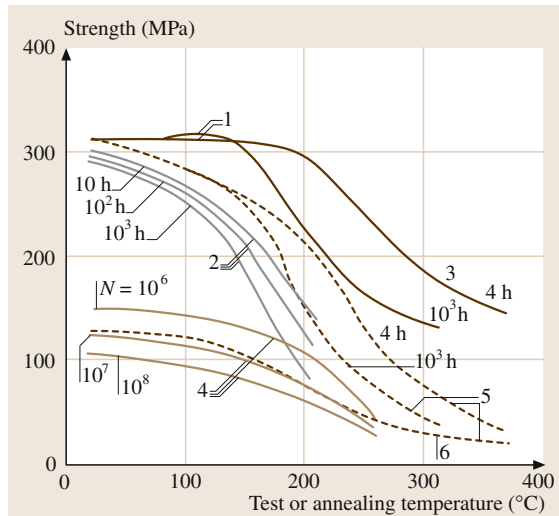


Fig. 3.1-37 Properties of 6061-T6 at elevated temperatures; 1.0 wt% Mg, 0.6 wt% Si, 0.3 wt% Cu, 0.25 wt% Cr, artificially aged [1.9]. (1) tensile strength R_m at 20 °C, (2) stress rupture strength, (3) duration of exposure, (4) fatigue strength, (5) tensile strength at test temperature, (6) solution treated

strength due to forming is diminished with increasing temperature and exposure time.

- Artificially aged alloys do not undergo any permanent changes on annealing up to approaching the ageing temperature. At higher temperatures, aging continues from the point where it was interrupted during the aging process (Figs. 3.1-38 and 3.1-39).
- Naturally aged alloys usually exhibit increased hardening when exposed to higher temperatures as a result of artificial ageing. At higher temperatures, the behavior is similar to that of artificially aged alloys.

High Temperature Mechanical Properties in Short-Term Tests. In materials that are not thermally stable, there will be an effect due to irreversible changes in properties. Its magnitude depends on the temperature and duration of exposure, Figs. 3.1-40 and 3.1-41.

Creep Behavior. Creep of Al alloys starts to play an important role at temperatures above 100 to 150 °C (Figs. 3.1-42 and 3.1-43). Material, amount of cold work

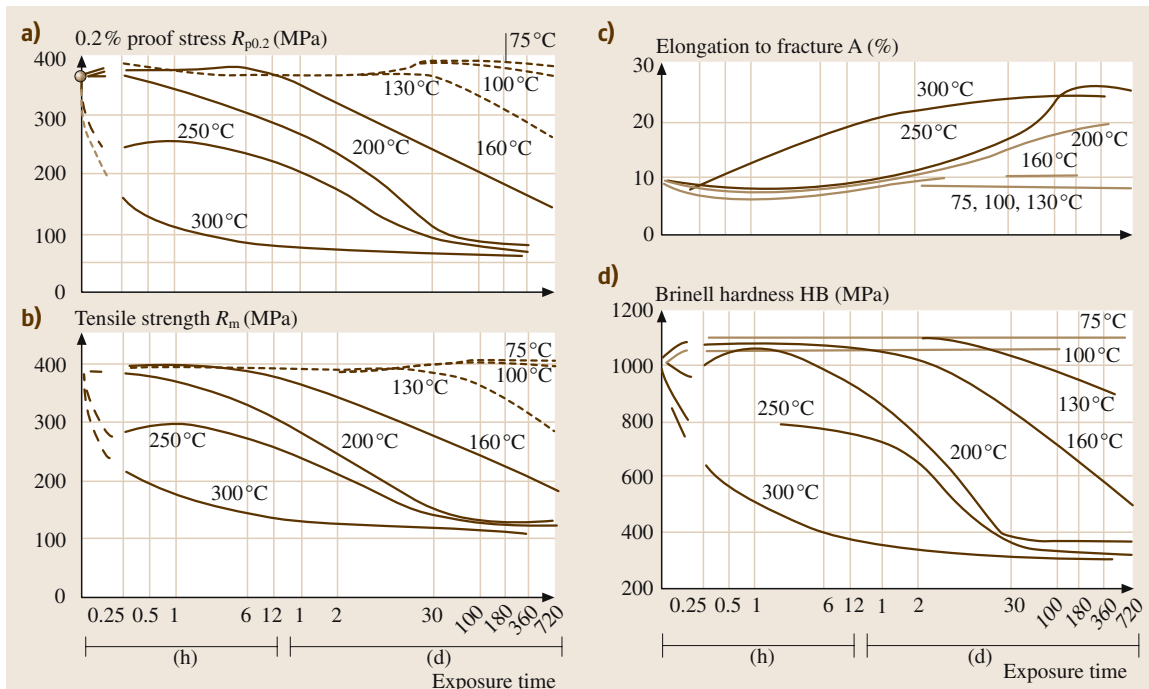


Fig. 3.1-38a-d Effect of temporary exposure to elevated temperature on the mechanical properties of artificially aged AlSi1MgMn [6082] at 20 °C [1.9]. (a) tensile strength; (b) 0.2% proofstress $R_{p0.2}$; (c) elongation to fracture A; (d) Brinell hardness

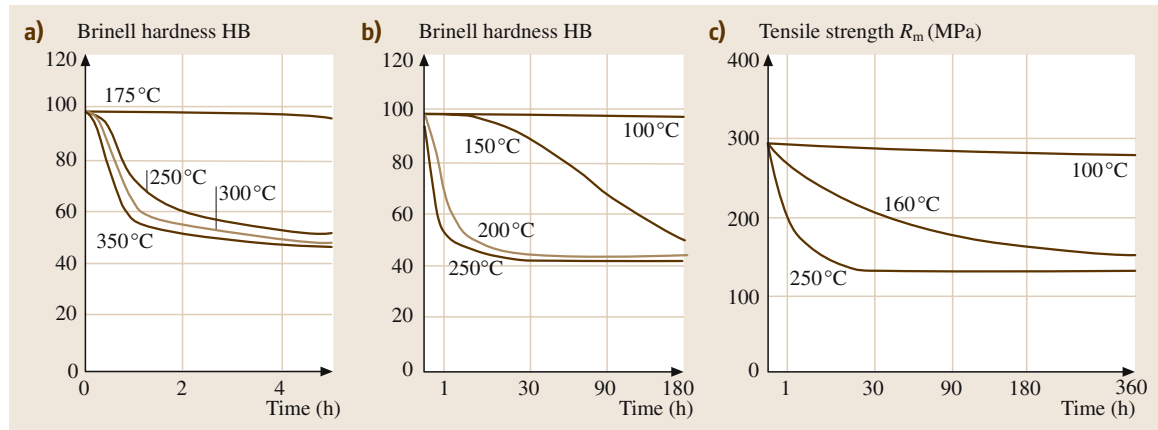


Fig. 3.1-39a–c Effect of temporary exposure to elevated temperature on the hardness and tensile strength at 20 °C of cast G-AlSi10Mg [43000, AlSi10Mg(a)] alloy, artificially aged [1.28]. **(a)** 0–4 h; **(b)** 1–180 d; **(c)** 1–360 d

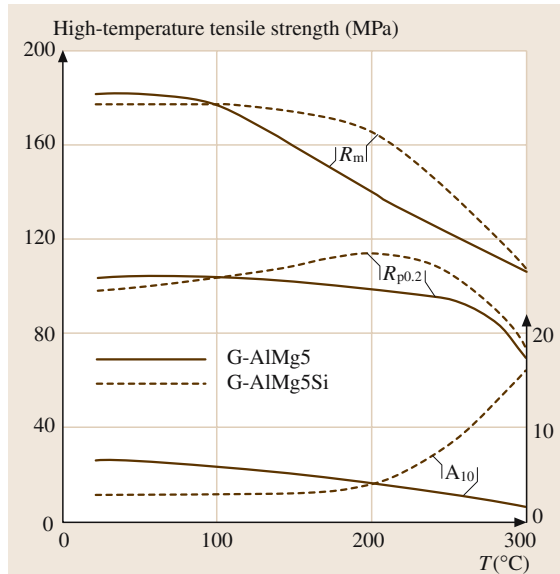


Fig. 3.1-40 High-temperature tensile strength of G-AlMg5 [51300] and G-AlMg5Si [51400] casting alloys, sand cast, after 30 min prior exposure to the test temperature [1.29]

and degree of age-hardening can affect creep behavior in various ways. With non-age-hardenable alloys, the effect of cold working is more pronounced at low temperatures, below about 150 °C. At higher temperatures, the behavior rapidly approaches that of the softened material. Thus, more highly alloyed materials in the soft temper may exhibit better creep properties than cold worked alloys that are less highly alloyed. Artificially

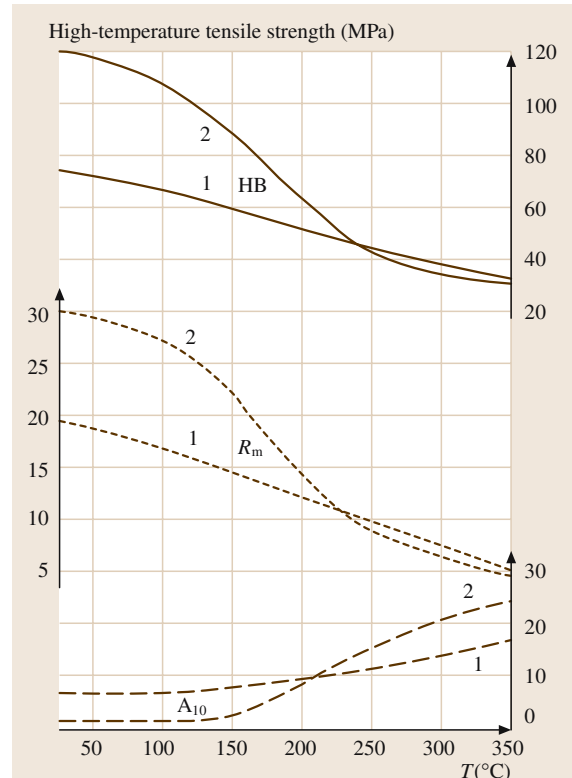


Fig. 3.1-41 High-temperature tensile strength of casting alloys [1.28]. **(1)** As-cast G-AlSi12 alloy [44300, AlSi12(Fe)]. **(2)** G-AlSi10Mg alloy [43000, AlSi10Mg(a)] after preheating for 8 days at the test temperature

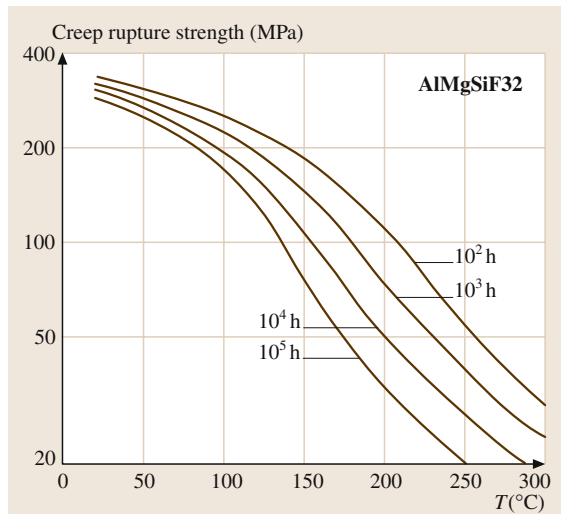


Fig. 3.1-42 Creep rupture behavior of 6082, AlSi1MgMn, T6 alloy, strain-hardened, min. tensile strength 320 MPa; extruded rods, 25 mm diameter [1.30, 31]

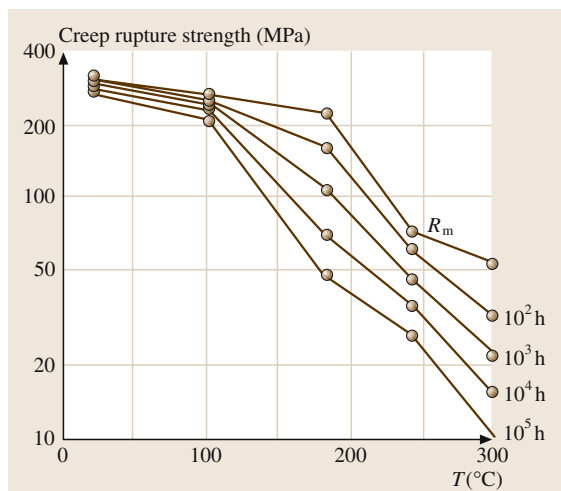


Fig. 3.1-43 Creep rupture behavior of AlSi10MgCa [43000] casting alloy, artificially aged, 100 h prior exposure to the test temperature [1.30, 31]

aged alloys should only be exposed for prolonged periods to temperatures that are significantly lower than the temperature of artificial ageing, otherwise over-ageing will lead to a complete loss of strength.

Mechanical Properties at Low Temperatures. Based on its fcc crystal structure, Al and its alloys show neither a rapid increase in yield stress nor a rapid de-

crease in fracture toughness with decreasing temperature (Figs. 3.1-44 – 3.1-46). Tests carried out on Al–Mn, Al–Mg, Al–Mg–Si, Al–Cu–Mg, and Al–Zn–Mg wrought alloys at -268°C showed that the values of elongation to fracture at extremely low temperatures were even higher than at room temperature. In most cases, tensile strength and 0.2% proof stress increased weakly with decreasing temperature. Casting alloys behave similar to wrought alloys at low temperatures. The behavior will depend on composition, temper (especially size, shape and distribution of precipitates), and on the casting process used (Fig. 3.1-47).

Fatigue. There is a marked effect of composition, heat treatment, and method of processing on fatigue strength. Solid solution hardening, cold work, and age hardening all lead to an increase in fatigue strength. For a given alloy composition, extruded sections usually have a higher fatigue strength than sheet or forgings. Fine grains are generally beneficial whereas coarse grains and coarse intermetallic phase particles can lead to a reduction in fatigue strength. Often there is an increase in fatigue strength with decreasing sample thickness, especially with bending stresses. Moreover, the effect of roughness or surface defects in thin specimens is usually less than that in thicker samples. With wrought aluminium alloys, there is a marked difference between age-hardenable alloys and non-age-hardenable alloys. It manifests itself in the shape of the S–N curve (Fig. 3.1-47), which is almost horizontal after about 10^6 cycles for non-age-hardenable alloys and after about 10^8 cycles for age-hardenable alloys. Fig-

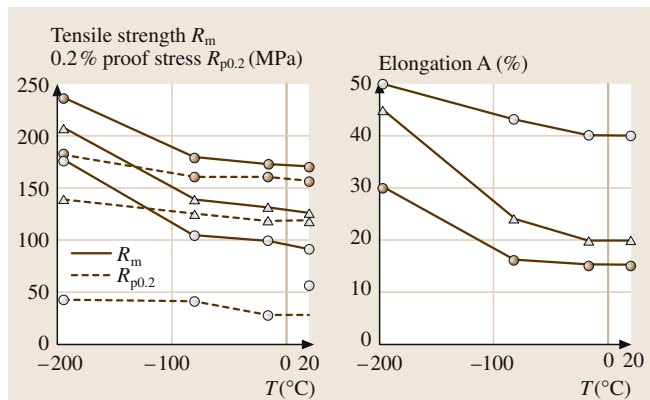


Fig. 3.1-44a,b Mechanical properties of unalloyed aluminium AA 1100 (Al99) at low temperatures [1.9]. (a) Tensile strength R_m ; (b) Elongation A

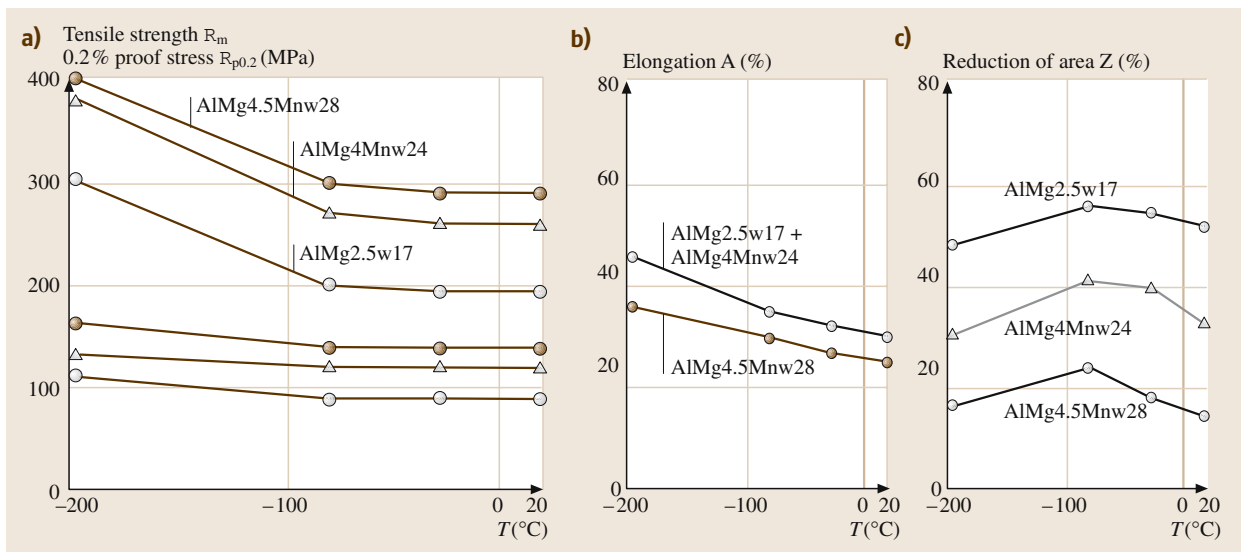


Fig. 3.1-45a–c Mechanical properties at low temperatures for some Al–Mg and Al–Mg–Mn alloys in the soft temper [1.9].
(a) Tensile strength R_m and 0.2 proof stress $R_{p0.2}$; **(b)** Elongation A''_2 ; **(c)** reduction of area AlMg4Mn (\approx 5086, AlMg4), W24 ~O/H111; AlMg2.5 (\approx 5052, AlMg2.5), W17 ~O/H111; AlMg4.5Mn (\approx 5083, AlMg4.5Mn), W28 ~O/H111

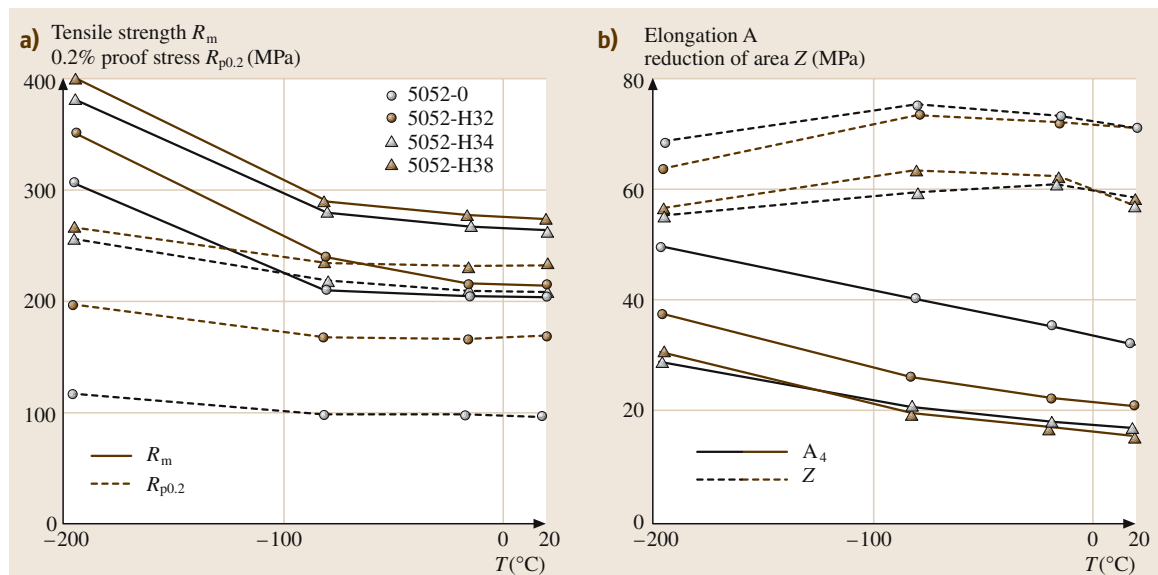


Fig. 3.1-46a,b Effect of cold working on the tensile properties of AlMg2.5 (5052) at low temperatures [1.9]. **(a)** Tensile strength and 0.2 proof stress; **(b)** Elongation and reduction of area

ure 3.1-48 illustrates that the choice of 10^8 cycles as the ultimate number of stress cycles is regarded as adequate. Figure 3.1-49 shows fatigue curves for a number of casting alloys.

Technological Properties

Abrasion Resistance. The wear resistance of Al alloys is low, especially in the absence of lubricants. There is no relation between hardness, strength and

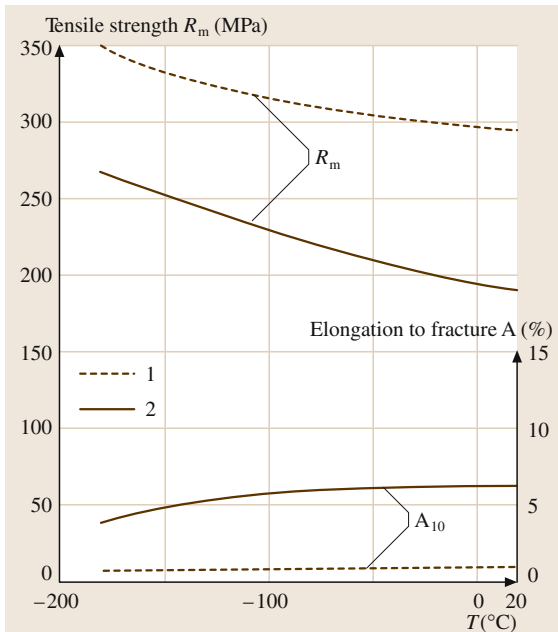


Fig. 3.1-47 Mechanical properties of artificially aged G-AlSi12 and G-AlSi10Mg casting alloys at low temperatures [1.28]. The solid line represents G-AlSi10Mg, artificially aged; the dotted line represents G-AlSi12, as-cast

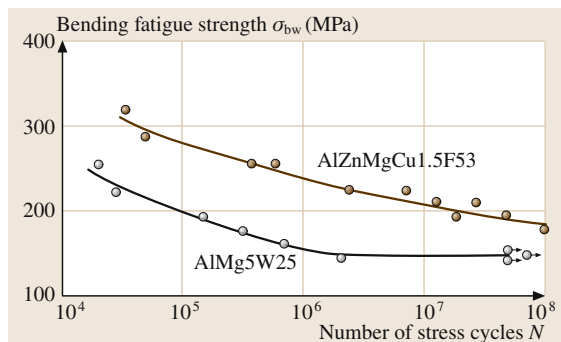


Fig. 3.1-48 Typical S-Ncurves for reverse bending tests on an age-hardenable and a non-age-hardenable alloy [1.9], AlZnMgCu1.5 F53 (\approx 7075, AlZn5.5MgCu, T651) and AlMg5 (\approx 5019, AlMg5), W25

Table 3.1-13 Typical values of strain-hardening exponent n and degree of anisotropy r for some aluminium-base materials based on data from various sources [1.9]; n.a. – not available

| Material, Alloy | Temper | n | r |
|-----------------|--------|------|------|
| Al99.5 | O/H111 | 0.25 | 0.62 |
| AlMn1 | O/H111 | 0.15 | n.a. |
| AlMg3 | O/H111 | 0.20 | 0.64 |
| AlMg3 | H14 | 0.16 | 0.75 |
| AlMg3 | H18 | 0.12 | 1.10 |
| AlMg2Mn0.8 | O/H111 | 0.20 | 0.66 |
| AlMg2Mn0.8 | H112 | 0.20 | 0.92 |
| AlMg4.5Mn | O/H111 | 0.15 | n.a. |

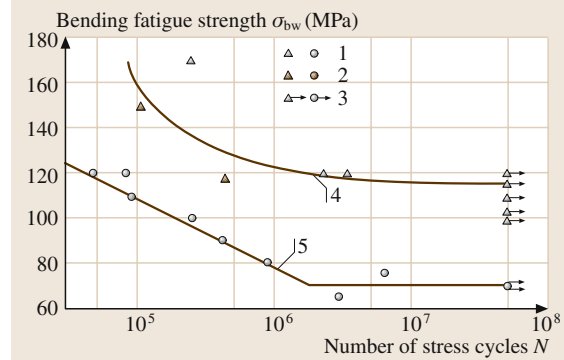


Fig. 3.1-49 Bending fatigue strength of two aluminium pressure die-casting alloys; flat samples with cast skin [1.9]. (1) Fracture; (2) Fracture, with evidence of defect; (3) No fracture; (4) GD-AlSi6Cu3; (not in EN); (5) GD-AlSi12 [\approx 44300, AlSi12(Fe)]

abrasion resistance. Under suitable conditions of lubrication, aluminium alloys can be safely used where they will encounter friction, as shown by their widespread use in the fabrication of pistons and sliding bearings. Wear can be drastically reduced by the suitable surface treatments.

Sheet Formability. Typical values for deep-drawing indices for commonly used sheet materials are shown in Fig. 3.1-50, whereas typical values of strain-hardening exponent n and degree of anisotropy r are given in Table 3.1-13. The r value is strongly dependent on the manufacturing process in particular, as is the case with all texture-dependent properties. In general, materials with high n and r values are deep-drawable.

Fig. 3.1-50 Typical S-Ncurves for reverse bending tests on an age-hardenable and a non-age-hardenable alloy [1.9], AlZnMgCu1.5 F53 (\approx 7075, AlZn5.5MgCu, T651) and AlMg5 (\approx 5019, AlMg5), W25

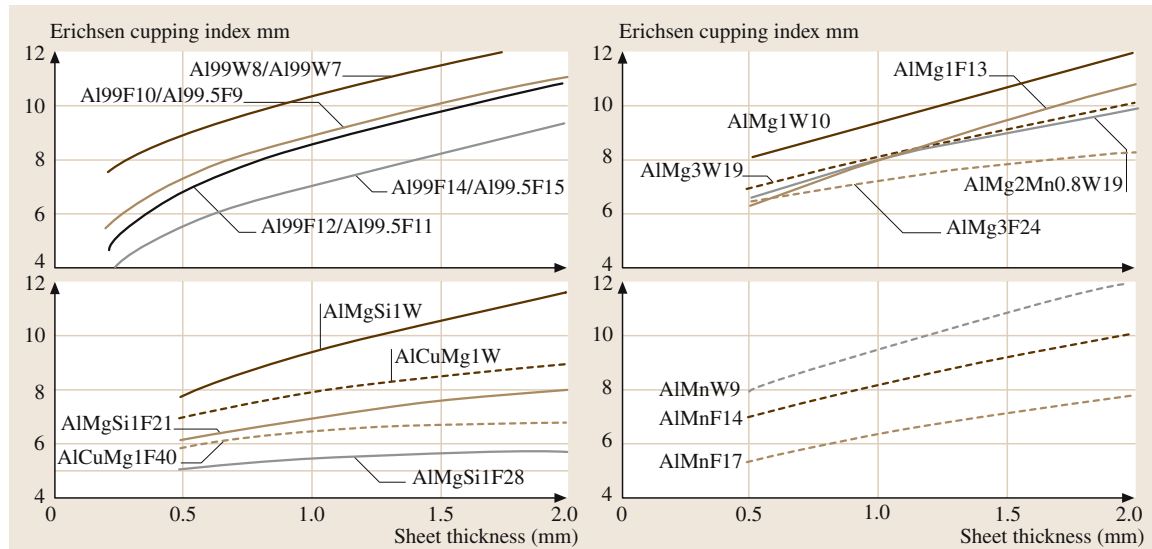


Fig. 3.1-50 Dependence of deep-drawing index on sheet thickness for different aluminium sheet alloys [1.9]

Machinability. There are difficulties to classify aluminium alloys according to their machinability. In general, soft wrought alloys perform worse than other materials regardless of the machining conditions because of chip shape. Harder wrought alloys perform somewhat better and special machining alloys and casting alloys perform best of all. In Si-containing alloys, including wrought alloys, there is a marked increase in tool wear with increasing Si content if the relatively hard Si is present in its elemental form.

Physical Properties

The most important physical properties of pure Al are listed in Chapt. 2.1, Table 3.1-11. Characteristic ranges of property variations with the amount of impurities or alloying elements are compiled in Table 3.1-14.

Coefficient of Thermal Expansion. Values of the average linear coefficient of thermal expansion for some Al-based materials at temperatures of practical significance are given in Table 3.1-15. Alloying leads to

Table 3.1-14 Examples for physical properties of aluminium alloys [1.9]^a

| Designation EN | EN former designation | Density (g cm^{-3}) | Freezing range ^b (°C) | Electrical conductivity ($\text{m } \Omega^{-1} \text{ mm}^{-2}$) | Thermal conductivity ($\text{W m}^{-1} \text{ K}^{-1}$) | Coefficient of linear expansion ($10^{-6}/\text{K}$) |
|-----------------------|--------------------------|-----------------------------------|--|---|---|--|
| Wrought alloys | | | | | | |
| 1098 | Al99.98 | Al99.98R | 2.70 | 660 | 37.6 | 232 |
| 1050A | Al99.5 | Al99.5 | 2.70 | 646–657 | 34–36 | 210–220 |
| 1200 | Al99 | Al99 | 2.71 | 644–657 | 33–34 | 205–210 |
| 8011A | AlFeSi(A) | AlFeSi | 2.71 | 640–655 | 34–35 | 210–220 |
| 3103 | AlMn1 | AlMn | 2.73 | 645–655 | 22–28 | 160–200 |
| 3003 | AlMn1Cu | AlMnCu | 2.73 | 643–654 | 23–29 | 160–200 |
| 3105 | AlMn0.5Mg0.5 | AlMn0.5Mg0.5 | 2.71 | 635–654 | 25–27 | 180–190 |
| 3004 | AlMn1Mg1 | AlMn1Mg1 | 2.72 | 629–654 | 23–25 | 160–190 |
| 5005A | AlMn1(C) | AlMg1 | 2.69 | 630–650 | 23–31 | 160–220 |
| 5052 | AlMg2.5 | AlMg2.5 | 2.68 | 607–649 | 19–21 | 130–150 |
| 5754 | AlMg3 | AlMg3 | 2.66 | 610–640 | 20–23 | 140–160 |
| 5019 | AlMg5 | AlMg5 | 2.64 | 575–630 | 15–19 | 110–140 |
| 5049 | AlMg2Mn0.8 | AlMg2Mn0.8 | 2.71 | 620–650 | 20–25 | 140–180 |

Table 3.1-14 Examples for physical properties of aluminium alloys [1.9]^a, cont.

| Designation EN | EN former designation | | Density (g cm ⁻³) | Freezing range ^b (°C) | Electrical conductivity (m Ω ⁻¹ mm ⁻²) | Thermal conductivity (W m ⁻¹ K ⁻¹) | Coefficient of linear expansion (10 ⁻⁶ /K) |
|-----------------------|--------------------------|----------------|----------------------------------|--|---|---|---|
| 5454 | AlMg2.7Mn | AlMg2.7Mn | 2.68 | 602–646 | 19–21 | 130–150 | 23.6 |
| 5086 | AlMg4 | AlMg4Mn | 2.66 | 585–641 | 17–19 | 120–140 | 23.8 |
| 5083 | AlMg4.5Mn0.7 | AlMg4.5Mn | 2.66 | 574–638 | 16–19 | 110–140 | 24.2 |
| 6060 | AlMgSi | AlMgSi0.5 | 2.70 | 585–650 | 28–34 | 200–220 | 23.4 |
| 6181 | AlSi1Mg0.8 | AlMgSi0.8 | 2.70 | 585–650 | 24–32 | 170–220 | 23.4 |
| 6082 | AlSi1MgMn | AlMgSi1 | 2.70 | 585–650 | 24–32 | 170–220 | 23.4 |
| 6012 | AlMgSiPb | AlMgSiPb | 2.75 | 585–650 | 24–32 | 170–220 | 23.4 |
| 2011 | AlCu6BiPb | AlCuBiPb | 2.82 | 535–640 | 22–26 | 160–180 | 23.1 |
| 2007 | AlCu4PbMgMn | AlCuMgPb | 2.85 | 507–650 | 18–22 | 130–160 | 23 |
| 2117 | AlCu2.5Mg0.5 | AlCu2.5Mg0.5 | 2.74 | 554–650 | 21–25 | 150–180 | 23.8 |
| 2017A | AlCu4MgSi(A) | AlCuMg1 | 2.80 | 512–650 | 18–28 | 130–200 | 23.0 |
| 2024 | AlCu4Mg1 | AlCuMg2 | 2.78 | 505–640 | 18–21 | 130–150 | 22.9 |
| 2014 | AlCu4SiMg | AlCuSiMn | 2.80 | 507–638 | 20–29 | 140–200 | 22.8 |
| 7020 | AlZn4.5Mg1 | AlZn4.5Mg1 | 2.77 | 600–650 | 19–23 | 130–160 | 23.1 |
| 7022 | AlZn5Mg3Cu | AlZnMgCu0.5 | 2.78 | 485–640 | 19–23 | 130–160 | 23.6 |
| 7075 | AlZn5.5MgCu | AlZnMgCu1.5 | 2.80 | 480–640 | 19–23 | 130–160 | 23.4 |
| Casting alloys | | | | | | | |
| 44100 | AlSi12(b) | G-AlSi12 | 2.65 | 575–585 | 17–27 | 120–190 | 20 |
| 47000 | AlSi12(Cu) | G-AlSi12(Cu) | 2.65 | 570–585 | 16–23 | 110–160 | 20 |
| 43000 | AlSi10Mg(a) | G-AlSi10Mg | 2.65 | 575–620 | 17–26 | 120–180 | 20 |
| 43200 | AlSi10Mg(Cu) | G-AlSi10Mg(Cu) | 2.65 | 570–620 | 16–20 | 110–140 | 20 |
| 42000 | AlSi7Mg | G-AlSi7Mg | 2.70 | 550–625 | 21–32 | 150–220 | 22 |
| 51000 | AlMg3(b) | G-AlMg3 | 2.70 | 580–650 | 16–24 | 110–170 | 23 |
| 51300 | AlMg5 | G-AlMg5 | 2.60 | 560–630 | 15–22 | 100–160 | 23 |
| 51400 | AlMg5(Si) | G-AlMg5Si | 2.60 | 560–630 | 16–21 | 110–150 | 23 |
| 51200 | AlMg9 | GD-AlMg9 | 2.60 | 510–620 | 11–15 | 80–110 | 24 |
| 46200 | AlSi8Cu3 | G-AlSi8Cu3 | 2.75 | 510–610 | 14–18 | 100–130 | 22 |
| 45000 | AlSi6Cu4 | G-AlSi6Cu4 | 2.75 | 510–620 | 15–18 | 110–130 | 22 |
| 21100 | AlCu4Ti | G-AlCu4Ti | 2.75 | 550–640 | 16–20 | 110–140 | 23 |
| 21000 | AlCu4MgTi | G-AlCu4TiMg | 2.75 | 540–640 | 16–20 | 110–140 | 23 |

^a The actual values will depend on the material composition within the permitted range; electrical and thermal conductivity will also depend on the material structure

^b Where a eutectic structure is expected to form because of segregation, this will solidify at the lowest temperature given

Table 3.1-15 Linear coefficient of thermal expansion of some Al alloys for different ranges of temperature [1.9]

| Designation (according to EN 573.3 and EN 1706) | | Average coefficient of linear expansion (10 ⁻⁶ K ⁻¹), for the range | | | |
|--|-----------|--|--------------|--------------|--------------|
| | | -50 to 20 °C | 20 to 100 °C | 20 to 200 °C | 20 to 300 °C |
| 1098 | Al99.98 | 21.8 | 23.6 | 24.5 | 25.5 |
| 1050A | Al99.5 | 21.7 | 23.5 | 24.4 | 25.4 |
| 3003 | AlMn1Cu | 21.5 | 23.2 | 24.1 | 25.2 |
| 3004 | AlMn1Mg1 | 21.5 | 23.2 | 24.1 | 25.1 |
| 5005A | AlMg1(C) | 21.8 | 23.6 | 24.5 | 25.5 |
| 5019 | AlMg5 | 22.5 | 24.1 | 25.1 | 26.1 |
| 5474 | AlMg3Mn | 21.9 | 23.7 | 24.6 | 25.6 |
| 6060 | AlMgSi0.5 | 21.8 | 23.4 | 24.5 | 25.6 |
| 2011 | AlCu6BiPb | 21.4 | 23.1 | 24.0 | 25.0 |
| 44100 | AlSi12(b) | — | 20.0 | 21.0 | 22.0 |

only small changes in the coefficient of thermal expansion (Tables 3.1-14 and 3.1-15). Si additions with 1.2% reduction in the coefficient of thermal expansion for each wt% Si have the greatest effect of the alloying elements commonly used. This effect is applied to the manufacture of piston alloys.

Specific Heat. The specific heat of aluminium in the solid state increases continuously from 0 at 0 K to a maximum at the melting point. This is only the case with alloys when there are no solid state reactions. The effect of alloying elements in solution is not very marked.

Elastic Properties. The Young's modulus of Al and its alloys is usually taken to be about 70 GPa. Values given in the literature for aluminium of all grades of purity and aluminium alloys range from about 60 GPa to 78 GPa. Unalloyed and low-alloyed materials are found in the lower part of the range. The age-hardenable alloys are in the middle to upper part. The Young's modulus is dependent on texture, because the elastic anisotropy as expressed by the ratio of the elastic moduli for single crystals with [111] and [100] orientations is 1.17. Furthermore, there is a marked effect of cold working and test temperature (Fig. 3.1-51).

Electrical Conductivity. The electrical conductivity is influenced largely by alloying or impurities and the

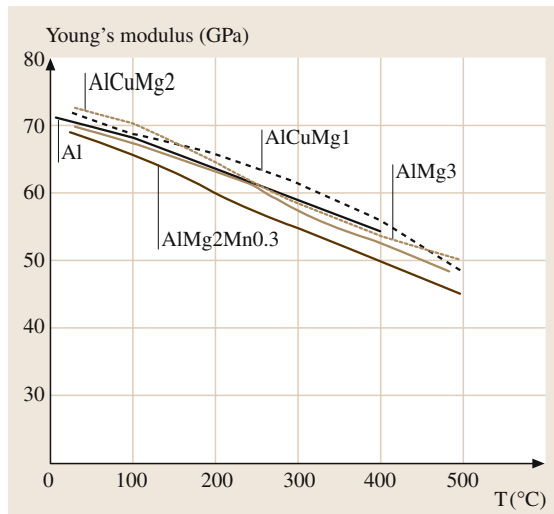


Fig. 3.1-51 Dependence of Young's modulus E of different Al alloys on temperature; determined using 9 mm thick plate [1.32]

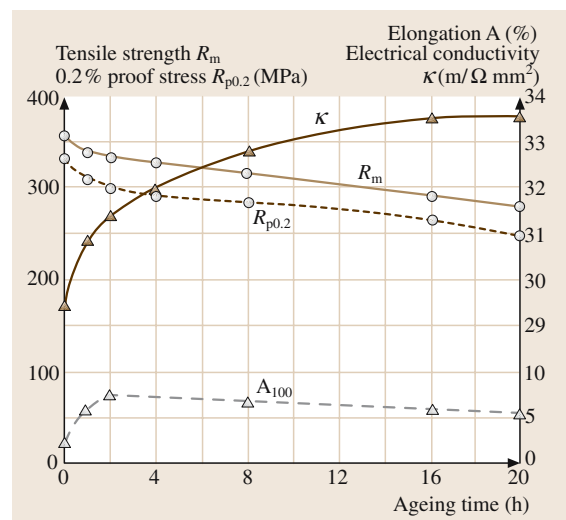


Fig. 3.1-52 Changes in the mechanical properties and electrical conductivity of electrical grade E-AlMgSi (\approx 6101) alloy wire during artificial ageing at 160°C; solution treated at 525°C, water quenched, naturally aged for 14 days, 95% cold-worked and then artificially aged [1.14]

structure. Elements present in solid solution lead to a greater reduction in electrical conductivity than precipitates (Figs. 3.1-7 and 3.1-8). By use of a suitable combination of heat treatment and cold working, it is possible to obtain microstructures with an adequate combination of tensile strength and electrical conductivity. This is shown in Fig. 3.1-52, using E-AlMgSi wire as an example.

Behavior in Magnetic Fields. Aluminium is weakly paramagnetic. The specific susceptibility of Al and its alloys is about $7.7 \times 10^{-9} \text{ m}^3 \text{ kg}^{-1}$ at room temperature.

Nuclear Properties. Thanks to its small absorption cross section for thermal neutrons, aluminium is often used in reactor components requiring low neutron absorption.

Optical Properties. The integral reflection is almost independent of the technical brightening process applied, but it depends on the purity of the metal. It is 84–85% for high-purity aluminium Al99.99 and 83–84% for unalloyed aluminium Al99.9. Higher amounts of diffuse reflection can be obtained by mechanical or chemical pre-treatment, such as sand blasting or strong pickling before brightening.

3.1.2.10 Thermal and Mechanical Treatment

Thermal and mechanical treatments have a great influence on the properties of aluminium and its alloys. Moreover these treatments influence some physical properties, for example the electrical conductivity. Thus these treatments are used to obtain a material with an optimum of properties required.

Work Hardening

Strengthening by work hardening can be achieved by both cold- and warm working. Figures 3.1-53–3.1-56 illustrate the effect of cold working. During hot working, strengthening and softening processes occur simultaneously; with aluminium-based materials, this will be above about 150–200 °C. Therefore hardness decreases with increasing hot-working temperature (Fig. 3.1-57). The formation of subgrains occurs in the microstructure; their size increases with increasing rolling temperature. Alloying atoms, such as Mg, impede growth or coarsening of the subgrains.

Thermal Softening

Figures 3.1-57a and 3.1-57b show typical softening curves for aluminium alloys in three characteristic stages: recovery, recrystallization, and grain-growth. In the case of the untreated continuously cast and rolled strip shown in Fig. 3.1-57a, recrystallization will occur at temperatures between about 260 and 290 °C. In Fig. 3.1-57b, recrystallization starts after about half an hour and is complete after about an hour. The

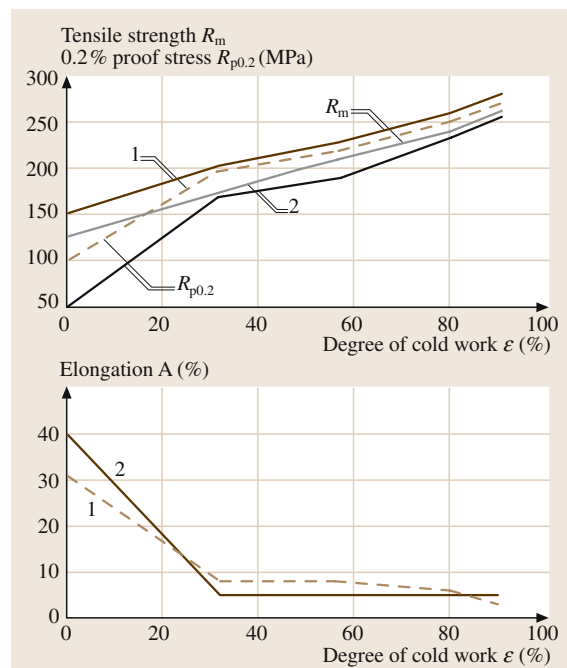


Fig. 3.1-54 Typical mechanical properties of (1) continuously cast and rolled strip and (2) strip produced conventionally by hot-rolling and then cold-rolling cast billets of AlMn1 (3103) [1.34]

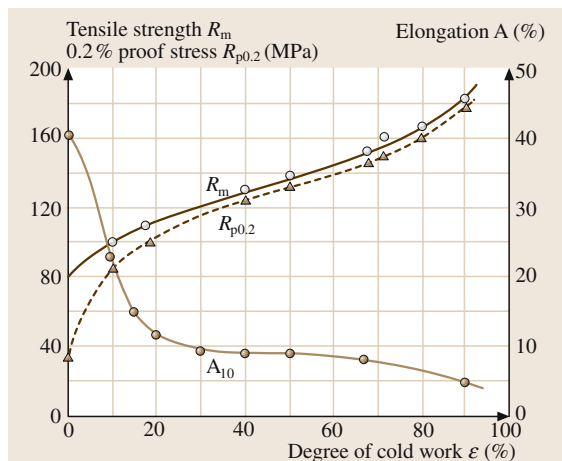


Fig. 3.1-53 Hardening of Al99.5 strip (0.15 wt% Si, 0.28 wt% Fe) after recrystallization annealing and subsequent cold-rolling [1.33]

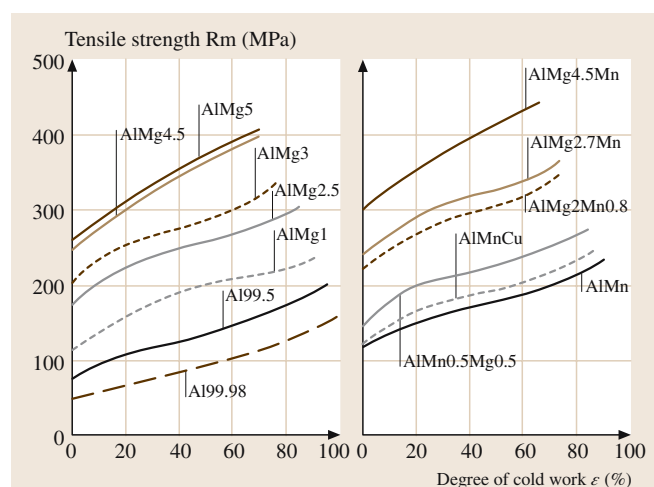


Fig. 3.1-55 Tensile strength of various wrought non-age-hardenable aluminium alloys as a function of the degree of cold work [1.33]: AlMg4.5 – 5082; AlMg5 – 5019; AlMg3 – 5754; AlMg2.5 – 5052; AlMg1 – 5005; Al99.5 – 1050A; Al99.8 – 1080°; AlMg4.5Mn – 5083; AlMg2.7Mn – 5454; AlMg2Mn0.8 – 5049; AlMn0.5Mg0.5 – 3105; AlMn – 3103; AlMnCu – 3003

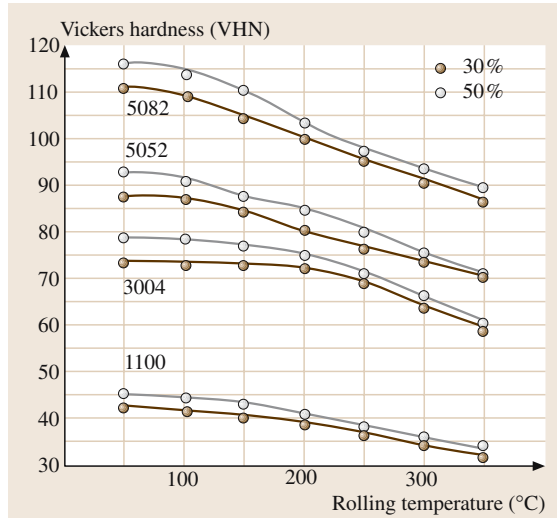


Fig. 3.1-56 Effect of rolling temperature on hardness; specimens quenched after hot-rolling: Al99.0Cu – 1100; AlMn1Mg2 – 3004; AlMg2.5 – 5052; AlMg4.5 – 5082

softening curves depend not only on the alloy composition but also on the degree of prior cold working to a marked extent. Further factors are the content of alloying and impurity elements, annealing time, heating rate, the microstructure prior to deformation and prior thermomechanical treatment, which can also include the casting process used to produce the starting material.

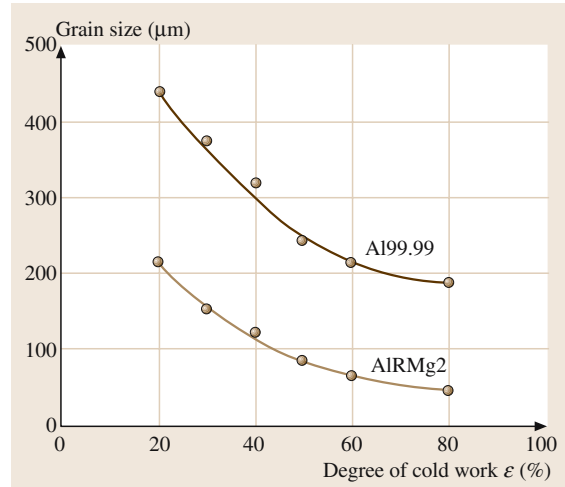


Fig. 3.1-58 Grain size after complete recrystallization of Al99.99 and AlRMg2 as a function of degree of cold work (annealed at 350 to 415 °C until complete recrystallization) [1.9]

The softening due to recovery or partial recrystallization is very important when producing semi-finished products of medium hardness (e.g., half hard). The relationship between the degree of cold work and grain size is apparent in Fig. 3.1-58. If the degree of cold work is below a critical value, no recrystallization will occur. This threshold depends on material and prior thermo-

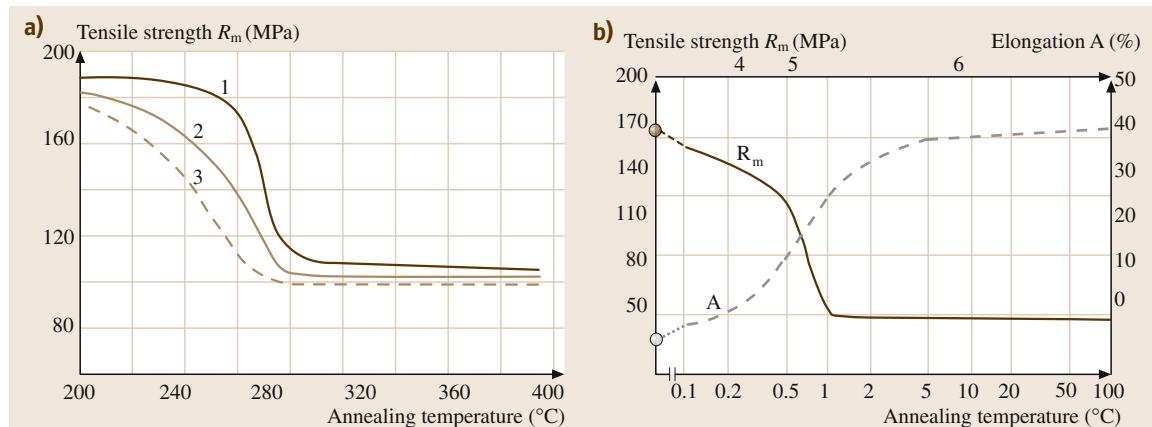


Fig. 3.1-57a,b Typical softening curves for cold-rolled Al99.5 [1.35, 36]. (a) Recrystallization after different initial temperatures to 90% cold work and subsequent annealing for 1 h at different temperatures: (1) Continuously cast and rolled strip, subsequently cold-worked without an intermediate annealing treatment; (2) as 1 but with an intermediate annealing treatment for 1 h at 580 °C; (3) Strip conventionally produced using permanent mould casting and hot-rolling. (b) Continuously cast and rolled strip, cold-worked 90% and then annealed at 320 °C for time shown: (4) Recovery; (5) Recrystallization; (6) Grain growth

mechanical treatment, and is about 2–15%. If the degree of cold work is near the critical value, coarse grains can form during recrystallization, as clearly shown in the three-dimensional diagram in Fig. 3.1-59.

Other elements can affect the recrystallization temperature and the grain size after recrystallization. Mg does not have a marked effect (Fig. 3.1-60), while Mn, Fe, Cr, Ti, V, and Zr increase the recrystallization temperature (Fig. 3.1-61 delaying effect = plateau).

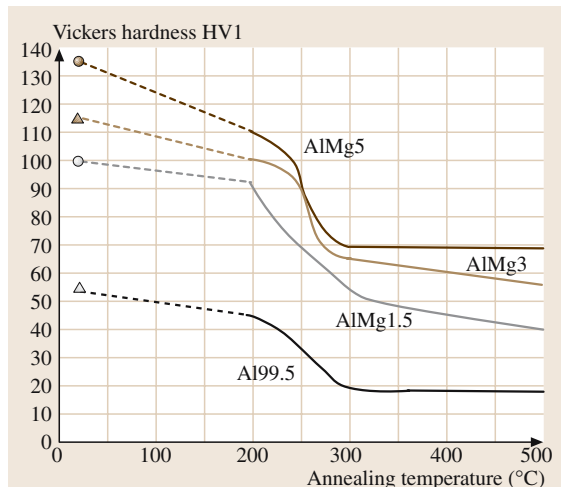


Fig. 3.1-60 Effect of Al–Mg alloy composition on the softening behavior; the material was 90% cold-worked and annealed for 1 h at temperature shown [1.36]

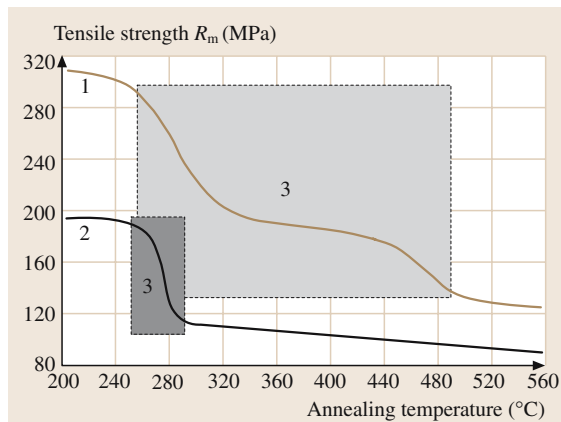


Fig. 3.1-61 Comparison of softening curves for cast and hot-rolled Al99.5 and AlMn1 strip; material cold-worked 90% and annealed for 1 h at the temperature shown [1.36]: (1) Cast and hot-rolled AlMn1 (3103) strip; (2) Cast and hot-rolled Al99.5 (1050A) strip; (3) Recrystallization range

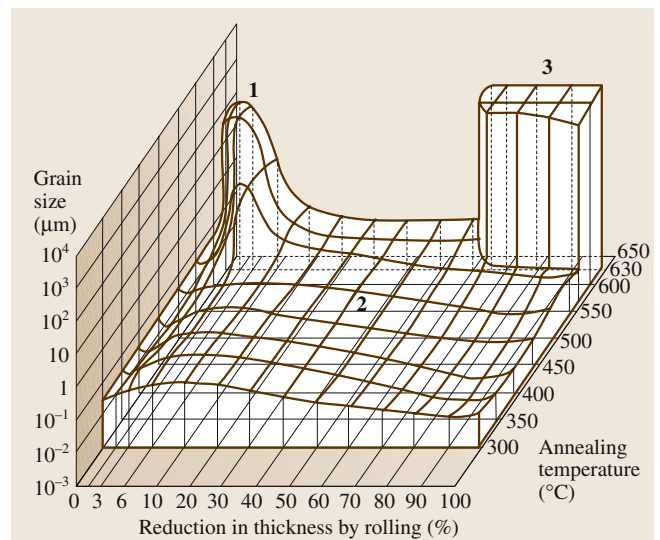


Fig. 3.1-59 Recrystallization diagram showing grain size of Al99.6 (1060) as a function of cold work and annealing for 2 h at the temperatures shown [1.9]: (1) Coarse grains in the region of critical degree of cold work (primary recrystallization); (2) Area of primary recrystallization with fine and medium-sized grains, (3) Coarse grains as a result of secondary recrystallization

This is dependent on the amount and distribution of these elements, i.e., whether they are present as precipitates or in supersaturated solid solution, and/or whether they form intermetallic phases. In Fig. 3.1-62 it is clearly apparent that solution treatment reduces the degree of supersaturation and that the range over which tensile strength and 0.2% proof stress decrease rapidly with temperature is thus shifted to significantly lower temperatures. Interactions between the various elements present can also affect recrystallization behavior.

Soft Annealing, Stabilization

With cold-worked materials, soft annealing consists of recrystallization annealing. The duration of the treatment, degree of cold work, and intermediate annealing treatments need to be selected with grain size in mind. In age-hardenable alloys, soft annealing permits most of the supersaturated components to precipitate out in coarse form or coherent or partially coherent phases to transform to incoherent stable phases. Soft annealing of casting alloys involves annealing the as-cast structure at 350 to 450 °C. With age-hardenable alloys, this is also possible using a solution treatment followed by furnace cooling

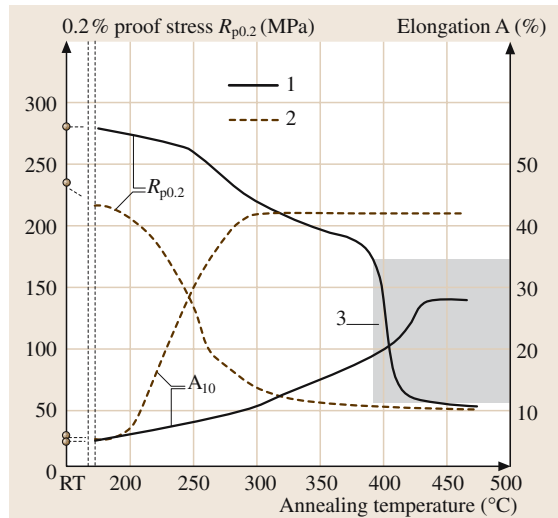


Fig. 3.1-62 Softening curves for continuously cast and rolled AlMn1 strip after annealing for 4 h at elevated temperatures [1.37,38]: (1) Untreated material, as-cast condition; (2) Homogenised at 540°C after cold working; (3) Coarse grains

or nonforced air cooling. Al–Mg alloys with more than 4 wt% Mg may have to be stabilized to produce a structure that is not susceptible to intergranular corrosion.

Stress-Relieving

The temperatures used for thermal stress relief are relatively low, i.e., at the lower end of the recovery range, or even lower, and between 200 and 300 °C for non-age-hardenable alloy castings, otherwise there will be an unacceptably large loss of strength.

Table 3.1-16 Conditions for aging treatments ^a

| Alloy | Annealing Temperature ^b (°C) | Quenching medium | Natural aging time (d) | Artificial aging Temperature (°C) | Time (h) |
|-----------|---|-------------------|------------------------|-----------------------------------|-------------------------------|
| E-AlMgSi | 525–540 | Water | 5–8 | 155–190 | 4–16 |
| AlMgSi0.5 | 525–540 | Air/water | 5–8 | 155–190 | 4–16 |
| AlMgSi1 | 525–540 | Water/air | 5–8 | 155–190 | 4–16 |
| AlMg1SiCu | 525–540 | Water/air | 5–8 | 155–190 | 4–16 |
| AlCuBiPb | 515–525 | Water up to 65 °C | 5–8 | 165–185 | 8–16 |
| AlCuMg1 | 495–505 | Water | 5–8 | d | 4 ^d |
| AlCuMg2 | 495–505 | Water | | 180–195 ^d | 16–24 ^d |
| AlZn4.5Mg | 460–485 | Air At least | 90 | I 90–100/ II 140–160 ^c | I 8–12/ II 16–24 ^c |

^a Recommendations only; exact specification as per agreement with semi-finishing plant

^b Metal temperature

^c Stages I and II of step annealing

^d Usually only naturally aged

Homogenization

This treatment is used for the elimination of residual casting stresses and segregation, for dissolution of eutectoid components at grain boundaries, or for producing a more uniform precipitation of supersaturated elements (e.g., Mn and Fe). Additionally, the elements which are responsible for hardening in age-hardenable alloys are taken into solid solution. A homogenization is carried out at temperatures which are composition-dependent and close to the solidus temperature of the alloy in question. Long exposure times are required, typically about 10–12 hr but possibly even longer, depending on the relevant diffusion coefficients and microstructure.

Aging

Age hardening treatments require the three steps of solution treatment, quenching, and aging (Fig. 3.1-63). The purpose of solution treatment is to produce a homogeneous α -Al solid solution. The annealing temperature is determined by the relevant phase. It should be as high as possible in order to avoid excessively long annealing times, but lower than the solidus of α and the melting point of the lowest melting phase (Table 3.1-16). It should be noted that segregation effects tend to displace the effective phase boundaries to lower temperatures and incipient melting may occur. In addition, the effect of the selected solution treatment temperature on strength levels attained after aging will vary with alloy (Figs. 3.1-64 and 3.1-65). The annealing time depends

Fig. 3.1-64 Effect of solution treatment temperature on the tensile strength of wrought aluminium alloys [1.9]: AlZnMgCu1.5 (\approx 7075, AlZn5.5MgCu), 24 h at 120 °C; AlCuMg1 [\approx 2017A, AlCu4MgSi(A)], 5 days at room temperature; AlZn4.5Mg1 7020, (\approx AlZn4.5Mhg1), 1 month at room temperature; AlMgSi1 (\approx 6082, AlSi1MgMn), 16 h at 160 °C ►

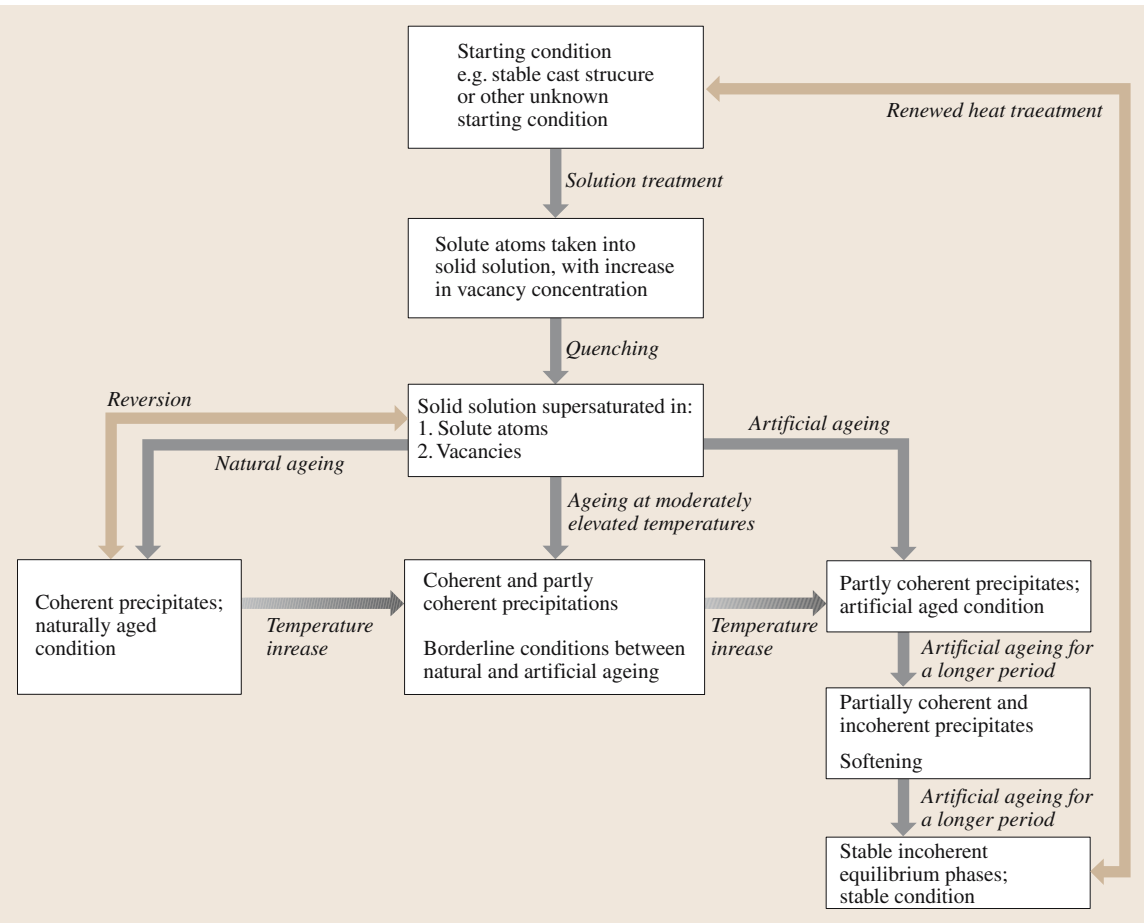


Fig. 3.1-63 Schematic of the age hardening process

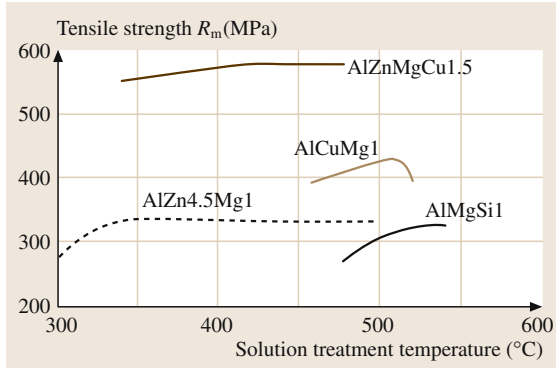
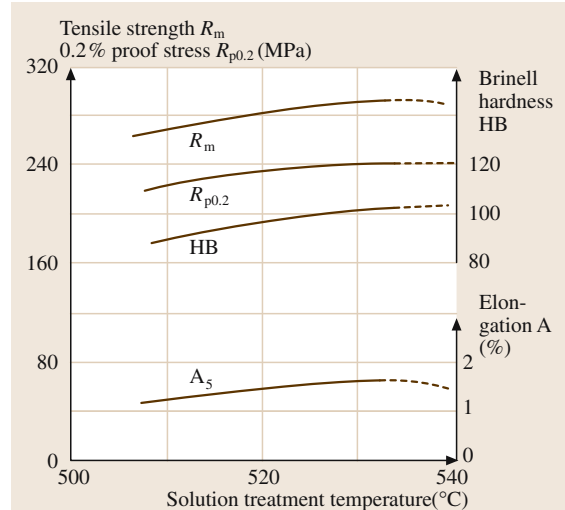


Fig. 3.1-65 Effect of solution treatment temperature on the mechanical properties of G-AlSi10Mg casting alloy after subsequent aging [$\approx 43\,000$, AlSi10Mg(a)] [1.9] ►



mainly on the initial condition of the semi-finished material, type of semi-finished product, and the wall thickness (Figs. 3.1-66 and 3.1-67).

During quenching, it is important to pass through the temperature range around 200 °C as quickly as pos-

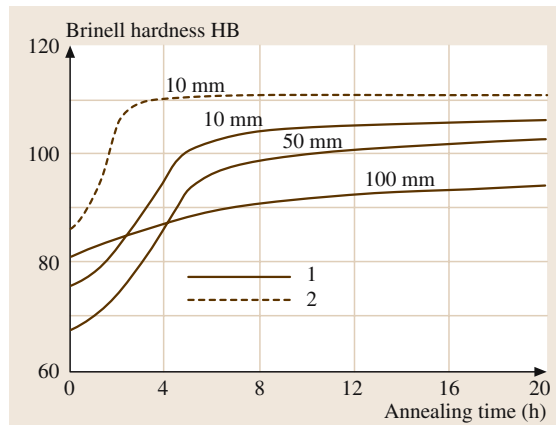


Fig. 3.1-66 Effect of annealing time on the hardness of artificially aged G-AlSi10Mg casting alloy for different casting techniques and specimen diameters [1.9]: (1) Sand cast; (2) Permanent mould cast

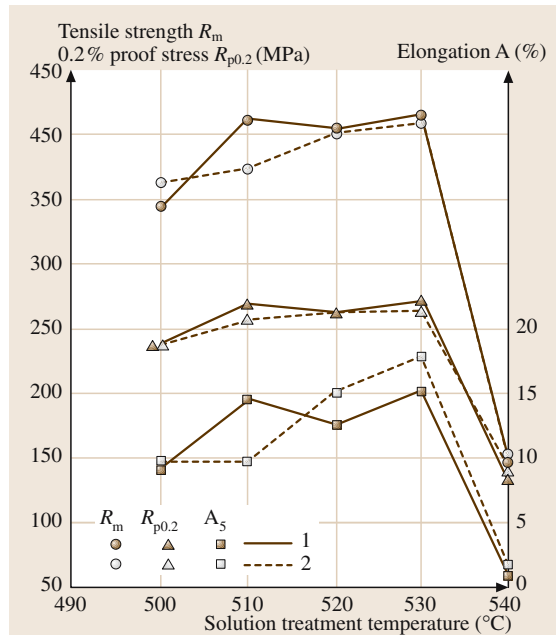


Fig. 3.1-67 Dependence of mechanical properties of naturally aged G-AlCu4TiMg casting alloy on the maximum solution treatment temperature: (1) Step annealing; (2) Single step annealing

sible, in order to prevent premature precipitation of the elements in supersaturated solid solution.

Some alloys require high cooling rates, such as those obtained by quenching in water. For others, especially with thinner sections, cooling in a forced draft of air or a mist spray suffices. In this case, quenching takes place immediately after hot working or even directly in the extrusion press. With most alloys it is important that the annealed material is rapidly transferred to the quenching bath as any delay (incipient cooling) can have a detrimental effect on strength and corrosion resistance.

After the first two stages of the hardening process, the solid solution will be supersaturated in both vacancies and solute atoms. It will tend to attain equilibrium conditions by precipitation of the supersaturated solute atoms. As the process is both temperature- and time-dependent, precipitation is basically possible either by natural or artificial aging, i.e., at room or elevated temperature respectively.

Aging at room temperature, or slightly elevated temperature, is accompanied by the formation of metastable Guinier-Preston zones (GP zones). These metastable phases increase the strength by differing amounts depending on their type, size, volume fraction, and distribution. With fully coherent precipitates, the crystal lattice is strongly strained locally, resulting in a marked increase in hardness and strength, while ductility and electrical conductivity decreases (Figs. 3.1-68 and 3.1-69).

At higher aging temperatures of about 100 °C to 200 °C, metastable phases form that are partially coherent. The local coherency strain is less pronounced

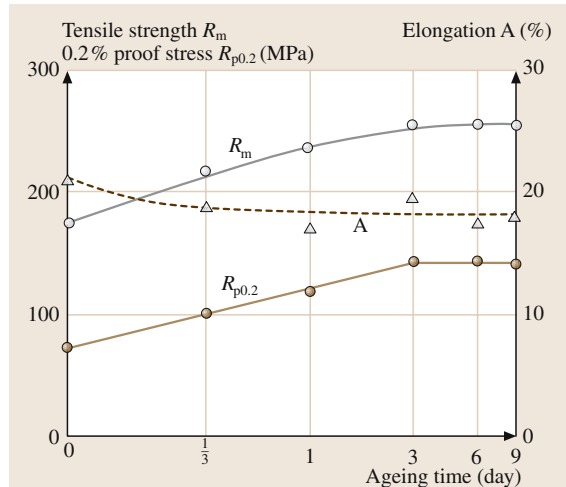


Fig. 3.1-68 Natural aging of AlMgSi1 alloy [1.39]

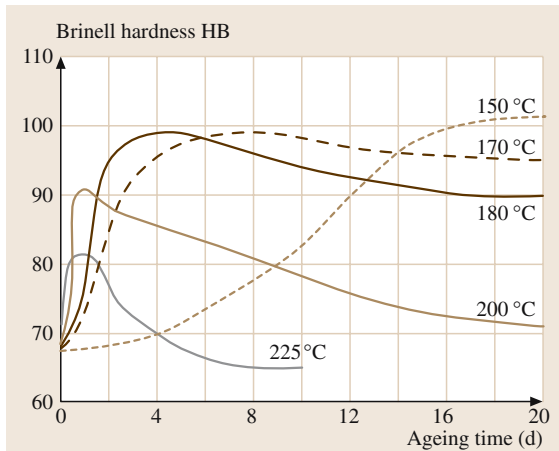


Fig. 3.1-69 Artificial aging of G-AlSi10Mg casting alloy [1.9]

because the stresses are partly reduced by the formation of interfacial dislocations. This would lead to a lower increase in strength in principle. However, since the particle size of the metastable phases formed in this range is often larger than that of the coherent phases which result from natural aging, there is a marked increase in strength (Figs. 3.1-70 and 3.1-71).

Higher temperatures and longer aging times lead to the formation of incoherent equilibrium phases (e.g., Al_2Cu , Mg_2Si , and MgZn_2) and there is a reduction in the hardening effect. This is called over-aging.

Effects of Plastic Deformation on Age-Hardening Behavior

For wrought age-hardenable aluminium alloys, the combination of heat treatments with hot and/or cold working (thermo-mechanical treatment) is of great practical significance. It can be a method to obtain a better combination of mechanical properties, such as moderate ductility and higher strength. The effects of thermo-mechanical treatments can be attributed to the fact that all processes occurring during heat treatment are influenced by the concentration of defects introduced during working. It is not necessary to carry out both steps simultaneously; the heat treatment can be carried out after forming [1.40]. As far as precipitation is concerned, lattice defects facilitate diffusion and at the same time act as nucleation sites. Thus, by deforming a material by a certain amount *prior* to aging and thereby obtaining the desired defect concentration, one can influence the size, quantity and distribution of the precipitates that form subsequently. It is important, however, that the

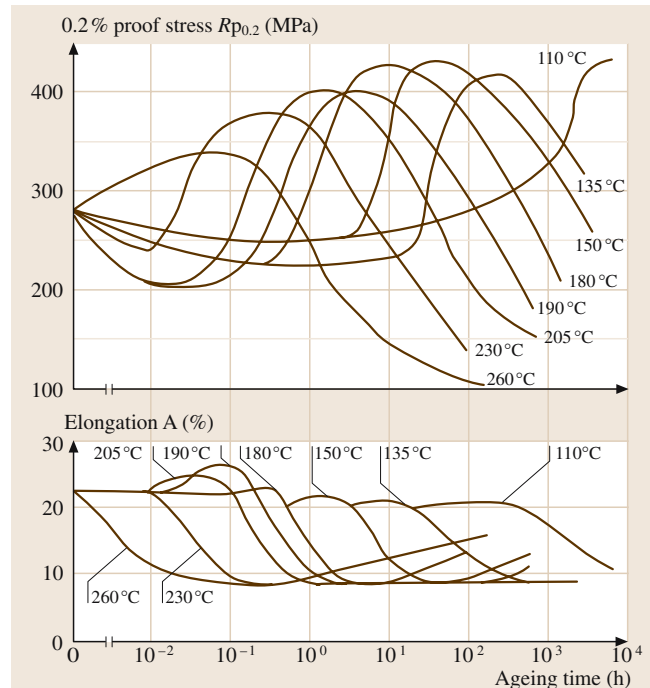


Fig. 3.1-70 Artificial aging curves for AlCuSiMn alloy [1.9]

final ageing treatment is carried out at a temperature below the recrystallization temperature, as the lattice defect concentration that is generated is fully effective only then.

Controlled hot working, often in combination with additional heat treatments, is another form of thermo-mechanical treatment and is used to improve fracture toughness, creep strength and fatigue strength. One tries to obtain a suitable recrystallized grain size and an optimum distribution of lattice defects and precipitates. Such treatments are very often used with high strength Al-Zn-Mg-Cu alloys. They usually consist of a series of solution treatments with controlled cooling and hot-rolling under well defined conditions. Cold working carried out between the various stages of a step-aging treatment is also referred to as thermomechanical treatment. Examples are shown in Fig. 3.1-72 and Fig. 3.1-73.

Simultaneous Softening and Precipitation

One of the factors that influence the softening of an alloy is the possible supersaturation by alloying of impurity elements. Supersaturation can be achieved deliberately, e.g., by solution treatment and subsequent quenching, or, as is often the case, it may be the result of rapid cool-

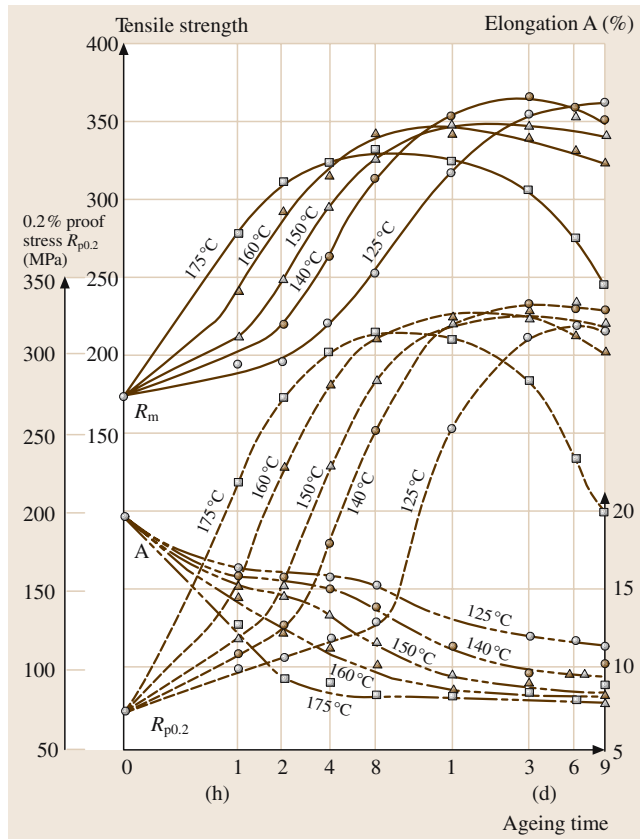


Fig. 3.1-71 Artificial aging curves for AlMgSi1 alloy after solution treatment at 520 °C and water quenching

ing, e.g., of castings. If such a supersaturated material is cold-worked and then aged, it reveals markedly different softening behavior because solute atom clusters or precipitates are formed during recovery at lattice defects in the deformed or recovered structure which pin lattice defects and the formation of solute atom clusters or of precipitates during recrystallization at the recrystallization front, which pin down the recrystallization front. There is a slowing down of the softening process as a result of these pinning effects (Figs. 3.1-74a and 3.1-74b).

The Stage III area in Fig. 3.1-74b is of particular interest, as by definition this is a thermomechanical treatment because the lattice defects introduced by working are fully effective during the formation of the precipitates. Dislocations, which are present in large quantities, act as nuclei for precipitation and this results in the formation of numerous finely-dispersed precipitates. These impair subsequent recrystallization at every stage – the

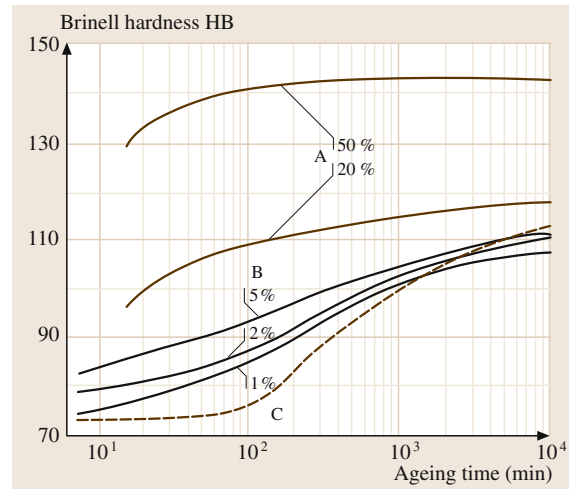


Fig. 3.1-72 Effect of cold work on the natural aging of AlCuMg1 (2017A) [1.9]; A – Rolled; B – Stretched; C – Without cold work

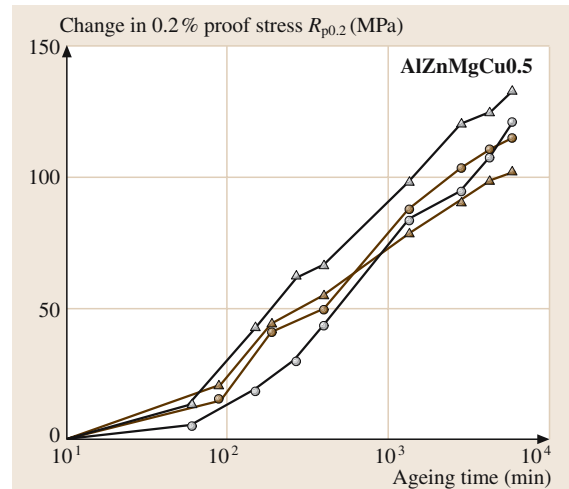


Fig. 3.1-73 Changes in the 0.2% proof stress during natural aging of 0.5 mm diameter wire specimens AlZnMgCu0.5 (7022) alloys after different degrees of cold working. The alloys were first solution-treated at 490 °C and then immediately subjected to cold working as indicated below [1.41]

formation of recrystallization nuclei, the moving of boundaries and the subsequent grain growth. These effects increase the thermal resistance and delay the loss of strength that occurs after prolonged exposure because of grain growth. The Figs. 3.1-77 to 3.1-79 show some examples of TTT-Diagrams for unalloyed aluminium and for alloys.

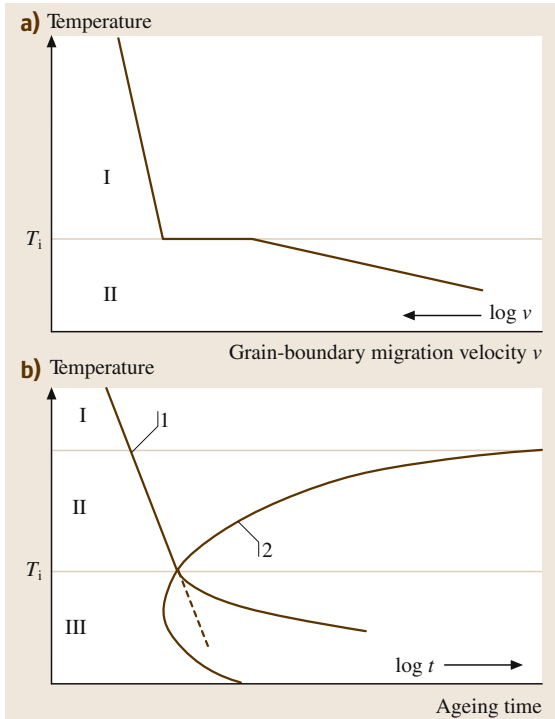


Fig. 3.1-74a,b Effect of segregation and precipitation on recrystallization (grain-boundary migration): (1) Start of recrystallization; (2) Start of precipitation. **(a)** Basic effects of solute atom clusters on the grain boundary migration velocity [1.42]. Region I, high temperatures: The grain boundary migration velocity is only weakly dependent on temperature because it is unaffected by the clustering (\rightarrow high velocity). Region II: Below T_i , the mobility of the boundaries is reduced because atom clusters have to be dragged along by the boundary, and the diffusion rate of these atoms determines the migration velocity of the boundary (\rightarrow low velocity). **(b)** Interrelationship between recrystallization and precipitation as TTT (time-temperature-transformation) diagram [1.43]. Region I: Recrystallization as a homogenous stable solid solution, unaffected by precipitation processes, i.e., at these temperatures there is no longer any supersaturation. Region II: Recrystallization in a supersaturated solid solution; the number of potential precipitation nuclei (dislocations) decreases. Result: Fewer but larger precipitations. Region III: Precipitation prior to recrystallization, or simultaneously (T_i) the precipitates delay recrystallization significantly

Fig. 3.1-77 TTT diagram for Al-0.5 wt% Fe-0.15 wt% Si alloy Harvey cast strip after 80% cold work [1.45] (1) Start of precipitation; (2) Recrystallization zone

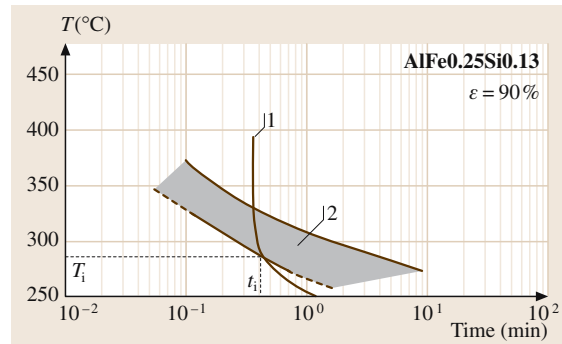


Fig. 3.1-75 TTT diagram for Al-0.25 wt% Fe-0.13 wt% Si alloy Hunter-Engineering cast strip after 90% cold work [1.35]. (1) First signs of precipitation; (2) Recrystallization zone

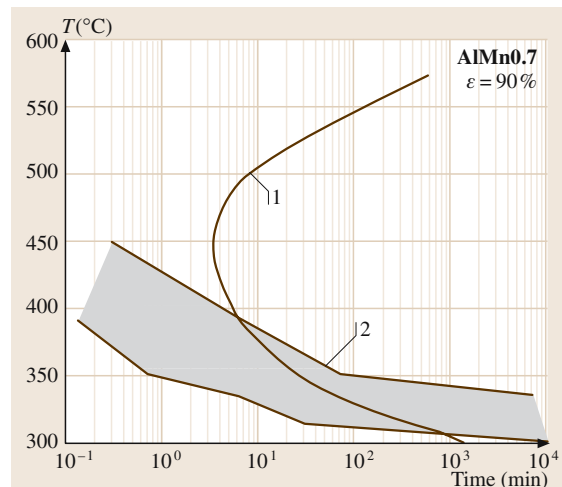
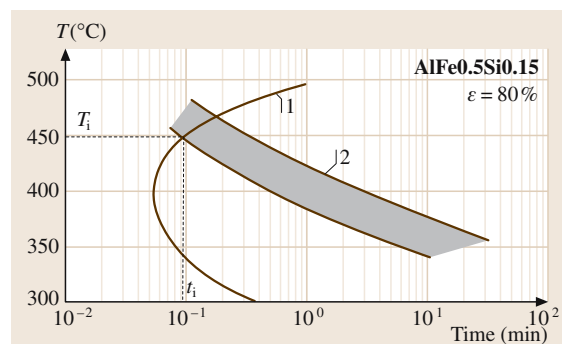


Fig. 3.1-76 TTT diagram showing precipitation and recrystallization in 90% cold-rolled, high-purity AlMn0.7 alloy, strip produced by permanent mould casting, hot-rolling, and then cold-rolling [1.44]. (1) Start of precipitation; (2) Recrystallization zone



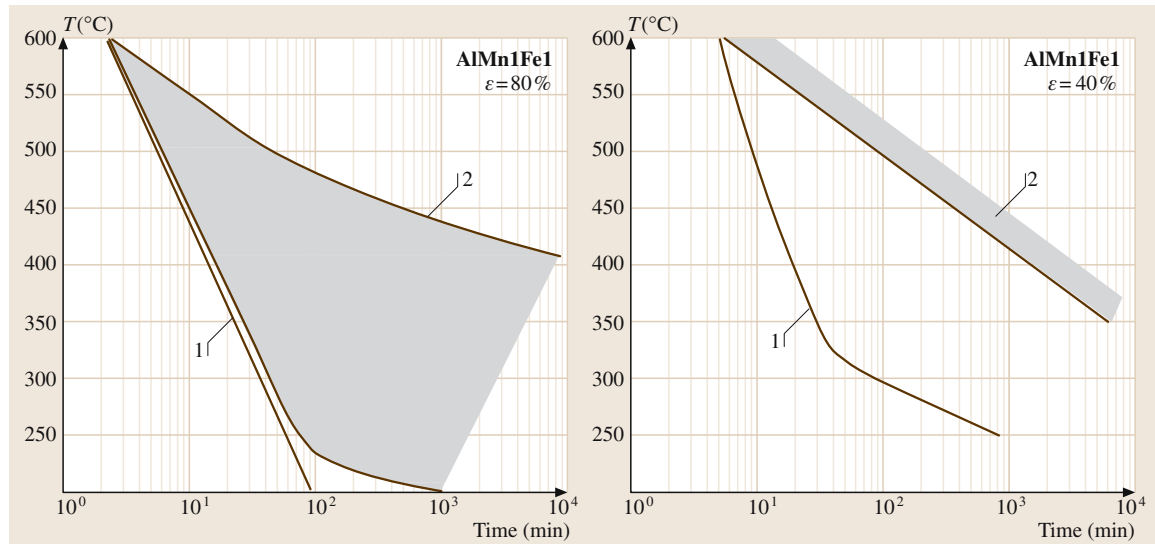
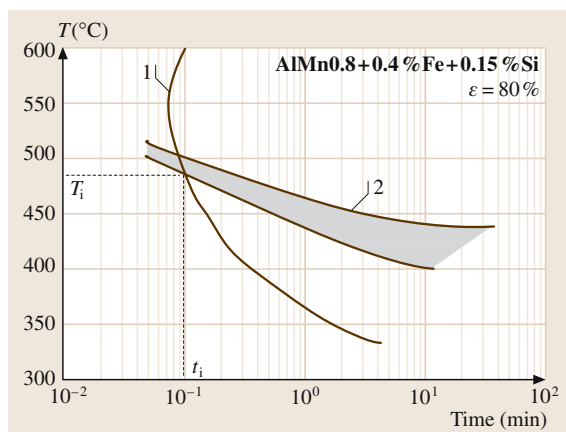


Fig. 3.1-79a,b TTT diagrams for precipitation and recrystallization in commercially pure AlMn1Fe1 (0.16 wt% Si), Hunter-Engineering cast strip after varying degrees of cold-rolling [1.49]. (1) Start of precipitation; (2) Recrystallization zone. (a) 90%. (b) 40%



3.1.2.11 Corrosion Behavior of Aluminium

From a thermodynamic point of view, aluminium would have to react with water to form hydrogen. However, Al and Al alloys have proven to be very corrosion-resistant in a wide range of practical applications. This corrosion resistance is attributable to the reaction of Al with oxygen or water vapor and the formation of a thin but compact natural oxide film when it is exposed to air, i. e. Al is passivated. In contrast to the oxide layers formed on many other materials, this oxide layer is strongly adherent and thus protects the underlying metal against further oxidation. This property explains the good re-

Fig. 3.1-78 TTT diagram showing precipitation and recrystallization in commercially pure AlMn0.8 alloy strip (0.4 wt% Fe and 0.15 wt% Si) produced by strip casting and 85% cold-rolled [1.46–48]. (1) Start of precipitation; (2) Recrystallization zone

sistance of aluminium when exposed to the weather or a large number of organic and inorganic substances. The corrosion resistance can be increased further by various surface treatments.

Aluminium and all standardized aluminium alloys are non-toxic. Aluminium products are easy to clean, can be sterilized and meet all hygienic and antitoxic requirements.

Surface Layers

Aluminium and Al alloys react with oxygen and water vapor in the air to produce a thin, compact surface oxide film which protects the underlying metal from further attack (Fig. 3.1-80). The surface layer contains mainly amorphous Al_2O_3 in several layers. The so-called barrier layer has an extremely low conductivity for electrons and ions and thus acts as an insulator in any interfacial electrochemical reactions. It thus affords effective protection against corrosion. If mechanical damage of the protective layer occurs, or if the layer is removed by pickling, it re-forms immediately. Aluminium and Al alloys thus exhibit good corrosion resistance to chemicals, seawater, and the weather.

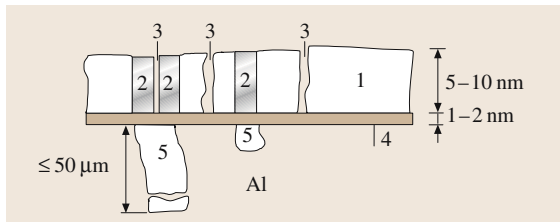


Fig. 3.1-80 Schematic representation of the structure of the oxide film formed on unalloyed aluminium in dry air; the total thickness is typically 0.005 to 0.02 mm [1.50]. Al = Aluminium; 1 = Surface layer; 2 = Mixed oxides; 3 = Pores; 4 = Barrier layer; 5 = Heterogeneous components

The oxide film which forms on bare aluminium in dry air at room temperature grows to a thickness of a few μm in a few minutes. It then grows to about two or three times this thickness in a few days at a continuously decreasing rate, so-called self-protection. Higher temperatures, such as those during heat treatments, accelerate the rate of growth of the natural oxide layer and lead to the growth of thicker films (Fig. 3.1-81). In moist air, the oxide films grow rapidly at first but then more slowly, and they are markedly thicker than the films formed in dry air.

The composition of the atmosphere has a significant effect on the behavior of the oxide layer. The aggressiveness of the atmosphere is particularly dependent on the amounts of sulfur dioxide, sulfur trioxide, dust, soot, and salts present. Rain water hitting the surface and running off flushes away these substances and thus reduces their influence.

Tap water or natural waters cause growth of the outer layer on top of the barrier layer of the oxide. The growth will depend on the alloy composition, the nature of the water and temperature. In aggressive waters, especially those containing chlorides and heavy metals, pitting corrosion can occur if oxygen from the air or other oxidizing media are introduced into the water. Traces of Cu (from copper piping or fittings containing copper) are particularly aggressive. Copper ions enter the oxide layer on the aluminium surface via defects and precipitate out as metallic Cu. Copper then acts as a cathode in the resulting local galvanic element such that Al is dissolved anodically.

Corrosion

If Al is exposed to acids or bases these dissolve the oxide film. The pH value of the electrolyte strongly influences corrosion in aqueous media. The protective film on aluminium is practically insoluble in the pH range from 4.5

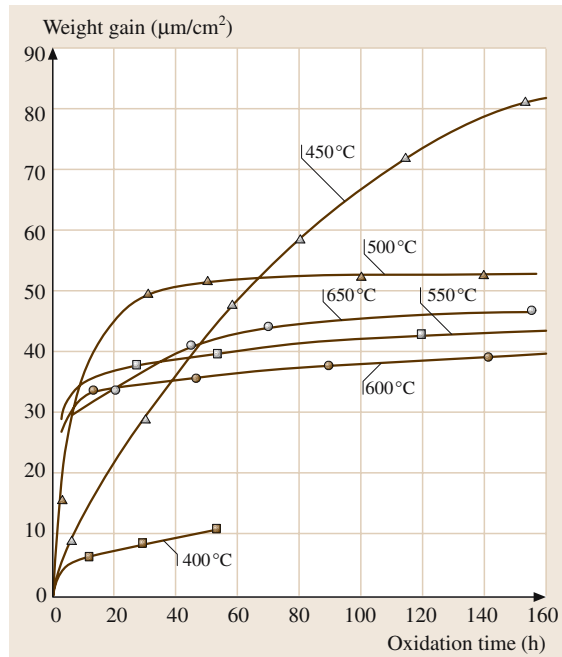


Fig. 3.1-81 Growth of the oxide film on super-purity aluminium in dry oxygen during the first 160 h [1.22]

to 8.5, which explains why aluminium is usually only used in this range.

Aluminium alloys have heterogeneous microstructural components such as intermetallic phases and resulting oxides in the surface and barrier layers. This explains why unalloyed aluminium and aluminium alloys have lower corrosion resistance than high-purity aluminium.

Apart from the effects of alloying and impurities, there are some other factors affecting corrosion, for example, changes in microstructure by thermal or mechanical treatments and ensuing changes of the surface condition.

Corrosion protection covers any measure aimed at modifying a corrosion system in order to mitigate corrosion damage. This can involve influencing the properties of the metal or the corrosive medium, or separating the metal from the medium by the use of protective layers. One can differentiate between active and passive measures. Passive measures, such as the use of organic polymer coatings (paints), will provide temporary protection, the level of which will depend on the nature, thickness, and quality of the layer. Active measures, such as the use of sacrificial magnesium or zinc anodes, offer long-term protection.

3.1.3 Titanium and Titanium Alloys

Titanium and its alloys are used as technical materials mainly because of the low density ($\rho = 4.5 \text{ g cm}^{-3}$) of Ti at technically useful levels of mechanical properties, and the formation of a passivating, protective oxide layer in air, which leads to a pronounced stability in corrosive media and at elevated temperatures. Further useful properties to be noted are its paramagnetic behavior, low temperature ductility, low thermal conductivity ($\kappa = 21 \text{ W m}^{-1} \text{ K}^{-1}$), low thermal expansion coefficient ($\lambda = 8.9 \times 10^{-6} \text{ K}^{-1}$), and its biocompatibility which is essentially due to its passivating oxide layer.

Five groups of materials based on Ti may be distinguished [1.51–53]: commercially pure (i.e., commercially available) Ti (cp-Ti), low-alloy Ti materials, Ti-base alloys, intermetallic Ti-Al materials, and highly alloyed functional materials: TiNi shape memory alloys, Nb-Ti superconducting materials (Sect. 4.2.1), and Ti-Fe-Mn materials for hydrogen storage.

Titanium undergoes a structural phase transformation at 882°C . Like in steels, this transformation is crucial for the microstructural design and the mechanical properties of Ti-based alloys. The low temperature phase α -Ti has an almost close packed hexagonal (A3) structure that is somewhat compressed along the c axis. Its

lattice parameters are $c = 0.4679 \text{ nm}$ and $a = 0.2951 \text{ nm}$ at room temperature. The high-temperature phase β -Ti has a body-centered cubic (A2) structure. The lattice parameter of β -Ti at room temperature can be obtained as $a = 0.3269 \text{ nm}$ by extrapolation from alloy solid solutions.

The binary phase diagrams of Ti [1.54] indicate that several interstitial components such as O, N, C, and H form extended solid solutions with α -Ti. As an example Fig. 3.1-82 shows the Ti-rich part of the Ti-O phase diagram. The high local lattice strains caused by the interstitial atoms lead to pronounced solid solution strengthening which is exploited, in particular, to harden commercially pure Ti by O additions. On average, the interstitials lead to a pronounced elongation of both the a and c axes of the α -Ti lattice, as shown in Fig. 3.1-83.

Figure 3.1-84 shows the influence of the concentration of residual impurity elements O, N, C, Fe, and Si on the increase of hardness HB.

Commercially pure grades of Ti, cp-Ti, are produced via the reduction of TiCl_4 by Mg (Kroll process). The product is Ti sponge. Table 3.1-17 gives typical concentration levels of the main impurity components and corresponding hardness values of the Ti sponge. Impu-

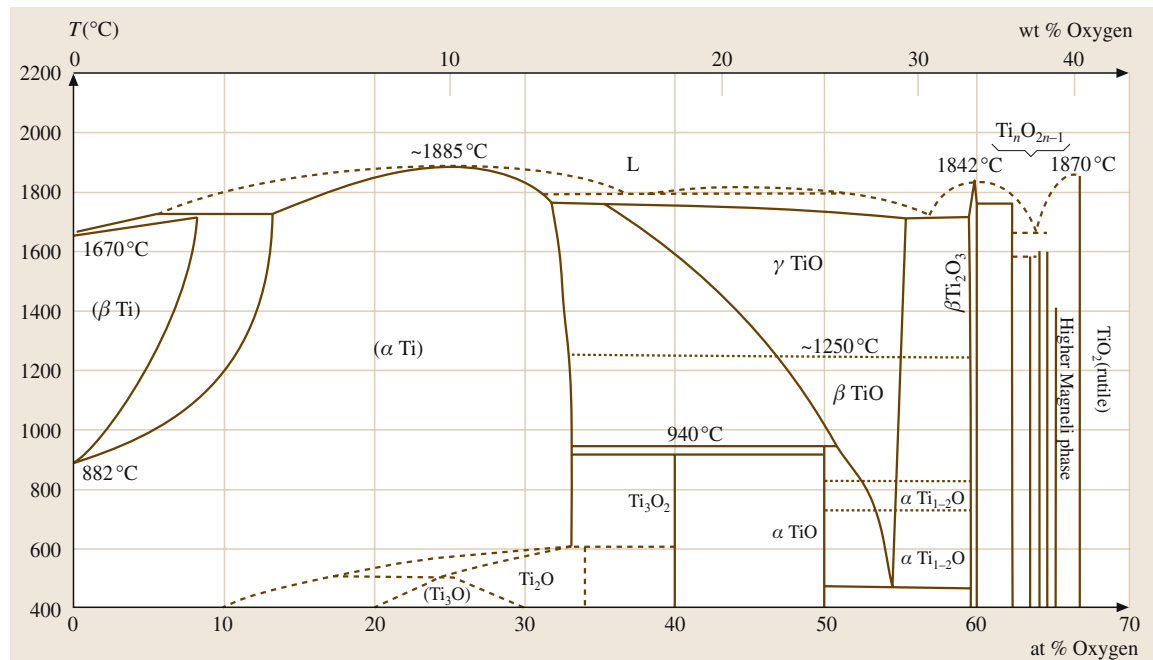
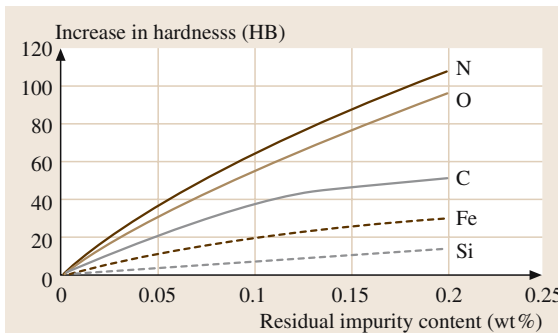


Fig. 3.1-82 Ti-O phase diagram

Table 3.1-17 Chemical composition of titanium sponge [1.53]

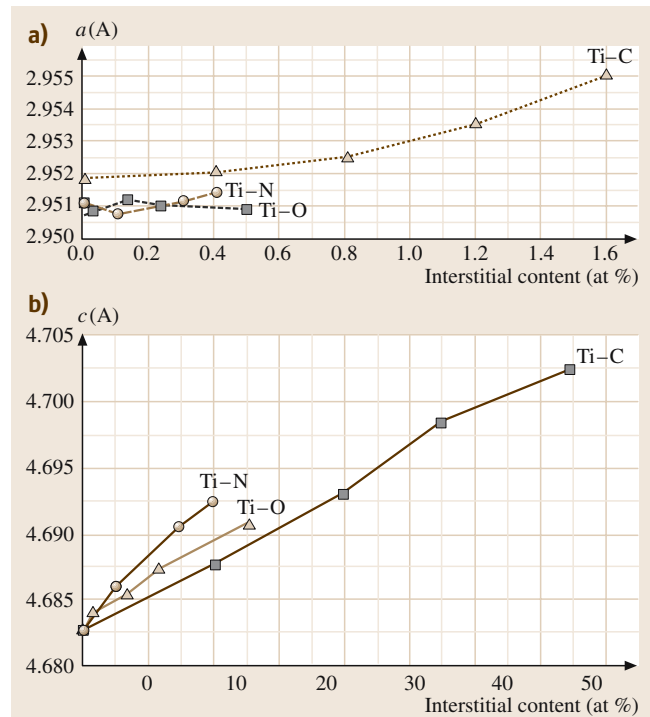
| Reduction process/ element | C | N | O | H | Fe | Mg | Na | Cl | Maximum hardness (HB) |
|-------------------------------|-------|-------|-------|-------|-------|------|------|------|-----------------------------|
| Magnesium | 0.006 | 0.003 | 0.045 | 0.002 | 0.02 | 0.03 | | 0.10 | 95 |
| | 0.008 | 0.005 | 0.05 | 0.002 | 0.04 | | | 0.09 | 100 |
| | 0.008 | 0.005 | 0.06 | 0.002 | 0.05 | 0.03 | | 0.08 | 110 |
| | 0.008 | 0.005 | 0.07 | 0.002 | 0.06 | 0.03 | | 0.09 | 120 |
| Sodium electrolysis | 0.009 | 0.004 | 0.07 | 0.01 | 0.016 | | 0.08 | 0.13 | 120 |
| | 0.003 | 0.002 | 0.01 | 0.003 | 0.001 | | | 0.08 | 60 |
| | 0.013 | 0.004 | 0.03 | 0.004 | 0.004 | | | 0.09 | 75 |
| | 0.018 | 0.004 | 0.04 | 0.004 | 0.020 | | | 0.16 | 90 |

**Fig. 3.1-84** Increase of hardness HB of Ti as a function of concentration of residual impurities O, N, C, Fe, and Si

rity levels resulting from earlier reduction processes by Na and electrolysis are also listed. The concentration of the residual content of the reducing elements Mg, Na, and their chlorides is lowered by the subsequent melting processes. High purity levels (5N) of Ti can be obtained by the iodide reduction process. These grades are used for electronic devices.

3.1.3.1 Commercially Pure Grades of Ti and Low-Alloy Ti Materials

Materials designated as commercially pure grades of Ti are interstitial solid solutions of O, N, C, and H in Ti. Oxygen is the only element added deliberately for solid solution strengthening. The other interstitial solutes are impurities resulting from the production process as indicated. Table 3.1-18 shows the chemical compositions and mechanical properties of commercially pure grades of Ti. The temperature dependence of their mechanical properties is shown in Fig. 3.1-85. Low-alloy Ti materials containing Pd, Ru, and Ni + Mo, respectively, are providing increased corrosion resistance at

**Fig. 3.1-83a, b** Lattice parameters a (a) and c (b) of α -Ti as a function of interstitial content

identical levels of mechanical properties as those of the corresponding cp-Ti grades. The compositions and mechanical properties of typical alloys are also shown in Table 3.1-18. All commercially pure and low-alloy Ti materials may be strengthened by cold work. The tensile strength R_m is about doubled by cold work, which amounts to 80 to 90% reduction in area, and the fracture strain A_5 and the reduction in area are about halved.

Table 3.1-18 Chemical composition (maximum contents) and mechanical properties of commercially pure and low-alloy grades of Ti

| O wt% | Tensile strength R_m (MPa) | Yield strength $R_{p0.2}$ (MPa) | Fracture strain A_{10} (%) | Standard grade ^a ep | Standard grade ^a low alloyed |
|-------|------------------------------|---------------------------------|------------------------------|--------------------------------|---|
| 0.12 | 290–410 | > 180 | > 30 | Grade 1 | Pd: grade 11 |
| 0.18 | 390–540 | > 250 | > 22 | Grade 2 | Pd: grade 7 Ru: grade 27 |
| 0.25 | 460–590 | > 320 | > 18 | Grade 3 | Ru: grade 26 |
| 0.35 | 540–740 | > 390 | > 16 | Grade 4 | |
| 0.25 | > 480 | > 345 | > 18 | | Ni+Mo: grade 12 |

^a ASTM B265, ed. 2001; N_{max}: 0.03 wt%; C_{max}: 0.08 wt%; H_{max}: 0.015 wt%

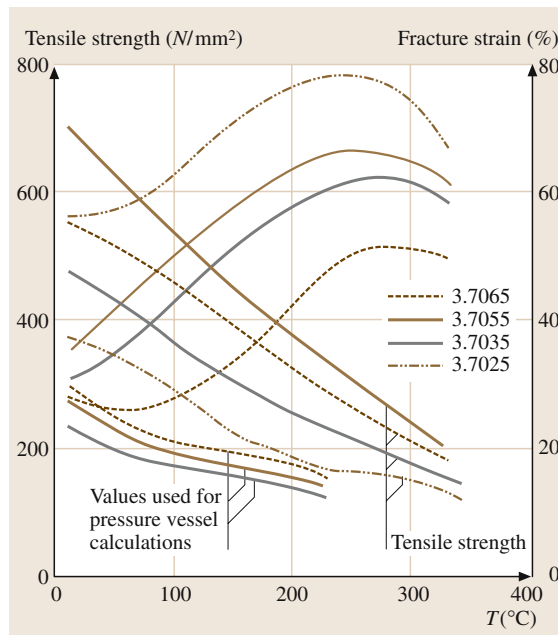


Fig. 3.1-85 High-temperature tensile strength and fracture strain of titanium, and values used for titanium pressure vessel calculations (105 h)

Most applications of cp-Ti and low-alloy Ti materials are based on their high corrosion resistance, such as components in chemical plants, heat exchangers, offshore technology, seawater desalination plants, Ni winning, electroplating plants, medical applications such as heart pacer casings, surgical implants including ear implants [1.55], and automotive applications. Applications of unalloyed Ti in architecture and jewellery are based on coloring the surface by oxide growth upon heat treatment in air. Unalloyed Ti grades are, also, applied at elevated temperature because of their favorable mechanical properties and oxidation resistance at high temperature. Figure 3.1-86 shows the creep date for grade 4 Ti.

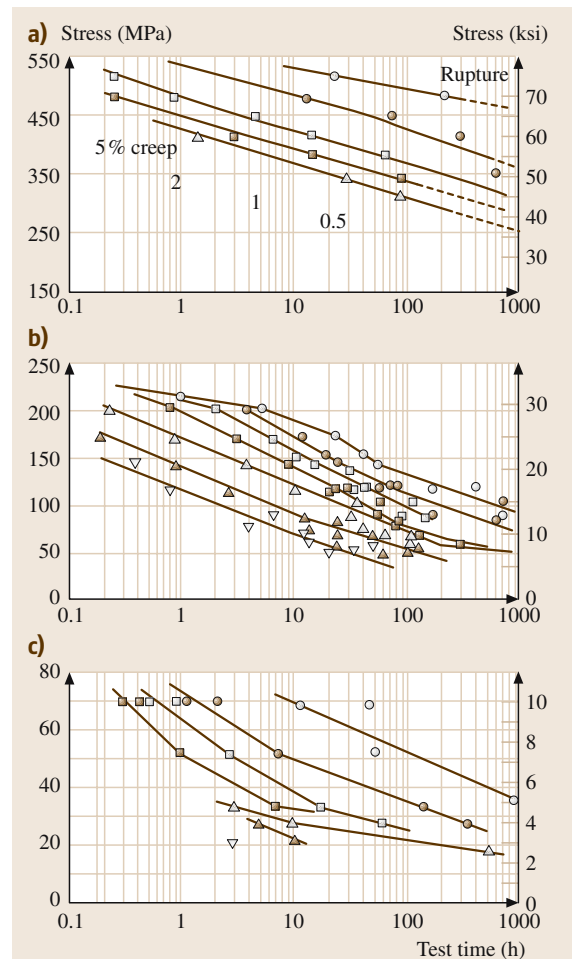


Fig. 3.1-86a-c Creep behavior of commercially pure Ti grade 4, mill annealed with a minimum yield stress of 480 MPa [1.56]. (a) 25 °C; (b) 425 °C; (c) 540 °C

3.1.3.2 Ti-Based Alloys

Alloying elements are added to Ti to improve its mechanical properties. Based on the phase transformation of pure Ti, alloying elements influence the phase equilibria and, thus, the transformations and the resulting microstructural states. The phase composition of the microstructure may be varied from pure α through ($\alpha + \beta$) to pure β , depending on the alloy content [1.54]. The α phase is stabilized by O, N, C, and Al. The β phase range is expanded by H, V, Mo, Fe, Cr, Cu, Pd, and Si. High solubility in α and β is exhibited by Zr and Sn. The alloy variants are characterized by the phases present in the annealed state at room temperature, as shown in Table 3.1-19. Alloys consisting partially or fully of the β phase are more easily deformed because of the larger number of slip systems in the bcc structure of the β phase compared to those in the hcp α phase. The alloying elements provide, also, solid solution strengthening. A further increase in yield strength may be attained by quenching and aging of β -phase alloys which leads to the coherent precipitation of the α and ω phases. However, the strength increase is moderate (10–20%) compared to

that caused by precipitation hardening effects in Al and Cu-based alloys.

Based on their high specific strength, Ti alloys are widely used in aerospace applications, furthermore for high-speed moving parts, corrosion resistant pressure vessels and pipes, and for sports gear. The high-temperature strength has been increased by alloying for elevated temperature applications, as shown in Table 3.1-20. The densely packed hcp structure of the α phase is more creep-resistant than the more open bcc structure of the β phase. Accordingly the creep strength of the α - and near- α -phase alloys is clearly higher than that of $\alpha + \beta$ -phase alloys, as shown in Fig. 3.1-87.

Titanium alloys may be processed like stainless steel. This leads to a cost effective production of a wide range of semi-finished and finished products and parts. If the tendency to oxidation and welding above approximately 350 °C and the low thermal conductivity are taken into account, parts can be manufactured from Ti alloys, quite similar to manufacturing from stainless steels. A wide variety of working, joining, and coating processes is well established.

Table 3.1-19 Chemical composition and mechanical properties of Ti-base alloys at room temperature (minimum values)

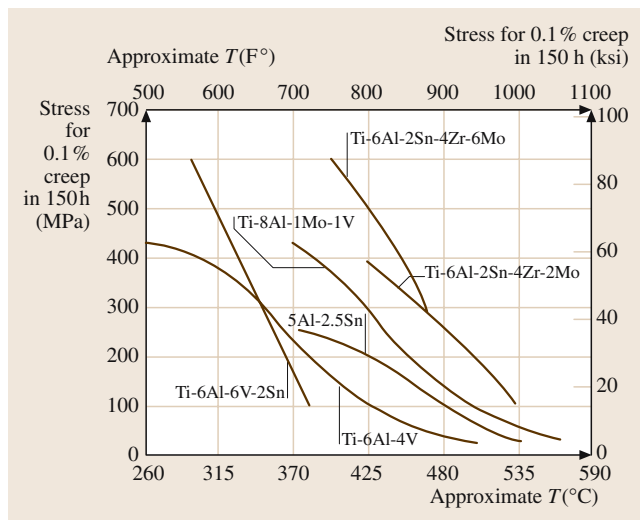
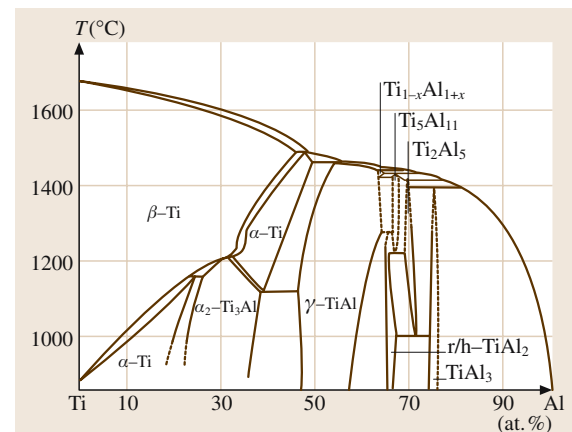
| Alloy composition ^a | Alloy type | Tensile strength R _m (MPa) | Yield strength R _{p0.2} (MPa) | Density ρ (g/cm ³) | Young's modulus E (GPa) | Main property | Standard grade ^b |
|--------------------------------------|------------------|---------------------------------------|--|--------------------------------|-------------------------|---------------------------------|-----------------------------|
| Ti5Al2.5Sn | α | 830 | 780 | 4.48 | 110 | High strength | |
| Ti6Al2Sn4Zr2MoSi | near α | 900 | 830 | 4.54 | 114 | High-temperature strength | 3.7145 |
| Ti6Al5Zr0.5MoSi | near α | 950 | 880 | 4.45 | 125 | High-temperature strength | 3.7155 |
| Ti5.8Al4Sn3.5Zr0.7Nb 0.5Mo0.2Si0.05C | near α | 1030 | 910 | 4.55 | 120 | High-temperature strength | |
| Ti6Al4V | $\alpha + \beta$ | 900 | 830 | 4.43 | 114 | High strength | |
| Ti4Al4Mo2Sn | $\alpha + \beta$ | 1100 | 960 | 4.60 | 114 | High strength | 3.7185 |
| Ti6Al6V2Sn | $\alpha + \beta$ | 1030 | 970 | 4.54 | 116 | High strength | 3.7175 |
| Ti10V2Fe3Al | near β | 1250 | 1100 | 4.65 | 103 | High strength | |
| Ti15V3Cr3Sn3Al | β | 1000 | 965 | 4.76 | 103 | High strength; cold formability | |
| Ti3Al8V6Cr4Zr4Mo | β | 1170 | 1100 | 4.82 | 103 | High corrosion; resistance | |
| Ti15Mo3Nb3AlSi | β | 1030 | 965 | 4.94 | 96 | High corrosion; resistance | |

^a Figure before chemical symbol denotes nominal wt%

^b according to DIN 17851, ASTM B 265 ed. 2001

Table 3.1-20 Upper temperature limit for Ti alloys developed for elevated-temperature applications

| Alloy | Alloy type | Year of introduction | Useful maximum °C |
|--|------------------------------------|----------------------|-------------------|
| Ti-6Al-4V (Ti-64) | $\alpha + \beta$ | 1954 | 300 |
| Ti-4Al-2Sn-4Mo-0.5Si (IMI-550) | $\alpha + \beta$ | 1956 | 400 |
| Ti-8Al-1Mo-1V (Ti-811) | near- α | 1961 | 425 |
| Ti-2Al-11Sn-5Zr-1Mo-0.2Si (IMI-679) | near- α | 1961 | 450 |
| Ti-6Al-2Sn-4Zr-6Mo (Ti-6246) | $\alpha + \beta$ | 1966 | 450 |
| Ti-6Al-2Sn-4Zr-2Mo (Ti-6242) | near- α | 1967 | 450 |
| Ti-3Al-6Sn-4Zr-0.5Mo-0.5Si (Hylite 65) | near- α | 1967 | 520 |
| Ti-6Al-5Zr-0.5Mo-0.25Si (IMI-685) | near- α | 1969 | 520 |
| Ti-5Al-5Sn-2Zr-2Mo-0.2Si (Ti5522S) | near- α or $\alpha + \beta$ | 1972 | 520 |
| Ti-6Al-2Sn-1.5Zr-1Mo-0.1Si-0.3Bi (Ti-11) | near- α | 1972 | 540 |
| Ti-6Al-2Sn-4Zr-2Mo-0.1Si (Ti-6242S) | near- α | 1974 | 520 |
| Ti-5Al-5Sn-2Zr-4Mo-0.1Si (Ti-5524S) | near- α or $\alpha + \beta$ | 1976 | 500 |
| Ti-5.5Al-3.5Sn-3Zr-0.3Mo-1Nb-0.3Si (IMI-829) | near- α | 1976 | 580 |
| Ti-5.5Al-4Sn-4Zr-0.3Mo-1Nb-0.5Si-0.06C (IMI-834) | near- α | 1984 | 590 |
| Ti-6Al-2.75Sn-4Zr-0.4Mo-0.45Si (Ti-1100) | near- α | 1987 | 590 |
| Ti-15Mo-3Al-2.75Nb-0.25Si (Beta-21S) | β | 1988 | 590 |

**Fig. 3.1-87** Creep strength for α (Ti-5Al-2.5Sn), near- α (Ti-8Al-1Mo-1V and Ti-6Al-2Sn-4Zr-2Mo), and $\alpha + \beta$ (Ti-6Al-4V and Ti-6Al-2Sn-4Zr-6Mo) alloys**Fig. 3.1-88** Ti-Al phase diagram

Various versions of the binary Ti-Al phase diagram are available [1.54] and are still under discussion because of conflicting results. The phase diagram shown in Fig. 3.1-88 incorporates recent results.

Ti₃Al-Based Alloys

Various Ti₃Al-based alloys have been developed with niobium as a major alloying element and further components for obtaining an optimised balance of strength, formability, toughness, and oxidation resistance. The alloys are two-phase or three-phase. Current Ti₃Al-based alloys with engineering significance are listed in Table 3.1-23.

3.1.3.3 Intermetallic Ti-Al Materials

The intermetallic compounds Ti₃Al and TiAl are studied for high-temperature materials developments. Extensive accounts [1.52, 57] are the sources of the data presented here. In Table 3.1-21 the property ranges of Ti₃Al- and TiAl-based alloys are compared to those of conventional Ti alloys and Ni-based superalloys.

Table 3.1-21 Properties of alloys based on the titanium aluminides Ti_3Al and $TiAl$ [1.50] and of conventional titanium alloys and nickel based superalloys

| Property | Ti-based alloys | Ti_3Al -based intermetallic materials | $TiAl$ -based intermetallic materials | Ni-based superalloys |
|--|-----------------|---|---------------------------------------|----------------------|
| Structure | A3/A2 | D0 ₁₉ /A2/B2 | L1 ₀ /D0 ₁₉ | A1/L1 ₂ |
| Density (g/cm ³) | 4.5–4.6 | 4.1–4.7 | 3.7–3.9 | 7.9–9.1 |
| Thermal conductivity (W/m K) | 21 | 7 | 22 | 11 |
| Young's modulus at room temperature (GN/m ²) | 95–115 | 100–145 | 160–180 | 195–220 |
| Yield strength at room temperature (MN/m ²) | 380–1150 | 700–990 | 400–650 | 250–1310 |
| Tensile strength at room temperature (MN/m ²) | 480–1200 | 800–1140 | 450–800 | 620–1620 |
| Temperature limit due to creep (°C) | 600 | 760 | 1000 | 1090 |
| Temperature limit due to oxidation (°C) | 600 | 650 | 900 | 1090 |
| Tensile strain to fracture at room temperature (%) | 10–25 | 2–26 | 1–4 | 3–50 |
| Tensile strain to fracture at high temperature (%) | 12–50 | 10–20 | 10–60 | 8–125 |
| Fracture toughness K_{Ic} at room temperature (MN/m ^{3/2}) | High | 13–42 | 10–20 | 25 |

Table 3.1-22 Crystal structure data

| Phase designation | Composition | Strukturbericht designation (prototype) |
|-----------------------|-----------------|---|
| α -Ti(Al) | 0–45 at.% Al | A3 (Mg) |
| β -Ti(Al) | 0–47.5 at.% Al | A2 (W) |
| β_1 | | B2 (CsCl) |
| α_2 - Ti_3Al | 22–39 at.% Al | DO ₁₉ (Ni_3Sn) |
| γ - $TiAl$ | 48–69.5 at.% Al | L1 ₀ (AuCu) |
| O | Ti_2AlNb | |
| ω | Ti_4Al_3Nb | B8 ₂ |

Table 3.1-23 Major Ti_3Al -based alloys [1.50]

| Alloy composition (at.%) | Phases | Designation |
|--------------------------|--------------------------|--------------|
| Ti-24Al-11Nb | $\alpha_2 + \beta$ | 24-11 |
| Ti-25Al-11Nb | $\alpha_2 + \beta$ | 25-11 |
| Ti-25Al-8Nb-2Mo-2Ta | $\alpha_2 + \beta$ | 8-2-2 |
| Ti-25Al-16Nb | $\alpha_2 + \beta + O$ | 25-16 |
| Ti-25Al-17Nb | $\alpha_2 + \beta + O$ | 25-17 |
| Ti-27Al-15Nb | $\alpha_2 + \beta + O$ | 27-15 |
| Ti-27Al-15Nb-1Mo | $\alpha_2 + \beta + O$ | 27-15-1 |
| Ti-22Al-17Nb-1Mo | $\alpha_2 + \beta + O$ | 22-17-1 |
| Ti-25Al-17Nb-1Mo | $\alpha_2 + \beta + O$ | 25-17-1 |
| Ti-25Al-10Nb-3V-1Mo | $\alpha_2 + \beta + O$ | 10-3-1 |
| Ti-25Al-24Nb | O + β | 25-24 |
| Ti-22Al-27Nb | O + β | 22-27 |
| Ti-30Al-20Nb | O + ω | 30-20 (1986) |
| SCS/6Ti-24Al-11Nb | $\alpha_2 + \beta + SiC$ | SCS-6/24-11 |

Alloy 24-11 and alloy 10-3-1 have already been produced on a production mill scale.

Mechanical Properties. The elastic properties of selected alloys are presented in Table 3.1-24. Strength, ductility, and toughness of the Ti_3Al -based alloys are sensitive functions of both composition and microstructure which are controlled by prior processing. Characteristic data are shown in Table 3.1-25 for various alloys. Different property data for the same alloy composition indicate the effect of different prior thermo-mechanical treatments. The effect of microstructure on toughness is exemplified by Table 3.1-26. Particularly high strengths can be obtained in intermetallic Ti_3Al -based matrix composites.

Table 3.1-26 Effect of microstructure variation on fracture toughness K_{Ic} at room temperature for a Ti-25Al-10Nb-3V-1Mo alloy

| Microstructure | K_{Ic} [MPa m ^{1/2}] |
|-----------------|----------------------------------|
| Coarse globular | 11 |
| Fine globular | 10 |
| Coarse bimodal | 11 |
| Fine bimodal | 14 |
| Fine lamellar | 8 |
| Coarse lamellar | 50 |

Table 3.1-24 Elastic moduli E , G , K , and Poisson's ratio ν at various temperatures T for selected simple Ti_3Al -based alloys

| Alloy (at.%) | T (°C) | E (GPa) | G (GPa) | ν | K (GPa) |
|---------------------------------------|----------|-------------------|------------------|-------------------|-----------|
| Ti-25.5Al | 27 | 144 | 56.2 | 0.283 | |
| Ti-25.5Al | -270 | 151 | 59.0 | 0.280 | |
| Ti-25Al-10Nb-3V-1Mo (coarse globular) | 23 | 72 | | | |
| Ti-25Al-10Nb-3V-1Mo (fine lamellar) | 23 | 120 | | | |
| Ti-25Al-10Nb-3V-1Mo (coarse lamellar) | 23 | 159 | | | |
| Ti-26.6Al-4.9Nb | 26–883 | 134.47–0.0482 T | 53.56–0.0180 T | 0.257–0.00004 T | |
| Ti-27.4Al-20.3Nb | 25 | 128.8 | 48.8 | 0.32 | 118.4 |
| Ti-22Al-23Nb/Ultra-SCS | 25 | 201 ± 8 | | | |
| Ti-22Al-23Nb/Ultra-SCS | 649 | 173 | | | |
| Ti-22Al-23Nb/Ultra-SCS | 760 | 135 ± 8 | | | |

Table 3.1-25 Selected tensile data for yield stress R_p , fracture stress R_m , total elongation A , fracture toughness K_{Ic} at room temperature, and creep time to rupture t_r at 650 °C and 380 MPa for various Ti_3Al -based alloys

| Alloy (at.%) | R_p (MPa) | R_m (MPa) | A (%) | K_{Ic} (MPa m ^{1/2}) | t_r (h) |
|---------------------|-------------|-------------|---------|----------------------------------|-----------|
| Ti-25Al | 538 | 538 | 0.3 | | |
| Ti-24Al-11Nb | 787 | 824 | 0.7 | | 44.7 |
| Ti-24Al-11Nb | 510 | | 2.0 | 20.7 | |
| Ti-24Al-11Nb | 761 | 967 | 4.8 | | |
| Ti-24Al-14Nb | 831 | 977 | 2.1 | | 59.5 |
| Ti-24Al-14Nb | 790 | | 3.3 | 15.8 | 60.4 |
| Ti-15Al-22.5Nb | 860 | 963 | 6.7 | 42.3 | 0.9 |
| Ti-25Al-10Nb-3V-1Mo | 825 | 1042 | 2.2 | 13.5 | 360 |
| Ti-25Al-10Nb-3V-1Mo | 823 | 950 | 0.8 | | |
| Ti-25Al-10Nb-3V-1Mo | 745 | 907 | 1.1 | | |
| Ti-25Al-10Nb-3V-1Mo | 759 | 963 | 2.6 | | |
| Ti-25Al-10Nb-3V-1Mo | 942 | 1097 | 2.7 | | |
| Ti-24.5Al-17Nb | 952 | 1010 | 5.8 | 28.3 | 62 |
| Ti-24.5Al-17Nb | 705 | 940 | 10.0 | | |
| Ti-25Al-17Nb-1Mo | 989 | 1133 | 3.4 | 20.9 | 476 |
| Ti-22Al-23Nb | 863 | 1077 | 5.6 | | |
| Ti-22Al-27Nb | 1000 | | 5.0 | 30.0 | |
| Ti-22Al-20Nb-5V | 900 | 1161 | 18.8 | | |
| Ti-22Al-20Nb-5V | 1092 | 1308 | 8.8 | | |

Chemical Properties. The oxidation resistance of the Ti₃Al-based alloys is higher than that of conventional Ti alloys with TiO₂ formation, but lower than that of Al₂O₃-forming alloys. The rate controlling mechanisms are complex and change with atmosphere, temperature, and time. Oxidation is moderate with porous scales up to 800 °C whereas spallation occurs at higher temperatures. The addition of Nb to the Ti₃Al-based alloys is beneficial to the oxidation resistance as well as nitrogen in the atmosphere [1.58]. Table 3.1-27 presents characteristic data for oxidation at 800 °C.

It should be noted that H is easily dissolved in Ti₃Al-based alloys, leading to embrittlement and stress corrosion cracking. Furthermore, the thermal stability of intermetallic Ti₃Al-based matrix composites – in particular SCS-6 SiC/Ti-25Al-10Nb-3V-1Mo – is affected by chemical reactions between the matrix and the strengthening phase.

TiAl-Based Alloys

Alloys based on γ -TiAl, also called gamma titanium aluminides, excel due to their high strength per unit density. These alloys contain the α_2 -phase Ti₃Al as a second phase and are further alloyed with other elements for property optimization. The composition range is Ti-(45–48)Al-(0–2)(Cr, Mn, V)-(0–5)(Nb, Ta, W)-(0–2)(Si, B, Fe, N) (at.%) . Further components such as Hf,

Sn, C, and/or 0.8–7 vol.% TiB₂ are added for dispersion strengthening [1.59]. Table 3.1-28 shows the standard microstructures and Table 3.1-29 lists the alloys of primary interest.

Various jet engine and car engine components have been identified for application of TiAl-based alloys. It is particularly noteworthy that large sheets, which are suitable for superplastic forming and joining by diffusion bonding, can be produced from these intrinsically brittle intermetallic compound alloys.

Physical Properties. Some thermal data for single crystalline and polycrystalline TiAl alloys are shown in Tables 3.1-30 and 3.1-31.

Mechanical Properties. Elastic properties of TiAl-based materials are compiled in Table 3.1-32. Strength, ductility, and toughness of the TiAl-based alloys are sensitive functions of both composition and microstructure which is controlled by prior processing [1.59]. Characteristic data are shown in Table 3.1-33 for various alloys. Different property data for the same alloy composition indicate the effect of different prior thermo-mechanical treatments. It is noted that TiAl-based alloys are prone to hydrogen/environmental embrittlement depending on the amount of α_2 from Ti₃Al [1.60]. Creep and fatigue data are available [1.59, 61].

Table 3.1-27 Characteristic oxidation data for various Ti₃Al-based alloys at 800 °C. Apparent parabolic rate constant k_p and apparent activation energy Q [1.58]

| Alloy (at.%) | Atmosphere | Test duration (h) | k_p (10 ⁻¹² g ² cm ⁻⁴ s ⁻¹) | Q (kJ mol ⁻¹) |
|---------------------|---|-------------------|--|-----------------------------|
| Ti-25Al | O ₂ | 9 | 19 | 289 |
| Ti-25Al-11Nb | O ₂ | 4 | 2.0 | 330 |
| Ti-24Al-15Nb | O ₂ | 6 | 2.2 | 329 |
| Ti-24Al-15Nb | 20% O ₂ + 80% N ₂ | 5 | 0.25 | 274 |
| Ti-24Al-10Nb-3V-1Mo | 20% O ₂ + 80% N ₂ | 15 | 1150 | 217 |
| Ti-25Al-10Nb-3V-1Mo | Air | 24 | 2.4 | 248 |

Table 3.1-28 Standard microstructures of TiAl-based alloys [1.59]

| Type | Phase distribution |
|----------------------|--|
| Near-gamma (NG) | γ grains + α_2 particles |
| Duplex (DP) | γ grains + α_2 plates or particles |
| Nearly lamellar (NL) | Lamellar γ + γ grains |
| Fully lamellar (FL) | Lamellar γ + residual γ grains on grain boundaries |
| Modified NL (MNL) | Lamellar γ + fine γ grains |
| Modified FL (MFL) | Lamellar γ |

Table 3.1-29 Important TiAl-based alloys with microstructures according to Table 3.1-28 [1.59]

| Composition (at.%) | Microstructure type | Designation |
|-------------------------------------|------------------------|---------------------|
| Ti-48Al-1V-0.3C-0.2O | DP | 48-1-(0.3C) |
| Ti-48Al-1V-0.2C-0.14O | DP/NL | 48-1-(0.2C) |
| Ti-48Al-2Cr-2Nb | DP, NL, DP/FL | 48-2-2 |
| Ti-47Al-1Cr-1V-2.6Nb | DP/FL | G1 |
| Ti-45Al-1.6Mn | NL | Sumitomo |
| Ti-47.3Al-0.7V-1.5Fe-0.7B | – | IHI Alloy |
| Ti-47Al-2W-0.5Si | DP | ABB Alloy |
| Ti-47Al-2Mn-2Nb-0.8TiB ₂ | NL + TiB ₂ | 47XD |
| Ti-45Al-2Mn-2Nb-0.8TiB ₂ | MFL + TiB ₂ | 45XD |
| Ti-46.2Al-xCr-y(Ta,Nb) | NL | GE Alloy 204b |
| Ti-47Al-2Nb-2Cr-1Ta | DP | Ti-47Al-2Nb-2Cr-1Ta |
| Ti-46Al-4Nb-1W | NL | Alloy 7 |
| Ti-46.5Al-2Cr-3Nb-0.2W | DP/MFL | Alloy K5 |
| Ti-48Al-2Cr | NG, DP, FL | Ti-48Al-2Cr |
| Ti-47Al-1.5Nb-1Cr-1Mn-0.7Si-0.5B | MFL | γ-TAB |
| Ti-46.5Al-4(Cr, Nb, Ta, B) | MFL | γ-Met |

Table 3.1-30 Temperature dependence of the thermal expansion coefficient α for single crystalline TiAl

| Alloy (at.%) | T (°C) | $\alpha_{[100]} (\text{K}^{-1})$ | $\alpha_{[001]} (\text{K}^{-1})$ |
|--------------|--------|--|--|
| Ti-56Al | 25–500 | $9.77 \times 10^{-6} + 4.46 \times 10^{-9}(T + 273)$ | $9.26 \times 10^{-6} + 3.76 \times 10^{-9}(T + 273)$ |

Table 3.1-31 Thermal expansion coefficient α , thermal conductivity λ and specific heat c_p at various temperatures T for polycrystalline TiAl alloys [1.62]

| Alloy (at.%) | T (°C) | $\alpha (\text{K}^{-1})$ | $\lambda (\text{W K}^{-1} \text{m}^{-1})$ | $c_p (\text{J g}^{-1} \text{K}^{-1})$ |
|--------------|--------|--------------------------|---|---------------------------------------|
| Ti-50Al | 27 | 11×10^{-6} | 11 | 0.4 |
| Ti-50Al | 850 | 13×10^{-6} | 19 | 0.5 |
| Ti-48Al-2Cr | 100 | 9.1×10^{-6} | – | – |
| Ti-48Al-2Cr | 700 | 11.8×10^{-6} | – | – |

Table 3.1-32 Young's modulus E , shear modulus G , Poisson's ratio ν and bulk modulus K for single-phase TiAl and a TiAl composite

| Alloy (at.%) | T (°C) | $E (\text{GPa})$ | $G (\text{GPa})$ | ν | $K (\text{GPa})$ |
|------------------------------------|--------|--------------------|-------------------|-------|------------------|
| Ti-49.4Al | 25–935 | $173.59 - 0.0342T$ | $70.39 - 0.0141T$ | 0.234 | – |
| Ti-50Al | 25 | 185 | 75.7 | – | 110 |
| Ti-50Al | -273 | 190 | 78.3 | – | 112 |
| Ti-47Al-2V-7 vol.%TiB ₂ | 27 | 180 | – | – | – |
| Ti-47Al-2V-7 vol.%TiB ₂ | 647 | 162 | – | – | – |

Table 3.1-33 Selected tensile data for yield stress R_p , fracture stress R_m , total elongation A , toughness K_{Ic} at room temperature (RT) or higher temperature T for the TiAl-based alloys of Table 3.1-29 with microstructures of Table 3.1-28 [1.59, 61]

| Alloy designation | Alloy condition, processing, microstructure | T [°C] | R_p (MPa) | R_m (MPa) | A (%) | K_{Ic} (MPa m $^{1/2}$) |
|---------------------|---|----------|-------------|-------------|---------|----------------------------|
| 48-1-(0.3C) | Forging + HT | RT | 392 | 406 | 1.4 | 12.3 |
| | | 760 | 320 | 470 | 10.8 | — |
| | Casting-duplex | RT | 490 | — | — | 24.3 |
| 48-1-(0.2C) | Forging + HT | RT | 480 | 530 | 1.5 | — |
| | | 815 | 360 | 450 | 720 | — |
| 48-2-2 | Casting + HIP + HT | RT | 331 | 413 | 2.3 | 20–30 |
| | | 760 | 310 | 430 | — | — |
| | Extrusion + HT: DP/FL | RT | 480/454 | — | 3.1/0.5 | — |
| | | 870 | 330/350 | — | 53/19 | — |
| | PM extrusion + HT | RT | 510 | 597 | 2.9 | — |
| G1 | Forging + HT: DP/FL | RT | 480/330 | 548/383 | 2.3/0.8 | 12/30-36 |
| | | 600 | 383/— | 507/— | 3.1/— | 16/— |
| | | 800 | 324/290 | 492/378 | 55/1.5 | —/40-70 |
| Sumitomo | Reactive sintering | RT | 465 | 566 | 1.4 | — |
| | | 800 | 370 | 540 | 14 | — |
| IHI Alloy | Casting | RT | — | 520 | 0.6 | — |
| | | 800 | — | 424 | 40 | — |
| ABB Alloy | Casting + HT | RT | 425 | 520 | 1.0 | 22 |
| | | 760 | 350 | 460 | 2.5 | — |
| 47XD | Casting + HIP + HT | RT | 402 | 482 | 1.5 | 15–16 |
| | | 760 | 344 | 458 | — | — |
| 45XD | Casting + HIP + HT | RT | 550–590 | 670–720 | 1.5 | 15–19 |
| | | 760 | 415 | 510 | 19 | — |
| GE Alloy 204b | Casting + HIP + HT | RT | 442 | 575 | 1.5 | 34.5 |
| | | 840 | 381 | 549 | 12.2 | — |
| Ti-47Al-2Nb-2Cr-1Ta | Casting + HIP + HT | RT | 430 | 515 | 1.0 | — |
| | | 870 | 334 | 403 | 14.6 | — |
| Alloy 7 | Extrusion + HT | RT | 648 | 717 | 1.6 | — |
| | | 760 | 517 | 692 | — | — |
| Alloy K5 | Forging + HT: DP/MFL | RT | 462/473 | 579/557 | 2.8/1.2 | 11/20-22 |
| | | 870 | —/362 | —/485 | —/12.0 | — |
| Ti-48Al-2Cr | Casting + HIP + HT | RT | 390 | 405 | 1.5 | — |
| | | 700 | 340 | 395 | 2.7 | — |
| γ -TAB | Casting + HIP + HT | RT | 475 | — | 1.6 | — |
| | | 700 | 385 | — | 6.0 | — |

Chemical Properties. The oxidation behavior of TiAl alloys is complex as both Al_2O_3 and/or TiO_2 are formed at parabolic rate constants ranging from 3×10^{-13} to $3 \times 10^{-9} \text{ g}^2 \text{ cm}^{-4} \text{ s}^{-1}$ at 950°C , depending not only on alloy composition, atmosphere, and temperature, but also on alloy surface quality. The oxidation rate is higher in air than in pure oxygen. Alloying additions of Nb, W, Ta, or Si generally improve the oxidation resis-

tance. Additions of V and Mo promote Al_2O_3 formation above 900°C , which is beneficial, but accelerates scale growth at lower temperatures, i.e., at possible service temperatures. Small additions of Cr reduce the oxidation resistance whereas larger amounts improve it. Small additions of P or Cl have been found to increase the oxidation resistance. Some characteristic data are shown in Table 3.1-34.

Table 3.1-34 Characteristic oxidation data for some TiAl-based alloys of Table 3.1-29. Apparent parabolic rate constant k_p at 800 °C in air

| Alloy designation | Test duration (h) | k_p ($10^{-12} \text{ g}^2 \text{ cm}^{-4} \text{ s}^{-1}$) |
|---------------------|-------------------|---|
| 48-2-2 | 500 | 2 |
| Alloy K5 | 1000 | 0.5 |
| Alloy 7 (5 at.% Nb) | 1000 | 0.1 |

Usually γ -TiAl-based alloys contain α_2 -Ti₃Al as a second phase and are, therefore, subject to hydrogen uptake and hydrogen/environmental embrittlement depending on the amount of α_2 -Ti₃Al.

3.1.3.4 TiNi Shape-Memory Alloys

The shape-memory effect is based on martensitic transformations of intermetallic phases with a high degree of reversibility [1.63]. The alloy TiNi is the most advanced and has widespread shape memory. The present state of development and applications is summarized in [1.63, 64]. The high-temperature TiNi phase, having a cubic B2 (CsCl type) structure, is transformed martensitically, i. e., by a combination of transformation shears, into a low-temperature phase with a monoclinic DO₁₉ structure upon cooling or upon applying a stress and strain. The transformation can be associated with a macroscopic shape change. The transformation and the associated shape change are reversed on heating (shape-memory effect) or on releasing the stress and strain isothermally (superelasticity). The range of transformation start temperatures M_s varies between -200°C and 110°C depending on the alloy composition, as shown in Fig. 3.1-89.

Further reversible, diffusionless, but non-martensitic transformation phenomena occur in the TiNi high temperature phase on approaching the temperature range of martensitic transformation. Microscopically, these transformation phenomena are associated with phonon softening. Crystallographically, they are observable as localised rhombohedral distortions of the B2 structure. Furthermore, these localized displacements appear to be stabilized by annealing. Annealing treatments in the temperature range of 300 to 800 °C are increasing the M_s temperature. Figure 3.1-90 shows a characteristic example.

The shape-memory effect is a complex function of composition, martensite start temperature M_s , stress, strain, microstructure, texture, and aging treatment. It consists essentially of a reversible transformation strain and the associated macroscopic shape change. At low numbers of transformation cycles (e.g., up to 100), the

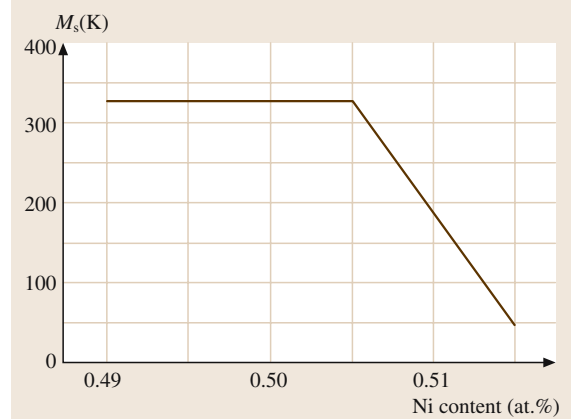


Fig. 3.1-89 Martensite start temperature M_s of the TiNi phase as a function of Ni content

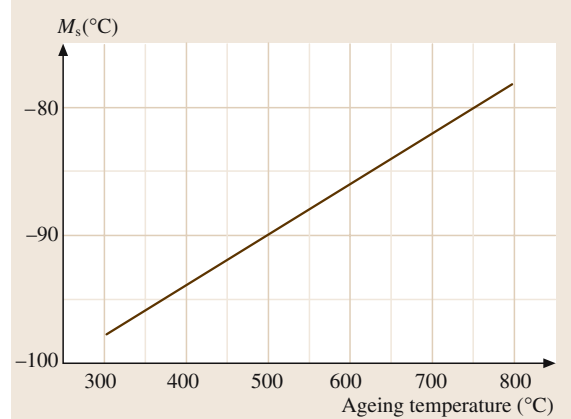


Fig. 3.1-90 Effect of aging temperature on the M_s temperature of an Ni_{47.3}Ti_{43.8}Nb_{8.9} alloy

reversible transformation strain decreases from a typical initial value 8% to about 6%; even after $\geq 100\,000$ transformation cycles it stays at a technically useful level of $\cong 2\%$. A considerable number and variety of technical and medical applications of the shape-memory effect and of the closely related effect of superelasticity have been developed [1.65, 66].

3.1.4 Zirconium and Zirconium Alloys

Zirconium is used – similarly to titanium but less extensively so – as a special structural material of high corrosion resistance due to its highly stable protective oxide layer. This oxide layer forms in air at ambient temperature spontaneously and can be increased in thickness and stability by heat treatment in air. More extensive treatments are found in [1.51, 67]. Technically-pure and low-alloy Zr materials are especially used in applications requiring structural parts of high chemical stability. The processing is closely analogous to that of Ti. Another main application of Zr is in high-purity Zr alloys used as cladding and structural materials in nuclear applications due to the low thermal neutron capture cross section of Zr. A third group of Zr-based materials with application potential is due to the fact that some Zr-based alloys form the amorphous state easily upon cooling at a comparatively low rate. They are suitable for the production of bulk glassy alloys.

At 1138 K, Zr undergoes a structural phase transformation from low-temperature, hexagonal close-packed α -Zr to high-temperature, body-centered cubic β -Zr. Alloying elements such as Nb stabilize the β phase. On slow cooling and annealing of the β phase, a metastable

ω phase can be obtained which forms by coherent precipitation.

3.1.4.1 Technically-Pure and Low-Alloy Zirconium Materials

Only two zirconium materials are standardised: Zr 702 which is essentially technically-pure Zr and consists of the α phase only, and Zr 705 which contains 2 to 3 wt% Nb, has an $\alpha + \beta$ microstructure and a higher yield stress. Their composition ranges and mechanical properties are listed in Tables 3.1-35 and 3.1-36. Since Hf is usually contained in the Zr ore zircon ($ZrSiO_4$) and is difficult to separate, the Zr materials are specified to contain Hf up to 4.5 wt%. The presence of Hf in Zr alloys up to this level of composition does not affect the mechanical and corrosion properties significantly.

The Zr–Nb phase diagram (Fig. 3.1-91) indicates that $\alpha + \beta$ microstructures can be obtained at the 2–3 wt% Nb level. This leads to both substitutional solid solution strengthening and dual phase strengthening effects. Oxygen has a high interstitial solubility in α -Zr. Fig. 3.1-92 shows the Zr–O phase diagram. It is inter-

Table 3.1-35 Composition of technically-pure and low-alloy Zr materials

| Common designation ASTM/UNS designation | Zr 702 R 60702 | Zr 705 R 60705 |
|--|-------------------|-------------------|
| Alloying, elements (wt%) | | |
| Zr+Hf, min | 99.2 | 95.5 |
| Hf, max | 4.5 | 4.5 |
| Fe+Cr, max | 0.20 | 0.20 |
| Nb | – | 2.0–3.0 |
| O, max | 0.16 | 0.18 |
| H, max | 0.005 | 0.005 |
| N, max | 0.025 | 0.025 |
| C, max | 0.05 | 0.05 |

Table 3.1-36 Mechanical properties of technically-pure and low-alloy Zr materials

| Alloy | Property | Test temperature (°C) | | | | |
|--------|------------------|-----------------------|------|------|------|------|
| | | 20 | 95 | 150 | 260 | 370 |
| Zr 702 | $R_{p0.2}$ (MPa) | 321 | 267 | 196 | 129 | 82 |
| | R_m (MPa) | 468 | 364 | 304 | 201 | 157 |
| | A (%) | 28.9 | 31.5 | 42.5 | 49.0 | 44.1 |
| Zr 705 | $R_{p0.2}$ (MPa) | 506 | | 272 | 196 | |
| | R_m (MPa) | 615 | | 389 | 326 | |
| | A (%) | 18.8 | | 31.7 | 28.9 | |

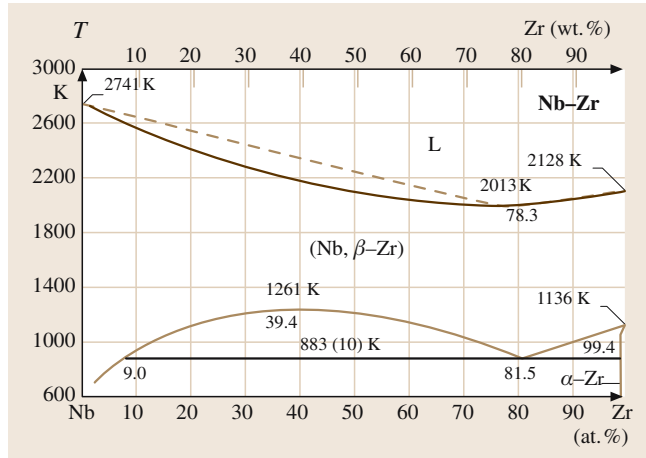


Fig. 3.1-91 Zr–Nb phase diagram

esting to note that the O atoms undergo ordering on the interstitial lattice sites of the α -Zr solid solution above about 10 at.% O. These interstitially ordered phases are termed suboxides. The interstitial O content leads to a strong interstitial solid solution strengthening effect: about 0.01 wt% O increases the yield stress by about 150 MPa.

Extensive data and references are available on the corrosion behavior of Zr in many types of media and under various conditions of exposure [1.67].

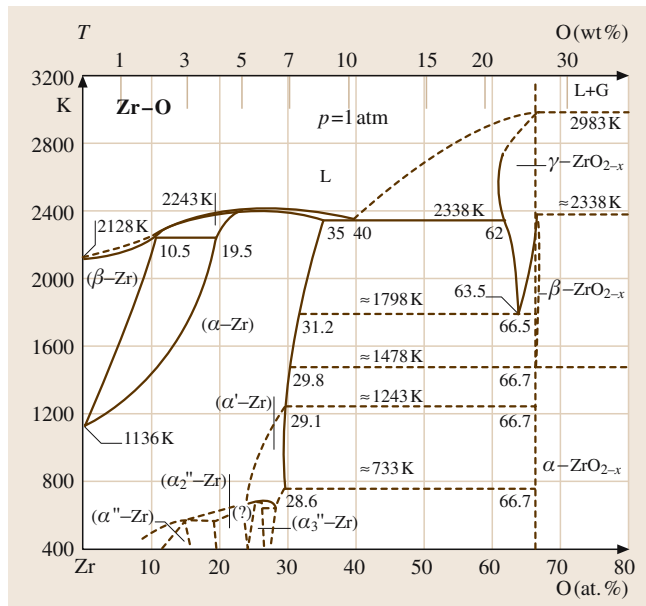


Fig. 3.1-92 Zr–O phase diagram

3.1.4.2 Zirconium Alloys in Nuclear Applications

Based on its low cross section for thermal neutrons and its high corrosion resistance in water, Zr is the preferred material for structural parts and cladding in pressurized and boiling water nuclear reactors. An extensive account of these materials and of their behavior under irradiation is given in [1.68]. Designations and composition ranges of the 4 standardized alloys are listed in Table 3.1-37. The addition of Sn gives rise to a strengthening contribution and increases corrosion resistance by reducing the deleterious effect of nitrogen. The metals Fe, Cr, and Ni, which are highly soluble in the β phase, have very low solubility in α -Zr (maximum solubility: Fe 120 ppm, Cr 200 ppm). This is the basis of a heat treatment involving a high-temperature solution annealing and a low-temperature precipitation treatment. The resulting precipitates are the Laves phases $Zr_2(Ni, Fe)$ and $Zr(Cr, Fe)_2$. In their presence the corrosion resistance is increased by reducing forms of localized corrosion. A specified O content serves to adjust the yield stress due to interstitial solid solution strengthening. Hafnium is removed and its upper limit is specified in Zr alloys for nuclear applications because of its high cross section for thermal neutrons.

The irradiation effects on the mechanical properties are significant. The interstitial atoms and vacancies resulting from irradiation-induced atomic displacements give rise to the formation of dislocation loops of interstitial and vacancy type. These dislocation loops act as obstacles to slip dislocations and lead to an increase in yield stress and decrease in elongation upon fracture as a function of dose, as shown in Fig. 3.1-93. The effect saturates at about 10^{24} nm^{-2} .

3.1.4.3 Zirconium-Based Bulk Glassy Alloys

Zirconium-based alloys were among the first non-noble metal-based alloys found to solidify in the amorphous state upon cooling from the melt at comparatively low rates R , such as 10 K s^{-1} [1.69, 70]. The term bulk glassy alloys refers to the fact that this solidification behavior permits us to obtain bulky parts with an amorphous structure by conventional casting procedures, e.g., in rod form, up to 30 mm. Data are given in [1.71, 72].

The tendency to solidification in the amorphous state is due to a low rate of nucleation of the equilibrium phase(s) at a particular alloy composition. An empirical method to determine the ease of glass formation has proved to be an evaluation of the glass-transition tem-

Table 3.1-37 Designations and compositions of the standardized Zr alloys for nuclear applications [1.68]

| Common designation ASTM/UNS designation | Zircaloy-2 R 60802 | Zircaloy-4 R 60804 | Zr-Nb R 60901 | Zr-Nb R 60904 |
|--|-----------------------------------|-----------------------|------------------|-----------------------|
| Alloying elements (wt%) | | | | |
| Sn | 1.2–1.7 | 1.2–1.7 | – | – |
| Fe | 0.07–0.2 | 0.18–0.24 | – | – |
| Cr | 0.05–0.15 | 0.07–0.13 | – | – |
| Ni | 0.03–0.08 | – | – | – |
| Nb | – | – | 2.4–2.8 | 2.5–2.8 |
| O | 0.010–0.014 (t.b.s.) ^a | | 0.09–0.13 | (t.b.s.) ^a |
| Impurity elements, maximum permissible content (wt ppm) | | | | |
| Al | 75 | 75 | 75 | 75 |
| C | 270 | 270 | 270 | 150 |
| Cu | 50 | 50 | 50 | 50 |
| Hf | 100 | 100 | 100 | 50 |
| Mn | 50 | 50 | 50 | 50 |
| Mo | 50 | 50 | 50 | 50 |
| Ni | – | 80 | 80 | 65 |
| Si | 120 | 120 | 120 | 120 |
| Ti | 50 | 50 | 50 | 50 |
| W | 100 | 100 | 100 | 100 |

^a t.b.s. – to be specified

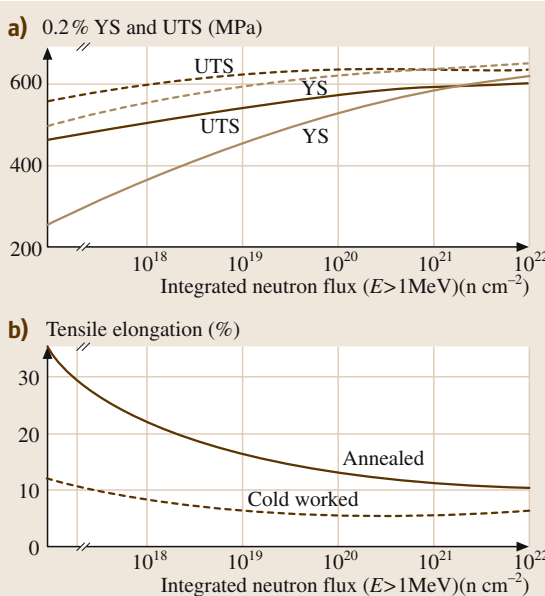


Fig. 3.1-93 Irradiation effects on mechanical properties of a zircaloy [1.68]. YS – yield stress; UTS – ultimate tensile strength. *Solid lines*: irradiation in the annealed state. *Dashed lines*: irradiation in the 10% cold worked state

perature T_g and the crystallization temperature T_x , which can be determined by thermal analysis of the amorphous alloy in question upon heating. For a great number of alloys which form the amorphous state upon cooling, it has been shown that the critical cooling rate R_c , i. e., lowest rate which is sufficient for complete glass formation, decreases strongly with two parameters:

- The relative glass-transition temperature $T_{rg} = T_g/T_{l/el}$, where $T_{l/el}$ is the liquidus temperature, and
- The magnitude of the temperature range $\Delta T_x = T_x - T_g$.

Figures 3.1-94 – 3.1-97 show characteristic data for Zr alloys which have been investigated in a wide range of compositions.

It is impossible to date to derive from first principles which alloy compositions are prone to easy glass formation. It has been found empirically that multi-component alloys with components of significantly different ionic radii are suitable candidates in principle. Examples of Zr-based systems that show bulk glassy solidification behavior are listed in Table 3.1-38.

Empirical findings have been subjected to a systematic treatment involving a mismatch entropy term S_σ and the enthalpy of mixing ΔH [1.73]. Such re-

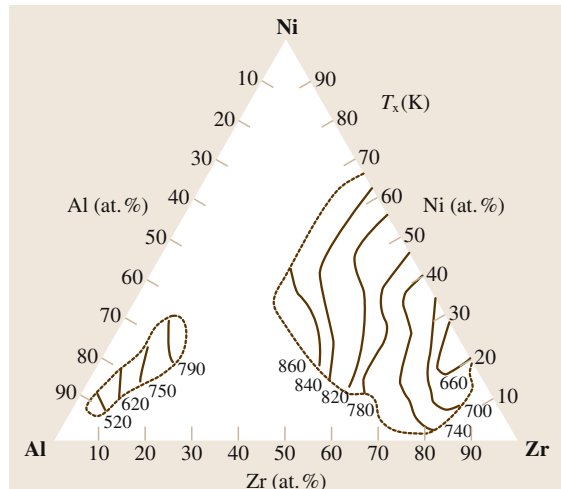


Fig. 3.1-94 Dependence of crystallization temperature T_x on composition in amorphous Zr–Al–Ni alloys [1.72]

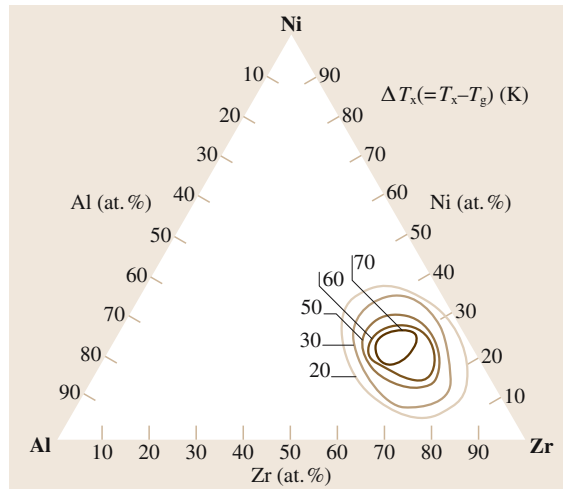


Fig. 3.1-96 Dependence of ΔT_x on composition in amorphous Zr–Al–Ni alloys [1.72]

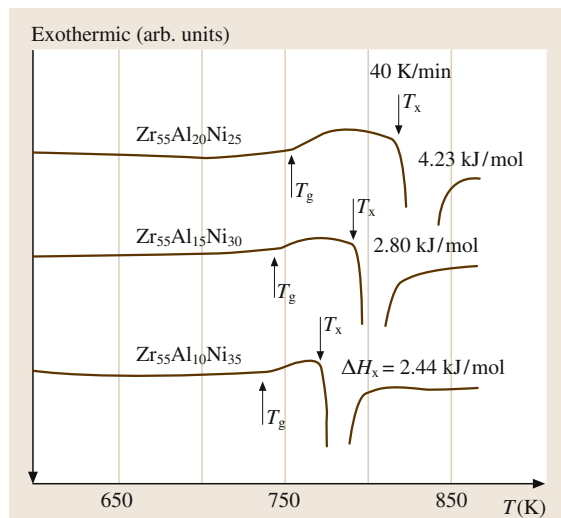


Fig. 3.1-95 Dependence of ΔT_x on composition as determined by differential thermal analysis of amorphous Zr–Al–Ni alloys [1.72]

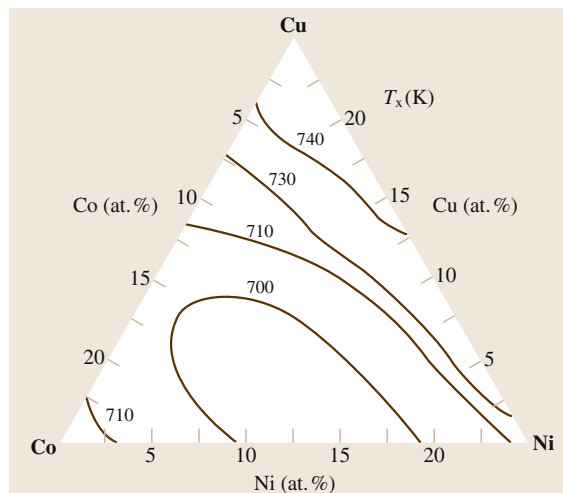


Fig. 3.1-97 Dependence of T_x on composition in amorphous $Zr_{65}Al_{7.5}Cu_{2.5}(Co_{1-x-y}Ni_xCu_y)_{25}$ alloys [1.72]

lations are based on systematic investigations of the effects of individual alloying elements on the characteristic properties T_g , T_x , and ΔT_x , as shown in Fig. 3.1-98 for a characteristic example.

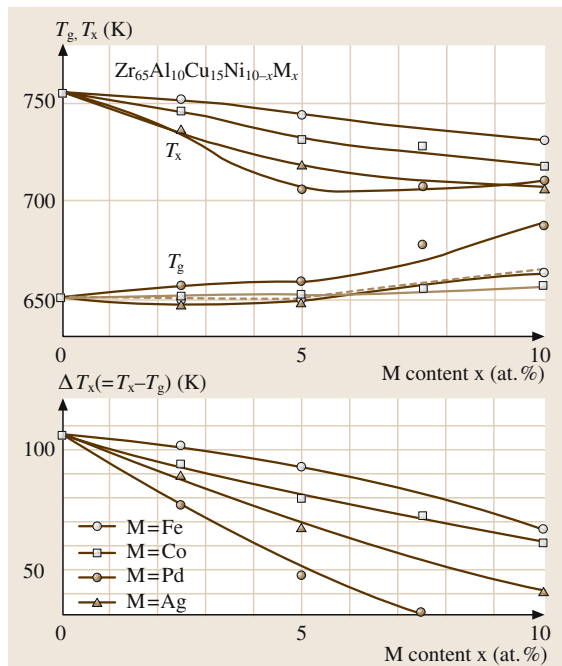
There are no tabulated data of the properties of Zr-based bulk glassy alloys available yet. A typical set of data is given in Table 3.1-39 [1.75].

Table 3.1-38 Zr-based alloy systems exhibiting bulk glassy behavior

| Alloy system | Reference |
|--------------------------|-----------|
| Zr–Al–TM | [1.72] |
| Zr–Al–Ni–Cu–(Ti, Nb, Pd) | [1.72] |
| Zr–Al–Co | [1.74] |
| Zr–Ti–Ni–Cu–(Be) | [1.75] |
| Zr–Cu–Ni–(Al, Ti, Ta) | [1.76] |

Table 3.1-39 Properties of amorphous Zr_{41.2}Ti_{13.8}Cu_{12.5}Ni₁₀Be_{22.5}

| <i>E</i> (GPa) | <i>G</i> (GPa) | <i>v</i> | Elastic strain limit % | <i>R_{p0.2}</i> (GPa) | HV | <i>ρ</i> g/cm ³ | <i>R_{p0.2}/ρ</i> (GPa cm ³ g ⁻¹) | <i>A_e^a</i> (%) | <i>A_c^b</i> (%) | <i>K_{1c}</i> (MN m ^{1/2}) |
|-------------------|-------------------|----------|---------------------------|----------------------------------|-----------|-------------------------------|---|---|---|---|
| 90±1 | 33±1 | 0.354 | 2.0–2.2 | 1.9±0.05 | 590 | 5.9 | 0.32 | ~ 1 | 1–20 | 20–40 |

^a Plastic strain to failure in tension^b Plastic strain to failure in compression**Fig. 3.1-98** Variation of *T_g*, *T_x*, and ΔT_x with M content for melt-spun Zr₆₅Al₁₀Cu₁₅Ni_{10-x}M_x (M = Fe, Co, Pd, Ag) amorphous alloys

3.1.5 Iron and Steels

Iron is technically the most versatile and economically the most important base metal for a great variety of structural and magnetic materials, most of which are called steels. With increasing temperature, iron undergoes two structural phase transitions,

$$\alpha \text{ (bcc)} \leftrightarrow \gamma \text{ (fcc)} \text{ at } 911^\circ\text{C}$$

and

$$\gamma \text{ (fcc)} \leftrightarrow \delta \text{ (bcc)} \text{ at } 1392^\circ\text{C},$$

and a magnetic phase transition,

$$\alpha_{\text{ferromagnetic}} \leftrightarrow \alpha_{\text{paramagnetic}} \text{ at } 769^\circ\text{C},$$

at ambient pressure. At elevated pressure levels, Fe forms a third structural phase ε (hcp). These phase

transitions, their variation upon alloying, and the concomitant phase transformations are the thermodynamic, structural and microstructural basis for the unique variety of iron-based alloys and of their properties [1.52, 77–80].

The wide variety of standards for steels which have developed from national standards and efforts of international standardization are compiled in [1.81]. In the present section we are using different standard designations as provided by the sources used. In the following sections, the SAE (Society of Automotive Engineers), AISI (American Iron and Steel Institute), and UNS (Unified Numbering System) designations are the dominating ones.

3.1.5.1 Phase Relations and Phase Transformations

Iron-Carbon Alloys

The most frequent alloying element of iron is carbon. The Fe–C phase diagram (Fig. 3.1-99) shows the important metastable phase equilibria involving the metastable carbide Fe_3C , called cementite, in dashed lines, whereas the stable equilibria with graphite C are shown in solid lines. The formation of Fe_3C predominates in most carbon and low-alloy steels because the activation energy of its nucleation is considerably lower than that of graphite. At higher carbon contents (2.5–4.0 wt% C) and in the presence of Si (1.0–3.0 wt% Si), graphite formation is favored. This is the basis of alloying and microstructure of gray cast iron (see Sect. 3.1.5.7).

The Fe–C phase forms interstitial solid solutions of α - and γ -Fe. The solid solution phase of α -Fe is called ferrite, the solid solution phase based on γ -Fe is called austenite in the binary Fe–C system. These

terms for the solid solutions phases of α - and γ -Fe are applied to all other Fe-based alloy systems as well. Since phase transformations induced by cooling from the austenite phase field play a major role to induce particular microstructures and properties, some resulting microstructures have also been given particular terms and form the basis of the nomenclature in steels. Cooling of Fe–C alloys from the austenite phase field can lead to three different phase transformations below the eutectoid temperature of 1009 K (736 °C). Their kinetics of formation depends on composition and cooling rate. The transformation products are:

- Pearlite, a lamellar product of ferrite and cementite. It is formed by a discontinuous (pearlitic) transformation, i.e., both phases are formed side by side in the reaction front. The lamellar spacing decreases with decreasing temperature of formation. The maximum rate of formation occurs at about 500 °C.

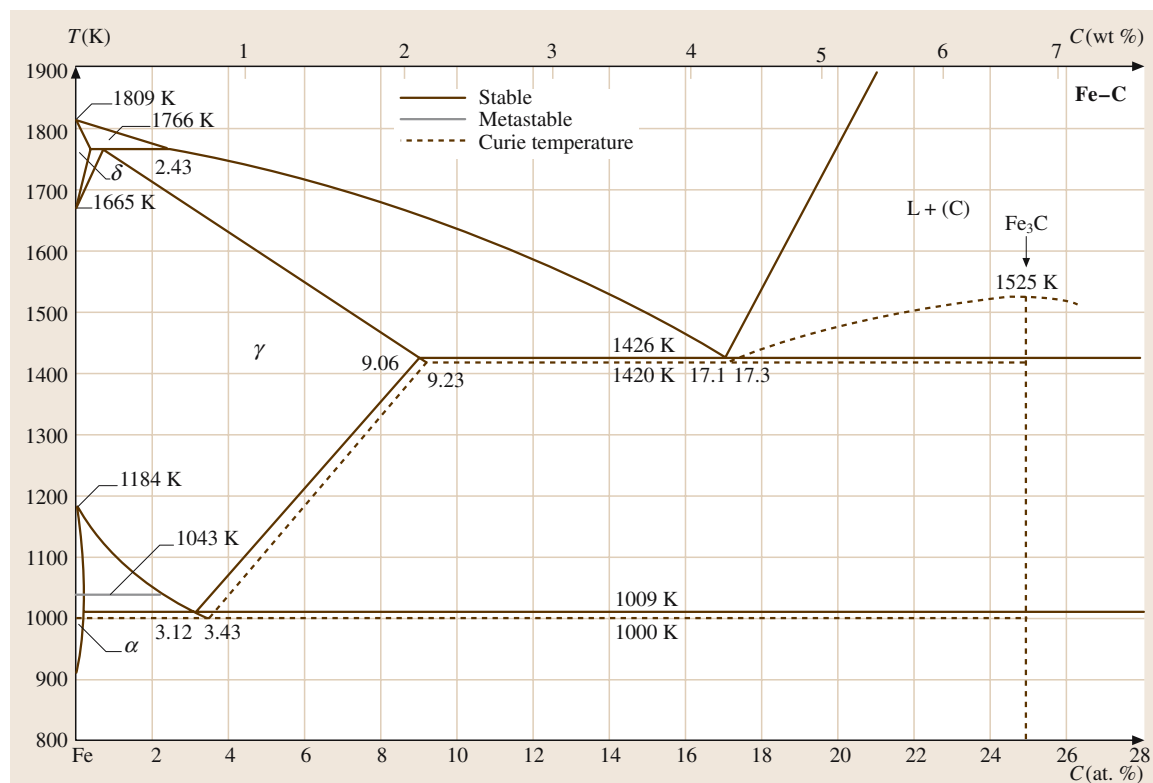


Fig. 3.1-99 Fe–C phase diagram. Metastable equilibria involving cementite Fe_3C are shown in dashed lines, stable equilibria with graphite C are shown in solid lines [1.82] (dotted lines – Curie temperature)

- Bainite, a plate- or spearhead-shaped product consisting of a ferrite matrix in which carbide particles are dispersed. The bainitic transformation mechanism depends sensitively on alloy composition and the temperature of transformation, yielding essentially two microstructural variants. A somewhat coarser transformation product formed at about 450°C is called upper bainite and a finer transformation product formed at about 350°C is termed lower bainite.
- Martensite, a plate-shaped product formed by a diffusionless, athermal transformation. Thermodynamically it is a metastable ferrite, designated as α' and supersaturated in carbon. But by the displacive mechanism of the transformation, the distribution of the C atoms in the martensite lattice is anisotropic such that it has a body-centered tetragonal crystal structure and its c and a parameters vary with the C content accordingly (Fig. 3.1-100). The temperature below which martensite begins to form upon quenching is termed martensite start temperature M_s and depends strongly on the C concentration (Fig. 3.1-101). M_f designates the temperature at which the transformation is complete. In order to promote the diffusionless martensitic transformation, the diffusion-dependent transformations to pearlite and bainite have to be suppressed by rapid cooling, usually termed quenching.

Since martensite formation is used as a main hardening mechanism in steels, the hardenability is a main concern of alloy design and consequence of alloy composition. The lower the rate of formation of the

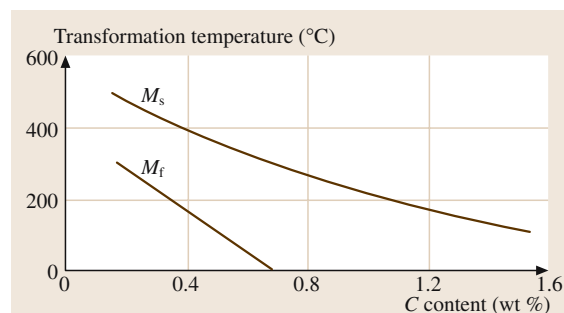


Fig. 3.1-101 Concentration dependence of the martensite transformation temperatures. M_s – martensite start; M_f – martensite finish, i.e., austenite is transformed completely

diffusion-dependent transformations, the higher is the fraction of martensite formed upon cooling from the austenite range, i.e., the hardenability (see Sect. 3.1.5.2). The rates of pearlite and bainite formation are reduced by alloying with carbon and all substitutional alloying elements except by Co. But the decrease of M_s with increasing alloy content has, also, to be taken into account.

Subsequent heat treatment of the phases formed is termed annealing with regard to ferrite and bainite, and tempering with regard to martensite. These heat treatments play a major role in optimizing the microstructure to obtain specific properties. Upon subsequent heat treatment the transformation products listed above undergo the following reactions:

- Pearlite is coarsened by the transition of the cementite lamellae into spherical particles, thus reducing the interfacial free energy per unit volume. The process is called spheroidization and consequently the resulting microstructural constituent is termed spheroidite.
- Bainite is coarsened as well both by recovery of the ferrite plates and by coarsening of the carbide particles.
- Martensite is essentially transformed into bcc ferrite by the precipitation of carbide particles during tempering. The tempering treatment usually leads to the precipitation of metastable carbides from the martensite phase. Different metastable carbides may be formed depending on alloy composition (including substitutional alloying elements), temperature, and time of annealing. A compilation of all metastable carbides occurring in Fe–C(–X) alloys is given in Table 3.1-40.

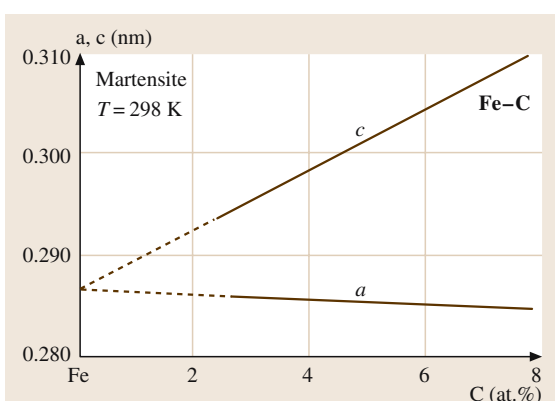


Fig. 3.1-100 Lattice parameters of Fe–C martensite as a function of composition [1.82]

Table 3.1-40 Metastable and stable carbide phases occurring in the Fe–C(–X) alloy system [1.82]

| Phase | Structure | Type | a (nm) | b (nm) | c (nm) |
|----------------------------------|-----------|---------------------------------|---------------------------------|---------|----------|
| Fe ₄ C | cub | | 0.3878 | | |
| Fe ₃ C | orth | Fe ₃ C | 0.50889 | 0.67433 | 0.452353 |
| ε -Fe ₃ C | hex | | 0.273 | | 0.433 |
| Fe ₂ – ₃ C | hex | | 0.4767 | | 0.4354 |
| Fe ₅ C ₂ | mon | Mn ₅ C ₂ | 1.1563 $\beta = 97.73^\circ$ | 0.4573 | 0.5058 |
| Fe ₇ C ₃ | hex | Th ₇ Fe ₃ | 0.6882 | | 0.4540 |
| Fe ₂₀ C ₉ | orth | | 0.9061 | 1.5695 | 0.7937 |

Heat Treatments

The heat treatments referred to above need to be specified rather succinctly such that they can be correlated with the ensuing microstructures and properties. Furthermore, the specifications of heat treatments require taking the cross section and form of the part to be heat treated into account (at least if the cross sections get larger than, say, 0.5 mm). The finite thermal conductivity and the heat capacity of the material will cause any temperature change applied to the surface to occur at a decreasing rate with increasing depth in the heat-treated part. Thus, not only the time and temperature of an isothermal treatment but also the rate of cooling or the rate of heating are common parameters to be specified. Beyond those referred to above, the following treatments are widely applied to steels:

Austenitizing. Heating to and holding in the range of the austenite phase is commonly the first stage of transformation heat treatments. The higher the austenitizing temperature, the more lattice defects such as dislocations and grain boundaries are annihilated. This lowers the rate of nucleation of subsequent phase transformations.

Soft Annealing. This term is used for heat treatment of hardenable steels containing ≥ 0.4 wt% C at temperatures closely below the eutectoid temperature for a duration of ≤ 100 h. It results in a microstructure of coarse grained, ductile ferrite, and coarsened cementite.

Normalizing. This heat treatment is applied to obtain a uniform, fine-grained microstructure. The first step consists of heating the metal rapidly to, and holding it at a temperature 30–50 K above the $(\alpha + \gamma)/\gamma$ phase boundary (also referred to as the A_{c3} line) for hypoeutectoid steels, and heating rapidly to and holding at about 50 K above the eutectoid temperature (also referred to as A_{c1} line). This step results in the formation of

a fairly fine-grained austenite and ferrite structure in the hypo-eutectoid and in a fine-grained austenite with coagulated grain boundary cementite in the hyper-eutectoid compositions. Upon cooling, the austenite transforms into pearlite and this microstructural state has a favorable combination of strength, ductility, and machinability.

Substitutional Iron-Based Alloys

For the phase diagrams with substitutional alloying components shown in later sections, a major aspect pertaining to both the binary alloys shown and the steels alloyed with these components is whether the α or the γ phase of Fe is stabilized. i.e., which phase field is expanded or contracted upon alloying.

Fe–Ni. Figure 3.1-102 shows the Fe–Ni phase equilibria indicating that Ni stabilizes the fcc γ phase. If Fe-rich alloys are quenched from the γ phase field they transform martensitically to bcc α' martensite. The transformation temperatures are shown in Fig. 3.1-103. The Fe–Ni phase diagram is particularly relevant for the controlled thermal expansion and constant-modulus alloys as well as for the soft magnetic Fe–Ni based materials at higher Ni contents. These, in turn, derive their magnetic properties in part from the occurrence of the superlattice phase FeNi₃.

Nickel is added to Fe–C alloys to increase the hardenability and to increase the yield strength of ferrite by solid solution hardening.

Fe–Mn. Figure 3.1-104 shows the Fe–Mn phase equilibria indicating that Mn is stabilizing the fcc γ phase similar to Ni. It should be noted that quenching Fe-rich alloys from the γ -phase field leads to two different martensitic transformations which may result in a bcc structure (α' martensite) or an hcp structure (ϵ' martensite). The transformation temperatures are shown in Fig. 3.1-105. The martensitic transformation can also be induced by deformation. This property is exploited

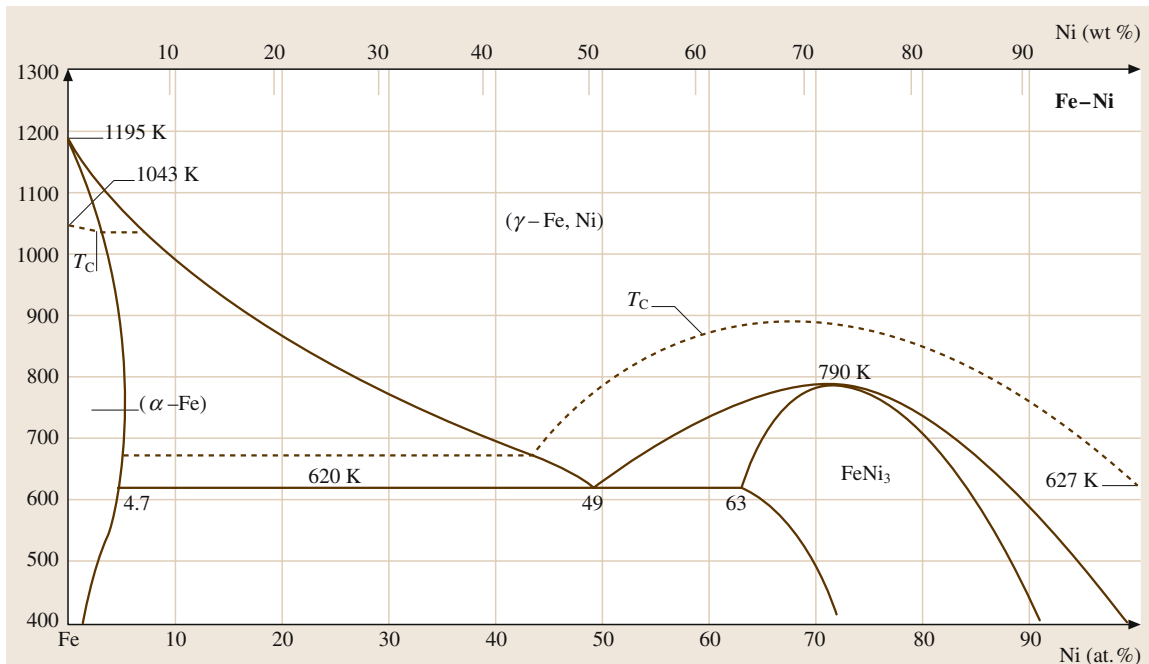


Fig. 3.1-102 Fe–Ni phase diagram. T_C – Curie temperature [1.82]

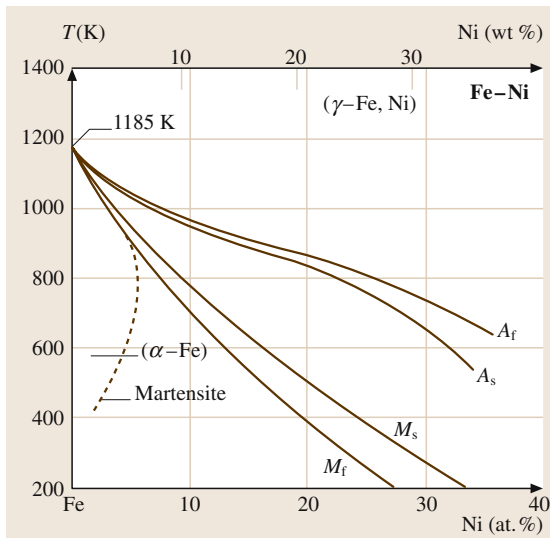


Fig. 3.1-103 Martensitic transformation temperatures of Fe-rich Fe–Ni alloys. The reverse transformation is characterized by the A_s (austenite start) and A_f (austenite finish) temperatures [1.82]

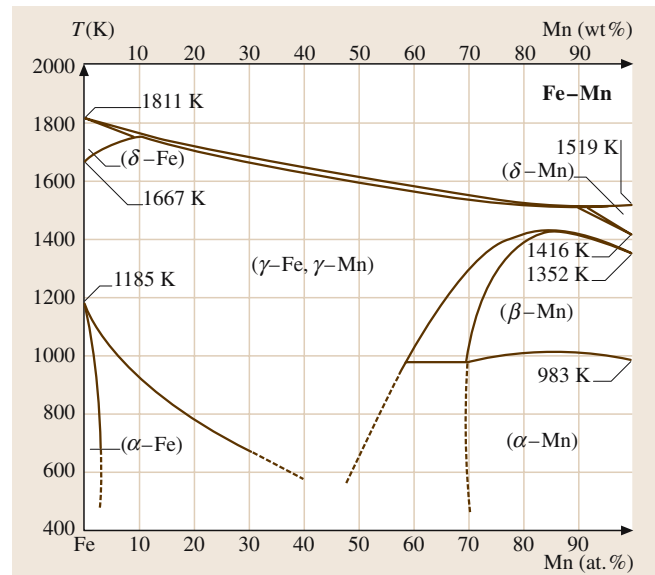


Fig. 3.1-104 Fe–Mn phase diagram [1.82]

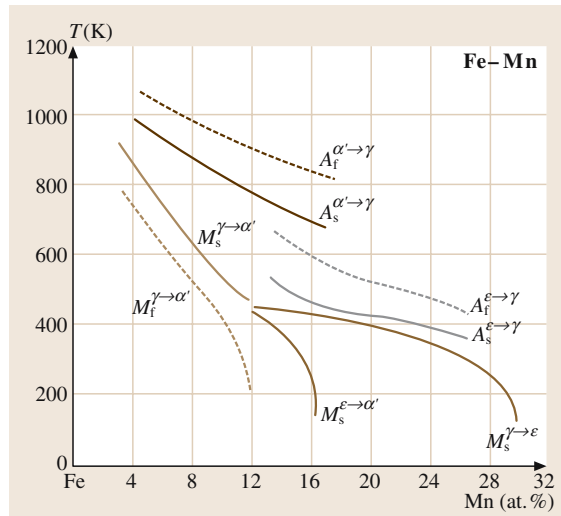


Fig. 3.1-105 Martensitic transformation temperatures of Fe-rich Fe–Mn alloys. The superscripts indicate the transforming phases [1.82]

in the design of wear-resistant steels (Hatfield steel: 12 wt% Mn, 1 wt% C).

Manganese is contained in practically all commercial steels because it is used for deoxidation of the melt. Typical contents are 0.3–0.9 wt% Mn. Manganese increases the hardenability of steels and contributes moderately to the yield strength by solid solution hardening.

Fe–Cr. The Fe–Cr phase diagram, Fig. 3.1-106, is the prototype of the case of an iron-based system with an α -phase stabilizing component. Chromium is the most important alloying element of corrosion resistant, ferritic stainless steels and ferritic heat-resistant steels. If α -Fe–Cr alloys are quenched from above 1105 K and subsequently annealed, they decompose according to a metastable miscibility gap shown in Fig. 3.1-107. This decomposition reaction can cause severe embrittlement which is called “475 °C-embrittlement” in ferritic chromium steels. Embrittlement can also occur upon formation of the σ phase.

In carbon steels, Cr is added to increase corrosion and oxidation resistance because it promotes the formation of stable passivating and protective oxide layers. Moreover, Cr is a strong carbide former which modifies and delays the formation of pearlite and bainite, thus increasing the hardenability. In heat-resistant steels Cr contributes to the high-temperature yield strength.

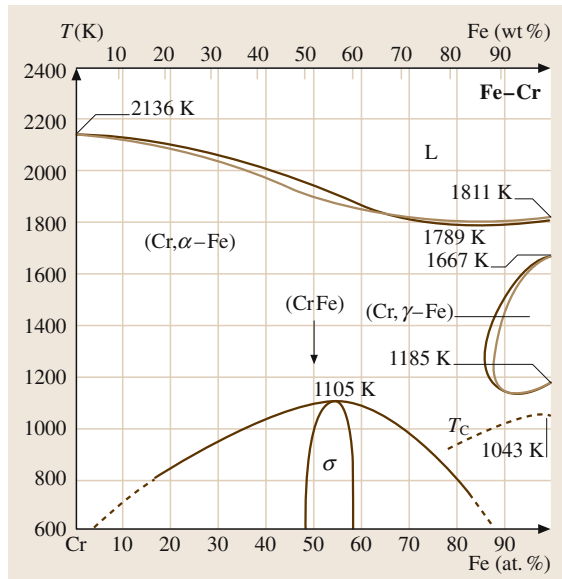


Fig. 3.1-106 Fe–Cr phase diagram [1.82]

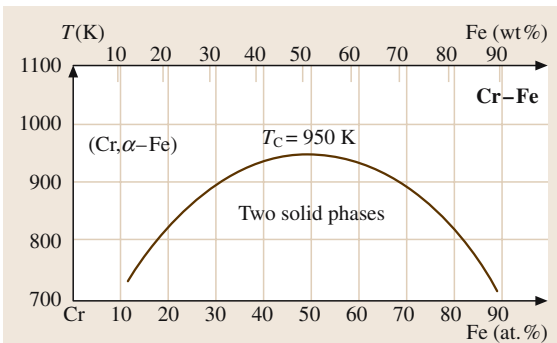


Fig. 3.1-107 Metastable miscibility gap in the Fe–Cr alloy system [1.82]

Fe–Si. The phase diagram Fe–Si, Fig. 3.1-108, shows that Si is a strong ferrite former. The main application of binary Fe–Si alloys is in the form of steels with ≤ 3.5 wt% Si which have an optimum combination of high magnetic moment, low magnetostriiction, and low magnetocrystalline anisotropy such that they are the ideal material for high induction and low magnetic power loss applications such as power transformers. Data are given in Sect. 4.3.2.3.

In Fe–C steelmaking, Si is one of the principal deoxidizers. It may amount to 0.05–0.3 wt% Si in the steel depending on the deoxidizing treatment and the amount of other deoxidants used. At these levels of concentration Si contributes only moderately to the strength of ferrite and causes no significant loss of ductility.

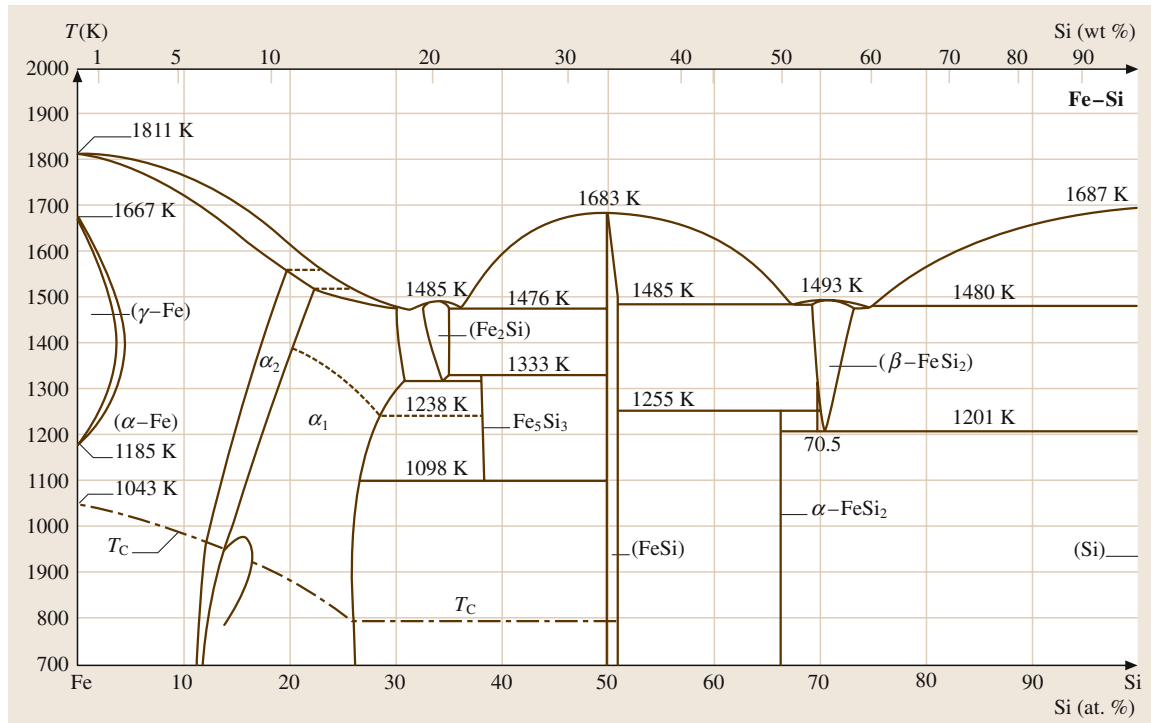


Fig. 3.1-108 Fe–Si phase diagram [1.82]

3.1.5.2 Carbon and Low-Alloy Steels

The largest group of steels produced both by number of variants and by volume is that of carbon and low-alloy steels. It is characterized by the fact that most of the phase relations and phase transformations may be referred to the binary Fe–C phase diagram or comparatively small deviations from it. These steels are treated extensively in [1.80].

Compositions and Properties of Carbon Steels

According to the effect of carbon concentration on the phases formed and on their properties, Fig. 3.1-109 shows the variation of the effective average mechanical properties of as-rolled 25-mm bars of plain carbon steels as an approximate survey of the typical concentration dependence.

Carbon steels are defined as containing up to 1 wt% C and a total of 2 wt% alloying elements. Apart from the deoxidizing alloying elements Mn and Si, two impurity elements are always present in carbon steels: phosphorous and sulfur. Phosphorus increases strength

and hardness significantly by solid solution hardening, but severely decreases ductility and toughness. Only in exceptional cases may P be added deliberately to increase machinability and corrosion resistance. Sulfur has essentially no effect on the strength properties since it is practically insoluble in ferrite. However, it decreases the ductility and fracture toughness. But S is added deliberately along with an increased Mn content to promote the formation of MnS. This compound is formed in small particles which are comparatively soft and serve as effective chip breakers in free-cutting steel grades, thus increasing machinability. On the basis of these effects of the most common alloying and impurity elements, carbon steel compositions are specified as listed in Table 3.1-41 and free-cutting carbon steel compositions are specified as listed in Table 3.1-42.

A survey of the alloying elements used and of the ranges of composition applied in carbon and low-alloy steels may be gained from the SAE-AISI system of designations for carbon and alloy steels listed in Table 3.1-43. Extensive cross references to other standards may be found in [1.81].

Table 3.1-41 Standard carbon steel compositions applicable to semi-finished products for forging, hot-rolled and cold-finished bars, wire rods, and seamless tubing [1.80]. Selected grades

| Designation UN number | SAE-AISI number | Cast or heat chemical ranges and limits ^a (wt%) | | | P_{\max} | S_{\max} |
|-----------------------------|--------------------|--|-----------|--|------------|------------|
| | | C | Mn | | | |
| G10050 | 1005 | 0.06 max | 0.35 max | | 0.040 | 0.050 |
| G10100 | 1010 | 0.08–0.13 | 0.30–0.60 | | 0.040 | 0.050 |
| G10200 | 1020 | 0.18–0.23 | 0.30–0.60 | | 0.040 | 0.050 |
| G10300 | 1030 | 0.28–0.34 | 0.60–0.90 | | 0.040 | 0.050 |
| G10400 | 1040 | 0.37–0.44 | 0.60–0.90 | | 0.040 | 0.050 |
| G10500 | 1050 | 0.48–0.55 | 0.60–0.90 | | 0.040 | 0.050 |
| G10600 | 1060 | 0.55–0.65 | 0.60–0.90 | | 0.040 | 0.050 |
| G10700 | 1070 | 0.65–0.75 | 0.60–0.90 | | 0.040 | 0.050 |
| G10800 | 1080 | 0.75–0.88 | 0.60–0.90 | | 0.040 | 0.050 |
| G10900 | 1090 | 0.85–0.98 | 0.60–0.90 | | 0.040 | 0.050 |

^a When silicon ranges or limits are required for bar and semifinished products, the following ranges are commonly used: 0.10% max; 0.10 to 0.20%; 0.15 to 0.35%; 0.20 to 0.40%; or 0.30 to 0.60%. For rods the following ranges are commonly used: 0.10 max; 0.07–0.15%; 0.10–0.20%; 0.15–0.35%; 0.20–0.40%; and 0.30–0.60%. Steels listed in this table can be produced with additions of lead or boron. Leaded steels typically contain 0.15–0.40% Pb and are identified by inserting the letter L in the designation (10L45); boron steels can be expected to contain 0.0005–0.003% B and are identified by inserting the letter B in the designation (10B46)

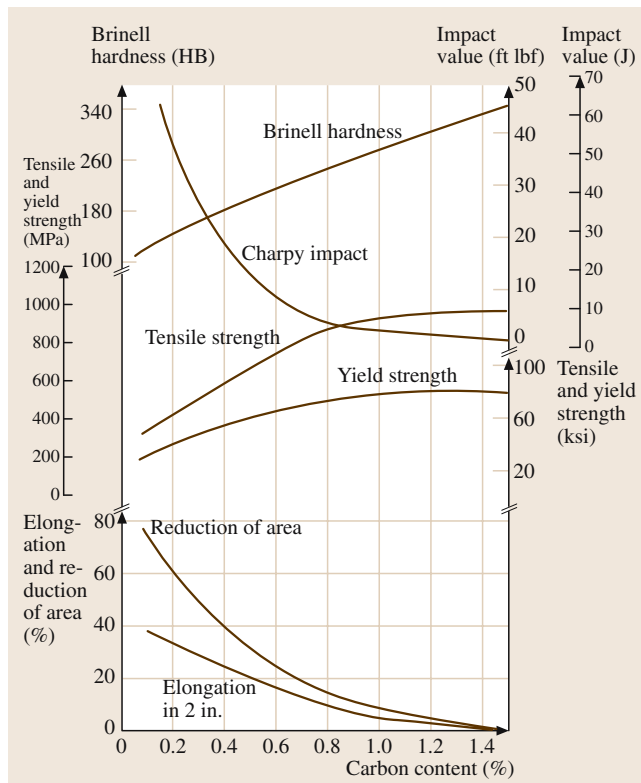


Fig. 3.1-109 Variations in average mechanical properties of as-rolled 25-mm-diam. bars of plain carbon steels as a function of carbon content [1.80]

Table 3.1-42 Standard free-cutting (re-sulfurized) carbon steel compositions applicable to semi-finished products for forging, hot-rolled and cold-finished bars, and seamless tubing [1.80]

| Designation UN number | SAE-AISI number | Cast or heat chemical ranges and limits ^a (wt%) | | | |
|-----------------------------|--------------------|--|-----------|------------------|-----------|
| | | C | Mn | P _{max} | S |
| G11080 | 1108 | 0.08–0.13 | 0.85–0.98 | 0.040 | 0.08–0.13 |
| G11100 | 1110 | 0.08–0.13 | 0.30–0.60 | 0.040 | 0.08–0.13 |
| G11170 | 1117 | 0.14–0.20 | 1.00–1.30 | 0.040 | 0.08–0.13 |
| G11180 | 1118 | 0.14–0.20 | 1.30–1.60 | 0.040 | 0.08–0.13 |
| G11370 | 1137 | 0.32–0.39 | 1.35–1.65 | 0.040 | 0.08–0.13 |
| G11390 | 1139 | 0.35–0.43 | 1.35–1.65 | 0.040 | 0.13–0.20 |
| G11400 | 1140 | 0.37–0.44 | 0.70–1.00 | 0.040 | 0.08–0.13 |
| G11410 | 1141 | 0.37–0.45 | 1.35–1.65 | 0.040 | 0.08–0.13 |
| G11440 | 1144 | 0.40–0.48 | 1.35–1.65 | 0.040 | 0.24–0.33 |
| G11460 | 1146 | 0.42–0.49 | 0.70–1.00 | 0.040 | 0.08–0.13 |
| G11510 | 1151 | 0.48–0.55 | 0.70–1.00 | 0.040 | 0.08–0.13 |

^a When lead ranges or limits are required or when silicon or limits are required for bars or semifinished products, the values in Table 5 apply. For rods, the following ranges and limits for silicon are commonly used: up to SAE 1110 inclusive, 0.10% max; SAE 1117 and over, 0.10%, 0.10–0.20%, or 0.15–0.35%

Table 3.1-43 SAE-AISI system of designations for carbon and low-alloy steels [1.80]

| Numerals and digits | Type of steel and nominal alloy content (wt%) |
|--|--|
| Carbon steels | |
| 10xx ^a | Plain carbon (Mn 100 max) |
| 11xx | Resulfurized |
| 12xx | Resulfurized and rephosphorized |
| 15xx | Plain carbon (max Mn range: 1.00–1.65) |
| Manganese steels | |
| 13xx | Mn 1.75 |
| Nickel steels | |
| 23xx | Ni 3.50 |
| 25xx | Ni 5.00 |
| Nickel-chromium steels | |
| 31xx | Ni 1.25; Cr 0.65 and 0.80 |
| 32xx | Ni 1.75; Cr 1.07 |
| 33xx | Ni 3.50; Cr 1.50 and 1.57 |
| 34xx | Ni 3.00; Cr 0.77 |
| Molybdenum steels | |
| 40xx | Mo 0.20 and 0.25 |
| 44xx | Mo 0.40 and 0.52 |
| Chromium-molybdenum steels | |
| 41xx | Cr 0.50, 0.80, and 0.95; Mo 0.12, 0.20, 0.25, and 0.30 |
| Nickel-chromium-molybdenum steels | |
| 43xx | Ni 1.82; Cr 0.50 and 0.80; Mo 0.25 |
| 43BVxx | Ni 1.82; Cr 0.50; Mo 0.12 and 0.25; V 0.03 min |
| 47xx | Ni 1.05; Cr 0.45; Mo 0.20 and 0.35 |
| 81xx | Ni 0.30; Cr 0.40; Mo 0.12 |
| 86xx | Ni 0.55; Cr 0.50; Mo 0.20 |

Table 3.1-43 SAE-AISI system of designations for carbon and low-alloy steels [1.80], cont.

| Numerals and digits | Type of steel and nominal alloy content (wt%) |
|---------------------------------|--|
| 87xx | Ni 0.55; Cr 0.50; Mo 0.25 |
| 88xx | Ni 0.55; Cr 0.50; Mo 0.35 |
| 93xx | Ni 3.25; Cr 1.20; Mo 0.12 |
| 94xx | Ni 0.45; Cr 0.40; Mo 0.12 |
| 97xx | Ni 0.55; Cr 0.20; Mo 0.20 |
| 98xx | Ni 1.00; Cr 0.80; Mo 0.25 |
| Nickel-molybdenum steels | |
| 46xx | Ni 0.85 and 1.82; Mo 0.20 and 0.25 |
| 48xx | Ni 3.50; Mo 0.25 |
| Chromium steels | |
| 50xx | Cr 0.27, 0.40, 0.50, and 0.65 |
| 51xx | Cr 0.80, 0.87, 0.92, 0.95, 1.00, and 1.05 |
| 50xxx | Cr 0.50; C 1.00 min |
| 51xxx | Cr 1.02; C 1.00 min |
| 52xxx | Cr 1.45; C 1.00 min |
| Chromium-vanadium steels | |
| 61xx | Cr 0.60, 0.80, and 0.95; V 0.10 and 0.15 min |
| Tungsten-chromium steels | |
| 72xx | W 1.75; Cr 0.75 |
| Silicon-manganese steels | |
| 92xx | Si 1.40 and 2.00; Mn 0.65, 0.82, and 0.85; Cr 0 and 0.65 |
| Boron steels | |
| xxBxx | B denotes boron steel |
| Leaded steels | |
| xxLxx | L denotes leaded steel |
| Vanadium steels | |
| xxVxx | V denotes vanadium steel |

^a The xx in the last two digits of these designations indicates that the carbon content (in hundredths of a weight percent) is to be inserted

Turning to the mechanical properties, it should be emphasized that the microstructure has a decisive influence on the properties of all steels. Therefore the composition and the prior thermal, mechanical, or thermomechanical treatments which determine the phase transformations and ensuing microstructural state of a steel will always have to be taken into account. Accordingly, tabulated property data will invariably be given with reference to mechanical and thermal treatments applied. The terms used and their specific definitions are outlined in Sect. 3.1.5.1.

In plain carbon steels the C content and microstructure are determining the mechanical properties. Manganese is providing moderate solid solution

strengthening and increases the hardenability. The properties of plain carbon steels are also affected by the other common residual elements Si, P, and S. Furthermore, the gasses O, N, and H and their reaction products may play a role. Their content depends largely on the melting, deoxidizing and pouring practice. While Fig. 3.1-109 illustrates the general effect of C content on the mechanical properties if the austenite grain size and transformation microstructure are held essentially constant. Tables 3.1-44 and 3.1-45 list the mechanical properties of representative carbon and low alloy steels in specified states as a function of deformation and heat treatment.

Table 3.1-44 Mechanical properties of selected carbon and low-alloy steels in the hot-rolled, normalized, and annealed conditions [1.80]

| AISI No. ^a | Treatment | Austenitizing temperature (°C) | Tensile strength (MPa) | Yield strength (MPa) | Elongation (%) | Reduction in area (%) | Hardness (HB) |
|-----------------------|------------|--------------------------------|------------------------|----------------------|----------------|-----------------------|---------------|
| 1015 | As-rolled | — | 420.6 | 313.7 | 39.0 | 61.0 | 126 |
| | Normalized | 925 | 424.0 | 324.1 | 37.0 | 69.6 | 121 |
| | Annealed | 870 | 386.1 | 284.4 | 37.0 | 69.7 | 111 |
| 1020 | As-rolled | — | 448.2 | 330.9 | 36.0 | 59.0 | 143 |
| | Normalized | 870 | 441.3 | 346.5 | 35.8 | 67.9 | 131 |
| | Annealed | 870 | 394.7 | 294.8 | 36.5 | 66.0 | 111 |
| 1022 | As-rolled | — | 503.3 | 358.5 | 35.0 | 67.0 | 149 |
| | Normalized | 925 | 482.6 | 358.5 | 34.0 | 67.5 | 143 |
| | Annealed | 870 | 429.2 | 317.2 | 35.0 | 63.6 | 137 |
| 1030 | As-rolled | — | 551.6 | 344.7 | 32.0 | 57.0 | 179 |
| | Normalized | 925 | 520.6 | 344.7 | 32.0 | 60.8 | 149 |
| | Annealed | 845 | 463.7 | 341.3 | 31.2 | 57.9 | 126 |
| 1040 | As-rolled | — | 620.5 | 413.7 | 25.0 | 50.0 | 201 |
| | Normalized | 900 | 589.5 | 374.0 | 28.0 | 54.9 | 170 |
| | Annealed | 790 | 518.8 | 353.4 | 30.2 | 57.2 | 149 |
| 1050 | As-rolled | — | 723.9 | 413.7 | 20.0 | 40.0 | 229 |
| | Normalized | 900 | 748.1 | 427.5 | 20.0 | 39.4 | 217 |
| | Annealed | 790 | 636.0 | 365.4 | 23.7 | 39.9 | 187 |
| 1060 | As-rolled | — | 813.6 | 482.6 | 17.0 | 34.0 | 241 |
| | Normalized | 900 | 775.7 | 420.6 | 18.0 | 37.2 | 229 |
| | Annealed | 790 | 625.7 | 372.3 | 22.5 | 38.2 | 179 |
| 1080 | As-rolled | — | 965.3 | 586.1 | 12.0 | 17.0 | 293 |
| | Normalized | 900 | 1010.1 | 524.0 | 11.0 | 20.6 | 293 |
| | Annealed | 790 | 615.4 | 375.8 | 24.7 | 45.0 | 174 |
| 1095 | As-rolled | — | 965.3 | 572.3 | 9.0 | 18.0 | 293 |
| | Normalized | 900 | 1013.5 | 499.9 | 9.5 | 13.5 | 293 |
| | Annealed | 790 | 656.7 | 379.2 | 13.0 | 20.6 | 192 |
| 1117 | As-rolled | — | 486.8 | 305.4 | 33.0 | 63.0 | 143 |
| | Normalized | 900 | 467.1 | 303.4 | 33.5 | 63.8 | 137 |
| | Annealed | 855 | 429.5 | 279.2 | 32.8 | 58.0 | 121 |
| 1118 | As-rolled | — | 521.2 | 316.5 | 32.0 | 70.0 | 149 |
| | Normalized | 925 | 477.8 | 319.2 | 33.5 | 65.9 | 143 |
| | Annealed | 790 | 450.2 | 284.8 | 34.5 | 66.8 | 131 |
| 1137 | As-rolled | — | 627.4 | 379.2 | 28.0 | 61.0 | 192 |
| | Normalized | 900 | 668.8 | 396.4 | 22.5 | 48.5 | 197 |
| | Annealed | 790 | 584.7 | 344.7 | 26.8 | 53.9 | 174 |
| 1141 | As-rolled | — | 675.7 | 358.5 | 22.0 | 38.0 | 192 |
| | Normalized | 900 | 706.7 | 405.4 | 22.7 | 55.5 | 201 |
| | Annealed | 815 | 598.5 | 353.0 | 25.5 | 49.3 | 163 |
| 1144 | As-rolled | — | 703.3 | 420.6 | 21.0 | 41.0 | 212 |
| | Normalized | 900 | 667.4 | 399.9 | 21.0 | 40.4 | 197 |
| | Annealed | 790 | 584.7 | 346.8 | 24.8 | 41.3 | 167 |
| 1340 | Normalized | 870 | 836.3 | 558.5 | 22.0 | 62.9 | 248 |
| | Annealed | 800 | 703.3 | 436.4 | 25.5 | 57.3 | 207 |
| 3140 | Normalized | 870 | 891.5 | 599.8 | 19.7 | 57.3 | 262 |
| | Annealed | 815 | 689.5 | 422.6 | 24.5 | 50.8 | 197 |

Table 3.1–44 Mechanical properties of selected carbon and low-alloy steels [1.80], cont.

| AISI No. ^a | Treatment | Austenitizing temperature (°C) | Tensile strength (MPa) | Yield strength (MPa) | Elongation (%) | Reduction in area (%) | Hardness (HB) |
|--------------------------|------------|--------------------------------------|------------------------------|----------------------------|-------------------|-----------------------------|------------------|
| 4130 | Normalized | 870 | 668.8 | 436.4 | 25.5 | 59.5 | 197 |
| | Annealed | 865 | 560.5 | 360.6 | 28.2 | 55.6 | 156 |
| 4140 | Normalized | 870 | 1020.4 | 655.0 | 17.7 | 46.8 | 302 |
| | Annealed | 815 | 655.0 | 417.1 | 25.7 | 56.9 | 197 |
| 4150 | Normalized | 870 | 1154.9 | 734.3 | 11.7 | 30.8 | 321 |
| | Annealed | 815 | 729.5 | 379.2 | 20.2 | 40.2 | 197 |
| 4320 | Normalized | 895 | 792.9 | 464.0 | 20.8 | 50.7 | 235 |
| | Annealed | 850 | 579.2 | 609.5 | 29.0 | 58.4 | 163 |
| 4340 | Normalized | 870 | 1279.0 | 861.8 | 12.2 | 36.3 | 363 |
| | Annealed | 810 | 744.6 | 472.3 | 22.0 | 49.9 | 217 |
| 4620 | Normalized | 900 | 574.3 | 366.1 | 29.0 | 66.7 | 174 |
| | Annealed | 855 | 512.3 | 372.3 | 31.3 | 60.3 | 149 |
| 4820 | Normalized | 860 | 75.0 | 484.7 | 24.0 | 59.2 | 229 |
| | Annealed | 815 | 681.2 | 464.0 | 22.3 | 58.8 | 197 |
| 5140 | Normalized | 870 | 792.9 | 472.3 | 22.7 | 59.2 | 229 |
| | Annealed | 830 | 572.3 | 293.0 | 28.6 | 57.3 | 167 |
| 5150 | Normalized | 870 | 870.8 | 529.0 | 20.7 | 58.7 | 255 |
| | Annealed | 825 | 675.7 | 357.1 | 22.0 | 43.7 | 197 |
| 5160 | Normalized | 855 | 957.0 | 530.9 | 17.5 | 44.8 | 269 |
| | Annealed | 815 | 722.6 | 275.8 | 17.2 | 30.6 | 197 |
| 6150 | Normalized | 815 | 722.6 | 275.8 | 17.2 | 30.6 | 197 |
| | Annealed | 815 | 667.4 | 412.3 | 23.0 | 48.4 | 197 |
| 8620 | Normalized | 915 | 632.9 | 357.1 | 26.3 | 59.7 | 183 |
| | Annealed | 870 | 536.4 | 385.4 | 31.3 | 62.1 | 149 |
| 8630 | Normalized | 870 | 650.2 | 429.5 | 23.5 | 53.5 | 187 |
| | Annealed | 845 | 564.0 | 372.3 | 29.0 | 58.9 | 156 |
| 8650 | Normalized | 870 | 1023.9 | 688.1 | 14.0 | 40.4 | 302 |
| | Annealed | 795 | 715.7 | 386.1 | 22.5 | 46.4 | 212 |
| 8740 | Normalized | 870 | 929.4 | 606.7 | 16.0 | 47.9 | 269 |
| | Annealed | 815 | 695.0 | 415.8 | 22.2 | 46.4 | 201 |
| 9255 | Normalized | 900 | 932.9 | 579.2 | 19.7 | 43.4 | 269 |
| | Annealed | 845 | 774.3 | 486.1 | 21.7 | 41.1 | 229 |
| 9310 | Normalized | 890 | 906.7 | 570.9 | 18.8 | 58.1 | 269 |
| | Annealed | 845 | 820.5 | 439.9 | 17.3 | 42.1 | 241 |

^a All grades are fine-grained except for those in the 1100 series, which are coarse-grained. Heat-treated specimens were oil quenched unless otherwise indicated

Table 3.1-45 Mechanical properties of selected carbon and alloy steels in the quenched-and-tempered condition, heat treated as 25 mm rounds [1.80]

| AISI No. ^a | Tempering temperature (°C) | Tensile strength (MPa) | Yield strength (MPa) | Elongation (%) | Reduction in area (%) | Hardness HB |
|--------------------------|----------------------------------|------------------------------|----------------------------|-------------------|-----------------------------|----------------|
| 1030 ^b | 205 | 848 | 648 | 17 | 47 | 495 |
| | 315 | 800 | 621 | 19 | 53 | 401 |
| | 425 | 731 | 579 | 23 | 60 | 302 |
| | 540 | 669 | 517 | 28 | 65 | 255 |
| | 650 | 586 | 441 | 32 | 70 | 207 |
| 1040 ^b | 205 | 896 | 662 | 16 | 45 | 514 |
| | 315 | 889 | 648 | 18 | 52 | 444 |
| | 425 | 841 | 634 | 21 | 57 | 352 |
| | 540 | 779 | 593 | 23 | 61 | 269 |
| | 650 | 669 | 496 | 28 | 68 | 201 |
| 1040 | 205 | 779 | 593 | 19 | 48 | 262 |
| | 315 | 779 | 593 | 20 | 53 | 255 |
| | 425 | 758 | 552 | 21 | 54 | 241 |
| | 540 | 717 | 490 | 26 | 57 | 212 |
| | 650 | 634 | 434 | 29 | 65 | 192 |
| 1050 ^b | 205 | 1124 | 807 | 9 | 27 | 514 |
| | 315 | 1089 | 793 | 13 | 36 | 444 |
| | 425 | 1000 | 758 | 19 | 48 | 375 |
| | 540 | 862 | 655 | 23 | 58 | 293 |
| | 650 | 717 | 538 | 28 | 65 | 235 |
| 1050 | 205 | — | — | — | — | — |
| | 315 | 979 | 724 | 14 | 47 | 321 |
| | 425 | 938 | 655 | 20 | 50 | 277 |
| | 540 | 876 | 579 | 23 | 53 | 262 |
| | 650 | 738 | 469 | 29 | 60 | 223 |
| 1060 | 205 | 1103 | 779 | 13 | 40 | 321 |
| | 315 | 1103 | 779 | 13 | 40 | 321 |
| | 425 | 1076 | 765 | 14 | 41 | 311 |
| | 540 | 965 | 669 | 17 | 45 | 277 |
| | 650 | 800 | 524 | 23 | 54 | 229 |
| 1080 | 205 | 1310 | 979 | 12 | 35 | 388 |
| | 315 | 1303 | 979 | 12 | 35 | 388 |
| | 425 | 1289 | 951 | 13 | 36 | 375 |
| | 540 | 1131 | 807 | 16 | 40 | 321 |
| | 650 | 889 | 600 | 21 | 50 | 255 |
| 1095 ^b | 205 | 1489 | 1048 | 10 | 31 | 601 |
| | 315 | 1462 | 1034 | 11 | 33 | 534 |
| | 425 | 1372 | 958 | 13 | 35 | 388 |
| | 540 | 1138 | 758 | 15 | 40 | 293 |
| | 650 | 841 | 586 | 20 | 47 | 235 |
| 1095 | 205 | 1289 | 827 | 10 | 30 | 401 |
| | 315 | 1262 | 813 | 10 | 30 | 375 |
| | 425 | 1213 | 772 | 12 | 32 | 363 |
| | 540 | 1089 | 676 | 15 | 37 | 321 |
| | 650 | 896 | 552 | 21 | 47 | 269 |

Table 3.1-45 Mechanical properties of selected carbon and alloy steels, cont.

| AISI No. ^a | Tempering temperature (°C) | Tensile strength (MPa) | Yield strength (MPa) | Elongation (%) | Reduction in area (%) | Hardness (HB) |
|--------------------------|----------------------------------|------------------------------|----------------------------|-------------------|-----------------------------|------------------|
| 1137 | 205 | 1082 | 938 | 5 | 22 | 352 |
| | 315 | 986 | 841 | 10 | 33 | 285 |
| | 425 | 876 | 731 | 15 | 48 | 262 |
| | 540 | 758 | 607 | 24 | 62 | 229 |
| | 650 | 655 | 483 | 28 | 69 | 197 |
| 1137 ^b | 205 | 1496 | 1165 | 5 | 17 | 415 |
| | 315 | 1372 | 1124 | 9 | 25 | 375 |
| | 425 | 1103 | 986 | 14 | 40 | 311 |
| | 540 | 827 | 724 | 19 | 60 | 262 |
| | 650 | 648 | 531 | 25 | 69 | 187 |
| 1141 | 205 | 1634 | 1213 | 6 | 17 | 461 |
| | 315 | 1462 | 1282 | 9 | 32 | 415 |
| | 425 | 1165 | 1034 | 12 | 47 | 331 |
| | 540 | 896 | 765 | 18 | 57 | 262 |
| | 650 | 710 | 593 | 23 | 62 | 217 |
| 1144 | 205 | 876 | 627 | 17 | 36 | 277 |
| | 315 | 869 | 621 | 17 | 40 | 262 |
| | 425 | 848 | 607 | 18 | 42 | 248 |
| | 540 | 807 | 572 | 20 | 46 | 235 |
| | 650 | 724 | 503 | 23 | 55 | 217 |
| 1330 ^b | 205 | 1600 | 1455 | 9 | 39 | 459 |
| | 315 | 1427 | 1282 | 9 | 44 | 402 |
| | 425 | 1158 | 1034 | 15 | 53 | 335 |
| | 540 | 876 | 772 | 18 | 60 | 263 |
| | 650 | 731 | 572 | 23 | 63 | 216 |
| 1340 | 205 | 1806 | 1593 | 11 | 35 | 505 |
| | 315 | 1586 | 1420 | 12 | 43 | 453 |
| | 425 | 1262 | 1151 | 14 | 51 | 375 |
| | 540 | 965 | 827 | 14 | 58 | 295 |
| | 650 | 800 | 621 | — | 66 | 252 |
| 4037 | 205 | 1027 | 758 | 6 | 38 | 310 |
| | 315 | 951 | 765 | 14 | 53 | 295 |
| | 425 | 876 | 731 | 20 | 60 | 270 |
| | 540 | 793 | 655 | 23 | 63 | 247 |
| | 650 | 696 | 421 | 29 | 60 | 220 |
| 4042 | 205 | 1800 | 1662 | 12 | 37 | 516 |
| | 315 | 1613 | 1455 | 13 | 42 | 455 |
| | 425 | 1289 | 1172 | 15 | 51 | 380 |
| | 540 | 986 | 883 | 20 | 59 | 300 |
| | 650 | 793 | 689 | 28 | 66 | 238 |
| 4130 ^b | 205 | 1627 | 1462 | 10 | 41 | 467 |
| | 315 | 1496 | 1379 | 11 | 43 | 435 |
| | 425 | 1282 | 1193 | 13 | 49 | 380 |
| | 540 | 1034 | 910 | 17 | 57 | 315 |
| | 650 | 814 | 703 | 22 | 64 | 245 |

Table 3.1-45 Mechanical properties of selected carbon and alloy steels, cont.

| AISI No. ^a | Tempering temperature (°C) | Tensile strength (MPa) | Yield strength (MPa) | Elongation (%) | Reduction in area (%) | Hardness (HB) |
|--------------------------|----------------------------------|------------------------------|----------------------------|-------------------|-----------------------------|------------------|
| 4140 | 205 | 1772 | 1641 | 8 | 38 | 510 |
| | 315 | 1551 | 1434 | 9 | 43 | 445 |
| | 425 | 1248 | 1138 | 13 | 49 | 370 |
| | 540 | 951 | 834 | 18 | 58 | 258 |
| | 650 | 758 | 655 | 22 | 63 | 230 |
| 4150 | 205 | 1931 | 1724 | 10 | 39 | 530 |
| | 315 | 1765 | 1593 | 10 | 40 | 495 |
| | 425 | 1517 | 1379 | 12 | 45 | 440 |
| | 540 | 1207 | 1103 | 15 | 52 | 370 |
| | 650 | 958 | 841 | 19 | 60 | 290 |
| 4340 | 205 | 1875 | 1675 | 10 | 38 | 520 |
| | 315 | 1724 | 1586 | 10 | 40 | 486 |
| | 425 | 1469 | 1365 | 10 | 44 | 430 |
| | 540 | 1172 | 1076 | 13 | 51 | 360 |
| | 650 | 965 | 855 | 19 | 60 | 280 |
| 5046 | 205 | 1744 | 1407 | 9 | 25 | 482 |
| | 315 | 1413 | 1158 | 10 | 37 | 401 |
| | 425 | 1138 | 931 | 13 | 50 | 336 |
| | 540 | 938 | 765 | 18 | 61 | 282 |
| | 650 | 786 | 655 | 24 | 66 | 235 |
| 50B46 | 205 | — | — | — | — | 560 |
| | 315 | 1779 | 1620 | 10 | 37 | 505 |
| | 425 | 1393 | 1248 | 13 | 47 | 405 |
| | 540 | 1082 | 979 | 17 | 51 | 322 |
| | 650 | 883 | 793 | 22 | 60 | 273 |
| 50B60 | 205 | — | — | — | — | 600 |
| | 315 | 1882 | 1772 | 8 | 32 | 525 |
| | 425 | 1510 | 1386 | 11 | 34 | 435 |
| | 540 | 1124 | 1000 | 15 | 38 | 350 |
| | 650 | 896 | 779 | 19 | 50 | 290 |
| 5130 | 205 | 1613 | 1517 | 10 | 40 | 475 |
| | 315 | 1496 | 1407 | 10 | 46 | 440 |
| | 425 | 1275 | 1207 | 12 | 51 | 379 |
| | 540 | 1034 | 938 | 15 | 56 | 305 |
| | 650 | 793 | 689 | 20 | 63 | 245 |
| 5140 | 205 | 1793 | 1641 | 9 | 38 | 490 |
| | 315 | 1579 | 1448 | 10 | 43 | 450 |
| | 425 | 1310 | 1172 | 13 | 50 | 365 |
| | 540 | 1000 | 862 | 17 | 58 | 280 |
| | 650 | 758 | 662 | 25 | 66 | 235 |
| 5150 | 205 | 1944 | 1731 | 5 | 37 | 525 |
| | 315 | 1737 | 1586 | 6 | 40 | 475 |
| | 425 | 1448 | 1310 | 9 | 47 | 410 |
| | 540 | 1124 | 1034 | 15 | 54 | 340 |
| | 650 | 807 | 814 | 20 | 60 | 270 |

Table 3.1-45 Mechanical properties of selected carbon and alloy steels, cont.

| AISI No. ^a | Tempering temperature (°C) | Tensile strength (MPa) | Yield strength (MPa) | Elongation (%) | Reduction in area (%) | Hardness (HB) |
|--------------------------|----------------------------------|------------------------------|----------------------------|-------------------|-----------------------------|------------------|
| 5160 | 205 | 2220 | 1793 | 4 | 10 | 627 |
| | 315 | 1999 | 1772 | 9 | 30 | 555 |
| | 425 | 1606 | 1462 | 10 | 37 | 461 |
| | 540 | 1165 | 1041 | 12 | 47 | 341 |
| | 650 | 896 | 800 | 20 | 56 | 269 |
| 51B60 | 205 | — | — | — | — | 600 |
| | 315 | — | — | — | — | 540 |
| | 425 | 1634 | 1489 | 11 | 36 | 460 |
| | 540 | 1207 | 1103 | 15 | 44 | 355 |
| | 650 | 965 | 869 | 20 | 47 | 290 |
| 6150 | 205 | 1931 | 1689 | 8 | 38 | 538 |
| | 315 | 1724 | 1572 | 8 | 39 | 483 |
| | 425 | 1434 | 1331 | 10 | 43 | 420 |
| | 540 | 1158 | 1069 | 13 | 50 | 345 |
| | 650 | 945 | 841 | 17 | 58 | 282 |
| 81B45 | 205 | 2034 | 1724 | 10 | 33 | 550 |
| | 315 | 1765 | 1572 | 8 | 42 | 475 |
| | 425 | 1407 | 1310 | 11 | 48 | 405 |
| | 540 | 1103 | 1027 | 16 | 53 | 338 |
| | 650 | 896 | 793 | 20 | 55 | 280 |
| 8630 | 205 | 1641 | 1503 | 9 | 38 | 465 |
| | 315 | 1482 | 1392 | 10 | 42 | 430 |
| | 425 | 1276 | 1172 | 13 | 47 | 375 |
| | 540 | 1034 | 896 | 17 | 54 | 310 |
| | 650 | 772 | 689 | 23 | 63 | 240 |
| 8640 | 205 | 1862 | 1669 | 10 | 40 | 505 |
| | 315 | 1655 | 1517 | 10 | 41 | 460 |
| | 425 | 1379 | 1296 | 12 | 45 | 400 |
| | 540 | 1103 | 1034 | 16 | 54 | 340 |
| | 650 | 896 | 800 | 20 | 62 | 280 |
| 86B45 | 205 | 1979 | 1641 | 9 | 31 | 525 |
| | 315 | 1696 | 1551 | 9 | 40 | 475 |
| | 425 | 1379 | 1317 | 11 | 41 | 395 |
| | 540 | 1103 | 1034 | 15 | 49 | 335 |
| | 650 | 903 | 876 | 19 | 58 | 280 |
| 8650 | 205 | 1937 | 1675 | 10 | 38 | 525 |
| | 315 | 1724 | 1551 | 10 | 40 | 490 |
| | 425 | 1448 | 1324 | 12 | 45 | 420 |
| | 540 | 1172 | 1055 | 15 | 51 | 340 |
| | 650 | 965 | 827 | 20 | 58 | 280 |
| 8660 | 205 | — | — | — | — | 580 |
| | 315 | — | — | — | — | 535 |
| | 425 | 1634 | 1551 | 13 | 37 | 460 |
| | 540 | 1310 | 1213 | 17 | 46 | 370 |
| | 650 | 1068 | 951 | 20 | 53 | 315 |

Table 3.1-45 Mechanical properties of selected carbon and alloy steels, cont.

| AISI No. ^a | Tempering temperature (°C) | Tensile strength (MPa) | Yield strength (MPa) | Elongation (%) | Reduction in area (%) | Hardness (HB) |
|--------------------------|----------------------------------|------------------------------|----------------------------|-------------------|-----------------------------|------------------|
| 8740 | 205 | 1999 | 1655 | 10 | 41 | 578 |
| | 315 | 1717 | 1551 | 11 | 46 | 495 |
| | 425 | 1434 | 1358 | 13 | 50 | 415 |
| | 540 | 1207 | 1138 | 15 | 55 | 363 |
| | 650 | 986 | 903 | 20 | 60 | 302 |
| 9255 | 205 | 2103 | 2048 | 1 | 3 | 601 |
| | 315 | 1937 | 1793 | 4 | 10 | 578 |
| | 425 | 1606 | 1489 | 8 | 22 | 477 |
| | 540 | 1255 | 1103 | 15 | 32 | 352 |
| | 650 | 993 | 814 | 20 | 42 | 285 |
| 9260 | 205 | — | — | — | — | 600 |
| | 315 | — | — | — | — | 540 |
| | 425 | 1758 | 1503 | 8 | 24 | 470 |
| | 540 | 1324 | 1131 | 12 | 30 | 390 |
| | 650 | 979 | 814 | 20 | 43 | 295 |
| 94B30 | 205 | 1724 | 1551 | 12 | 46 | 475 |
| | 315 | 1600 | 1420 | 12 | 49 | 445 |
| | 425 | 1344 | 1207 | 13 | 57 | 382 |
| | 540 | 1000 | 931 | 16 | 65 | 307 |
| | 650 | 827 | 724 | 21 | 69 | 250 |

^a All grades are fine-grained except for those in the 1100 series, which are coarse-grained. Heat-treated specimens were oil quenched unless otherwise indicated

^b Water quenched

Hardenability

Hardening of steels is the heat treatment consisting of heating to the range of austenite, cooling in water, oil, or air, and subsequent tempering. The term hardenability refers to the suitability of a steel to be transformed partially or completely from austenite to martensite to a specified depth below the free surface of a workpiece when cooled under specified conditions. This definition reflects that the term hardenability does not only refer to the magnitude of hardness which can be attained for a particular steel, but it relates the extent of hardening achievable to the macroscopic or local cooling rate or isothermal holding time in the transformation range and, thus, to the mechanisms, kinetic phase transformations, and their effects on the mechanical properties.

The amount of martensite formed upon cooling is a function of C content and total steel composition. This behavior is due to two decisive factors of influence:

- The temperature range of transformation of austenite to martensite depends on the C content, as shown in Fig. 3.1-101 of Sect. 3.1.5.1, and
- The diffusion-dependent transformations of austenite (to ferrite, pearlite, and bainite) compete with the martensitic transformation such that the volume fraction available for the latter will decrease as the volume transformed by the former increases. This transformation kinetics of the diffusional phase transformations is strongly dependent on alloy composition.

The lower the cooling rate may be while still permitting one to obtain a high fraction of martensite, the higher the hardenability of steel. This can best be tested by varying the cooling rate and analyzing the resulting microstructure and its hardness (and other mechanical properties). The method used most widely is an ingeniously simple testing procedure, the Jominy end-quench test illustrated in Fig. 3.1-110. The mater-

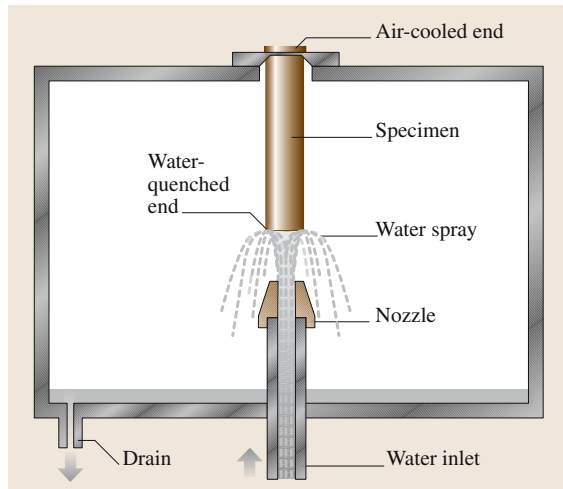


Fig. 3.1-110 Jominy end-quench apparatus

ial to be tested is normalized and a test bar 100 mm long and 25 mm in diameter is machined. This specimen is austenitized and transferred to the fixture (shown in Fig. 3.1-110) holding it vertically 13 mm above the nozzle through which water is directed against the bottom face of the specimen. While the bottom end is quenched by water, the top end is slowly cooled in air and intermediate cooling rates occur at intermediate positions. After the test, hardness readings and microstructural analyses may be taken along the bar. They can be correlated to the pre-determined approximate cooling rate at a given temperature, as shown for a characteristic example in Fig. 3.1-111.

The hardenability of numerous commonly used steels has been characterised quantitatively by extensive investigations of their transformation behavior as a function of temperature and time. These investigations have been carried out in two modes of heat treatment:

- Quenching from the austenite range to a temperature in the transformation range at which the specimen is held isothermally in a salt or a lead bath for different times, and finally quenched to room temperature to be investigated regarding the transformation products by microstructural and supplementary measurements. The resulting plots of the beginning of formation of the different transforma-

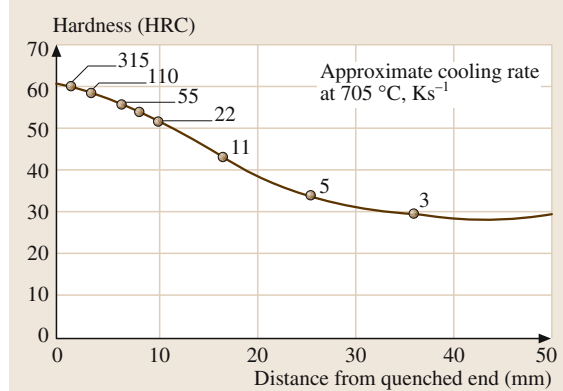


Fig. 3.1-111 Plot of end-quench hardenability data of an AISI 8650 steel (0.49 wt% C, 0.98 wt% Mn, 0.29 wt% Si, 0.59 wt% Ni, 0.47 wt% Cr, 0.19 wt% Mo) [1.80]

tion products (sometimes including the fractional amounts and end of transformation) are termed time-temperature-transformation (TTT) or isothermal transformation (IT) diagrams. An example is shown as Fig. 3.1-112.

- Cooling from the austenite range through the transformation range at different cooling rates, and investigating the temperature of onset of transformation of the different products for different cooling rates by microstructural and supplementary measurements, e.g., dilatometry. The resulting plot is called a continuous-cooling-transformation (CCT) diagram. An example is shown in Fig. 3.1-113. The critical cooling rate means the lowest rate for which a fully martensitic state can be obtained.

Apart from empirical determinations of these transformation diagrams, methods of prediction based on nucleation theory and phenomenological growth theory using the Johnson–Mehl–Avrami equation have been devised to estimate TTT diagrams [1.83].

The hardenability increases with increasing carbon and metallic alloy element concentration (with the exception of Co). The transformation kinetics and ensuing hardenability properties are documented extensively in compilations of TTT and CCT diagrams such as [1.84].

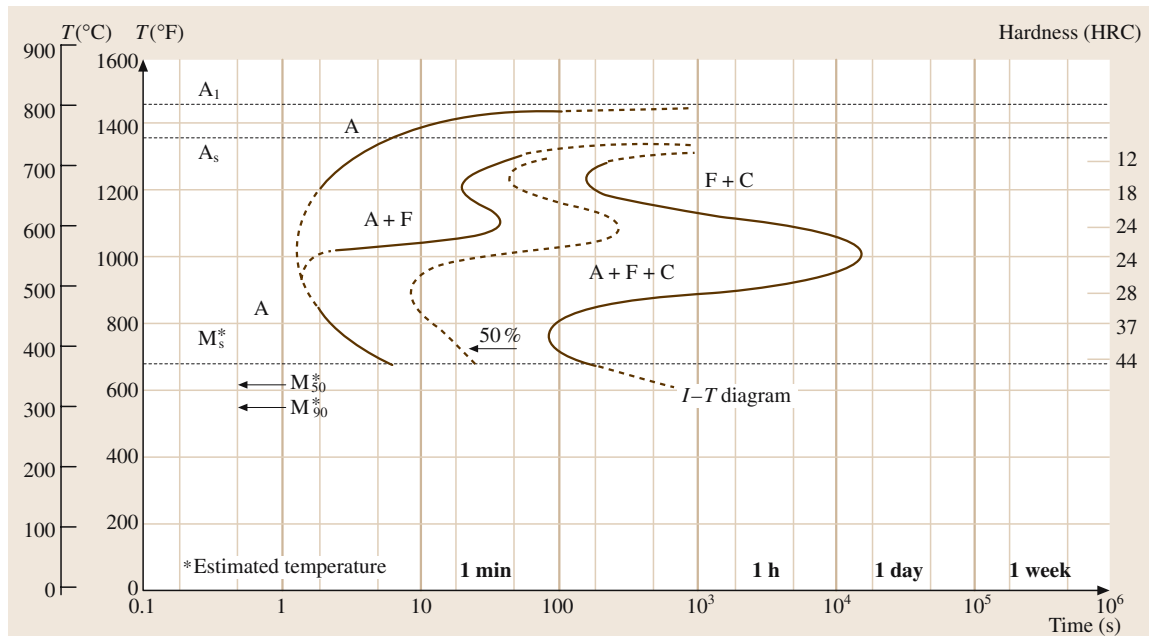


Fig. 3.1-112 Time-temperature-transformation (TTT) diagram of a 4130 grade low-alloy steel. A – austenite; F – ferrite; C – cementite; M – Martensite (the suffix indicates the amount of martensite formed in vol.%)

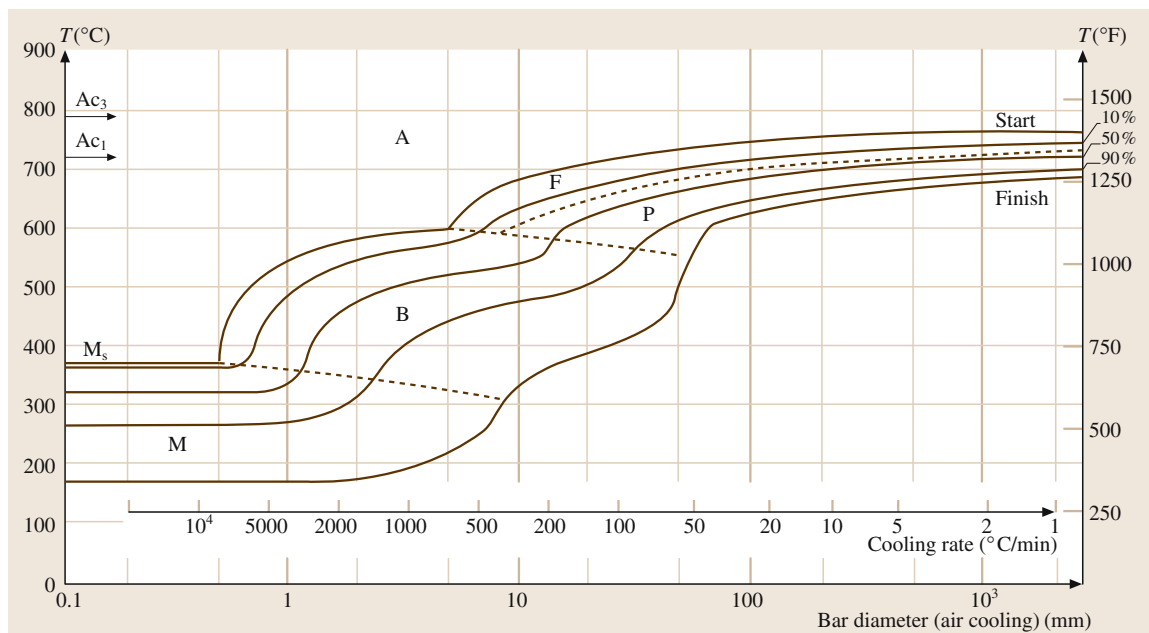


Fig. 3.1-113 Continuous-cooling-transformation (CCT) diagram for a 4130 grade low-alloy steel. Ac₃ and Ac₁ signify the temperatures of the γ /(γ + α) and eutectoid reaction, respectively. A – austenite, F – ferrite, B – bainite, P – pearlite, M – martensite. The cooling rate is measured at 705 °C. The calculated critical cooling rate is 143 K/s [1.80]

3.1.5.3 High-Strength Low-Alloy Steels

High-strength low-alloy (HSLA) steels are designed to provide higher mechanical property values and/or higher resistance to atmospheric corrosion than conventional low-alloy steels of comparable level of alloy content. Higher yield stress is achieved by adding ≤ 0.1 wt% N, Nb, V, Ti, and/or Zr (micro-alloying) which form carbide or carbonitrite precipitates, and by special, closely-controlled processing which yields mostly fine-grained microstructures.

HSLA steels contain 0.05 to 0.25 wt% C, ≤ 2 wt% Mn and mainly Cr, Ni, Mo, and Cu as further alloying elements. Their yield stress is in the range ≥ 275 MPa. They are primarily hot-rolled into usual wrought product forms and commonly delivered in the as-rolled condition.

The particular processing methods of HSLA steels include [1.80]:

- *Controlled rolling* of micro-alloyed, precipitation hardening variants to obtain fine equiaxial and/or highly deformed, pancake-shaped austenite grains. During cooling these austenite grains transform into fine ferrite grains, providing an optimum combination of high yield strength and ductility.
- *Accelerated cooling* of controlled-rolled steels to enhance the formation of fine ferrite grains.
- *Quenching of steels containing ≤ 0.08 wt% C* such that acicular ferrite or low-carbon bainite is formed. This microstructural state provides an excellent combination of high yield strengths of 275 to 690 MPa, ductility, formability, and weldability.
- *Normalizing of V-alloyed steel*, thus increasing yield strength and ductility.
- *Intercritical annealing*, i. e., annealing in the $\gamma + \alpha$ phase field to obtain a dual-phase microstructure which, after cooling, consists of martensite islands dispersed in a ferrite matrix. This microstructure exhibits a somewhat lower yield strength but a high rate of work-hardening, providing a better combination of tensile strength, ductility, and formability than conventional HSLA steels.

HSLA steels include numerous standard and proprietary grades designed to provide specific desirable combinations of properties such as strength, ductility, weldability, and atmospheric corrosion resistance. Table 3.1-46 lists characteristic compositions and Table 3.1-47 lists mechanical properties of these characteristic variants.

In view of the multitude of compositional and processing variants of HSLA steels it is useful to have a summarizing overview as provided in Table 3.1-48.

3.1.5.4 Stainless Steels

Stainless steels are treated extensively in [1.79]. Compared to carbon or low-alloy steels, they are characterized by an increased resistance against corrosion in aggressive media. The corrosion resistance is achieved basically by an alloy content of at least 11–12 wt% Cr. This content is required to form a dense, pore-free protective surface layer consisting mainly of chromium oxides and hydroxides. The corrosion resistance can be further increased by additional alloying with elements such as Ni, Mo, W, Mn, Si, Cu, Co, Al, or N.

Since chromium has a high affinity to carbon, the formation of chromium carbides may reduce the local concentration of Cr in solution and thus deteriorate the corrosion resistance. This can be avoided by

- Low carbon content of the steel.
- Suitable heat treatment.
- Bonding of carbon by other elements with higher carbon affinity, such as Ti and Nb, so-called stabilization.

Similar effects can be attained by the formation of chromium nitrides. Thus, in addition to the chemical composition of the steel, its corrosion properties are strongly influenced by its heat treatment condition.

Depending on the intended field of application, the corrosion resistance of the steel must often be combined with other useful properties such as high strength or hardness, high temperature strength, good formability, low temperature fracture toughness, weldability or machinability. However, since optimization of one property is generally only possible at the expense of others, the property spectrum of a stainless steel is often the result of a compromise. Consequently, a large number of steel grades has been developed to meet different property requirements. Some steels have been developed just for a single application. The following section gives typical representatives of the various types of stainless steel grades.

Depending on alloy composition and cooling conditions from elevated temperature, stainless steels may occur in different types of microstructure: ferritic (bcc), austenitic (fcc), martensitic, or mixtures of two or all three of these phases. The bcc structure is promoted by the ferrite forming elements Cr, Mo, W, Ti, V, Nb, Al, and Si, whereas the fcc structure is promoted by the austenite

Table 3.1-46 Compositional limits of HSLA steel grades according to ASTM standards [1.80]

| ASTM specification ^a | Type or grade | UNS designation | C | Mn | Heat compositional limits (wt%) ^b | | | | Cu | V | Other |
|---------------------------------|---------------|-----------------|-------------------|------------------------|--|-------|-------------------|-----------|-----------|-----------------------|---|
| | | | | | P | S | Si | Cr | | | |
| A 242 | Type 1 | K11510 | 0.15 | 1.00 | 0.45 | 0.05 | — | — | — | 0.20 min | — |
| A 572 | Grade 42 | — | 0.21 | 1.35 ^c | 0.04 | 0.05 | 0.30 ^e | — | — | 0.20 min ^d | — |
| | Grade 50 | — | 0.23 | 1.35 ^c | 0.04 | 0.05 | 0.30 ^e | — | — | 0.20 min ^d | — |
| | Grade 60 | — | 0.26 | 1.35 ^c | 0.04 | 0.05 | 0.30 | — | — | 0.20 min ^d | — |
| | Grade 65 | — | 0.23 ^c | 1.65 ^c | 0.04 | 0.05 | 0.30 | — | — | 0.20 min ^d | — |
| A 588 | Grade A | K11430 | 0.10–0.19 | 0.90–1.25 | 0.04 | 0.05 | 0.15–0.30 | 0.40–0.65 | — | 0.25–0.40 | 0.02–0.10 |
| | Grade B | K12043 | 0.20 | 0.75–1.25 | 0.04 | 0.05 | 0.15–0.30 | 0.40–0.70 | 0.25–0.50 | 0.20–0.40 | 0.01–0.10 |
| | Grade C | K11538 | 0.15 | 0.80–1.35 | 0.04 | 0.05 | 0.15–0.30 | 0.30–0.50 | 0.25–0.50 | 0.20–0.50 | 0.01–0.10 |
| | Grade D | K11552 | 0.10–0.20 | 0.75–1.25 | 0.04 | 0.05 | 0.50–0.90 | 0.50–0.90 | — | 0.30 | — |
| | Grade K | — | 0.17 | 0.50–1.20 | 0.04 | 0.05 | 0.25–0.50 | 0.40–0.70 | 0.40 | 0.30–0.50 | — |
| A 606 | — | — | 0.22 | 1.25 | — | 0.05 | — | — | — | — | — |
| A 607 | Grade 45 | — | 0.22 | 1.35 | 0.04 | 0.05 | — | — | — | 0.20 min ^d | — |
| | Grade 50 | — | 0.23 | 1.35 | 0.04 | 0.05 | — | — | — | 0.20 min ^d | — |
| | Grade 55 | — | 0.25 | 1.35 | 0.04 | 0.05 | — | — | — | 0.20 min ^d | — |
| | Grade 60 | — | 0.26 | 1.50 | 0.04 | 0.05 | — | — | — | 0.20 min ^d | — |
| | Grade 65 | — | 0.26 | 1.50 | 0.04 | 0.05 | — | — | — | 0.20 min ^d | — |
| | Grade 70 | — | 0.26 | 1.65 | 0.04 | 0.05 | — | — | — | 0.20 min ^d | — |
| A 618 | Grade Ia | — | 0.15 | 1.00 | 0.15 | 0.05 | — | — | — | 0.20 min | — |
| | Grade Ib | — | 0.20 | 1.35 | 0.04 | 0.05 | — | — | — | 0.20 min ^f | — |
| | Grade II | K12609 | 0.22 | 0.85–1.25 | 0.04 | 0.05 | 0.30 | — | — | 0.02 min | — |
| | Grade III | K12700 | 0.23 | 1.35 | 0.04 | 0.05 | 0.30 | — | — | 0.02 min | 0.005 Nb min ^g |
| A 633 | Grade A | K01802 | 0.18 | 1.00–1.35 | 0.04 | 0.05 | 0.15–0.30 | — | — | — | 0.05 Nb |
| | Grade C | K12000 | 0.20 | 1.15–1.50 | 0.04 | 0.05 | 0.15–0.50 | — | — | — | 0.05–0.05 Nb |
| | Grade D | K02003 | 0.20 | 0.70–1.60 ^c | 0.04 | 0.05 | 0.15–0.50 | 0.25 | 0.35 | — | 0.08 Mo |
| | Grade E | K12202 | 0.22 | 1.15–1.50 | 0.04 | 0.05 | 0.15–0.50 | — | — | 0.04–0.11 | 0.01–0.05 Nb ^d , 0.01–0.03 N |
| A 656 | Type 3 | — | 0.18 | 1.65 | 0.025 | 0.035 | 0.60 | — | — | — | 0.08 0.020 N, |
| | Type 7 | — | 0.18 | 1.65 | 0.025 | 0.035 | 0.60 | — | — | — | 0.005–0.15 0.020 N, |
| | | | | | | | | | — | — | 0.005–0.10 Nb |

Table 3.1-46 Compositional limits of HSLA steel grades according to ASTM standards [1.80], cont.

| ASTM specification ^a | Type or grade | UNS designation | Heat compositional limits (wt%) ^b | | | | | | Other |
|---------------------------------|------------------|-----------------|--|-----------|-----------|-----------------------|------------------------|------|------------------------------------|
| | | | C | Mn | P | S | Si | Cr | |
| A 690 | — | K12249 | 0.22 | 0.60–0.90 | 0.08–0.15 | 0.05 | 0.10 | — | 0.40–0.75 0.50 min |
| A 709 | Grade 50, type 1 | — | 0.23 | 1.35 | 0.04 | 0.05 | 0.40 | — | — |
| | Grade 50, type 2 | — | 0.23 | 1.35 | 0.04 | 0.05 | 0.40 | — | 0.01–0.15 |
| | Grade 50, type 3 | — | 0.23 | 1.35 | 0.04 | 0.05 | 0.40 | — | 0.05 Nb max |
| | Grade 50, type 4 | — | 0.23 | 1.35 | 0.04 | 0.05 | 0.40 | — | 0.015 Nb max |
| A 715 | — | — | 0.15 | 1.65 | 0.025 | 0.035 | — | — | Added as Ti, Nb added as necessary |
| A 808 | — | — | 0.12 | 1.65 | 0.04 | 0.05 max or 0.15–0.50 | — | — | 0.10 |
| | | | | | | 0.010 max | | | V + Nb = 0.15 max |
| A 812 | 65 | — | 0.23 | 1.40 | 0.035 | 0.04 | 0.15–0.50 ^j | — | — |
| | 80 | — | 0.23 | 1.50 | 0.035 | 0.04 | 0.15–0.50 | 0.35 | — |
| A 841 | — | — | 0.20 ^k | — | 0.030 | 0.030 | 0.15–0.50 | 0.25 | 0.35 |
| A 871 | — | — | 0.20 | 1.50 | 0.04 | 0.05 | 0.90 | 1.25 | 1.00 |
| | | | | | | | | | 0.10 |
| | | | | | | | | | 0.25 Mo, 0.15 Zr, 0.05 Nb, 0.05 Ti |

^a For characteristics and intended uses, see Table 3.1-48; for mechanical properties, see Table 3.1-47.^b If a single value is shown, it is a maximum unless otherwise stated.^c Values may vary, or minimum value may exist, depending on product size and mill form.^d Optional or when specified^e May purchased as type 1 (0.005–0.05 Nb), type 2 (0.01–0.15 V), type 3 (0.05 Nb, max, plus 0.02–0.15 V) or type 4 (0.015 N, max, plus V ≥ 4 N).^f If chromium and silicon are each 0.50% min, the copper minimum does not apply.^g May be substituted for all or part of V.^h Niobium plus vanadium, 0.02 to 0.15%.ⁱ Nitrogen with vanadium content of 0.015% (max) with a minimum vanadium-to-nitrogen ratio of 4:1.^j When silicon-killed steel is specified.^k For plate under 40 mm (1.5 in.), manganese contents are 0.70 to 1.35% or up to 1.60% if carbon equivalents do not exceed 0.47%.

For plate thicker than 40 mm (1 to 5 in.), ASTM A 841 specifies manganese contents of 1.00 to 1.60%.

Table 3.1-47 Tensile properties of HSLA steel grades specified in ASTM standards [1.80]

| ASTM specification ^a | Type, grade or condition | Product thickness ^b (mm) | Minimum tensile strength ^c (MPa) | Minimum yield strength ^c (MPa) | Minimum elongation (%) ^c in 200 mm | Minimum elongation (%) ^c in 50 mm | Bend radius ^c Longitudinal | Transverse |
|---------------------------------|---------------------------------------|-------------------------------------|---|---|--|---|--|------------|
| A242 | Type 1 | 20 | 480 | 345 | 18 | — | — | — |
| | | 20–40 | 460 | 315 | 18 | 21 | — | — |
| | | 40–100 | 435 | 290 | 18 | 21 | — | — |
| A572 | Grade 42 | 150 | 415 | 290 | 20 | 24 | d | — |
| | Grade 50 | 100 | 450 | 345 | 18 | 21 | d | — |
| | Grade 60 | 32 | 520 | 415 | 16 | 18 | d | — |
| | Grade 65 | 32 | 550 | 450 | 15 | 17 | d | — |
| A588 | Grades A–K | 100 | 485 | 345 | 18 | 21 | d | — |
| | | 100–125 | 460 | 315 | — | 21 | d | — |
| | | 125–200 | 435 | 290 | — | 21 | d | — |
| A606 | Hot rolled | sheet | 480 | 345 | — | 22 | t | 2t – 3t |
| | Hot rolled and annealed or normalized | sheet | 450 | 310 | — | 22 | t | 2t – 3t |
| | Cold rolled | sheet | 450 | 310 | — | 22 | t | 2t – 3t |
| A607 | Grade 45 | sheet | 410 | 310 | — | 22–25 | t | 1.5t |
| | Grade 50 | sheet | 450 | 345 | — | 20–22 | t | 1.5t |
| | Grade 55 | sheet | 480 | 380 | — | 18–20 | 1.5t | 2t |
| | Grade 60 | sheet | 520 | 415 | — | 16–18 | 2t | 3t |
| | Grade 65 | sheet | 550 | 450 | — | 15–16 | 2.5t | 3.5t |
| | Grade 70 | sheet | 590 | 485 | — | 14 | 3t | 4t |
| A618 | Ia, Ib, II | 19 | 485 | 345 | 19 | 22 | t – 2t | — |
| | Ia, Ib, II, III | 19–38 | 460 | 315 | 18 | 22 | t – 2t | — |
| A633 | A | 100 | 430–570 | 290 | 18 | 23 | d | — |
| | C, D | 65 | 485–620 | 345 | 18 | 23 | d | — |
| | C, D | 65–100 | 450–590 | 315 | 18 | 23 | d | — |
| | E | 100 | 550–690 | 415 | 18 | 23 | d | — |
| | E | 100–150 | 515–655 | 380 | 18 | 23 | d | — |
| A656 | 50 | 50 | 415 | 345 | 20 | — | d | — |
| | 60 | 40 | 485 | 415 | 17 | — | d | — |
| | 70 | 25 | 550 | 485 | 14 | — | d | — |
| | 80 | 20 | 620 | 550 | 12 | — | d | — |
| A690 | — | 100 | 485 | 345 | 18 | — | 2t | — |
| A709 | 50 | 100 | 450 | 345 | 18 | 21 | — | — |
| | 50W | 100 | 450 | 345 | 18 | 21 | — | — |
| A715 | Grade 50 | sheet | 415 | 345 | — | 22–24 | 0 | t |
| | Grade 60 | sheet | 485 | 415 | — | 20–22 | 0 | t |
| | Grade 70 | sheet | 550 | 485 | — | 18–20 | t | 1.5t |
| | Grade 80 | sheet | 620 | 550 | — | 16–18 | t | 1.5t |
| A808 | — | 40 | 450 | 345 | 18 | 22 | — | — |
| | | 40–50 | 450 | 315 | 18 | 22 | — | — |
| | | 50–65 | 415 | 290 | 18 | 22 | — | — |

Table 3.1-47 Tensile properties of HSLA steel grades specified in ASTM standards [1.80], cont.

| ASTM specification ^a | Type, grade or condition | Product thickness ^b (mm) | Minimum tensile strength ^c (MPa) | Minimum yield strength ^c (MPa) | Minimum elongation (%) ^c in 200 mm | Minimum elongation (%) ^c in 50 mm | Bend radius ^c Longitudinal | Transverse |
|---------------------------------|--------------------------|-------------------------------------|---|---|--|---|--|------------|
| A812 | 65 | sheet | 585 | 450 | — | 13–15 | — | — |
| | 80 | sheet | 690 | 550 | — | 11–13 | — | — |
| A841 | — | 65 | 485–620 | 345 | 18 | 22 | — | — |
| | | 65–100 | 450–585 | 310 | 18 | 22 | — | — |
| A871 | 60, as-hot-rolled | 5–35 | 520 | 415 | 16 | 18 | — | — |
| | 65, as-hot-rolled | 5–20 | 550 | 450 | 15 | 17 | — | — |

^a For characteristics and intended uses, see Table 3.1-48; for specified composition limits, see Table 3.1-46^b Maximum product thickness except when a range is given. No thickness are specified for sheet products.^c May vary with product size and mill form^d Optional supplementary requirement given in ASTM A6**Table 3.1-48** Summary of characteristics and uses of HSLA steels according to ASTM standards [1.80]

| ASTM specification ^a | Title | Alloying elements ^b | Available mill forms | Special characteristics | Intended uses |
|---------------------------------|--|-----------------------------------|--|---|--|
| A 242 | High-strength low-alloy structural steel | Cr, Cu, N, Ni, Si, Ti, V, Zr | Plate, bar, and shapes ≤ 100 mm in thickness | Atmospheric-corrosion resistance four times of carbon steel | Structural members in welded, bolted, or riveted construction |
| A 572 | High-strength low-alloy niobium-vanadium steels of structural quality | Nb, V, N | Plate, bar, and sheet piling ≤ 150 mm in thickness | Yield strength of 290 to 450 MPa in six grades | Welded, bolted, or riveted structures, but many bolted or riveted bridges and buildings |
| A 588 | High-strength low-alloy structural steel with 345 MPa minimum yield point ≤ 100 mm in thickness | Nb, V, Cr, Ni, Mo, Cu, Si, Ti, Zr | Plate, bar, and shapes ≤ 200 mm in thickness | Atmospheric-corrosion resistance four times of carbon steel; nine grades of similar strength | Welded, bolted, or riveted structures, but primarily welded bridges and buildings in which weight savings or added durability is important |
| A 606 | Steel sheet and strip hot-rolled steel and cold-rolled, high-strength low-alloy with improved corrosion resistance | Not specified | Hot-rolled and cold-rolled sheet and strip | Atmospheric-corrosion twice that of carbon steel (type 2) or four times of carbon steel (type 4) | Structural and miscellaneous purposes for which weight savings or added durability is important |
| A 607 | Steel sheet and strip hot-rolled steel and cold-rolled, high-strength low-alloy niobium and/or vanadium | Nb, V, N, Cu | Hot-rolled and cold-rolled sheet and strip | Atmospheric-corrosion twice that of carbon steel, but only when copper content is specified; yield strength of 310 to 485 MPa in six grades | Structural and miscellaneous purposes for which greater strength or weight savings is important |
| A 618 | Hot formed welded and seamless high-strength low-alloy structural tubing | Nb, V, Si, Cu | Square, rectangular round and special-shape structural welded or seamless tubing | Three grades of similar yield strength; may be purchased with atmospheric-corrosion resistance twice that of carbon steel | General structural purposes include welded, bolted or riveted bridges and buildings |

Table 3.1-48 Summary of characteristics and uses of HSLA steels according to ASTM standards [1.80], cont.

| ASTM specification ^a | Title | Alloying elements ^b | Available mill forms | Special characteristics | Intended uses |
|---------------------------------|--|--------------------------------|---|--|--|
| A 633 | Normalized high-strength low-alloy structural steel | Nb, V, Cr, Ni, Mo, Cu, N, Si | Plate, bar, and shapes ≤ 150 mm in thickness | Enhanced notch toughness; yield strength of 290 to 415 MPa in five grades | Welded, bolted, or riveted structures for service at temperatures at or above -45°C |
| A 656 | High strength low-alloy, hot rolled structural vanadium-aluminium-nitrogen and titanium-aluminium steels | V, Al, N, Ti, Si | Plate, normally ≤ 16 mm in thickness | Yield strength of 552 MPa | Truck frames, brackets, crane booms, rail cars and other applications for which weight savings is important |
| A 690 | High-strength low-alloy steel H-piles and sheet piling | Ni, Cu, Si | Structural-quality H-piles and sheet piling | Corrosion resistance two to three times greater than that of carbon steel in the splash zone of marine marine structures | Dock walls, sea walls Bulkheads, excavations and similar structures exposed to seawater |
| A 709, grade 50 and 50W | Structural steel | V, Nb, N, Cr, Ni, Mo | All structural-shape groups and plate ≤ 100 mm in thickness | Minimum yield strength of 345 MPa, Grade 50W is a weathering steel | Bridges |
| A 714 | High-strength low-alloy welded and seamless steel pipe | V, Ni, Cr, Mo, Cu, Nb | Pipe with nominal pipe size diameters of 13 to 660 mm | Minimum yield strength of ≤ 345 MPa and corrosion resistance two or four times that of carbon steel | Piping |
| A 715 | Steel sheet and strip hot-rolled, high-strength low-alloy with improved formability | Nb, V, Cr, Mo, N, Ti, Zr, B | Hot-rolled sheet and strip | Improved formability ^c compared to A 606 and A 607; yield strength of 345 to 550 MPa in four grades | Structural and miscellaneous applications for which high strength, weight savings, improved formability and good weldability are important |
| A 808 | High-strength low-alloy steel with improved notch toughness | V, Nb | Hot-rolled plate ≤ 65 mm in thickness | Charpy V-notch impact energies of 40–60 J (40–60 ft lbf) at -45°C | Railway tank cars |
| A 812 | High-strength low-alloy steels | V, Nb | Steel sheet in coil form | Yield strength of 450–550 MPa | Welded layered pressure vessels |
| A 841 | Plate produced by themomechanical controlled processes | V, Nb, Cr Mo, Ni | Plates ≤ 100 mm in thickness | Yield strength of 310–345 MPa | Welded pressure vessels |
| A 847 | Cold formed welded and seamless high-strength low-alloy structural tubing with improved atmospheric corrosion resistance | Cu, Cr, Ni, Si, V, Ti, Zr, Nb | Welded tubing with maximum periphery of 1625 mm and wall thickness of 16 mm or seamless tubing with maximum periphery of 810 mm and wall thickness of 13 mm | Minimum yield strength ≤ 345 MPa with atmospheric-corrosion twice that of carbon steel | Round, square, or specially shaped structural tubing for welded, riveted or bolted construction of bridges and buildings |

Table 3.1-48 Summary of characteristics and uses of HSLA steels according to ASTM standards [1.80], cont.

| ASTM specification ^a | Title | Alloying elements ^b | Available mill forms | Special characteristics | Intended uses |
|---------------------------------|--|--------------------------------|--|---|--|
| A 860 | High-strength butt-welding fittings of wrought high-strength low-alloy steel | Cu, Cr, Ni, Mo, V, Nb, Ti | Normalized or quenched-and-tempered wrought fittings | Minimum yield strength ≤ 485 MPa | High-pressure gas and oil transmission lines |
| A 871 | High-strength low-alloy steel with atmospheric corrosion resistance | V, Nb, Ti Cu, Mo, Cr | As-rolled plate ≤ 35 mm in thickness | Atmospheric-corrosion resistance four times that of carbon structural steel | Tubular structures and poles |

^a For grades and mechanical properties, see Table 3.1-47.

^b In addition to carbon, manganese, phosphorus, and sulfur. A given grade may contain one or more of the listed elements, but not necessarily all of them; for specified compositional limits, see Table 3.1-46.

^c Obtained by producing killed steel, made to fine grain practice, and with microalloying elements such as niobium, vanadium titanium, and zirconium in the composition.

forming elements C, N, Ni, Mn, Cu, and Co. All alloying elements suppress the austenite to martensite transformation by reducing the M_s temperature, so that the steel may remain fcc at and below room temperature at a sufficiently high alloy content. For a rough estimate of the structural components of a stainless steel as a function of alloy composition, the so-called Schaeffler diagram (initially determined by M. Strauss and E. Maurer in 1920) can be used (see Fig. 3.1-114 [1.77]). It relates the equivalent Cr and Ni content to the observed fractions of martensite, austenite, and ferrite. One of the formulas of the Ni and Cr equivalent used most frequently is that of Schneider [1.85] (in wt%):

$$\text{Cr}_{\text{equ}} = \text{Cr} + 2 \text{Si} + 1.5 \text{Mo} + 5 \text{V} + 5.5 \text{Al} + 1.5 \text{Ti} + 0.7 \text{W}$$

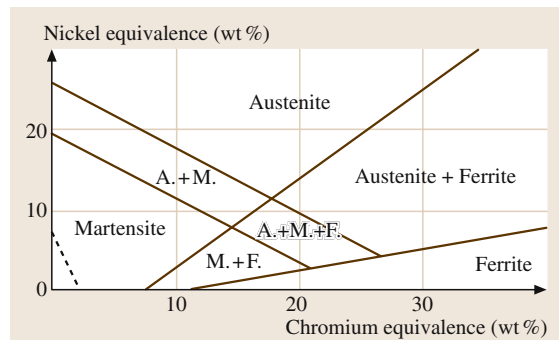


Fig. 3.1-114 Structure of iron-based alloys as a function of the concentrations of the chromium and nickel equivalent elements. A: austenite (face centered cubic); F: ferrite (body centered cubic); M: martensite (tetragonal-body centered cubic) [1.77]

and

$$\text{Ni}_{\text{equ}} = \text{Ni} + 0.5 \text{Mn} + 0.3 \text{Cu} + 25 \text{N} + 30 \text{C} .$$

Ferritic Chromium Steels

High chromium (≥ 18 wt% Cr) and low carbon concentrations result in a fully ferritic structure of the steels at all temperatures, i.e., with a bcc delta ferrite structure and no phase transformations. Therefore these steels cannot be strengthened by quenching and tempering. The possibility to increase strength by cold deformation is limited since it decreases ductility and toughness. Steels containing < 18 wt% Cr form some austenite during heating which can be transformed into martensite by fast cooling, thus strengthening the steel. A tempering treatment just below Ar_1 results in a mixture of δ -ferrite, α -ferrite, and carbides formed from tempered martensite.

In general the toughness of the conventional stainless ferritic chromium steels is not very high, the impact transition temperature often being at or above room temperature and reaching 100°C after welding (see curve (e) in Fig. 3.1-115). This is due to (i) the tendency of the ferritic stainless steels to pronounced grain coarsening on heat treatments, leading to a relatively large grain size (which cannot be refined by phase transformation) and (ii) the precipitation of chromium carbides at the grain boundaries. Both effects render the steel rather brittle after welding. Furthermore, precipitation of chromium carbides at the grain boundaries causes susceptibility to intergranular corrosion due to the formation of zones with local chromium depletion along the grain boundaries. Some improvement can be achieved

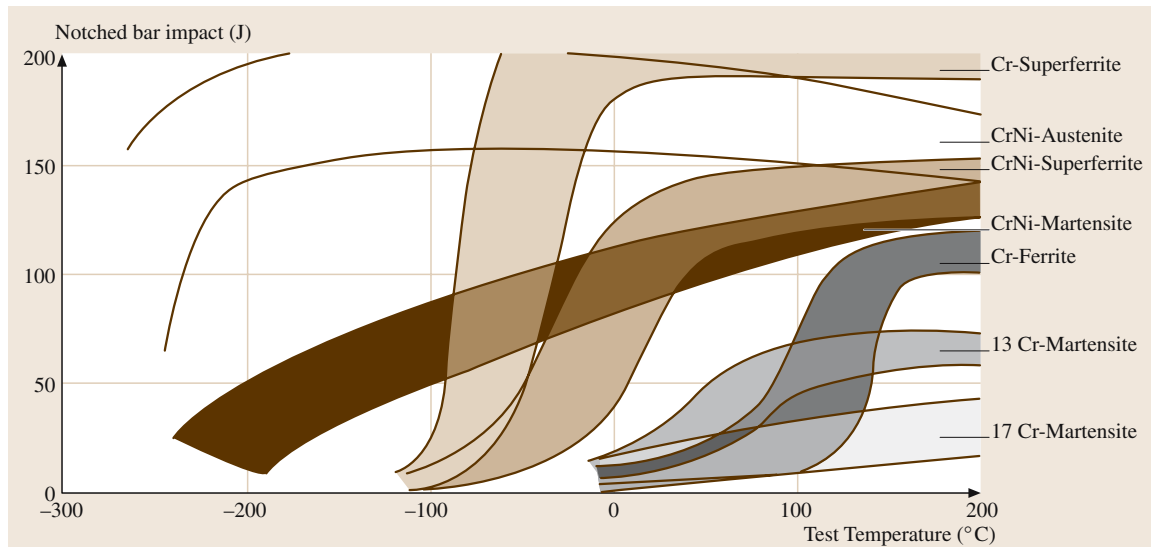


Fig. 3.1-115 Notched bar impact energy as a function of test temperature of various types of stainless steels (DVM samples: dimension $10 \times 10 \times 55 \text{ mm}^3$, notch depth 3 mm, notch root radius 1 mm)

(i) by quenching or a suitable diffusion heat treatment for equilibration of the chromium distribution, and (ii) by a stabilization of the steels with small amounts of Ti and/or Nb which are added to bind the carbon and nitrogen in more stable compounds. In unstabilized steels the carbon content is generally restricted to $\leq 0.1 \text{ wt\%}$. Up to 2 wt% Mo improves the corrosion resistance of ferritic chromium steels, especially in chloride-containing media.

In Table 3.1-49 the chemical composition of a number of ferritic stainless steels is given. The most common representative is the grade X6Cr17/AISI 430. Table 3.1-50 presents some information on hot deformation and recommended heat treatment parameters. Tables 3.1-51 and 3.1-52 show typical data of the mechanical and physical properties, respectively, and Table 3.1-53 reviews the weldability of these steels.

Good ductility and toughness at sub-zero temperatures can be achieved when the carbon and nitrogen content in ferritic steels is reduced to very low concentrations (below 100 ppm) (see curve (a) in

Fig. 3.1-115). With higher alloy concentrations on the order of 26–30 wt% Cr, up to 2 wt% Mo, and up to 4 wt% Ni, these so-called superferritic steels exhibit excellent corrosion properties, i. e., high resistance against transcrystalline stress corrosion cracking and chloride-induced pitting corrosion, as well as intercrystalline and general corrosion. However, in order to maintain the low C and N contents even after welding, an effective inert gas shielding is required during welding as it is known for welding of Ti. Obviously, the high purity requirements which have to be observed during melting, hot forming and welding, and some embrittling effects which occur in high Cr steels after lengthy high temperature exposure (475° embrittlement and σ -phase formation) have precluded as yet a wider application of these steels, in spite of their attractive properties. In addition to their good corrosion resistance these steels possess a higher thermal conductivity than austenitic stainless steels, which is of special interest in heat exchanger applications, and a lower rate of work hardening on cold deformation.

Table 3.1-49 Chemical composition of ferritic stainless steels

| Grade no. (EN 10088) | Steel designation | ASTM A 276/ AISI grade | Chemical composition (wt %) | | | | | | | |
|-------------------------|-------------------|---------------------------------|-----------------------------|-----------------|------------|--------------|--------------|-----------|------------------------------------|--|
| | | C | Si | Mn | S | P | Cr | Mo | Others | |
| 1.4016 | X6Cr17 | 430 | ≤ 0.08 | ≤ 1 | ≤ 1 | ≤ 0.03 | 15.5–17.5 | | | |
| 1.4104 | X12CrMoS17 | 430F | 0.10–0.17 | ≤ 1.5 | ≤ 1 | 0.15–0.35 | ≤ 0.06 | 15.5–17.5 | 0.2–0.6 | |
| 1.4105 | X4CrMoS18 | | ≤ 0.06 | ≤ 1.5 | ≤ 1 | 0.15–0.35 | ≤ 0.06 | 16.5–18.5 | 0.2–0.6 | |
| 1.4509 | X2CrTiNb18 | 441 | ≤ 0.03 | ≤ 1 | ≤ 1 | ≤ 0.015 | 17.5–18.5 | | Ti 0.1–0.6 Nb 9x% C+ 0.3–1.0 | |
| 1.4510 | X3CrTi17 | 430Ti | ≤ 0.08 | ≤ 1 | ≤ 1 | ≤ 0.03 | ≤ 0.045 | 16–18 | | |
| 1.4511 | X3CrNb17 | | ≤ 0.08 | ≤ 1 | ≤ 1 | ≤ 0.03 | ≤ 0.045 | 16–18 | Nb $\geq 12x\%$ C up to 1.20% | |
| 1.4113 | X6Cr Mo17-1 | 434 | ≤ 0.08 | ≤ 1 | ≤ 1 | ≤ 0.03 | ≤ 0.045 | 16–18 | 0.9–1.3 | |
| 1.4520 | X2CrTi15 | | ≤ 0.015 | ≤ 0.5 | ≤ 0.5 | ≤ 0.020 | ≤ 0.025 | 14–16 | | |
| 1.4521 | X2CrMoTi18-2 | 444 | ≤ 0.025 | ≤ 1 | ≤ 1 | ≤ 0.03 | ≤ 0.045 | 17–19 | 1.8–2.3 | |
| | X20Cr20 | 442 | ≤ 0.2 | ≤ 1 | ≤ 1 | ≤ 0.03 | ≤ 0.04 | 18–23 | | |
| 1.3810 | X20Cr25 | 446 | ≤ 0.25 | ≤ 0.5 –2.0 | ≤ 0.5 | ≤ 0.03 | ≤ 0.04 | 23–27 | | |
| a | X1CrMo26-1 | | 0.002 | 0.1 | 0.3 | 0.015 | 0.01 | 26 | 1 | |
| a | X1CrMo29-4 | | 0.003 | 0.1 | 0.04 | 0.01 | 0.01 | 29.5 | 4 | |
| a | X1CrMoNi29-4-2 | | 0.002 | 0.1 | 0.1 | 0.01 | 0.01 | 29.5 | 4 | |
| a | X2CrMoNiTi25-4-4 | | 0.012 | 0.04 | 0.3 | 0.006 | | 25 | 4 | |
| a Typical values | | | | | | | | | | |

Table 3.1-50 Heat treatment conditions of ferritic stainless steels

| Grade no. | Rolling and forging (°C) | Soft annealing Temperature (°C) | Time (min) | Cooling |
|------------------|--------------------------|------------------------------------|------------|-------------|
| 1.4016 | 1100–800 | 750–850 | 20–30 | Air/water |
| 1.4104 | 1100–800 | 750–850 | 120–180 | Air/furnace |
| 1.4105 | 1100–800 | 750–850 | | Air/water |
| 1.4510 | 1100–800 | 750–850 | 20–30 | Air/water |
| 1.4511 | 1050–750 | 750–850 | 20–30 | Air/water |
| 1.4113 | 1050–750 | 750–850 | 20–30 | Air/water |
| 1.4521 | 1150–750 | 750–900 | | Air/water |
| X1CrMo26-1 | 1150–750 | 750–900 | | Air/water |
| X1CrMo29-4 | 1100–800 | 750–800 | 120–360 | Air/furnace |
| X1CrMoNi29-4-2 | 1150–750 | 750–800 | 15–30 | Air |
| X2CrMoNiTi25-4-4 | 1100–800 | 730–780 | 120–360 | Air/furnace |

Table 3.1–51 Mechanical properties of ferritic stainless steels

| Grade no. | Heat treatment condition | Tensile properties of flat products ≤ 25 mm in thickness | | |
|------------------|--------------------------|--|---------------------------------|---|
| | | Min. yield strength or 0.2% proof strength (MPa) | Ultimate tensile strength (MPa) | Min. fracture elongation A ₅ (%) |
| 1.4016 | Annealed | 270 | 450–600 | 20 |
| 1.4104 | Annealed | 300 | 540–740 | 16 |
| 1.4105 | Annealed | 270 | 450–650 | 20 |
| 1.4510 | Annealed | 270 | 450–600 | 20 |
| 1.4511 | Annealed | 250 | 450–600 | 20 |
| 1.4113 | Annealed | 260 | 480–630 | 20 |
| 1.4521 | Annealed | 320 | 450–650 | 20 |
| X1CrMo26-1 | Annealed | 275 ^a | 450 ^a | 22 ^a |
| X1CrMo29-4 | Annealed | 415 ^a | 550 ^a | 20 ^a |
| X1CrMoNi29-4-2 | Annealed | 415 ^a | 550 ^a | 20 ^a |
| X2CrMoNiTi25-4-4 | Annealed | 550 ^a | 650 ^a | 20 ^a |

^a Typical values**Table 3.1–52** Physical properties of ferritic stainless steels

| Grade no. | Mean thermal expansion coefficient between 20 °C and T (°C) in 10 ⁻⁶ K ⁻¹ | | | | Density (kg/dm ³) | Thermal conductivity at 20 °C (W/K m) | Specific heat at 20 °C (J/g K) | Electrical resistivity at 20 °C (Ω mm ² /m) | Modulus of elasticity (kN/mm ²) | Magnetizable |
|-----------|---|------|------|------|-------------------------------|---------------------------------------|--------------------------------|--|---|--------------|
| | 100 | 200 | 300 | 400 | | | | | | |
| 1.4016 | 10.0 | 10.0 | 10.5 | 10.5 | 7.7 | 25 | 0.46 | 0.60 | 220 | yes |
| 1.4104 | 10.0 | 10.5 | 10.5 | 10.5 | 7.7 | 25 | 0.46 | 0.70 | 216 | yes |
| 1.4105 | 10.0 | 10.5 | 10.5 | 10.5 | 7.7 | 25 | 0.46 | 0.70 | 216 | yes |
| 1.4510 | 10.0 | 10.0 | 10.5 | 10.5 | 7.7 | 25 | 0.46 | 0.60 | 220 | yes |
| 1.4511 | 10.0 | 10.0 | 10.5 | 10.5 | 7.7 | 25 | 0.46 | 0.60 | 220 | yes |
| 1.4113 | 10.0 | 10.0 | 10.5 | 10.5 | 7.7 | 25 | 0.46 | 0.70 | 216 | yes |
| 1.4521 | 10.4 | 10.8 | 11.2 | 11.6 | 7.7 | 15 | 0.43 | 0.80 | 220 | yes |

Table 3.1–53 Weldability of ferritic stainless steels

| Grade no. | Weldable | Welding method | | Arc welding | Resistance welding | Autogenous welding | Preheating (°C) | After-treatment | |
|----------------|----------|---------------------|---|-------------|--------------------|--------------------|-----------------|-----------------|-----------|
| | | SAW/MIG/TIG welding | | | | | | Annealing | at T (°C) |
| 1.4016 | Yes | + | + | + | + | (+) | 200 | (+) | 700 |
| 1.4104 | No | — | — | — | — | — | — | — | — |
| 1.4105 | No | — | — | — | — | — | — | — | — |
| 1.4510 | Yes | + | + | + | + | — | 200 | (+) | 750 |
| 1.4511 | Yes | + | + | + | + | — | 200 | (+) | 750 |
| 1.4113 | Yes | + | + | + | — | — | — | + | 750 |
| 1.4521 | Yes | + | + | — | — | — | — | — | — |
| X2CrMoTi29-4 | Yes | + | — | — | — | — | — | — | — |
| X1CrMo26-1 | Yes | + | — | — | — | — | — | — | — |
| X1CrMo29-4 | Yes | + | — | — | — | — | — | — | — |
| X1CrMoNi29-4-2 | Yes | + | — | — | — | — | — | — | — |

Martensitic and Martensitic-Ferritic Chromium Steels

Steels with 11.5 to 18 wt% Cr and up to 1.2 wt% C are austenitic at high temperatures and can be transformed into martensite by fast cooling. Due to the high chromium content, the hardenability of these steels is relatively high, so a fully martensitic transformation can be achieved even with relatively large cross sections and moderate cooling rates. They are normally used for applications requiring a combination of high hardness with good corrosion and wear resistance. With carbon contents below about 0.35 wt% C the steels are hypo-eutectic, and some ferrite will be present after heat treatment. They can be austenitized at $\geq 960^{\circ}\text{C}$. Steels with ≥ 0.40 wt% C and 13 wt% Cr are already hyper-eutectic and will contain some undissolved primary carbides after quenching. To dissolve more carbon, these steels are usually quenched from a higher austenitization temperature around 1050°C . The steels cannot be hardened if the carbon concentration is below 0.12 wt% C and the chromium content ≥ 16 wt% Cr.

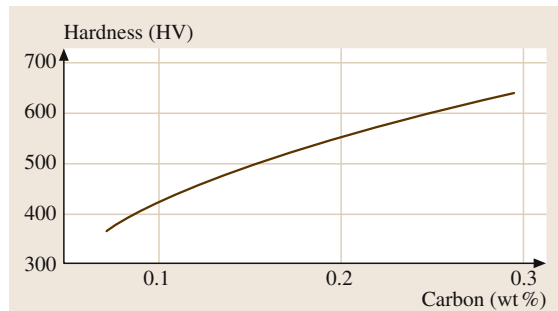


Fig. 3.1-116 As-quenched hardness as a function of the carbon content of a martensitic 12 wt% Cr steel

In some grades a small content of 0.5–1 wt% Mo (and sometimes some W, V, or Nb) is used to increase the tempering resistance, i.e., to retain higher hardness on tempering by means of precipitation reactions. Increased S contents or Se additions improve the machinability of the steels. About 1–2.5 wt% Ni together with reduced carbon content is applied if hardenability of higher cross sections and an improved weldability are required.

The hardness after quenching depends on the carbon content, as illustrated in Fig. 3.1-116 for a 12 wt% Cr steel [1.77]. In the as-quenched state the steels are hard but very brittle. Thus a tempering treatment is necessary to adjust toughness and strength to the level required for a specific application. For high hardness, annealing temperatures of about $100\text{--}300^{\circ}\text{C}$ are applied, whereas increases in ductility and toughness require tempering at or above 650°C .

The chemical composition for a number of martensitic Cr steels is given in Table 3.1-54. Tables 3.1-55–3.1-58 review data on recommended heat treatment conditions, mechanical properties, physical properties, and weldability, respectively.

It should be noted that a different way to produce stainless steels with high hardness is by precipitation hardening. Such steels have a low carbon content and contain in addition to chromium a few wt% of Ni and Cu. The hardening is caused by Cu precipitates. Others use precipitation hardening by intermetallic phases such as NiTi, TiAl, or NiAl.

Table 3.1-54 Chemical composition of martensitic and martensitic-ferritic chromium steels

| Grade no. (EN 10088) | Steel designation | ASTM A 276/ AISI grade | Chemical composition (wt %) | | | | | | | |
|----------------------|-------------------|------------------------|-----------------------------|------------|------------|--------------|--------------|-----------|-----------|-----------|
| | | | C | Si | Mn | P | S | Cr | Mo | Ni |
| 1.4006 | X12Cr13 | 410 | 0.08–0.12 | ≤ 1.0 | ≤ 1.0 | ≤ 0.045 | ≤ 0.030 | 12.0–14.0 | – | – |
| 1.4005 | X12CrS13 | 416 | ≤ 0.15 | ≤ 1.0 | ≤ 1.0 | 0.15–0.25 | ≤ 0.045 | 12.0–13.0 | – | – |
| 1.4021 | X20Cr13 | 420 | 0.17–0.25 | ≤ 1.0 | ≤ 1.0 | ≤ 0.045 | ≤ 0.030 | 12.0–14.0 | – | – |
| 1.4028 | X30Cr13 | 420 | 0.28–0.35 | ≤ 1.0 | ≤ 1.0 | ≤ 0.045 | ≤ 0.030 | 12.0–14.0 | – | – |
| 1.4104 | X12CrMoS17-2 | 430F | 0.10–0.17 | ≤ 1.0 | ≤ 1.5 | ≤ 0.060 | 0.15–0.35 | 15.5–17.5 | 0.2–0.6 | – |
| 1.4057 | X20CrNi17-2 | 431 | 0.14–0.23 | ≤ 1.0 | ≤ 1.0 | ≤ 0.045 | ≤ 0.030 | 15.5–17.5 | – | 1.50–2.50 |
| 1.4109 | X70CrMo15 | 440A | 0.60–0.75 | ≤ 1.0 | ≤ 1.0 | ≤ 0.045 | ≤ 0.030 | 13.0–15.0 | 0.50–0.60 | – |
| 1.4125 | X105CrMo17 | 440C | 0.95–1.20 | ≤ 1.0 | ≤ 1.0 | ≤ 0.045 | ≤ 0.030 | 16.0–18.0 | 0.40–0.80 | – |

Table 3.1-55 Heat treatment conditions of martensitic and martensitic-ferritic chromium steels

| Grade no. | Rolling and forging <i>T</i> (°C) | Soft annealing | | | Quenching | | | | Annealing <i>T</i> (°C) |
|-----------|--------------------------------------|----------------|------------|-------------|---------------|---------|------------------|--|----------------------------|
| | | <i>T</i> (°C) | Time (min) | Cooling | <i>T</i> (°C) | Medium | Hardness HRC ca. | | |
| 1.4006 | 1100–800 | 750–800 | 120–360 | Air/furnace | 950–1000 | Air/oil | 31 | | 780–680 |
| 1.4005 | 1150–750 | 750–800 | 15–30 | Air | 950–1000 | Oil | 31 | | 700–600 |
| 1.4021 | 1100–800 | 730–780 | 120–360 | Air/furnace | 980–1030 | Air/oil | 47 | | 750–650 |
| 1.4028 | 1100–800 | 730–780 | | Air/furnace | 980–1030 | Air/oil | | | 740–640 |
| 1.4104 | 1100–800 | 750–850 | 120–180 | Air/furnace | 980–1030 | Air/oil | 27 | | 650–550 |
| 1.4057 | 1100–800 | 650–750 | 180–240 | Air/furnace | 980–1030 | Air/oil | 47 | | 720–620 |
| 1.4109 | 1100–900 | 790–840 | 120–360 | Furnace | 1020–1060 | Oil | 59 | | 200–150 |
| 1.4125 | 1100–900 | 800–850 | 160–240 | Furnace | 1000–1050 | Oil | 61 | | 300–100 |

Table 3.1-56 Mechanical properties of martensitic and martensitic-ferritic chromium steels

| Grade no. | Heat treatment condition | Tensile properties of flat products ≤25 mm thickness | | | CVN impact energy at room temperature (J) longitudinal/transversal | Min. yield strength or 0.2% proof strength at <i>T</i> (°C) in MPa | | | |
|-----------|--------------------------|--|---------------------------------|--|--|--|-----|-----|-----|
| | | Min. yield strength or 0.2% proof strength (MPa) | Ultimate tensile strength (MPa) | Fracture elongation A ₅ (%) long./transv. | | 100 | 200 | 300 | 400 |
| 1.4006 | Annealed | 250 | 450–650 | 20/15 | –/– | 235 | 225 | 220 | 195 |
| | Quenched and tempered | 420 | 600–800 | 16/12 | –/– | 420 | 400 | 365 | 305 |
| 1.4005 | Quenched and tempered | 440 | 590–780 | 12/– | –/– | – | – | – | – |
| 1.4021 | Annealed | – | ≤740 | – | –/– | | | | |
| | Quenched and tempered | 450 | 650–800 | 15/11 | 30/– | 420 | 400 | 365 | 305 |
| | | 550 | 750–950 | 13/10 | 25/– | | | | |
| 1.4028 | Annealed | – | ≤780 | – | –/– | | | | |
| | Quenched and tempered | 600 | 800–1000 | – | 11/– | | | | |
| 1.4104 | Annealed | 300 | 540–740 | – | –/– | | | | |
| | Quenched and tempered | 450 | 640–840 | – | –/– | | | | |
| 1.4057 | Annealed | – | ≤950 | – | –/– | | | | |
| | Quenched and tempered | 550 | 750–950 | 14/10 | 20/– | 495 | 460 | 430 | 345 |

Table 3.1-57 Physical properties of martensitic and martensitic-ferritic chromium steels

| Grade no. | Mean thermal expansion coefficient between 20 °C and T (°C) in 10 ⁻⁶ K ⁻¹ | | | | Density (kg/dm ³) | Thermal conductivity at 20 °C (W/Km) | Specific heat at 20 °C (J/g K) | Electrical resistivity at 20 °C (Ω mm ² /m) | Modulus of elasticity (kN/mm ²) | Magnetizable |
|-----------|---|------|------|------|-------------------------------|--------------------------------------|--------------------------------|--|---|--------------|
| | 100 | 200 | 300 | 400 | | | | | | |
| 1.4006 | 10.5 | 11.0 | 11.5 | 12.0 | 7.7 | 30 | 0.46 | 0.60 | 216 | yes |
| 1.4005 | 10.5 | 11.0 | 11.5 | 12.0 | 7.7 | 30 | 0.46 | 0.60 | 216 | yes |
| 1.4021 | 10.0 | 10.0 | 10.5 | 10.5 | 7.7 | 30 | 0.46 | 0.60 | 216 | yes |
| 1.4028 | 10.5 | 11.0 | 11.5 | 12.0 | 7.7 | 30 | 0.46 | 0.65 | 220 | yes |
| 1.4104 | 10.0 | 10.5 | 10.5 | 10.5 | 7.7 | 25 | 0.46 | 0.70 | 216 | yes |
| 1.4057 | 10.0 | 10.5 | 11.0 | 11.0 | 7.7 | 25 | 0.46 | 0.70 | 216 | yes |
| 1.4109 | 10.5 | 11.0 | 11.0 | 11.5 | 7.7 | 30 | 0.46 | 0.65 | 210 | yes |
| 1.4125 | 10.4 | 10.8 | 11.2 | 11.6 | 7.7 | 15 | 0.43 | 0.80 | 220 | yes |

Table 3.1-58 Weldability of martensitic and martensitic-ferritic chromium steels

| Grade no. | Weldable | Welding method | | | | Pre-heating (°C) | After-treatment | | | Q+T anew |
|-----------|----------|----------------|-------------|-------------|--------------------|------------------|-----------------|-----------|-----|----------|
| | | SAW/MIG | TIG welding | Arc welding | Resistance welding | | Annealing | at T (°C) | | |
| 1.4006 | Yes | + | | + | + | (+) | 250 | + | 750 | — |
| 1.4005 | No | — | | — | — | — | — | — | — | — |
| 1.4021 | Condit. | + | | + | — | — | 350 | + | 720 | (+) |
| 1.4028 | Yes | — | | + | — | — | — | + | 720 | — |
| 1.4104 | No | — | | — | — | — | — | — | — | — |
| 1.4057 | Condit. | + | | + | — | — | 200 | + | 700 | (+) |
| 1.4109 | No | — | | — | — | — | — | — | — | — |
| 1.4125 | No | — | | — | — | — | — | — | — | — |

Austenitic Stainless Steels

By adding of austenite forming elements, mainly Ni, the range of stability of the fcc phase is extended down to and below room temperature. The favorable combinations of ductility, toughness, hot and cold formability, weldability, and corrosion resistance have made the austenitic CrNi steels by far the most important and popular stainless steels. The most widespread representatives are the steel grades AISI 304 (X5CrNi18-10, 1.4301) and AISI 316 (X5CrNiMo17-12-2, 1.4401). The austenitic steels are applied in the solution-annealed (at 1000–1100 °C) and fast-cooled state which yields a microstructure that is free of carbide precipitates and has a homogeneous distribution of the alloying elements necessary for good corrosion resistance.

Compared to the bcc ferrite phase the fcc austenite phase is characterized by a higher solubility but a lower diffusivity of almost all alloying elements. The first fact allows the production of single phase fcc alloys with a broad composition spectrum. This permits adjustment of the properties of the steel to specific requirements of

corrosion and oxidation resistance, cold and hot strength etc. The low diffusivity makes precipitation processes rather sluggish.

The austenite of the quenched steels can be unstable and can transform into martensite as a result of cold deformation or cooling to sub-zero temperatures, especially if these steels are relatively weakly-alloyed. This transformation leads to increased strength and reduced ductility. Martensite can be detected by magnetization measurements because the austenite is paramagnetic whereas the martensite is ferromagnetic. Since the fcc austenitic steels do not exhibit the ductile-brittle transition characteristic of ferritic alloys, the austenitic steels stay sufficiently ductile even at liquid He temperature (4.2 K) and are thus preferred materials for cryogenic applications. Their yield strength of 200–250 MPa is lower than that of the ferritic steels, but due to their pronounced work hardening by cold deformation (making extensive cold-forming operations difficult and often requiring intermediate soft annealing heat treatments), they have a higher tensile strength and fracture elon-

gation. A pronounced solid solution strengthening is possible, especially by higher concentrations of nitrogen (up to about 0.4 wt% N). The nitrogen-alloyed CrNi steels are characterized by particularly favorable combinations of mechanical and corrosion properties.

As mentioned above, after fast cooling from $\geq 1000^{\circ}\text{C}$, the austenitic stainless steels are free of carbide precipitates. But since steels with ≥ 0.05 wt% C are already carbon-supersaturated at temperatures below 900°C , holding the material at temperatures between about 400 and 900°C will lead to precipitation of chromium carbides (mainly M_{23}C_6 type), preferentially at the grain boundaries. This will result in an increased susceptibility to intergranular corrosion due to local chromium depletion. The means to avoid this undesir-

able effect are the same as for the ferritic steels: bonding of the carbon (and nitrogen) atoms by an overstoichiometric alloying with Nb, Ta, or Ti (so-called stabilization of the steels), or the reduction of the carbon content to below 0.03 wt% C resulting in the development of the extra low carbon (ELC) steels. However, in strongly oxidative media (such as concentrated nitric acid) even steels that have been sufficiently stabilized by Ti may exhibit intergranular corrosion due to selective dissolution of the TiC. Under less severe corrosion conditions, the Ti stabilized steels are as stable as the Nb stabilized grades but at somewhat lower costs.

Chemical compositions, heat treatment conditions, physical properties, and hints to weldability of austenitic stainless steels are presented in Tables 3.1-59 – 3.1-63.

Table 3.1-59 Heat treatment conditions of austenitic stainless steels

| Grade no. | Rolling and forging temperature ($^{\circ}\text{C}$) | Cooling | Quenching temperature ($^{\circ}\text{C}$) | Cooling |
|-----------|--|--|--|-------------------|
| 1.4541 | 1150–750 | Air | 1020–1100 | Air, > 2 mm water |
| 1.4401 | | | | |
| 1.4402 | | | | |
| 1.4406 | | | | |
| 1.4436 | | | | |
| 1.4571 | | | | |
| 1.4580 | | | | |
| 1.4301 | 1150–750 | Air | 1000–1080 | Air, > 2 mm water |
| 1.4303 | | | | |
| 1.4305 | | | | |
| 1.4306 | | | | |
| 1.4311 | | | | |
| 1.4550 | 1150–750 | Air | 1050–1150 | Air, > 2 mm water |
| 1.4429 | 1150–750 | Air | 1040–1120 | Air, > 2 mm water |
| 1.4438 | | | | |
| 1.4439 | | | | |
| 1.4435 | 1150–750 | Air, below 600°C furnace | 1020–1100 | Air, > 2 mm water |

Table 3.1-60 Chemical composition of austenitic stainless steels

| Grade no. (EN 10088) | Steel designation | ASTM A 276/ AISI grade | | | Chemical composition (wt%) | | | P | S | Cr | Ni | Mo | Others |
|-------------------------|-------------------|---------------------------------|-------|------|----------------------------|-----------|-----------|-----------|-----------|-------------|-------------|----|--------|
| | | C | Si | Mn | | | | | | | | | |
| 1.4310 | X12CrNi17-7 | 301 | ≤0.12 | ≤1.5 | ≤2.0 | ≤0.045 | 0.030 | 16.0–18.0 | 6.0–9.0 | | | | |
| 1.4301 | X5CrNi18-10 | 304 | ≤0.07 | ≤1.0 | ≤2.0 | ≤0.045 | ≤0.030 | 17.0–19.0 | 8.5–10.5 | | | | |
| 1.4303 | X5CrNi18-12 | 305, 308 | ≤0.07 | ≤1.0 | ≤2.0 | 0.15–0.25 | ≤0.045 | 17.0–19.0 | 11.0–13.0 | | | | |
| 1.4305 | X10CrNiS18-9 | 303 | ≤0.12 | ≤1.0 | ≤2.0 | ≤0.060 | 0.15–0.35 | 17.0–19.0 | 8.0–10.0 | | | | |
| 1.4306 | X2CrNi19-11 | 304L | ≤0.03 | ≤1.0 | ≤2.0 | ≤0.045 | ≤0.030 | 18.0–20.0 | 10.0–12.5 | | | | |
| 1.4311 | X2CrNiN18-10 | 304LN | ≤0.03 | ≤1.0 | ≤2.0 | ≤0.060 | 0.15–0.35 | 17.0–19.0 | 8.5–11.5 | N 0.12–0.22 | | | |
| 1.4541 | X6CrNiTi18-10 | 321 | ≤0.08 | ≤1.0 | ≤2.0 | ≤0.045 | ≤0.030 | 17.0–19.0 | 9.0–12.0 | Ti 5x% C | | | |
| 1.4550 | X6CrNiNb18-10 | 347 | ≤0.08 | ≤1.0 | ≤2.0 | ≤0.045 | ≤0.030 | 17.0–19.0 | 9.0–12.0 | Nb 10x% C | | | |
| 1.4401 | X5CrNiMo17-12-2 | 316 | ≤0.07 | ≤1.0 | ≤2.0 | ≤0.045 | ≤0.030 | 16.5–18.5 | 10.5–13.5 | up to 1.0 | | | |
| 1.4404 | X2CrNiMo17-13-2 | 316L | ≤0.03 | ≤1.0 | ≤2.0 | ≤0.045 | ≤0.030 | 16.5–18.5 | 11.0–14.0 | 2.0–2.5 | | | |
| 1.4406 | X2CrNiMoN17-12-2 | 316LN | ≤0.03 | ≤1.0 | ≤2.0 | ≤0.045 | ≤0.030 | 16.5–18.5 | 10.5–13.5 | N 0.12–0.22 | | | |
| 1.4571 | X6CrNiMoTi17-12-2 | 316Ti | ≤0.08 | ≤1.0 | ≤2.0 | ≤0.045 | ≤0.030 | 16.5–18.5 | 10.5–13.5 | Ti 5x% C | up to 0.80 | | |
| 1.4580 | X6CrNiMoNb17-12-2 | 316Cb | ≤0.08 | ≤1.0 | ≤2.0 | ≤0.045 | ≤0.030 | 16.5–18.5 | 10.5–13.5 | Nb 10x% C | up to 0.80 | | |
| 1.4429 | X2CrNiMoN17-13-3 | 316LN | ≤0.03 | ≤1.0 | ≤2.0 | ≤0.045 | ≤0.025 | 16.5–18.5 | 11.5–14.5 | up to 1.0 | | | |
| 1.4435 | X2CrNiMo18-14-3 | 316L | ≤0.03 | ≤1.0 | ≤2.0 | ≤0.045 | ≤0.025 | 17.0–18.5 | 12.5–15.0 | N 0.14–0.22 | | | |
| 1.4436 | X5CrNiMo17-13-3 | 316 | ≤0.07 | ≤1.0 | ≤2.0 | ≤0.045 | ≤0.025 | 16.5–18.5 | 11.0–14.0 | 2.5–3.0 | | | |
| 1.4438 | X2CrNiMo18-16-4 | 317L | ≤0.03 | ≤1.0 | ≤2.0 | ≤0.045 | ≤0.025 | 17.5–19.5 | 14.0–17.0 | 3.0–4.0 | | | |
| 1.4439 | X2CrNiMoN17-13-5 | F48 | ≤0.03 | ≤1.0 | ≤2.0 | ≤0.045 | ≤0.025 | 16.5–18.5 | 12.5–14.5 | 4.0–5.0 | N 0.12–0.22 | | |
| | | 201 | ≤0.15 | ≤1.0 | 5.5–7.5 | ≤0.06 | ≤0.03 | 16.8–18.0 | 3.5–5.5 | N 0.25 | | | |
| | | 202 | ≤0.15 | ≤1.0 | 7.5–10.0 | ≤0.06 | ≤0.03 | 17.0–19.0 | 4.0–6.0 | N 0.25 | | | |
| (1.4828) | (X15CrNiSi20-12) | 309 | ≤0.20 | ≤1.0 | ≤2.0 | ≤0.045 | ≤0.03 | 22.0–24.0 | 12.0–15.0 | | | | |
| (1.4845) | (X12CrNi25-21) | 310 | ≤0.25 | ≤1.5 | ≤2.0 | ≤0.045 | ≤0.03 | 24.0–26.0 | 19.0–22.0 | | | | |

Table 3.1-61 Mechanical properties of austenitic stainless steels

| Grade no. | Heat treatment condition | Tensile properties of flat products ≤ 25 mm thickness | | | Min. CVN impact energy at room temperature (J) | Min. yield strength or 0.2% proof strength at T (°C) in MPa | | | | |
|-----------|--------------------------|---|---------------------------------|---|--|---|-----|-----|-----|-----|
| | | Min. yield strength or 0.2% proof strength (MPa) | Ultimate tensile strength (MPa) | Min. fracture elongation A ₅ (%) | | 100 | 200 | 300 | 400 | 500 |
| 1.4310 | Quenched | 260 | 600–950 | 35 | 105 | — | — | — | — | — |
| 1.4301 | Quenched | 195 | 500–700 | 45 | 85 | 157 | 127 | 110 | 98 | 92 |
| 1.4303 | Quenched | 185 | 490–690 | 45 | 85 | 155 | 127 | 110 | 98 | 92 |
| 1.4305 | Quenched | 195 | 500–700 | 35 | — | — | — | — | — | — |
| 1.4306 | Quenched | 180 | 460–680 | 45 | 85 | 147 | 118 | 100 | 89 | 81 |
| 1.4311 | Quenched | 270 | 550–760 | 40 | 85 | 205 | 157 | 136 | 125 | 119 |
| 1.4541 | Quenched | 200 | 500–730 | 40 | 85 | 176 | 157 | 136 | 125 | 119 |
| 1.4550 | Quenched | 205 | 510–740 | 40 | 85 | 177 | 157 | 136 | 125 | 119 |
| 1.4401 | Quenched | 205 | 510–710 | 40 | 85 | 177 | 147 | 127 | 115 | 110 |
| 1.4404 | Quenched | 190 | 490–690 | 40 | 85 | 166 | 137 | 118 | 108 | 100 |
| 1.4406 | Quenched | 280 | 580–800 | 40 | 85 | 211 | 167 | 145 | 135 | 129 |
| 1.4571 | Quenched | 210 | 500–730 | 35 | 85 | 185 | 167 | 145 | 135 | 129 |
| 1.4580 | Quenched | 215 | 510–740 | 35 | 85 | 186 | 167 | 145 | 135 | 129 |
| 1.4429 | Quenched | 295 | 580–800 | 40 | 85 | 225 | 178 | 155 | 145 | 138 |
| 1.4435 | Quenched | 190 | 490–690 | 35 | 85 | 166 | 137 | 118 | 108 | 100 |
| 1.4436 | Quenched | 205 | 510–710 | 40 | 85 | 177 | 147 | 127 | 115 | 110 |
| 1.4438 | Quenched | 195 | 490–690 | 35 | 85 | 172 | 147 | 127 | 115 | 110 |
| 1.4439 | Quenched | 285 | 580–800 | 35 | 85 | 225 | 185 | 165 | 150 | — |
| AISI 201 | | 370 ^a | 1125 ^a | 57 ^a | | | | | | |
| AISI 202 | | 359 ^a | 1110 ^a | 55 ^a | | | | | | |
| AISI 309 | | 334 ^a | 691 ^a | 48 ^a | | | | | | |
| AISI 310 | | 319 ^a | 678 ^a | 50 ^a | | | | | | |

^a Typical values

Table 3.1-62 Physical properties of austenitic stainless steels

Duplex Stainless Steels

Duplex steels have a mixed structure of ferrite and austenite. They contain the ferrite-forming elements Cr and Mo at levels of 20–29 wt% Cr and up to 4 wt% Mo, respectively, and the austenite-forming elements of about 4–9 wt% Ni and up to 0.3 wt% N. Typical examples are presented in Table 3.1-64. These steels solidify as δ -ferrite which will partly transform into austenite upon cooling. Thus, the phase fractions of ferrite and austenite depend not only on the chemical composition, but also on the annealing and cooling conditions.

The advantages of the duplex steels compared to the austenitic steels are a substantially higher yield and tensile strength (cf. Table 3.1-66) and a better resistance against stress corrosion cracking. A few data on heat treatment conditions, physical properties, and weldability are given in Tables 3.1-65, 3.1-67, and 3.1-68. In comparison with ferritic stainless steels, the duplex steels have a better weldability, a higher low temperature toughness, and a lower susceptibility to general and

intergranular corrosion. With respect to optimum toughness, the δ -ferrite content of duplex steels should be below 60 vol%. The influence of annealing temperature and cooling conditions on the ferrite content of a steel with 0.05 wt% C, 25 wt% Cr, 8 wt% Ni, 2.5 wt% Mo, and 1.5 wt% Cu is illustrated in Table 3.1-69 [1.78]. During the partial phase transformation of ferrite into austenite below 1350 °C, a redistribution of the alloying elements occurs with the ferrite-forming elements Cr, Mo, and Ti enriched in the α -phase and the austenite-forming elements C, N, Ni, and Mn enriched in the γ -phase. The reduced C content in the α -phase delays the formation of chromium carbides. The relatively high Mo and N contents ensure good resistance against pitting corrosion.

The formation of the brittle Cr-rich σ -phase, which can form in the temperature range of 1000–500 °C and can lead to a drastic reduction of toughness and corrosion resistance, requires special attention. Therefore, duplex steels are usually water quenched from a solution treatment at 1100–1150 °C.

Table 3.1-64 Chemical composition of duplex stainless steels

| Grade no. (EN 10088) | Steel designation | ASTM A 276/AISI grade | Chemical composition (wt%) | | | | | | | | |
|----------------------|-------------------|-----------------------|----------------------------|----|----|-------|--------|-----------|---------|---------|-----------|
| | | | C | Si | Mn | S | P | Cr | Ni | Mo | N |
| 1.4460 | X4CrNiMoN27-5-2 | 329 | ≤0.05 | ≤1 | ≤2 | ≤0.03 | ≤0.045 | 25.0–28.0 | 4.5–6.0 | 1.3–2.0 | 0.05–0.20 |
| 1.4462 | X2CrNiMoN22-5-3 | F51 | ≤0.03 | ≤1 | ≤2 | ≤0.02 | ≤0.03 | 21.0–23.0 | 4.5–6.5 | 2.5–3.5 | 0.08–0.20 |

Table 3.1-65 Heat treatment conditions of duplex stainless steels

| Grade no. | Rolling and forging temperature (°C) | Cooling | Quenching temperature (°C) | Cooling |
|-----------|--------------------------------------|---------|----------------------------|------------|
| 1.4460 | 1150–900 | Air | 1020–1100 | Air, water |
| 1.4462 | 1150–900 | Air | 1020–1100 | Air, water |

Table 3.1-66 Mechanical properties of duplex stainless steels

| Grade no. | Heat treatment condition | Tensile properties of flat products ≤ 25 mm thickness | | | Min. CVN impact energy at room temp. (J) | Min. yield strength or 0.2% proof strength at T (°C) in MPa | | | | |
|-----------|--------------------------|--|---------------------------------|---|--|---|-----|-----|-----|-----|
| | | Min. yield strength or 0.2% proof strength (MPa) | Ultimate tensile strength (MPa) | Min. fracture elongation A ₅ (%) | | 100 | 200 | 300 | 400 | 500 |
| 1.4460 | Quenched | 450 | 600–800 | 20 | 55 | 360 | 310 | — | — | — |
| 1.4462 | Quenched | 450 | 640–900 | 30 | 120 | 360 | 310 | 280 | — | — |

Table 3.1–67 Physical properties of duplex stainless steels

| Grade no. | Mean thermal expansion coefficient between 20 °C and T (°C) in 10 ⁻⁶ K ⁻¹ | | | | | | | | Density (kg/dm ³) | Thermal conductivity at 20 °C (W/K m) | Specific heat at 20 °C (J/g) | Electrical resistivity at 20 °C (Ω mm ² /m) | Modulus of elasticity at 20 °C (kN/mm ²) | Magnetizable |
|-----------|---|------|------|------|-----|-----|-----|-----|-------------------------------|---------------------------------------|------------------------------|--|--|--------------|
| | 100 | 200 | 300 | 400 | 500 | 600 | 700 | 800 | | | | | | |
| 1.4460 | 12.0 | 12.5 | 13.0 | 13.5 | — | — | — | — | 7.8 | 15 | 0.45 | 0.80 | 200 | Yes |
| 1.4462 | 12.0 | 12.5 | 13.0 | — | — | — | — | — | 7.8 | 15 | 0.45 | 0.80 | 200 | Yes |

Table 3.1–68 Weldability of duplex stainless steels

| Grade no. | Weldable | Welding method SAW/MIG/TIG welding | Arc welding | Resistance welding | Autogenous welding | Preheating (°C) | Aftertreatment |
|-----------|----------|------------------------------------|-------------|--------------------|--------------------|-----------------|----------------|
| 1.4460 | Yes | + | + | + | + | — | 1020 °C |
| 1.4462 | Yes | + | + | + | — | — | — |

Table 3.1–69 Influence of annealing temperature and cooling conditions on the ferrite content of a steel with 0.05 wt% C, 25 wt% Cr, 8 wt% Ni, 2.5 wt% Mo and 1.5 wt% Cu [1.10]

| Annealing temperature (°C) (holding time 15 min) | Ferrite content (vol. %) after water quenching | air cooling |
|---|---|-------------|
| 1350 | 93.0 | 78.8 |
| 1300 | 70.2 | 61.8 |
| 1250 | 43.5 | 37.5 |
| 1150 | 35.7 | 34.2 |
| 1050 | 24.0 | 23.7 |
| 1000 | 7.6 | 7.6 |

3.1.5.5 Heat-Resistant Steels

Heat-resistant steels are treated extensively in [1.52], creep data are compiled in [1.86]. Steels are considered heat-resistant if they possess—in addition to good mechanical properties at ambient temperature—special resistance against short or long term exposure to hot gases, combustion products and melts of metals or salts at temperatures above about 550 °C where non- or low-alloyed steels are no longer applicable due to extensive scaling and creep.

Thus, heat-resistant steels are characterized by a combination of good high temperature strength, scaling resistance, a sufficient hot and cold formability, and weldability. They are sufficiently stable against embrittling processes at the high application temperatures. The resistance against scaling and hot gas corrosion is affected by the formation of a protective dense, pore-free, and tightly adherent oxide layer at the surface. The main alloying elements leading to such an oxide layer are Cr, Al, and Si. The oxidation and scaling resistance increases with increasing Cr content between about 6 and 25 wt% Cr. Higher Cr concentrations do not lead to fur-

ther improvement. Additions of up to 2 wt% Al and up to 3 wt% Si enhance the effect of Cr. Small additions of rare earth metals, e.g., of Ce, can improve the adherence and the ductility of the oxide layer. In order to keep the protective oxide layer intact during temperature changes, the steels should exhibit low volume changes and, if possible, no phase transformations during heating and cooling. Consequently, there are two main groups of heat resistant steels: ferritic and austenitic steels, both showing no phase transformations.

The *ferritic* Cr (or Cr–Al–Si) steels are less expensive but have a lower creep strength above 800 °C. They may suffer from three embrittling mechanisms:

- The “475 °C embrittlement” due to decomposition in the metastable miscibility gap of the Fe–Cr solid solution, occurring between about 350 and 550 °C at Cr contents above 15 wt% Cr (Fig. 3.1–107);
- The formation of the brittle intermetallic FeCr σ -phase at temperatures between about 550 and 900 °C (Sect. 3.1.5.1, Fig. 3.1–106);
- Grain coarsening at temperatures above about 900 °C.

However, these embrittling mechanisms will not impair the behavior at high operating temperatures if taken into account properly, but will deteriorate the toughness after cooling to room temperature. Heating to temperatures above the range of occurrence of the embrittling phases followed by sufficiently fast cooling will suppress the embrittling effects.

The Cr and Ni alloyed austenitic steels possess a higher temperature strength and better ductility, toughness, and weldability. The susceptibility to embrittling effects is considerably lower. At Ni contents above 30 wt% Ni, they are outside the stability region of the brittle σ -phase.

The properties of the *ferritic-austenitic* steels lie between those of the ferritic and austenitic steels. They are characterized by a higher fracture toughness, cold formability, high temperature strength, and weldability than the fully ferritic grades, and by a higher chemical resistance in sulphurous gases than the austenitic grades.

It is obvious that the scaling resistance of the heat-resisting steels will be detrimentally influenced by any other corrosion mechanism which may be destroying the oxide layer, e.g., by chemical reactions with other metal oxides, chlorine, or chlorides. Thus in general, the heat resistance cannot be characterized by a single test method or measuring parameter but will depend on the specific environmental conditions.

In Table 3.1-70 chemical compositions of the most important grades of heat resistant steels are presented [1.87]. Table 3.1-71 contains some information about recommended temperature ranges for heat treatment and hot forming. In Tables 3.1-72 and 3.1-73 the mechanical properties at room temperature and at high temperatures are listed, respectively. Table 3.1-74 shows some physical properties. The ferritic and ferritic-austenitic steels are magnetisable while the austenitic grades are nonmagnetic. Qualitative data on the high temperature behavior in special gas atmospheres are given in Table 3.1-75. In carburizing atmospheres carbon can diffuse into the steel, reacting with the chromium to form chromium carbides which can lead to embrittlement and reduced scaling resistance due to chromium depletion in the matrix. Higher Ni and Si contents reduce the carburization susceptibility. In sulfur-containing atmospheres, which contain the sulfur mostly in the form of SO_2 or H_2S , the formation of sulfides at the surface may inhibit the formation of the protecting oxide layer. Under oxidizing conditions this process will proceed rather slowly, but under reducing conditions the pick-up of sulfur occurs very

Table 3.1-70 Chemical composition of heat-resistant steels according to SEW [1.87]

| Grade ^a | Steel designation | ASTM/AISI grade | Chemical composition (wt%) | | | | Mn | P | S | Al | Cr | Ni | Others |
|-----------------------------------|-------------------|-----------------|----------------------------|---------|------|--------|-------|----------|-----------|-----------|------------------------|----|--------|
| Ferritic steels | | | | | | | | | | | | | |
| 1.4713 | X10CrAlSi7 | — | ≤0.12 | 0.5–1.0 | ≤1 | ≤0.04 | ≤0.03 | 0.5–1.0 | 6.0–8.0 | — | — | — | — |
| 1.4720 | X7CrTi12 | — | ≤0.08 | ≤1.0 | ≤1 | ≤0.04 | ≤0.03 | — | 10.5–12.5 | — | Ti ≥ 6 wt% C up to 1.0 | — | — |
| 1.4724 | X10CrAlSi13 | 405 | ≤0.12 | 0.7–1.4 | ≤1 | ≤0.04 | ≤0.03 | 0.7–1.2 | 12.0–14.0 | — | — | — | — |
| 1.4742 | X10CrAlSi18 | 430 | ≤0.12 | 0.7–1.4 | ≤1 | ≤0.04 | ≤0.03 | 0.7–1.2 | 17.0–19.0 | — | — | — | — |
| 1.4762 | X10CrAlSi25 | 446 | ≤0.12 | 0.7–1.4 | ≤1 | ≤0.04 | ≤0.03 | 1.2–1.7 | 23.0–26.0 | — | — | — | — |
| Ferritic-austenitic steels | | | | | | | | | | | | | |
| 1.4821 | X15CrNiSi25-4 | 327 | 0.10–0.20 | 0.8–1.5 | 2.0 | ≤0.04 | ≤0.03 | — | 24.0–27.0 | 3.5–5.5 | — | — | — |
| Austenitic steels | | | | | | | | | | | | | |
| 1.4878 | X10CrNiTi18-10 | 321 | ≤0.12 | ≤1 | ≤2.0 | ≤0.045 | ≤0.03 | — | 17.0–19.0 | 9.0–12.0 | Ti ≥ 4 wt% C up to 0.8 | — | — |
| 1.4828 | X15CrNiSi20-12 | 309 | ≤0.20 | 1.5–2.5 | ≤2.0 | ≤0.045 | ≤0.03 | — | 19.0–21.0 | 11.0–13.0 | — | — | — |
| 1.4833 | X12CrNi23-12 | 309S | ≤0.08 | ≤1 | ≤2.0 | ≤0.045 | ≤0.03 | — | 21.0–23.0 | 12.0–15.0 | — | — | — |
| 1.4845 | X8CrNi25-21-12 | 310S | ≤0.15 | ≤0.75 | ≤2.0 | ≤0.045 | ≤0.03 | — | 24.0–26.0 | 19.0–22.0 | — | — | — |
| 1.4841 | X15CrNiSi25-20 | 310/314 | ≤0.20 | 1.5–2.5 | ≤2.0 | ≤0.045 | ≤0.03 | — | 24.0–26.0 | 19.0–22.0 | — | — | — |
| 1.4864 | X12NiCrSi36-18 | 330 | ≤0.15 | 1.0–2.0 | ≤2.0 | ≤0.030 | ≤0.02 | — | 15.0–17.0 | 33.0–37.0 | — | — | — |
| 1.4876 | X10NiCrAlTi32-21 | B163 | ≤0.12 | ≤1 | ≤2.0 | 0.030 | ≤0.02 | 0.15–0.6 | 19.0–23.0 | 30.0–34.0 | Ti 0.15–0.6 | — | — |

a According to SEW [1.87]

Table 3.1-71 Recommended conditions for heat treatment and hot forming of heat-resistant steels

| Grade ^a | Hot forming temperature (°C) | Soft annealing (°C) Cooling in air (water) | Quenching temperature (°C) Cooling in water (air) | Limiting scaling temperature in air (°C) |
|-----------------------------------|------------------------------|---|--|--|
| Ferritic steels | | | | |
| 1.4713 | 1100–750 | 750–800 | – | 620 |
| 1.4720 | 1050–750 | 750–850 | – | 800 |
| 1.4724 | 1100–750 | 800–850 | – | 850 |
| 1.4742 | 1100–750 | 800–850 | – | 1000 |
| 1.4762 | 1100–750 | 800–850 | – | 1150 |
| Ferritic-austenitic steels | | | | |
| 1.4821 | 1150–800 | – | 1000–1050 | 1100 |
| Austenitic steels | | | | |
| 1.4878 | 1150–800 | – | 1020–1070 | 850 |
| 1.4828 | 1150–800 | – | 1050–1100 | 1000 |
| 1.4833 | 1150–900 | – | 1050–1100 | 1000 |
| 1.4845 | 1150–800 | – | 1050–1100 | 1050 |
| 1.4841 | 1150–800 | – | 1050–1100 | 1150 |
| 1.4864 | 1150–800 | – | 1050–1100 | 1100 |
| 1.4876 | 1150–800 | 900–980 (recrystallization annealing) | 1100–1150 (solution annealing) | 1100 |

^a According to SEW [1.87]

Table 3.1-72 Mechanical properties of heat-resistant steels at 20 °C

| Grade ^a | Heat treatment condition | Hardness (HB) max. | 0.2% proof stress (MPa) min. | Ultimate tensile strength (MPa) | Elongation $L_0 = 5d_0$ min. (%) long. transv. |
|-----------------------------------|--------------------------|--------------------|------------------------------|---------------------------------|---|
| Ferritic steels | | | | | |
| 1.4713 | Annealed | 192 | 220 | 420–620 | 20 |
| 1.4720 | Annealed | 179 | 210 | 400–600 | 25 |
| 1.4724 | Annealed | 192 | 250 | 450–650 | 15 |
| 1.4742 | Annealed | 212 | 270 | 500–700 | 12 |
| 1.4762 | Annealed | 223 | 280 | 520–720 | 10 |
| Ferritic-austenitic steels | | | | | |
| 1.4821 | Quenched | 235 | 400 | 600–850 | 16 |
| Austenitic steels | | | | | |
| 1.4878 | Quenched | 192 | 210 | 500–750 | 40 |
| 1.4828 | Quenched | 223 | 230 | 500–750 | 30 |
| 1.4833 | Quenched | 192 | 210 | 500–750 | 35 |
| 1.4845 | Quenched | 192 | 210 | 500–750 | 35 |
| 1.4841 | Quenched | 223 | 230 | 550–800 | 30 |
| 1.4864 | Quenched | 223 | 230 | 550–800 | 30 |
| 1.4876 | Recryst. annealed | 192 | 210 | 500–750 | 30 |
| | Solution annealed | 192 | 170 | 450–700 | 30 |

^a According to SEW [1.87]

Table 3.1-73 Long-term mechanical properties of heat-resistant steels at high temperatures; average values of scatter bands

| Grade ^a | Temperature (°C) | 1% creep limit (MPa) at <i>t</i> = | | Creep rupture strength (MPa) at <i>t</i> = | | | |
|--|------------------|------------------------------------|----------|--|----------|-----------|--|
| | | 1000 h | 10 000 h | 1000 h | 10 000 h | 100 000 h | |
| Ferritic and ferritic-austenitic steels | | | | | | | |
| 1.4713 | 500 | 80 | 50 | 160 | 100 | 55 | |
| 1.4720 | 600 | 27.5 | 17.5 | 55 | 35 | 20 | |
| 1.4724 | 700 | 8.5 | 4.7 | 17 | 9.5 | 5 | |
| 1.4742 | 800 | 3.7 | 2.1 | 7.5 | 4.3 | 2.3 | |
| 1.4762 | 900 | 1.8 | 1.0 | 3.6 | 1.9 | 1.0 | |
| 1.4821 | | | | | | | |
| Austenitic steels | | | | | | | |
| 1.4878 | 600 | 110 | 85 | 185 | 115 | 65 | |
| | 700 | 45 | 30 | 80 | 45 | 22 | |
| | 800 | 15 | 10 | 35 | 20 | 10 | |
| 1.4828 | 600 | 120 | 80 | 190 | 120 | 65 | |
| 1.4833 | 700 | 50 | 25 | 75 | 36 | 16 | |
| | 800 | 20 | 10 | 35 | 18 | 7.5 | |
| | 900 | 8 | 4 | 15 | 8.5 | 3.0 | |
| 1.4845 | 600 | 150 | 105 | 230 | 160 | 80 | |
| 1.4841 | 700 | 53 | 37 | 80 | 40 | 18 | |
| | 800 | 23 | 12 | 35 | 18 | 7 | |
| | 900 | 10 | 5.7 | 15 | 8.5 | 3.0 | |
| 1.4864 | 600 | 105 | 80 | 180 | 125 | 75 | |
| | 700 | 50 | 35 | 75 | 45 | 25 | |
| | 800 | 25 | 15 | 35 | 20 | 7 | |
| | 900 | 12 | 5 | 15 | 8 | 3 | |
| 1.4876 | 600 | 130 | 90 | 200 | 152 | 114 | |
| (solution annealed) | 700 | 70 | 40 | 90 | 68 | 47 | |
| | 800 | 30 | 15 | 45 | 30 | 19 | |
| | 900 | 13 | 5 | 20 | 11 | 4 | |

^a According to SEW [1.87]

Table 3.1-74 Physical properties of heat-resistant steels

| Grade ^a | Density at 20 °C (g cm ⁻³) | Average coefficient of thermal expansion between 20 °C and <i>T</i> (°C) ($\times 10^{-6}$ K ⁻¹) | | | | | Thermal conductivity at <i>T</i> (°C) (W m ⁻¹ K ⁻¹) | | Specific heat at 20 °C (J g ⁻¹ K ⁻¹) | Specific electrical resistivity at 20 °C (Ω mm ² m ⁻¹) | |
|-----------------------------------|--|--|------|------|------|------|---|----|---|---|------|
| | | 200 | 400 | 600 | 800 | 1000 | 1200 | 20 | 500 | | |
| Ferritic steels | | | | | | | | | | | |
| 1.4713 | 7.7 | 11.5 | 12.0 | 12.5 | 13.0 | — | — | 23 | 25 | 0.45 | 0.70 |
| 1.4720 | 7.7 | 11.0 | 12.0 | 12.5 | 13.0 | — | — | 25 | 28 | 0.45 | 0.60 |
| 1.4724 | 7.7 | 11.0 | 11.5 | 12.0 | 12.5 | 13.5 | — | 21 | 23 | 0.45 | 0.90 |
| 1.4742 | 7.7 | 10.5 | 11.5 | 12.0 | 12.5 | 13.5 | — | 19 | 25 | 0.45 | 0.95 |
| 1.4762 | 7.7 | 10.5 | 11.5 | 12.0 | 12.5 | 13.5 | 15.0 | 17 | 23 | 0.45 | 1.10 |
| Ferritic-austenitic steels | | | | | | | | | | | |
| 1.4821 | 7.7 | 13.0 | 13.5 | 14.0 | 14.5 | 15.0 | 15.5 | 17 | 23 | 0.50 | 0.90 |

Table 3.1-74 Physical properties of heat-resistant steels, cont.

| Grade ^a | Density at 20 °C (g cm ⁻³) | Average coefficient of thermal expansion between 20 °C and T (°C) ($\times 10^{-6}$ K ⁻¹) | | | | | | Thermal conductivity at T (°C) (W m ⁻¹ K ⁻¹) | | Specific heat at 20 °C (J g ⁻¹ K ⁻¹) | Specific electrical resistivity at 20 °C (Ω mm ² m ⁻¹) | |
|--------------------------|--|--|------|------|------|------|------|---|-----|---|---|--|
| | | 200 | 400 | 600 | 800 | 1000 | 1200 | 20 | 500 | | | |
| Austenitic steels | | | | | | | | | | | | |
| 1.4878 | 7.9 | 17.0 | 18.0 | 18.5 | 19.0 | — | — | 15 | 21 | 0.50 | 0.75 | |
| 1.4828 | 7.9 | 16.5 | 17.5 | 18.0 | 18.5 | 19.5 | — | 15 | 21 | 0.50 | 0.85 | |
| 1.4833 | 7.9 | 16.0 | 17.5 | 18.0 | 18.5 | 19.5 | — | 15 | 19 | 0.50 | 0.80 | |
| 1.4845 | 7.9 | 15.5 | 17.0 | 17.5 | 18.0 | 19.0 | — | 14 | 19 | 0.50 | 0.85 | |
| 1.4841 | 7.9 | 15.5 | 17.0 | 17.5 | 18.0 | 19.0 | 19.5 | 15 | 19 | 0.50 | 0.90 | |
| 1.4864 | 8.0 | 15.0 | 16.0 | 17.0 | 17.5 | 18.5 | — | 13 | 19 | 0.50 | 1.00 | |
| 1.4876 | 8.0 | 15.0 | 16.0 | 17.0 | 17.5 | 18.5 | — | 12 | 19 | 0.50 | 1.00 | |

^a According to SEW [1.87]

Table 3.1-75 Resistance of heat-resistant steels in various media

| Grade ^a | Resistance to Carburization | Sulphurous gases | | Reducing | Nitrogenous and low-oxygen gases | Maximum operating temperature in air (°C) |
|-----------------------------------|-----------------------------|------------------|----------|----------|----------------------------------|---|
| | | Oxidizing | Reducing | | | |
| Ferritic steels | | | | | | |
| 1.4713 | Medium | Very high | Medium | Low | 800 | |
| 1.4762 | Medium | Very high | High | Low | 1150 | |
| Ferritic-austenitic steels | | | | | | |
| 1.4821 | Medium | High | Medium | Medium | 1100 | |
| Austenitic steels | | | | | | |
| 1.4878 | Low | Medium | Low | High | 850 | |
| 1.4828 | Low | Medium | Low | High | 1000 | |
| 1.4841 | Low | Medium | Low | High | 1150 | |
| 1.4864 | High | Medium | Low | High | 1100 | |

^a According to SEW [1.87]

fast. This is especially true with Ni-alloyed steels due to the formation at about 650 °C of a low-melting Ni/NiS eutectic. Thus under such conditions the ferritic steels are more stable than the austenitic grades. In sulfur-containing atmospheres the maximum service temperatures will be about 100 to 200 °C lower than in air.

The heat-resistant steels are weldable by the usual processes, with arc welding preferred over gas fusion welding. For the ferritic steels, the tendency to grain coarsening in the heat affected zone has to be kept in mind. The application of austenitic filler metals will lead to better mechanical properties of the weld connection than those of the base metal (however, with respect to the scaling resistance, different thermal expansions of the ferritic and austenitic materials may be a problem). Filler materials should be at least as highly alloyed as the base metal. In sulfurizing atmospheres it is advisable to use ferritic electrodes for the cap passes only in order

to ensure a tough weld. Post-weld heat treatments are generally not necessary.

3.1.5.6 Tool Steels

Tool steels are the largest group of materials used to make tools for cutting, forming, or otherwise shaping a material into a part or component. An extensive account is given in [1.88]. Other major groups of tool materials are cemented carbides (Sect. 3.1.6.6), and ceramics including diamond (Chapt. 3.2).

The most commonly used materials are wrought tool steels, which are either carbon, alloy, or high-speed steels capable of being hardened by quenching and tempering to hardness levels ≤ 70 HRC. High-speed tool steels are so named because of their suitability to machine materials at high cutting speed. Other steels used for metalworking applications include steels produced by powder metallurgy, medium-carbon alloy steels,

high-carbon martensitic stainless steels, and maraging steels.

Wrought tool steels are essentially hardenable alloy steels with relatively high contents of the carbide forming elements Cr, Mo, W, and V. If the steels are quenched and tempered, the dependence of their hardness on tempering temperature indicates the level of hardening achieved as well as its temperature stability, (Fig. 3.1-117). The rate of effective softening at tempering temperatures up to about 300 °C is mainly due to the competing effects of recovery and the precipitation of iron carbides (Table 3.1-40). The hardening at higher temperatures is associated with the precipitation of alloy carbides which can form at elevated temperatures only because of their high melting points and transformation kinetics. They give rise to a second maximum on isothermal tempering curves, as curves 3 and 4 in Fig. 3.1-117, which is referred to as secondary hardening.

The alloy carbide phases which precipitate and give rise to secondary hardening are listed in Table 3.1-76.

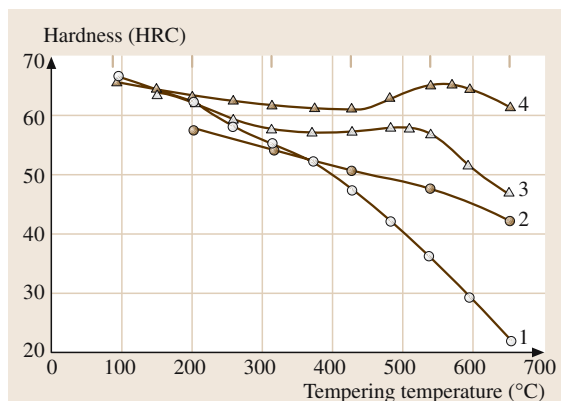


Fig. 3.1-117 Isothermal (1 h) tempering curves of 4 typical tool steels. Curves 1 and 2: softening of AISI grade W (water-hardening) and O (oil-hardening) steels; Curves 3 and 4: softening and secondary hardening of AISI grade A2 (air-hardening medium alloy) and M2 (Mo high-speed) steels [1.88]

Table 3.1-76 Alloy carbides occurring in tool steels

| Type of carbide | Prototype | Lattice type | Occurrence, composition ^a |
|--------------------------------|---------------------------------|---------------------|--------------------------------------|
| M ₇ C ₃ | Cr ₇ C ₃ | Hexagonal | In Cr alloy steels M = Cr |
| M ₂₃ C ₆ | Cr ₂₃ C ₆ | Face-centered cubic | In high-Cr steels M = Cr, Fe, W, Mo |
| M ₆ C | W ₆ C | Face-centered cubic | M = W, Mo, Cr, V, Co |
| M ₂ C | W ₂ C | Hexagonal | M = W, Mo, Cr |
| MC | VC | Face-centered cubic | VC |

^a Bold letters indicate major components

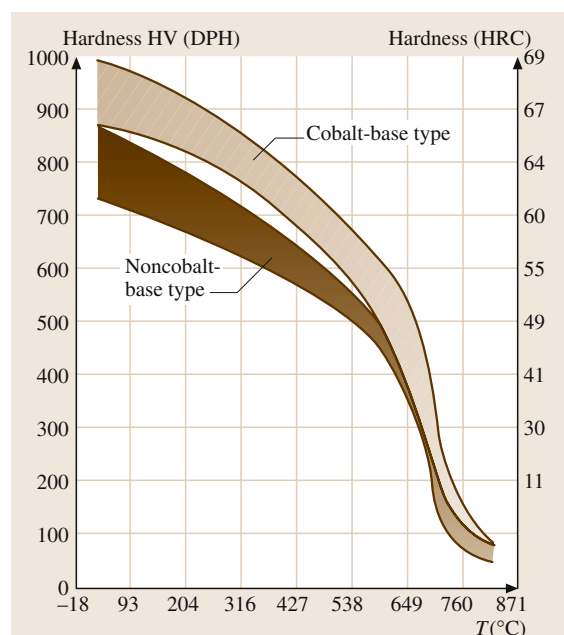


Fig. 3.1-118 Comparison of the hot hardness of Co-bearing versus non-Co bearing high-speed tool steels [1.88]

Co is an alloying element which raises the high temperature stability of tool steels by raising their melting temperature. Figure 3.1-118 shows this effect by a comparison of the hardness vs. temperature data for non-Co-based and Co-based high-speed tool steels.

Table 3.1-77 gives composition ranges for the tool steels most commonly used. According to the AISI classification, each group of similar composition and properties is given a capital letter, somewhat related to the major alloying element. Thus, high-speed steels are classified by M for molybdenum and T for tungsten. Within each group individual types are assigned code numbers.

The basic properties of tool steels that determine their performance in service are hardness, wear

Table 3.1-77 Composition ranges of principle types of tool steels according to AISI and UNS classifications [1.88]

| Designation | UNS No. | Composition ^b (wt%) | Mn | Si | Cr | Ni | Mo | W | V | C ₀ |
|---------------------------------------|---------|--------------------------------|-----------|-----------|-----------|----------|-------------|-------------|-----------|----------------|
| Molybdenum high-speed steels | | | | | | | | | | |
| M1 | T11301 | 0.78–0.88 | 0.15–0.40 | 0.20–0.50 | 3.50–4.00 | 0.30 max | 8.20–9.20 | 1.40–2.10 | 1.00–1.35 | – |
| M2 | T11302 | 0.78–0.88; 0.95–1.05 | 0.15–0.40 | 0.20–0.45 | 3.75–4.50 | 0.30 max | 4.50–5.50 | 5.50–6.75 | 1.75–2.20 | – |
| M3, class 1 | T11313 | 1.00–1.10 | 0.15–0.40 | 0.20–0.45 | 3.75–4.50 | 0.30 max | 4.75–6.50 | 5.00–6.75 | 2.25–2.75 | – |
| M3, class 2 | T11323 | 1.15–1.25 | 0.15–0.40 | 0.20–0.45 | 3.75–4.50 | 0.30 max | 4.75–6.50 | 5.00–6.75 | 2.75–3.75 | – |
| M4 | T11304 | 1.25–1.40 | 0.15–0.40 | 0.20–0.45 | 3.75–4.75 | 0.30 max | 4.25–5.50 | 5.25–6.50 | 3.75–4.50 | – |
| M7 | T11307 | 0.97–1.05 | 0.15–0.40 | 0.20–0.55 | 3.50–4.00 | 0.30 max | 8.20–9.20 | 1.40–2.10 | 1.75–2.25 | – |
| M10 | T11310 | 0.84–0.94; 0.95–1.05 | 0.10–0.40 | 0.20–0.45 | 3.75–4.50 | 0.30 max | 7.75–8.50 | – | 1.80–2.20 | – |
| M30 | T11330 | 0.75–0.85 | 0.15–0.40 | 0.20–0.45 | 3.50–4.25 | 0.30 max | 7.75–9.00 | 1.30–2.30 | 1.00–1.40 | 4.50–5.50 |
| M33 | T11333 | 0.85–0.92 | 0.15–0.40 | 0.15–0.50 | 3.50–4.00 | 0.30 max | 9.00–10.00 | 1.30–2.10 | 1.00–1.35 | 7.75–8.75 |
| M34 | T11334 | 0.85–0.92 | 0.15–0.40 | 0.20–0.45 | 3.50–4.00 | 0.30 max | 7.75–9.20 | 1.40–2.10 | 1.90–2.30 | 7.75–8.75 |
| M35 | T11335 | 0.82–0.88 | 0.15–0.40 | 0.20–0.45 | 3.75–4.50 | 0.30 max | 4.50–5.50 | 5.50–6.75 | 1.75–2.20 | 4.50–5.50 |
| M36 | T11336 | 0.80–0.90 | 0.15–0.40 | 0.20–0.45 | 3.75–4.50 | 0.30 max | 4.50–5.50 | 5.50–6.50 | 1.75–2.25 | 7.75–8.75 |
| M41 | T11341 | 1.05–1.15 | 0.20–0.60 | 0.15–0.50 | 3.75–4.50 | 0.30 max | 3.25–4.25 | 6.25–7.00 | 1.75–2.25 | 4.75–5.75 |
| M42 | T11342 | 1.05–1.15 | 0.15–0.40 | 0.15–0.65 | 3.50–4.25 | 0.30 max | 9.00–10.00 | 1.15–1.85 | 0.95–1.35 | 7.75–8.75 |
| M43 | T11343 | 1.15–1.25 | 0.20–0.40 | 0.15–0.65 | 3.50–4.25 | 0.30 max | 7.50–8.50 | 2.25–3.00 | 1.50–1.75 | 7.75–8.75 |
| M44 | T11344 | 1.10–1.20 | 0.20–0.40 | 0.30–0.55 | 4.00–4.75 | 0.30 max | 6.00–7.00 | 5.00–5.75 | 1.85–2.20 | 11.00–12.25 |
| M46 | T11346 | 1.22–1.30 | 0.20–0.40 | 0.40–0.65 | 3.70–4.20 | 0.30 max | 8.00–8.50 | 1.90–2.20 | 3.00–3.30 | 7.80–8.80 |
| M47 | T11347 | 1.05–1.15 | 0.15–0.40 | 0.20–0.45 | 3.50–4.00 | 0.30 max | 9.25–10.00 | 1.30–1.80 | 1.15–1.35 | 4.75–5.25 |
| M48 | T11348 | 1.42–1.52 | 0.15–0.40 | 0.15–0.40 | 3.50–4.00 | 0.30 max | 4.75–5.50 | 9.50–10.50 | 2.75–3.25 | 8.00–10.00 |
| M62 | T11362 | 1.25–1.35 | 0.15–0.40 | 0.15–0.40 | 3.50–4.00 | 0.30 max | 10.00–11.00 | 5.75–6.50 | 1.80–2.10 | – |
| Tungsten high-speed steels | | | | | | | | | | |
| T1 | T12001 | 0.65–0.80 | 0.10–0.40 | 0.20–0.40 | 3.75–4.50 | 0.30 max | – | 17.25–18.75 | 0.90–1.30 | – |
| T2 | T12002 | 0.80–0.90 | 0.20–0.40 | 0.20–0.40 | 3.75–4.50 | 0.30 max | 1.0 max | 17.50–19.00 | 1.80–2.40 | – |
| T4 | T12004 | 0.70–0.80 | 0.10–0.40 | 0.20–0.40 | 3.75–4.50 | 0.30 max | 0.40–1.00 | 17.50–19.00 | 0.80–1.20 | 4.25–5.75 |
| T5 | T12005 | 0.75–0.85 | 0.20–0.40 | 0.20–0.40 | 3.75–5.00 | 0.30 max | 0.50–1.25 | 17.50–19.00 | 1.80–2.40 | 7.00–9.50 |
| T6 | T12006 | 0.75–0.85 | 0.20–0.40 | 0.20–0.40 | 4.00–4.75 | 0.30 max | 0.40–1.00 | 18.50–21.00 | 1.50–2.10 | 11.00–13.00 |
| T8 | T12008 | 0.75–0.85 | 0.20–0.40 | 0.20–0.40 | 3.75–4.50 | 0.30 max | 0.40–1.00 | 13.25–14.75 | 1.80–2.40 | 4.25–5.75 |
| T15 | T12015 | 1.50–1.60 | 0.15–0.40 | 0.15–0.40 | 3.75–5.00 | 0.30 max | 1.00 max | 11.75–13.00 | 4.50–5.25 | 4.75–5.25 |
| Intermediate high-speed steels | | | | | | | | | | |
| M50 | T11350 | 0.78–0.88 | 0.15–0.45 | 0.20–0.60 | 3.75–4.50 | 0.30 max | 3.90–4.75 | – | 0.80–1.25 | – |
| M52 | T11352 | 0.85–0.95 | 0.15–0.45 | 0.20–0.60 | 3.50–4.30 | 0.30 max | 4.00–4.90 | 0.75–1.50 | 1.65–2.25 | – |

Table 3.1-77 Composition ranges of principle types of tool steels according to AISI and UNS classifications [1.88], cont.

| Designation | UNS No. | Composition ^b (wt%) | Mn | Si | Cr | Ni | Mo | W | V | C |
|--|---------|--------------------------------|-----------|-----------|-------------|-----------|-----------|-------------|-----------|-----------|
| AISI | | | | | | | | | | |
| Chromium hot-worked steels | | | | | | | | | | |
| H10 | T20810 | 0.35–0.45 | 0.25–0.70 | 0.80–1.20 | 3.00–3.75 | 0.30 max | 2.00–3.00 | — | 0.25–0.75 | — |
| H11 | T20811 | 0.33–0.43 | 0.20–0.50 | 0.80–1.20 | 4.75–5.50 | 0.30 max | 1.10–1.60 | — | 0.30–0.60 | — |
| H12 | T20812 | 0.30–0.40 | 0.20–0.50 | 0.80–1.20 | 4.75–5.50 | 0.30 max | 1.25–1.75 | 1.00–1.70 | 0.50 max | — |
| H13 | T20813 | 0.32–0.45 | 0.20–0.50 | 0.80–1.20 | 4.75–5.50 | 0.30 max | 1.10–1.75 | — | 0.80–1.20 | — |
| H14 | T20814 | 0.35–0.45 | 0.20–0.50 | 0.80–1.20 | 4.75–5.50 | 0.30 max | — | 4.00–5.25 | — | — |
| H19 | T20819 | 0.32–0.45 | 0.20–0.50 | 0.20–0.50 | 4.00–4.75 | 0.30 max | 0.30–0.55 | 3.75–4.50 | 1.75–2.20 | 4.00–4.50 |
| Tungsten hot-worked steels | | | | | | | | | | |
| H21 | T20821 | 0.26–0.36 | 0.15–0.40 | 0.15–0.50 | 3.00–3.75 | 0.30 max | — | 8.50–10.00 | 0.30–0.60 | — |
| H22 | T20822 | 0.30–0.40 | 0.15–0.40 | 0.15–0.40 | 1.75–3.75 | 0.30 max | — | 10.00–11.75 | 0.25–0.50 | — |
| H23 | T20823 | 0.25–0.45 | 0.15–0.40 | 0.15–0.60 | 11.00–12.75 | 0.30 max | — | 11.00–12.75 | 0.75–1.25 | — |
| H24 | T20824 | 0.42–0.53 | 0.15–0.40 | 0.15–0.40 | 2.50–3.50 | 0.30 max | — | 14.00–16.00 | 0.40–0.60 | — |
| H25 | T20825 | 0.22–0.32 | 0.15–0.40 | 0.15–0.40 | 3.75–4.50 | 0.30 max | — | 14.00–16.00 | 0.40–0.60 | — |
| H26 | T20826 | 0.45–0.55 ^b | 0.15–0.40 | 0.15–0.40 | 3.75–4.50 | 0.30 max | — | 17.25–19.00 | 0.75–1.25 | — |
| Molybdenum hot-worked steels | | | | | | | | | | |
| H42 | T20842 | 0.55–0.70 ^b | 0.15–0.40 | — | 3.75–4.50 | 0.30 max | 4.50–5.50 | 5.50–6.75 | 1.75–2.20 | — |
| Air-hardening, medium-alloy, cold-worked steels | | | | | | | | | | |
| A2 | T30102 | 0.95–1.05 | 1.00 max | 0.50 max | 4.75–5.50 | 0.30 max | 0.90–1.40 | — | 0.15–0.50 | — |
| A3 | T30103 | 1.20–1.30 | 0.40–0.60 | 0.50 max | 4.75–5.50 | 0.30 max | 0.90–1.40 | — | 0.80–1.40 | — |
| A4 | T30104 | 0.95–1.05 | 1.80–2.20 | 0.50 max | 0.90–2.20 | 0.30 max | 0.90–1.40 | — | — | — |
| A6 | T30106 | 0.65–0.75 | 1.80–2.50 | 0.50 max | 0.90–1.20 | 0.30 max | 0.90–1.40 | — | — | — |
| A7 | T30107 | 2.00–2.85 | 0.80 max | 0.50 max | 5.00–5.75 | 0.30 max | 0.90–1.40 | 0.50–1.50 | 3.90–5.15 | — |
| A8 | T30108 | 0.50–0.60 | 0.50 max | 0.75–1.10 | 4.75–5.50 | 0.30 max | 1.15–1.65 | 1.00–1.50 | — | — |
| A9 | T30109 | 0.45–0.55 | 0.50 max | 0.95–1.15 | 4.75–5.50 | 1.25–1.75 | 1.30–1.80 | — | 0.80–1.40 | — |
| A10 | T30110 | 1.25–1.50 ^b | 1.60–2.10 | 1.00–1.50 | — | 1.55–2.05 | 1.25–1.75 | — | — | — |
| High-carbon, high-chromium, cold-worked steels | | | | | | | | | | |
| D2 | T30402 | 1.40–1.60 | 0.60 max | 0.60 max | 11.00–13.00 | 0.30 max | 0.70–1.20 | — | 1.10 max | — |
| D3 | T30403 | 2.00–2.35 | 0.60 max | 0.60 max | 11.00–13.50 | 0.30 max | — | 1.00 max | 1.00 max | — |
| D4 | T30404 | 2.05–2.40 | 0.60 max | 0.60 max | 11.00–13.00 | 0.30 max | 0.70–1.20 | — | 1.00 max | — |
| D5 | T30405 | 1.40–1.60 | 0.60 max | 0.60 max | 11.00–13.00 | 0.30 max | 0.70–1.20 | — | 1.00 max | 2.50–3.50 |
| D7 | T30407 | 2.15–2.50 | 0.60 max | 0.60 max | 11.50–13.50 | 0.30 max | 0.70–1.20 | — | 3.80–4.40 | — |

Table 3.1-77 Composition ranges of principle types of tool steels according to AISI and UNS classifications [1.88], cont.

| AISI | UNs No. | Composition ^b (wt%) | Mn | Si | Cr | Ni | Mo | W | V | C |
|--|---------|--------------------------------|-----------|-----------|-----------|-----------|-----------|-----------|------------------------|-------------|
| Oil-hardening cold-worked steels | | | | | | | | | | |
| O1 | T31501 | 0.85–1.00 | 1.00–1.40 | 0.50 max | 0.40–0.60 | 0.30 max | — | 0.40–0.60 | 0.30 max | — |
| O2 | T31502 | 0.85–0.95 | 1.40–1.80 | 0.50 max | 0.50 max | 0.30 max | 0.30 max | — | 0.30 max | — |
| O6 | T31506 | 1.25–1.55 ^c | 0.30–1.10 | 0.55–1.50 | 0.30 max | 0.30 max | 0.20–0.30 | — | — | — |
| O7 | T31507 | 1.10–1.30 | 1.00 max | 0.60 max | 0.35–0.85 | 0.30 max | 0.30 max | 1.00–2.00 | 0.40 max | — |
| Shock-resisting steels | | | | | | | | | | |
| S1 | T41901 | 0.40–0.55 | 0.10–0.40 | 0.15–1.20 | 1.00–1.80 | 0.30 max | 0.50 max | 1.50–3.00 | 0.15–0.30 | — |
| S2 | T41902 | 0.40–0.55 | 0.30–0.50 | 0.90–1.20 | — | 0.30 max | 0.30–0.60 | — | 0.50 max | — |
| S5 | T41905 | 0.50–0.65 | 0.60–1.00 | 1.75–2.25 | 0.50 max | — | 0.20–1.35 | — | 0.35 max | — |
| S6 | T41906 | 0.40–0.50 | 1.20–1.50 | 2.00–2.50 | 1.20–1.50 | — | 0.30–0.50 | — | 0.20–0.40 | — |
| S7 | T41907 | 0.45–0.55 | 0.20–0.90 | 0.20–1.00 | 3.00–3.50 | — | 1.30–1.80 | — | 0.20–0.30 ^d | — |
| Low-alloy special-purpose tool steels | | | | | | | | | | |
| L2 | T61202 | 0.45–1.00 ^b | 0.10–0.90 | 0.50 max | 0.70–1.20 | — | 0.25 max | — | 0.10–0.30 | — |
| L6 | T61206 | 0.65–0.75 | 0.25–0.80 | 0.50 max | 0.60–1.20 | 1.25–2.00 | 0.50 max | — | 0.20–0.30 ^d | — |
| Low-carbon mold steels | | | | | | | | | | |
| P2 | T51602 | 0.10 max | 0.10–0.40 | 0.10–0.40 | 0.75–1.25 | 0.10–0.50 | 0.15–0.40 | — | — | — |
| P3 | T51603 | 0.10 max | 0.20–0.60 | 0.40 max | 0.40–0.75 | 1.00–1.50 | — | — | — | — |
| P4 | T51604 | 0.12 max | 0.20–0.60 | 0.10–0.40 | 4.00–5.25 | — | 0.40–1.00 | — | — | — |
| P5 | T51605 | 0.10 max | 0.20–0.60 | 0.40 max | 2.00–2.50 | 0.35 max | — | — | — | — |
| P6 | T51606 | 0.05–0.15 | 0.35–0.70 | 0.10–0.40 | 1.25–1.75 | 3.25–3.75 | — | — | — | — |
| P20 | T51620 | 0.28–0.40 | 0.60–1.00 | 0.20–0.80 | 1.40–2.00 | — | 0.30–0.55 | — | — | — |
| P21 | T51621 | 0.18–0.22 | 0.20–0.40 | 0.20–0.40 | 0.50 max | 3.90–4.25 | — | — | 0.15–0.25 | 1.05–1.25Al |
| Water-hardening tool steels | | | | | | | | | | |
| W1 | T72301 | 0.70–1.50 ^e | 0.10–0.40 | 0.10–0.40 | 0.15 max | 0.20 max | 0.10 max | 0.15 max | 0.10 max | — |
| W2 | T72302 | 0.85–1.50 ^e | 0.10–0.40 | 0.10–0.40 | 0.15 max | 0.20 max | 0.10 max | 0.15 max | 0.15–0.35 | — |
| W3 | T72303 | 1.05–1.15 | 0.10–0.40 | 0.10–0.40 | 0.40–0.60 | 0.20 max | 0.10 max | 0.15 max | 0.10 max | — |

^a All steels except group W contain 0.25 max Cu, 0.03 max P, and 0.03 max S; group W steels contain 0.20 max Cu, 0.025 max P, and 0.025 max S. Where specified, sulfur may be increased to 0.06 to 0.15% to improve machinability of group A, D, H, M and T steels.

^b Available in several carbon ranges.

^c Contains free graphite in the microstructure.

^d Optional.

^e Specified carbon ranges are designated by suffix numbers.

resistance, ductility and fracture toughness, and in many applications stability against softening at elevated temperatures. Characteristic mechanical properties at

room temperature as a function of hardening treatment are listed for group L and group S steels in Table 3.1-78.

Table 3.1-78 Mechanical properties of group L and group S tool steels at room temperature as a function of hardening treatment [1.88]

| Type | Condition | Tensile strength (MPa) | 0.2% yield strength (MPa) | Elongation ^a (%) | Reduction in area (%) | Hardness (HRc) |
|------|--|------------------------|---------------------------|-----------------------------|-----------------------|----------------|
| L2 | Annealed | 710 | 510 | 25 | 50 | 96 HRB |
| | Oil quenched from 855 °C and single tempered at: | | | | | |
| | 205 °C | 2000 | 1790 | 5 | 15 | 54 |
| | 315 °C | 1790 | 1655 | 10 | 30 | 52 |
| | 425 °C | 1550 | 1380 | 12 | 35 | 47 |
| | 540 °C | 1275 | 1170 | 15 | 45 | 41 |
| L6 | Annealed | 655 | 380 | 25 | 55 | 93 HRB |
| | Oil quenched from 845 °C and single tempered at: | | | | | |
| | 315 °C | 2000 | 1790 | 4 | 9 | 54 |
| | 425 °C | 1585 | 1380 | 8 | 20 | 46 |
| | 540 °C | 1345 | 1100 | 12 | 30 | 42 |
| | 650 °C | 965 | 830 | 20 | 48 | 32 |
| S1 | Annealed | 690 | 415 | 24 | 52 | 96 HRB |
| | Oil quenched from 925 °C and single tempered at: | | | | | |
| | 205 °C | 2070 | 1895 | — | — | 57.5 |
| | 315 °C | 2025 | 1860 | 4 | 12 | 54 |
| | 425 °C | 1790 | 1690 | 5 | 17 | 50.5 |
| | 540 °C | 1680 | 11525 | 9 | 23 | 47.5 |
| S5 | Annealed | 725 | 440 | 25 | 50 | 96 HRB |
| | Oil quenched from 870 °C and single tempered at: | | | | | |
| | 205 °C | 2345 | 1930 | 5 | 20 | 59 |
| | 315 °C | 2240 | 1860 | 7 | 24 | 58 |
| | 425 °C | 1895 | 1690 | 9 | 28 | 52 |
| | 540 °C | 1515 | 1380 | 10 | 30 | 48 |
| S7 | Annealed | 640 | 380 | 25 | 55 | 95 HRB |
| | Oil quenched from 940 °C and single tempered at: | | | | | |
| | 205 °C | 2170 | 1450 | 7 | 20 | 58 |
| | 315 °C | 1965 | 1585 | 9 | 25 | 55 |
| | 425 °C | 1895 | 1410 | 10 | 29 | 53 |
| | 540 °C | 1820 | 1380 | 10 | 33 | 51 |
| | 650 °C | 1240 | 1035 | 14 | 45 | 39 |

^a In 50 mm

3.1.5.7 Cast Irons

The term cast iron pertains to a large family of multi-component Fe–C–Si alloys which solidify according to the eutectic of the Fe–C system (Sect. 3.1.5.1; Fig. 3.1-99). They are treated extensively in [1.89]. Their comparatively high C and Si contents lead to solidification either according to the metastable equilibria involving Fe_3C or according to the stable equilibria involving graphite, depending, also, on the content of further alloying elements, melt treatment, and rate of cooling. Since, in addition, the metallic phases can be alloyed and their microstructures varied by annealing and transformation treatments as in other ferrous alloys, a multitude of microstructural states and associated properties result.

Classification

The C rich phases determine the basic classification of cast irons. According to the color of their fracture surfaces, Fe_3C -containing grades are called white, graphite-containing grades are called gray, and alloys which solidify in mixed states are called mottled. In addition, the shape of the graphite phase particles and the microstructure of the metallic matrix phases are taken into account since they are also characterizing the mechanical properties.

Shape of Graphite Phase Particles. Lamellar (flake) graphite (FG) is characteristic of cast irons with near-zero ductility; spheroidal (nodular) graphite (SG) is characteristic of ductile cast iron; compacted (vermicular) graphite (CG) is a transition form between flake and nodule shape; temper graphite (TG) results from a tempering treatment and consists of small clusters of branched graphite lamellae.

Microstructure of Metallic Matrix Phases. Ferritic, pearlitic, austenitic, bainitic (austempered). More details are presented in Fig. 3.1-119 and Table 3.1-79.

Iron–Carbon–Silicon Equilibria and Carbon Equivalent

Since C and Si are the alloying elements which dominate the solidification behavior and the resulting microstructures of cast irons, their phase equilibria need to be taken into account. Figure 3.1-120 shows a section through the metastable ternary Fe–C–Si diagram at 2 wt% Si which approximates the Si content of many cast irons. Compared to the binary Fe–C system, the addition of Si decreases the stability of Fe_3C and increases the stability of ferrite, as indicated by the expansion of the α -phase field. With increasing Si concentration, the C concentrations of the eutectic and the eutectoid equilibria decrease while their temperatures increase.

These relations are the basis for correlating the C and Si concentrations with the ranges of formation of steels and of the main groups of cast irons as shown in Fig. 3.1-121. The relations are expressed in terms of the carbon equivalent $\text{CE} = (\text{wt\% C}) + (1/3)(\text{wt\% Si})$. The concentration of the eutectic (upper dashed line) is given by $\text{CE}_e = 4.3$. Accordingly, alloys with $\text{CE} < 4.3$ are hypoeutectic and alloys with $\text{CE} > 4.3$ are hypereutectic. In P-containing cast irons the relation is $\text{CE} = (\text{wt\% C}) + (1/3)(\text{wt\% Si} + \text{wt\% P})$. In addition, Fig. 3.1-121 shows the limit of solubility of C in austenite (lower dashed line), which is the upper limit of the range of steels. It is given by $\text{CE}_{\gamma_{\max}} = 2.1 = (\text{wt\% C}) + (1/6)(\text{wt\% Si})$.

Grades of Cast Irons

Table 3.1-80 lists the composition ranges of typical unalloyed cast irons, indicating that they are classified mainly by the type of carbon-rich phase formed and by the basic mechanical behavior.

Table 3.1-79 Classification of cast irons according to commercial designation, microstructure and color of fracture surface [1.89]

| Commercial designation | Carbon-rich phase | Matrix ^a | Fracture | Final structure after |
|--------------------------|-------------------------------------|---------------------|-------------|--|
| Gray iron | Lamellar graphite | P | Gray | Solidification |
| Ductile iron | Spheroidal graphite | F, P, A | Silver-gray | Solidification or heat treatment |
| Compacted graphite iron | Compacted (vermicular) graphite | F, P | Gray | Solidification |
| White iron | Fe_3C | P, M | White | Solidification and heat treatment ^b |
| Mortled iron | Lamellar Gr + Fe_3C | P | Mottled | Solidification |
| Malleable iron | Temper graphite | F, P | Silver-gray | Heat treatment |
| Austempered ductile iron | Spheroidal graphite | At | Silver-gray | Heat treatment |

^a F, ferrite; P, pearlite; A, austenite; M, martensite; At, austempered (bainite)

^b White irons are not usually heat treated, except for stress relief and to continue austenite transformation

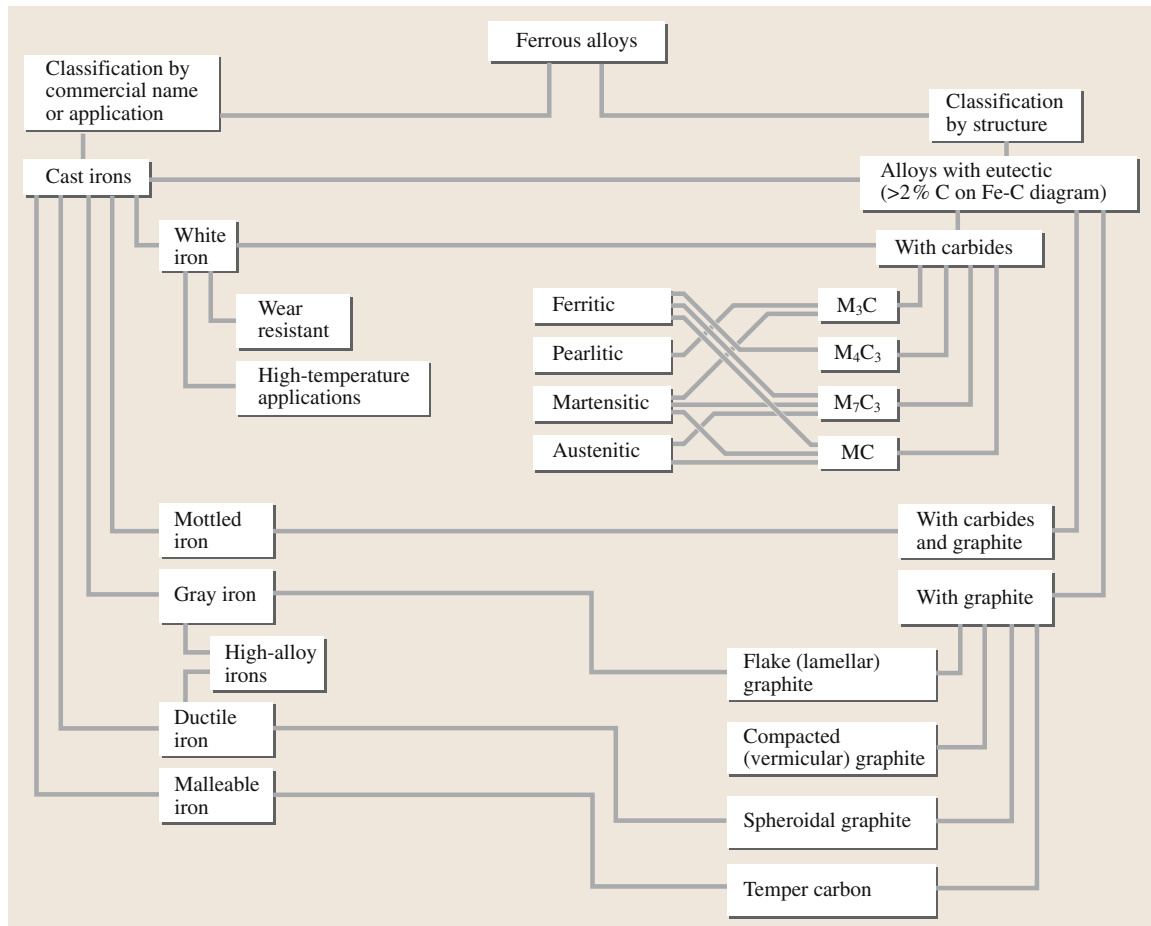


Fig. 3.1-119 Classification of cast irons [1.89]

Table 3.1-80 Range of composition, microstructural and mechanical characteristics of typical unalloyed cast irons [1.89]

| Type | Carbon phase | Concentration range (wt%) | | Mn | P | S |
|--------------------|----------------------|---------------------------|---------|----------|-----------|-----------|
| | | C | Si | | | |
| Gray | FG | 2.5–4.0 | 1.0–3.0 | 0.2–1.0 | 0.002–1.0 | 0.02–0.25 |
| Compacted graphite | CG | 2.5–4.0 | 1.0–3.0 | 0.2–1.0 | 0.01–0.1 | 0.01–0.03 |
| Ductile | SG | 3.0–4.0 | 1.8–2.8 | 0.1–1.0 | 0.01–0.1 | 0.01–0.03 |
| White | Fe ₃ C | 1.8–3.6 | 0.5–1.9 | 0.25–0.8 | 0.06–0.2 | 0.06–0.2 |
| Malleable | Fe ₃ C/TG | 2.2–2.9 | 0.9–1.9 | 0.15–1.2 | 0.02–0.2 | 0.02–0.2 |

Gray Iron. This most common type of cast iron is characterised by flake graphite and requires a high CE to ensure a sufficient graphitization potential which is also increased by Al addition. Gray irons may be moderately alloyed, e.g., by 0.2–0.6 wt% Cr, 0.2–1 wt% Mo, and 0.1–0.2 wt% V which promote the formation of alloy carbides and pearlite. Upon plastic deformation the flake form of graphite promotes early internal crack

formation and, thus, causes the low ductility of gray iron.

Ductile Iron. This cast iron is characterized by the spheroidal graphite phase (SG) in its microstructure. Spheroidal graphite is formed during solidification if the melt has been treated by the addition of a component which promotes the particular nucleation and

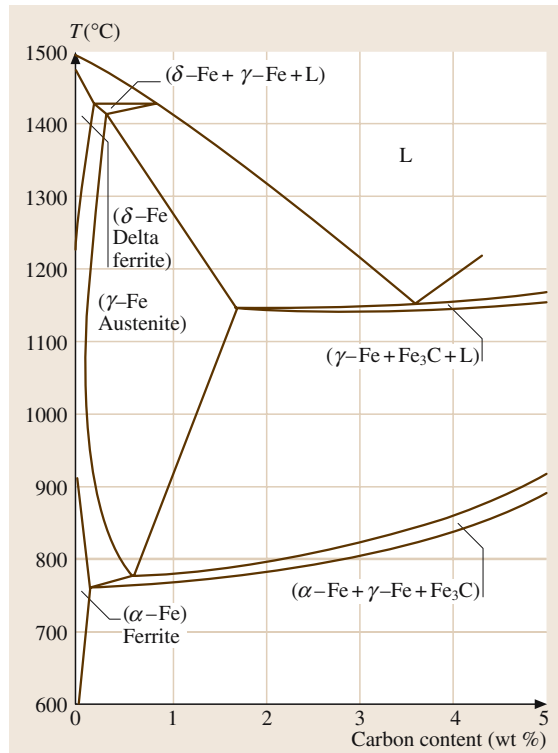


Fig. 3.1-120 Section through the metastable Fe–C–Si phase diagram at 2 wt% Si [1.89]

growth behavior of graphite in the form of nodules. The most common alloying component added to nucleate spheroidal graphite is Mg, but Ca, Ce, La, and Y have also been found to favour spheroidal graphite formation. Basically this microstructural modification leads to higher yield strength and higher ductility because the plastic deformation of the metallic matrix phases can be extended to higher strains than in gray iron before fracture sets in.

Malleable Irons. The melt treatment of malleable cast irons involves Mg, Ca, Bi, or Te additions. But malleable irons have an as-cast structure consisting of Fe₃C in a pearlitic matrix. By heat treatment in the range of 800–970 °C the cementite phase is transformed into graphite (TG). The cooling is controlled in such a way as to promote pearlite formation, ferrite formation, or a mixture of the two.

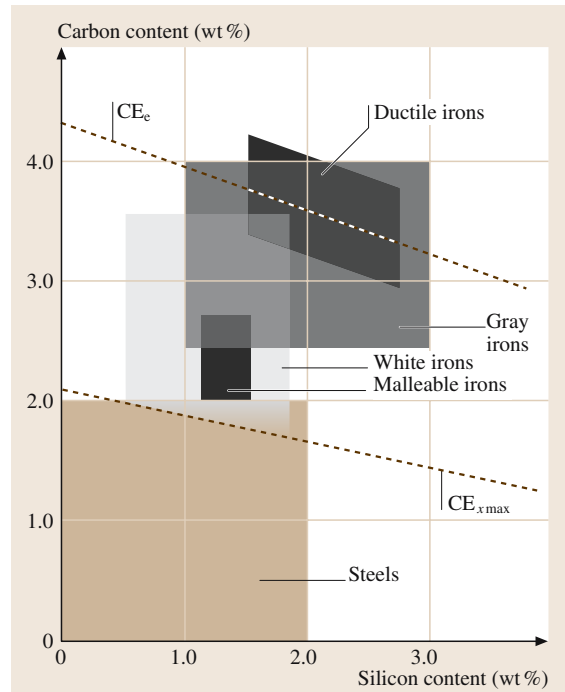


Fig. 3.1-121 Approximate C and Si concentrations for the composition ranges of steels and different grades of cast irons [1.89]

Alloy Cast Irons. Alloying elements beyond the levels mentioned above are added to cast irons almost exclusively to enhance resistance to abrasive wear or chemical corrosion, or to extend their stability for application at elevated temperature. The function of the alloying elements is essentially the same as in steels. Table 3.1-81 lists the groups of grades with typical compositions and the microstructural constituents present in the as-cast state.

Mechanical Properties of Cast Irons

Due to the multitude of as-cast structures as a function of alloy composition, melt treatment, cooling rate (as influenced by the cooling conditions and the cross section of the work piece), and subsequent heat treatment, there is a wide range of mechanical properties which can be achieved according to the requirements of the application. Table 3.1-82 gives a survey in terms of characteristic examples.

Table 3.1-81 Ranges of alloy content of typical alloy cast irons [1.89]

| Description | Composition (wt%) ^a | | | | | | | | | | Matrix structure as-cast ^c |
|---|--------------------------------|---------|------|------|-----------|-----------|--------------|---------|------|------|---------------------------------------|
| | TC ^b | Mn | P | S | Si | Ni | Cr | Mo | Cu | | |
| Abrasion-resistant white irons | | | | | | | | | | | |
| Low-carbon white iron ^d | 2.2–2.8 | 0.2–0.6 | 0.15 | 0.15 | 1.0–1.6 | 1.5 | 1.0 | 0.5 | e | CP | |
| High-carbon, low-silicon white iron | 2.8–3.6 | 0.3–2.0 | 0.30 | 0.15 | 0.3–1.0 | 2.5 | 3.0 | 1.0 | e | CP | |
| Martensitic nickel-chromium iron | 2.5–3.7 | 1.3 | 0.30 | 0.15 | 0.8 | 2.7–5.0 | 1.1–4.0 | 1.0 | – | M, A | |
| Martensitic nickel, high-chromium iron | 2.5–3.6 | 1.3 | 0.10 | 0.15 | 1.0–2.2 | 5.0–7.0 | 7.0–11.0 | 1.0 | – | M, A | |
| Martensitic chromium-molybdenum iron | 2.0–3.6 | 0.5–1.5 | 0.10 | 0.06 | 1.0 | 1.5 | 11.0–23.0 | 0.5–3.5 | 1.2 | M, A | |
| High-chromium iron | 2.3–3.0 | 0.5–1.5 | 0.10 | 0.06 | 1.0 | 1.5 | 23.0–28.0 | 1.5 | 1.2 | M | |
| Corrosion-resistant irons | | | | | | | | | | | |
| High-silicon iron ^f | 0.4–1.1 | 1.5 | 0.15 | 0.15 | 14.0–17.0 | – | 5.0 | 1.0 | 0.5 | F | |
| High-chromium iron | 1.2–4.0 | 0.3–1.5 | 0.15 | 0.15 | 0.5–3.0 | 5.0 | 12.0–35.0 | 4.0 | 3.0 | M, A | |
| Nickel-chromium gray iron ^g | 3.0 | 0.5–1.5 | 0.08 | 0.12 | 1.0–2.8 | 13.5–36.0 | 1.5–6.0 | 1.0 | 7.5 | A | |
| Nickel-chromium ductile iron ^h | 3.0 | 0.7–4.5 | 0.08 | 0.12 | 1.0–3.0 | 18.0–36.0 | 1.0–5.5 | 1.0 | – | A | |
| High-resistant gray iron | | | | | | | | | | | |
| Medium-silicon iron ⁱ | 1.6–2.5 | 0.4–0.8 | 0.30 | 0.10 | 4.0–7.0 | – | – | – | – | F | |
| Nickel-chromium iron ^g | 1.8–3.0 | 0.4–1.5 | 0.15 | 0.15 | 1.0–2.75 | 13.5–36.0 | 1.8–6.0 | 1.0 | 7.5 | A | |
| Nickel-chromium-silicon iron ^j | 1.8–2.6 | 0.4–1.0 | 0.10 | 0.10 | 5.0–6.0 | 13.0–43.0 | 1.8–5.5 | 1.0 | 10.0 | A | |
| High-aluminium iron | 1.3–2.0 | 0.4–1.0 | 0.15 | 0.15 | 1.3–6.0 | – | 20.0–25.0 Al | – | – | F | |
| Heat resistant ductile irons | | | | | | | | | | | |
| Medium-silicon ductile iron | 2.8–3.8 | 0.2–0.6 | 0.08 | 0.12 | 2.5–6.0 | 1.5 | – | 2.0 | – | F | |
| Nickel-chromium ductile iron ^h | 3.0 | 0.7–2.4 | 0.08 | 0.12 | 1.75–5.5 | 18.0–36.0 | 1.75–3.5 | 1.0 | – | A | |
| Heat-resistant white irons | | | | | | | | | | | |
| Ferritic grade | 1.0–2.5 | 0.3–1.5 | – | – | 0.5–2.5 | – | 30.0–35.0 | – | – | F | |
| Austenitic grade | 1.0–2.0 | 0.3–1.5 | – | – | 0.5–2.5 | 10.0–15.0 | 15.0–30.0 | – | – | A | |

^a Where a single value is given rather than a range, that value is a maximum limit^b Total carbon^c CP, coarse pearlite; M, martensite; A, austenite; F, ferrite^d Can be produced from a malleable-iron base composition^e Copper can replace all or part of the nickel^f Such as Durion, Durichlor 51, Superchlor^g Such as Ni-Resist austenitic iron (ASTM A 436)^h Such as Ni-Resist austenitic ductile iron (ASTM A 439)ⁱ Such as Silal^j Such as Nicrosilal**Table 3.1-82** Mechanical properties of cast irons

| Material | R _{p0.2} (N mm ⁻²) (min.) | R _m (N mm ⁻²) (min.) | A ₅ (%) (min.) | Matrix microstructure | Material number ^a | Short code ^a |
|-------------------------------------|--|--|---|--|------------------------------|----------------------------|
| Gray cast irons (FG) DIN 1691 | | 100 ^b 200 ^b 350 ^b | | Mainly ferritic Unspecified | 0.6010 0.6020 0.6035 | GG-10 GG-20 GG-35 |
| Ductile cast irons (SG) DIN 1693 | 250 ^c 360 ^c 400 ^c | 390 ^c 600 ^c 700 ^c | 15 ^d 2 ^d 2 ^d | Pearlitic-ferritic Mainly pearlitic Wide variation permissible | 0.7040 0.7060 0.7070 | GGG-40 GGG-60 GGG-70 |

Table 3.1-82 Mechanical properties of cast irons, cont.

| Material | $R_{p0.2}$ (N mm $^{-2}$) (min.) | R_m (N mm $^{-2}$) (min.) | A_5 (%) (min.) | Matrix microstructure | Material number ^a | Short code ^a |
|-------------------------------------|---|--------------------------------------|--|---|--------------------------------------|--|
| White malleable irons (TG) | 260 ^b | 350 ^d 450 ^d | 4 7 | Core: ganular pearlite Core: lamellar to granular pearlite | 0.8035 0.8045 | GTW-35-04 GTW-45-07 |
| DIN 1692 | 220 ^b | 400 ^d | 5 | Ferrite | 0.8040 | GTW-40-05 |
| Black malleable irons (TG) | 200 ^c 270 ^c | 350 ^d 450 ^d | 10 6 | Pearlite, ferrite Pearlite | 0.8135 0.8145 | GTS-35-10 GTS-45-06 |
| DIN 1692 | 430 ^c 530 ^c | 650 ^d 700 ^d | 2 2 | Hardened | 0.8165 0.8170 | GTS-65-02 GTS-70-02 |
| Austenitic alloy cast irons (FG) | | 140/220 190/240 170/240 | — 12 — | | 0.6652 0.6661 0.6680 | GGL-NiMn13-7 GGL NiCr20-3 GGL-NiSiCr30-5-5 |
| DIN 1694 | 210 210 240 210 | 390 390 390 370 | 15 ^d 7 ^d — 7 ^d | | 0.7652 0.7661 0.7680 0.7685 | GGG-NiMn13-7 GGG NiCr20-3 GGG-NiSiCr30-5-5 GGG-NiCr35-3 |

^a According to German Materials Standard

^b The values refer to a cylindrical test specimen of 30 mm in diameter corresponding to a wall thickness of 15 mm. The tensile strength values to be expected depend on the wall thickness Example: GG-20.

Wall thickness (mm) 2.5–5.5 5.5–10 10–20 20–40 40–80 80–150

R_m (N/mm 2) 230 205 180 155 130 115

^c Diameter of the test rod: 12 or 15 mm. For cast parts with a thickness < 6 mm tensile test specimens.

^d For a cylindrical test specimen of 12 mm in diameter. The mechanical properties depend on the diameter of the test specimen Example: GTW-45-07

Diameter of the test rod (mm) 9 12 15

R_m (N/mm 2) 400 450 480

$R_{p0.2}$ (N/mm 2) 230 260 280

3.1.6 Cobalt and Cobalt Alloys

Cobalt is applied as a base metal for a number of alloys, as an alloying element, and as a component of numerous inorganic compounds. Table 3.1-83 lists its major applications. Cobalt and cobalt-based materials are treated extensively in [1.90, 91].

Data on the electronic structure of Co and Co alloys may be found in [1.92]. Phase diagrams, crystal structures, and thermodynamic data of binary Co alloys may be found in [1.93].

3.1.6.1 Co-Based Alloys

Cobalt-based alloys with a carbon content in the range of 1 to 3 wt% C are widely used as wear-resistant

solid materials and weld overlays. Depending on the alloy composition and heat treatment, $M_{23}C_6$, M_6C , and MC carbides are formed. Materials with lower carbon content are mostly designed for corrosion resistance and for heat resistance, sometimes combined with wear resistance. The metals W, Mo, and Ta are essentially added for solid solution strengthening. In a few alloys Ti and Al are added. They serve to form a coherent ordered $Co_3(Ti, Al)$ phase which precipitates and leads to strengthening by age hardening. The Cr content is generally rather high to provide oxidation and hot corrosion resistance. Table 3.1-84 presents a survey of Co-based alloys.

Table 3.1-83 Applications of cobalt [1.91]

| Application | Co consumption (%) | Form | Section |
|---|--------------------|---|----------------------------|
| Co-based alloys, Co-based superalloys, steels | 24.3 | Base and alloying element | Sects. 3.1.5, 3.1.6, 3.1.7 |
| Hard facing and related materials | 6.9 | Base and alloying element | Sect. 3.1.6 |
| Soft and hard magnetic materials, and controlled thermal expansion alloys | 8.5 | Base and alloying element, oxide | Chapt. 4.3 |
| Cemented carbides, diamond tooling | 15.2 | Metal, binder | Sect. 3.1.6 |
| Catalysts | 8.0 | Metal, sulfates | — |
| Colorizer for glass, enamel, ceramics, plastics, fabrics | 11.6 | Oxides, salts | — |
| Batteries | 9.5 | Powder, hydroxide, LiCoO ₂ | — |
| Tire adhesives, soaps, driers | 11.0 | Soaps, complexes made from metal powder | — |
| Feedstuff, anodizing, electrolysis, copper winning | 5.0 | Sulphate, carbonate, hydroxide | — |

Table 3.1-84 Compositions of Co-based alloys

| Alloy tradename | UNS No. | Nominal composition (wt%) | | | | | | | | | |
|---|---------|---------------------------|------|------|-----------|------|---------|-----------|-----------|-----------|------------------|
| | | Co | Cr | W | Mo | C | Fe | Ni | Si | Mn | Others |
| Cast, P/M and weld overlay wear-resistant alloys | | | | | | | | | | | |
| Stellite 1 | R30001 | bal | 30 | 13 | 0.5 | 2.5 | 3 | 1.5 | 1.3 | 0.5 | — |
| Stellite 3 (P/M) | R30103 | bal | 30.5 | 12.5 | — | 2.4 | 5 (max) | 3.5 (max) | 2 (max) | 2 (max) | 1 B (max) |
| Stellite 4 | R30404 | bal | 30 | 14 | 1 (max) | 0.57 | 3 (max) | 3 (max) | 2 (max) | 1 (max) | — |
| Stellite 6 | R30006 | bal | 29 | 4.5 | 1.5 (max) | 1.2 | 3 (max) | 3 (max) | 1.5 (max) | 1 (max) | — |
| Stellite 6 (P/M) | R30106 | bal | 28.5 | 4.5 | 1.5 (max) | 1 | 5 (max) | 3 (max) | 2 (max) | 2 (max) | 1 B (max) |
| Stellite 12 | R30012 | bal | 30 | 8.3 | — | 1.4 | 3 (min) | 1.5 | 0.7 | 2.5 | — |
| Stellite 21 | R30021 | bal | 27 | — | 5.5 | 0.25 | 3 (max) | 2.75 | 1 (max) | 1 (max) | 0.007 B (max) |
| Stellite 98M2 (P/M) | — | bal | 30 | 18.5 | 0.8 (max) | 2 | 5 (max) | 3.5 | 1 (max) | 1 (max) | 4.2 V, 1 B (max) |
| Stellite 703 | — | bal | 32 | — | 12 | 2.4 | 3 (max) | 3 (max) | 1.5 (max) | 1.5 (max) | — |
| Stellite 706 | — | bal | 29 | — | 5 | 1.2 | 3 (max) | 3 (max) | 1.5 (max) | 1.5 (max) | — |
| Stellite 712 | — | bal | 29 | — | 8.5 | 2 | 3 (max) | 3 (max) | 1.5 (max) | 1.5 (max) | — |
| Stellite 720 | — | bal | 33 | — | 18 | 2.5 | 3 (max) | 3 (max) | 1.5 (max) | 1.5 (max) | 0.3 B |
| Stellite F | R30002 | bal | 25 | 12.3 | 1 (max) | 1.75 | 3 (max) | 22 | 2 (max) | 1 (max) | — |
| Stellite Star J (P/M) | R30102 | bal | 32.5 | 17.5 | — | 2.5 | 3 (max) | 2.5 (max) | 2 (max) | 2 (max) | 1 B (max) |
| Stellite Star J | R31001 | bal | 32.5 | 17.5 | — | 2.5 | 3 (max) | 2.5 (max) | 2 (max) | 2 (max) | — |
| Tantung G | — | bal | 29.5 | 16.5 | — | 3 | 3.5 | 7 (max) | — | 2 (max) | 4.5 Ta/Nb |
| Tantung 144 | — | bal | 27.5 | 18.5 | — | 3 | 3.5 | 7 (max) | — | — | 5.5 Ta/Nb |
| Laves-phase wear-resistant alloys | | | | | | | | | | | |
| Tribaloy T-400 | R30400 | bal | 9 | — | 29 | — | — | — | 2.5 | — | — |
| Tribaloy T-800 | — | bal | 18 | — | 29 | — | — | — | 3.5 | — | — |
| Wrought wear-resistant alloys | | | | | | | | | | | |
| Stellite 6B | R30016 | bal | 30 | 4 | 1.5 (max) | 1 | 3 (max) | 2.5 | 0.7 | 1.4 | — |
| Stellite 6K | — | bal | 30 | 4.5 | 1.5 (max) | 1.6 | 3 (max) | 3 (max) | 2 (max) | 2 (max) | — |

Table 3.1-84 Compositions of Co-based alloys, cont.

| Alloy tradename | UNS No. | Nominal composition (wt%) | | | | C | Fe | Ni | Si | Mn | Others |
|--|---------|---------------------------|----|-----|-----|------------|---------|------|-----------|-----------|-------------------------------|
| Wrought heat-resistant alloys (see Table 3.1-86 for cast alloy compositions) | | | | | | | | | | | |
| Haynes 25 (L605) | R30605 | bal | 20 | 15 | — | 0.1 | 3 (max) | 10 | 0.4 (max) | 1.5 | — |
| Haynes 188 | R30188 | bal | 22 | 14 | — | 0.1 | 3 (max) | 22 | 0.35 | 1.25 | 0.03 La |
| Inconel 783 | R30783 | bal | 3 | — | — | 0.03 (max) | 25.5 | 28 | 0.5 (max) | 0.5 (max) | 5.5 Al, 3 Nb, 3.4 Ti (max) |
| UMCo-50 | — | bal | 28 | — | — | 0.02 (max) | 21 | — | 0.75 | 0.75 | — |
| S-816 | R30816 | 40 (min) | 20 | 4 | 4 | 0.37 | 5 (max) | 20 | 1 (max) | 1.5 | 4 Nb |
| Corrosion-resistant alloys | | | | | | | | | | | |
| Ultimet (1233) | R31233 | bal | 26 | 2 | 5 | 0.06 | 3 | 9 | 0.3 | 0.8 | 0.08 N |
| MP 159 | R30159 | bal | 19 | — | 7 | — | 9 | 25.5 | — | — | 3 Ti, 0.6 Nb, 0.2 Al |
| MP35N | R30035 | 35 | 20 | — | 10 | — | — | 35 | — | — | — |
| Duratherm 600 | R30600 | 41.5 | 12 | 3.9 | 4 | 0.05 (max) | 8.7 | bal | 0.4 | 0.75 | 2 Ti, 0.7 Al, 0.05 Be |
| Elgiloy | R30003 | 40 | 20 | — | 7 | 0.15 (max) | bal | 15.5 | — | 2 | 1 Be (max) |
| Havar | R30004 | 42.5 | 20 | 2.8 | 2.4 | 0.2 | bal | 13 | — | 1.6 | 0.06 Be (max) |

P/M: powder metallurgy; bal: balance

3.1.6.2 Co-Based Hard-Facing Alloys and Related Materials

The behavior of Co-based wear resistant alloys is based on a coarse dispersion of hard carbide phases embedded in a tough Co-rich metallic matrix. The volume fraction of the hard carbide phase is comparatively high: e.g., at 2.4 wt% C the carbide content is 30 wt%. The carbide phases are M_7C_3 (Cr_7C_3 type) and M_6C (W_6C type). Table 3.1-85 lists characteristic properties of Co-based hard facing alloys the compositions of which are listed Table 3.1-83.

3.1.6.3 Co-Based Heat-Resistant Alloys, Superalloys

Both wrought and cast Co-based heat resistant alloys, listed in Tables 3.1-84 and 3.1-86, respectively, are also referred to as Co superalloys. They are based on the face-centered cubic high temperature phase of Co which is stabilized between room temperature and the solidus temperature by alloying with ≥ 10 wt% Ni. They are solid-solution strengthened by alloying with W, Ta, and Mo. Furthermore, they are dispersion strengthened by carbides.

Table 3.1-85 Properties of selected Co-based hard-facing alloys

| Property | Stellite 21 | Stellite 6 | Stellite 12 | Stellite 1 | Tribaloy T-800 |
|---|---|---|---|---|---|
| Density, $g\text{ cm}^{-3}$ (lb in^{-3}) | 8.3 (0.30) | 8.3 (0.30) | 8.6 (0.31) | 8.6 (0.31) | 8.6 (0.31) |
| Ultimate compressive strength, MPa (ksi) | 1295 (188) | 1515 (220) | 1765 (256) | 1930 (280) | 1780 (258) |
| Ultimate tensile strength, MPa (ksi) | 710 (103) | 834 (121) | 827 (120) | 620 (90) | 690 (100) |
| Elongation, % | 8 | 1.2 | 1 | 1 | <1 |
| Coefficient of thermal expansion, $^{\circ}\text{C}^{-1}$ ($^{\circ}\text{F}^{-1}$) | 14.8×10^{-6} (8.2×10^{-6}) | 15.7×10^{-6} (8.7×10^{-6}) | 14×10^{-6} (7.8×10^{-6}) | 13.1×10^{-6} (7.3×10^{-6}) | 12.3×10^{-6} (6.8×10^{-6}) |
| Hot hardness, HV, at: | | | | | |
| 445 °C (800 °F) | 150 | 300 | 345 | 510 | 659 |
| 540 °C (1000 °F) | 145 | 275 | 325 | 465 | 622 |
| 650 °C (1200 °F) | 135 | 260 | 285 | 390 | 490 |
| 760 °C (1400 °F) | 115 | 185 | 245 | 230 | 308 |

Table 3.1-85 Properties of selected Co-based hard-facing alloys, cont.

| Property | Stellite 21 | Stellite 6 | Stellite 12 | Stellite 1 | Tribaloy T-800 |
|--|-------------|-------------|-------------|------------|----------------|
| Unlubricated sliding wear ^a , mm ³ (in ³ × 10 ⁻³) at: | | | | | |
| 670 N (150 lbf) | 5.2 (0.32) | 2.6 (0.16) | 2.4 (0.15) | 0.6 (0.04) | 1.7 (0.11) |
| 1330 N (300 lbf) | 14.5 (0.90) | 18.8 (1.17) | 18.4 (1.14) | 0.8 (0.05) | 2.1 (0.13) |
| Abrasive wear ^b , mm ³ (in ³ × 10 ⁻³) | | | | | |
| OAW | — | 29 (1.80) | 12 (0.75) | 8 (0.50) | — |
| GTAW | 86 (5.33) | 64 (3.97) | 57 (3.53) | 52 (3.22) | 24 (1.49) |
| Unnotched Charpy impact strength, J (ft × lbf) | 37 (27) | 23 (17) | 5 (4) | 5 (4) | 1.4 (1) |
| Corrosion resistance ^c : | | | | | |
| 65% nitric acid at 65 °C (150 °F) | U | U | U | U | S |
| 5% sulfuric acid at 65 °C (150 °F) | E | E | E | E | — |
| 50% phosphoric acid at 400 °C (750 °F) | E | E | E | E | E |

^a Wear measured from tests conducted on Dow-Corning LFW-1 against 4620 steel ring at 80 rev/min for 2000 rev varying the applied load

^b Wear measured from dry sand rubber wheel abrasion tests. Tested for 2000 rev at a load of 135 N (30 lbf) using a 230 mm (9 in) diam rubber wheel and American Foundrymen's Society test sand. OAW, oxyacetylene welding; GTAW, gas-tungsten arc welding

^c E, less than 0.05 mm/yr (2 mils/year); S, 0.5 to less than 1.25 mm/yr (over 20 to less than 50 mils/year); U, more than 1.25 mm/year (50 mils/year)

Table 3.1-86 Nominal compositions of cast cobalt-based heat-resistant alloys

| Alloy designation | Nominal composition (wt%) | | | | | | | | | | | | |
|--------------------|---------------------------|-----|------|------|-----|-----|-----|-------|------|-----|-----|-----|----------------------------|
| | C | Ni | Cr | Co | Mo | Fe | Al | B | Ti | Ta | W | Zr | Other |
| AlResist 13 | 0.45 | — | 21 | 62 | — | — | 3.4 | — | — | 2 | 11 | — | 0.1 Y |
| AlResist 213 | 0.20 | 0.5 | 20 | 64 | — | 0.5 | 3.5 | — | — | 6.5 | 4.5 | 0.1 | 0.1 Y |
| AlResist 215 | 0.35 | 0.5 | 19 | 63 | — | 0.5 | 4.3 | — | — | 7.5 | 4.5 | 0.1 | 0.1 Y |
| FSX-414 | 0.25 | 10 | 29 | 52.5 | — | 1 | — | 0.010 | — | — | 7.5 | — | — |
| Haynes 25 (L-605) | 0.1 | 10 | 20 | 54 | — | 1 | — | — | — | — | 15 | — | — |
| J-1650 | 0.20 | 27 | 19 | 36 | — | — | — | 0.02 | 3.8 | 2 | 12 | — | — |
| MAR-M 302 | 0.85 | — | 21.5 | 58 | — | 0.5 | — | 0.005 | — | 9 | 10 | 0.2 | — |
| MAR-M 322 | 1.0 | — | 21.5 | 60.5 | — | 0.5 | — | — | 0.75 | 4.5 | 9 | 2 | — |
| MAR-M 509 | 0.6 | 10 | 23.5 | 54.5 | — | — | — | — | 0.2 | 3.5 | 7.5 | 0.5 | — |
| NASA (Co-W-Re) | 0.40 | — | 3 | 67.5 | — | — | — | — | 1 | — | 25 | 1 | 2Re |
| S-816 | 0.4 | 20 | 20 | 42 | — | 4 | — | — | — | — | 4 | — | 4 Mo, 4 Nb, 1.2 Mn, 0.4 Si |
| V-36 | 0.27 | 20 | 25 | 42 | — | 3 | — | — | — | — | 2 | — | 4 Mo, 2 Nb, 1 Mn, 0.4 Si |
| WI-52 | 0.45 | — | 21 | 63.5 | — | 2 | — | — | — | — | 11 | — | 2 Nb + Ta |
| Stellite 23 | 0.40 | 2 | 24 | 65.5 | — | 1 | — | — | — | — | 5 | — | 0.3 Mn, 0.6 Si |
| Stellite 27 | 0.40 | 32 | 25 | 35 | 5.5 | 1 | — | — | — | — | — | — | 0.3 Mn, 0.6 Si |
| Stellite 30 | 0.45 | 15 | 26 | 50.5 | 6 | 1 | — | — | — | — | — | — | 0.6 Mn, 0.6 Si |
| Stellite 31 (X-40) | 0.50 | 10 | 22 | 57.5 | — | 1.5 | — | — | — | — | 7.5 | — | 0.5 Mn, 0.5 Si |

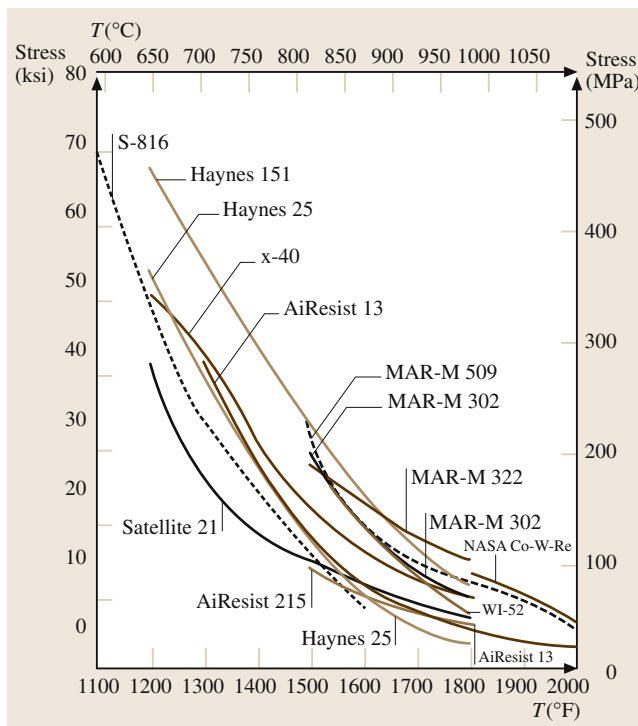


Fig. 3.1-122 Stress–rupture curves for 1000-h life of cast Co-based superalloys

Differences of the high-temperature mechanical behavior of these materials are shown in terms of stress–rupture curves in Fig. 3.1-122.

Investment-cast Co alloys are generally used for parts of complex shape such as first- and second-stage vanes and nozzles in gas turbine engines.

3.1.6.4 Co-Based Corrosion-Resistant Alloys

Compared to the heat resistant Co-based alloys, the corrosion-resistant alloys have low C concentrations and

Table 3.1-87 Co-based corrosion resistant alloys

| Alloy tradename | UNS No. | Nominal Composition (wt%) | | | | | | | | | |
|--------------------|---------|---------------------------|----|-----|-----|------------|-----|------|-----|------|-----------------------|
| | | Co | Cr | W | Mo | C | Fe | Ni | Si | Mn | Others |
| Ultimet (1233) | R31233 | bal | 26 | 2 | 5 | 0.06 | 3 | 9 | 0.3 | 0.8 | 0.08 N |
| MP 159 | R30159 | bal | 19 | — | 7 | — | 9 | 25.5 | — | — | 3 Ti, 0.6 Nb, 0.2 Al |
| MP35N | R30035 | 35 | 20 | — | 10 | — | — | 35 | — | — | — |
| Duratherm 600 | R30600 | 41.5 | 12 | 3.9 | 4 | 0.05 (max) | 8.7 | bal | 0.4 | 0.75 | 2 Ti, 0.7 Al, 0.05 Be |
| Elgiloy | R30003 | 40 | 20 | — | 7 | 0.15 (max) | bal | 15.5 | — | 2 | 1 Be (max) |
| Havar | R30004 | 42.5 | 20 | 2.8 | 2.4 | 0.2 | bal | 13 | — | 1.6 | 0.06 Be (max) |

bal: balance

are alloyed with higher Mo contents rather than with W since Mo contributes to their corrosion and oxidation resistance. Table 3.1-87 shows the compositions of various Co-based corrosion-resistant alloys.

The multiphase (MP) alloys MP35N and MP159 combine ultra-high strength, high ductility, and corrosion resistance, including resistance to stress-corrosion cracking in the work-hardened state. The prime strengthening is based on the deformation-induced martensitic transformation of the fcc matrix phase into the hcp phase which has been termed a multiphase reaction. The multiphase microstructure provides an increased density of barriers for slip dislocations. Subsequent annealing leads to a stabilization of the two-phase structure by solute partitioning. Figures 3.1-123 and 3.1-124 show the increase in strength and decrease in ductility for alloys MP35N and Duratherm 600 with work hardening and aging.

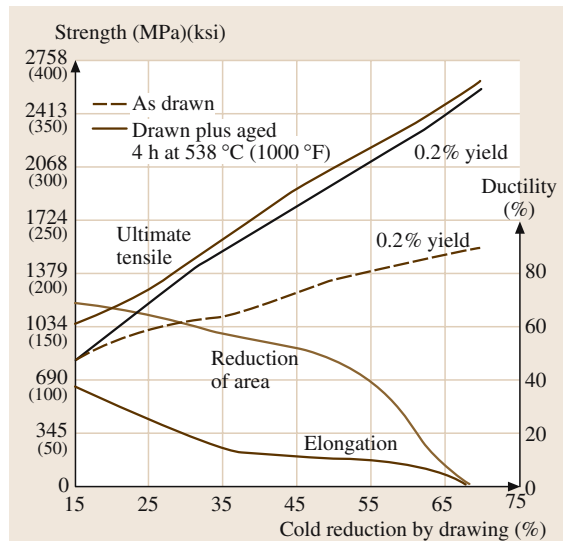


Fig. 3.1-123 Tensile properties of cold-drawn and aged MP35N

3.1.6.5 Co-Based Surgical Implant Alloys

Co-based surgical implant alloys (see Table 3.1-88 for compositions) are used to fabricate a variety of implant parts and devices. These are predominantly implants for hip and knee joint replacements, implants that fix bone fractures such as bone screws, staples, plates, support structures for heart valves, and dental implants. The mechanical properties (shown in Table 3.1-89) depend sensitively on the thermal and thermomechanical treatments of the materials.

3.1.6.6 Cemented Carbides

The term cemented carbides, also called hardmetals, refers to powder-composite materials consisting of carbide particles bonded with metals or alloys. Extensive treatments are given in [1.94, 95]. The most common cemented carbide is WC bonded with Co. Cobalt is used as a binder since it wets the angular WC particles particularly well. Nickel is added to increase corrosion and oxidation resistance of the Co binder phase. The metals Ta, Nb, and Ti may be added to form a (W, Ta, Nb, or Ti)C solid solution carbide phase which is an additional microstructural constituent in the form of rounded particles in the so-called complex grade, multigrade, or steel-cutting grade cemented carbides. Table 3.1-90 lists representative materials.

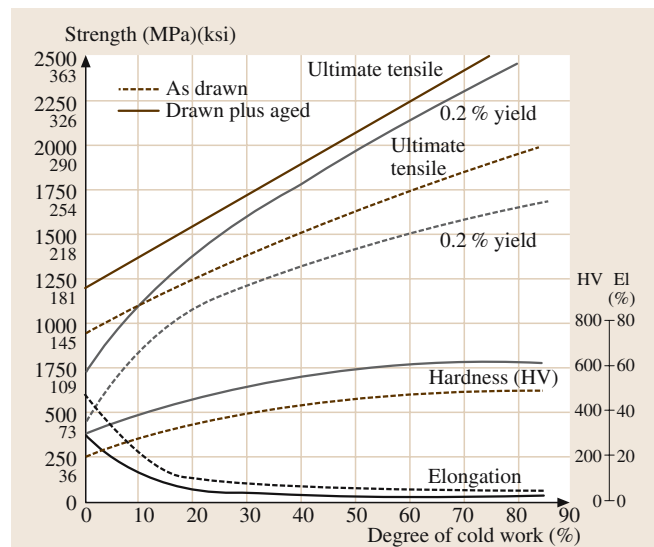


Fig. 3.1-124 Tensile properties of cold-drawn and aged Duratherm 600

Table 3.1-88 Compositions of Co-based surgical implant alloys

| ASTM specification | Composition (wt%) | | | | | | | | |
|--------------------|-------------------|-----------|-----------|----------|---------|-------------|------------|------------|--------------|
| | Co | Cr | Ni | Mo | Fe | C | Mn | Si | Other |
| F75 | bal | 27.0–30.0 | 1.0 | 5.0–7.0 | 0.75 | 0.35 | 1.0 | 1.0 | — |
| F90 | bal | 19.0–21.0 | 9.0–11.0 | — | 3 (max) | 0.05–0.15 | 1.0–2.0 | 0.4 | 14.0–16.0 W |
| F562 | bal | 19.0–21.0 | 33.0–37.0 | 9.0–10.5 | 1 (max) | 0.025 (max) | 0.15 (max) | 0.15 (max) | 1.0 Ti (max) |

bal: balance

Table 3.1-89 Mechanical properties of Co-based surgical implant alloys

| ASTM specification | Alloy system | Condition | Yield strength (MPa) | (ksi) | Tensile strength (MPa) | (ksi) | Elongation (%) | Elastic modulus (GPa) | (10 ⁶ ksi) |
|--------------------|--------------|--------------------------------|----------------------|-------|------------------------|---------|----------------|-----------------------|-----------------------|
| F75 | Co–Cr–Mo | Cast | 450 | 65 | 655 | 95 | 8 | 248 | 36 |
| F799 | Co–Cr–Mo | Thermomechanically processed | 827 | 120 | 1172 | 170 | 12 | — | — |
| F90 | Co–Cr–W–Ni | Wrought | 379 | 55 | 896 | 130 | — | 242 | 35 |
| F562 | Co–Ni–Cr–Mo | Annealed, cold-worked and aged | 241–448 | 35–65 | 793–1000 | 115–145 | 50 | 228 | 33 |
| | | | 1586 | 230 | 1793 | 260 | 8 | — | — |

Table 3.1-90 Compositions, microstructures and properties of representative Co-bonded cemented carbides

| Nominal composition | Grain size | Hardness (HR _A) | Density (g cm ⁻³) | Transverse strength (oz in ⁻²) | Compressive strength (MPa) | Modulus of elasticit (ksi) | Modulus (GPa) | Relative abrasion resistance ^a | Coefficient of thermal expansion (μm/mK) at 200 °C (390 °F) | Thermal conductivity (W/mK) at 1000 °C (1830 °F) | | | | |
|---------------------|------------|-----------------------------|-------------------------------|--|----------------------------|----------------------------|---------------|---|---|--|-----|-----|-----|-----|
| 97WC-3Co | Medium | 92.5–93.2 | 15.3 | 8.85 | 1590 | 230 | 5860 | 850 | 641 | 93 | 100 | 4.0 | — | 121 |
| 94WC-6Co | Fine | 92.5–93.1 | 15.0 | 8.67 | 1790 | 260 | 5930 | 860 | 614 | 89 | 100 | 4.3 | 5.9 | — |
| | Medium | 91.7–92.2 | 15.0 | 8.67 | 2000 | 290 | 5450 | 790 | 648 | 94 | 58 | 4.3 | 5.4 | 100 |
| | Coarse | 90.5–91.5 | 15.0 | 8.67 | 2210 | 320 | 5170 | 750 | 641 | 93 | 25 | 4.3 | 5.6 | 121 |
| 90WC-10Co | Fine | 90.7–91.3 | 14.6 | 8.44 | 3100 | 450 | 5170 | 750 | 620 | 90 | 22 | — | — | — |
| | Coarse | 87.4–88.2 | 14.5 | 8.38 | 2760 | 400 | 4000 | 580 | 552 | 80 | 7 | 5.2 | — | 112 |
| 84WC-16Co | Fine | 89 | 13.9 | 8.04 | 3380 | 490 | 4070 | 590 | 524 | 76 | 5 | — | — | — |
| | Coarse | 86.0–87.5 | 13.9 | 8.04 | 2900 | 420 | 3860 | 560 | 524 | 76 | 5 | 5.8 | 7.0 | 88 |
| 75WC-22Co | Medium | 83–85 | 13.0 | 7.52 | 2550 | 370 | 3100 | 450 | 483 | 70 | 3 | 6.3 | — | 71 |
| 71WC-12.5TiC | Medium | 92.1–92.8 | 12.0 | 6.94 | 1380 | 200 | 5790 | 840 | 565 | 82 | 11 | 5.2 | 6.5 | 35 |
| -12TaC-4.5Co | | | | | | | | | | | | | | |
| 72WC-8TiC | Medium | 90.7–91.5 | 12.6 | 7.29 | 1720 | 250 | 5170 | 750 | 558 | 81 | 13 | 5.8 | 6.8 | 50 |
| -11.5TaC-8.5Co | | | | | | | | | | | | | | |

^a Based on a value of 100 for the most abrasion-resistant material

3.1.7 Nickel and Nickel Alloys

Nickel is the base element for a variety of Ni alloys. But it is mainly used as a major alloying element in Fe- and Cu-based alloys, especially in stainless steels. A further major use is Ni plating. A survey of its applications is given in Table 3.1-91. It also indicates where Ni bearing alloys are covered in this handbook. Nickel materials are treated extensively in [1.96] and the special group of heat resistant alloys and superalloys in [1.97]. Alloys of Ni–Fe show ferromagnetism in a wide range of compositions. This, in combination with other intrinsic magnetic properties, is the basis for the Ni–Fe based alloys with soft magnetic and controlled thermal expansion properties, respectively, covered in Chapt. 3.4.3. NiTi shape memory alloys are treated in Sect. 3.1.3.4.

Data on the electronic structure of Ni and Ni alloys may be found in [1.98, 99], phase diagrams, crystal structures and thermodynamic data of binary Ni alloys are contained in [1.100].

3.1.7.1 Commercially Pure and Low-Alloy Nickels

Commercially pure and low-alloy nickels are used as corrosion-resistant materials with very good formability. Some Ni-based alloys are precipitation hardened; Ni–2 wt% Be (Duranickel 301) shows pronounced precipitation hardening. Commonly used, commercially pure and low-alloy nickels are listed in Table 3.1-92. Room-temperature mechanical properties of these and

Table 3.1-91 Uses of nickel

| Use | Fraction of total Ni consumption (%) | Section |
|----------------------------|--------------------------------------|---------------|
| Stainless steels | 63 | Sect. 3.1.5.4 |
| Nickel-based alloys | 12 | Sect. 3.1.7 |
| Nickel plating | 10 | Sect. 3.1.7 |
| Nickel in alloy steels | 9 | Sect. 3.1.5 |
| Nickel in foundry products | 3.5 | Sect. 3.1.5.7 |
| Nickel in copper alloys | 1.5 | Sect. 3.1.8 |
| Others | 1 | — |

Table 3.1-92 Nominal compositions of corrosion-resistant nickels and nickel-base alloys

| Alloy | UNS No. | Composition (wt%) | | | | | | | | Other |
|----------------------------------|---------|-------------------|-------|-------|-----------|------|------------|-------|------------------------------|-------|
| | | Ni | Cu | Fe | Mn | C | Si | S | | |
| Commercially pure nickels | | | | | | | | | | |
| Nickel 200 | N02200 | 99.0 (min) | 0.25 | 0.40 | 0.35 | 0.15 | 0.35 | 0.01 | — | |
| Nickel 201 | N02201 | 99.0 (min) | 0.25 | 0.40 | 0.35 | 0.02 | 0.35 | 0.01 | — | |
| Nickel 205 | N02205 | 99.0 (min(b)) | 0.15 | 0.20 | 0.35 | 0.15 | 0.15 | 0.008 | 0.01–0.08 Mg, 0.01–0.05 Ti | |
| Nickel 212 | — | 97.0 (min) | 0.20 | 0.25 | 1.5–2.5 | 0.10 | 0.20 | — | 0.20 Mg | |
| Nickel 220 | N02220 | 99.0 (min) | 0.10 | 0.10 | 0.20 | 0.15 | 0.01–0.05 | 0.008 | 0.01–0.08 Mg | |
| Nickel 225 | N02225 | 99.0 (min) | 0.10 | 0.10 | 0.20 | 0.15 | 0.15–0.25 | 0.008 | 0.01–0.08 Mg, 0.01–0.05 Ti | |
| Nickel 230 | N02230 | 99.0 (min) | 0.10 | 0.10 | 0.15 | 0.15 | 0.01–0.035 | 0.008 | 0.04–0.08 Mg, 0.005 Ti | |
| Nickel 270 | N02270 | 99.97 (min) | 0.001 | 0.005 | 0.02 | 0.02 | 0.001 | 0.001 | 0.001 Co, 0.001 Cr, 0.001 Ti | |
| Low-alloy nickels | | | | | | | | | | |
| Nickel 211 | N02211 | 93.7 (min) | 0.25 | 0.75 | 4.25–5.25 | 0.20 | 0.15 | 0.015 | — | |
| Duranickel 301 | N03301 | 93.00 (min) | 0.25 | 0.60 | 0.50 | 0.30 | 1.00 | 0.01 | 4.00–4.75 Al, 0.25–1.00 Ti | |
| Alloy 360 | N03360 | bal | — | — | — | — | — | — | 1.85–2.05 Be, 0.4–0.6 Ti | |

bal: balance

Table 3.1–93 Mechanical properties of nickel-based alloys at room temperature

| Alloy | Ultimate tensile strength (MPa) | | Yield strength (0.2% offset) (MPa) | | Elongation in 50 mm (2 in) (%) | Elastic modulus (tension) (GPa) | | Hardness |
|--|------------------------------------|-------|--|------|--------------------------------------|---------------------------------------|------|------------|
| | (ksi) | (ksi) | (ksi) | (%) | | (10 ⁶ psi) | | |
| Nickel 200 | 462 | 67 | 148 | 21.5 | 47 | 204 | 29.6 | 109 HB |
| Nickel 201 | 403 | 58.5 | 103 | 15 | 50 | 207 | 30 | 129 HB |
| Nickel 205 | 345 | 50 | 90 | 13 | 45 | — | — | — |
| Nickel 211 | 530 | 77 | 240 | 35 | 40 | — | — | — |
| Nickel 212 | 483 | 70 | — | — | — | — | — | — |
| Nickel 222 | 380 | 55 | — | — | — | — | — | — |
| Nickel 270 | 345 | 50 | 110 | 16 | 50 | — | — | 30 HRB |
| Duranickel 301 (precipitation hardened) | 1170 | 170 | 862 | 125 | 25 | 207 | 30 | 30–40 HRC |
| Alloy 400 | 550 | 80 | 240 | 35 | 40 | 180 | 26 | 110–150 HB |
| Alloy 401 | 440 | 64 | 134 | 19.5 | 51 | — | — | — |
| Alloy R-405 | 550 | 80 | 240 | 35 | 40 | 180 | 26 | 110–140 HB |
| Alloy K-500 (precipitation hardened) | 1100 | 160 | 790 | 115 | 20 | 180 | 26 | 300 HB |
| Alloy 600 | 655 | 95 | 310 | 45 | 40 | 207 | 30 | 75 HRB |
| Alloy 601 | 620 | 90 | 275 | 40 | 45 | 207 | 30 | 65–80 HRB |
| Alloy 617 (solution annealed) | 755 | 110 | 350 | 51 | 58 | 211 | 30.6 | 173 HB |
| Alloy 625 | 930 | 135 | 517 | 75 | 42.5 | 207 | 30 | 190 HB |
| Alloy 690 | 725 | 105 | 348 | 50.5 | 41 | 211 | 30.6 | 88 HRB |
| Alloy 718 (precipitation hardened) | 1240 | 180 | 1036 | 150 | 12 | 211 | 30.6 | 36 HRC |
| Alloy C-22 | 785 | 114 | 372 | 54 | 62 | — | — | 209 HB |
| Alloy C-276 | 790 | 115 | 355 | 52 | 61 | 205 | 29.8 | 90 HRB |
| Alloy G3 | 690 | 100 | 320 | 47 | 50 | 199 | 28.9 | 79 HRB |
| Alloy 800 | 600 | 87 | 295 | 43 | 44 | 193 | 28 | 138 HB |
| Alloy 825 | 690 | 100 | 310 | 45 | 45 | 206 | 29.8 | — |
| Alloy 925 ^a | 1210 | 176 | 815 | 118 | 24 | — | — | 36.5 HRC |

Properties are for annealed sheet unless otherwise indicated.

^a Annealed at 980 °C (1800 °F) for 30 min, air cooled, and aged at 760 °C (1400 °F) for 8 h, furnace at a rate of 55 °C (1150 °F) for 8 h, air cooled

some further Ni alloys which are dealt with in the next section are listed in Table 3.1–93.

3.1.7.2 Highly Alloyed Ni-Based Materials

Nickel forms extensive solid solutions with many alloying elements: complete solid solutions with Fe and Cu, and limited solid solutions with ≤ 35 wt% Cr, ≤ 20 wt% Mo, ≤ 5 –10 wt% Al, Ti, and Mn; and V. Nickel and its alloys are providing favorable properties for uses in corrosive environments and at elevated temperatures.

The extensive solubility of several of the alloying elements is the basis of solid solution hardening which scales roughly with the atomic-size difference of the solute and is, therefore, pronounced with W, Mo, Nb, Ta, and Al. Based on the face-centered cubic structure, Ni-based solid solutions show high ductility, fracture toughness, and formability. The basic corrosion resistance of Ni is strongly increased by alloying additions of Cr, Mo, and W.

On the basis of these possibilities of materials design, a number of corrosion-resistant materials have been developed according to the criteria shown in

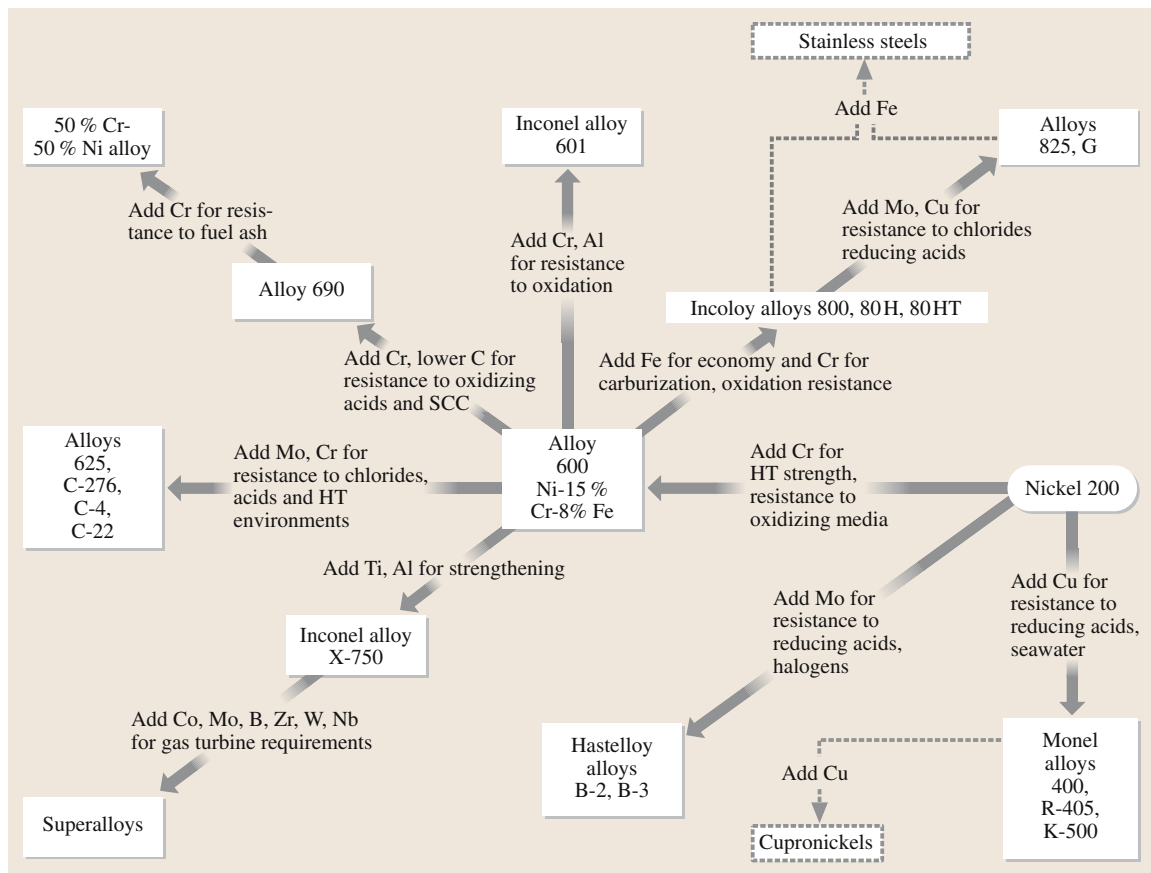


Fig. 3.1-125 Effects of alloying additions on the corrosion resistance of nickel alloys. (HT denotes high temperature)

Fig. 3.1-125. The materials listed in Table 3.1-94 are the main representatives of high-Ni alloys.

Mechanical properties are listed in Table 3.1-93. Characteristic creep data are shown in Fig. 3.1-126.

Table 3.1-94 Nominal compositions of highly-alloyed Ni

| Designation | UNS Nr | Ni | Cr | Fe (wt%) | Co | Mo |
|--|--------|---------------|------------|------------|-----------|-----------|
| Nickel-molybdenum alloys | | | | | | |
| Hastelloy B | N10001 | bal | 1.0 | 6.0 | 2.5 | 26.0–33.0 |
| Hastelloy B-2 | N10665 | bal | 1.0 | 2.0 | 1.0 | 26.0–30.0 |
| Hastelloy B-3 | N10675 | 65.0 | 1.0–3.0 | 1.0–3.0 | 3.0 | 27.0–32.0 |
| Nicrofer 6629 (B-4) | N10629 | bal | 0.5–1.5 | 1.0–6.0 | 2.5 | 26.0–30.0 |
| Nickel-chromium-iron alloys | | | | | | |
| Inconel 600 | N06600 | 72.0 (min(b)) | 14.0–17.0 | 6.0–10.0 | — | — |
| Inconel 601 | N06601 | 58.0–63.0 | 21.0–25.0 | bal | — | — |
| Inconel 690 | N06690 | 58.0 (min) | 27.0–31.0 | 7.0–11.0 | — | — |
| Haynes 214 | N07214 | bal | 15.0–17.0 | 2.0–4.0 | 2.0 | 0.5 |
| Iron-nickel-chromium alloys | | | | | | |
| Incoloy 800 | N08800 | 30.0–35.0 | 19.0–23.0 | 39.5 (min) | — | — |
| Incoloy 800HT | N08811 | 30.0–35.0 | 19.0–23.0 | 39.5 (min) | — | — |
| Incoloy 801 | N08801 | 30.0–34.0 | 19.0–22.0 | bal | — | — |
| Incoloy 803 | S35045 | 32.0–37.0 | 25.0–29.0 | 37.0 (min) | — | — |
| Nickel-chromium-molybdenum alloys | | | | | | |
| Hastelloy C | N10002 | bal | 14.5–16.50 | 4.0–7.0 | 2.5 | 15.0–17.0 |
| Hastelloy C-4 | N06455 | bal | 14.0–18.0 | 3.0 | 2.0 | 14.0–17.0 |
| Hastelloy C-22 | N06022 | bal | 20.0–22.5 | 2.0–6.0 | 2.5 | 12.5–14.5 |
| Hastelloy C-276 | N10276 | bal | 14.5–16.50 | 4.0–7.0 | 2.5 | 15.0–17.0 |
| Hastelloy C-2000 | N06200 | bal | 22.0–24.0 | 3.0 | 2.0 | 15.0–17.0 |
| Nicrofer 5923 (Alloy 59) | N06059 | bal | 22.0–24.0 | 1.5 | 0.3 | 15.0–16.5 |
| Inconel 617 | N06617 | 44.5 (min) | 20.0–24.0 | 3.0 | 10.0–15.0 | 8.0–10.0 |
| Inconel 625 | N06625 | 58.0 (min) | 20.0–23.0 | 5.0 | 1.0 | 8.0–10.0 |
| Inconel 686 | N06686 | bal | 19.0–23.0 | 5.0 | — | 15.0–17.0 |
| Hastelloy S | N06635 | bal | 14.5–17.0 | 3.0 | 2.0 | 14.0–16.5 |
| Allcorr | N06110 | bal | 27.0–33.0 | — | 12.0 | 8.0–12.0 |
| Nickel-chromium-iron-molybdenum alloys | | | | | | |
| Incoloy 825 | N08825 | 38.0–46.0 | 19.5–23.5 | bal | — | 2.5–3.5 |
| Hastelloy G | N06007 | bal | 21.0–23.5 | 18.0–21.0 | 2.5 | 5.5–7.5 |
| Hastelloy G-2 | N06975 | 47.0–52.0 | 23.0–26.0 | bal | — | 5.0–7.0 |
| Hastelloy G-3 | N06985 | bal | 21.0–23.5 | 18.0–21.0 | 5.0 | 6.0–8.0 |
| Hastelloy G-30 | N06030 | bal | 28.0–31.5 | 13.0–17.0 | 5.0 | 4.0–6.0 |
| Hastelloy G-50 | N06950 | 50.0 (min) | 19.0–21.0 | 15.0–20.0 | 2.5 | 8.0–10.0 |
| Hastelloy D-205 | — | 65.0 | 20.0 | 6.0 | — | 2.5 |
| Hastelloy N | N10003 | bal | 6.0–8.0 | 5.0 | 0.2 | 15.0–18.0 |
| Hastelloy X | N06002 | bal | 20.5–23.0 | 17.0–20.0 | 0.5–2.5 | 8.0–10.0 |
| Nicrofer 3033 (Alloy 33) | R20033 | 30.0–33.0 | 31.0–35.0 | bal | — | 0.5–2.0 |
| Nickel-chromium-tungsten, nickel-iron-chromium, and nickel-cobalt-chromium-silicon alloys | | | | | | |
| Haynes 230 | N06230 | bal | 20.0–24.0 | 3.0 | — | 1.0–3.0 |
| Haynes HR-120 | N08120 | 35.0–39.0 | 23.0–27.0 | bal | 3.0 | 2.5 |
| Haynes HR-160 | N12160 | bal | 26.0–30.0 | 3.5 | 27.0–33.0 | 1.0 |
| Precipitation-hardening alloys | | | | | | |
| Alloy 625 Plus | N07716 | 57.0–63.0 | 19.0–22.0 | bal | — | 7.0–9.50 |
| Inconel 718 | N07718 | 50.0–55.0 | 17.0–21.0 | bal | 1.0 | 2.80–3.30 |
| Inconel 725 | N07725 | 55.0–59.0 | 19.0–22.5 | bal | — | 7.0–9.50 |
| Inconel 925 | N09925 | 38.0–46.0 | 19.5–23.5 | 22.0 (min) | — | 2.50–3.50 |

(a) Single values are maximum unless otherwise indicated; (b) Nickel plus cobalt content; bal: balance

Table 3.1-94 Nominal compositions of highly alloyed Ni alloys, cont.

| | W | Nb | Ti | Al | C (wt%) | Mn | Si | B | Others |
|--|-----------|-----------|-----------|-----------|------------|-----------|-------|---------|--------------------------|
| Nickel-molybdenum alloys | | | | | | | | | |
| — | — | — | — | — | 0.12 | 1.0 | 1.0 | — | 0.60 V |
| — | — | — | — | — | 0.02 | 1.0 | 0.10 | — | — |
| 3.0 | 0.20 | 0.20 | 0.50 | 0.01 | 3.0 | 0.10 | — | — | 0.20 Ta |
| — | — | — | 0.1–0.5 | 0.01 | 1.5 | 0.05 | — | — | — |
| Nickel-chromium-iron alloys | | | | | | | | | |
| — | — | — | — | 0.15 | 1.0 | 0.5 | — | 0.5 Cu | — |
| — | — | — | 1.0–1.7 | 0.10 | 1.0 | 0.50 | — | 1.0 Cu | — |
| — | — | — | — | 0.05 | 0.50 | 0.50 | — | 0.50 Cu | — |
| 0.5 | — | 0.5 | 4.0–5.0 | 0.05 | 0.5 | 0.2 | 0.006 | — | 0.05 Zr, 0.002–0.040 Y |
| Iron-nickel-chromium alloys | | | | | | | | | |
| — | — | 0.15–0.60 | 0.15–0.60 | 0.10 | 1.5 | 1.0 | — | — | — |
| — | — | 0.15–0.60 | 0.15–0.60 | 0.06–0.10 | 1.5 | 1.0 | — | — | 0.895–1.20 Al + Ti |
| — | — | 0.75–1.5 | — | 0.10 | 1.5 | 1.0 | — | — | 0.5 Cu |
| — | — | 0.15–0.60 | 0.15–0.60 | 0.06–0.10 | 1.5 | 1.0 | — | — | 0.75 Cu |
| Nickel-chromium-molybdenum alloys | | | | | | | | | |
| 3.0–4.5 | — | — | — | — | 0.08 | 1.0 | 1.0 | — | 0.35 V |
| — | — | 0.70 | — | 0.015 | 1.0 | 0.08 | — | — | — |
| 2.5–3.5 | — | — | — | — | 0.015 | 0.5 | 0.08 | — | 0.35 V |
| 3.0–4.5 | — | — | — | — | 0.02 | 1.0 | 0.08 | — | 0.35 V |
| — | — | — | 0.5 | 0.010 | 0.5 | 0.08 | — | — | 1.3–1.9 Cu |
| — | — | — | 0.1–0.4 | 0.010 | 0.5 | 0.10 | — | — | — |
| — | — | 0.6 | 0.8–1.5 | 0.05–0.15 | 1.0 | 1.0 | 0.006 | — | 0.5 Cu |
| — | 3.15–4.15 | 0.40 | 0.40 | 0.10 | 0.50 | 0.50 | — | — | — |
| 3.0–4.4 | — | 0.02–0.25 | — | 0.010 | 0.75 | 0.08 | — | — | — |
| 1.0 | — | — | 0.1–0.50 | 0.02 | 0.3–1.0 | 0.20–0.75 | 0.015 | — | 0.35 Cu, 0.01–0.10 La |
| 4.0 | 2.0 | 1.50 | 1.50 | 0.15 | — | — | — | — | — |
| Nickel-chromium-iron-molybdenum alloys | | | | | | | | | |
| — | — | 0.6–1.2 | 0.2 | 0.05 | 1.0 | 0.5 | — | — | — |
| 1.0 | 1.75–2.5 | — | — | 0.05 | 1.0–2.0 | 1.0 | — | — | — |
| — | — | 0.70–1.5 | — | 0.03 | 1.0 | 1.0 | — | — | 0.7–1.20 Cu |
| 1.5 | — | — | — | 0.015 | 1.0 | 1.0 | — | — | 1.5–2.5 Cu, 0.50 Nb + Ta |
| 1.5–4.0 | 0.3–1.5 | — | — | 0.03 | 1.5 | 0.8 | — | — | 1.0–2.4 Cu |
| 1.0 | 0.5 | — | — | 0.015 | 1.0 | 1.0 | — | — | 0.5 Cu |
| — | — | — | — | 0.03 | — | 5.0 | — | — | 2.0 Cu |
| 0.5 | — | — | — | 0.010 | 1.0 | 1.0 | 0.010 | — | 0.50 V, 0.35 Cu |
| 0.20–1.0 | — | — | — | 0.05–0.15 | 1.0 | 1.0 | — | — | — |
| — | — | — | — | 0.015 | 2.0 | 0.5 | — | — | 0.3–1.2 Cu |
| Nickel-chromium-tungsten, nickel-iron-chromium, and nickel-cobalt-chromium-silicon alloys | | | | | | | | | |
| 13.0–15.0 | — | — | 0.20–0.50 | 0.05–0.15 | 0.3–1.0 | 0.25–0.75 | 0.015 | — | 0.005–0.05 La |
| 2.5 | 0.4–0.9 | 0.20 | 0.40 | 0.02–0.1 | 1.5 | 1.0 | 0.010 | — | 0.5 Cu |
| 1.0 | — | 0.20–0.80 | — | 0.15 | 1.5 | 2.4–3.0 | — | — | — |
| Precipitation-hardening alloys | | | | | | | | | |
| — | 2.75–4.0 | 1.0–1.60 | 0.35 | 0.03 | 0.20 | 0.20 | — | — | — |
| — | 4.75–5.50 | 0.35 | 0.20–0.80 | 0.08 | 0.35 | 0.35 | 0.06 | — | 0.3 Cu |
| — | 2.75–4.0 | 1.0–1.70 | 0.35 | 0.03 | 0.35 | 0.50 | — | — | — |
| — | 0.50 | 1.9–2.40 | 0.10–0.50 | 0.03 | 1.0 | 0.50 | — | — | 1.5–3.0 Cu |

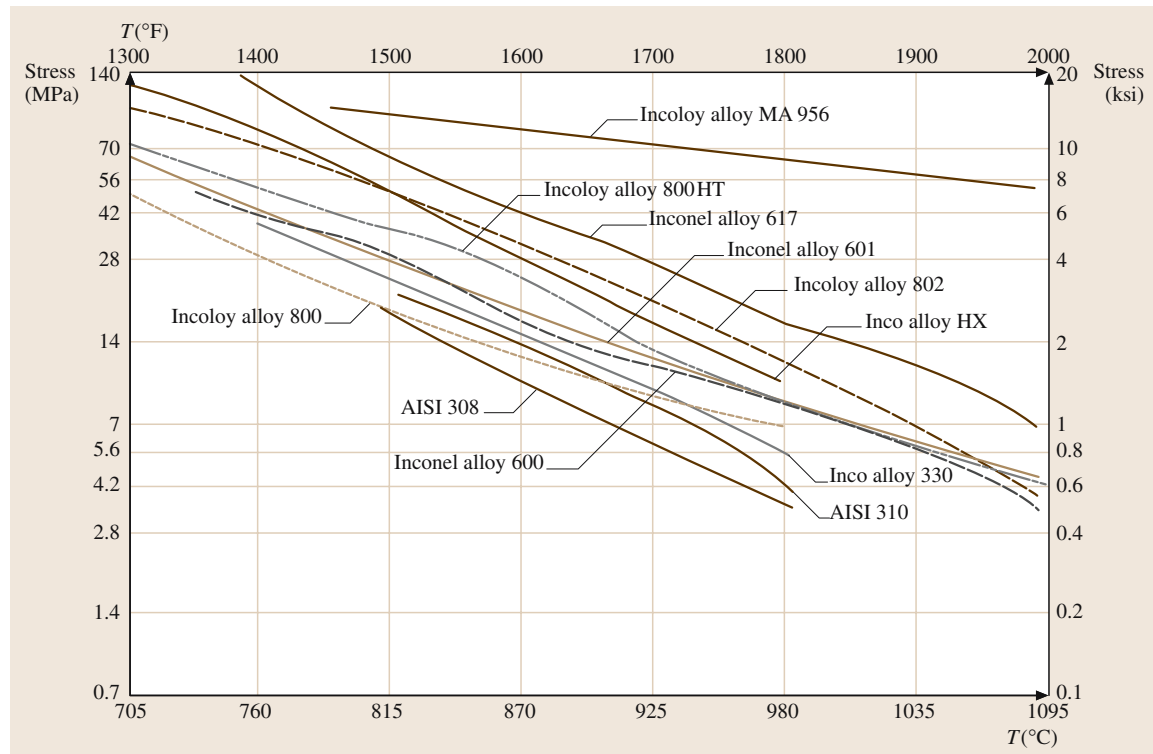


Fig. 3.1-126 Rupture strength (10 000 h) of Ni-based alloys and stainless steels

3.1.7.3 Ni-Based Superalloys

The term superalloy is used for a group of nickel-, iron–nickel-, and cobalt-based high-temperature materials for applications at temperatures $\geq 540^\circ\text{C}$. It is useful to compare the main subgroups in terms of the strengthening mechanisms applied and stress–rupture characteristics achieved, as shown in Fig. 3.1-127. In this section iron–nickel- and nickel-based superalloys are covered whereas cobalt-based superalloys are dealt with in Sect. 3.1.6.3. Nickel-based superalloys are among the most complex metallic materials with numerous alloying elements serving particular functions, as briefly outlined here.

All Ni and Fe–Ni-based superalloys are alloyed with Al. This leads to a two-phase matrix consisting of the γ' ($\text{Ni}, \text{Fe}, \text{Al}$) solid solution phase (fcc, A1 structure) and the intermetallic $\gamma''-\text{Ni}_3\text{Al}$ phase ($\text{L}1_2$ structure), which has a superlattice structure relative to the fcc structure of the γ' phase. The binary Al–Ni phase diagram in Fig. 3.1-128 shows clearly that the γ' phase is stable up to the melting range. The matrix phase γ is solid solution strengthened by alloying additions of Cr, Mo, W, and

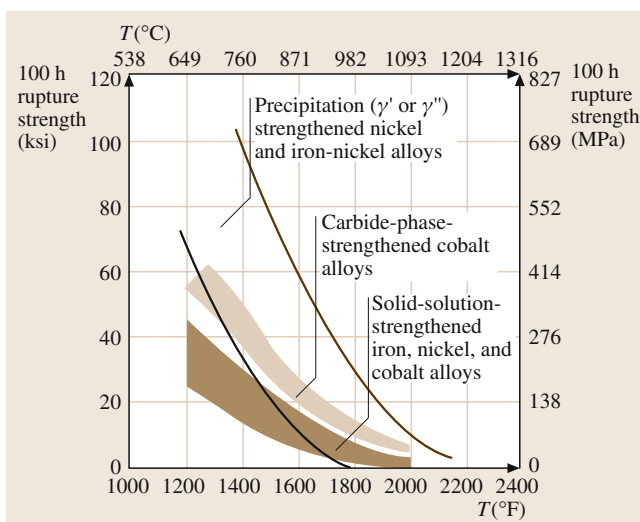


Fig. 3.1-127 Stress–rupture characteristics of wrought superalloys

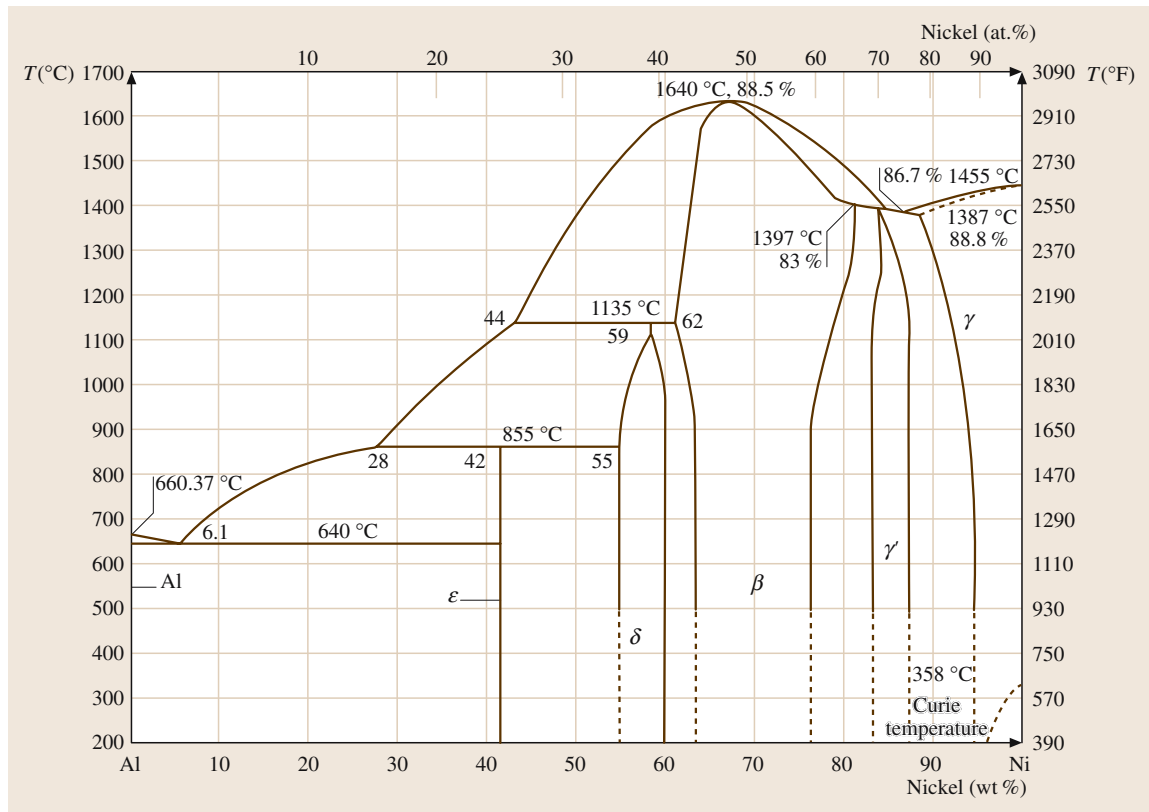


Fig. 3.1-128 Al–Ni phase diagram indicating the high thermal stability of the γ' phase

Ta. The γ' - Ni_3Al phase is precipitated coherently from the γ phase by appropriate heat treatment in amounts ranging from 20 to 45 vol% γ' in wrought superalloys and about 60 vol% γ' in cast superalloys. The hardening effect of γ' in these alloys is due to its high yield stress which increases with increasing temperature to a maximum at about 650 °C, as shown in Fig. 3.1-129. The anomalous temperature dependence is due to the fact that the plastic deformation is associated with the formation and motion of partial dislocations, giving rise to local disordering of the ordered structure. Figure 3.1-129 shows also that alloying additions such as Cr, Ti, and Nb increase the yield stress and tend to shift its maximum to higher temperatures. This is because several alloying elements substitute Ni (Fe, Co, Cr) or Al (Ti, Nb) in the Ni_3Al structure and raise its critical resolved shear stress. Another major alloying addition is carbon in combination with carbide forming alloy components such as Ti, Cr, Mo, W, and Nb (which are partly added to achieve hardening of the metallic phases as well, as described above). The carbides (MC , M_7C_3 , M_{23}C_6 , and M_6C) are

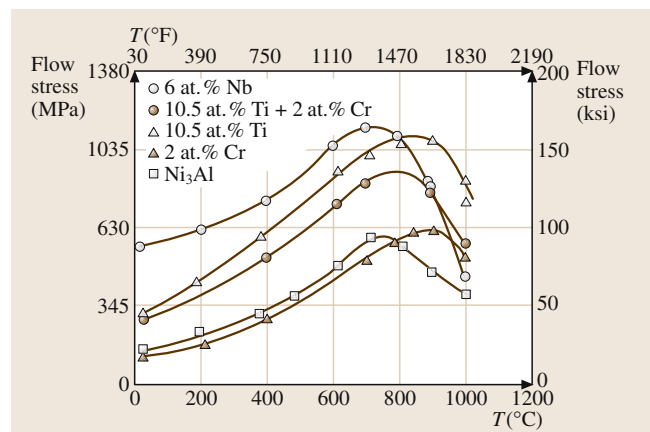


Fig. 3.1-129 Temperature dependence of the flow stress of the γ' - Ni_3Al phase and effects of Nb, Ti, and Cr alloying additions

precipitated or formed by secondary reactions as intra-grain or grain boundary precipitates further stabilizing the microstructure against creep deformation.

Taking these factors of influence into account the wrought superalloys listed in Table 3.1-95 and the cast superalloys listed in Table 3.1-96 have been developed.

Table 3.1-95 Nominal compositions of Fe–Ni-based and Ni-based wrought superalloys

| Alloy | UNS No. | Composition (wt%) | Cr | Ni | Co | Mo | W | Nb | Ti | Al | Fe | C | Other |
|---------------------------------------|---------|-------------------|------|----------|------|------|------|-----|----------|------|----------|-----------|--------------------------------|
| Solid-solution alloys | | | | | | | | | | | | | |
| Iron-nickel-based | | | | | | | | | | | | | |
| Alloy N-155 (Multimet) | R30155 | 21.0 | 20.0 | 20.0 | — | 3.00 | 2.5 | 1.0 | — | — | 32.2 | 0.15 | 0.15 N, 0.2 La, 0.02 Zr |
| Haynes 556 | R30556 | 22.0 | 21.0 | 20.0 | — | 3.0 | 2.5 | 0.1 | — | 0.3 | 29.0 | 0.10 | 0.50 Ta, 0.02 La, 0.002 Zr |
| 19-9 DL | S63198 | 19.0 | 9.0 | — | — | 1.25 | 1.25 | 0.4 | 0.3 | — | 66.8 | 0.30 | 1.10 Mn, 0.60 Si |
| Incoloy 800 | N08800 | 21.0 | 32.5 | — | — | — | — | — | 0.38 | 0.38 | 45.7 | 0.05 | — |
| Incoloy 800H | N08810 | 21.0 | 33.0 | — | — | — | — | — | — | — | 45.8 | 0.08 | — |
| Incoloy 800HT | N08811 | 21.0 | 32.5 | — | — | — | — | — | 0.4 | 0.4 | 46.0 | 0.08 | 0.8 Mn, 0.5 Si, 0.4 Cu |
| Incoloy 801 | N08801 | 20.5 | 32.0 | — | — | — | — | — | 1.13 | — | 46.3 | 0.05 | — |
| Incoloy 802 | — | 21.0 | 32.5 | — | — | — | — | — | 0.75 | 0.58 | 44.8 | 0.35 | — |
| Nickel-based | | | | | | | | | | | | | |
| Haynes 214 | — | 16.0 | 76.5 | — | — | — | — | — | — | 4.5 | 3.0 | 0.03 | — |
| Haynes 230 | N06230 | 22.0 | 55.0 | 5.0(max) | 2.0 | 14.0 | — | — | — | 0.35 | 3.0(max) | 0.10 | 0.015(max) B, 0.02 La |
| Inconel 600 | N06600 | 15.5 | 76.0 | — | — | — | — | — | — | — | 8.0 | 0.08 | 0.25 Cu |
| Inconel 601 | N06601 | 23.0 | 60.5 | — | — | — | — | — | — | 1.35 | 14.1 | 0.05 | 0.5 Cu |
| Inconel 617 | N06617 | 22.0 | 55.0 | 12.5 | — | 9.0 | — | — | — | 1.0 | — | 0.07 | — |
| Inconel 625 | N06625 | 21.5 | 61.0 | — | — | 9.0 | — | 3.6 | 0.2 | 0.2 | 2.5 | 0.05 | — |
| RA 333 | N06333 | 25.0 | 45.0 | 3.0 | — | 3.0 | 3.0 | — | — | — | 18.0 | 0.05 | — |
| Hastelloy B | N01001 | 1.0(max) | 63.0 | 2.5(max) | 28.0 | — | — | — | — | — | 5.0 | 0.05(max) | 0.03 V |
| Hastelloy N | N01003 | 7.0 | 72.0 | — | — | 16.0 | — | — | 0.5(max) | — | 5.0(max) | 0.06 | — |
| Hastelloy S | N06635 | 15.5 | 67.0 | — | — | 15.5 | — | — | — | 0.2 | 1.0 | 0.02(max) | 0.02 La |
| Hastelloy W | N10004 | 5.0 | 61.0 | 2.5(max) | 24.5 | — | — | — | — | — | 5.5 | 0.12(max) | 0.6 V |
| Hastelloy X | N06002 | 22.0 | 49.0 | 1.5(max) | — | 9.0 | 0.6 | — | — | 2.0 | 15.8 | 0.15 | — |
| Hastelloy C-276 | N10276 | 15.5 | 59.0 | — | — | 16.0 | 3.7 | — | — | — | 5.0 | 0.02(max) | — |
| Haynes HR-120 | N08120 | 25.0 | 37.0 | 3.0 | — | 2.5 | 2.5 | 0.7 | — | 0.1 | 33.0 | 0.05 | 0.7 Mn, 0.6 Si, 0.2 N, 0.004 B |
| Haynes HR-160 | N12160 | 28.0 | 37.0 | 29.0 | — | — | — | — | — | — | 2.0 | 0.05 | 2.75 Si, 0.5 Mn |
| Nimonic 75 | N06075 | 19.5 | 75.0 | — | — | — | — | — | 0.4 | 0.15 | 2.5 | 0.12 | 0.25(max) Cu |
| Nimonic 86 | — | 25.0 | 65.0 | — | — | 10.0 | — | — | — | — | — | 0.05 | 0.03 Ce, 0.015 Mg |
| Precipitation-hardening alloys | | | | | | | | | | | | | |
| Iron-nickel-based | | | | | | | | | | | | | |
| A-286 | S66286 | 15.0 | 26.0 | — | — | 1.25 | — | — | 2.0 | 0.2 | 55.2 | 0.04 | 0.005 B, 0.3 V |
| Discaloy | S66220 | 14.0 | 26.0 | — | — | 3.0 | — | — | 1.7 | 0.25 | 55.0 | 0.06 | — |
| Incoloy 903 | N19903 | 0.1(max) | 38.0 | 15.0 | — | 0.1 | — | 3.0 | 1.4 | 0.7 | 41.0 | 0.04 | — |
| Pyromet CTX-1 | — | 0.1(max) | 37.7 | 16.0 | — | 0.1 | — | 3.0 | 1.7 | 1.0 | 39.0 | 0.03 | — |
| Incoloy 907 | N19907 | — | 38.4 | 13.0 | — | — | — | 4.7 | 1.5 | 0.03 | 42.0 | 0.01 | 0.15 Si |
| Incoloy 909 | N19909 | — | 38.0 | 13.0 | — | — | — | 4.7 | 1.5 | 0.03 | 42.0 | 0.01 | 0.4 Si |
| Incoloy 925 | N09925 | 20.5 | 44.0 | — | — | 2.8 | — | — | 2.1 | 0.2 | 29 | 0.01 | 1.8 Cu |
| V-57 | — | 14.8 | 27.0 | — | — | 1.25 | — | — | 3.0 | 0.25 | 48.6 | 0.08(max) | 0.01 B, 0.5(max) V |
| W-545 | S66545 | 13.5 | 26.0 | — | — | 1.5 | — | — | 2.85 | 0.2 | 55.8 | 0.08(max) | 0.05 B |

Table 3.1-95 Nominal compositions of Fe–Ni-based and Ni-based wrought superalloys, cont.

| Alloy | UNS No. | Composition (wt%) | | | | Mo | W | Nb | Ti | Al | Fe | C | Other |
|---------------------|---------|-------------------|------|-----------|------|-----|-----|------|------------|-----------|------------|------------------------------|-------|
| Nickel-based | | | | | | | | | | | | | |
| Astroloy | N13017 | 15.0 | 56.5 | 15.0 | 5.25 | — | — | 3.5 | 4.4 | <0.3 | 0.06 | 0.03 B, 0.06 Zr | |
| Custom Age 625 PLUS | N07716 | 21.0 | 61.0 | — | 8.0 | — | 3.4 | 1.3 | 0.2 | 5.0 | 0.01 | — | |
| Haynes 242 | — | 8.0 | 62.5 | 2.5 (max) | 25.0 | — | — | — | 0.5 (max) | 2.0 (max) | 0.10 (max) | 0.006 (max) B | |
| Haynes 263 | N07263 | 20.0 | 52.0 | — | 6.0 | — | — | 2.4 | 0.6 | 0.7 | 0.06 | 0.6 Mn, 0.4 Si, 0.2 Cu | |
| Haynes R-41 | N07041 | 19.0 | 52.0 | 11.0 | 10.0 | — | — | 3.1 | 1.5 | 5.0 | 0.09 | 0.5 Si, 0.1 Mn, 0.006 B | |
| Inconel 100 | N13100 | 10.0 | 60.0 | 15.0 | 3.0 | — | — | 4.7 | 5.5 | <0.6 | 0.15 | 1.0 V, 0.06 Zr, 0.015 B | |
| Inconel 102 | N06102 | 15.0 | 67.0 | — | 2.9 | 3.0 | 2.9 | 0.5 | 0.5 | 7.0 | 0.06 | 0.005 B, 0.02 Mg, 0.03 Zr | |
| Incoloy 901 | N09901 | 12.5 | 42.5 | — | 6.0 | — | — | 2.7 | — | 36.2 | 0.10 (max) | — | |
| Inconel 702 | N07702 | 15.5 | 79.5 | — | — | — | — | 0.6 | 3.2 | 1.0 | 0.05 | 0.5 Mn, 0.2 Cu, 0.4 Si | |
| Inconel 706 | N09706 | 16.0 | 41.5 | — | — | — | — | 1.75 | 0.2 | 37.5 | 0.03 | 2.9 (Nb + Ta), 0.15 (max) Cu | |
| Inconel 718 | N07718 | 19.0 | 52.5 | — | 3.0 | — | 5.1 | 0.9 | 0.5 | 18.5 | 0.08 (max) | 0.15 (max) Cu | |
| Inconel 721 | N07721 | 16.0 | 71.0 | — | — | — | — | 3.0 | — | 6.5 | 0.04 | 2.2 Mn, 0.1 Cu | |
| Inconel 722 | N07722 | 15.5 | 75.0 | — | — | — | — | 2.4 | 0.7 | 7.0 | 0.04 | 0.5 Mn, 0.2 Cu, 0.4 Si | |
| Inconel 725 | N07725 | 21.0 | 57.0 | — | 8.0 | — | 3.5 | 1.5 | 0.35 (max) | 9.0 | 0.03 (max) | — | |
| Inconel 751 | N07751 | 15.5 | 72.5 | — | — | — | 1.0 | 2.3 | 1.2 | 7.0 | 0.05 | 0.25 (max) Cu | |
| Inconel X-750 | N07750 | 15.5 | 73.0 | — | — | — | 1.0 | 2.5 | 0.7 | 7.0 | 0.04 | 0.25 (max) Cu | |
| M-252 | N07252 | 19.0 | 56.5 | 10.0 | 10.0 | — | — | 2.6 | 1.0 | <0.75 | 0.15 | 0.005 B | |
| Nimonic 80A | N07080 | 19.5 | 73.0 | 1.0 | — | — | — | 2.25 | 1.4 | 1.5 | 0.05 | 0.10 (max) Cu | |
| Nimonic 90 | N07090 | 19.5 | 55.5 | 18.0 | — | — | — | 2.4 | 1.4 | 1.5 | 0.06 | — | |
| Nimonic 95 | — | 19.5 | 53.5 | 18.0 | — | — | — | 2.9 | 2.0 | 5.0 (max) | 0.15 (max) | +B, +Zr | |
| Nimonic 100 | — | 11.0 | 56.0 | 20.0 | 5.0 | — | — | 1.5 | 5.0 | 2.0 (max) | 0.30 (max) | +B, +Zr | |
| Nimonic 105 | — | 15.0 | 54.0 | 20.0 | 5.0 | — | — | 1.2 | 4.7 | — | 0.08 | 0.005 B | |
| Nimonic 115 | — | 15.0 | 55.0 | 15.0 | 4.0 | — | — | 4.0 | 5.0 | 1.0 | 0.20 | 0.04 Zr | |
| C-263 | N07263 | 20.0 | 51.0 | 20.0 | 5.9 | — | — | 2.1 | 0.45 | 0.7 (max) | 0.06 | — | |
| Pyromet 860 | — | 13.0 | 44.0 | 4.0 | 6.0 | — | — | 3.0 | 1.0 | 28.9 | 0.05 | 0.01 B | |
| Pyromet 31 | N07031 | 22.7 | 55.5 | — | 2.0 | — | 1.1 | 2.5 | 1.5 | 14.5 | 0.04 | 0.005 B | |
| Refractaloy 26 | — | 18.0 | 38.0 | 20.0 | 3.2 | — | — | 2.6 | 0.2 | 16.0 | 0.03 | 0.015 B | |
| René 41 | N07041 | 19.0 | 55.0 | 11.0 | 10.0 | — | — | 3.1 | 1.5 | <0.3 | 0.09 | 0.01 B | |
| René 95 | — | 14.0 | 61.0 | 8.0 | 3.5 | 3.5 | 3.5 | 2.5 | 3.5 | <0.3 | 0.16 | 0.01 B, 0.05 Zr | |
| René 100 | — | 9.5 | 61.0 | 15.0 | 3.0 | — | — | 4.2 | 5.5 | 1.0 (max) | 0.16 | 0.015 B, 0.06 Zr, 1.0 V | |
| Udimet 500 | N07500 | 19.0 | 48.0 | 19.0 | 4.0 | — | — | 3.0 | 3.0 | 4.0 (max) | 0.08 | 0.005 B | |
| Udimet 520 | — | 19.0 | 57.0 | 12.0 | 6.0 | 1.0 | — | 3.0 | 2.0 | — | 0.08 | 0.005 B | |
| Udimet 630 | — | 17.0 | 50.0 | — | 3.0 | 3.0 | 6.5 | 1.0 | 0.7 | 18.0 | 0.04 | 0.004 B | |
| Udimet 700 | — | 15.0 | 53.0 | 18.5 | 5.0 | — | — | 3.4 | 4.3 | <1.0 | 0.07 | 0.03 B | |
| Udimet 710 | — | 18.0 | 55.0 | 14.8 | 3.0 | 1.5 | — | 5.0 | 2.5 | — | 0.07 | 0.01 B | |
| Unitemp AF2-1DA | N07012 | 12.0 | 59.0 | 10.0 | 3.0 | 6.0 | — | 3.0 | 4.6 | <0.5 | 0.35 | 1.5 Ta, 0.015 B, 0.1 Zr | |
| Waspaloy | N07001 | 19.5 | 57.0 | 13.5 | 4.3 | — | — | 3.0 | 1.4 | 2.0 (max) | 0.07 | 0.006 B, 0.09 Zr | |

Table 3.1-96 Nominal compositions of Ni-based cast superalloys

| Alloy designation | Nominal composition (wt%) | | | | | | | | | | | | |
|---------------------|---------------------------|------|------|------|------|-----|------|-------|-----|----------------|------|------|-------------------|
| | C | Ni | Cr | Co | Mo | Fe | Al | B | Ti | Ta | W | Zr | Other |
| Nickel-based | | | | | | | | | | | | | |
| B-1900 | 0.1 | 64 | 8 | 10 | 6 | — | 6 | 0.015 | 1 | 4 ^a | — | 0.10 | — |
| CMSX-2 | — | 66.2 | 8 | 4.6 | 0.6 | — | 56 | — | 1 | 6 | 8 | 6 | — |
| Hastelloy X | 0.1 | 50 | 21 | 1 | 9 | 18 | — | — | — | — | 1 | — | — |
| Inconel 100 | 0.18 | 60.5 | 10 | 15 | 3 | — | 5.5 | 0.01 | 5 | — | — | 0.06 | 1 V |
| Inconel 713C | 0.12 | 74 | 12.5 | — | 4.2 | — | 6 | 0.012 | 0.8 | 1.75 | — | 0.1 | 0.9 Nb |
| Inconel 713LC | 0.05 | 75 | 12 | — | 4.5 | — | 6 | 0.01 | 0.6 | 4 | — | 0.1 | — |
| Inconel 738 | 0.17 | 61.5 | 16 | 8.5 | 1.75 | — | 3.4 | 0.01 | 3.4 | — | 2.6 | 0.1 | 2 Nb |
| Inconel 792 | 0.2 | 60 | 13 | 9 | 2.0 | — | 3.2 | 0.02 | 4.2 | — | 4 | 0.1 | 2 Nb |
| Inconel 718 | 0.04 | 53 | 19 | — | 3 | 18 | 0.5 | — | 0.9 | — | — | — | 0.1 Cu, 5 Nb |
| X-750 | 0.04 | 73 | 15 | — | — | 7 | 0.7 | — | 2.5 | — | — | — | 0.25 Cu, 0.9 Nb |
| M-252 | 0.15 | 56 | 20 | 10 | 10 | — | 1 | 0.005 | 2.6 | — | — | — | — |
| MAR-M 200 | 0.15 | 59 | 9 | 10 | — | 1 | 5 | 0.015 | 2 | — | 12.5 | 0.05 | 1 Nb ^b |
| MAR-M 246 | 0.15 | 60 | 9 | 10 | 2.5 | — | 5.5 | 0.015 | 1.5 | 1.5 | 10 | 0.05 | — |
| MAR-M 247 | 0.15 | 59 | 8.25 | 10 | 0.7 | 0.5 | 5.5 | 0.015 | 1 | 3 | 10 | 0.05 | 1.5 Hf |
| PWA 1480 | — | bal | 10 | 5.0 | — | — | 5.0 | — | 1.5 | 12 | 4.0 | — | — |
| René 41 | 0.09 | 55 | 19 | 11.0 | 10.0 | — | 1.5 | 0.01 | 3.1 | — | — | — | — |
| René 77 | 0.07 | 58 | 15 | 15 | 4.2 | — | 4.3 | 0.015 | 3.3 | — | — | 0.04 | — |
| René 80 | 0.17 | 60 | 14 | 9.5 | 4 | — | 3 | 0.015 | 5 | — | 4 | 0.03 | — |
| René 80 Hf | 0.08 | 60 | 14 | 9.5 | 4 | — | 3 | 0.015 | 4.8 | — | 4 | 0.02 | 0.75 Hf |
| René 100 | 0.18 | 61 | 9.5 | 15 | 3 | — | 5.5 | 0.015 | 4.2 | — | — | 0.06 | 1 V |
| René N4 | 0.06 | 62 | 9.8 | 7.5 | 1.5 | — | 4.2 | 0.004 | 3.5 | 4.8 | 6 | — | 0.5 Nb, 0.15 Hf |
| Udimet 500 | 0.1 | 53 | 18 | 17 | 4 | 2 | 3 | — | 3 | — | — | — | — |
| Udimet 700 | 0.1 | 53.5 | 15 | 18.5 | 5.25 | — | 4.25 | 0.03 | 3.5 | — | — | — | — |
| Udimet 710 | 0.13 | 55 | 18 | 15 | 3 | — | 2.5 | — | 5 | — | 1.5 | 0.08 | — |
| Waspaloy | 0.07 | 57.5 | 19.5 | 13.5 | 4.2 | 1 | 1.2 | 0.005 | 3 | — | — | 0.09 | — |
| WAX-20 (DS) | 0.20 | 72 | — | — | — | — | 6.5 | — | — | — | 20 | 1.5 | — |

^a B-1900 + Hf also contains 1.5% Hf^b MAR-M 200 + Hf also contains 1.5% Hf

bal: balance

The mechanical properties as a function of temperature of the wrought superalloys are listed in Tables 3.1-97 and 3.1-98, those for the cast alloys in Table 3.1-99. The temperature dependence of the mechanical properties is essentially dependent on the volume fraction, composition, and resulting flow stress of the γ' phase.

Figure 3.1-126 shows some typical results of stress rupture tests characterising the time-dependent high temperature behavior dominated by creep deformation. A compilation of creep data may be found in [1.101].

3.1.7.4 Ni Plating

Nickel plating is used extensively for decorative applications (80%) and for engineering and electroforming purposes (20%).

Electroless Ni coatings are produced by autocatalytical reduction of Ni ions from aqueous solution. Three electroless coatings are applied most frequently: nickel-phosphorus (6–12 wt% P), nickel–boron (\approx 5 wt% B), and composite coatings (Ni–P with SiC, fluorocarbons, and diamond). A more extensive account is given in [1.96].

Table 3.1-97 Effect of temperature on the ultimate tensile strength of wrought Ni-based superalloys

| Alloy | Form | Ultimate tensile strength at: | | | | Condition of test material ^a | | | |
|--------------------------|-------|-------------------------------|---------------------|---------------------|---------------------|---|-------|-------|-------|
| | | 21 °C (70 °F) | 540 °C (1000 °F) | 650 °C (1200 °F) | 870 °C (1600 °F) | 760 °C (1400 °F) | (MPa) | (ksi) | (MPa) |
| Nickel-based | | | | | | | | | |
| Astroloy | Bar | 1415 | 205 | 1240 | 180 | 1310 | 190 | 1160 | 168 |
| Cabot 214 | — | 915 | 133 | 715 | 104 | 675 | 98 | 560 | 84 |
| D-979 | Bar | 1410 | 204 | 1295 | 188 | 1105 | 160 | 720 | 104 |
| Hastelloy C-22 | Sheet | 800 | 116 | 625 | 91 | 585 | 85 | 525 | 76 |
| Hastelloy G-30 | Sheet | 690 | 100 | 490 | 71 | — | — | — | — |
| Hastelloy S | Bar | 845 | 130 | 775 | 112 | 720 | 105 | 575 | 84 |
| Hastelloy X | Sheet | 785 | 114 | 650 | 94 | 570 | 83 | 435 | 63 |
| Haynes230 | — | 870 | 126 | 720 | 105 | 675 | 98 | 575 | 84 |
| Inconel 587 ^b | Bar | 1180 | 171 | 1035 | 150 | 1005 | 146 | 830 | 120 |
| Inconel 597 ^b | Bar | 1220 | 177 | 1140 | 165 | 1060 | 154 | 930 | 135 |
| Inconel 600 | Bar | 660 | 96 | 560 | 81 | 450 | 65 | 260 | 38 |
| Inconel 601 | Sheet | 740 | 107 | 725 | 105 | 525 | 76 | 290 | 42 |
| Inconel 617 | Bar | 740 | 107 | 580 | 84 | 565 | 82 | 440 | 64 |
| Inconel 617 | Sheet | 770 | 112 | 590 | 86 | 590 | 86 | 470 | 68 |
| Inconel 625 | Bar | 965 | 140 | 910 | 132 | 835 | 121 | 550 | 80 |
| Inconel 706 | Bar | 1310 | 190 | 1145 | 166 | 1035 | 150 | 725 | 105 |
| Inconel 718 | Bar | 1435 | 208 | 1275 | 185 | 1228 | 178 | 950 | 138 |
| Inconel 718 | Bar | 1530 | 222 | 1350 | 196 | 1235 | 179 | — | — |
| Inconel 718 Direct Age | Bar | 1530 | 196 | 1200 | 174 | 1130 | 164 | — | — |
| Inconel 718 Super | — | — | — | — | — | — | — | — | — |

Table 3.1-97 Effect of temperature on the ultimate tensile strength of wrought Ni-based superalloys, cont.

| Alloy | Form | Ultimate tensile strength at: | | | | Condition of test material ^a | | | |
|---------------------|-------|-------------------------------|---------------------|---------------------|---------------------|---|-------|-------|-----|
| | | 21 °C (70 °F) | 540 °C (1000 °F) | 650 °C (1200 °F) | 760 °C (1400 °F) | 870 °C (1600 °F) | (MPa) | (ksi) | |
| Nickel-based | | | | | | | | | |
| Inconel X750 | Bar | 1200 | 174 | 1050 | 152 | 940 | 136 | — | — |
| M-252 | Bar | 1240 | 180 | 1230 | 178 | 1160 | 168 | 945 | 137 |
| Nimonic 75 | Bar | 745 | 108 | 675 | 98 | 540 | 78 | 310 | 45 |
| Nimonic 80A | Bar | 1000 | 145 | 875 | 127 | 795 | 115 | 600 | 87 |
| Nimonic 90 | Bar | 1235 | 179 | 1075 | 156 | 940 | 136 | 655 | 95 |
| Nimonic 105 | Bar | 1180 | 171 | 1130 | 164 | 1095 | 159 | 930 | 135 |
| Nimonic 115 | Bar | 1240 | 180 | 1090 | 158 | 1125 | 163 | 1085 | 157 |
| Nimonic 263 | Sheet | 970 | 141 | 800 | 116 | 770 | 112 | 650 | 94 |
| Nimonic 942 | Bar | 1405 | 204 | 1300 | 189 | 1240 | 180 | 900 | 131 |
| Nimonic PE.11 | Bar | 1080 | 157 | 1000 | 145 | 940 | 136 | 760 | 110 |
| Nimonic PE.16 | Bar | 885 | 128 | 740 | 107 | 660 | 96 | 510 | 74 |
| Nimonic PK.33 | Sheet | 1180 | 171 | 1000 | 145 | 1000 | 145 | 885 | 128 |
| Pyromet 860 | Bar | 1295 | 188 | 1255 | 182 | 1110 | 161 | 910 | 132 |
| René 41 | Bar | 1420 | 206 | 1400 | 203 | 1340 | 194 | 1105 | 160 |
| René 95 | Bar | 1620 | 235 | 1550 | 224 | 1460 | 212 | 1170 | 170 |
| Udimet 400 | Bar | 1310 | 190 | 1185 | 172 | — | — | — | — |
| Udimet 500 | Bar | 1310 | 190 | 1240 | 180 | 1215 | 176 | 1040 | 151 |
| Udimet 520 | Bar | 1310 | 190 | 1240 | 180 | 1175 | 170 | 725 | 105 |
| Udimet 630 | Bar | 1520 | 220 | 1380 | 200 | 1275 | 185 | 965 | 140 |
| Udimet 700 | Bar | 1410 | 204 | 1275 | 185 | 1240 | 180 | 1035 | 150 |

Table 3.1-97 Effect of temperature on the ultimate tensile strength of wrought Ni-based superalloys, cont.

| Alloy | Form | Ultimate tensile strength at: | | | | Condition of test material ^a | | | |
|--|-------|-------------------------------|---------------------|---------------------|---------------------|---|-------|-------|-------|
| | | 21 °C (70 °F) | 540 °C (1000 °F) | 650 °C (1200 °F) | 870 °C (1600 °F) | 760 °C (1400 °F) | (MPa) | (ksi) | (MPa) |
| Nickel-based | | | | | | | | | |
| Udimet 710 | Bar | 1185 | 172 | 1150 | 167 | 1290 | 187 | 1020 | 148 |
| Udimet 720 | Bar | 1570 | 228 | — | — | 1455 | 211 | 1150 | 167 |
| Unitemp AF2-1DA6 | Bar | 1560 | 226 | 1480 | 215 | 1400 | 203 | 1290 | 187 |
| Waspaloy | Bar | 1275 | 185 | 1170 | 170 | 1115 | 162 | 650 | 94 |
| Iron base | | | | | | | | | |
| A-286 | Bar | 1005 | 146 | 905 | 131 | 720 | 104 | 440 | 64 |
| Alloy 901 | Bar | 1205 | 175 | 1030 | 149 | 960 | 139 | 725 | 105 |
| Discaloy | Bar | 1000 | 145 | 865 | 125 | 720 | 104 | 485 | 70 |
| Haynes 556 | Sheet | 815 | 118 | 645 | 93 | 590 | 85 | 470 | 69 |
| Incoloy 800 | Bar | 595 | 86 | 510 | 74 | 405 | 59 | 235 | 34 |
| ^a OQ, oil quench; AC, air cool; RQ, rapid quench; RAC-WQ, rapid air cool-water quench; FC, furnace cool; SC, slow cool; CW, cold worked | | | | | | | | | |
| ^b Annealed | | | | | | | | | |
| ^c Precipitation hardened | | | | | | | | | |
| ^d Ref 15. | | | | | | | | | |
| ^e Ref 1. | | | | | | | | | |
| ^f Work strengthened and aged | | | | | | | | | |
| ^g At 700 °C(1290 °F) | | | | | | | | | |
| ^h At 900 °C(1650 °F). Source: Ref 12, except as noted | | | | | | | | | |
| ⁱ At 900 °C(1650 °F). Source: Ref 12, except as noted | | | | | | | | | |
| ^j At 900 °C(1650 °F). Source: Ref 12, except as noted | | | | | | | | | |

Table 3.1-98 Effect of temperature on the mechanical properties of wrought Ni-based superalloys

| Alloy | Form | Yield strength at 0.2% offset at | | | | Tensile elongation (%) at | | | | | |
|-------------------------|-------|----------------------------------|------------------|------------------|------------------|---------------------------|---------------|------------------|------------------|------------------|------------------|
| | | 21 °C (70 °F) | 540 °C (1000 °F) | 650 °C (1200 °F) | 760 °C (1400 °F) | 870 °C (1600 °F) | 21 °C (70 °F) | 540 °C (1000 °F) | 650 °C (1200 °F) | 760 °C (1400 °F) | 870 °C (1600 °F) |
| | | (MPa) | (ksi) | (MPa) | (ksi) | (MPa) | (ksi) | (MPa) | (ksi) | | |
| Nickel-based | | | | | | | | | | | |
| Astroloy | Bar | 1050 | 152 | 965 | 140 | 965 | 132 | 690 | 100 | 16 | 18 |
| Cabot 214 | — | 560 | 81 | 510 | 74 | 505 | 73 | 310 | 45 | 38 | 19 |
| D-979 | Bar | 1005 | 146 | 925 | 134 | 980 | 129 | 655 | 95 | 305 | 44 |
| Hastelloy C-22 | Sheet | 405 | 59 | 275 | 40 | 250 | 36 | 240 | 35 | — | 57 |
| Hastelloy G-30 | Sheet | 315 | 46 | 170 | 25 | — | — | — | — | 64 | 65 |
| Hastelloy S | Bar | 455 | 65 | 340 | 49 | 320 | 47 | 310 | 45 | 220 | 32 |
| Hastelloy X | Sheet | 360 | 52 | 290 | 42 | 275 | 40 | 260 | 38 | 180 | 26 |
| Haynes 230 ^a | Sheet | 390 | 57 | 275 | 40 | 270 | 39 | 285 | 41 | 225 | 32 |
| Inconel 587 | Bar | 705 | 102 | 620 | 90 | 615 | 89 | 605 | 88 | 400 | 58 |
| Inconel 597 | Bar | 760 | 110 | 720 | 104 | 675 | 98 | 665 | 96 | — | 15 |
| Inconel 600 | Bar | 285 | 41 | 220 | 32 | 205 | 30 | 180 | 26 | 40 | 6 |
| Inconel 601 | Sheet | 455 | 66 | 350 | 51 | 310 | 45 | 220 | 32 | 55 | 8 |
| Inconel 617 | Bar | 295 | 43 | 200 | 29 | 170 | 25 | 180 | 26 | 195 | 28 |
| Inconel 617 | Sheet | 345 | 50 | 230 | 33 | 220 | 32 | 230 | 33 | 205 | 30 |
| Inconel 625 | Bar | 490 | 71 | 415 | 60 | 420 | 61 | 415 | 60 | 275 | 40 |
| Inconel 706 | Bar | 1005 | 146 | 910 | 132 | 860 | 125 | 660 | 96 | — | 20 |
| Inconel 718 | Bar | 1185 | 172 | 1065 | 154 | 1020 | 148 | 740 | 107 | 330 | 48 |
| Inconel 718/Direct Age | Bar | 1365 | 198 | 1180 | 171 | 1090 | 158 | — | — | — | 16 |
| Inconel 718/Super | Bar | 1105 | 160 | 1020 | 148 | 960 | 139 | — | — | — | 16 |
| Inconel X750 | Bar | 815 | 118 | 725 | 105 | 710 | 103 | — | — | — | 27 |
| M-252 | Bar | 840 | 122 | 765 | 111 | 745 | 108 | 720 | 104 | 485 | 70 |
| Nimonic 75 | Bar | 285 | 41 | 200 | 29 | 200 | 29 | 160 | 23 | 90 | 13 |
| Nimonic 80A | Bar | 620 | 90 | 530 | 77 | 550 | 80 | 505 | 73 | 260 | 38 |
| Nimonic 90 | Bar | 810 | 117 | 725 | 105 | 685 | 99 | 540 | 78 | 260 | 38 |
| Nimonic 105 | Bar | 830 | 120 | 775 | 112 | 765 | 111 | 740 | 107 | 490 | 71 |
| Nimonic 115 | Bar | 865 | 125 | 795 | 115 | 815 | 118 | 800 | 116 | 550 | 80 |
| Nimonic 263 | Sheet | 580 | 84 | 485 | 70 | 485 | 70 | 460 | 67 | 180 | 26 |
| Nimonic 942 | Bar | 1060 | 154 | 970 | 141 | 1000 | 145 | 860 | 125 | — | — |
| Nimonic PE-11 | Bar | 720 | 105 | 690 | 100 | 670 | 97 | 560 | 81 | — | — |
| Nimonic PE-16 | Bar | 530 | 77 | 485 | 70 | 485 | 70 | 370 | 54 | 140 | 20 |
| Nimonic 860 | Sheet | 780 | 113 | 725 | 105 | 725 | 105 | 670 | 97 | 420 | 61 |
| Pyromet 860 | Bar | 835 | 121 | 840 | 122 | 850 | 123 | 835 | 121 | — | 22 |
| René 41 | Bar | 1060 | 154 | 1020 | 147 | 1000 | 145 | 940 | 136 | 550 | 80 |
| René 95 | Bar | 1310 | 190 | 1255 | 182 | 1220 | 177 | 1100 | 160 | — | 15 |

Table 3.1-98 Effect of temperature on the mechanical properties of wrought Ni-based superalloys, cont.

| Alloy | Form | Yield strength at 0.2% offset at | | | | Tensile elongation (%) at | | | | | | | | | | | | | | | |
|-------------------|----------|----------------------------------|------------------|------------------|-------------|---------------------------|------------------|------------------|-------------|---------------|------------------|------------------|-------------|---------------|------------------|------------------|-------------|---------------|------------------|------------------|-------------|
| | | 21 °C (70 °F) | 540 °C (1000 °F) | 650 °C (1200 °F) | (MPa) (ksi) | 21 °C (70 °F) | 540 °C (1200 °F) | 650 °C (1400 °F) | (MPa) (ksi) | 21 °C (70 °F) | 540 °C (1200 °F) | 650 °C (1400 °F) | (MPa) (ksi) | 21 °C (70 °F) | 540 °C (1200 °F) | 650 °C (1400 °F) | (MPa) (ksi) | 21 °C (70 °F) | 540 °C (1200 °F) | 650 °C (1400 °F) | (MPa) (ksi) |
| Udimet 400 | Bar | 930 | 135 | 830 | 120 | — | — | — | — | — | — | — | — | 30 | 26 | — | — | — | — | — | — |
| Udimet 500 | Bar | 840 | 122 | 795 | 115 | 760 | 110 | 730 | 106 | 495 | 72 | 32 | 28 | 20 | 17 | 15 | 15 | 15 | 15 | 15 | 20 |
| Udimet 520 | Bar | 860 | 125 | 825 | 120 | 795 | 115 | 725 | 105 | 520 | 75 | 21 | 20 | 17 | 15 | 5 | 5 | — | — | — | — |
| Udimet 630 | Bar | 1310 | 190 | 1170 | 170 | 1105 | 160 | 860 | 125 | — | — | 15 | 15 | 7 | 5 | — | — | — | — | — | — |
| Udimet 700 | Bar | 965 | 140 | 895 | 130 | 855 | 124 | 825 | 120 | 635 | 92 | 17 | 16 | 16 | 16 | 20 | 20 | 20 | 20 | 20 | 27 |
| Udimet 710 | Bar | 910 | 132 | 850 | 123 | 860 | 125 | 815 | 118 | 635 | 92 | 7 | 10 | 15 | 15 | 25 | 25 | 25 | 25 | 25 | 29 |
| Udimet 720 | Bar | 1195 | 173 | — | — | 1130 | 164 | 1050 | 152 | — | — | 13 | — | 17 | 9 | — | — | — | — | — | — |
| Unitemp | Bar | 1015 | 147 | 1040 | 151 | 1020 | 148 | 995 | 144 | — | — | 20 | 19 | 18 | 18 | 16 | 16 | 16 | 16 | 16 | — |
| AF2-IDA6 | Waspaloy | Bar | 795 | 115 | 725 | 105 | 690 | 100 | 675 | 98 | 520 | 75 | 25 | 23 | 34 | 28 | 28 | 35 | 35 | 35 | 35 |
| Iron-based | | | | | | | | | | | | | | | | | | | | | |
| A-286 | Bar | 725 | 105 | 605 | 88 | 605 | 88 | 430 | 62 | — | — | 25 | 19 | 13 | 13 | 19 | 19 | — | — | — | — |
| Alloy 901 | Bar | 895 | 130 | 780 | 113 | 760 | 110 | 635 | 92 | — | — | 14 | 14 | 13 | 13 | 19 | 19 | — | — | — | — |
| Discaloy | Bar | 730 | 106 | 650 | 94 | 630 | 91 | 430 | 62 | — | — | 19 | 16 | 19 | 19 | — | — | — | — | — | — |
| Haynes 256 | Sheet | 410 | 60 | 240 | 35 | 225 | 33 | 220 | 32 | 195 | 29 | 48 | 54 | 52 | 52 | 49 | 49 | 53 | 53 | 53 | 53 |
| Incoloy 800 | Bar | 250 | 36 | 180 | 26 | 180 | 26 | 150 | 22 | — | — | 44 | 38 | 51 | 51 | 83 | 83 | — | — | — | — |
| Incoloy 801 | Bar | 385 | 56 | 310 | 45 | 305 | 44 | 290 | 42 | — | — | 30 | 28 | 26 | 26 | 55 | 55 | — | — | — | — |
| Incoloy 802 | Bar | 290 | 42 | 195 | 28 | 200 | 29 | 200 | 29 | 150 | 22 | 44 | 39 | 39 | 39 | 25 | 25 | 25 | 25 | 25 | 38 |
| Incoloy 807 | Bar | 380 | 55 | 255 | 37 | 240 | 35 | 225 | 32.5 | 185 | 26.5 | 48 | 40 | 35 | 34 | 71 | 71 | 71 | 71 | 71 | 71 |
| Incoloy 825 | — | 310 | 45 | ≈234 | ≈34 | ≈220 | ≈32 | 180 | ≈26 | ≈105 | ≈15 | 45 | ≈44 | ≈35 | ≈35 | ≈86 | ≈86 | ≈100 | ≈100 | ≈100 | ≈100 |
| Incoloy 903 | Bar | 1105 | 160 | — | — | 895 | 130 | — | — | — | — | 14 | — | 18 | 18 | — | — | — | — | — | — |
| Incoloy 907 | — | ≈1110 | ≈161 | ≈960 | ≈139 | ≈895 | ≈130 | ≈565 | ≈82 | — | — | ≈12 | ≈11 | ≈10 | ≈10 | ≈20 | ≈20 | — | — | — | — |
| Incoloy 909 | Bar | 1020 | 148 | 945 | 137 | 870 | 126 | 540 | 78 | — | — | 16 | 14 | 24 | 24 | 34 | 34 | — | — | — | — |
| N-155 | Bar | 400 | 58 | 340 | 49 | 295 | 43 | 250 | 36 | 175 | 25 | 40 | 33 | 32 | 32 | 33 | 33 | 33 | 33 | 33 | 33 |
| V-57 | Bar | 830 | 120 | 760 | 110 | 745 | 108 | 485 | 70 | — | — | 26 | 19 | 22 | 22 | 34 | 34 | — | — | — | — |
| 19-9 DL | — | 570 | 83 | 395 | 57 | 360 | 52 | — | — | — | — | 43 | 30 | 30 | 30 | — | — | — | — | — | — |
| 16-25-6 | — | 770 | 112 | — | — | 517 | 75 | 345 | 50 | 255 | 37 | 23 | — | 12 | 11 | 9 | 9 | 9 | 9 | 9 | 9 |

^a Cold-rolled and solution-annealed sheet, 1.2 to 1.6 mm thick

Table 3.1-99 Effect of temperature on the mechanical properties of cast Ni-based superalloys

| Alloy | Ultimate tensile strength at: | | | | 0.2% yield strength at: | | | | | | | |
|---------------------------|-------------------------------|----------------------------|-----------------------------|------------------|-------------------------|----------------------------|------|-----------------------------|-------------------|-------------------------|----------------------------|-----------------|
| | 21 °C (70 °F) MPa | 538 °C (1000 °F) MPa | 1093 °C (2000 °F) MPa | ksi | 21 °C (70 °F) MPa | 538 °C (1000 °F) MPa | ksi | 1093 °C (2000 °F) MPa | ksi | 21 °C (70 °F) MPa | 538 °C (1000 °F) MPa | ksi |
| Nickel-base | | | | | | | | | | | | |
| IN-713 C | 850 | 123 | 860 | 125 | — | — | 740 | 107 | 705 | 102 | — | — |
| IN-713 LC | 895 | 130 | 895 | 130 | — | — | 750 | 109 | 760 | 110 | — | — |
| B-1900 | 970 | 141 | 1005 | 146 | 270 | 38 | 825 | 120 | 870 | 126 | 195 | 28 |
| IN-625 | 710 | 103 | 510 | 74 | — | — | 350 | 51 | 235 | 34 | — | — |
| IN-718 | 1090 | 158 | — | — | — | — | 915 | 133 | — | — | — | — |
| IN-100 | 1018 | 147 | 1090 | 150 | (380) | (55) | 850 | 123 | 885 | 128 | (240) | (35) |
| IN-162 | 1005 | 146 | 1020 | 148 | — | — | 815 | 118 | 795 | 115 | — | — |
| IN-731 | 835 | 121 | — | — | 275 | 40 | 725 | 105 | — | — | 170 | 25 |
| IN-738 | 1095 | 159 | — | — | — | — | 950 | 138 | — | — | — | — |
| IN-792 | 1070 | 170 | — | — | — | — | 1060 | 154 | — | — | — | — |
| IN-22 | 730 | 106 | 780 | 113 | — | — | 685 | 99 | 730 | 106 | — | — |
| MAR-M 200 | 930 | 135 | 945 | 137 | 325 | 47 | 840 | 122 | 880 | 123 | — | — |
| MAR-M 246 | 965 | 140 | 1000 | 145 | 345 | 50 | 860 | 125 | 860 | 125 | — | — |
| MAR-M 247 | 965 | 140 | 1035 | 150 | — | — | 815 | 118 | 825 | 120 | — | — |
| MAR-M 421 | 1085 | 157 | 995 | 147 | — | — | 930 | 135 | 815 | 118 | — | — |
| MAR-M 432 | 1240 | 180 | 1105 | 160 | — | — | 1070 | 155 | 910 | 132 | — | — |
| MC-102 | 675 | 98 | 655 | 95 | — | — | 605 | 88 | 540 | 78 | — | — |
| Nimocast 75 | 500 | 72 | — | — | — | — | 179 | 26 | — | — | — | — |
| Nimocast 80 | 730 | 106 | — | — | — | — | 520 | 75 | — | — | — | — |
| Nimocast 90 | 700 | 102 | 595 | 86 | — | — | 520 | 75 | 420 | 61 | — | — |
| Nimocast 242 | 460 | 67 | — | — | — | — | 300 | 44 | — | — | — | — |
| Nimocast 263 | 730 | 106 | — | — | — | — | 510 | 74 | — | — | — | — |
| René 77 | — | — | — | — | — | — | — | — | — | — | — | — |
| René 80 | — | — | — | — | — | — | — | — | — | — | — | — |
| Udimet 500 | 930 | 135 | 895 | 130 | — | — | 815 | 118 | 725 | 105 | — | — |
| Udimet 710 | 1075 | 156 | — | — | 240 | 35 | 895 | 130 | — | — | 170 | 25 |
| CMSX-2 ^a | 1185 | 172 | 1295 ^b | 188 ^b | — | — | 1135 | 165 | 1245 ^b | 181 ^b | — | — |
| GMR-235 | 710 | 103 | — | — | — | — | 640 | 93 | — | — | — | — |
| IN-939 | 1050 | 152 | 915 ^b | 133 ^b | 325 ^c | 47 ^c | 800 | 116 | 635 ^b | 92 ^b | 205 ^c | 30 ^c |
| MM 002 ^d | 1035 | 150 | 1035 ^b | 150 ^b | 550 ^c | 80 ^c | 825 | 120 | 860 ^b | 125 ^b | 345 ^c | 50 ^c |
| IN-713 Hf ^e | 1000 | 145 | 895 ^b | 130 ^b | 380 ^c | 55 ^c | 760 | 110 | 620 ^b | 90 ^b | 240 ^c | 35 ^c |
| René 125 Hf ^f | 1070 | 155 | 1070 ^b | 155 ^b | 550 ^c | 80 ^c | 825 | 120 | 860 ^b | 125 ^b | 345 ^c | 50 ^c |
| MAR-M 246 Hf ^g | 1105 | 160 | 1070 ^b | 155 ^b | 565 ^c | 82 ^c | 860 | 125 | 860 ^b | 125 ^b | 345 ^c | 50 ^c |
| MAR-M 200 Hf ^h | 1035 | 150 | 1035 ^b | 150 ^b | 540 ^c | 78 ^c | 825 | 120 | 860 ^b | 125 ^b | 345 ^c | 50 ^c |
| PWA-1480 ^a | — | — | 1130 ^b | 164 ^b | 685 ^c | 99 ^c | 895 | 130 | 905 ^b | 131 ^b | 495 ^c | 72 ^c |
| SEL | 1020 | 148 | 875 ^b | 127 ^b | — | — | 905 | 131 | 795 ^b | 115 ^b | — | — |
| UDM 56 | 945 | 137 | 945 ^b | 137 ^b | — | — | 850 | 123 | 725 ^b | 105 ^b | — | — |
| SEL 15 | 1060 | 154 | 1090 ^b | 158 ^b | — | — | 895 | 130 | 815 ^b | 118 ^b | — | — |

^a Single-crystal [001]^b At 760 °C (1400 °F)^c At 980 °C (1800 °F)^d RR-7080^e MM 004

Table 3.1-99 Effect of temperature on the mechanical properties of cast Ni-base superalloys, cont.

| | Tensile elongation % at: 21°C (70°F) | 538°C (1000°F) | 1093°C (2000°F) | Dynamic modulus of elasticity at: 21°C (70°F) GPa | 10 ⁶ psi | 538°C (1000°F) GPa | 10 ⁶ psi | 1093°C (2000°F) GPa | 10 ⁶ psi |
|--------------------|--|-------------------|--------------------|--|---------------------|--------------------------|---------------------|---------------------------|---------------------|
| Nickel-base | | | | | | | | | |
| 8 | 10 | — | 206 | 29.9 | 179 | 26.2 | — | — | — |
| 15 | 11 | — | 197 | 28.6 | 172 | 25.0 | — | — | — |
| 8 | 7 | 11 | 214 | 31.0 | 183 | 27.0 | — | — | — |
| 48 | 50 | — | — | — | — | — | — | — | — |
| 11 | — | — | — | — | — | — | — | — | — |
| 9 | 9 | — | 215 | 31.2 | 187 | 27.1 | — | — | — |
| 7 | 6.5 | — | 197 | 28.5 | 172 | 24.9 | — | — | — |
| 6.5 | — | — | — | — | — | — | — | — | — |
| — | — | — | 201 | 29.2 | 175 | 25.4 | — | — | — |
| 4 | — | — | — | — | — | — | — | — | — |
| 5.5 | 4.5 | — | — | — | — | — | — | — | — |
| 7 | 5 | — | 218 | 31.6 | 184 | 26.7 | — | — | — |
| 5 | 5 | — | 205 | 29.8 | 178 | 25.8 | 145 | 21.1 | |
| 7 | — | — | — | — | — | — | — | — | — |
| 4.5 | 3 | — | 203 | 29.4 | — | — | 141 | 20.4 | |
| 6 | — | — | — | — | — | — | — | — | — |
| 5 | 9 | — | — | — | — | — | — | — | — |
| 39 | — | — | — | — | — | — | — | — | — |
| 15 | — | — | — | — | — | — | — | — | — |
| 14 | 15 | — | — | — | — | — | — | — | — |
| 8 | — | — | — | — | — | — | — | — | — |
| 18 | — | — | — | — | — | — | — | — | — |
| — | — | — | — | — | — | — | — | — | — |
| — | — | — | 208 | 30.2 | — | — | — | — | — |
| 13 | 13 | — | — | — | — | — | — | — | — |
| 8 | — | — | — | — | — | — | — | — | — |
| 10 | 17 ^b | — | — | — | — | — | — | — | — |
| 3 | — | 18 ^c | — | — | — | — | — | — | — |
| 5 | 7 ^b | 25 ^c | — | — | — | — | — | — | — |
| 7 | 5 ^b | 12 ^c | — | — | — | — | — | — | — |
| 11 | 6 ^b | 20 ^c | — | — | — | — | — | — | — |
| 5 | 5 ^b | 12 ^c | — | — | — | — | — | — | — |
| 6 | 7 ^b | 14 ^c | — | — | — | — | — | — | — |
| 5 | 5 ^b | 10 ^c | — | — | — | — | — | — | — |
| 4 | 8 ^b | 20 ^c | — | — | — | — | — | — | — |
| 6 | 7 ^b | — | — | — | — | — | — | — | — |
| 3 | 5 ^b | — | — | — | — | — | — | — | — |
| 9 | 5 ^b | — | — | — | — | — | — | — | — |

^f M 005^g MM 006^h MM 009ⁱ Data from Metals Handbook, 9th edn., Vol. 3, 1980^j At 650°C (1200°F)

Source: Nickel Development Institute, except as noted

3.1.8 Copper and Copper Alloys

Copper and copper alloys are used as materials mainly because of the high electrical and thermal conductivity of Cu and because of the variability and favorable combination of electrical, mechanical, and corrosion properties and of color (from copper red to silver white) by alloying and heat treatment. The basic properties of Cu are covered in Sect. 2.2.3. The electrical resistivity of Cu, $\sigma = 16.78 \text{ n}\Omega \text{ m}$ (293 K), is the highest among the metals of moderate cost. The corresponding high thermal conductivity $\lambda = 397 \text{ W m}^{-1} \text{ K}^{-1}$ of Cu gives rise to numerous applications in heat exchangers. Its high corrosion resistance and good formability are the basis of its use as gas and water pipes, in the chemical and food industries, and – combined with its color – in architecture.

The alloying of Cu with group IIB to IVB metals results in a series of alloy systems with a characteristic sequence of intermetallic phases characterised by their outer electron to atom ratio (e/a), as first recognised by and named after Hume-Rothery. This behavior is attributed to the fact that the electronic structure rather than ionic radius, directed bonds, or other factors of influence for alloy formation is dominating the and crystal

structure formation of the intermetallic phases. The same is true for Ag- and Au-based alloy systems. A survey is given in Table 3.1-100.

The solid solution phase α of Cu, dominating in most Cu materials, is hardened by the solute elements s through solid solution hardening which is proportional to the misfit parameter η_s , given by the relative difference in atomic radius r_s to r_{Cu} : $\eta_s = 2(r_s - r_{\text{Cu}})/(r_s + r_{\text{Cu}})$. Since $r_{\text{Cu}} = 1.28$, $r_{\text{Ni}} = 1.25$, $r_{\text{Zn}} = 1.33$, and $r_{\text{Sn}} = 1.51$, it follows that the increase in yield stress per at.% of solute increases in the order Ni < Zn < Sn.

The materials on copper basis may be subdivided into the groups shown in Table 3.1-101. Standards for copper and copper materials have been issued by ASTM, DIN, DKE, CEN, CENELEC, ISO, and IEC. In the USA, the Unified Numbering System for Metals and Alloys (UNS) applied to Cu materials consists of the letter C and a 5 digit number. More extensive accounts of Cu and Cu alloys as materials are given in [1.102–104].

3.1.8.1 Unalloyed Coppers

Cu is used as the technical standard for the conductivity of metals and alloys. The International Annealed Copper Standard (IACS) is defined by a Cu wire, 1 m long and weighing 0.1 kg, the resistance of which is 0.15327Ω at 20°C . Accordingly, a conductivity of 100% IACS = 58.00 MS m^{-1} (or $\text{m} \Omega^{-1} \text{ mm}^{-2}$), which corresponds to a resistivity of $1.7243793 (\mu\Omega \text{ cm})$. The electrical conductivity is specifically and strongly dependent on the kind and concentration of impurities (Fig. 3.1-130).

Table 3.1-100 Characteristics of Hume-Rothery phases in Cu-, Ag- and Au-based alloy systems

| e/a | Phase designation | Crystal structure | Example |
|-------|-------------------|--------------------------|---------------------------------|
| 3/2 | β | bcc | CuZn |
| 3/2 | ζ | hcp | CuGa, CuGe |
| 21/13 | γ | γ brass structure | Cu ₅ Zn ₈ |
| 7/4 | ε | hcp | CuZn ₃ |

Table 3.1-101 Groups of copper materials according to ASTM

| Designation | Maximum alloying range, wt%, further alloying elements | Wrought alloys | Cast alloys | Particular alloying range for castings |
|--------------------|---|----------------|-------------|--|
| Coppers | – | + | + | – |
| High copper alloys | 1.2Cd, 2Be, 3Fe, 2.7Co, 3Ni, 2.5Sn, 1.5Cr, 0.7Zn, 0.25Si, 3.4Ti, 1Zr, 3.5Pb | + | + | |
| Brasses | 43Zn, 3Pb, 2Al, Co, Si, Mn, Fe | + | + | |
| Bronzes | 8Sn, Zn | + | + | 12Sn, 2Pb, 2Ni |
| Cu–Pb–Sn | – | – | + | 10Sn, 20Pb |
| Copper–Nickels | 30Ni, 1Fe, 1Mn, 2Sn | + | + | |
| Nickel–Silvers | 18Ni, 39Zn, 3Pb, 2Mn | + | – | – |
| Cu–Sn–Zn | – | – | + | 7Sn, 8Zn, 7Pb |
| Cu–Al | 8Al | + | + | |

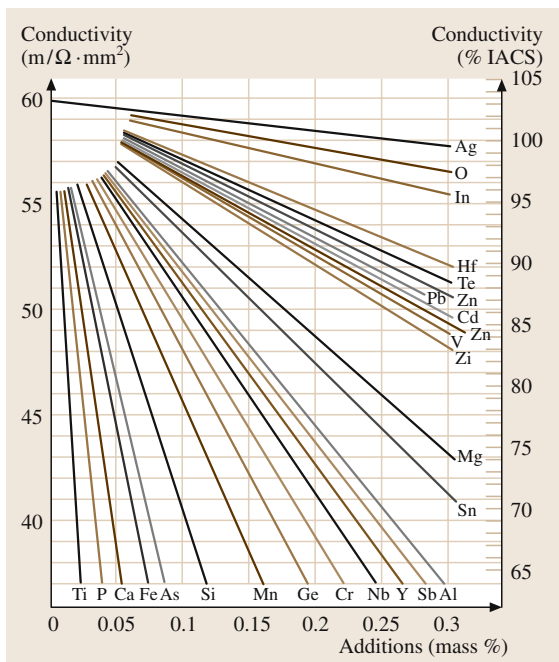


Fig. 3.1-130 Effect of solute elements on the conductivity of Cu

Unalloyed coppers contain ≥ 99.3 wt% Cu. The elements O, P, and/or As are deliberate additions.

Table 3.1-102 Composition and properties of characteristic unalloyed coppers

| Material | UNS No. | Purity; other elements (wt%) | Yield stress $R_{\text{po},2}$ (MPa) | Ultimate tensile strength R_m (MPa) | Fracture strain A_f (%) | Thermal conductivity κ ($\text{W m}^{-1} \text{K}^{-1}$) | Electrical resistivity ρ ($\mu\Omega \text{ cm}$) |
|------------------------------------|---------|------------------------------|--------------------------------------|---------------------------------------|---------------------------|---|--|
| Pure Cu (oxygen-free electronic) | C10100 | 99.99 Cu | 69–365 | 221–455 | 4–55 | 392 | 1.741 |
| Pure Cu (oxygen-free) | C10200 | 99.95 Cu | 69–365 | 221–455 | 4–55 | 397 | 1.741 |
| Electrolytic tough pitch Cu | C11000 | 99.90 Cu–0.04 O | 69–365 | 224–455 | 4–55 | 397 | 1.707 |
| Oxygen-free low phosphorus Cu | C10800 | 99.95 Cu–0.009 P | 69–345 | 221–379 | 4–50 | 397 | 2.028 |
| Phosphorus deoxidized arsenical Cu | C14200 | 99.68 Cu–0.35 As –0.02 P | 69–345 | 221–379 | 8–45 | 397 | 3.831 |

Table 3.1-103 Composition of high copper alloys

| Basic alloy system | UNS No. | Major alloying elements (mass%) | Minor elements |
|--------------------|---------------|------------------------------------|----------------|
| Cu–Cd | C16200 | 0.7–1.2 Cd | |
| Cu–Be | C17000–C17300 | 1.6–2.0 Be | Al, Pb |
| Cu–Ni–Be | C17450–C17460 | 0.5–1.4 Ni, 0.15–0.50 Be | Al, Zr |
| Cu–Co–Be | C17500 | 2.4–2.7 Co, 0.4–0.7 Be | |
| Cu–Ni–Cr–Si | C18000 | 1.8–3.0 Ni, 0.1–0.8 Cr, 0.4–0.8 Si | |
| Cu–Sn–Cr | C18030–C18040 | 0.08–0.3 Sn, 0.1–0.35 Cr | P |

Small oxygen additions to Cu in the range of 0.005 to 0.04 wt% O are used to oxidize the metallic impurities which may be dissolved in small Cu_2O particles or form their own oxides. Thus the conductivity of the Cu is increased. Alternatively ultra-high purity cathodes from the electrolytic copper refining process are used as raw material. Oxygen-bearing Cu is unsuitable for applications requiring exposure to hydrogen, or requiring bonding by soldering or by brazing, because reactions between oxygen and hydrogen or between oxygen and the braze or solder components, respectively, lead to embrittlement. Gas evolution may occur in ultra-high-vacuum equipment if the Cu applied contains oxygen additions or higher contents of other impurities with a higher vapor pressure. Therefore, use of oxygen-free high purity copper is mandatory in these cases. In less critical cases, deoxidation by phosphorus is applied to the copper with an ensuing loss in conductivity. These measures lead to the different technical coppers ranging from about 40 to 58 MS m^{-1} in conductivity and from 99.90 to 99.99 wt% in purity. Table 3.1-102 lists major unalloyed coppers.

3.1.8.2 High Copper Alloys

This group of materials comprises essentially a number of age-hardenable alloys which are listed in Table 3.1-103.

Table 3.1-104 Properties of high copper alloys

| Material | UNS No. | Yield stress $R_{\text{po},2}$ (MPa) | Ultimate tensile strength R_m (MPa) | Fracture strain A_f (%) | Brinell Hardness (HB) | Thermal conductivity κ ($\text{W m}^{-1} \text{K}^{-1}$) | Electrical resistivity ρ ($\mu\Omega \text{ cm}$) |
|-------------------------|---------|--------------------------------------|---------------------------------------|---------------------------|-----------------------|---|--|
| Beryllium copper | C17200 | 172–1344 | 469–1462 | 1–48 | 100–363 | ≤ 95 | 4.009 |
| Beryllium copper | C17000 | 221–1172 | 483–1310 | 3–45 | 100–363 | ≤ 95 | 2.053 |
| Cadmium copper | C16200 | 600 | 649 | n.a. | n.a. | 376 | 2.028 |
| Chromium copper | C18200 | 479–531 | 232–593 | 14–60 | 58–140 | 188 | 3.831 |
| Cobalt beryllium copper | C17500 | 172–758 | 310–793 | 5–28 | 67–215 | 84 | 7.496 |
| Lead copper | C18700 | 69–345 | 221–379 | 8–45 | n.a. | n.a. | n.a. |
| Silver-bearing copper | C11300 | 69–365 | 221–455 | 4–55 | 55–90 | 397 | 1.741 |
| Sulfur copper | C14700 | 69–379 | 221–393 | 8–52 | 55–85 | 373 | 1.815 |
| Tellurium copper | C14500 | 69–352 | 221–386 | 8–45 | 49–80 | 382 | 1.759 |
| Zirconium copper | C15000 | 41–496 | 200–524 | 2–54 | n.a. | n.a. | n.a. |
| n.a. not available | | | | | | | |

The age-hardening behavior is based on the fact that the solubility of Cd, Be, and Cr in Cu decreases with decreasing temperature. On this basis a heat treatment is applied, that leads to age-hardening. A high-temperature solution treatment is followed by a low-temperature annealing, or aging, treatment. This serves to precipitate a dispersion of small metastable or stable particles which give rise to hardening by several hardening mechanisms that depend in detail on the microstructural, chemical, crystallographic and mechanical properties of the precipitated particles (see Table 3.1-104).

3.1.8.3 Brasses

The term brass was originally applied to binary Cu–Zn alloys (Fig. 3.1-131) but was extended to Cu–Zn-based multi-component alloys, mainly containing Fe, Al, Ni, and Si.

The phases of technical interest are the fcc α phase and the bcc β phase. The high-temperature β phase transforms to its ordered (CsCl type) variant β' at temperatures below 727 to 741 K depending on composition, as shown in Fig. 3.1-131. The intermetallic phases with higher Zn content are brittle and have no technical relevance.

Brasses and other Cu-based alloys are mainly supplied as wrought alloys which designate the state of the final material which is obtained by a final shaping operation (rolling, rod, and wire drawing etc.) with a controlled degree of cold work. The work-hardening behavior of the alloys is, thus, exploited to vary the final mechanical properties in comparatively wide limits

(see Table 3.1-105). By way of an example, Fig. 3.1-132 shows the mechanical properties of CuZn15 as a function of the degree of cold work.

The dependence of the mechanical properties on the effect of annealing is similarly important. Figure 3.1-133 shows the changes upon isothermal annealing for the same alloy as in Fig. 3.1-132. Table 3.1-105 lists the nominal compositions and property ranges of brasses.

3.1.8.4 Bronzes

Bronze is the original term for Cu–Sn alloys, Fig. 3.1-134. The term bronze has, also, been extended to Cu–Al and Cu–Si based alloys. Table 3.1-106 lists the composition and properties of characteristic bronzes. As referred to in the introduction the α solid solution of Cu–Sn is increasing in yield stress as a function of solute content most strongly of all common Cu alloys because of the high misfit of Sn in Cu.

Aluminium bronzes, especially ternary alloys containing Ni and Mn, have an increased high temperature oxidation resistance due to the formation of a protective Al_2O_3 layer upon exposure to higher temperature. The Cu–Al alloys and the related systems have been studied extensively as prototype systems which show martensitic transformations upon cooling and upon plastic deformation [1.105]. This transformation behavior is, also, the basis of shape memory and superplastic properties. Table 3.1-106 lists the nominal compositions and property ranges of bronzes. Figure 3.1-135 shows a phase diagram of Cu–Al.

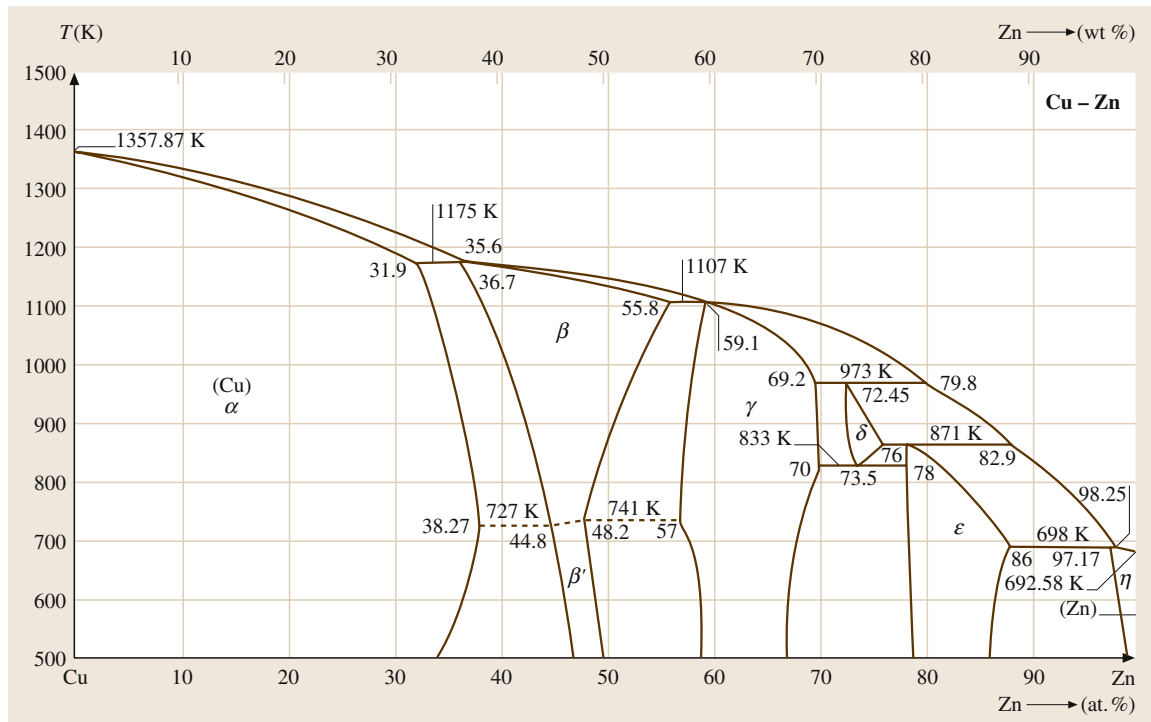


Fig. 3.1-131 Cu-Zn phase diagram [1.106]

Table 3.1-105 Composition and properties of characteristic brasses

| Material | UNS No. | Composition (wt %) | Yield stress $R_{\text{po.2}}$ (MPa) | Ultimate tensile strength R_m (MPa) | Fracture strain A_f (%) | Thermal conductivity κ ($\text{W m}^{-1} \text{K}^{-1}$) | Electrical resistivity ρ ($\mu\Omega \text{ cm}$) |
|---|---------|-------------------------|--------------------------------------|---------------------------------------|---------------------------|---|--|
| Admiralty brass | C44300 | 71 Cu–28 Zn –1 Sn | 124–152 | 331–379 | 60–65 | | |
| Aluminium brass | C68700 | 77.5 Cu–20.5 Zn –2 Al | 186 | 414 | 55 | 101 | 7.496 |
| Cartridge brass | C68700 | 70 Cu–30 Zn | 76–448 | 303–896 | 3–66 | 121 | 6.152 |
| Free-cutting brass | C36000 | 61.5 Cu–35.5 Zn –3 Pb | 124–310 | 338–469 | 18–53 | 109 | 6.631 |
| Gilding metal (cap copper) | C21000 | 95.0 Cu–5.0 Zn | 69–400 | 234–441 | 8–45 | 234 | 3.079 |
| High tensile brass (architectural bronze) | C38500 | 57 Cu–40 Zn –3 Pb | 138 | 414 | 30 | 88–109 | 8.620 |
| Hot stamping brass (forging) | C37700 | 59 Cu–39 Zn –2 Pb | 138 | 359 | 45 | 109 | 6.631 |
| Low brass | C24000 | 80 Cu–20 Zn | 83–448 | 290–862 | 3–55 | 138 | 4.660 |
| Muntz metal | C28000 | 60 Cu–40 Zn | 145–379 | 372–510 | 10–52 | 126 | 6.157 |
| Naval brass | C46400 | 60 Cu–39.25 Zn –0.75 Sn | 172–455 | 379–607 | 17–50 | 117 | 6.631 |
| Red brass | C23000 | 85 Cu–15 Zn | 69–434 | 269–724 | 3–55 | 159 | 3.918 |
| Yellow brass | C26800 | 65 Cu–35 Zn | 97–427 | 317–883 | 3–65 | 121 | 6.631 |

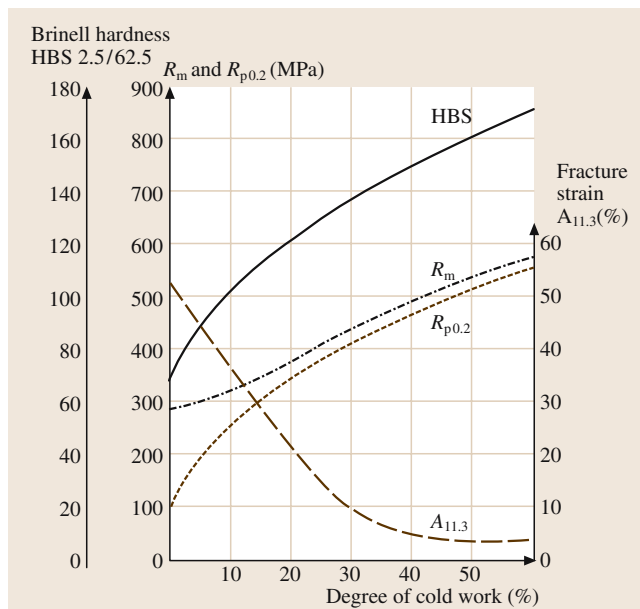


Fig. 3.1-132 Effect of work hardening, expressed as % reduction in thickness by rolling, on the mechanical properties of CuZn15 brass. This relation is a typical example for the control of the mechanical properties of wrought copper alloys by work hardening

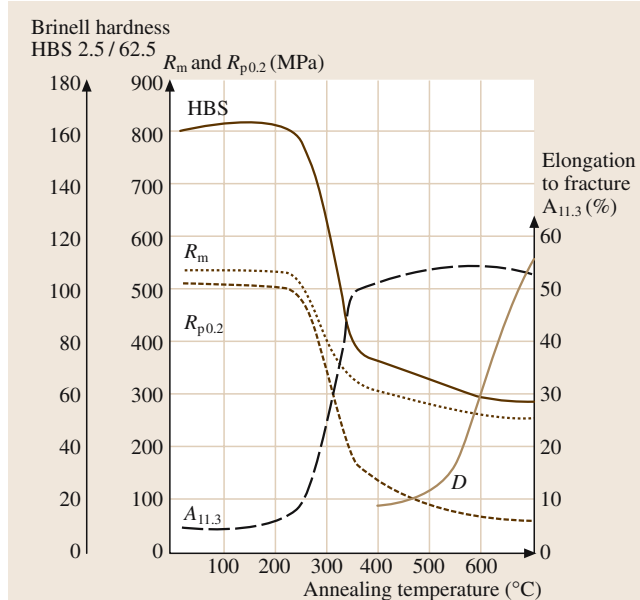


Fig. 3.1-133 Annealing behavior of a CuZn15 brass (cold worked 50%; Annealing time 3 h)

3.1.8.5 Copper–Nickel and Copper–Nickel–Zinc Alloys

Copper–Nickel Alloys

Figure 3.1-136 shows the Cu–Ni phase diagram which is characterized by a continuous solid solution which extends to room temperature. The metal Cu is solution-hardened only weakly by alloying with Ni because of the low misfit between the two components. But Cu–Ni alloys show an excellent corrosion resistance against seawater and are used, e.g., in desalination plants, accordingly. Another outstanding effect of Ni in Cu is the drastic decrease in electrical and thermal conductivity with increasing Ni content, as shown in Figs. 3.1-137 and 3.1-138. The interrelation through the Wiedemann–Franz law is obvious. A prominent application of the low thermal conductivity of Cu–Ni material is its use in equipment for operation at cryogenic temperature where heat loss by conduction is a major concern.

Copper–Nickel–Zinc Alloys. Nickel–Silvers

The designation of these Cu–Ni–Zn alloys is based on the silver-like color. Their composition ranges from 45 to 49 wt% Cu, 10 to 12 wt% Ni, with the balance composing Zn. Up to 2 wt% Pb is added for better drilling and turning behavior. Ni increases the yield stress and decreases the electrical and thermal conductivity (see Table 3.1-107).

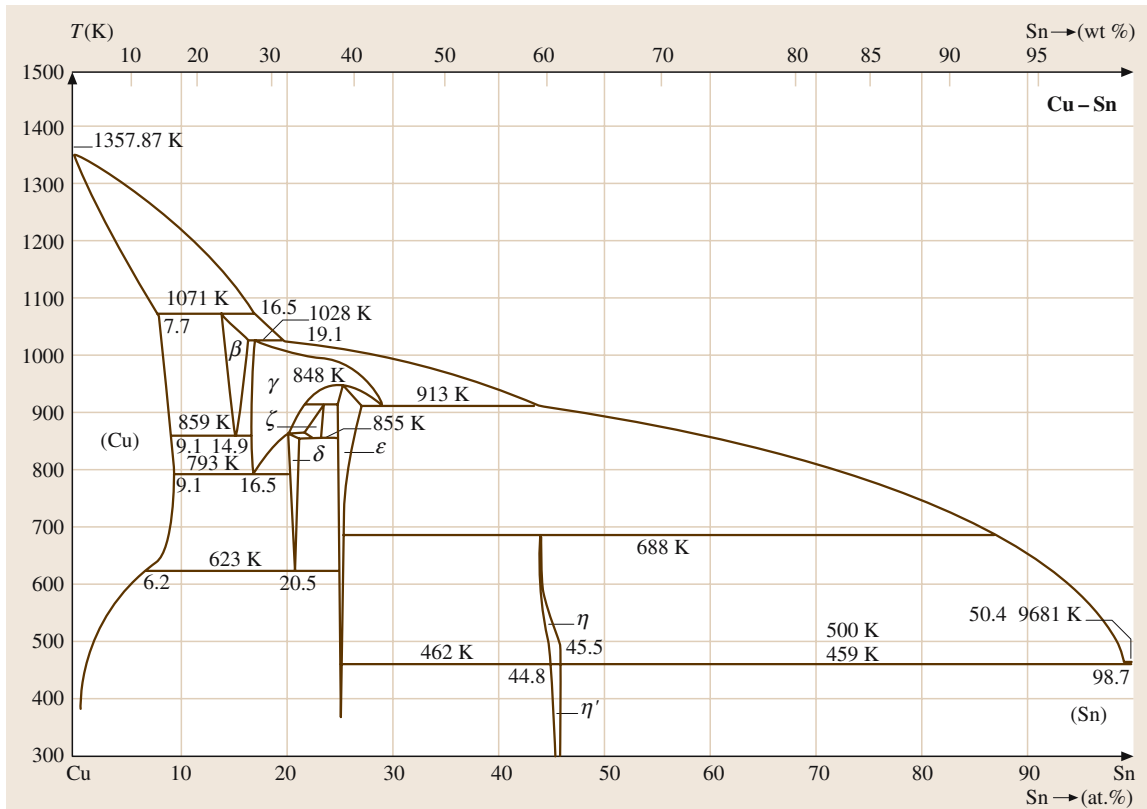


Fig. 3.1-134 Cu–Sn phase diagram [1.106]

Table 3.1-106 Composition and properties of characteristic bronzes

| Material | UNS No. | Purity; other elements (wt%) | Yield stress $R_{p0.2}$ (MPa) | Ultimate tensile strength R_m (MPa) | Fracture strain A_f (%) | Thermal conductivity κ ($\text{W m}^{-1} \text{K}^{-1}$) | Electrical resistivity ρ ($\mu\Omega \text{cm}$) |
|--------------------|---------|------------------------------|-------------------------------|---------------------------------------|---------------------------|---|---|
| Phosphor bronze | C51100 | 96 Cu–3.5 Sn –0.12 P | 345–552 | 317–710 | 2–48 | 85 | 9.171 |
| Phosphor bronze A | C51000 | 95 Cu–5 Sn –0.09 P | 131–552 | 324–965 | 2–64 | 75 | 10.26 |
| Phosphor bronze C | C52100 | 92 Cu–7 Sn –0.12 P | 165–552 | 379–965 | 2–70 | 67 | 12.32 |
| Phosphor bronze D | C52400 | 90 Cu–10 Sn | 193 | 455–1014 | 3–70 | 63 | 12.32 |
| Silicon bronze A | C65500 | 97 Cu–3.0 Si | 145–483 | 386–1000 | 3–63 | 50 | 21.29 |
| Silicon bronze B | C65100 | 98.5 Cu–1.5 Si | 103–476 | 276–655 | 11–55 | not available | not available |
| Aluminium bronze D | C61400 | 91 Cu–7 Al–2 Fe | 228–414 | 524–614 | 32–45 | not available | 12.32 |
| Aluminium bronze | C60800 | 95 Cu–5 Al | 186 | 414 | 55 | 85 | 9.741 |
| Aluminium bronze | C63000 | Cu–9.5 Al–4 Fe –5 Ni–1 Mn | 345–517 | 621–814 | 15–20 | 62 | 13.26 |

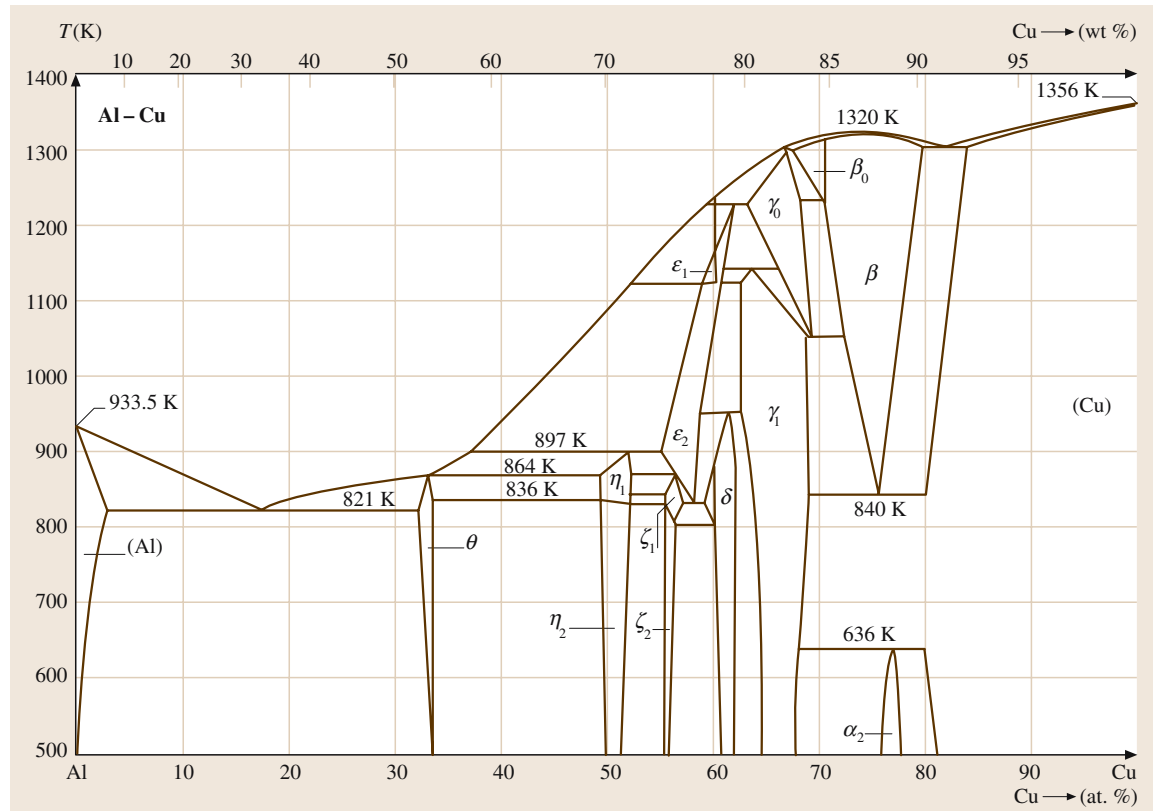


Fig. 3.1-135 Cu-Al phase diagram [1.106]

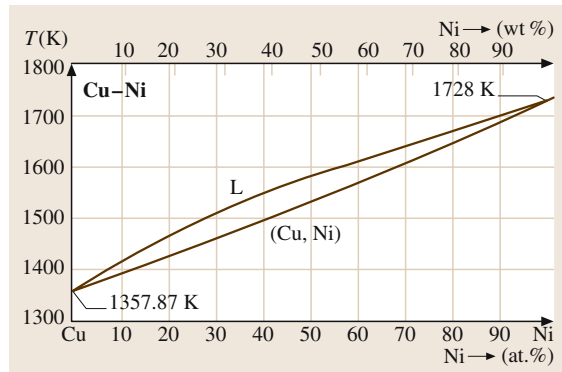


Fig. 3.1-136 Cu-Ni phase diagram [1.106]

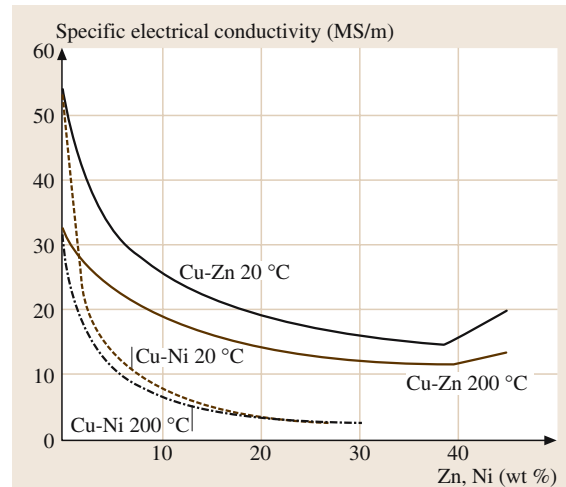
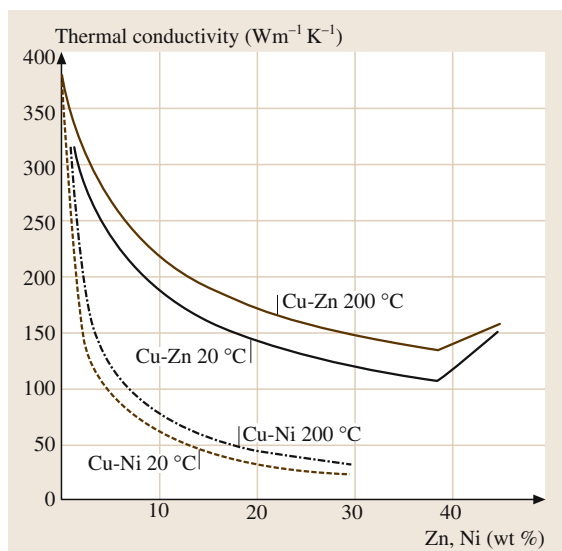


Fig. 3.1-137 Electrical conductivity of Cu-Ni and Cu-Zn alloys [1.103]

Table 3.1-107 Composition and properties of characteristic copper–nickel and copper–nickel–zinc alloys

| Material | UNS No. | Purity; other elements (wt %) | Yield stress $R_{\text{p}0.2}$ (MPa) | Ultimate tensile strength R_m (MPa) | Fracture strain A_f (%) | Thermal conductivity κ ($\text{W m}^{-1} \text{K}^{-1}$) | Electrical resistivity ρ ($\mu\Omega \text{ cm}$) |
|-------------------|---------|----------------------------------|--------------------------------------|---------------------------------------|---------------------------|---|--|
| Copper nickel | C70400 | 92.4 Cu–5.5 Ni –1.5 Fe–0.6 Mn | 276–524 | 262–531 | 2–46 | 67 | 13.79 |
| Copper nickel | C70600 | 87.7 Cu–10 Ni –1.5 Fe–0.6 Mn | 110–393 | 303–414 | 10–42 | 42 | 21.55 |
| Copper nickel | C71500 | 67 Cu–31 Ni –0.7 Fe–0.5 Be | 138–483 | 372–517 | 15–45 | 21 | 38.31 |
| Nickel silver 10% | C74500 | 65 Cu–25 Zn–10 Ni | 124–524 | 338–896 | 1–50 | 37 | 20.75 |
| Nickel silver 12% | C74500 | 65 Cu–23 Zn–12 Ni | 124–545 | 359–641 | 2–48 | 30 | 22.36 |
| Nickel silver 15% | C75200 | 65 Cu–20 Zn–15 Ni | 124–545 | 365–634 | 2–43 | 27 | 24.59 |
| Nickel silver 18% | C74500 | 65 Cu–17 Zn–18 Ni | 172–621 | 386–710 | 3–45 | 28 | 27.37 |

**Fig. 3.1-138** Thermal conductivity of Cu–Ni and Cu–Zn alloys [1.103]

3.1.9 Refractory Metals and Alloys

Several books and reviews have been published on the technology and properties of refractory metals and their alloys [1.107–116]. According to the most common definition, refractory metals comprise elements of the Group VB and VIB with a melting point higher than 2000 °C; these are niobium, tantalum, molybdenum, and tungsten. In some publications the VIIB metal rhenium is also included, as it does not fit in any other classification. Less common definitions describe a refractory metal as metal with a melting point equal to or greater than that of chromium, thus additionally including vanadium, technetium, the reactive metal hafnium, and the noble metals

ruthenium, osmium, ruthenium, and iridium. This chapter will give data on molybdenum, tungsten, tantalum, niobium, and their alloys. Powder metallurgy (P/M) is the only production route for commercial W and W alloys and for 97% of Mo, the remainder is processed by electron-beam melting (EB) and vacuum-arc casting (VAC) [1.117]. The finer grain structure of P/M-material is advantageous for both the further processing and the mechanical properties of the finished product. For some alloys such as those doped with potassium silicate, La_2O_3 , and Y_2O_3 , P/M is the only possible production technique.

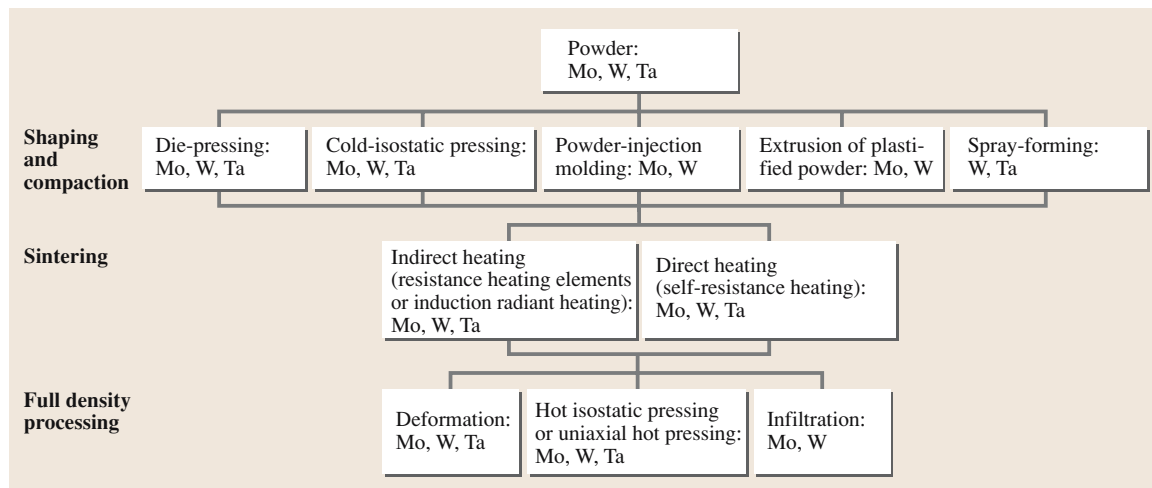


Fig. 3.1-139 Large-scale P/M production routes for Mo, W and Ta [1.118]

The mechanical properties and homogenous microstructure required are again the reasons to apply P/M in producing Ta wire as employed extensively in the manufacture of capacitors. The larger fraction of the Ta sheet production is based on the use of EB sheet bars, as this is more economical. The techniques of VAC and EB dominate in the production of Nb and Nb alloys. The industrial P/M production routes of Mo, W, Ta, and their alloys are given in Fig. 3.1-139.

Net shape techniques such as powder injection molding and spraying on a lost core (vacuum-plasma-spraying, chemical vapor deposition) are limited to some specific applications in the field of electronic devices and aerospace products. Less than 10% of the production quantity is delivered in the as-sintered state. The most common fully-dense-processing techniques are deformation by rolling, forging, swaging, and drawing.

Initially refractory metals were applied mainly in the pure state. Extensive developments mainly driven by US aerospace programs led to a wide variety of alloys now commercially available. The compositions of solid-solution, precipitation- and dispersion-strengthened alloys are given in Table 3.1-108. Tungsten heavy metals and refractory-metal-based composite materials are not included here.

Carbide precipitation hardening (in TZM, MHC) is effective up to 1400 °C. The addition of the deformable oxides La_2O_3 (in ML) and $x\text{K}_2\text{O} \cdot y\text{SiO}_2$ (in K–Si–Mo), respectively, results in oxide refinement by deformation and in the possibility of tailoring the mechanical properties. This is the main alloying mechanism for Mo applied in lamps [1.119].

The tungsten alloy which is commercially most important is Al–K-silicate doped W (AKS–W). It is a dispersion-strengthened, micro-alloyed metal with a directionally recrystallized microstructure. Spherical bubbles stabilized by containing K gas are interacting with dislocations, sub-boundaries and high-angle boundaries [1.120, 121]. The high stability of these bubbles can be explained by the low solubility of K in W, even at operating temperatures up to 3200 °C.

A current task is to reduce the low-temperature brittleness of Mo and W, which is essentially due to a rigid covalent component of the interatomic bond along the edges of the bcc unit cell. This causes a low solubility for interstitial elements which occupy the octahedral sites of the lattice and give rise to its tetragonal distortion and a strong interaction of dislocations with the elastic strain field surrounding the interstitial solutes, thus impeding the dislocation movement [1.122]. One possibility to increase the low-temperature ductility is alloying with Re which lowers the brittle-to-ductile-transition temperature of both W and Mo [1.123–125]. But the insufficient supply and the high price of Re limit the application of these alloys.

The addition of oxides such as ThO_2 , BaO , SrO , Y_2O_3 , and Sc_2O_3 lowers the electron work function of W, which is important for its application in electrodes. The production quantities of W– La_2O_3 and W– Ce_2O_3 as electron emitting materials are increasing at the expense of the slightly radioactive W– ThO_2 material.

The production of capacitors, the dominating application of Ta, requires material in its purest

Table 3.1-108 Typical compositions of commercial refractory metal alloys (in weight percent, analyses of base-metal correspond to metallic purity) [1, 118]

state. Solid-solution-strengthened Ta_{2.5}W is used for components in chemical apparatus. Superconducting Nb_{46.5}Ti accounts for more than half of all Nb alloys produced. Hafnium is the main addition for niobium-based alloys used by the aerospace industry.

Refractory metals and their alloys are used in a wide variety of fields of application and products such as electrical and electronic devices; light sources; medical equipment; automotive, aerospace, and defense industry; chemical and pharmaceutical industry; or premium and sporting goods.

The producers of electrical and electronic devices, including the lighting industry, are the largest consumers of refractory metal products. In 1998, 1850 t of W products was used for filaments and electrodes in lamps only. Significant quantities of Mo are used for semiconductor base-plates for power rectifiers and in various products for lamps, such as dipped beam shields or support wires. Rapid growth in multimedia and wireless communication networks systems has boosted the need for W–Cu and Mo–Cu heat sink materials. These materials possess a high thermal conductivity combined with a low thermal expansion, close to those of Si and GaAs semiconductors or certain packaging materials. Also, the amount of Mo sputtering targets applied in the production of wiring for large format thin-film transistor LCDs and PDPs has risen significantly owing to the unique combination of low resistivity and high resistance against hillock formation. The electronic industry is the largest market (around 70%) for Ta products, employing the metal mainly in the manufacture of capacitors.

Refractory metals are also widely used by the materials processing industry. Molybdenum glass melting electrodes, TZM and MHC isothermal forging tools, weighing several tons per part, TZM piercing plugs for the production of stainless steel tubes, Mo and Ta crucibles for synthesizing artificial diamond, or TIG-welding electrodes are examples of products in this field. In order to improve the tribological properties of transmission and engine components for automobiles they are coated with Mo.

Recent products in the field of aerospace and defense industry are shaped charge liners made of Mo and Ta penetrators formed explosively. The X-ray anode, a composite product made of W₅Re or W₁₀Re, TZM and optionally graphite, is the essential item of computer-

tomography equipment, a very demanding application that critically depends on the users' expertise.

3.1.9.1 Physical Properties

The atomic and structural properties of the pure refractory metals are listed in Chapt. 2.1, Tables 2.1-16 and 2.1-18. Special features of refractory metals are their low vapor pressure, low coefficient of thermal expansion, and the high thermal and electrical conductivity of Mo and W. This combination of physical properties has opened up a wide range of new applications during the last decade, especially in the field of electronics.

The coefficient of linear thermal expansion, the thermal conductivity, the specific heat, and the electrical resistivity as function of temperature are shown in Figs. 3.1-140 – 3.1-143. The vapor pressure and rate of evaporation are shown in Fig. 3.1-144. In the case of precipitation- and dispersion-strengthened Mo alloys, such as TZM, MHC, ML, MY, and K–Si–Mo,

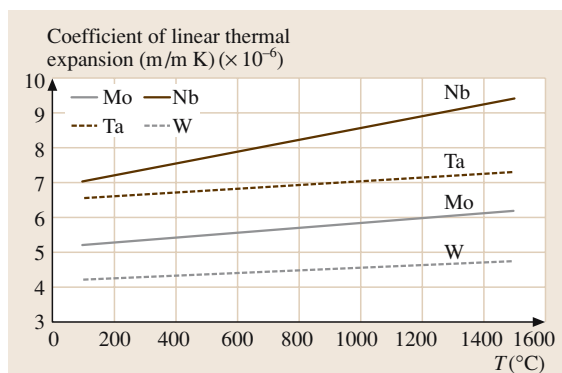


Fig. 3.1-140 Coefficient of linear thermal expansion versus temperature of molybdenum [1.126], tungsten [1.129], niobium [1.127], and tantalum [1.128]

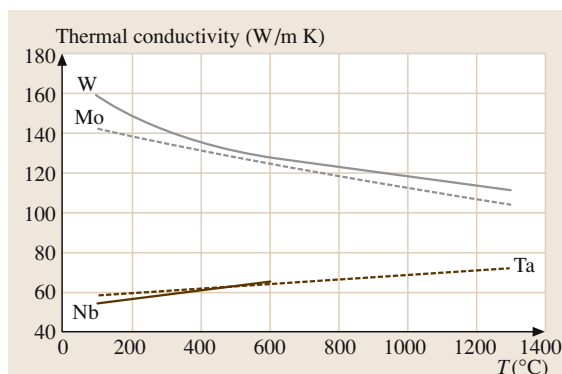


Fig. 3.1-141 Thermal conductivity versus temperature of molybdenum [1.126], tungsten [1.129], niobium [1.127], and tantalum [1.127]

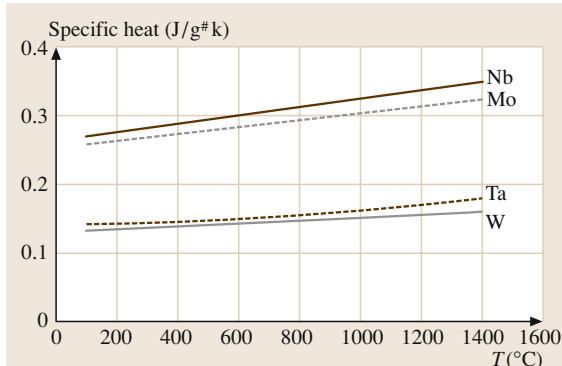


Fig. 3.1-142 Specific heat versus temperature of molybdenum, tungsten, niobium, and tantalum [1.126]

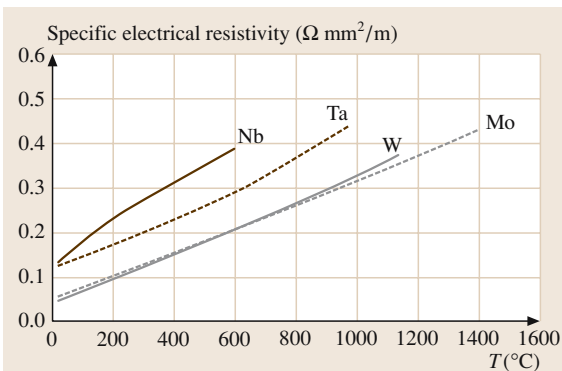


Fig. 3.1-143 Specific electrical resistivity versus temperature of molybdenum [1.126], tungsten [1.126], niobium [1.127], and tantalum [1.127]

as well as the tungsten based alloys AKS–W, WL, WC, and WT, the physical properties do not differ significantly from those of the pure metals. Values for the Young's modulus and its temperature dependence are plotted in Fig. 3.1-145. The Young's moduli of the Group VA metals are considerably lower than those of the Group VIA metals due to the differences in electronic structure.

The strong influence of the surface conditions on the emissivity and lack of information in the literature concerning pre-treatment make it difficult to interpret emissivity data. An overview of emissivity measurements for W, Nb, and Ta at 684.5 nm from 1500 °C up to the liquid phase using laser polarimetry is given in [1.130].

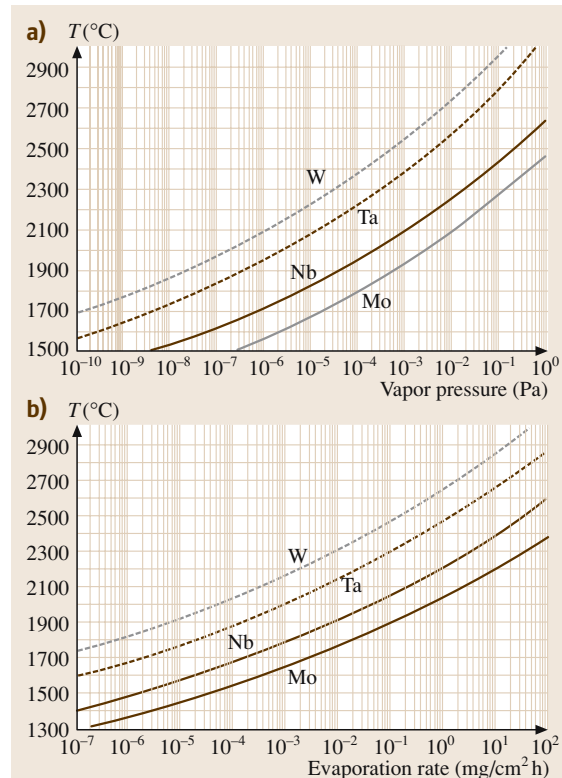


Fig. 3.1-144a,b Vapor pressure (a) and evaporation rate (b) versus temperature of molybdenum, tungsten, niobium, and tantalum [1.129]

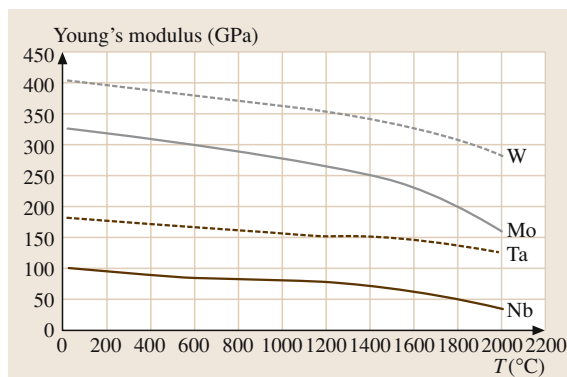


Fig. 3.1-145 Young's moduli versus temperature of molybdenum, tungsten, niobium, and tantalum [1.128]

3.1.9.2 Chemical Properties

Refractory metals are highly resistant to many chemical agents. Tantalum is outstanding in its performance as it is inert to all concentrations of hydrochloric and nitric acid, 98% sulphuric acid, 85% phosphoric acid, and aqua regia below 150 °C. Tantalum is attacked by hydrofluoric acid and strong alkalis, however. The excellent corrosion resistance of Ta is attributed to dense natural oxide layers which prevent the chemical attack of the metal. Niobium is less resistant than Ta and embrittles more easily. Nevertheless the more economical Nb has replaced Ta in some applications. Molybdenum and W are highly resistant to many molten glasses and metals as long as free oxygen is absent.

The interaction with H, N, and O is widely different for Mo and W on the one hand, and Nb and Ta on the other. Molybdenum and W have almost no solubility, whereas Nb and Ta can dissolve a considerable amount of these elements. Hydrogen can be removed from Nb at 300 °C to 1600 °C and from Ta at 800 °C to 1800 °C without metal loss by degassing in high vacuum. For the removal of N, temperatures higher than 1600 °C are recommended. The evaporation of volatile oxides at temperatures above 1600 °C in high vacuum leads to a reduction of the oxygen content in Nb and Ta. But during such heat treatments, metal is evaporated simultaneously.

An overview on the resistance of pure Mo, W, Nb, and Ta against different media is given in Tables 3.1-109 to 3.1-111. In accordance with the definition given

in [1.131], a material is considered “stable” against a corrosive medium if the metal loss is < 0.1 mm per year. If the loss of material is between 0.1 and 1.0 mm per year, the material is “considerably stable;” and it is “fairly unstable” if the loss of material is between 1.0 and 3.0 mm. The material is “unsuitable” in an environment if the metal loss is > 3.0 mm per year.

Oxidation Behavior

Refractory metals require protection from oxidizing environment as they do not form protective oxide layers. Oxidation of Mo and W leads to a loss of material by the formation of volatile oxides above 600 °C in case of Mo and 750 °C in case of W, respectively, but without any significant impact on the mechanical properties.

The low temperature oxidation of Mo and W often causes problems in practical use as thin corrosion films are formed during storage in moist air. The surface topography of Mo has a strong impact on the reaction rate. The corrosion film contains oxygen but also chemically-bonded nitrogen, which is incorporated in the film during film growth. C_xH_y residues are the nuclei for the oxidative attack in the early stage of film growth [1.132].

There is extensive evidence that between 300 and 500 °C, oxide-dispersion-strengthened (ODS) refractory metal alloys (e.g., Mo–La₂O₃ and Mo–Y₂O₃ grades) possess markedly reduced oxidation rates compared to the pure metals [1.133]. In-situ oxidation and evaluation of the binding state reveal that MoO₂ dominates over MoO₃ both for Mo and Mo–

Table 3.1-109 Metal loss of Mo, W, Nb and Ta in millimeter per year (mm/yr) in acids, alkalis and salt solutions

| Corroding agent (aqueous solution) | Temperature | Metal loss (mm/yr) | | | |
|---------------------------------------|-------------|--------------------|--------|-----------------------|-------------------------|
| | | Mo | W | Nb | Ta |
| 10% HCl | 20 °C | < 0.003 | 0.002 | 0 | < 0.001 |
| 10% H ₂ SO ₄ | 20 °C | < 0.005 | < 0.1 | < 0.1 | < 0.1 |
| 10% HNO ₃ | 20 °C | 18.6 | < 0.25 | < 0.013 | < 0.013 |
| 3% HF | 20 °C | < 0.001 | < 0.1 | > 3.0 | > 3.0 |
| 10% CH ₃ COOH | 20 °C | 0.07 | < 0.05 | < 0.1 | < 0.013 |
| 10% KOH | 20 °C | < 0.1 | < 0.1 | < 0.2 | < 0.1 |
| 3% NaCl | 20 °C | < 0.1 | < 0.1 | < 0.1 | < 0.1 |
| 10% HCl | 100 °C | < 0.025 | 0.005 | 0.005 (embrittlement) | < 0.025 |
| 10% H ₂ SO ₄ | 100 °C | 0.17 | < 0.25 | < 0.001 | 0 |
| 10% HNO ₃ | 100 °C | 150 | < 0.25 | < 0.076 | < 0.025 |
| 3% HF | 100 °C | 0.18 | 0.15 | > 3.0 | > 3.0 |
| 10% CH ₃ COOH | 100 °C | 0.033 | < 0.05 | < 0.1 | < 0.013 |
| 10% KOH | 100 °C | 0.054 | 0.01 | 1.2 (embrittlement) | < 0.003 (embrittlement) |
| 3% NaCl | 100 °C | < 0.1 | < 0.1 | < 0.1 | < 0.1 |

Table 3.1-110 Maximum temperatures for the resistance of Mo, W, Nb, and Ta against metal melts (up to the stated temperatures the solubility of the refractory metal in the metal melts and vice versa is negligible)

| Metal melt | Maximum resistance temperature (°C) | | | |
|------------|-------------------------------------|---------------|---------------|---------------|
| | Mo | W | Nb | Ta |
| Al | Not resistant | 680 | Not resistant | Not resistant |
| Pb | 1100 | 1100 | 850 | 1000 |
| Fe | Not resistant | Not resistant | Not resistant | Not resistant |
| Ga | 300 | 800 | 400 | 450 |
| K | 1200 | 900 | 1000 | 1000 |
| Cu | 1300 | Resistant | Resistant | Resistant |
| Mg | 1000 | 600 | 950 | 1150 |
| Na | 1030 | 900 | 1000 | 1000 |
| Hg | 600 | 600 | 600 | 600 |
| Zn | 500 | 750 | Not resistant | 500 |
| Sn | 550 | 980 | Not resistant | 260 |
| Ag | Resistant | Resistant | Resistant | 1200 |

Table 3.1-111 Maximum temperatures for the resistance of Mo, W, Nb, and Ta against gaseous media at atmospheric pressure

| Gaseous media | Maximum resistance temperature | | | |
|-----------------|--|---|--|--|
| | Mo | W | Nb | Ta |
| Air and oxygen | see Sect. 3.1.9.2 | | | |
| Hydrogen | Resistant | Resistant | 250 °C ($T > 250$ °C embrittlement owing to dissolved hydrogen) | 300 °C ($T > 300$ °C embrittlement owing to dissolved hydrogen) |
| Nitrogen | Resistant | Resistant | 300 °C ($T > 300$ °C embrittlement owing to dissolved nitrogen) | 400 °C ($T > 400$ °C embrittlement owing to dissolved nitrogen) |
| Ammonia | Resistant (except 1000–1100 °C: nitration) | Resistant (except 700–1150 °C: nitration) | 300 °C ($T > 300$ °C embrittlement owing to dissolved nitrogen) | 700 °C ($T > 700$ °C embrittlement owing to dissolved nitrogen) |
| Water vapor | 700 °C | 700 °C | 200 °C | 200 °C |
| Carbon monoxide | 800 °C ($T > 800$ °C carburization) | 1000 °C ($T > 800$ °C carburization) | 800 °C | 1100 °C |
| Carbon dioxide | 1200 °C ($T > 1200$ °C oxidation) | 1200 °C ($T > 1200$ °C oxidation) | 400 °C | 500 °C |

0.47 wt% Y₂O₃–0.08 wt% Ce₂O₃ (Fig. 3.1-146). These results are confirmed when comparing the thickness of the oxide layer formed at 500 °C in air (Fig. 3.1-147). The enhanced oxidation resistance of doped samples cannot be attributed to a chemical but rather to a morphological-mechanical effect. Investigations of the surface of pure Mo samples subjected to long-term oxidation reveal a network of cracks in the MoO₂ layer which drastically diminishes the passivating effect of

this layer by facilitating a further attack by O. Such cracks cannot be found on the surface of oxidized Mo–La₂O₃ and Mo–Y₂O₃ samples [1.133].

Above 700 °C for Mo and approximately 900 °C for W, evaporation of the volatile oxides MoO₃ and WO₃ is the rate-controlling process and the oxidation follows a linear time dependence. Above 2000 °C for Mo and 2400 °C for W, the metal loss increases because of the increasing vapor pressure of the pure metals. The time

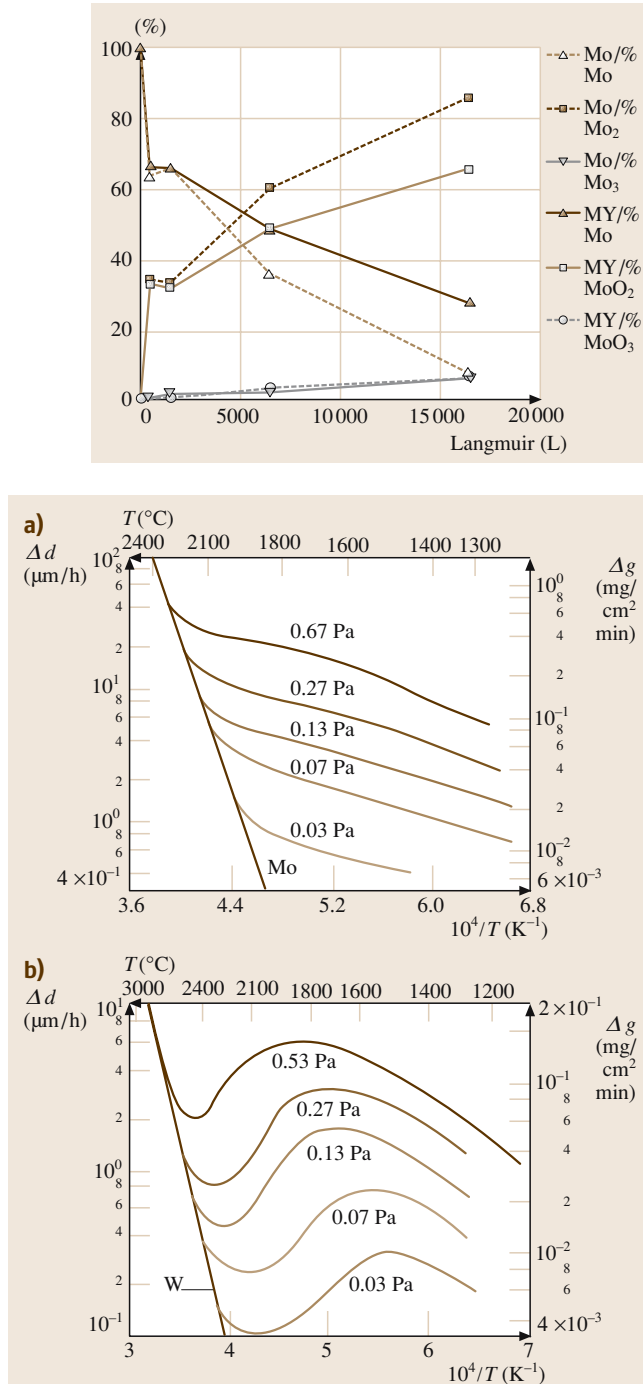


Fig. 3.1-148a,b Metal loss in air for Mo (a) and W (b) at $T \geq 1200^\circ\text{C}$ [1.134]

The dependence of metal loss for Mo and W at $T \geq 1200^\circ\text{C}$ is shown in Fig. 3.1-148 [1.134].

The oxidation rates of Nb and Ta strongly depend on temperature, pressure, and time. Different mechanisms causing different oxidation rates can be observed and metastable sub-oxides are formed during use in O-containing atmospheres [1.131, 134]. Oxygen is dissolved in the metal matrix which leads to significant changes of the mechanical properties. A poorly adherent, porous pentoxide is formed on the metal surface which does not protect the metal from further attack. Oxygen which has penetrated the porous oxide layer diffuses along the grain boundaries of the metal, leading to drastic embrittlement.

The metal loss at 1100 °C due to oxidation in air is shown for Mo, W, Nb, and Ta in Fig. 3.1-149 [1.135]. The embrittled zone caused by oxygen diffusion into the substrate is not considered in this diagram.

Only a few coating systems have been found to prevent the refractory metals from oxidation. In the case of Mo, Pt-clad components with a diffusion barrier interlayer on the basis of alumina, which prevents the formation of brittle intermetallic molybdenum–platinum

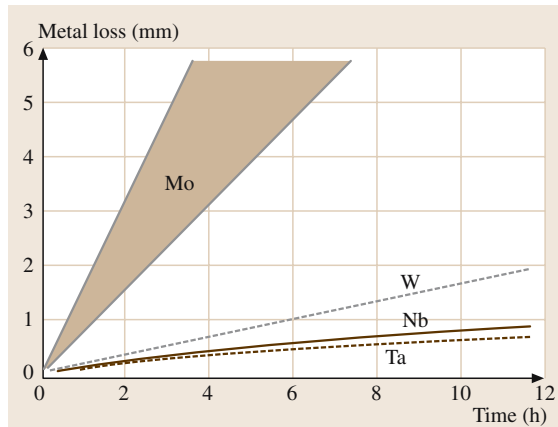


Fig. 3.1-149 Oxidation behavior of Mo, W, Nb, and Ta at 1100 °C [1.135]

phases, are used; e.g., for stirrers used to homogenize special glasses. Mo components for glass tanks and glass melting electrodes are protected from oxidation by coatings based on silicides, such as Si–B [1.136]. Silicon–boron and other silicide based coatings, such as Si–Cr–Fe or Si–Cr–Ti, are also used to protect Mo and Nb based alloys from oxidation in aerospace applications [1.135, 137–139]

3.1.9.3 Recrystallization Behavior

The mechanisms and kinetics of recovery and recrystallization processes significantly affect the processing and application of refractory metals. The homologous temperatures (T/T_M in K) for obtaining 50% recrystallized structure during annealing for one hour, range from 0.39 for Mo, 0.41 for W, 0.42 for Nb, to 0.43 for P/M Ta. The fraction of recrystallized structure as a function of the annealing temperature of Mo, W, P/M Ta, TZM, and Mo–0.7 wt%La₂O₃ sheets of 1 mm thickness is shown in Fig. 3.1-150. Experimental data on the evolution of grain size with the annealing temperature for pure Mo and Ta sheets of 1 mm thickness are shown in Fig. 3.1-151 [1.126, 140]. A recrystallization diagram for Mo is published in [1.141], and for P/M Ta in [1.142].

Compared to pure Mo, the recrystallization temperature of the carbide-precipitation-hardened alloy TZM is increased by 450 °C and that of Mo–0.7 wt%La₂O₃ by 550 °C. The data listed in Table 3.1-112 show that all those alloys containing particles, which deform together with the matrix metal (ML, K–Si–Mo, WL10, WL15, WT20, and AKS–W–ThO₂), reveal a significantly increased recrystallization temperature in the highly de-

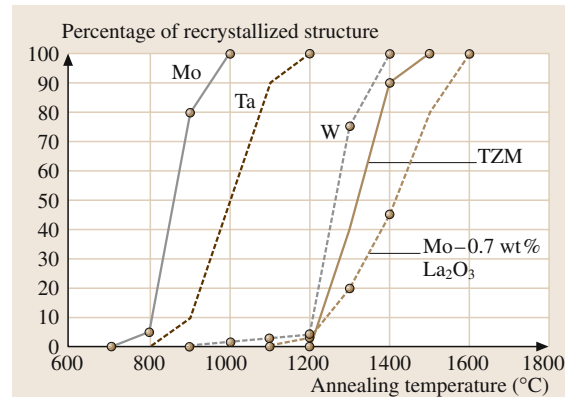


Fig. 3.1-150 Fraction of recrystallized structure versus annealing temperature (annealing time $t_a = 1$ h) for Mo, P/M Ta, W, TZM, and Mo–0.7 wt%La₂O₃ sheets with a thickness of 1 mm, degree of deformation, $\varphi = \frac{th_p - th_s}{th_p} 100[\%]$, where th_p = thickness of sintered plate, and th_s = thickness of rolled sheet. Mo: $\varphi = 94\%$, P/M Ta: $\varphi = 98\%$, W: $\varphi = 94\%$, TZM: $\varphi = 98\%$, Mo–0.7 wt%La₂O₃: $\varphi = 99\%$ [1.126]

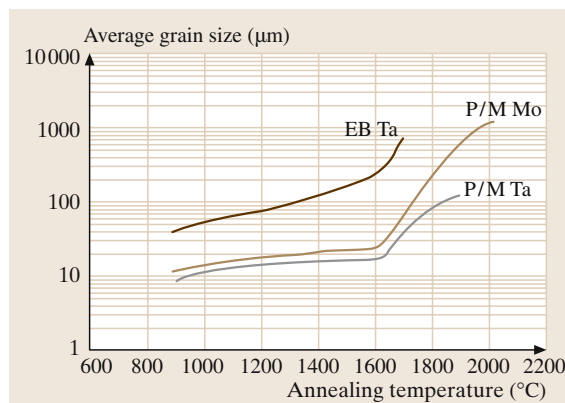


Fig. 3.1-151 Grain size versus annealing temperature (annealing time $t_a = 1$ h) for Mo, P/M Ta, and EB Ta sheets with a thickness of 1 mm. Mo: $\varphi = 94\%$, P/M Ta: $\varphi = 98\%$, EB Ta: $\varphi = 98\%$ [1.126, 140]

formed state. Increasing the degree of deformation from $\varphi = 90\%$ to $\varphi = 99.99\%$ leads to a further increase of the recrystallization temperature (100% recrystallized structure, 1 h annealing time) ranging from 600 °C for K–Si–Mo, 700 °C for ML, 950 °C for WT20, 1000 °C for WL10, to 1050 °C for WL15 and WC20. This can be explained by particle refinement. During the deformation process the particles are elongated. During annealing they break up and rows of smaller particles

Table 3.1–112 Typical recrystallization temperature and ultimate tensile strength of commercial Mo and W based rod and wire materials with a defined degree of total deformation φ [1.118]

| Alloy designation | Composition (wt%) | Temperature for 100% recrystallized structure ($t = 1\text{ h}$) (°C) | Typical ultimate tensile strength at 1000 °C (MPa) |
|------------------------|---|---|--|
| Pure Mo | | 1100 ($\varphi = 90\%$) | 250 ($\varphi = 90\%$) |
| TZM | Mo, 0.5% Ti, 0.08% Zr, 0.025% C | 1400 ($\varphi = 90\%$) | 600 ($\varphi = 90\%$) |
| MHC | Mo, 1.2% Hf, 0.08% C | 1550 ($\varphi = 90\%$) | 800 ($\varphi = 90\%$) |
| ML | Mo, 0.3% La_2O_3 | 1300 ($\varphi = 90\%$), 2000 ($\varphi = 99.99\%$) | 300 ($\varphi = 90\%$) |
| MY | Mo, 0.48% La_2O_3 , 0.07% Ce_2O_3 | 1100 ($\varphi = 90\%$), 1350 ($\varphi = 99.99\%$) | 300 ($\varphi = 90\%$) |
| K–Si–Mo | Mo, 0.05% Si, 0.025% K | 1200 ($\varphi = 90\%$), 1800 ($\varphi = 99.99\%$) | 300 ($\varphi = 90\%$) |
| Mo50Re | Mo, 47.5% Re | 1300 ($\varphi = 90\%$) | 600 ($\varphi = 90\%$) |
| Mo30W | Mo, 30% W | 1200 ($\varphi = 90\%$) | 350 ($\varphi = 90\%$) |
| Pure W | | 1350 ($\varphi = 90\%$) | 350 ($\varphi = 90\%$) |
| AKS-W | W, 0.005% K | 2000 ($\varphi = 99.9\%$) | 800 ($\varphi = 99.9\%$) |
| WL10 | W, 1.0% La_2O_3 | 1500 ($\varphi = 90\%$), 2500 ($\varphi = 99.99\%$) | 400 ($\varphi = 90\%$) |
| WL15 | W, 1.5% La_2O_3 | 1550 ($\varphi = 90\%$), 2600 ($\varphi = 99.99\%$) | 420 ($\varphi = 90\%$) |
| WC20 | W, 1.9% Ce_2O_3 | 1550 ($\varphi = 90\%$), 2600 ($\varphi = 99.99\%$) | 420 ($\varphi = 90\%$) |
| WT20 | W, 2% ThO_2 | 1450 ($\varphi = 90\%$), 2400 ($\varphi = 99.99\%$) | 400 ($\varphi = 90\%$) |
| AKS-W–ThO ₂ | W, 1% ThO_2 , 0.004% K | 2400 ($\varphi = 99.9\%$) | 1000 ($\varphi = 99.9\%$) |
| W5Re | W, 5 Re | 1700 ($\varphi = 90\%$) | 500 ($\varphi = 90\%$) |
| W26Re | W, 26 Re | 1750 ($\varphi = 90\%$) | 900 ($\varphi = 90\%$) |

are formed. With the increase in number of particles, the subgrain boundaries are pinned more effectively, resulting in an increase of the recrystallization temperature [1.119].

Experiments with various oxide-dispersion-strengthened (ODS) Mo materials with 2 vol.% of oxide, mean oxide particle sizes in the as-sintered state of around $0.8\text{ }\mu\text{m}$, and a degree of deformation $\ln(A_0/A) = 8.5$ (A_0 = cross section as-sintered, A = cross section as-deformed), revealed differences in the recrystallization temperature of up to 750 °C depending on the oxide used. It could be shown that this effect is caused by particle refinement during deformation and subsequent heat treatment. Particles which increase the recrystallization temperature very effectively, as is the case with La_2O_3 , show a high particle deformability [1.143].

Whether oxide particles deform in a pseudo-plastic manner or not depends on a multitude of parameters, such as the yield stress of the particles, the yield stress of the matrix, the particle/matrix bonding strength, the crystallite size, the defect density, or the state of stresses. Most of these parameters are unknown or difficult to measure. Good correlation could be found between the particle deformability, with its effect on the increase of the recrystallization temperature, and the fraction of ionic bonding character of the oxide, following the definition of Pauling [1.143]. Figure 3.1–152 shows that

compounds with a high fraction of ionic bonding character, such as La_2O_3 or SrO , raise the recrystallization temperature very effectively. Slight particle multiplication could also be found for Al_2O_3 , ZrO_2 , and HfO_2 compounds with a marked covalent bonding character, but because of breakage of the particles during the deformation process.

The recrystallization temperature can be tailored by varying both the type and the content of the oxide, the lat-

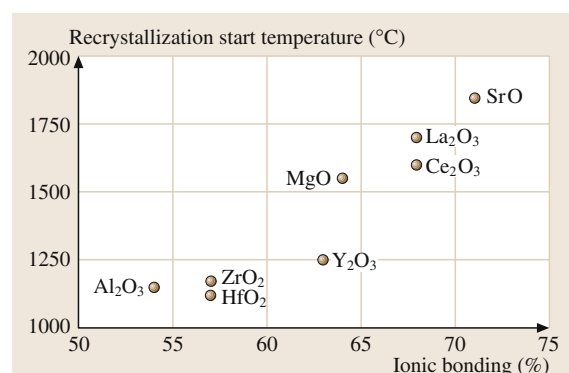


Fig. 3.1–152 Recrystallization start temperature of various ODS Mo materials versus fraction of ionic bonding (according to Pauling) of the respective oxides. Oxide content = 2 vol.%, wire diameter = 0.6 mm [1.143]

ter shown in Fig. 3.1-153 for Mo–0.03 wt%La₂O₃ (ILQ) and Mo–0.3 wt%La₂O₃ (ML).

AKS-W shows a similar effect where the K-containing bubbles are effective pinning centers. The recovery and recrystallization mechanisms of AKS-W as a function the annealing temperature are summarized in Table 3.1-113.

The recrystallization temperature of AKS-W is determined by the relation of the driving to dragging forces. The driving forces are determined by the thermomechanical treatment (TMT), the dragging forces depend on the number, size, and distribution of the K bubbles. With increasing degree of deformation, both the driving forces (increasing dislocation density and low-angle/high-angle boundary volume) and dragging forces (increasing length of stringers of K-filled pores and, as a consequence, increasing number of K bubbles formed) become larger. During the first deformation

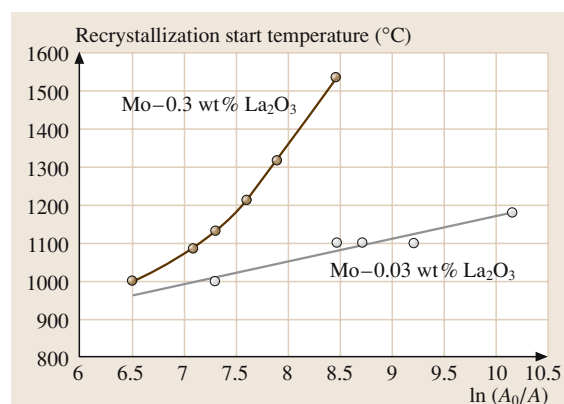


Fig. 3.1-153 Recrystallization start temperature of Mo–0.03 wt%La₂O₃ and Mo–0.3 wt%La₂O₃ wires versus degree of deformation $\ln(A_0/A)$ [1.133]

Table 3.1-113 Recrystallization mechanisms for AKS-W wires [1.120, 144, 145]

| Microstructural state | Processes |
|--|--|
| Evolution of the microstructure during wire drawing | <ul style="list-style-type: none"> Formation of a dislocation cell structure by static and dynamic recovery processes |
| Coarsening of the microstructure during annealing | <ul style="list-style-type: none"> Annealing temperature 800 to 1400 °C: <ul style="list-style-type: none"> Reduction of the dislocation density within the cell walls; Break-up of the K-containing stringers into pearl rows of bubbles; Migration of longitudinal grain boundaries is strongly reduced by pearl rows of bubbles; Similar ⟨110⟩ texture as in the as-worked state. For low heating rates, partial or even entire bubble rows can be dragged by the boundaries moving in the transverse direction. As a result, row/row collision and bubble coalescence can occur The temperature up to which the coarsened substructure remains stable depends on the degree of deformation (e.g., diameter 0.18 mm: 2100 °C/15 min). The coarsened substructure has a significant portion of high-angle grain boundaries (misorientation angles higher than 15°) |
| Exaggerated grain growth | <p>Nucleation and growth of large interlocking grains occur by primary recrystallization, whereby a subgrain begins to grow laterally at the expense of neighboring polygonized subgrains.</p> <ul style="list-style-type: none"> Because of the pearl row of bubbles, the rate of grain boundary movement is higher in the axial, than in the transverse direction Because of the interaction between the bubbles and the growing grains, the grain boundaries possess a wave-like, interlocking structure The grain aspect ratio of the recrystallized structure increases with increasing number of K bubbles. The number of K bubbles is a function of the K-content, the degree of deformation and the TMT. Highly deformed, recrystallized wires reveal a ⟨531⟩ texture. |

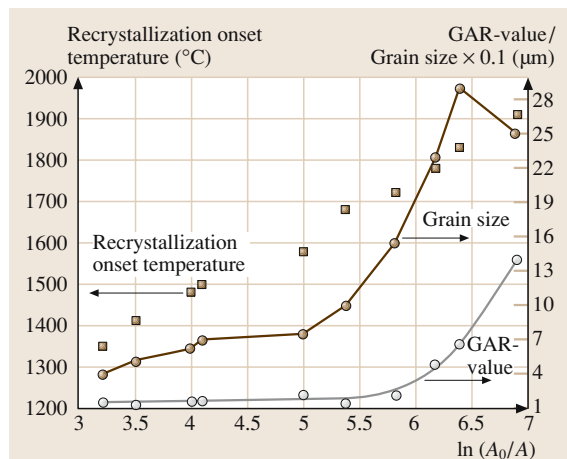


Fig. 3.1-154 Recrystallization onset temperature, grain size, and grain aspect ratio (GAR) versus $\ln(A_0/A)$. AKS-W grade with K content of 42 $\mu\text{g/g}$; deformation temperature below the onset temperature of recrystallization; no intermediate heat treatments above recrystallization temperature; annealing time = 15 min; heating rate = 3 K/s; annealing atmosphere = hydrogen; annealing temperature for GAR evaluation = 2200 °C ($t_a = 5$ min); grain size measured in transverse direction [1.133]

steps the increase of the driving forces outweighs that of the dragging forces. Then the rise of the dragging forces starts to dominate, resulting in an increase of the recrystallization temperature (see Fig. 3.1-154). With increasing length of the K stringers/number of K bubbles, the significance of the dragging effect in the transverse direction increases, resulting in an increase of the grain aspect ratio (GAR) in the recrystallized state. A marked increase of the GAR starts at a degree of deformation that coincides with a pronounced increase of the transverse grain size, as illustrated in Fig. 3.1-154.

3.1.9.4 Mechanical Properties

Influence of Thermomechanical Treatment (TMT) and Impurities

Molybdenum and Tungsten Alloys [1.133]. The formation of a cellular dislocation structure increases both strength and fracture toughness [1.146, 147]. Additionally, the mechanical properties depend on the type of deformation process, purity, and heat treatment. The thermomechanical treatment (TMT) serves to obtain the specified shape, to eliminate the porosity, and to adjust the mechanical and structural properties. In particular,

the evolution of the density distribution, pore size and shape, and its interaction with the mechanical properties are of high importance [1.120, 148–150].

During hot deformation which is usually the primary working step for both Mo and W, high-angle grain boundaries are formed and migrate, grains are subdivided by low-angle boundaries, and new large-angle boundaries are formed by coarsening of the substructure [1.151]. Grains with an aspect ratio close to one and a low dislocation density are formed.

Following this hot deformation, the material is processed at temperatures below the recrystallization onset temperature, but above the onset temperature of polygonization, leading to a cellular dislocation structure. The cell boundaries become impenetrable for slip dislocations and behave like grain boundaries, when the misorientation between neighboring cells is higher than a critical value of about 4° for Mo and W [1.146]. The formation of a misoriented cellular dislocation structure results both in an increase of strength and a decrease of the ductile-brittle-transition temperature (DBTT). Both effects become more and more significant with increasing degree of deformation which results in a smaller effective grain size [1.146]. The size of the misoriented cellular dislocation structure depends sensitively on the deformation temperature. A high deformation temperature implies large grains [1.152]. It is essential to control the deformation temperature carefully. The control of the microstructure at intermediate steps has also been recommended [1.153].

The production yield is mainly decreased by the formation of grain boundary cracks. The cohesion of the grain boundaries is believed to be the controlling factor limiting the ductility of Mo and W [1.154]. Impurities segregated at the grain boundaries can lead to a strong decrease in ductility. Based on both semi-empirical and first principle modeling of the energetics and the electronic structures of impurities on a $\Sigma 3$ (111) grain boundary in W, it was concluded that the impurities N, O, P, S, and Si weaken the intergranular cohesion, while B and C enhance the interatomic interaction across the grain boundary [1.154].

The amount of O in Mo ($\approx 10 \mu\text{g/g}$) and W ($\approx 5 \mu\text{g/g}$) is sufficient to form a monolayer of O on the grain boundaries as long as the grain size is not smaller than 10 μm . During recrystallization a migrating grain boundary can be saturated by collecting impurities while sweeping the volume. Based on the investigation of arc-cast Mo samples, a beneficial effect of C was found and attributed to the following mechanisms [1.155]:

- Suppression of oxygen segregation
- Precipitation of carbides, acting as dislocation sources
- Formation of an epitaxial relationship between precipitates and bulk crystals at grain boundaries

From these findings it was proposed that a C/O atomic ratio of >2 should improve the mechanical properties of Mo. The results obtained with arc-cast samples published in [1.155] could not be reproduced for samples produced by a P/M route [1.157].

As a consequence of the above mentioned effects, but in contrast to many other metallic materials, the fracture toughness of Mo and W is strongly reduced with increasing degree of recrystallization. With increasing plastic deformation, the fracture toughness increases (see Sect. 3.1.9.4), combined with a transition from intercrystalline to transcrystalline cleavage and to a transcrystalline ductile fracture [1.147, 158, 159].

With increasing degree of deformation the working temperature can be progressively reduced. In particular, products with a high degree of deformation such as wires, thin sheets, and foils can be subjected to a high degree of deformation at a temperature below the polygonization temperature. The reduction of grain boundaries oriented transversely to the drawing direction increases the bending ductility of W [1.160]. Tungsten wire with an optimum ductility can only be obtained, when deformed in such a way that dynamic recovery processes occur without polygonization [1.161]. Other recovery phenomena, besides polygonization, are described in [1.162]. However a high degree of deformation below the onset temperature for dynamic polygonization favors the formation of longitudinal cracks.

Thin sheets and foils, annealed under conditions resulting in a small fraction of primarily recrystallized grains, can show a very specific fracture behavior, i. e., cracks running at an angle of 45° to the rolling direction [1.163, 164]. Such 45° embrittlement is caused by the nucleation of critical cracks at isolated grains formed by recrystallization of weak secondary components of the texture. Cracks propagate under 45° to the rolling direction owing to the alignment of the cleavage planes in the rolling texture.

Niobium and Tantalum Alloys. Contrary to Mo and W, pure Nb and Ta are deformed at room temperature. Only highly-alloyed materials require breaking down the ingot microstructure either by forging or extrusion at elevated temperatures. In these

cases the ingot has to be protected to prevent an interaction with the atmosphere. The mechanical behavior of pure annealed Nb and Ta is characterized by a high ductility and low work-hardening rate. The influence of deformation on the yield strength and fracture elongation of pure Ta is shown in Fig. 3.1-155.

Mechanical properties of Nb- and Ta-based alloys are strongly influenced by interstitial impurities, e.g., oxygen, nitrogen, carbon, and hydrogen. The generally lower content of impurities and the larger grain size are the reasons why melt-processed Nb and Ta have a lower room-temperature tensile strength compared to sintered material. As an example, the influence of oxygen on the mechanical properties of Ta is presented in Fig. 3.1-156.

After deformation both Nb- and Ta-based alloys are usually heat treated in high vacuum before delivering in order to achieve a fine grained primarily recrystallized microstructure.

Static Mechanical Properties

Properties at Low Temperatures and Low Strain Rates.

The flow stress of the transition metals Mo, W, Nb, and Ta is strongly dependent on temperature and a strain rate below a characteristic transition temperature T_K ("knee" temperature) (corresponding to 0.1 to 0.2 of the absolute melting temperature) and plastic strain rates below $1 \times 10^{-5} \text{ s}^{-1}$ [1.165]. As an example, experimental data on the temperature dependence of the flow stress of recrystallized Ta are shown in Fig. 3.1-157. This dependence has

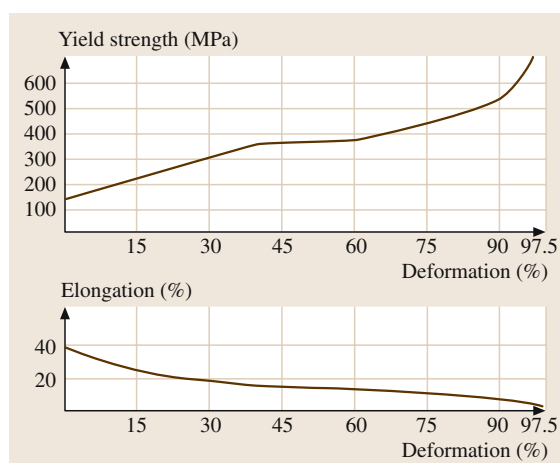


Fig. 3.1-155 Yield strength and fracture elongation of tantalum versus degree of deformation [1.156]

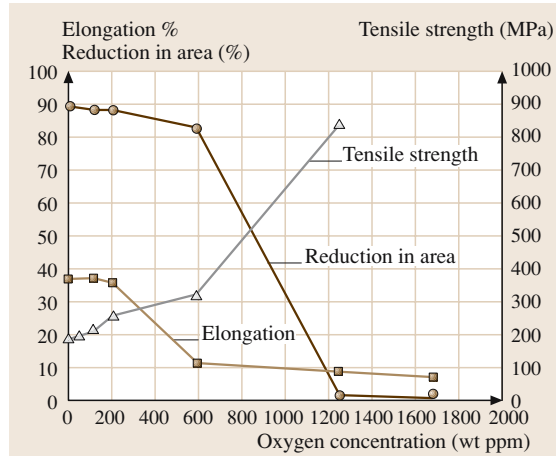


Fig. 3.1-156 Tensile strength, fracture elongation, and reduction in area versus oxygen concentration of tantalum specimens tested at room temperature [1.168]

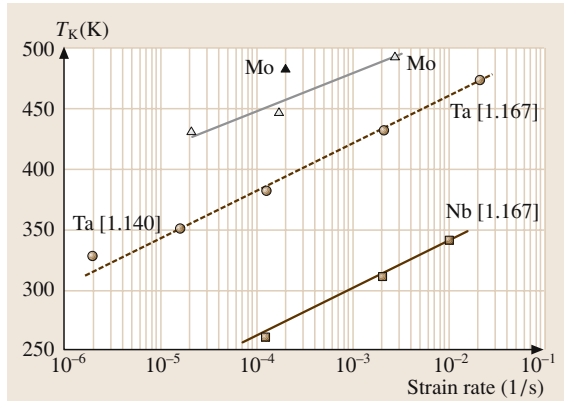


Fig. 3.1-158 Dependence of T_K on strain rate [1.140, 167]

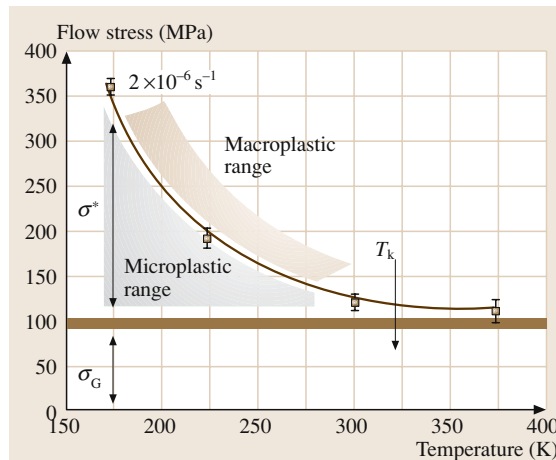


Fig. 3.1-157 Temperature dependence of the flow stress (at $\epsilon_{pl} = 1 \times 10^{-5}$) of recrystallized Ta under monotonic loading and $d\epsilon/dt = 2 \times 10^{-6} \text{ s}^{-1}$, T_K = ‘knee’ temperature, σ_G = athermal range, σ^* = thermal range [1.140]

been attributed to the characteristic behavior of screw dislocations [1.166]. The transition temperature T_K was shown to depend on the strain rate (Fig. 3.1-158) [1.140, 167].

For test temperatures $T < T_K$ the flow stress increases markedly. Borderlines between elastic/anelastic strain (σ_A) and microstrain/macrostrain deformation ranges can be deduced, subdivided into athermal (σ_G) and thermal (σ^*) ranges. The lower borderline of the microplastic region is almost independent of tem-

perature and may be called the intrinsic flow stress which is much lower than the conventionally determined flow stress (technical flow stress). In the stress range between the intrinsic and the technical flow stress below T_K , strains of up to several percent were observed after extended loading times for Mo and Ta [1.169, 170]. The effect of temperature and strain rate on the monotonic microflow behavior of bcc metals as functions of temperature and strain rate was presented schematically [1.171]. Experimental data for Mo and Ta in constant load tests (low temperature creep tests) for stresses considerably below the technical flow stress are shown in Figs. 3.1-159 and 3.1-160. After a considerable incubation period, depending on the test temperature and stress, a rapid increase in strain can be noticed approaching a saturation strain which depends on the stress level. The effect of the loading rate on the instantaneous plas-

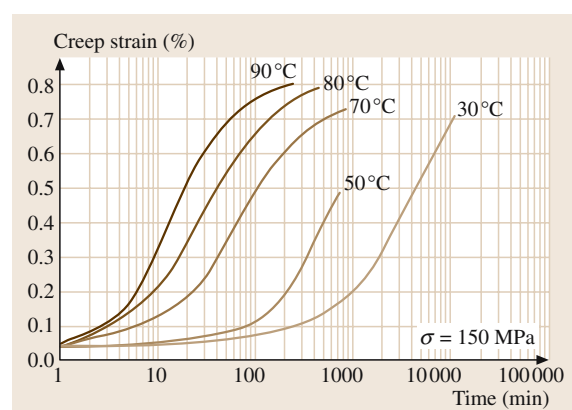


Fig. 3.1-159 Creep elongation of recrystallized Mo at $\sigma = 150 \text{ MPa}$ for $30^\circ\text{C} \leq T \leq 90^\circ\text{C}$ [1.126]

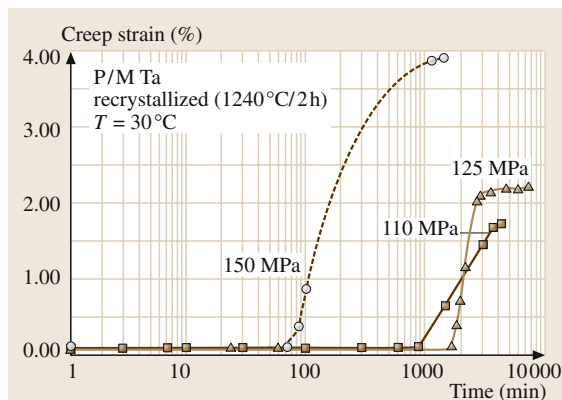


Fig. 3.1-160 Creep elongation of recrystallized Ta sheets (thickness = 2 mm) at 30 °C for $110 \text{ MPa} \leq \sigma \leq 150 \text{ MPa}$ [1.126]

tic strain can be revealed with high resolution in loading-unloading tests under various constant loading rates [1.140, 170]. This microflow behavior may be significant for components at low temperatures and low loads, e.g., under storage conditions. Internal stresses in semi-finished products may be reduced even at room temperature to levels corresponding to the intrinsic flow stress [1.170].

A significant influence of the strain rate on the tensile properties at room temperature was determined for recrystallized Mo and Ta (Fig. 3.1-161) [1.140], in close agreement with literature data [1.172]. This strain rate effect makes it imperative for comparison of test data to list the test conditions.

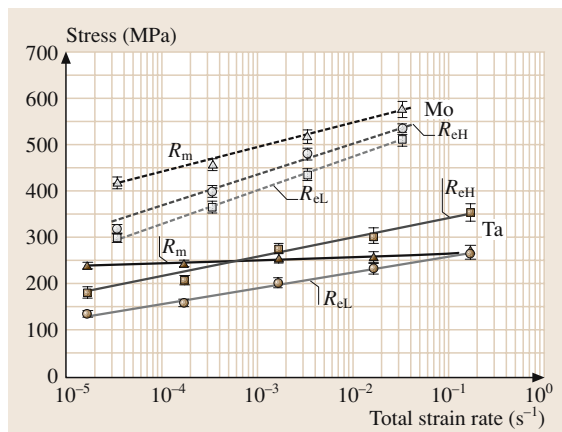


Fig. 3.1-161 Effect of strain rate on tensile properties at room temperature of recrystallized Mo and recrystallized Ta [1.140]

Properties at Elevated Temperatures. A rough ranking of the high temperature strength of Mo and W alloys can be obtained from the comparison presented in Table 3.1-112 (Sect. 3.1.9.3). Carbide-precipitation-strengthened Mo-based alloys (MHC, TZM) and alloys high in Re (Mo-50 wt%Re, W-26 wt%Re) have the highest tensile strength. Alloys containing K (AKS-W, AKS-W-ThO₂) exhibit high strength only in the case of a high preceding plastic deformation.

A comparison of the high-temperature strength of rods made of Mo, W, Nb, and Ta in their usual state of delivery is given in Fig. 3.1-162. The typical microstructure of stress-relieved Mo is a highly polygonized structure with up to 5% recrystallized grains. Depending on the product shape W is delivered in the as-worked state, especially in case of sheet material and wires, or stress-relieved with a polygonized microstructure.

The decrease of tensile strength and the increase of reduction in area with increasing test temperature can be related to changes in the fracture mode (Fig. 3.1-163), i.e., cleavage fracture, brittle grain boundary failure, and ductile transcrystalline failure [1.158].

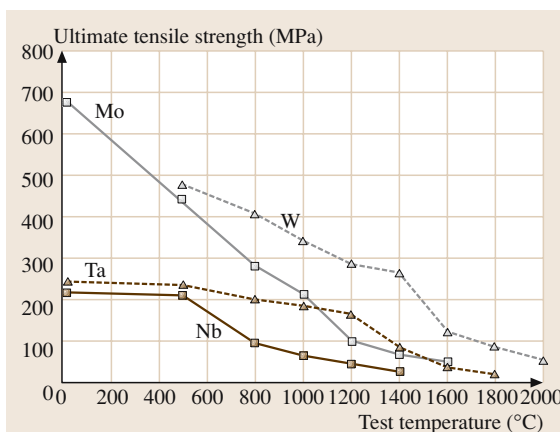


Fig. 3.1-162 Ultimate tensile strength versus test temperature for Mo, W, Ta, and Nb rods in their usual delivering condition. Mo, W: diameter = 25 mm (stress relieved); Ta, Nb: diameter = 12 mm (recrystallized); technical strain rates = $1.0 \times 10^{-4} \text{ s}^{-1}$ up to the 0.2% yield strength followed by $3.3 \times 10^{-3} \text{ s}^{-1}$ (Mo, room temperature), $1.7 \times 10^{-3} \text{ s}^{-1}$ (Mo, elevated temperatures), $8.3 \times 10^{-4} \text{ s}^{-1}$ (W, elevated temperatures), $6.7 \times 10^{-4} \text{ s}^{-1}$ up to the 0.2% yield strength followed by $3.3 \times 10^{-3} \text{ s}^{-1}$ (Nb, Ta for all test temperatures) [1.118]

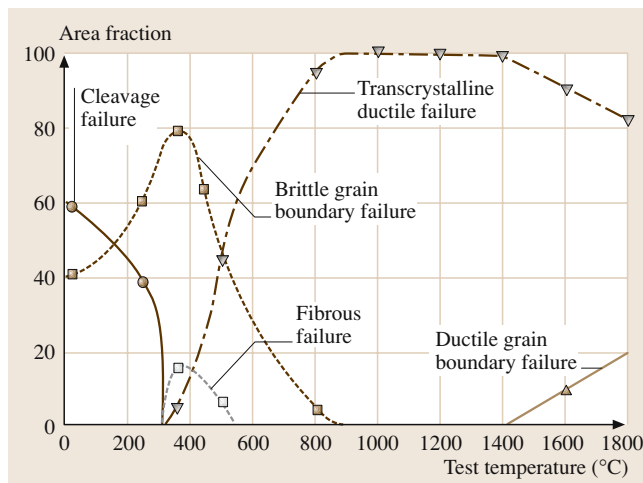


Fig. 3.1-163 Effect of test temperature on fracture modes of pure W, stress relieved at 1000 °C/6 h [1.158]

Fig. 3.1-164a,b The ultimate tensile strength R_m (a) and the yield strength $R_{p0.2}$ (b) versus test temperature of P/M Ta, P/M Ta2.5W, and P/M Ta10W sheets that are 1 mm thick, with impurity content ($\mu\text{g/g}$) Ta: O = 60, N = 10, H = 1.8, C < 5; Ta2.5W: O = 70, N = 12, H = 2.4, C = 5; Ta10W: O = 31, N < 5, H < 1, C = 21; material condition = recrystallized, technical strain rates = $6.7 \times 10^{-4} \text{ s}^{-1}$ up to $R_{p0.2}$, followed by $3.3 \times 10^{-3} \text{ s}^{-1}$ [1.126]

The influence of alloying Ta with W is illustrated in Fig. 3.1-164 for Ta2.5W and Ta10W, which are the main commercial Ta-based alloys.

Figure 3.1-165 summarizes values of $R_{p0.2}$ of the most common Nb-based alloys at elevated temperatures. All of these alloys are hardened primarily by solid solution strengthening; however, small amounts of precipitates are present.

For comparison, the high-temperature strength of stress-relieved 1 mm sheets made of Mo- and W-based materials is shown in Fig. 3.1-166. For short-term application under high stresses, the precipitation-strengthened Mo alloys TZM and MHC offer the best performance up to a service temperature of 1500 °C. For higher temperatures, W-based materials should be applied. Tantalum-based alloys are used only if additional high ductility is required after cooling to room temperature.

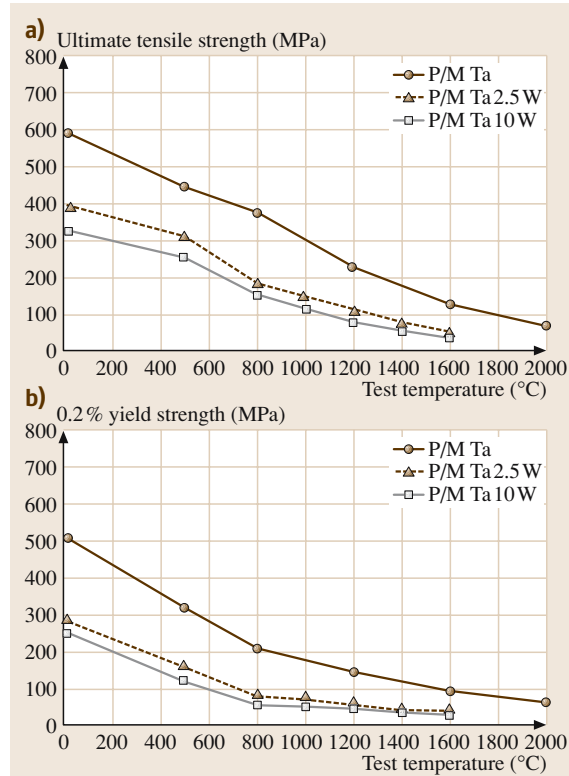


Fig. 3.1-165 Effect of temperature on $R_{p0.2}$ for common Nb-based alloys [1.173]

Dynamic Properties

Microplasticity Effects under Cyclic Loading at Low Temperatures. Microplasticity effects under monotonic loading have been reported in the literature for single- and polycrystalline Mo and Ta [1.171, 174]; information regarding effects of strain rate and temperature on the cyclic stress-strain response is given in [1.140, 170]. Most experiments on cyclic stress-strain behavior have

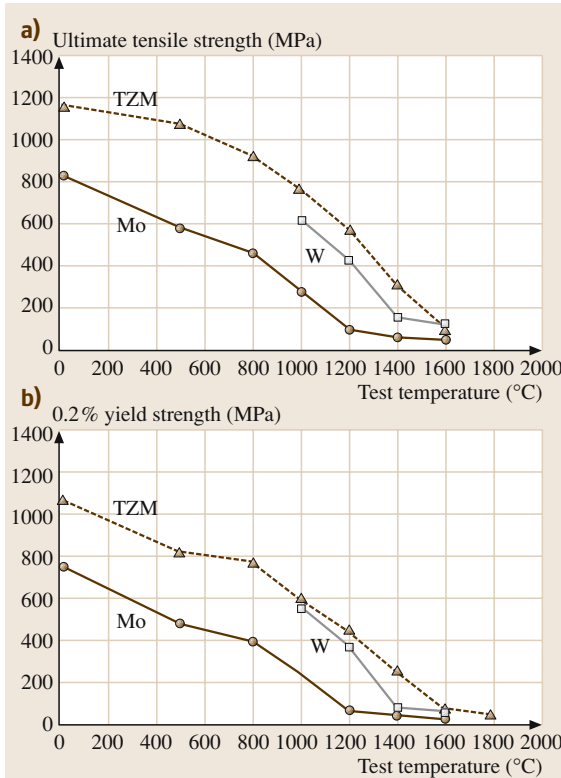


Fig. 3.1-166a,b The ultimate tensile strength R_m (a) and the yield strength $R_{p0.2}$ (b) versus test temperature for Mo, TZM, and W sheets that are 1 mm thick. Material condition = stress relieved, technical strain rates = $2.0 \times 10^{-3} \text{ s}^{-1}$ (Mo, TZM, room temperature), $1.3 \times 10^{-3} \text{ s}^{-1}$ (Mo, TZM, elevated temperatures), $3.3 \times 10^{-4} \text{ s}^{-1}$ up to $R_{p0.2}$, followed by $6.7 \times 10^{-4} \text{ s}^{-1}$ (W, elevated temperatures) [1.126]

been carried out at room temperature. When bcc metals are deformed at $T < 0.2 T_m$, microstrain ($\varepsilon_{pl} < 10^{-3}$) is characterized as the plastic strain, accommodated by the motion of non-screw dislocations [1.166, 169]. These differences are manifested in the temperature and strain-rate dependence of the flow behavior [1.171, 175]. Investigations of Mo and Ta showed that a true microplastic deformation can only be considered at plastic strains of less than 5×10^{-4} [1.140]. The critical temperature below which the marked increase in the cyclic flow stress occurs is in the range of 25 °C to 80 °C for Ta and between 200 °C and 280 °C for Mo, depending on the strain rate. The experimental results for Ta showed that the highest cyclic plastic strains are obtained under strain rates between $1 \times 10^{-8} \text{ s}^{-1}$ and $2 \times 10^{-6} \text{ s}^{-1}$. As an example, the effect of the loading rate on the

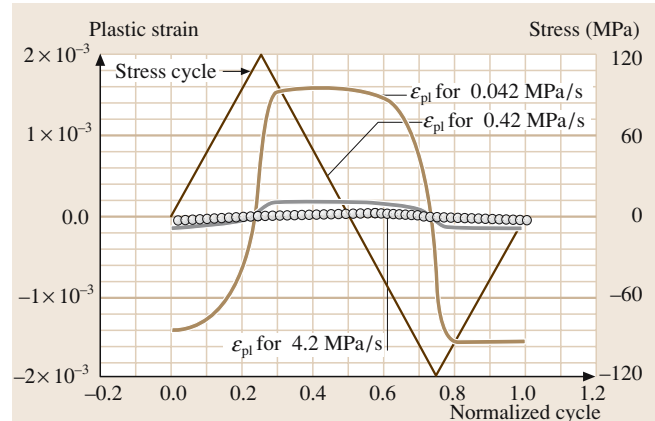


Fig. 3.1-167 Effect of loading rate on cyclic plastic strain of recrystallized Ta during a tension-compression cycle ($R = -1$). Stress amplitude = 120 MPa; test temperature = 25 °C; duration of a cycle at 0.042 MPa/s = 190 min, at 4.2 MPa/s = 1.9 min; maximum plastic strain rate at all loading rates = approx. $3 \times 10^{-6} \text{ s}^{-1}$ [1.140]

cyclic plastic strain of recrystallized tantalum during tension-compression cycles at loading rates between 0.042 MPa/s (duration of one cycle = 190 min) and 4.2 MPa/s (duration of one cycle = 1.9 min) is shown in Fig. 3.1-167 [1.140].

High-Cycle Fatigue Properties. Most of the fatigue data are reported in form of stress vs. number of cycles to failure (S-N) curves. For Mo a fatigue limit may be approached for $N > 10^7$ under stress-controlled conditions [1.176]. Experiments were conducted at test frequencies up to 20 kHz. The results of such tests should be considered with caution, taking into account the temperature and strain-rate sensitivity of bcc metals. Representative S-N curves for as-worked and recrystallized Mo, and a comparison of push-pull- and bending-fatigue-tested Mo sheet specimens are shown in Figs. 3.1-168 [1.126] and 3.1-169 [1.126].

The reported fatigue test data for various test methods are summarized in Table 3.1-114 with the fatigue limit (S_e) and the ratio of fatigue limit to tensile-stress (S_e/R_m) as characteristic parameters. Methods of statistical evaluation of test data were published [1.176, 177]. A decrease in fatigue limits with decreasing cyclic frequency was found.

Cyclic hardening/softening was deduced and cyclic stress-strain curves over wide ranges of plastic strain amplitudes were published in [1.178, 179] for Mo, in [1.172, 180, 181] for Ta, and in [1.182] for Nb and

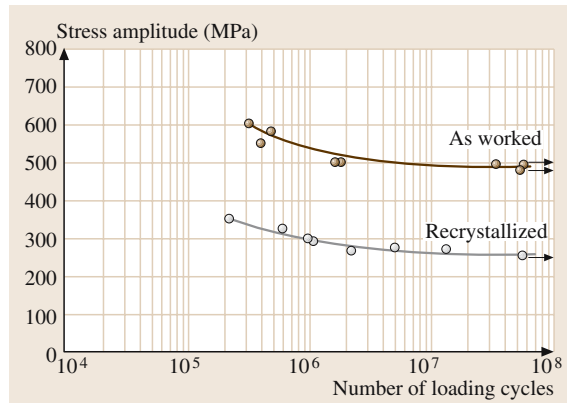


Fig. 3.1-168 Rotating-bending fatigue test results for as-received and recrystallized Mo rods (diameter = 25 mm) at room temperature [1.126]

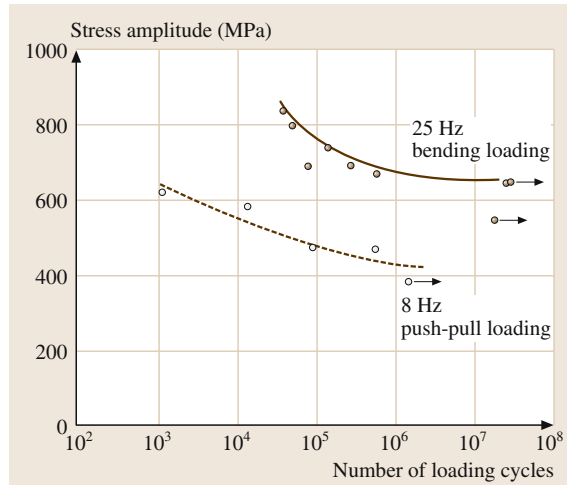


Fig. 3.1-169 Comparison of test results of bending (at 25 Hz) and push-pull fatigue (at 8 Hz) tests of stress-relieved Mo sheet specimens ($800^\circ\text{C}/6\text{ h}$) [1.126] at room temperature

Nb1Zr. Cyclic stress–plastic-strain curves are given in Figs. 3.1-170 and 3.1-171 for Mo and Ta at various test temperatures. The ranges of microplastic and macroplastic strain can be differentiated, based on the different slopes.

The elevated temperature fatigue behavior of TZM was investigated for test temperatures between 300°C and 500°C [1.183]. Brittle failure under high cycle fatigue conditions was found over the entire temperature range, with a significant decrease in fatigue strength with increasing temperature.

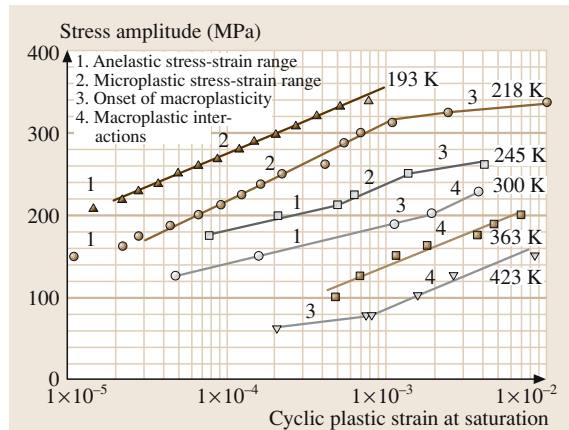


Fig. 3.1-170 Cyclic-stress–plastic-strain curves of recrystallized Mo at different temperatures at a loading rate of 60 MPa/s [1.140]

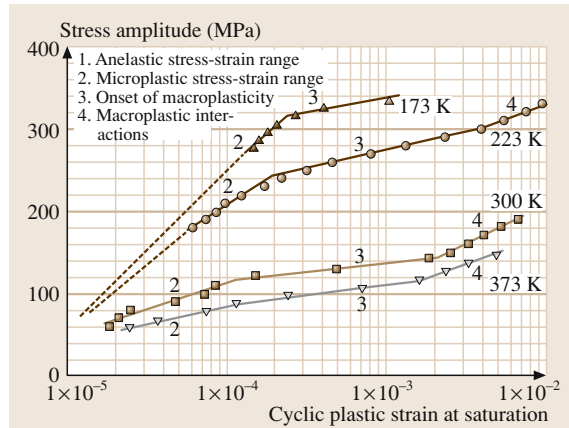


Fig. 3.1-171 Cyclic-stress–plastic-strain curves of recrystallized Ta at different temperatures at a loading rate of 0.42 MPa/s [1.140]

Low-Cycle Fatigue Properties. Results of low-cycle fatigue experiments under strain control on as-worked W plate material at 815°C are shown in Fig. 3.1-172. Low-cycle fatigue tests of pure W were performed in the temperature range between 1650°C and 3300°C [1.184]. A relationship $N_{\text{failure}} \approx \exp(-\alpha T)$ was found to be valid up to test temperatures of 2700°C [1.185]. In all cases the failure mode was intercrystalline. Similar results were also obtained at a test temperature of 1232°C [1.186]. The deformation behavior of Nb and Nb1Zr under plastic-strain control at room temperature was investigated and cyclic stress–strain curves published [1.182].

Table 3.1-114 Summary of fatigue data of refractory metals, pretreatment: Aw = as worked, Sr = stress relieved, Rxx = recrystallized. RT = room temperature

| Test mode | Material | Production process | Dimension (mm) (plate: thickness, bar: diameter) | Pretreatment $T(^{\circ}\text{C})/t_a$ (h) | Test conditions, temperature, frequency | S_e (MPa) | S_e/R_m | Ref. |
|--|--------------------|--------------------|--|---|--|--------------------------|----------------------|---------|
| Rotating bending fatigue, $R = -1$, fatigue limit S_e for 50% probability at $N = 5 \times 10^7$ | | | | | | | | |
| | Mo | P/M | bar 12 | Aw Rxx 1200/1 | RT, 100 Hz RT, 100 Hz | 450 220 | 0.68 0.44 | [1.126] |
| | Mo5Re | P/M | bar 12 | Aw Sr 900/6 Rxx 1300/1 | RT, 100 Hz RT, 100 Hz RT, 100 Hz RT, 100 Hz | 450 400 230 | 0.68 0.68 0.48 | [1.126] |
| | Mo41Re | P/M | bar 12 | Aw Sr 1050/6 Rxx 1400/1 | RT, 100 Hz RT, 100 Hz RT, 100 Hz | 690 620 320 | 0.62 0.36 | [1.126] |
| | TZM | P/M | bar 12 | Aw Sr Rxx 1500/1 | RT, 100 Hz RT, 100 Hz RT, 100 Hz | 550 560 340 | 0.62 0.57 | [1.126] |
| | W | P/M | bar 12 | Aw Rxx 1600/1 | RT, 100 Hz RT, 100 Hz | 760 310 | 0.48 0.70 | [1.126] |
| | W5Re | P/M | bar 12 | Aw Rxx 1800/1 | RT, 100 Hz RT, 100 Hz | 770 440 | 0.71 0.65 | [1.126] |
| | W26Re | P/M | bar 12 | Aw Rxx 1700/1 | RT, 100 Hz RT, 100 Hz | 820 450 | 0.54 0.39 | [1.126] |
| | W2ThO ₂ | P/M | bar 12 | Rxx 1900/1 | RT, 100 Hz | 365 | 0.64 | [1.126] |
| | Nb | P/M | bar 5.9 | Aw Rxx | RT, 100 Hz RT, 100 Hz | 225 220 | 0.42 0.51 | [1.190] |
| | Ta | P/M | bar 5.9 | Aw Rxx | RT, 100 Hz RT, 100 Hz | 290 270 | 0.92 0.95 | [1.190] |
| Push-pull fatigue, $R = -1$, fatigue limit S_e for 50% probability at $N = 1 \times 10^7$ | | | | | | | | |
| | Mo | P/M | plate 1 | Rxx 1200/1 | RT, 0.05 Hz | 195 | | [1.179] |
| | TZM | P/M | bar 50 | Aw Aw | RT, 25 Hz 850 °C, 25 Hz | 440 250 | | [1.191] |
| | Ta | | plate 2 | Aw Aw Rxx 1200/2 Rxx 1200/2 | RT, 0.05 Hz RT, 10 Hz RT, 0.05 Hz RT, 10 Hz | 205 225 180 210 | | [1.179] |
| Bending fatigue, $R = -1$, fatigue limit S_e for 50% fracture probability at $N = 1 \times 10^7$ | | | | | | | | |
| | Mo | P/M | plate 2 | Aw Sr 780/6 Rxx 1200/1 | RT, 25 Hz RT, 25 Hz RT, 25 Hz | 520 540 280 | | [1.126] |
| | Mo5Re | P/M | plate 1.6 | Sr | RT, 25 Hz | 460 | 0.56 | [1.126] |
| | Mo41Re | P/M | plate 1.6 | Sr | RT, 25 Hz | 680 | 0.61 | [1.126] |
| | TZM | P/M | plate 2 | Aw Sr 1150/6 Rxx 1500/1 | RT, 25 Hz RT, 25 Hz RT, 25 Hz | 650 750 460 | | [1.126] |
| | W | P/M | plate 2 | Aw Rxx 1600/1 | RT, 25 Hz RT, 25 Hz | 520 225 | | [1.126] |
| | Ta | P/M | plate 1 | Aw Rxx 1200/1 | RT, 25 Hz RT, 25 Hz | 335 240 | 0.56 0.75 | [1.126] |
| | Ta | EB | plate 1 | Aw Rxx 1200/1 | RT, 25 Hz RT, 25 Hz | 270 220 | 0.61 0.96 | [1.126] |
| | Ta2.5W | P/M | plate 1 | Rxx 1300/1 | RT, 25 Hz | 310 | 0.79 | [1.126] |
| | Ta2.5W | EB | plate 1 | Rxx 1300/1 | RT, 25 Hz | 270 | 0.69 | [1.126] |
| | Ta10W | EB | plate 0.64 | Aw | RT, 25 Hz | 480 | | [1.168] |

Table 3.1-114 (cont.) Summary of fatigue data of refractory metals, pretreatment: Aw = as worked, Sr = stress relieved, Rxx = recrystallized

| Test mode | Material | Production process | Dimension (mm) plate: thickness, bar: diameter | Pretreatment $T(^{\circ}\text{C})/t_a (\text{h})$ | Test conditions, temperature, frequency | $S_e (\text{MPa})$ | S_e/R_m | Ref. |
|---|----------|--------------------|--|--|---|--------------------|-----------|---------|
| High-frequency push-pull fatigue, $R = -1$, fatigue limit S_e for 50% fracture probability at $N = 10^8$ | Mo | P/M | bar 11 | Rxx 1300/4 | RT, 20 kHz | 278 | 0.56 | [1.176] |
| | TZM | P/M | bar 11 | Rxx 1600/2 | RT, 20 kHz | 383 | 0.69 | [1.176] |
| | Ta | EB | bar 3 | Aw | RT, 20 kHz | 383 | 0.72 | [1.126] |
| | | | | Sr | RT, 20 kHz | 286 | 0.92 | [1.126] |
| | Ta2.5W | P/M | plate 2 | Rxx | RT, 20 kHz | 300 | | [1.126] |
| | Ta10W | P/M | bar 12 | Rxx | RT, 20 kHz | 580 | | [1.126] |
| | Nb | | bar 3 | Aw | RT, 20 kHz | 230 | 0.80 | [1.177] |
| | | | | Rxx | RT, 20 kHz | 220 | 0.65 | [1.177] |

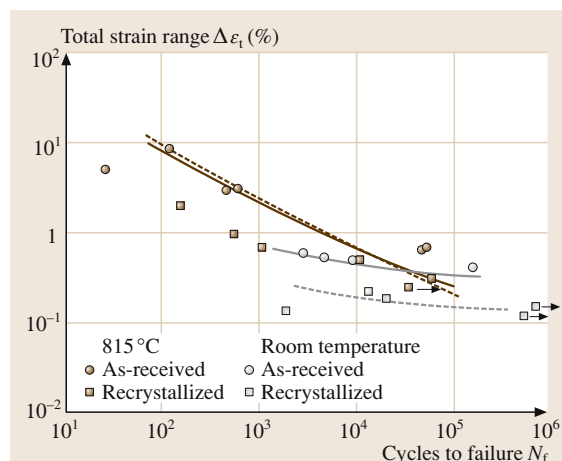


Fig. 3.1-172 Low-cycle fatigue data of as-received and recrystallized W at room temperature and 815 °C [1.186]

Low-cycle fatigue test data of Mo at high test temperatures were reported in [1.187]. The influence of microstructural changes in cold-worked Mo on the low-cycle fatigue behavior was reported for test temperatures between 300 °C and 950 °C [1.188]. Deformation experiments under low-cycle fatigue conditions between room temperature and 100 °C showed that recrystallized Mo, in spite of the low temperature and stress level, exhibits considerable plastic strains which depend sensitively on the loading frequency [1.189]. Data on the high temperature (350 °C and 500 °C) isothermal mechanical fatigue behavior of TZM were reported and a model for lifetime prediction was proposed [1.183].

Fig. 3.1-173 K_{lc} of forged Mo rods ($\varphi = 74\%$) versus degree of recrystallization [1.147]

Fracture Mechanics Properties

Fracture Toughness. Fracture toughness properties are affected by many parameters (thermomechanical pretreatments, microstructure, specimen and crack plane orientation; testing procedures as well as the preparation of the starting notch and of the fatigue precrack). Due to the peculiarities of the P/M production process, it is frequently not possible to introduce sufficient deformation into products of larger dimension in order to completely eliminate sinter pores which may affect the dynamic properties. The increase of fracture toughness with increasing degree of hot working of disc-shaped compact tension specimens, cut from a hot forged Mo bar is shown in Fig. 3.1-173 and the decrease of fracture toughness with increasing fraction of recrystallized microstructure in Fig. 3.1-174 [1.147].

Fracture toughness data for Mo, TZM, and W materials are summarized in Table 3.1-115. Data taken at elevated temperature for Mo and W are shown in Fig. 3.1-175 [1.192], and for TZM in Fig. 3.1-176 [1.193]. Data for Nb could only

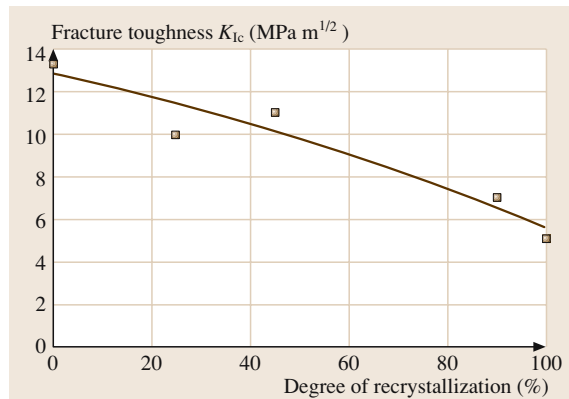


Table 3.1-115 Fracture mechanical data for various refractory metals, pretreatment: Aw = as worked, Sr = stress relieved, Rxx = recrystallized. RT = room temperature

| Fracture toughness data | | | | Specimen type: CT compact tension, SCT center surface cracked tension, DCT disk-shaped compact tension, SNB side notched bend, CNT center through-thickness notched tension | | | | |
|---|--------------------|---|--|---|----------------------|-----------------------------|--|--------------|
| Material | Production process | Dimension (mm) plate: thickness, bar: diameter | Pretreatment T (°C)/t _a (h) | Specimen type | Crack plane ASTM 399 | Test temperature | Fracture toughness (MPa m ^{1/2}) | Ref. |
| Mo | P/M | plate 6.5 | Rxx 1300/2 | CNT | L-T | RT | 9.5 | [1.126] |
| Mo | P/M | bar 50 | Sintered | DCT | R-C | RT | 6 | [1.147] |
| | | | Hot forged | DCT | R-C | RT | 12 | |
| | | | Rxx 1400/2 | DCT | R-C | RT | 5 | |
| Mo | VAC | plate 6.4 | Sr | CT | L-T/T-L | RT | 20/21 | [1.195] |
| | | | Rxx | CT | L-T/T-L | RT | 18/19 | |
| | | | Sr | CT | L-T/T-L | 300 °C | 74/70 | |
| | | | Rxx | CT | L-T/T-L | 300 °C | 60/67 | |
| Mo5Re | | bar 54 | Rxx 1300/1 | DCT | R-C | RT/450 °C | 18/27 | [1.193] |
| Mo-0.3 wt% La ₂ O ₃ | P/M | plate | Sintered | CT | L-T | RT | 25 | [1.196] |
| TZM | VAC | plate 6.4 | Sr | CT | T-L/L-T | RT | 19/15 | [1.195] |
| | | | Rxx | CT | T-L/L-T | RT | 15/18 | |
| | | | Sr | CT | T-L/L-T | 300 °C | 85/89 | |
| | | | Rxx | CT | T-L/L-T | 300 °C | 59/68 | |
| TZM | P/M | bar 54 Machined to 12 Swaged to 12 | Aw | DCT | R-C | RT | 19 | [1.159, 197] |
| | | | Aw | SCT | L-C | RT | 37 | |
| | | | Rxx 1400/2 | SCT | L-C | RT | 19 | |
| W | | bar 10 | | SNB | C-R/L-R | -196 °C | 11/6 | [1.198] |
| | | | | SNB | C-R/L-R | RT | 13/8 | |
| W | | bar 25 | Aw | SNB | R-L | RT/150 °C/ 300 °C/500 °C | 9/10/13/14 | [1.199] |
| W | Single crystal | bar 16 (111)[011] bar 16 (011)[100] bar 16 (100)[001] | | SNB | | -196 °C/RT | 9/31 | [1.198] |
| | | | | SNB | | -196 °C/RT | 4/20 | |
| | | | | SNB | | -196 °C/RT | 3/9 | |
| W | | | Aw | SNB | | RT/400/600/ 800 | 15/21/26/39 | [1.200] |
| W5Re | | | Aw | SNB | | RT/400 °C/ 600 °C | 11/26/58 | [1.200] |
| W-1 wt% La ₂ O ₃ | P/M | bar 25 | Aw | SNB | R-L | RT/150 °C/ 300 °C/500 °C | 9/10/11/13 | [1.199] |
| Nb | | plate 1.25 | Sr | CNT | L-T | -253 °C | 40 | [1.192] |
| | | | Rxx | CNT | L-T | -253 °C | 72 | |
| Nb | | | Rxx | SNB | | -196 °C | 37 | [1.194] |
| | | | Rxx | SNB | | RT | 37 | |

be determined below -200 °C [1.192]. Data on the impact and dynamic toughness of Nb between -196 °C and 25 °C were reported in [1.194]. The dy-

namic cleavage fracture toughness was shown to be 37 MPa m^{1/2}, relatively independent on grain size and test temperature.

Table 3.1-115 Fracture mechanical data for various refractory metals, pretreatment: Aw = as worked, Sr = stress relieved, Rxx = recrystallized, RT = room temperature, cont.

| Material | Fatigue crack growth and threshold data | | | Specimen type: | | | | | | | | |
|----------|---|----------------|---------------------------------|--|---------------|--|---|----------------------|---------------------------|-----------------------------------|------|---------|
| | Production process | Dimension (mm) | plate: thickness, bar: diameter | CNT center through-thickness notched tension | | | SCT center surface cracked tension | | | $\Delta K_{\text{th},\text{eff}}$ | ASTM | Ref. |
| | | | | CCT corner cracked tension | Specimen type | Crack plane conditions, ASTM frequency | Test conditions, temperature, frequency | Stress ratio R | da/dN -range, (m/cycle) | | | |
| Mo | P/M | plate 6.5 | Rxx | 1300/2 | CNT | L-T | RT, 20 kHz | -1 | $10^{-13} - 10^{-9}$ | 5.8 | E647 | [1.126] |
| Mo | P/M | bar 12 | Aw | SCT | | L-C | RT, 20 kHz | -1 | $10^{-13} - 10^{-9}$ | 11.3 | E647 | [1.159] |
| Mo | P/M | bar 12 | Rxx | 1400/2 | SNT | C-R | RT, 20 kHz | -1 | $10^{-13} - 10^{-9}$ | 10.7 | | |
| Mo | P/M | bar 12 | Sr | 850/1 | SNT | C-R | RT, 20 kHz | -1 | $10^{-13} - 10^{-9}$ | 10.3 | E647 | [1.201] |
| TZM | P/M | bar 12 | Rxx | 1700/2 | SNT | RT, 20 kHz | -1 | $10^{-13} - 10^{-9}$ | 8.5 | 6.6 | | |
| Mo5Re | P/M | bar 12 | Rxx | 1300/1 | SCT | L-C | RT, 20 kHz | -1 | $10^{-13} - 10^{-9}$ | 10.1 | E647 | [1.201] |
| Mo5Re | P/M | bar 12 | Rxx | 1300/1 | SCT | | | | | 9.9 | E647 | [1.126] |

20 kHz resonance test method, crack growth monitored by traveling light microscope,

ΔK_{th} corresponding to a crack growth rate of $da/dN < 10^{-13}$ m/cycle,

$\Delta K_{\text{th},\text{eff}}$ calculated from crack closure measurements based on strain gauge method

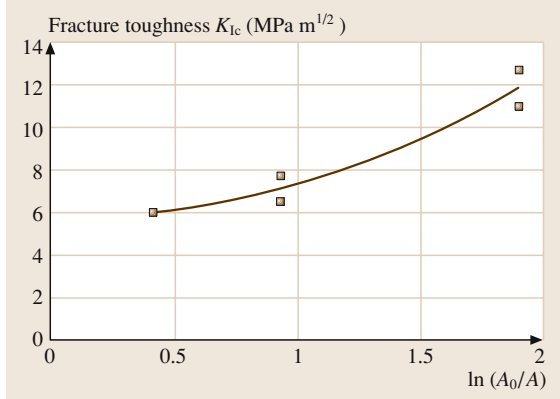


Fig. 3.1-174 K_{Ic} of forged Mo rods versus $\ln(A_0/A)$ [1.147]

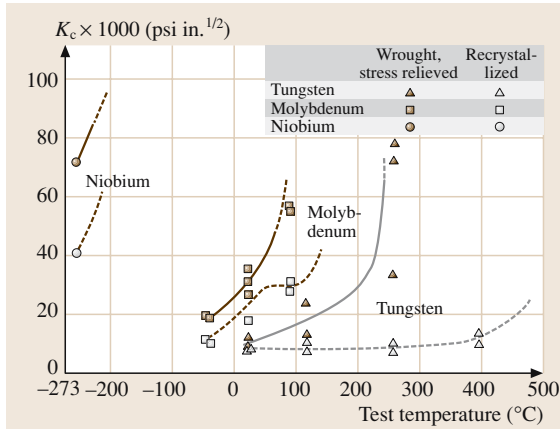


Fig. 3.1-175 Effect of test temperature on fracture toughness of unalloyed W, Mo, and Nb sheet specimens [1.192]

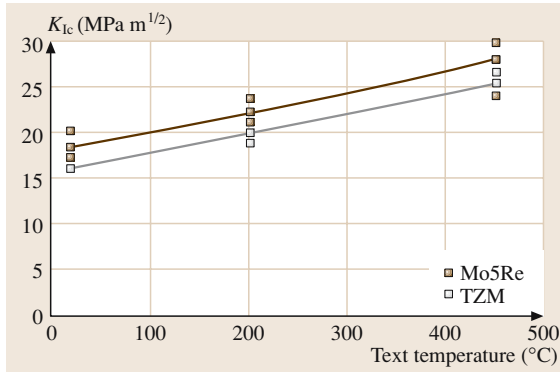


Fig. 3.1-176 Effect of test temperature on static fracture toughness of TZM and Mo5Re specimens [1.193]

Fatigue Crack Growth. Few data on the linear region of crack growth were published for Ta10W (Fig. 3.1-177), and a Nb–W–Zr alloy [1.202, 203].

Threshold Stress Intensity for Fatigue Crack Growth. The fatigue crack growth behavior of Mo, TZM, and W in the region near the threshold stress intensity, ΔK_{th} , considered to correspond to fatigue crack growth rates of $da/dN < 10^{-13} \text{ m/cycle}$, is shown in Fig. 3.1-178 [1.126]. The available crack growth and threshold data are included in Table 3.1-115.

An effective threshold value for fatigue crack growth, $\Delta K_{\text{th,eff}}$, can be computed. Methods for the determination of this effective threshold stress intensity range are described in [1.197]. The available data on $\Delta K_{\text{th,eff}}$ of Mo and TZM are listed in Table 3.1-115.

Short Fatigue Crack Growth Behavior. The nucleation and growth behavior of short fatigue cracks is of considerable practical and theoretical significance. Differences in the growth behavior exist between initial short cracks (length comparable with microstructural features) and long cracks of macroscopic dimensions. The irregular growth rate of such short cracks

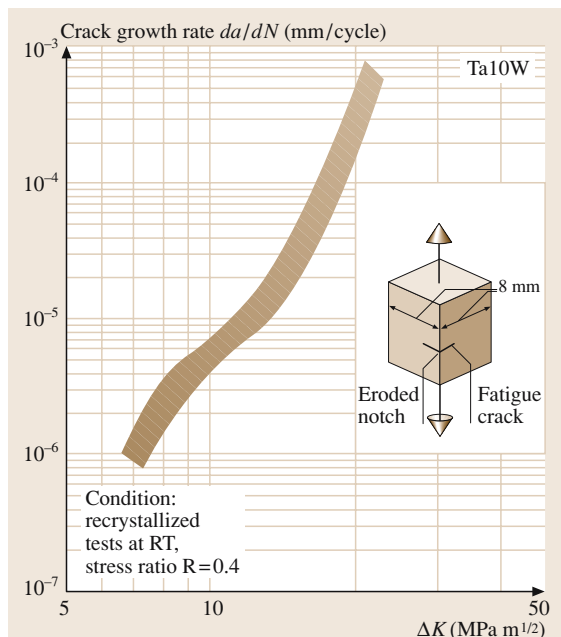


Fig. 3.1-177 Crack propagation behavior of recrystallized P/M Ta10W specimens at room temperature at a stress ratio of $R = 0.4$ [1.202]

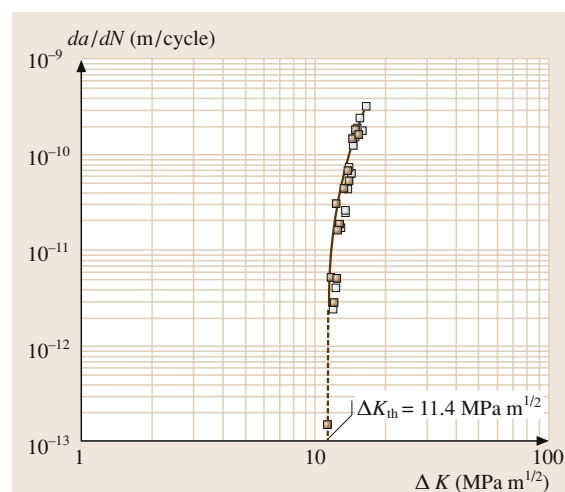


Fig. 3.1-178 Crack growth curve near threshold stress intensity of a center surface cracked specimen machined from a recrystallized Mo5Re rod, tested at a stress ratio of $R = -1$, test temperature = 50°C, and 20 kHz cyclic frequency; open symbols test under increasing load, solid symbols tests under decreasing load [1.126]

(Fig. 3.1-179) may pose problems for a conservative prediction of fatigue life [1.201]. Microscopic observations during fatigue exposure of specimens, loaded at stress amplitudes slightly above the fatigue limit, show initially a surface deformation very early in fatigue life, followed by short crack initiation and growth up to the final long crack growth. The number of fatigue cycles of the various stages depends on the microstructure and the presence of second phase particles (Fig. 3.1-180) [1.204].

It is known that fatigue failures occur in defect-containing materials after a high number of loading cycles ($N > 10^8$) at stresses considerably below the fatigue limit determined by conventional test procedures ($N < 10^7$). A fracture mechanics approach to this problem was proposed by Kitagawa et al. [1.205]. Based on a diagram relating a cyclic stress amplitude with crack length, a critical defect size (a_t) can be deduced which, when exceeded, causes a reduction of the fatigue strength. A modification of this diagram by introducing the value of the effective stress intensity range is shown in Fig. 3.1-181 [1.201]. Good agreement between predicted values and experimental results are obtained for hemispherical surface notches of various sizes [1.206, 207].

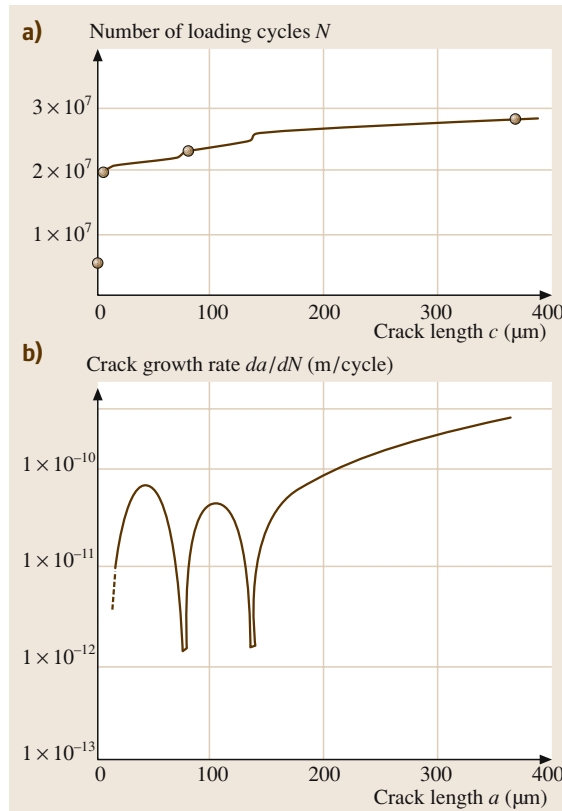


Fig. 3.1-179a,b Growth behavior of short surface cracks in a TZM specimen, tested at a stress amplitude of 375 MPa [1.201,204]. (a) Crack length as function of number of loading cycles. (b) Crack growth rate as function of crack length

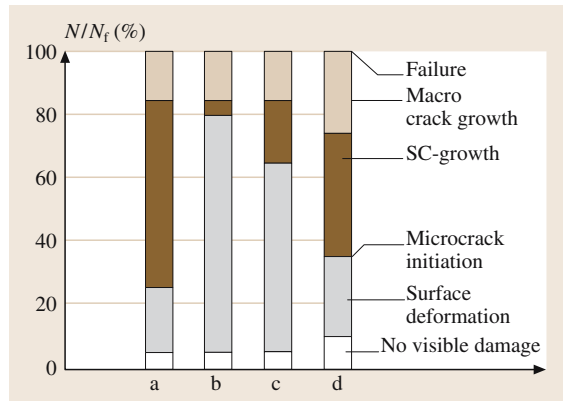


Fig. 3.1-180 Fraction of total fatigue life spent on damage accumulation and crack growth in specimens of stress relieved Mo (a), recrystallized Mo (b), TZM with fine particles (c), and TZM with coarse particles (d) [1.204]

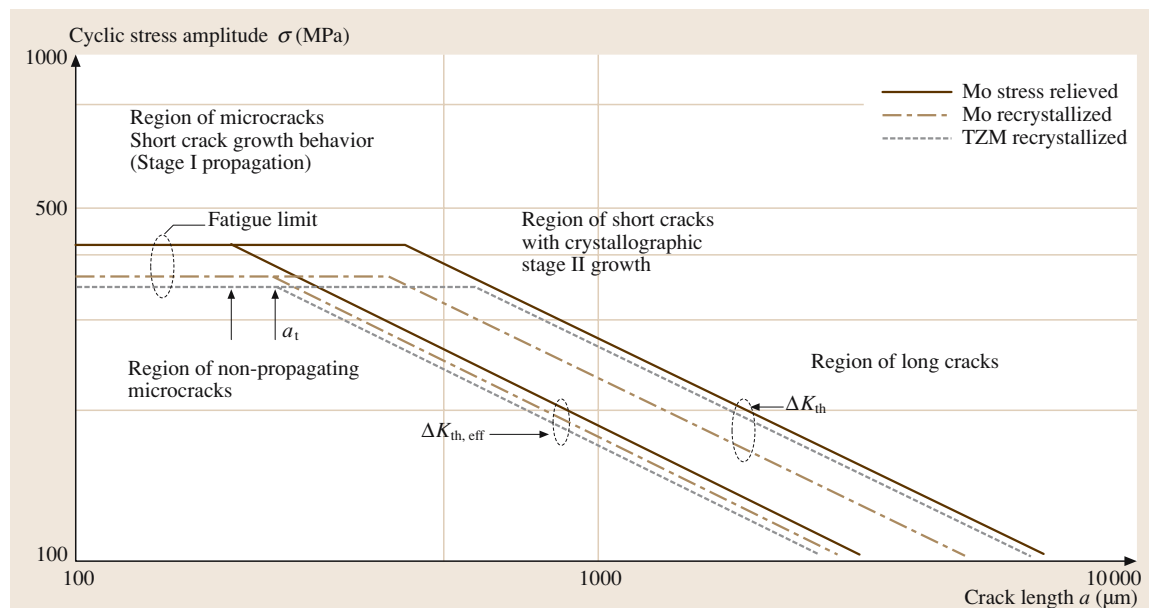


Fig. 3.1-181 Effect of crack length on stress amplitude for crack growth in specimens of stress relieved Mo, recrystallized Mo, and recrystallized TZM (modified Kitagawa diagram) [1.201]

Creep Properties

Creep-rupture data available up to 1970 were collected in [1.107]. The fairly wide scatter results from minor differences in microstructure, thermomechanical pre-treatment, and impurity levels, but possibly also from impurities picked up from the environment in the high-temperature test systems. A summary of 10 000 h/1% creep data for Mo, W, and TZM is given in Fig. 3.1-182; the 100 h creep-rupture data for Mo, W, Nb, Ta, W25Re and TZM are given in Fig. 3.1-183, based on [1.107]. Up to 1100 °C the carbide-precipitation-hardened material TZM reveals the highest creep strength, only outperformed by Mo and W alloys precipitation hardened with hafnium carbide, which are not considered in these figures. Comparing the stress causing a steady state creep rate of 1×10^{-4} /h, as illustrated in Fig. 3.1-184, it can be concluded that precipitation hardening is effective up to 1600 °C. At higher temperatures, the creep strength of TZM deteriorates to the level of Mo or even below. Above 1600 °C, W-based materials offer the best performance.

The influence of the microstructure on the creep mechanisms of Mo is illustrated in Fig. 3.1-185 for 1450 °C [1.208]. For a test stress of 35 MPa the steady state creep rate is almost independent of the grain size. In this stress regime a stress exponent of 5.4 was obtained, indicating dislocation creep as the rate-controlling mechanism. Lowering the test stress to 14 MPa and 7 MPa, grain-size-dependent creep mechanisms, such as diffusion creep and grain boundary sliding, become active, and as a consequence, the steady state creep rate increases with decreasing grain size [1.208].

The steady state creep rates of Mo rods made of VAC ingots, VAC and P/M Mo sheets, and P/M Mo-0.7 wt%La₂O₃ sheets are summarized in Fig. 3.1-186. Stress exponents of 4.3 (P/M Mo sheet/1800 °C), 4.5–4.7 (VAC Mo sheet/1600 °C), 4.6 (VAC Mo rod/1600 °C), 5.0 (Mo-0.7 wt% La₂O₃/1800 °C), and 5.5 (VAC Mo sheet/2200 °C) indicate that dislocation-controlled creep is rate-controlling in the stress regime investigated.

For AKS-W wires, used as lamp filaments, creep resistance is one of the most important requirements. The fine, K filled bubbles act as an effective barrier against dislocation movement, thereby reducing the deformation rate in the power-law creep

Fig. 3.1-184 Stress for steady state creep rate of 1×10^{-4} /h versus $1/T$ for Mo and TZM, deformed samples, various shapes [1.208]

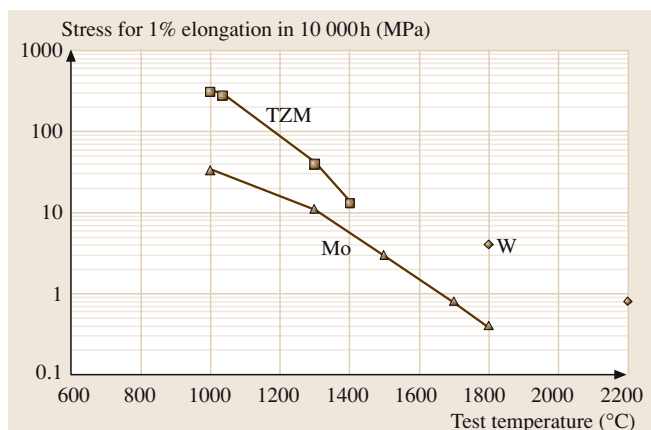


Fig. 3.1-182 Comparison of 10 000 h/1% creep data for Mo, TZM, and W based on [1.107]

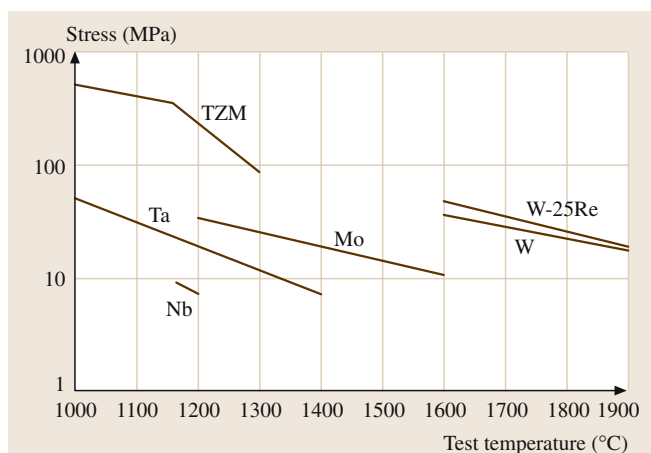
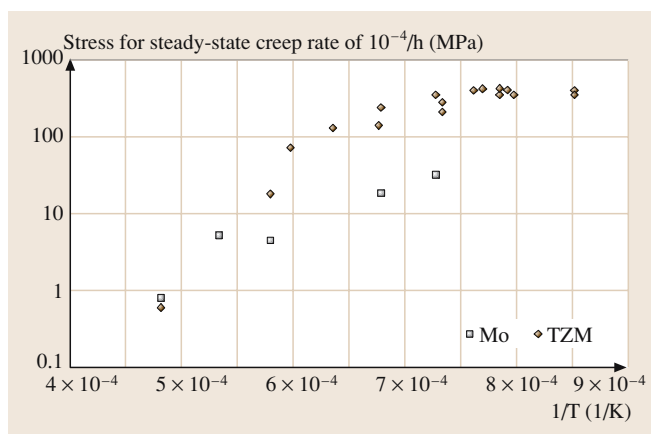


Fig. 3.1-183 Comparison of 100 h of rupture data for selected refractory metals based on [1.107]



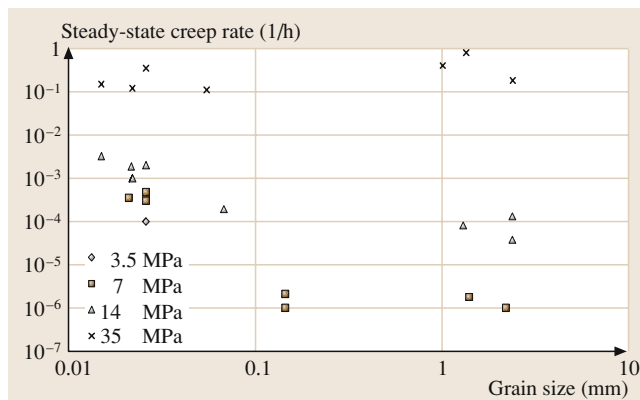


Fig. 3.1-185 Steady state creep rate of molybdenum sheets versus grain size. Sheet thickness = 2 mm/6 mm; test temperature = 1450 °C; test atmosphere = hydrogen [1.208]

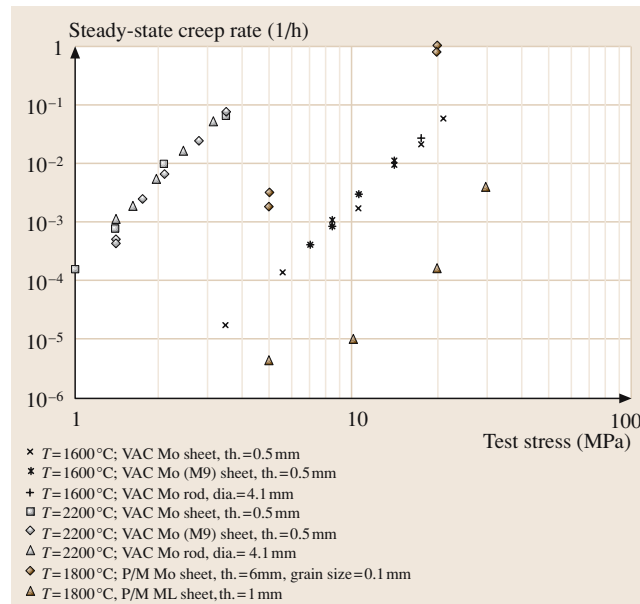


Fig. 3.1-186 Steady state creep rate at various test temperatures of vacuum-arc-cast (VAC) Mo sheet (thickness = 0.5 mm), VAC Mo rod (diameter = 4.1 mm), P/M Mo sheet (thickness = 6 mm), and P/M ML (Mo-0.7 wt% La₂O₃) sheet, recrystallized (thickness = 1 mm) versus test stress [1.107, 208]

regime. Nabarro–Herring and/or Coble creep is suppressed because of the large diffusion distances in a structure with large, highly elongated grains. Grain boundaries resist sliding because of the interlocking structure. A comparison of creep rupture data of pure tungsten and two AKS–W grades with

different grain aspect ratios (GAR) is given in Fig. 3.1-187.

In the high stress regime (> 60 MPa) and at temperatures between 2500 °C and 3000 °C, stress exponents between 8 and 25 were found [1.162, 209, 210]. This high stress dependence led to the introduction of a threshold stress (σ_{th}) below which a component does not reveal any measurable creep deformation under usual service conditions. For this threshold stress, which is lower than the Orowan stress, the detachment of the dislocations from the second phase particles or bubbles is the controlling factor [1.211, 212].

In the second phase particle/metal matrix interface, the dislocation line energy is lower compared to the dislocation line energy in the metal matrix. Of all dispersion strengthened materials investigated, potassium bubbles in AKS–W exert the most attractive interaction on dislocations [1.213].

For material produced in the 1970s with a mean, but strongly scattered, grain aspect ratio of around 35, dislocation creep dominated at stresses > 60 MPa (stress exponent = 25), as can be seen in Fig. 3.1-188. For material produced 20 years later with a similar grain aspect ratio of 31, a stress exponent of 1.2 was found in the stress regime from 30 to 80 MPa, indicating a diffusion-controlled creep process [1.214]. The evaluation of the strain rate/stress dependence of the values

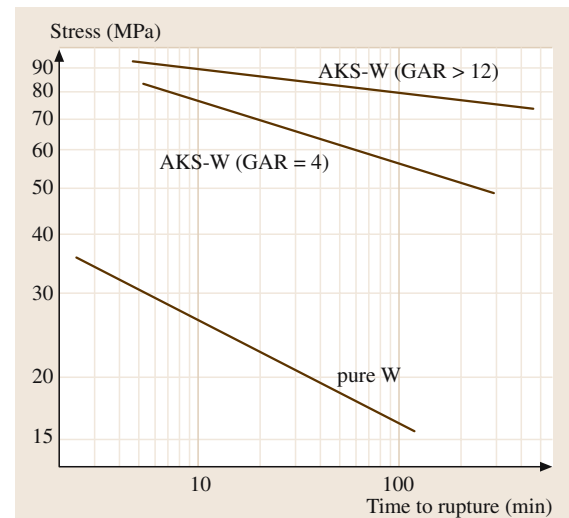


Fig. 3.1-187 Creep rupture data for AKS–W wires in comparison with pure tungsten. Wire diameter = 0.183 mm; test temperature = 2527 °C; atmosphere = vacuum better than 7×10^{-5} Pa; heating rate = approximately 2000 °C/s [1.162]

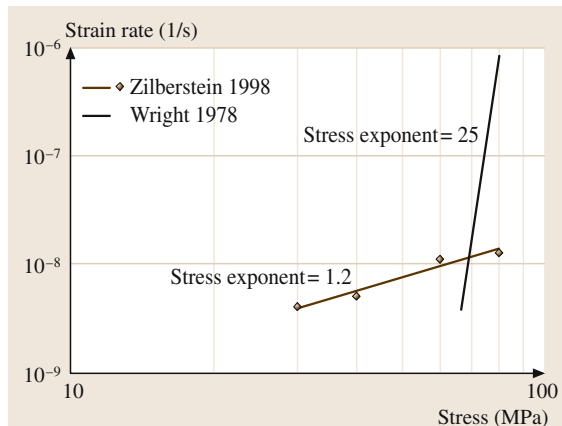
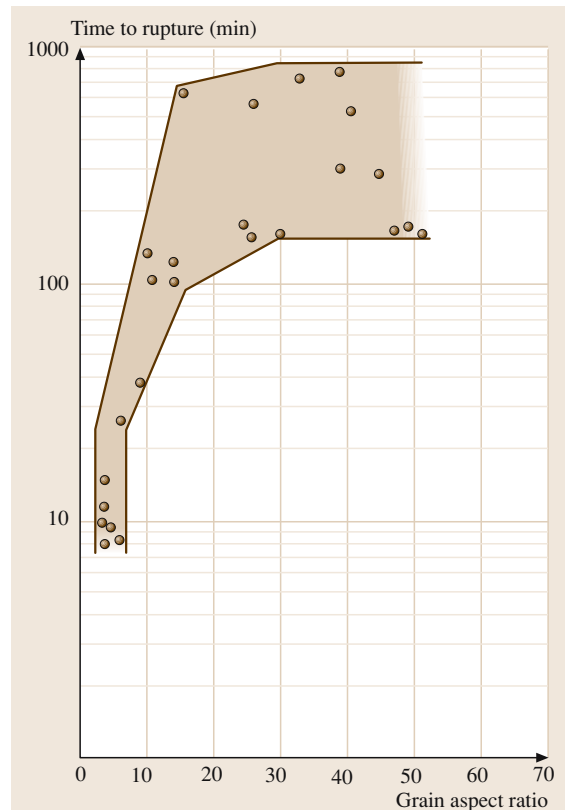


Fig. 3.1-188 Strain rate versus stress for AKS–W wires tested at 2527 °C. Wright 1978 [1.162]: AKS–W wire with a diameter of 0.183 mm; atmosphere = vacuum better than 7×10^{-5} Pa; heating rate = approximately 2000 °C/s; GAR = 35 ± 10 ; pre-recrystallized at 2527 °C/10 min. Zilberstein 1998 [1.215]: AKS–W wire with a diameter of 0.178 mm; atmosphere = vacuum; GAR = 31 ± 1 ; pre-recrystallized at 2527 °C/15 min

Fig. 3.1-189 Time-to-rupture versus grain aspect ratio for AKS–W wires with a diameter of 0.183 mm. Test temperature = 2527 °C; test stress = 73.6 MPa; atmosphere = vacuum better than 7×10^{-5} Pa; heating rate = approximately 2000 °C/s [1.162]

generated under vacuum also reveals a stress exponent close to 1 [1.215]. Data for the stress exponents are summarized in [1.113].

By lowering the grain aspect ratio, the transition temperature between dislocation and diffusion creep is shifted towards lower stresses. In the low



GAR regime a strong dependence of the creep resistance on microstructural features can be observed, as grain boundary related phenomena, such as grain boundary sliding and diffusion creep resulting in cavitations become rate-controlling. The influence of the GAR on time to creep rupture is demonstrated in Fig. 3.1-189.

3.1.10 Noble Metals and Noble Metal Alloys

The noble metals Ag, Au, Pd, Pt, Rh, Ir, Ru, and Os are characterized by their positive reduction potentials against hydrogen, high densities, high melting temperatures, high vapor pressures (Fig. 3.1-190), high electrical and thermal conductivities, optical reflectivity (Fig. 3.1-191), and catalytic properties. The electronic density of states (DOS) near the Fermi surface is nearly the same for all noble metals. Individual differences of electrical conductivity, magnetic, and optical behavior are related to different posi-

tions of the Fermi level relative to the DOS function (Fig. 3.1-192). Small energy differences between their outer s and d electronic states result in multiple oxidation states.

Silver, Au, Pd, and Pt are comparatively soft and ductile. Their hardness increases in the order Rh < Ir < Ru < Os. Strengthening of the alloys is affected by solid solution and dispersion hardening. The corrosion resistance against different agents decreases in the order Ir > Ru > Rh > Os > Au > Pt > Pd > Ag.

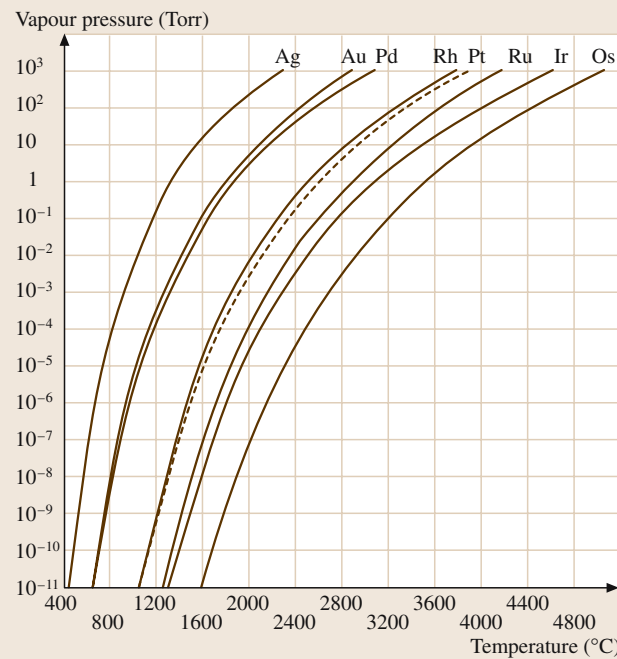


Fig. 3.1-190 Vapour pressures of the noble metals [1.216, p. 43]

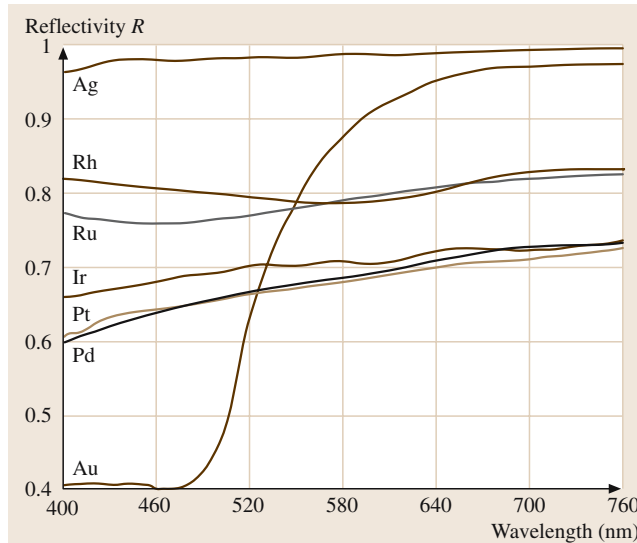


Fig. 3.1-191 Optical reflectivity in the visible spectral range [1.217, p. 173]

The purity grades of the elements are standardized according to ASTM (American Society for Testing and Materials) standards from 99.8 to 99.999 wt%: Ag (B 413–69), Au (B 562–86), Pd (B 589–82), Pt (B 561–86), Rh (B 616–78), Ir (B 671–91), Ru (B 717).

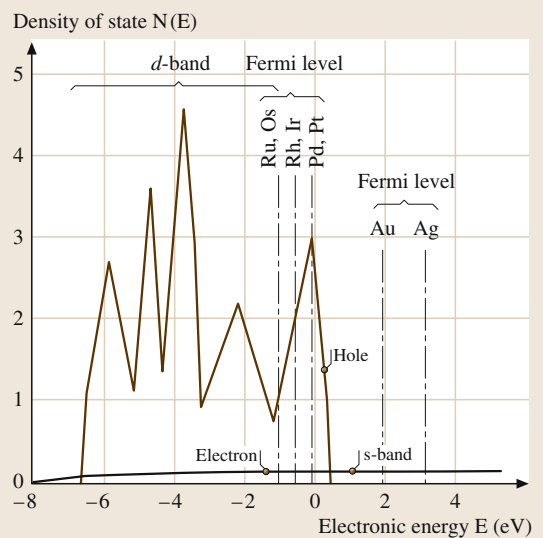


Fig. 3.1-192 Schematic density of states (DOS) curve of the noble metals [1.218, p. 30]

The pure elements and their alloys are key materials in electronics and electrical engineering (Ag, Au, Pd, Pt, and Ru) and serve to manufacture high strength, corrosion-resistant, high temperature, and highly oxidation-resistant structural parts (Pt, Au, Rh, and Ir). The platinum group metals, Ag, and Au, in both the metallic state and in the form of chemical compounds are effective heterogeneous or homogeneous catalysts for a wide variety of chemical reactions. Traditional applications of noble metals and their alloys are in dentistry (Au, Pt, Ag, Pd, and Ir), jewellery (Au, Ag, Pt, Pd, Rh, and Ir), and in coins and medals (Au and Ag).

3.1.10.1 Silver and Silver Alloys

Application

Silver and silver alloys are used for electrical contacts, connecting leads in semiconductor devices, solders and brazes, corrosion-resistant structural parts, batteries, oxidation catalysts, optical and heat reflecting mirrors, table ware, jewellery, dentistry, and coins. Silver halides are base components in photographic emulsions.

Production

Silver is extracted from ores through lead melts and precipitation with zinc by the Parkes process. Zinc is removed by distillation, while the remaining lead

and base metals are removed by oxidation (cupellation) up to $\approx 99\%$ Ag. True silver ores are extracted by cyanide leaching. High purity grades are produced by electrolysis. Bars, sheets, and wires are produced by classical metallurgical processing, powder by chemical and by electrolytic precipitation from solutions, and nano-crystalline powder grades by dispersion in organic solutions. Coatings and laminate structures are produced by cladding, by electroplating, in thick film layers by applying pastes of silver or in silver alloy powder with organic binder and glass frits onto ceramic surfaces and firing, in thin film coatings by evaporation, and by sputtering. Composite materials are made by powder technology, or by infiltration of liquid Ag into sintered refractory metal skeletons. Commercial grades of Ag are listed in Table 3.1-116. Standard purities of crystal powder and bars range from 99.9% to 99.999 wt% (ASTM B 413-69) [1.217].

Phases and Phase Equilibria

Selected phase diagrams are shown in Figs. 3.1-193–3.1-198 [1.219, 220]. Silver forms continuous solid solutions with Au and Pd, with miscibility gaps occurring in alloy systems with Mn, Ni, Os, P, Rh. Data for the solubility of oxygen are given in Table 3.1-117 [1.216]. Thermodynamic data are given in Tables 3.1-118–3.1-121. The entropy of fusion (L/T) of completely disordered intermetallic phases can generally be calculated by fractional addition from those of the components. For the completely ordered state the term $-19.146(N_1 \log N_1 + N_2 \log N_2)$ is to be added to the calculated entropy of fusion [1.216–218, 221, 222]. The molar heat capacity of the homogeneous alloy phases and intermetallic compounds, as calculated approximately from the atomic heat capacities of the components using Neumann-Kopp's rule, is obeyed to within $\pm 3\%$ in the temperature range 0–500 °C in the Ag–Au, Ag–Al, Ag–Al, and Ag–Mg alloy systems. The heat capacities of heterogeneous alloys may be calculated by fractional addition from those of the components by the empirical relation $c_p = 4.1816(a + 10^{-3}bT + 10^5cT^{-2})J/(K\text{ mol})$ to satisfactory accuracy.

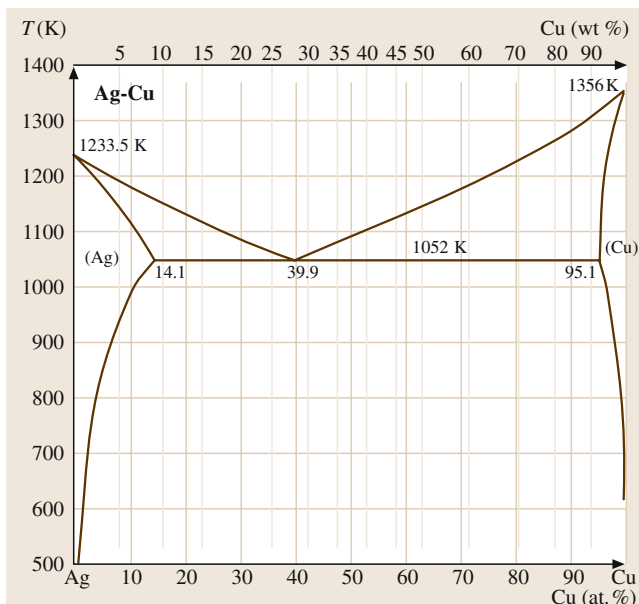


Fig. 3.1-193 Binary phase diagram: Ag–Cu [1.219, p. 38]

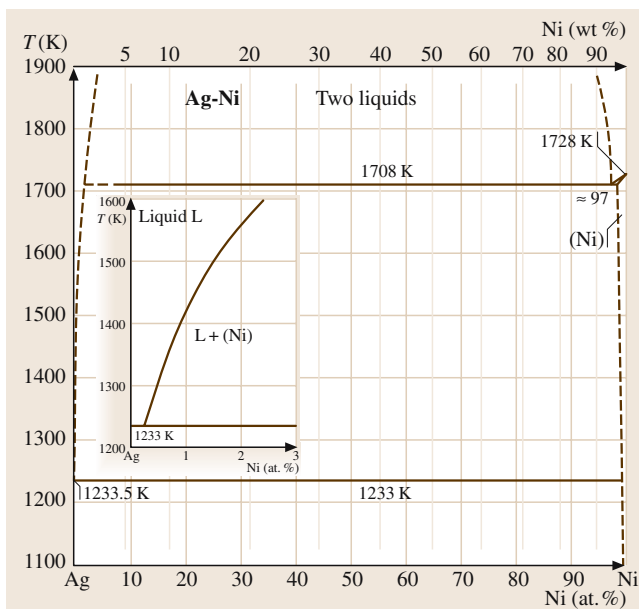


Fig. 3.1-194 Binary phase diagram: Ag–Ni [1.219, p. 88]

Table 3.1-116 Specifications of fine silver grades [1.217, p. 51]

| Designation | Grade (wt%) | Impurity | Maximum content (ppm) |
|---------------------|-------------|-------------------------|-----------------------------|
| “Good delivery” | > 99.9 | any, Cu | 1000 |
| Fine silver | > 99.97 | Cu/Pb/Bi/Se/Te | 300/10/10/5/5 |
| Fine silver 999.9 | > 99.99 | Cu/Pb/Bi/Se/Te | 100/10/10/5/5 |
| F. silver high pure | < 99.999 | Fe/Pb/Au/Cu/Cd/Bi/Se/Te | 2/1/1/1/0.5/0.5/0.5/0.5/0.5 |

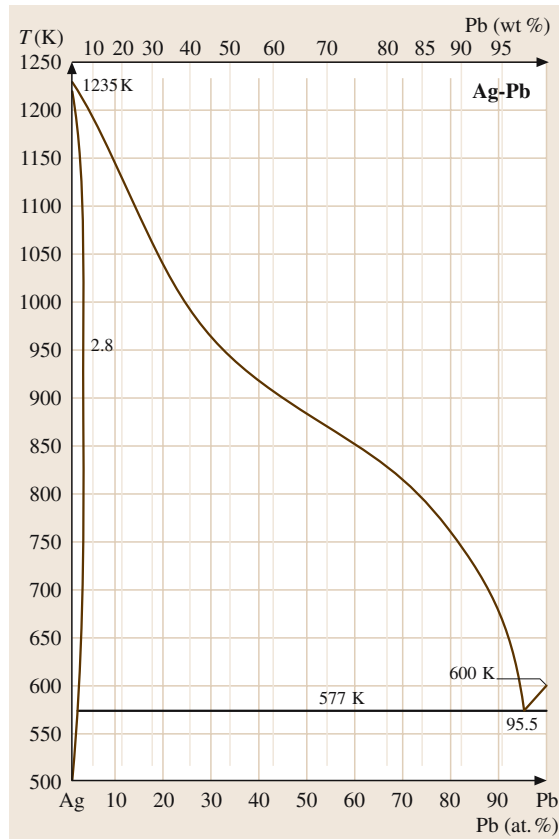


Fig. 3.1-195 Binary phase diagram: Ag–Pb [1.219, p. 92]

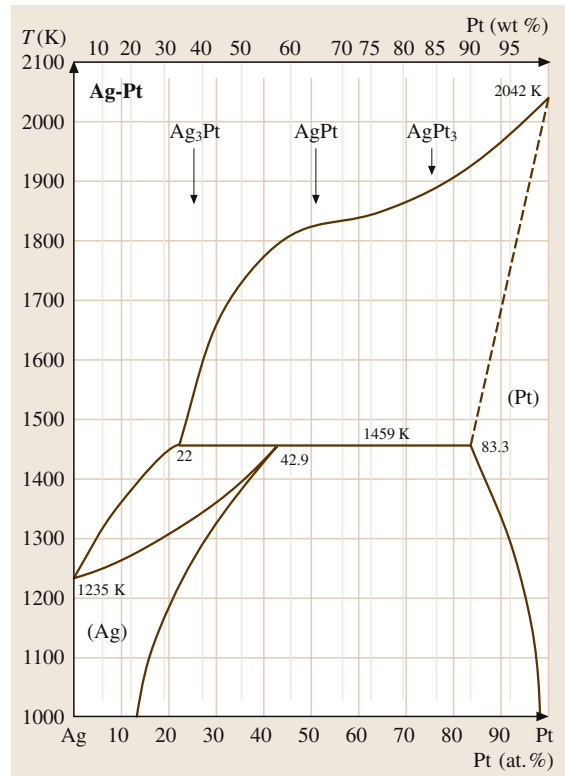


Fig. 3.1-196 Binary phase diagram: Ag–Pt [1.219, p. 101]

Table 3.1-117 Solubility L (ppm) of oxygen in solid and liquid Ag (O_2 pressure 1 bar) [1.216, p. 57]

| T (°C) | 200 | 400 | 600 | 800 | 973 | 1000 | 1200 |
|----------|------|-----|------|------|------|------|------|
| L ppm | 0.03 | 1.4 | 10.6 | 38.1 | 3050 | 3000 | 2500 |

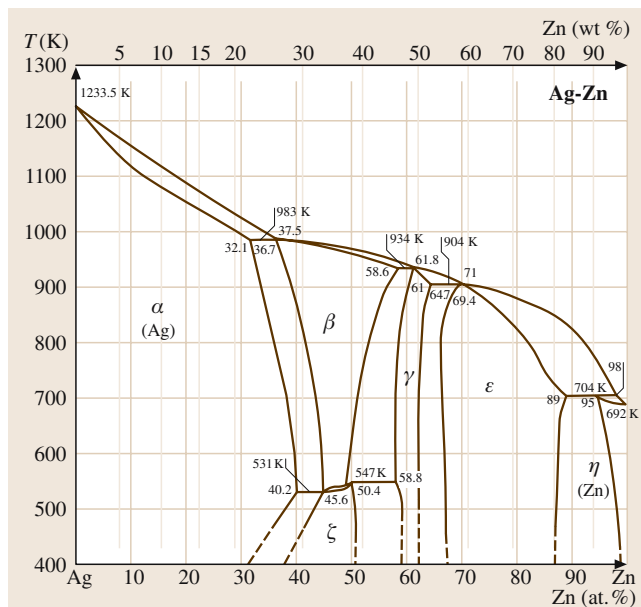


Fig. 3.1-197 Binary phase diagram: Ag–Zn [1.219, p. 144]

Table 3.1-119 Molar heat capacities of solid Ag and Au,
 $c_p = 4.1868 (a + 10^{-3}bT + 10^{-5}T^{-2}) \text{ J/K}$ [1.222, p. 219]

| Element | <i>a</i> | <i>b</i> | <i>c</i> | Temperature range (K) |
|---------|----------|----------|----------|-----------------------|
| Ag | 5.09 | 2.04 | 0.36 | 298–mp* |
| Au | 5.66 | 1.24 | — | 298–mp* |

* = melting point

Table 3.1-120 Latent heat and temperatures of transition of Ag and Au intermediate compounds [1.222, p. 189]

| Phase | N_2 | Transition | T_t | L_t |
|---------------------|-------------------------|-----------------------|-------------------------|-------------------------|
| $\beta\text{-AgCd}$ | 50 | $\beta'\text{-}\beta$ | 211 | 712 |
| AgZn | 50 | order-disorder | 258 | 2449 |
| AuCu | 50 | order-disorder | 408 | 1779 |
| AuCu ₃ | 75 | order-disorder | 390 | 1214 |
| AuSb ₂ | 66.7 | $\beta\text{-}\gamma$ | 355 | 335 |

T_t = transition temperature, L_t = latent heat of transition,
 N_2 = mole fraction of the second component

Table 3.1-121 Latent heats and temperatures of fusion of Ag and Au intermediate compounds [1.222, p. 188]

| Phase | N_2 | T_m (°C) | L_m (hJ/g-at.) | |
|----------------|-------|------------|------------------|------|
| β -AgCd | 67.5 | 592 | 8.46 | 0.42 |
| γ -AgZn | 61.8 | 664 | 7.79 | 0.33 |
| AgZn | 72.1 | 632 | 8.75 | 0.42 |
| δ -AuCd | 50.0 | 627 | 8.96 | 0.50 |
| AuSn | 50.0 | 418 | 12.81 | 0.33 |
| β -AuZn | 50.0 | 760 | 12.31 | 0.54 |

N_2 = mole fraction of the second component, T_m = melting point, L_m = Latent heat of fusion.

For compositions and crystal structures, see Tables 3.1-122–3.1-124 [1.217, 218, 223, 224]. Primary solid solutions have the fcc structure of Ag and the lattice parameters correspond roughly to Vegard's rule with a few exceptions. Alloys with Pt, In, Mg, Cd, and Zn form superlattice phases with tetrahedral and rhombo-

Table 3.1-118 Thermodynamic data of Ag [1.217, p. 107]

| T (K) | c_p (J/K mol) | H (J/K mol) | S (J/mol) | G (J/mol) | p (at) |
|------------|--------------------|------------------|----------------|----------------|------------------------|
| 298.15 | 25.397 | 42.551 | 0 | -12.687 | 1.09×10^{-43} |
| 400 | 25.812 | 50.069 | 2.606 | -17.421 | 5.02×10^{-31} |
| 800 | 28.279 | 68.661 | 13.392 | -41.537 | 1.45×10^{-12} |

T = Temperature, c_p = specific heat capacity, S = Entropy,

H = Enthalpy, G = free Enthalpy.

p = partial pressure of the pure elements

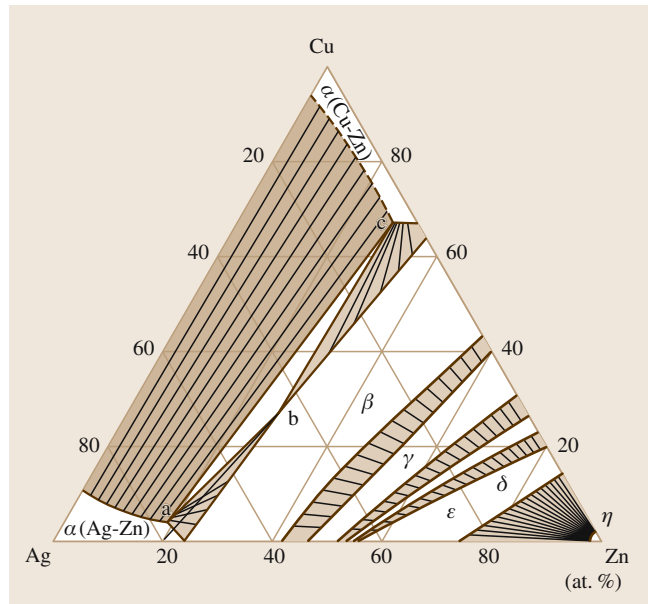


Fig. 3.1-198 Ternary phase diagram: Ag–Cu–Zn [1.220, p. 153]

hedral symmetry. A characteristic series of structures of intermetallic phases are formed with B-metals at compositions corresponding to e/a values (valence electrons per atom) of $3/2$, $21/13$, and $7/4$ (Hume-Rothery phases) [1.225].

| Phase | Pearson symbol | a (nm) | b (nm) | c (nm) | c/a | Remarks | Concentration x : A(1-x)B(x) |
|--------------------|----------------|----------|----------|----------|--------|---------|--------------------------------|
| Ag-Al | cF4 | 0.4064 | | | | | 0.18 |
| Ag ₂ Al | hP2 | 0.28777 | | 0.46223 | 1.6062 | | |
| Ag-Cd | hP2 | 0.2987 | | 0.553 | 1.8514 | | 0.97 |
| AgCd | cP2 | 0.3332 | | | | 293 K | 0.5 |
| AgCd | hP2 | 0.3016 | | 0.4863 | 1.6124 | 673 K | 0.5 |
| Ag-Cu | cF4 | 0.3603 | | | | | 0.95 |
| Ag-Mg | cF4 | 0.4116 | | | | | 0.26 |
| Ag-Mg | hP2 | 0.3197 | | 0.51838 | 1.6215 | | 0.98 |
| AgO | cF8 | 0.4816 | | | | | |
| AgO | mP8 | 0.5852 | 0.3478 | 0.5495 | | | |
| Ag-O | cP6 | 0.4728 | | | | | |
| Ag-O | hP3 | 0.3072 | | 0.4941 | 1.6084 | HP/HT | |
| Ag-Zn | hP2 | 0.28227 | | 0.44274 | 1.5685 | | 0.775 |
| Ag-Zn | hP9 | 0.7636 | | 0.28179 | 0.369 | | 0.38–0.52 |

HT = High-temperature modification, HP = High-pressure modification

Table 3.1-122

Structure and lattice parameter of intermediate Ag compounds [1.217, p. 112]

| Atomic ratio | Composition | | | | Superlattice structure | Fundamental structure |
|--------------|--------------------|-------------------|----------------------|-------------------|------------------------|-----------------------|
| 3:1 or 1:3 | Pd ₃ Fe | PdCu ₃ | Au ₃ Cu | AuCu ₃ | | |
| | Pt ₃ Fe | PtCu ₃ | Au ₃ Pd | | | |
| | Pt ₃ Ti | PtNi ₃ | Ag ₃ Pt | | L1 ₂ | fcc |
| | | PtMn ₃ | | | | |
| | Rh ₃ Mo | | Ag ₃ In | | | |
| | Rh ₃ W | | | | DO ₁₄ | |
| | Ir ₃ Mo | | | | | |
| | Ir ₂ W | | (Au ₂ Mn) | | DO ₂₂ | fcc |
| | Pd ₃ V | | | | | |
| | Pd ₃ Nb | | | | | |
| | Pt ₃ V | | | | | |
| | | | Au ₃ Cd | | DO ₂₃ | fcc |
| | | | Au ₃ Zn | | | |
| | | | Ag ₃ Mg | | | |
| 2:1 | Pd ₂ V | | | | Ni ₂ Cr | fcc |
| | Pt ₂ V | | | | | |
| | Pt ₂ Mo | | | | | |
| 1:1 | PdFe | | AuCu | | | |
| | PtFe | | | | L1 ₀ | fcc |
| | PtV | | | | | |
| | PtNi | | | | | |
| | PtCo | | | | | |
| | PtCu | | | | | fcc |
| | PdCu | | AuMn | | L1 ₁ | bcc |
| | | | AgCd | | L2 ₀ or B2 | |
| | | | AgZn | | | |
| | RhMo | | | | | hcp |
| | IrMo | | | | B19 | |
| | PtMo | | | | | |
| | IrW | | | | | |
| | PtNb | | | | | |

Table 3.1-123

Composition and structures of superlattices in NM-alloy systems [1.218, p. 105]

Table 3.1-124 Compositions and structures of *e/a* (Hume-Rothery) compounds [1.225, p. 197]

| Electron: atom ratio = 3:2 | | | Electron: atom ratio = 21:13 γ -brass structure | Electron: atom ratio = 7:4 Close packed hexagonal structure |
|-------------------------------|---|----------------------------------|---|--|
| Body-centered cubic structure | Complex cubic (β -manganese) structure | Close-packed hexagonal structure | | |
| AgMg | AgHg | AgZn | Ag ₅ Zn ₈ | AgZn ₃ |
| AgZn | Ag ₃ Al | AgCd | Ag ₅ Cd ₈ | AgCd ₃ |
| AgCd | Au ₃ Al | Ag ₃ Al | Ag ₅ Hg ₈ | Ag ₃ Sn |
| Ag ₃ Al | | Ag ₃ Ga | Ag ₉ In ₄ | Ag ₅ Al ₃ |
| Ag ₃ In | | Ag ₃ In | Au ₃ Zn ₈ | AuZn ₃ |
| AuMg | | Ag ₅ Sn | Au ₅ Cd ₈ | AuCd ₃ |
| AuZn | | Ag ₇ Sb | Au ₉ In ₄ | Au ₃ Sn |
| AuCd | | Au ₃ In | Rh ₅ Zn ₂₁ | Au ₅ Al ₃ |
| | | Au ₅ Sn | Pd ₅ Zn ₂₁ | |
| | | | Pt ₅ Be ₂₁ | |
| | | | Pt ₅ Zn ₂₁ | |

Mechanical Properties

In Tables 3.1-125–3.1-135 and Figs. 3.1-199–3.1-204 characteristic data are shown [1.217, 220, 225–229]. References for data of elastic constants of Ag alloys are given in [1.222]. Pure silver is very soft. Strengthening is affected by solid solution and by dispersion hardening [1.216, 230]. Alloying with 0.15 wt% Ni affects grain refinement and stabilizes against recrystallization. The high solubility of oxygen in silver (Table 3.1-117) permits the induction of dispersion hardening by internal oxidation of Ag alloys containing Al, Cd, Sn, and/or Zr.

Table 3.1-125 Module of elasticity of Ag in crystal directions (GPa) [1.217, p. 204]

| E(100) | E(110) | E(111) |
|--------|--------|--------|
| 44 | 82 | 115 |

Table 3.1-126 Elastic constants of Ag (GPa) [1.217, p. 204]

| T (°C) | c11 | c12 | c14 |
|--------|-------|------|------|
| -273 | 131.4 | 97.3 | 51.1 |
| +20 | 124.0 | 93.4 | 46.1 |

Table 3.1-129 Hardness of Ag–Mn alloys [1.226, p. 473]

| wt% Mn | 0.5 | 4.9 | 6.2 | 12.0 |
|--------------------------|-----|-----|-----|------|
| HV (kg/mm ²) | 31 | 39 | 40 | 58 |

| Composition (wt%) | | | BS ^a 1845 | Density (g/cm ³) | Melting range (°C) | Tensile strength (kg/mm ²) | Elongation (%) |
|-------------------|----|---|-------------------------|---------------------------------|-----------------------|---|-------------------|
| Ag | Cu | P | | | | | |
| 15 | 80 | 5 | CP1 | 8.40 | 645–719 | 25 | 10 |
| 5 | 89 | 6 | CP4 | 8.20 | 645–750 | 25 | 5 |
| 2 | 91 | 7 | CP3 | 8.15 | 645–770 | 25 | 5 |

^a = British standard (1966/1971) designation

Table 3.1-127 Mechanical properties of Ag (99.97%) at different temperatures (°C) [1.217, p. 204]

| T (°C) | E (GPa) | R _m (MPa) | A (%) | R _{p0.2} (MPa) | HV |
|--------|---------|----------------------|-------|-------------------------|----|
| 20 | 82 | 150 | 50 | 28 | 26 |
| 200 | 77 | 130 | — | 25 | 22 |
| 400 | 67 | 100 | 30 | 20 | 17 |
| 800 | 46 | 35 | — | 17 | 5 |

A = Elongation, E = Module of elasticity, R_p = Limit of proportionality, HV = Vickers hardness, R_m = Tensile strength

Table 3.1-128 Tensile strength R_m (MPa) of binary Ag alloys [1.217, p. 207]

| Content (wt%) Alloying elements | 2 | 5 | 10 | 20 |
|------------------------------------|----------------------|-----|-----|-----|
| | R _m (MPa) | | | |
| Au | 160 | 170 | 180 | 200 |
| Cd | 160 | 170 | 180 | 210 |
| Cu | 190 | 240 | 280 | 310 |
| Pd | 160 | 180 | 21 | |
| Sb | 190 | 240 | 300 | |
| Sn | 190 | 240 | 300 | |

Table 3.1-130 Mechanical properties of Ag–Cu–P alloys [1.226, p. 477]

| Composition (wt%) | | | Specific weight (cast) | Tensile strength (kg/mm ²) | Elongation (%) | Electrical conductivity (% of Cu) |
|-------------------|-----|----|---------------------------|---|-------------------|--------------------------------------|
| Cu | Zn | Ag | | | | |
| 36 | 24 | 40 | 9.11 | 40.5 | 6.2 | 19.7 |
| 25 | 15 | 60 | 9.52 | 45.0 | 7.7 | 20.5 |
| 22 | 3.0 | 75 | 10.35 | 29.3 | 5.3 | 53.4 |
| 16 | 4.0 | 80 | 10.05 | 35.1 | 16.0 | 45.8 |

Table 3.1-131

Mechanical properties of Ag–Cu–Zn alloys [1.220, p. 154]

| Alloy Ag–X (wt%) | HV5 | | <i>R_{p0.2}</i> (MPa) | | <i>R_{on}</i> (MPa) | | A (%) | |
|---------------------|-----|-----|-------------------------------|-----|-----------------------------|-----|-------|---|
| | s | h | s | h | s | h | s | h |
| Pd27.5 | 55 | | 80 | | 230 | | 33 | |
| Pd27.4Cu10.5 | 140 | 310 | 320 | 940 | 510 | 950 | 31 | 3 |
| Pd39.9Zn4 | 160 | 270 | 285 | 595 | 560 | 790 | 18 | 6 |

s = soft, h = hard

| Alloy AgX (wt%) | Temperature (°C) | | | | |
|-------------------------|------------------|--------|--------|--------|--------|
| | 20 | 200 | 400 | 600 | 800 |
| <i>R_m</i> /A | | | | | |
| Cd 4 | 170/60 | 150/50 | – | – | – |
| Cd 8 | 480/5 | 260/20 | 200/55 | – | – |
| Cu 3 | 190/35 | 170/40 | 140/40 | 90/80 | 30/150 |
| Cu 7.5 | 250.46 | 220/48 | 180/47 | 120/55 | 60/78 |
| Ni 0.3 | 190/60 | 170/60 | 130/65 | 100/65 | 60/50 |
| Si 3 | 260/39 | 220/33 | 180/35 | 90/52 | 20/55 |

Table 3.1-134 Strengthening of Ag (99.975%) by cold forming as a function of reduction in cross section in % [1.217, p. 204]

| V (%) | | <i>R_m</i> (MPa) | A (%) | HV |
|-------|---|----------------------------|-------|----|
| 0 | | 150 | 50 | 26 |
| 10 | | 180 | 30 | 54 |
| 30 | | 260 | 5 | 70 |
| 80 | 2 | 90 | | |

V = reduction of cross section

Table 3.1-135 Strengthening of Ag alloys by cold forming (HV 10) (reduction in % of thickness) [1.217, p. 207]

| Reduction (%) | 0 | 40 | 80 |
|------------------|----|-----|------|
| Alloying element | | | |
| Cu 5 | 58 | 108 | 134 |
| Cu 15 | 76 | 126 | 158 |
| Cu 28 | 98 | 136 | 177 |
| Cu 50 | 84 | 130 | 166 |
| Ni 0.15 | 40 | 86 | 100 |
| Pd 30 | 70 | 132 | 164 |
| Pd 30 Cu 5 | 92 | 174 | 2165 |

Table 3.1-133

Tensile strength *R_m* (MPa) and elongation *A* (%) of Ag alloys at different temperatures [1.217, p. 207]

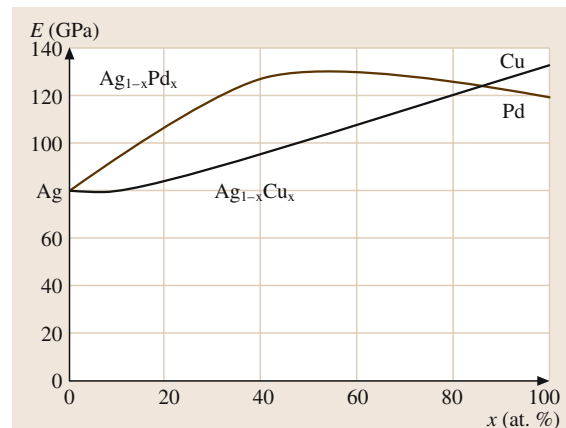


Fig. 3.1-199 Module of elasticity of Ag–Pd and Ag–Cu alloys [1.217, p. 206]

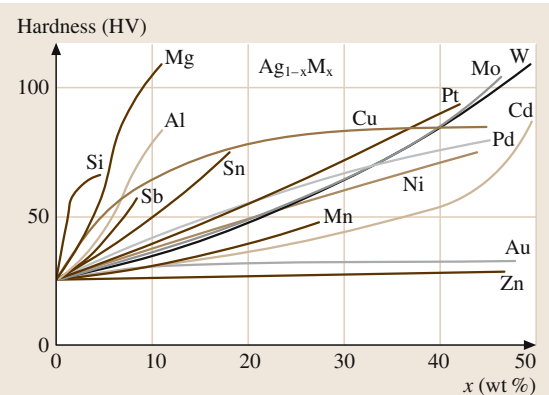


Fig. 3.1-200 Influence of alloying elements on the hardness of binary Ag alloys [1.217, p. 206]

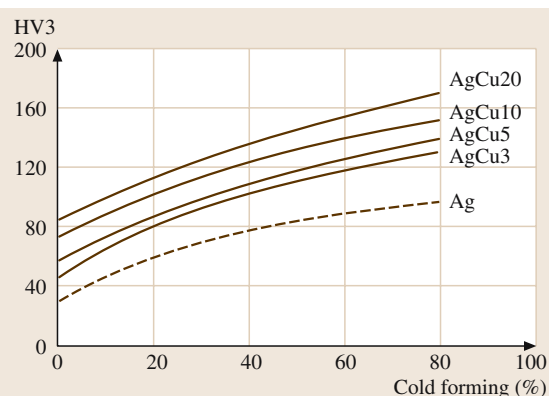


Fig. 3.1-201 Hardening of Ag–Cu alloys by cold forming [1.217, p. 432]

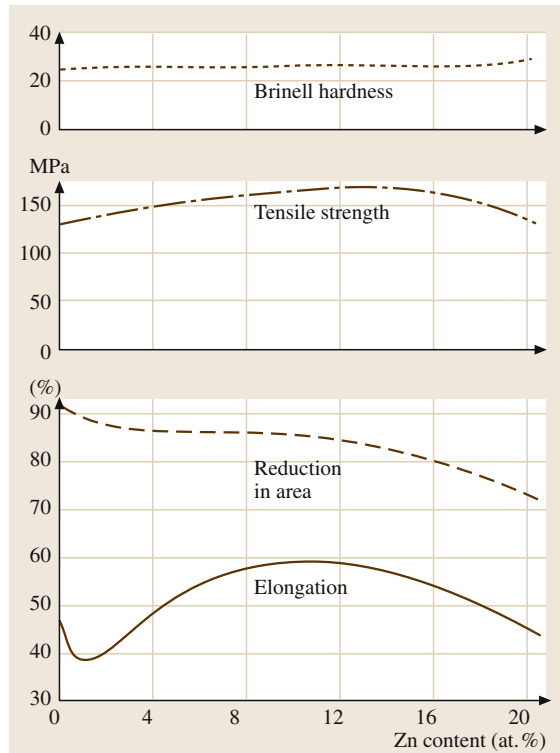


Fig. 3.1-202 Plastic properties of Ag–Zn crystals [1.220, p. 135]

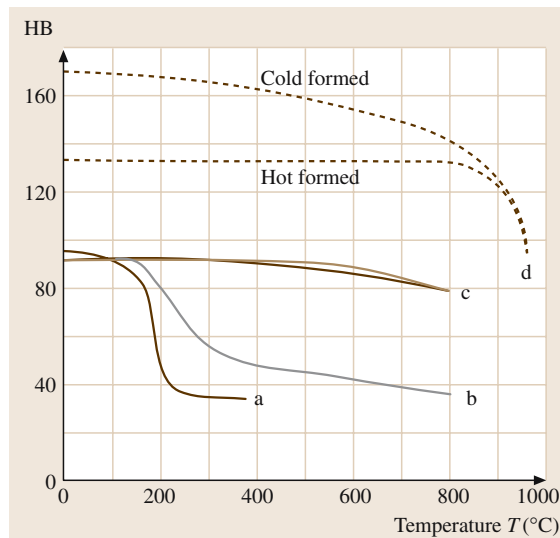


Fig. 3.1-203 Hardness of fine grain and dispersion-hardened Ag [1.216, p. 36]

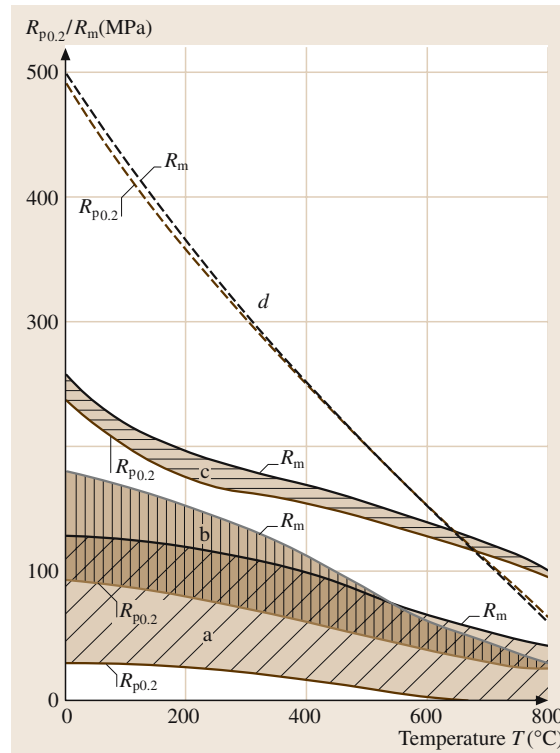


Fig. 3.1-204 Tensile strength and 0.2% proof stress of silver grades at different temperatures [1.216, p. 37]

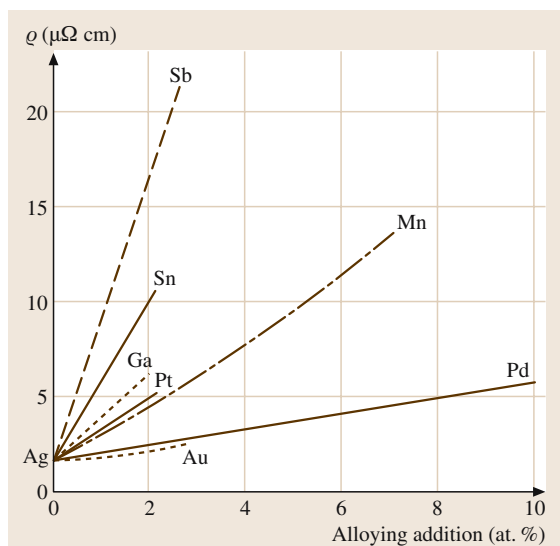


Fig. 3.1-205 Influence of alloying elements on the electrical conductivity of binary Ag alloys [1.231, p. 20]

Electrical Properties

Tables 3.1-136–3.1-139 and Fig. 3.1-205 [1.217, 231–233] show characteristic data. The residual resistivity ratio (RRR) of pure Ag ranges up to 2100. Ag alloys with Pb and Sn show superconductivity in the composition ranges: $\text{Ag}_{0.95-0.66}\text{Pb}_{0.05-0.34}$ with $T_c = 6.6-7.3 \text{ K}$ and $\text{Ag}_{0.72-0.52}\text{Sn}_{0.28-0.48}$ with $T_c = 3.5-3.65 \text{ K}$ [1.234].

Table 3.1-136 Specific electrical resistivity $\rho(T) = \rho_0 + \rho_i(T)$ of Ag ($\rho_0 = 0.0008 \mu\Omega \text{ cm}$) at different temperatures [1.217, p. 156]

| T (K) | $\rho(T)$ ($\mu\Omega \text{ cm}$) |
|---------|--------------------------------------|
| 10 | 0.0001 |
| 50 | 0.1032 |
| 120 | 0.5448 |
| 273 | 1.470 |
| 500 | 2.860 |
| 700 | 4.172 |
| 900 | 5.562 |
| 1100 | 7.031 |

Table 3.1-137 Increase of atomic electrical resistivity of Ag by alloying elements $\Delta\rho/C$ ($\mu\Omega \text{ cm}/\text{at.}\%$) [1.217, p. 157]

| Base element | Alloying elements |
|--------------|--|
| Ag | Al 1.87, As 8, Au 0.36, Cd 0.35, Cr 6.5, Cu 0.07, Fe 3.2, Ga 2.3, Ge 5, Hg 0.8, In 1.6, Pb 4.6, Pd 0.44, Pt 1.5, Sn 4.5, Zn 0.63 |

Table 3.1-138 Specific electrical resistivity ρ_i and coefficient of electrical resistivity (TCR) of noble metal solid solution alloy phases [1.217, p. 158]

| Base/ solute-metal | | Solute content | | | |
|-----------------------|----------|----------------|------|-------|------|
| | | 20 | 40 | 60 | 80 |
| Rh/Ni | ρ_i | 21 | 37 | 51 | 50 |
| | TCR | 3.8 | 1.8 | < 0.1 | 3 |
| Ag/Au | ρ_i | 8.3 | 11.0 | 11.0 | 8.1 |
| | TCR | 0.93 | 0.83 | 0.84 | 1.1 |
| Ag/Pd | ρ_i | 11 | 22 | 41 | 34 |
| | TCR | 0.58 | 0.40 | — | 0.75 |
| Ag/Pt | ρ_i | 33 | 60 | 46 | 35 |
| | TCR | 0.88 | 0.61 | 0.45 | 1.2 |
| Au/Pd | ρ_i | 9.8 | 17 | 30 | 26 |
| | TCR | 0.88 | 0.61 | 0.45 | 1.2 |
| Au/Pt | ρ_i | 28 | 44 | 0.82 | 0.8 |
| | TCR | 0.28 | 0.26 | 0.82 | 0.8 |

Table 3.1-139 Specific electrical resistivity ρ_{25} of annealed (8 h at 550 °C) Ag–Cu wire at 25 °C and 100 °C (ρ_{100}) and temperature coefficient of resistivity (TCR) α for 25–100 °C [1.226, p. 380]

| at.% Ag | 5 | 15 | 45 | 75 | 96 |
|--|-------|-------|-------|-------|-------|
| $\rho_{25} \times 10^{-6}$ ($\mu\Omega \text{ cm}$) | 1.832 | 1.895 | 1.913 | 1.645 | 1.822 |
| $\rho_{100} \times 10^{-6}$ ($\mu\Omega \text{ cm}$) | 2.369 | 2.320 | 2.411 | 2.308 | 2.297 |
| TCR $\times 10^5$ | 389 | 387 | 380 | 365 | 381 |

Thermoelectric Properties

In Tables 3.1-140–3.1-142 and Fig. 3.1-206, characteristic data are shown: absolute thermoelectric power, thermo-electromotive force of pure Ag as well as Ag–Au, Ag–Pd, and Ag–Pt alloys at different temperatures against a reference junction at 0 °C [1.217, 235, 236].

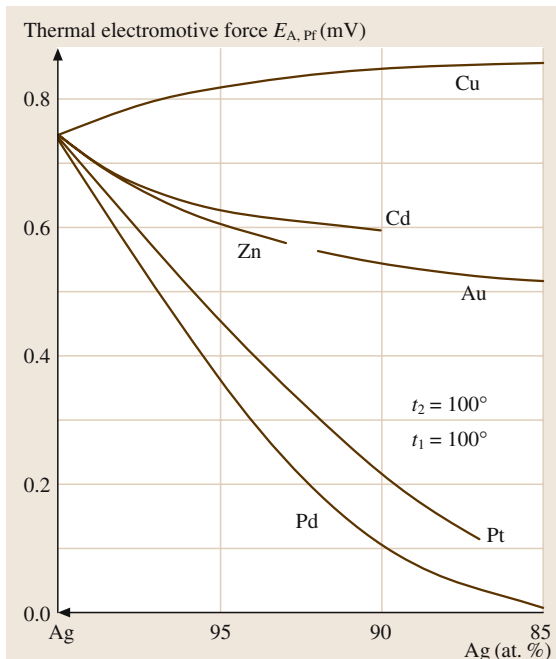


Fig. 3.1-206 Thermal electromotive force of binary Ag alloys [1.216, p. 98]

Table 3.1-140 Thermal electromotive force $E_{\text{Ag},\text{Pt}}$ (mV) of Ag at different temperatures; reference junction at 0 °C [1.217, p. 159]

| T (°C) | -200 | -100 | -50 | +100 | +200 | +400 | +800 |
|--------------------------------|-------|-------|-------|------|------|------|-------|
| $E_{\text{Ag},\text{Pt}}$ (mV) | -0.39 | -0.21 | -0.10 | 0.74 | 1.77 | 4.57 | 13.36 |

Table 3.1-142 Thermal electromotive force of Ag–Au alloys in mV at 100 °C and 700 °C reference junction at 0 °C [1.217, p. 160]

| T (°C) | Composition (wt%) | | | | | |
|--------|-------------------|------|------|------|------|-------|
| | 0 | 20 | 40 | 60 | 80 | 100 |
| 100 | 0.74 | 0.47 | 0.42 | 0.42 | 0.49 | 0.78 |
| 700 | 10.75 | 7.7 | 6.7 | 6.8 | 7.3 | 10.15 |

Magnetic Properties

Silver is diamagnetic (Table 3.1-143). The magnetic susceptibility remains constant from 0 K to the melting point. Alloying with B metals causes only minor variations compared to pure Ag. In the continuous solid solution range the molar susceptibilities remain negative and the alloys are diamagnetic. Ni, Pd, and Pt dissolve up to 25 at.% diamagnetically. Cr, Fe, and Mn give rise to paramagnetism, while Co causes ferromagnetism [1.216, 217].

Table 3.1-143 Atom susceptibility of Ag and Au alloys at room temperature [1.216, p. 90]

| Base metal | Alloying element | Base metal content (at. %) | | | | |
|------------|------------------|----------------------------|-----|-------|-------|-------|
| | | 100 | 99 | 95 | 90 | 80 |
| Ag | Au | -19 | | -20.2 | -20.8 | -22.2 |
| | Pd | -20 | | | -21 | -22 |
| Au | Cu | -26 | | -25.2 | -24.2 | -22.4 |
| | Ni | -28 | -22 | ±0 | +16 | - |
| | Pd | -28 | | | -20 | -15 |
| | Pt | -28 | | | -6 | ±0 |

Table 3.1-141 Absolute thermoelectric power of Ag at different temperatures [1.216, p. 94]

| Temperature (°C) | -255 | -200 | -100 | -20 | 0 | 100 | 300 | 500 | 800 |
|---|-------|-------|-------|-----|------|------|------|------|------|
| Thermoelectric power ($\mu\text{V}/^\circ\text{C}$) | +0.62 | +0.82 | +1.00 | - | +1.4 | +1.9 | +3.0 | +4.6 | +8.3 |

Thermal Properties

Selected data of thermal expansion, thermal conductivity, and melting temperatures of Ag alloys are given in Tables 3.1-144–3.1-150 and in Fig. 3.1-207 [1.216, 220].

Table 3.1-144 Recrystallization temperatures ($^{\circ}\text{C}$) of Ag 99.95 and 99.995% purity after different degrees of deformation V ; annealing time 1 h [1.217, p. 205]

| V (%) | $T_{\text{recryst.}}$ | |
|---------|-----------------------|---------|
| | Purity 99.95% | 99.995% |
| 40 | 190 | 125 |
| 60 | 160 | 100 |
| 99 | 127 | 70 |

Table 3.1-145 Mean coefficients of thermal expansion α (10^{-6} K^{-1}) of Ag and Au [1.217, p. 154]

| T (K) | α (10^{-6} K^{-1}) | |
|---------|---------------------------------------|------|
| | Ag | Au |
| 373 | 17.9 | 13.9 |
| 473 | 19.1 | 14.8 |
| 673 | 19.9 | 15.3 |
| 873 | 21.1 | 15.7 |
| 1073 | 23.6 | 16.2 |

Table 3.1-146 Mean coefficients of thermal expansion α (10^{-6} K^{-1}) of Ag and Au alloys [1.217, p. 154]

| Base metal | Au | Au | Au | Au | Ag |
|------------------|---------------------------------------|------|------|------|------|
| 2nd metal | Ag | Ag | Cu | Ni | Pd |
| Temp. range (K) | 273 | 293 | 273 | 273 | 373 |
| | 373 | 1073 | 593 | 373 | 473 |
| wt% of 2nd metal | α (10^{-6} K^{-1}) | | | | |
| 20 | 15.5 | 17.0 | 14.9 | 14.4 | 16.2 |
| 40 | 16.5 | 18.7 | — | 13.9 | — |
| 50 | 17.0 | — | 15.7 | 14.0 | 14.7 |
| 60 | 17.5 | 20.1 | 15.8 | 13.9 | — |
| 80 | 18.2 | 20.8 | 15.9 | 13.4 | 12.4 |

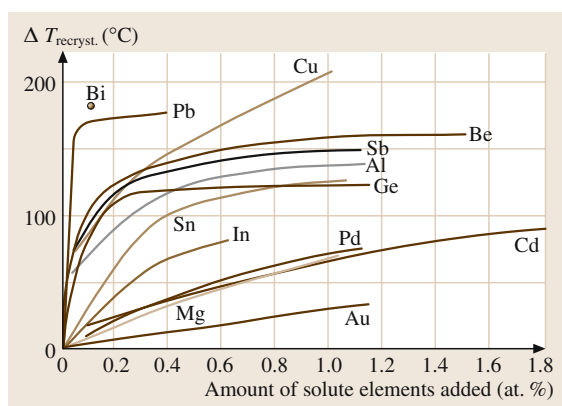


Fig. 3.1-207 Increase of the recrystallization temperature of Ag by solute elements [1.218, p. 452]

Table 3.1-149 Thermal conductivity λ (W/m K) of Ag and Au at different temperatures [1.217, p. 153]

| T (K) | λ (W/m K) | |
|---------|-------------------|-----|
| | Ag | Au |
| 40 | 1050 | 420 |
| 100 | 475 | 360 |
| 273 | 435 | 318 |
| 600 | 411 | 296 |
| 800 | 397 | 284 |

Table 3.1-150 Melting range of Ag–Cu–Sn and Ag–Cu–In solder alloys

| Composition (wt%) | | | | Melting range (°C) |
|-------------------|----|----|----|--------------------|
| Ag | Cu | Sn | In | |
| 60 | 23 | 17 | | 557–592 |
| 50 | 30 | 20 | | 555–578 |
| 47 | 20 | 33 | | 472–515 |
| 50 | 10 | 40 | | 435–456 |
| 49 | 19 | | 32 | 549–556 |
| 50 | 25 | | 25 | 594–601 |
| 45 | 17 | | 38 | 534–548 |
| 25 | 45 | | 30 | 581–610 |

Table 3.1-147 Specific heat of Ag at different temperatures [1.220, p. 9]

| T (°C) | -259.46 | -240.86 | -141.93 | -67.90 | +98.7 | +249.0 | +399.5 | +652.2 |
|---------------|----------|---------|---------|---------|--------|--------|--------|--------|
| c_p (cal/g) | 0.001177 | 0.01259 | 0.04910 | 0.05334 | 0.0569 | 0.0583 | 0.0600 | 0.0635 |

Table 3.1-148 Vapor pressure of liquid Ag [1.220, p. 8]

| T (°C) | 1550 | 1611 | 1742 | 1838 | 1944 | 2152 |
|-------------------------|------|------|------|------|------|-----------------|
| Vapour pressure (mm Hg) | 8.5 | 15.7 | 54 | 100 | 190 | 760 (extrapol.) |

Optical Properties

Table 3.1-151 and Figs. 3.1-208, 3.1-209 [1.237] show characteristic data of optical properties. Ag has the highest reflectivity of all noble metals. An interband transition takes place in the ultraviolet range at 3.9 eV. Ag–Al alloys between 10 at.% and 28 at.% Ag show higher reflectance in the low wavelength range than the pure elements. In Ag–Pd alloys, the threshold energy at 3.9 eV for the interband transition remains constant up to \approx 34 at.% Pd. Examples of colored Ag alloys are given in Table 3.1-152 [1.237].

Table 3.1-151 Spectral emissivity of Ag and Au at different temperatures [1.217, p. 171]

| | Surface | Temperature (°C) | Spectral degree of emission |
|----|---------|------------------|-----------------------------|
| Ag | Solid | 940 | 0.044 |
| | Liquid | 1060 | 0.0722 |
| Au | Solid | 1000 | 0.154 |
| | Liquid | 1067 | 0.222 |

Table 3.1-152 Colored noble metal alloys [1.237, p. 178]

| Alloy | Color | Remarks |
|-------------------------|--------------|----------|
| Ag–Zn (β -phase) | Rose | |
| Ag–Au(70) | Green-yellow | |
| Al ₂ Au | Violet | |
| KAu ₂ | Violet | |
| Au–Zn–Cu–Ag | Green | |
| AuIn ₂ | Blue | |
| <i>Zintl Phases</i> | | |
| Li ₂ AgAl | Yellow-rose | VEC 1.5 |
| Li ₂ AgGa | Yellowish | VEC 1.5 |
| Li ₂ AgIn | Gold-yellow | VEC 1.5 |
| Li ₂ AgTl | Violet-rose | VEC 1.5 |
| Li ₂ AuTl | Green-yellow | VEC 1.5 |
| Li ₂ AgSi | Rose-violet | VEC 1.75 |
| Li ₂ AgGe | Rose-violet | VEC 1.75 |
| Li ₂ AgSn | Violet | VEC 1.75 |
| Li ₂ AgPb | Blue-violet | VEC 1.75 |
| Li ₂ AuPb | Violet | VEC 1.75 |

VEC = Valence electron concentration

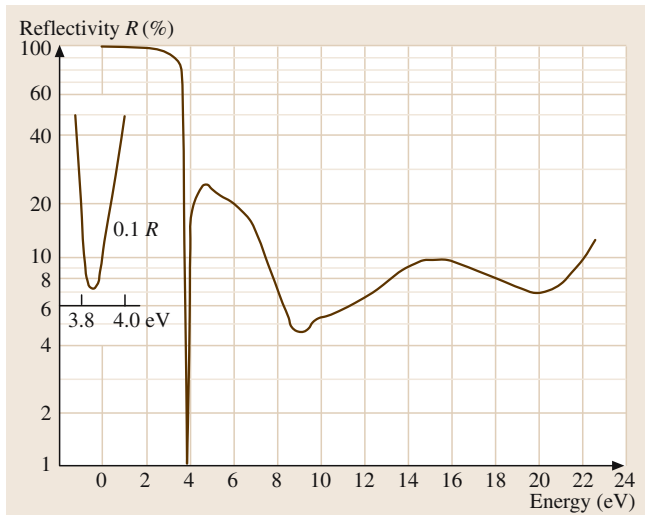


Fig. 3.1-208 Reflectance versus radiation energy of Ag [1.237, p. 158]

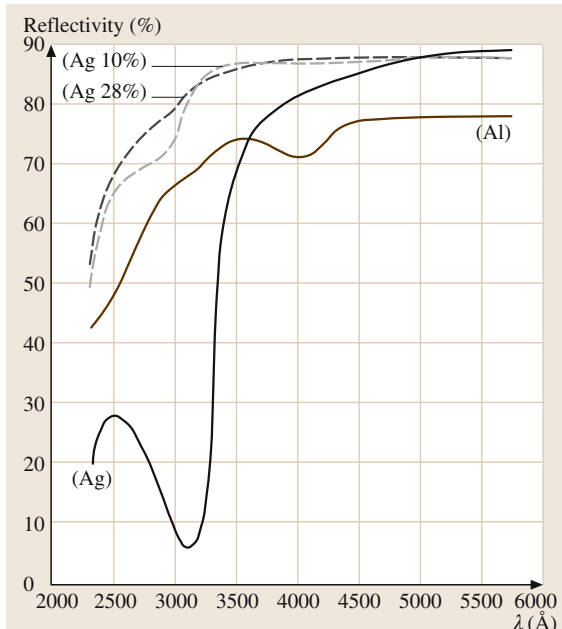


Fig. 3.1-209 Reflectivity of Ag–Al alloys [1.220, p. 142]

Diffusion

Data for self-diffusion of Ag in Ag alloys and diffusion of tracer impurity elements are shown in Tables 3.1-153–3.1-158 and Figs. 3.1-210–3.1-212. Diffusion of H and O is of importance for annealing treatments and dispersion hardening [1.217, 220, 226, 235].

Table 3.1-153 Self-diffusion in binary homogeneous Ag–Au alloys [1.217, p. 150]

| Au (at.%) | ΔT (K) | D^0 ($10^4 \text{ m}^2/\text{s}$) | Q (kJ/mol) |
|--|----------------|---------------------------------------|--------------|
| Ag–Au (^{110}m Ag diffusion) | | | |
| 8 | 927–1218 | 0.52 | 187.5 |
| 17 | 908–1225 | 0.32 | 184.4 |
| 83 | 923–1284 | 0.09 | 171.7 |
| 94 | 936–1234 | 0.072 | 168.5 |
| Ag–Au (^{198}Au diffusion) | | | |
| 8 | 991–1213 | 0.82 | 202.2 |
| 17 | 991–1220 | 0.48 | 198.0 |
| 83 | 985–1274 | 0.12 | 180.2 |
| 94 | 991–1283 | 0.09 | 176.1 |

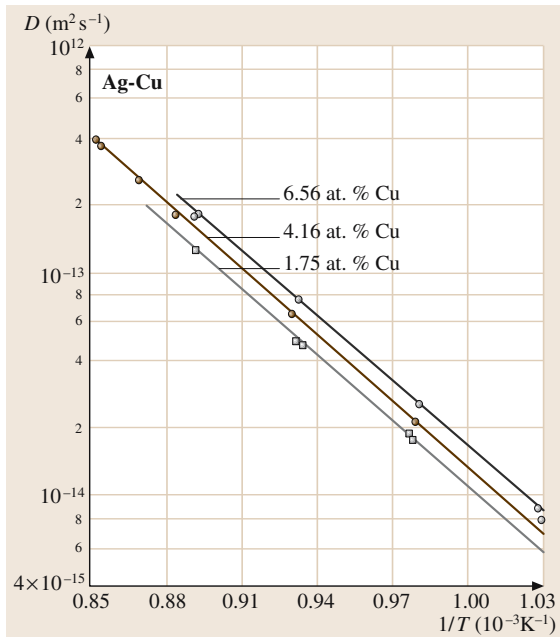


Fig. 3.1-210 Self-diffusion of Ag(^{110}m) in Ag–Cu (1.75–6.56 at.% Cu) alloys [1.238, p. 189]

| | Element | D^0 (m^2/s) | Q (kJ/mol) | T (K) |
|----------------|--------------------|---------------------------------|--------------|-----------------------------|
| Lattice | Ag | 0.278 | 181.7 | 1038–1218 |
| | Ag(s) ^a | 0.67 | 190.1 | 913–1221 |
| | Au | 0.107 | 176.9 | 623–733 |
| | Au(s) ^a | 0.027 | 165 | 603–866 |
| Surface | Ag | 1×10^4 | 264 | 873–1173 (H ₂) |
| | Ag | 3×10^{-5} | 49 | 580–730 (Vac.) |
| | Au(110) | 1×10^2 | 227 | 1138–1329 (H ₂) |
| | Au | 8×10^2 | 272 | 1200–1300 (Vac.) |
| Grain-boundary | Ag | 7.24×10^{-5} | 190.4 | ~790–680 |
| | Au | 9.10×10^{-6} | 174.6 | 625–521 |

^a (s) = single crystal

Table 3.1-154 Self-diffusion in pure Ag and Au [frequency factor D^0 ($10^{-4} \text{ m}^2/\text{s}$)], activation energy Q (kJ/mol) [1.217, p. 149]

| Ag in Cu | | | | | |
|-----------------|-----------------------|-----------------------|------------------------|-----------------------|------------------------|
| T (°C) | 485 | 574 | 625 | 731 | 794 |
| D_{Ag} | 4.9×10^{-14} | 8.2×10^{-13} | 2.91×10^{-12} | 7.7×10^{-11} | 1.65×10^{-10} |
| | ± 0.1 | ± 0.6 | ± 0.08 | | |

$$D = D_0 \exp(-E_A/RT) \text{ with } D_0 = 0.61 \text{ cm}^2/\text{s}, E_A = 46.5 \text{ kcal/g-at.}$$

| Cu in Ag | | | | | |
|-----------------|------------------------|------------------------|------------------------|-----------------------|-----------------------|
| T (°C) | 498 | 597 | 760 | 800 | 895 |
| D_{Cu} | 2.87×10^{-13} | 5.08×10^{-12} | 3.55×10^{-10} | 5.9×10^{-10} | 9.4×10^{-10} |
| | ± 0.45 | ± 0.54 | | | |

$$D_0 = 1.23 \text{ cm}^2/\text{s}, E_A = (46.1 \pm 0.9) \text{ kcal/g-at.}$$

Table 3.1-156 Diffusion of impurities in Ag, Au, Pt and Pd [1.217, p. 151]

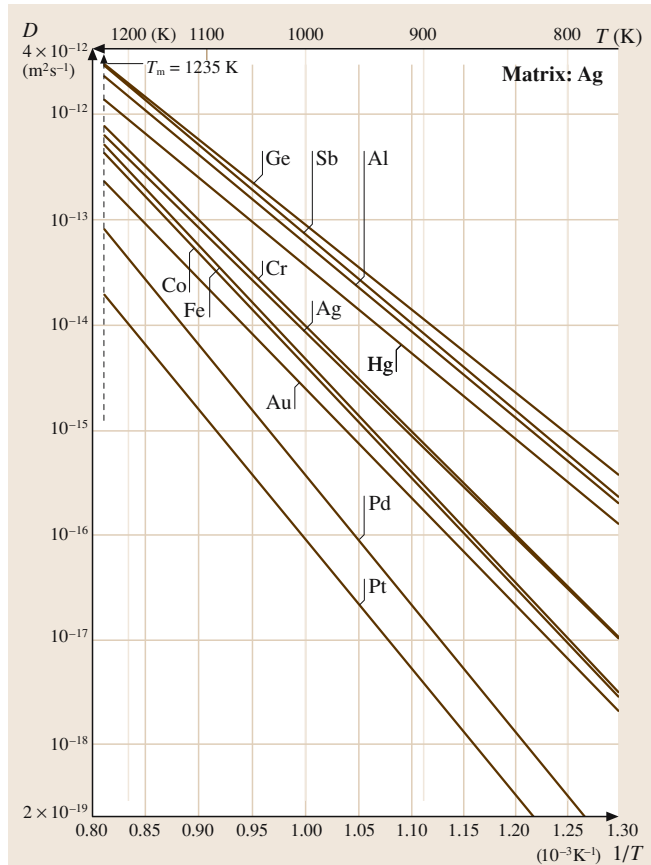
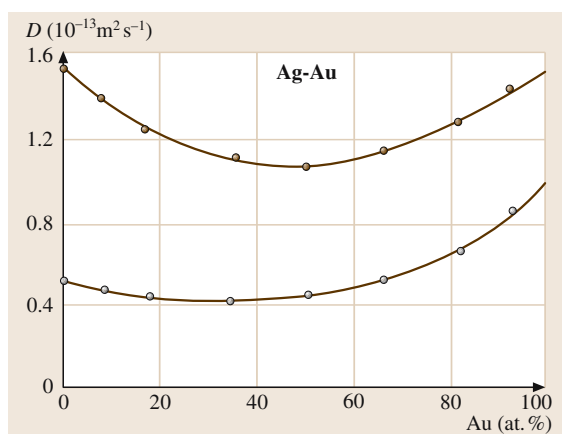
| Tracer | D^0 (10^{-4} m 2 /s) | Q (kJ/mol) | ΔT (K) | Tracer | D^0 (10^{-4} m 2 /s) | Q (kJ/mol) | ΔT (K) | | | | |
|---------------------|------------------------------|--------------|----------------|------------------------|------------------------------|--------------|----------------|--|--|--|--|
| Matrix: Silver (Ag) | | | | | | | | | | | |
| Cu | 1.23 | 193.0 | 990–1218 | Pd | 0.076 | 195.1 | 973–1273 | | | | |
| | 0.029 | 164.1 | 699–897 | Pt | 0.095 | 201.4 | 973–1273 | | | | |
| Au | 0.262 | 190.5 | 923–1223 | Ag | 0.072 | 168.3 | 943–1281 | | | | |
| | 0.41 | 194.3 | 929–1178 | | 0.08 | 169.1 | 1046–1312 | | | | |
| | 0.85 | 202.1 | 991–1198 | | 0.086 | 169.3 | 1004–1323 | | | | |
| | 0.62 | 199.0 | | Hg | 0.116 | 156.5 | 877–1300 | | | | |
| Pd | 9.57 | 237.6 | 1009–1212 | Matrix: Platin (Pt) | | | | | | | |
| Pt | 6.0 | 238.2 | 923–1223 | Ag | 0.13 | 258.1 | 1473–1873 | | | | |
| | 1.9 | 235.7 | 1094–1232 | Au | 0.13 | 252.0 | 850–1265 | | | | |
| Ru | 180 | 275.5 | 1066–1219 | Matrix: Palladium (Pd) | | | | | | | |
| | | | | Fe | 0.18 | 260 | 1373–1523 | | | | |

Table 3.1-157 Grain boundary tracer diffusion in pure Ag [1.217, p. 150]

| Matrix metal | Tracer | D^0 (m 2 /s) | Q (kJ/mol) | T (K) |
|--------------|--------|--------------------|--------------|---------|
| Ag | Cd | 5.04×10^4 | 176.6 | 772–557 |
| | In | 5.50×10^4 | 174.8 | 764–469 |
| | Sb | 2.34×10^4 | 163.5 | 771–471 |
| | Sn | 4.72×10^4 | 170.9 | 776–527 |
| | Te | 2.10×10^4 | 154.7 | 970–650 |

Table 3.1-158 Diffusion of hydrogen and oxygen in Ag, Pd, Pt, and Au [1.217, p. 151]

| Matrix | Gas | D^0 (10^{-4} m 2 /s) | Q (kJ/mol) | ΔT (K) |
|--------|-----|------------------------------|--------------|----------------|
| Ag | H | 8.55×10^{-3} | 30.11 | 947–1123 |
| Ag | O | 3.66×10^{-3} | 46.1 | 680–1140 |
| Pd | H | 2.9×10^{-3} | 22.19 | 473–1548 |
| | D | 1.7×10^{-3} | 19.88 | 218–233 |
| | T | 7.2×10^{-3} | 23.8 | 273–323 |
| Pt | H | 6×10^{-3} | 24.70 | 600–900 |
| Au | H | 5.6×10^{-4} | 23.61 | 773–1213 |

**Fig. 3.1-211** Diffusion of impurities in Ag [1.238, p. 244]**Fig. 3.1-212** Self-diffusion of Ag(110w) (brown circles) and Au(198) (gray circles) in Ag–Au (8–94 at.%) Ag–Au alloys [1.238, p. 190]

Chemical Properties

Silver has the reduction potential of $E_0 = +0.8$ V for Ag/Ag⁺. It is resistant against dry oxygen, air, non-oxidizing acids, organic acids, and alkali. Water and water vapor do not attack Ag up to 600 °C. Ag is dissolved in alkaline cyanide solutions in the presence of oxidizing agents, air, and oxygen. H₂S attacks Ag readily at room temperature, forming black Ag₂S layers (tarnish) [1.217].

Metallic Ag and Ag–Au alloys are heterogeneous catalysts for oxidation processes, e.g., in the production of ethylene oxide and formaldehyde applied as grids or as powder preparations on Al₂O₃ or carbon substrates [1.217].

Ag-Based Materials

Binary alloys (Tables 3.1-159–3.1-161) [1.218]: Ag–Ni alloys are grain-stabilized materials usually containing 0.15 wt% Ni. Ag–Cu alloys have manifold applications in jewelry, silverware, brazes, and solders. Jewelry, sil-

Table 3.1-161 Physical properties of noble-metal-containing vacuum braze alloys [1.217, p. 560]

| | Composition | Solidus (°C) | Liquidus (°C) |
|-------|------------------|--------------------|------------------|
| Ag–Cu | Ag40Cu19Zn21Cd20 | 595 | 630 |
| | Ag60Cu27In13 | 605 | 710 |
| | Ag44Cu30Zn26 | 675 | 735 |
| | Ag72Cu28 | 779 E ^a | |
| Ag–Mn | Ag85Mn15 | 950 | 950 |
| Ag–Pd | Ag68.4Pd5Cu26.6 | 807 | 810 |
| | Ag54Pd25Cu21 | 901 | 950 |
| | Ag75Pd20Mn5 | 100 | 1120 |
| Pd–Cu | Pd18Cu72 | 1080 | 1090 |
| Pd–Ni | Pd60Ni40 | 1237 | 1237 |
| Au–Cu | Au80Cu20 | 890 | 890 |
| | Au33Cu65 | 990 | 1010 |
| Au–Ni | Au82Ni18 | 950 | 950 |

^a E = Eutectic composition

Table 3.1-159 Noble metal containing soft solders [1.217]

| Alloy (wt%) | Melting range (°C) | Density (g/cm ³) | Tensile strength (N/mm ²) | Elongation (%) | Elasticity module (N/mm ²) | Thermal expansion (10 ⁻⁶ K ⁻¹) | Electrical conductivity (m/Ω mm ²) | Thermal conductivity (W/m K) |
|----------------|-----------------------|---------------------------------|---|--------------------|--|---|--|------------------------------------|
| AuSn20 | 280 | 14.57 | 275 | < 1 | 59 200 | 16 | < 5 | 57.3 |
| AuGe12 | 356 | 14.70 | 150–200 | < 1 | 69 300 | 13.4 | 7 | 44.4 |
| AuSi2 | 363–740 | 14.50 | 500–600 ^a | 0.5–3 ^a | | 12.6 | 33 | 50 |
| SnAg25Sb10 | 228–395 | 7.86 | 80–120 | 1–4 | 23 000 | 19 | 6.5 | 55 |
| SnAg3.5 | 221 | 7.38 | 25–35 | 20–30 | 41 100 | 27.9 | 7.5 | 57 |
| PbSn5Ag2.5 | 280 | 11.70 | 25–35 | 20–30 | 21 300 | 29 | < 5 | 44 |
| PbIn5Ag2.5 | 307 | 11.60 | 35–40 | 28–34 | 19 900 | 29 | < 5 | 42 |

^a Hard rolled condition

Table 3.1-160 Noble-metal-containing brazing alloys [1.217, p. 560]

| Alloy (wt%) | Melting range (°C) | Density (g/cm ³) | Tensile strength (N/mm ²) | Elongation (%) | E-Modul. (N/mm ²) | Thermal expansn. (10 ⁻⁶ K ⁻¹) | Electrical condet. (m/Ω mm ²) | Thermal condet. (W/m K) | ISO Type 3677 |
|----------------|-----------------------|---------------------------------|---|-------------------|----------------------------------|--|---|-------------------------------|--------------------|
| AgCu28 | 779 | 10.00 | 250–350 | 20–28 | 100 000 | 19.8 | 10 | | B Ag72 Cu780 |
| AgCu27In13 | 605–710 | 9.70 | 400–500 | 20–30 | 85 000 | 17.8 | 46.1 | 352 | B Ag60CuIn 695–710 |
| AgCu26.6Pd5 | 807–810 | 10.10 | 370–410 | 12–20 | 120 000 | 22 | 26 | 215 | B Ag68CuPd 807–810 |
| AgCu31.5Pd10 | 824–852 | 10.10 | 500–540 | 2–5 | 140 000 | 17.5 | 19 | 150 | B Ag58CuPd 824–852 |
| AgCu20Pd15 | 850–900 | 10.40 | 510–550 | 5–9 | 140 000 | 22 | 15 | 100 | B Ag65CuPd 850–900 |
| AgCu21Pd25 | 910–950 | 10.50 | 540–580 | 13–21 | 140 000 | 17.5 | 8 | 80 | B Ag54PdCu 901–950 |
| AgPd5 | 970–1010 | 10.50 | 180–220 | 26–34 | 40 000 | 22 | 25 | 220 | B Ag95Pd 970–1010 |
| CuPd18 | 1080–1090 | 9.40 | 380–420 | 31–39 | 135 000 | 18.9 | 9.1 | 100 | B Cu82Pd 1080–1090 |
| AgCu28Pd20 | 879–898 | 10.30 | 580–620 | 6–10 | 100 000 | 18.6 | 9.5 | 95 | B Ag52CuPd 879–898 |
| AuNi18 | 950 | 15.96 | 550–650 | 8 | | 14.6 | 5.9 | | B Au82Ni 950 |

Table 3.1-162 Typical powder grades of Ag, Pd, and Ag–Pd preparations for capacitors

| Metal | Manufacturing method | Grain shape | Grain size (μm) | Tap density (g/cm^3) | Specific surface ^a (m^2/g) |
|---------|-------------------------|--------------------------|------------------------------|--|---|
| Ag | Chemical reduction | Microcrystalline | 0.5–2.0 | 0.8–5.0 | 0.1–2.0 |
| | Electrolytic deposition | Dendritic ↓ Flakes | 1–200 2–40 | 4.5–4 2.5–5 | 0.1–0.5 0.2–1.8 |
| | Ball milling | | | | |
| Pd | Chemical reduction | Crystalline spheres | < 20 < 1.2 | 0.8 4.0 | 2.5 2.3 |
| | | | | | |
| Ag–Pd30 | Coprecipitation | Spheres ↓ Flakes | < 1.2 < 9 | 3.3 3.4 | 2.2 3.3 |
| | | | | | |

^a BET in N_2 adsorption

ver ware alloys, and coins usually contain between 7.5 wt% Cu (“sterling silver”) and 20 wt% Cu. The material Ag–28 wt% Cu is the most common silver brazing alloy. Alloys of Ag–Mn are special solders for hard metal and refractory metals (Mo, W). The alloy Ag–1 wt% Pt is applied in thick film layers for conductor paths in passive electronic devices. Ag–Pd powder preparations containing 10 to 30 wt% Pd form the conductor layers in multilayer capacitors (Table 3.1-162) [1.217].

Ternary and Higher Alloys

Alloys of the systems Ag–Cu–Sn, Ag–Cu–Zn, and Ag–Cu–Cu₃P are used as solders and brazes. Ag–Cu–P solder alloys can be applied without flux. Ti-containing solder alloys (active solders) allow di-

rect bonding to ceramics (Table 3.1-162) [1.239]. Alloys of the systems Ag–Au–Cu, Ag–Au–Ni, and Ag–Cu–Pd are applied in jewelry and dentistry (Tables 3.1-186, 3.1-187).

The oxide AgO forms the cathode of AgO/Zn button type batteries with a cell voltage of 1.55 V and with energy densities in the range of 80–250 Wh/dm² [1.218, 240–242].

Composite materials with SnO₂, CdO, carbon, Ni, and refractory carbides as dispersoids are base materials of electrical (Tables 3.1-163, 3.1-164, and Fig. 3.1-213) [1.226, 231, 243]. Extruded powder composites show preferred alignment of the dispersoid particles along the rod axes. Silver–nickel fiber composites are magnetic. Their coercivity increases with decreasing diameter of the Ni fibers [1.244].

Table 3.1-163 Hardness and electrical conductivity of Ag–Ni–C (contact) alloys [1.226, p. 436]

| | | | | | |
|---|------|------|------|------|-------|
| Alloy content wt% C | 3 | 2 | 2.5 | 2.5 | 2.5 |
| Alloy content wt% Ni0.5 | 0.5 | 0.5 | 1 | 5 | 10 |
| HV (kg/mm ²) ^{40.5} | 43 | 53 | 50 | 53 | 56–57 |
| Electrical conductivity in % of standard Cu | 63.7 | 74.8 | 69.8 | 67.3 | 64.5 |

Table 3.1-164 Silver bearing composite contact materials [1.243, p. 156]

| Type | Composition (at.%) | Hardness HV | Electrical conductivity ($\text{m}/\Omega \text{ mm}^2$) |
|----------------------------|--------------------------|-------------|--|
| Alloys | AgNi(0.15) | 100 | 58 |
| | AgCu(3) | 120 | 52 |
| | ↓ AgCu(20) | 150 | 49 |
| Composites with: | | | |
| Metals | Ag–Ni(10) | 90 | 54 |
| | ↓ Ag–Ni(40) | 115 | 37 |
| Oxides | Ag–CdO(10) | 80 | 48 |
| | ↓ | | |
| | Ag–CdO(15) | 115 | 45.5 |
| | Ag–ZnO(88) | 95 | 49 |
| | Ag–SnO ₂ (8) | 92 | 51 |
| Carbon | Ag–SnO ₂ (12) | 100 | 42 |
| | Ag–C(2) | 40 | 48 |
| | Ag–C(5) | 40 | 43.5 |
| Refractory metal compounds | Ag–W(20) | 240 | 26–28 |
| | ↓ | | |
| | Ag–W(80) | 80 | 42 |
| | Ag–WC(40) | 130 | 24–30 |
| Ag–WC(80) | 470 | | |

^a Composite made by infiltration of liquid silver into a tungsten skeleton

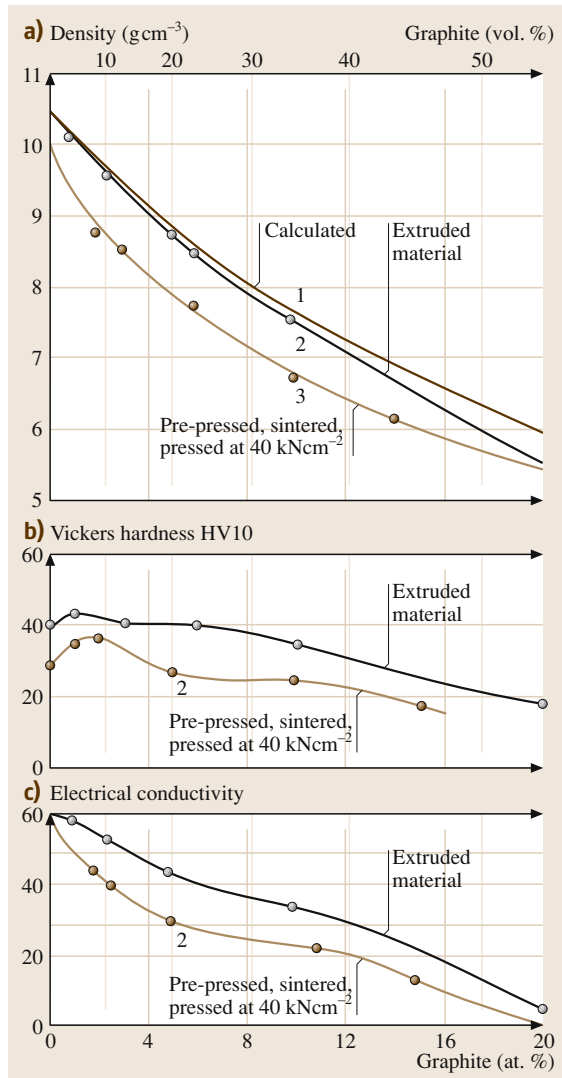


Fig. 3.1-213 (a) Density, (b) hardness, and (c) electrical conductivity of Ag–C alloys [1.231, p. 44f.]

3.1.10.2 Gold and Gold Alloys

Application

Gold and gold alloys are used for electrical contacts, bonding wires and conductor paths in semiconductor devices, chemical and corrosion resistant materials, thin surface coatings for optical and heat reflecting mirrors, special thermocouples, and catalysts for organic chemical reactions. Classical applications are jewelry, dentistry, monetary bars, and coins. Commercial grades: Table 3.1-165. The purity grades of gold bars are standardized in the range of 99.9 to 99.999 wt% (ASTM B 562-86), Tables 3.1-165, and 3.1-166 [1.217].

Production

Elementary gold is extracted from ores by cyanide leaching and precipitated with zinc, and by electrolysis. Refining is achieved by application of chlorine gas up to 99.5%, and to 99.9% and higher by electrolysis. Bars, sheets and wires are made by casting, rolling and drawing; powder is formed by chemical and by electrolytic precipitation from solutions; and nanocrystalline powders are formed by dispersion in organic solutions. Coatings are produced by cladding; electroplating; and applying powder preparations followed by firing. Thin films are produced by evaporation and cathode sputtering. Very fine gold leaves are made by traditional hammering to a thickness of $\sim 0.2 \mu\text{m}$, or by cathode sputtering.

Phases and Phase Equilibria

Selected phase diagrams are shown in Figs. 3.1-214–3.1-223 [1.245, 246]. Continuous solid solutions are

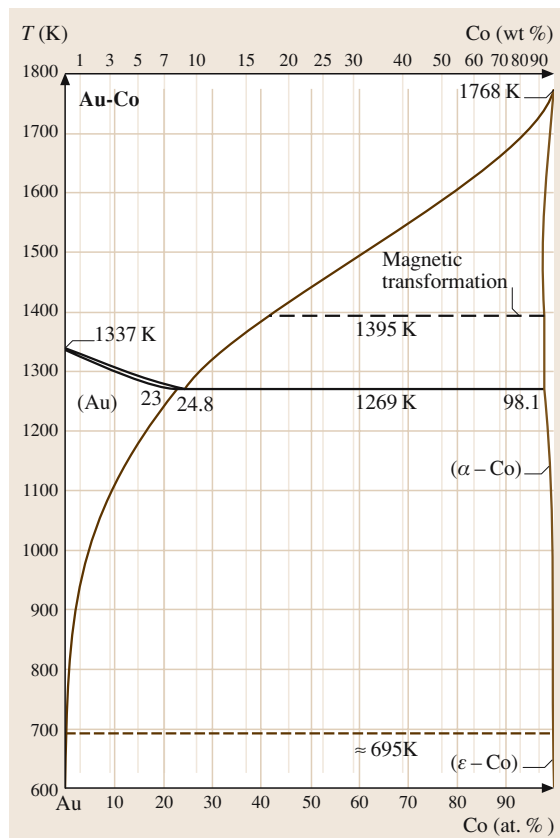


Fig. 3.1-214 Binary phase diagram of Au–Co [1.245]

formed with Ag, Co, Cu, Fe, Ni, Pd, and Pt. Misibility gaps occur with Be, Ni, Pt, Rh, and Ru. Thermochemical data are listed in Tables 3.1-167,

Table 3.1-165 Specifications of fine gold [1.217, p. 52]

| Designation | Grade (wt%) | Impurity | Maximum content (ppm) |
|----------------------------|-------------|---------------------------------|-----------------------|
| “Good delivery” gold | 99.5 | any, total | 5000 |
| Fine gold | 99.99 | Ag/Cu/others/total | 100/20/30/100 |
| Fine gold, chemically pure | 99.995 | Ag/others/total | 25/25/50 |
| Fine gold, high purity | 99.999 | Ag/Fe/Bi/Al/Cu/Ni/Pd + Pt/total | 3/3/2/0.5/0.5/0.5/10 |

Table 3.1-166 Standard fineness of noble metal alloys and corresponding carat of jewelry [1.217, p. 52]

| | Fineness (wt%) | | | | | |
|-------|----------------|-----|-----|-----|-----------------|------|
| Au | | 375 | 585 | 750 | 916,999 | |
| Ag | | | | | 800,925,999 | |
| Pd | | | 500 | | 850,900,950,999 | |
| Pt | | | 500 | | 950,999 | |
| | 333 | 375 | 585 | 750 | | 1000 |
| Carat | 8 | 9 | 14 | 18 | | 24 |

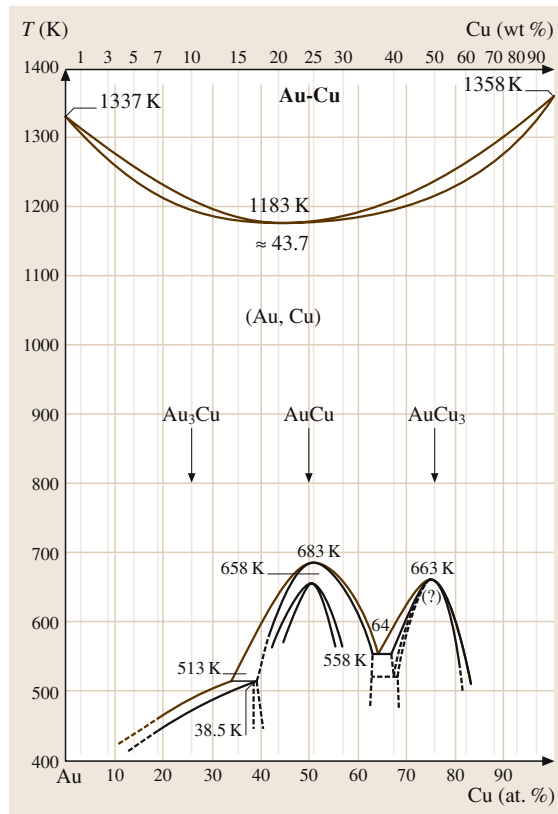


Fig. 3.1-215 Binary phase diagram of Au–Cu [1.245]

and 3.1-168 [1.217, 222]. Compositions, crystal structures and lattice parameters of selected intermetallic compounds are given in Table 3.1-169 [1.217] and in Figs. 3.1-224 and 3.1-225 [1.245]. Primary solid solutions have the fcc structure of Au. The lattice parameters of the substitutional solid solutions correspond roughly to Vegard's law with a few exceptions [1.247].

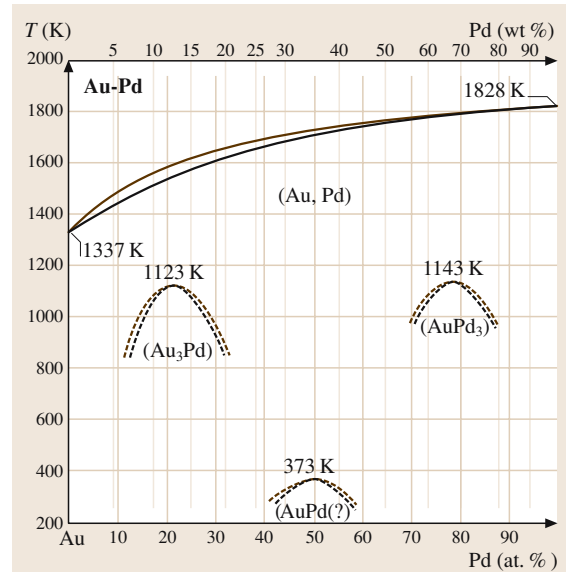


Fig. 3.1-217 Binary phase diagram of Au–Pd [1.245]

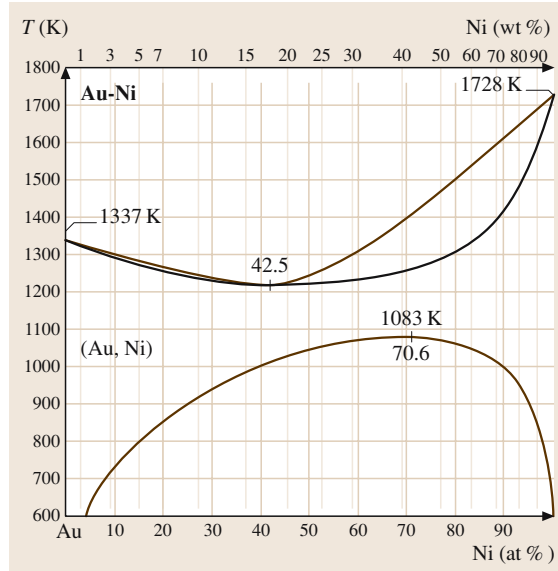


Fig. 3.1-216 Binary phase diagram of Au–Ni [1.245]

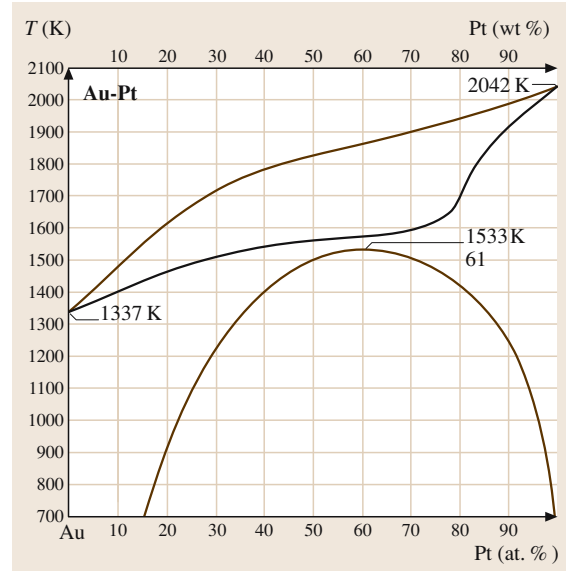
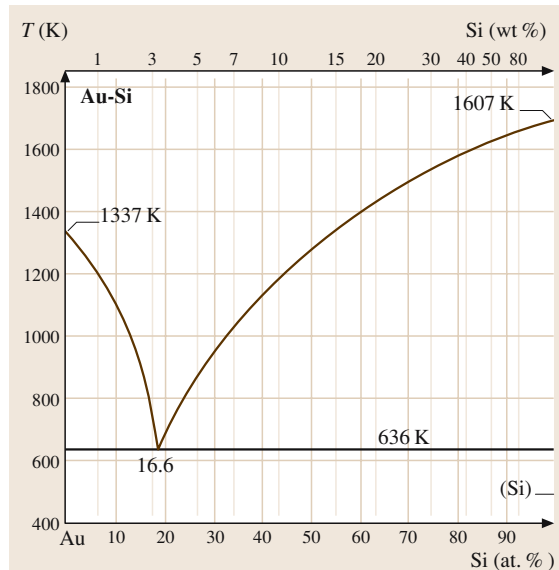
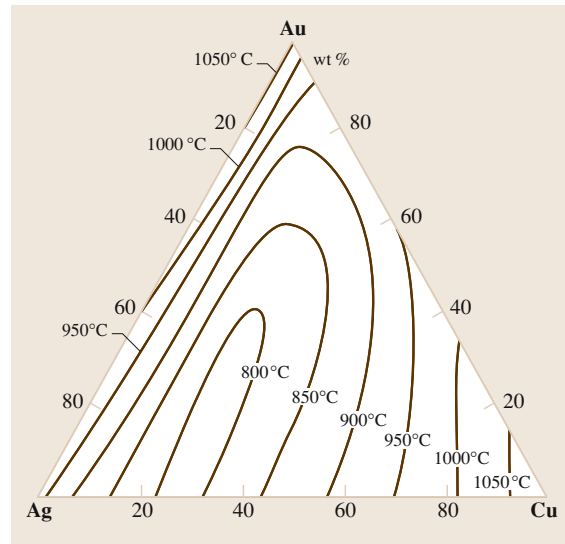
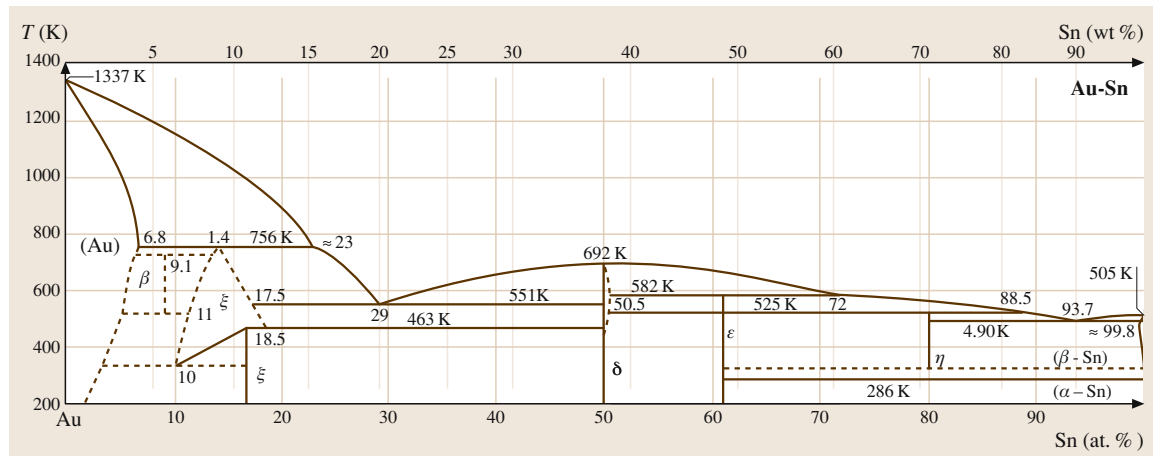


Fig. 3.1-218 Binary phase diagram of Au–Pt [1.245]

Table 3.1-167 Thermodynamic data of Au [1.217, p. 107]

| T (K) | c_p (J/K mol) | S (J/K mol) | H (J/mol) | G (J/mol) | p (at) |
|-------|-----------------|-------------|-----------|-----------|------------------------|
| 300 | 25.303 | 47.645 | 0.047 | -14.247 | 6.87×10^{-58} |
| 500 | 26.158 | 60.757 | 5.188 | -25.191 | 2.82×10^{-32} |
| 700 | 27.028 | 69.701 | 10.509 | -38.282 | 2.49×10^{-21} |

T = Temperature, c_p = specific heat capacity, S = Entropy, H = Enthalpy, p = partial pressure of the pure elements

**Fig. 3.1-219** Binary phase diagram of Au–Si [1.245]**Fig. 3.1-220** Liquidus sections through the miscibility gap of the Au–Ag–Cu system [1.246]**Fig. 3.1-221** Binary phase diagram of Au–Sn [1.245]

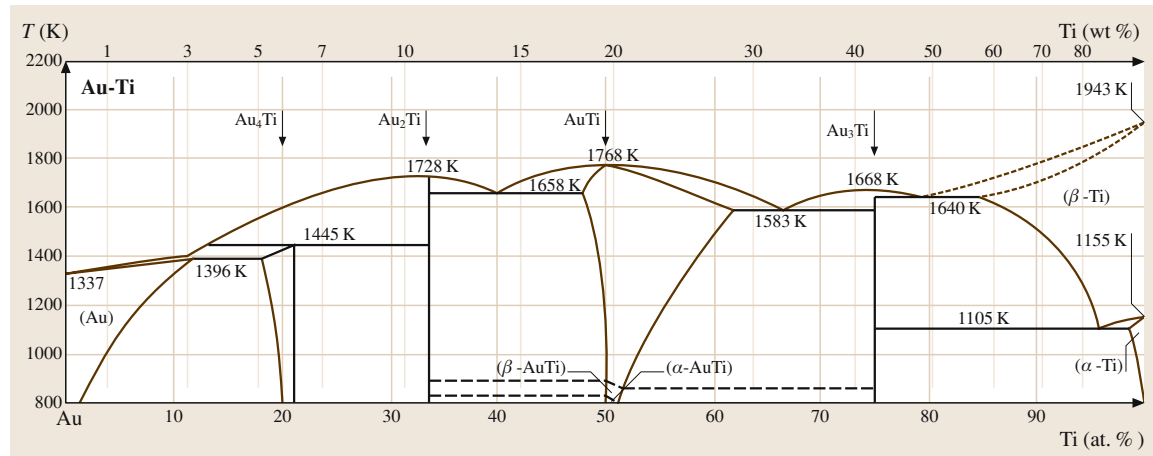


Fig. 3.1-222 Binary phase diagram of Au–Ti [1.245]

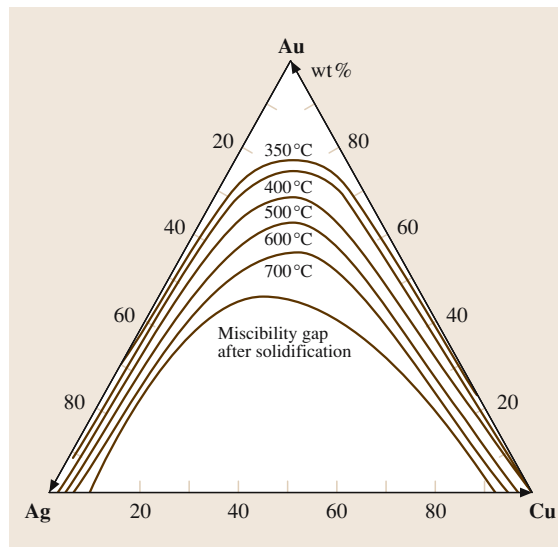


Fig. 3.1-223 Isothermal sections through the miscibility gap of the Au–Ag–Cu system [1.246]

Superlattice phases occur in alloys with Cd, Cu, Mn, Pd, Pt, Rh, Ru, and Zn. The superlattice structures have tetrahedral or rhombohedral symmetry. Typical compositions are AB_3 and A_3B [1.218]. If they are not precipitated as second phases, superlattice

Table 3.1-168 Heats, entropies and free energies of formation of Au compounds [1.222, p. 196]

| Phase | N_2 | T (°C) | H (J/mol) | G (J/mol) | S (J/K mol) |
|------------------------|-------|----------|-------------|-------------|---------------|
| AuCu s.s. | 0.58 | 500 | 5.32 | 9.67 | 5.65 |
| Au_3Cu | 0.26 | 25 | 4.03 | 4.90 | 2.97 |
| AuCu I | 0.50 | 25 | 8.96 | 8.96 | — |
| AuCu II | 0.50 | 400 | 6.03 | 8.79 | 4.10 |
| AuCu_3 | 0.75 | 25 | 6.87 | 7.24 | 1.26 |
| AuNi s.s. | 0.53 | 877 | −7.5 | — | 8.71 |
| AuSn | 0.50 | 25 | 14.24 | — | −0.4 |

N_2 = mole fraction of second compound,

ΔS = entropy of formation, s.s. = solid solution

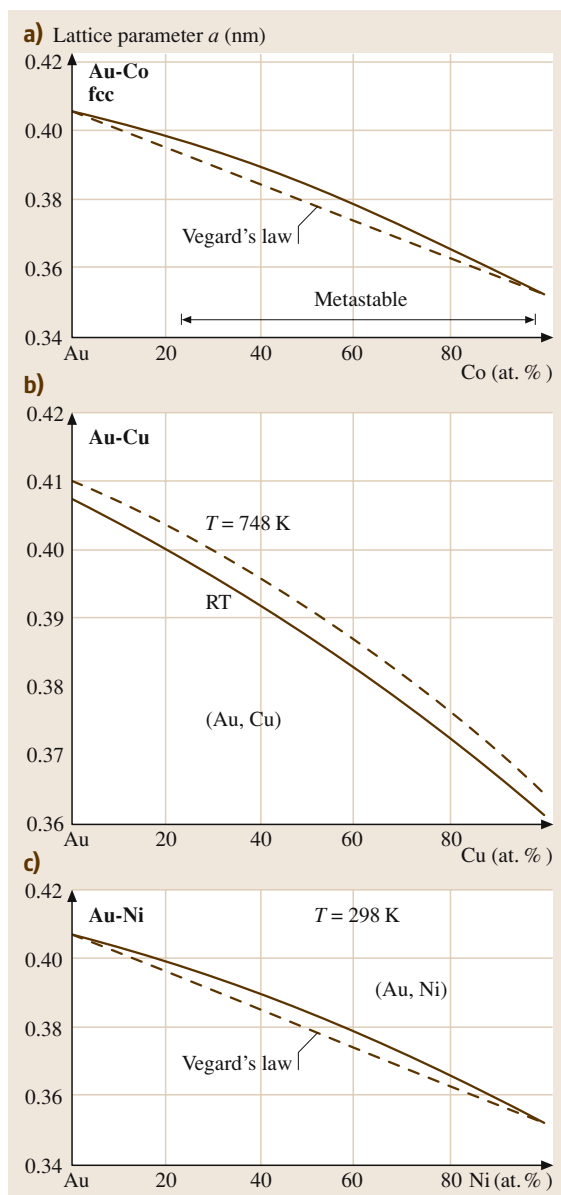
s.s. = solid solution

phases form antiphase domains on different sublattices separated by antiphase domain boundaries. Intermetallic compounds are formed with numerous elements with different and complex crystal structures [1.225]. Metastable phases exist with Ni and Pt. Alloys with B-metals form intermetallic phases at compositions corresponding to e/a values of $3/2$, $21/13$, and $7/4$ (Hume-Rothery phases). Structural types of intermetallic compounds of gold with rare earth metals are listed in [1.248].

Table 3.1-169 Structure and lattice parameters of selected intermediate Au compounds [1.217, p. 113]

| Phase | Pearson Symbol | <i>a</i> (nm) | <i>b</i> (nm) | <i>c</i> (nm) | <i>c/a</i> | Remarks | Concentration (A/1 - x)B(x) |
|--------------------|----------------|---------------|---------------|---------------|------------|---------|-----------------------------|
| AuAl | mPs | 0.6415 | 0.3331 | 0.6339 | | | |
| Au ₂ Al | oP30 | 0.8801 | 1.6772 | 0.3219 | | LT | 0.664–0.667 |
| Au ₅ Al | cP20 | 0.69208 | | | | LT | |
| Au–Al ₂ | cF12 | 0.59973 | | | | | 0.334 |
| AuCu | oI40 | 0.3676 | 0.3972 | | | 773 K | |
| AuCu | oP8 | 0.456 | 0.892 | 0.283 | | | |
| AuCu | iP4 | 0.3966 | | 0.3673 | 0.9261 | | 0.46–0.54 |
| Au ₃ Cu | cP4 | 0.39853 | | | | | |
| Au–Pd | cP4 | 0.3991 | | | | | 0.552 |
| Au–Pt | cF4 | 0.3996 | | | | | 0.5 |
| Au–Sn | hP2 | 0.29228 | | 0.47823 | 1.6329 | | 0.14 |
| AuSn | hP4 | 0.43218 | | 0.5523 | 1.2779 | | |
| AuSn ₄ | oC20 | 0.6502 | 0.6543 | 1.1705 | | 475 K | |
| Au ₄ Ti | tI10 | | 0.6485 | 0.4002 | 0.6171 | | |

LT = low-temperature modification

**Fig. 3.1-224a–c** Lattice parameter versus composition in the systems (a) Au–Co, (b) Au–Cu, (c) Au–Ni [1.245]

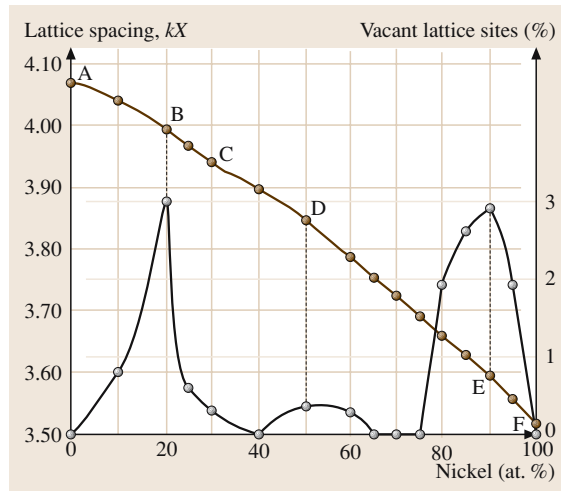


Fig. 3.1-225 Vacant lattice sites in Au–Ni alloys [1.225, p. 141]

Mechanical Properties

The mechanical properties of gold are given in Tables 3.1-170–3.1-176 and Figs. 3.1-226–3.1-237 [1.216, 217]. References for data of elastic constants of Au alloys are given in [1.217]. Pure gold is very soft. It can be cold-worked to more than 90% by

Table 3.1-170 Modulus of elasticity of Au in crystal directions (GPa) [1.217, p. 208]

| E (100) | E (110) | E (111) |
|---------|---------|---------|
| 42 | 81 | 114 |

Table 3.1-171 Elastic constants of Au (GPa) [1.217, p. 209]

| T (°C) | c11 | c12 | c14 |
|--------|-------|------|------|
| -273 | 131.4 | 97.3 | 51.1 |
| 20 | 124.0 | 93.4 | 46.1 |

Table 3.1-172 Mechanical properties of Au (99.99%) at different temperatures [1.217, p. 209]

| T (°C) | E (GPa) | R _m (MPa) | R _{p0.2} (MPa) | HV |
|--------|---------|----------------------|-------------------------|----|
| 20 | 79 | 125 | 30 | 28 |
| 200 | 75 | 110 | 20 | 19 |
| 400 | 70 | 92 | — | 16 |
| 700 | 58 | 40 | — | 5 |

E = Modul of elasticity, R_m = Tensile strength, R_p = Limit of proportionality, HV = Vickers hardness

Table 3.1-176 Mechanical properties of AuPt alloys in annealed and aged condition, Pt in wt% [1.217, p. 211] ►

Table 3.1-173 Tensile strength R_m (MPa) of binary Au alloys [1.217, p. 210]

| Content (wt%) Alloying element | 2 | 5 | 10 | 20 |
|-----------------------------------|-----|-----|-----|-----|
| Ag | 140 | 150 | 170 | 190 |
| Co | 240 | — | — | — |
| Cr | 200 | — | — | — |
| Cu | 190 | 290 | 400 | 500 |
| Fe | 190 | — | — | — |
| Ni | 220 | 350 | 470 | 680 |
| Pd | 150 | 170 | 220 | 290 |
| Pt | 150 | 189 | 240 | 370 |

Table 3.1-174 Mechanical properties of Au (99.99%) as a function of the reduction V (%) in thickness by cold forming [1.217, p. 209]

| V (%) | R _m (MPa) | A (%) | HV |
|-------|----------------------|-------|----|
| 0 | 120 | 45 | 28 |
| 10 | 140 | 22 | 55 |
| 30 | 180 | 75 | 63 |
| 50 | 220 | 4 | 65 |

R_m = Tensile strength, A = Elongation of rupture,

HV = Vickers hardness

Table 3.1-175 Change of hardness (HV 10) of Au alloys by cold forming (Degree of reduction in thickness in %) [1.217, p. 210]

| Degree of reduction in thickness (%) Alloying element | 0 | 40 | 80 |
|---|-----|-----|------|
| Ag20 | 40 | 95 | 1141 |
| Ag25Cu5 | 92 | 160 | 188 |
| Ag20Cu10 | 120 | 190 | 240 |
| Co5 | 92 | 126 | 154 |
| Ni5 | 120 | 162 | 188 |
| Pt10 | 78 | 102 | 118 |
| Pd30Cu5 | 92 | 174 | 216 |

| Alloy | R _m (MPa) | A (%) | HV |
|-------------------|----------------------|-------|-----|
| Pt10 ^a | 250 | 38 | 42 |
| Pt30 ^a | 430 | 12 | 120 |
| Pt30 ^b | 740 | — | 300 |
| Pt50 ^a | 900 | 3 | 240 |
| Pt50 ^c | 1460 | 2 | 420 |

^a annealed at 1000–1150 °C and quenched

^b stored 70 h at 500 °C,

^c stored 25 h at 500 °C

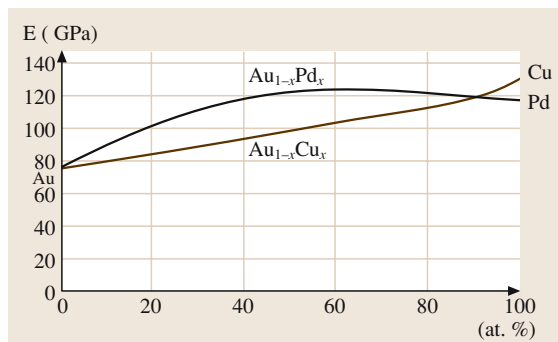


Fig. 3.1-226 Modulus of elasticity of Au–Cu and Au–Pd alloys [1.217, p. 219]

Fig. 3.1-227 Influence of alloying elements on the hardness of binary Au alloys [1.217, p. 211] ▶

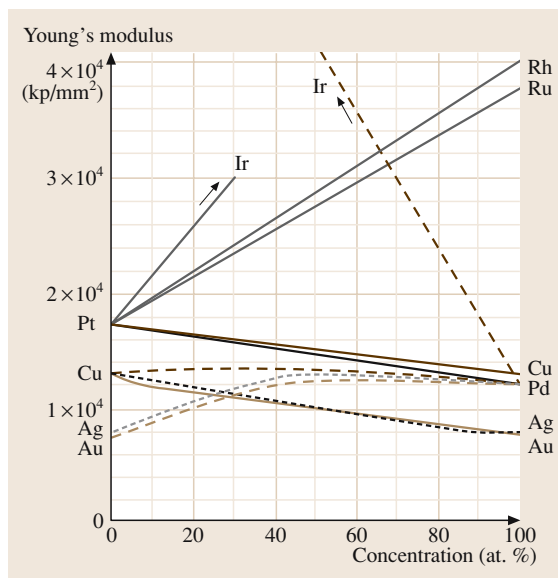


Fig. 3.1-228 Modulus of elasticity versus composition of binary noble-metal alloys [1.216, p. 77]

rolling or drawing. Cold hard drawn wires (about 90% deformation) have predominantly $\langle 111 \rangle$ fiber texture, which is converted by annealing into $\langle 100 \rangle$ orientation [1.249]. Strengthening of pure gold is affected by alloying (solid solution hardening, precipitation hardening) or by dispersion hardening. Ternary Au–Ag–Cu

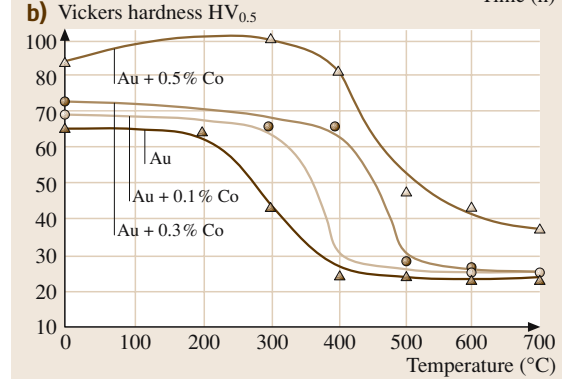
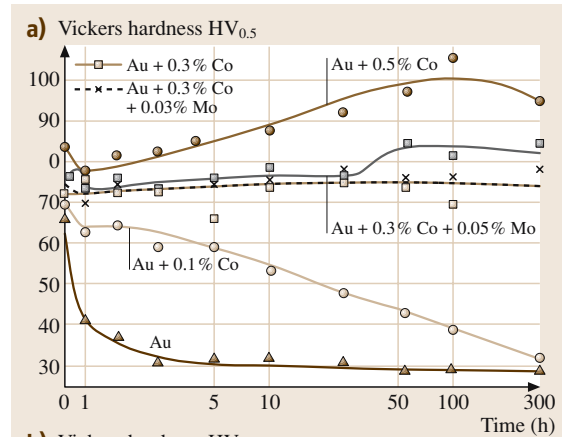
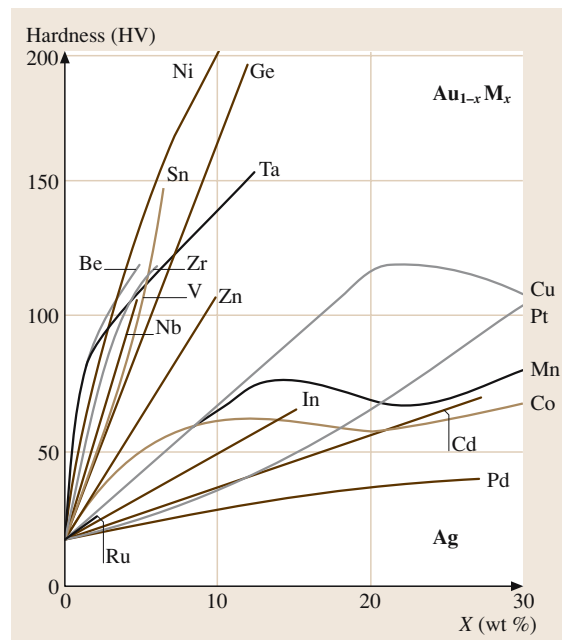


Fig. 3.1-229a,b Hardness of Au–Co alloys by annealing; (a) influence of time, (b) influence of temperature T [1.231, p. 62]

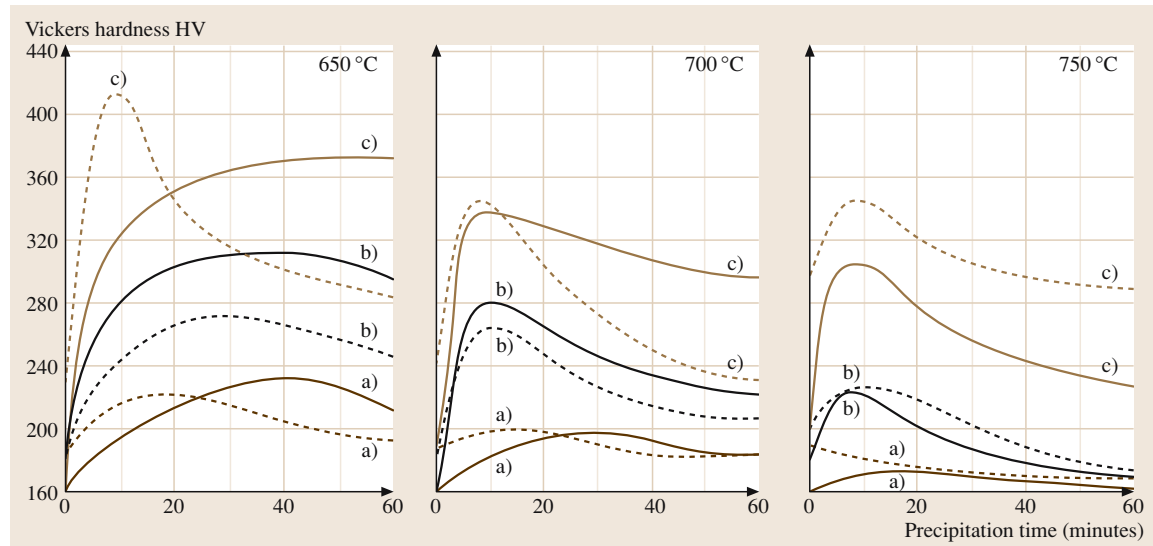


Fig. 3.1-230 Precipitation hardening of Au/Pt-40 (solid curve) and Au/Pt-50 (broken curve): solution treatment 15 min at a) 950 °C, b) 1050 °C and c) 1150 °C. Precipitation hardening performed at 650 °C, 700 °C, and 750 °C [1.218, p. 610]

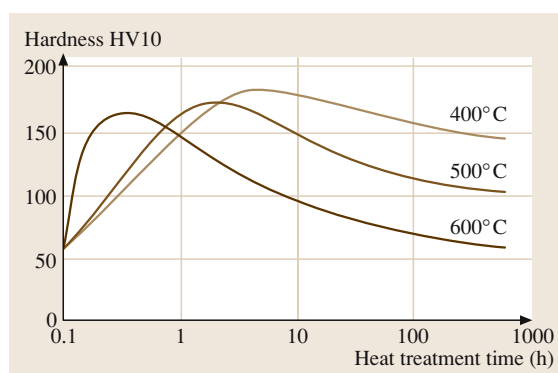


Fig. 3.1-231 Precipitation-hardening characteristic of Au-1% Ti alloy by annealing [1.252, p. 139]

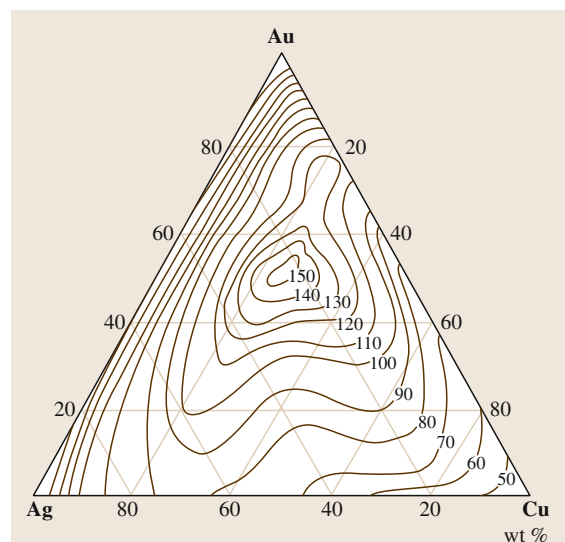
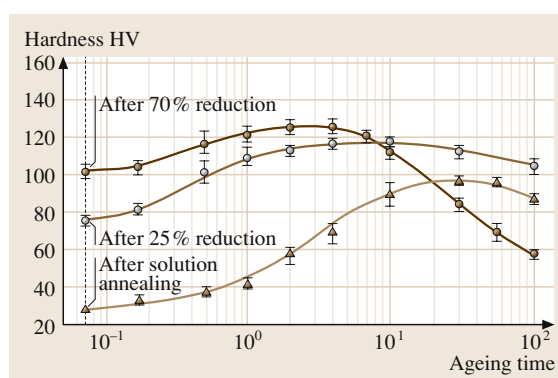


Fig. 3.1-232 Hardness of annealed and quenched Au–Ag–Cu alloys [1.253, p. 517]



alloys can be hardened by decomposition into Cu-rich Cu–Au and Ag-rich Ag–Au phases during annealing below the critical temperature of the miscibility gap and

Fig. 3.1-233 Hardness of the alloy AuSb0.3Co0.2 as a function of the reduction in thickness and of annealing time [1.254, p. 49]

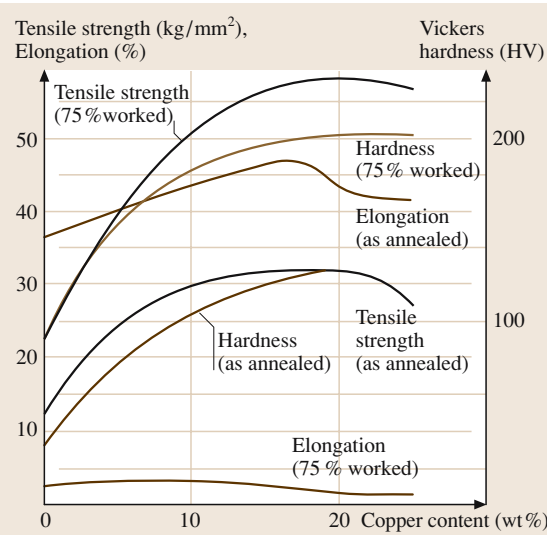


Fig. 3.1-235 Tensile strength and hardness of 18 carat Au–Ag–Cu alloys as a function of Cu content [1.218, p. 437]

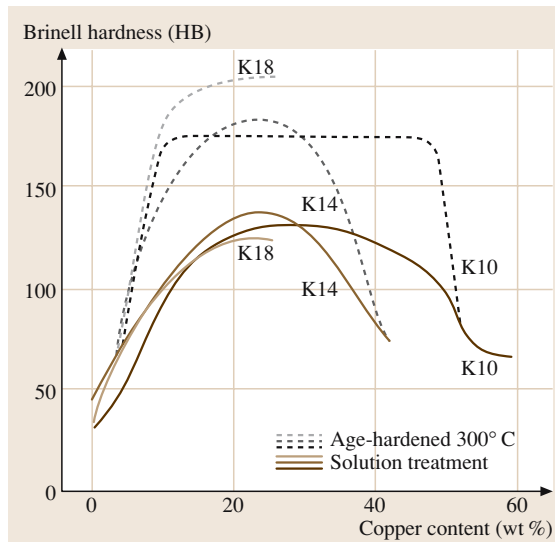


Fig. 3.1-236 Influence of Cu content on age hardening of 14 carat and 18 carat Au–Ag–Cu alloys [1.218, p. 437]

by formation of the ordered Au–Cu-phase at more than 75 wt% Au. Hardening of Au by alloying with rare-earth metals is described in detail in [1.248]. Grain refinement, applied especially to jewelry and dentistry alloys, is affected by the addition of 0.05–1 at.% of Ir, Ru, or Co [1.250, 251].

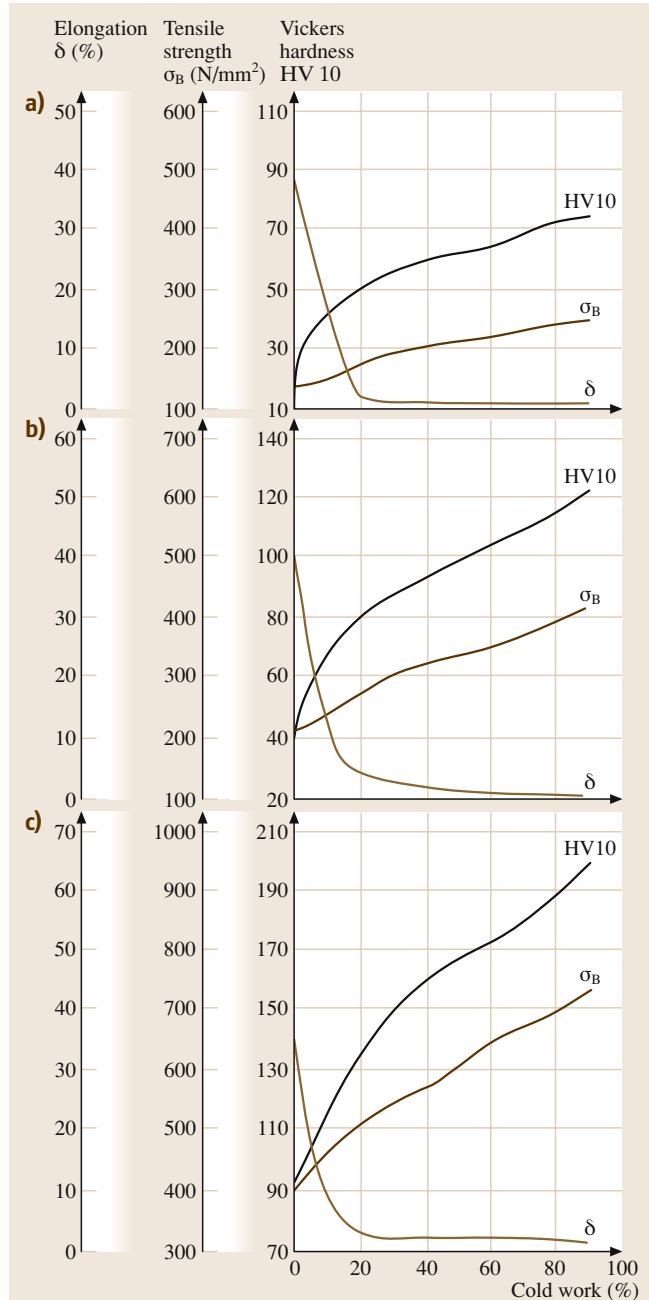


Fig. 3.1-234a-c Mechanical properties of (a) Au, (b) AuAg30, and (c) AuAg25Cu5 as a function of the reduction in thickness (%) [1.231, p. 58f.]

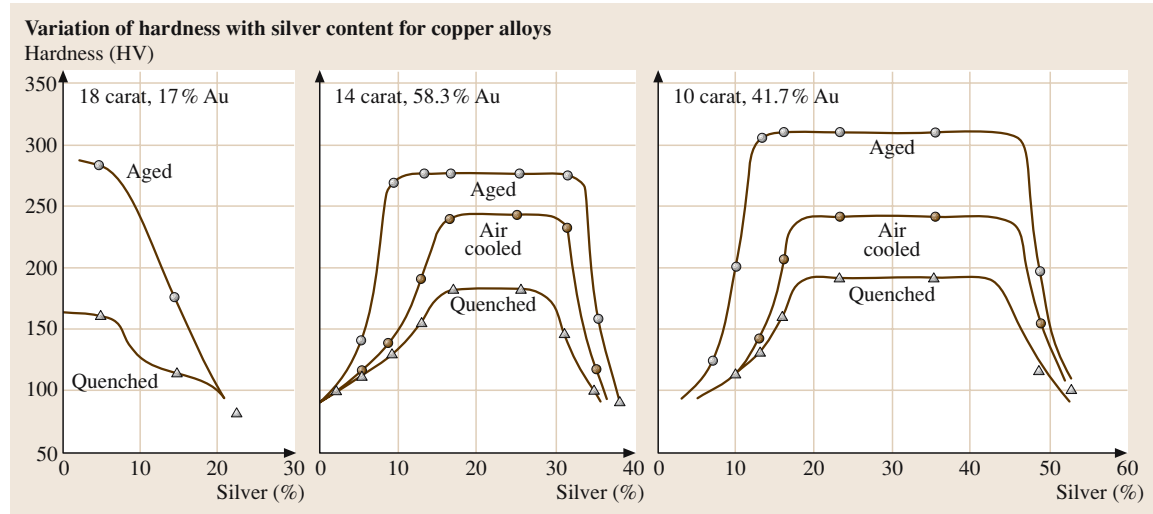


Fig. 3.1-237 Variation of hardness with silver content for Au–Ag–Cu alloys [1.217]

Electrical Properties

Tables 3.1-177–3.1-179 and Figs. 3.1-238, 3.1-239 [1.217, 231, 255] summarize the electrical properties of gold and gold alloys. The residual resistivity ratio for high purity gold amounts to 300. The electrical conductivity of gold alloys decreases in the low concentration range roughly linearly with the atomic concentration of

the solute. Au alloys with 1.15 at.% Mn show increasing temperature coefficients of the electrical resistivity (positive TCR) due to the Kondo effect. This behavior is applied in resistance thermometers for temperature measurements below 20 K. Superconductivity occurs in intermetallic phases of Au–Ge with $2.99 < T_c < 3.16$ K and Au–Sn with $T_c = 1.25$ K [1.256, 257].

Table 3.1-177 Specific electrical resistivity $\rho = \rho_0 + \rho_i(T)$ of Au at different temperatures ($\rho_0 = 0.0222 \mu\Omega \text{ cm}$) [1.217, p. 157]

| T (K) | 20 | 60 | 120 | 273.2 | 400 | 800 | 1000 | 1200 |
|------------------------------|--------|-------|-------|-------|-------|-------|-------|--------|
| $\rho(\mu\Omega \text{ cm})$ | 0.0138 | 0.287 | 0.796 | 2.031 | 3.094 | 6.742 | 8.871 | 11.299 |

at $T < 400$ K, $\rho_0 = 0.014 \mu\Omega \text{ cm}$ at $T > 400$ K

Table 3.1-178 Specific electrical resistivity (ρ_{25}) and temperature coefficient of resistivity (TCR) of Au–Pd and Au–Pt alloys [1.217, p. 158]

| Solute Content | Content | | | | |
|---|-------------|------|------|------|-----|
| | 80 | 60 | 40 | 30 | |
| Pd | ρ_{25} | 9.8 | 17 | 30 | 26 |
| | TCR | 0.88 | 0.61 | 0.45 | 1.2 |
| Pt | ρ_{25} | 28 | 44 | 37 | 34 |
| | TCR | 0.28 | 0.26 | 0.82 | 0.8 |
| $\text{TCR}_{T_1 T_2} = \frac{1}{\rho_1} \frac{\rho_{T_2} - \rho_{T_1}}{T_2 - T_1}$ | | | | | |

Table 3.1-179 Increase of atomic electrical resistivity of Au by alloying elements $\Delta \rho/C$ ($\mu\Omega \text{ cm}/\text{at.}\%$) [1.217, p. 157]

| Base element | Alloying elements | $\Delta \rho/C$ ($\mu\Omega \text{ cm}/\text{at.}\%$) |
|--------------|-------------------|---|
| Au | Ag | 0.35 |
| | Al | 1.9 |
| | Cd 0.60 | |
| | Co | 6.2 |
| | Cr | 4.5 |
| | Cu | 0.4 |
| | Fe | 8 |
| | Ga | 2.2 |
| | Ge | 5.5 |
| | Hg | 0.4 |
| | In | 1.4 |
| | Mn | 2.4 |
| | Mo | 4 |
| | Ni | 0.8 |
| | Pb | 3.9 |
| | Pt | 1 |
| | Rh | 3.3 |
| | Ru | 1.6 |
| | Sn | 3.5 |
| | Ti | 13 |
| | V | 13 |
| | Zn | 0.94 |

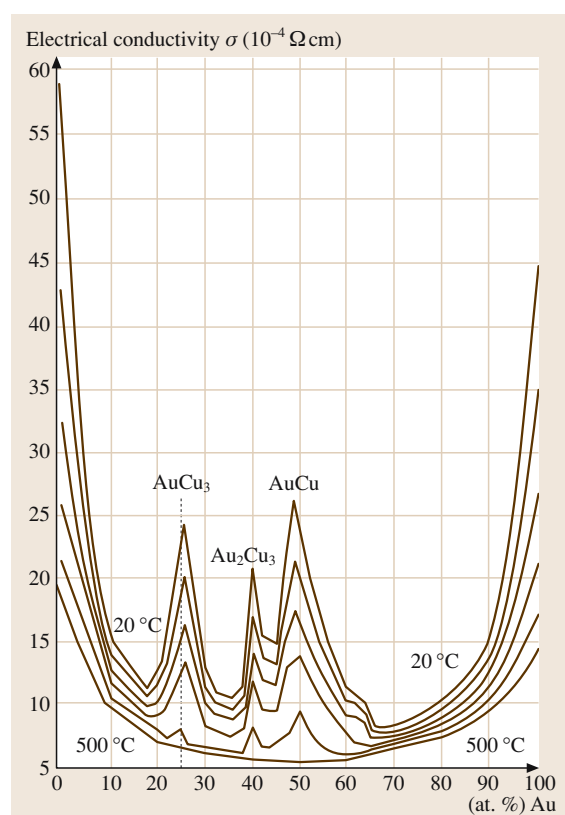


Fig. 3.1-238 Specific electrical conductivity of Au–Cu alloy phases [1.255, p. 619]

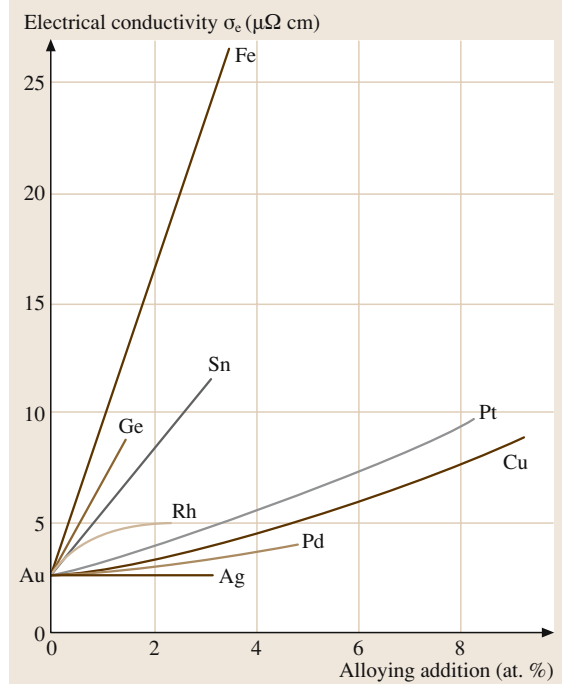


Fig. 3.1-239 Influence of alloying elements on the electric conductivity of binary Au alloys [1.231, p. 50]

Thermoelectric Properties

Tables 3.1-180–3.1-183 [1.216] and Figs. 3.1-240–3.1-242 [1.216, 218] list the thermoelectric properties of gold and its alloys. Au–Fe and Au–Co-alloys are used in thermocouples for measuring very low temperatures [1.258], Au–Pd and Au–Pd–Pt alloys in thermocouples working under highly corrosive conditions.

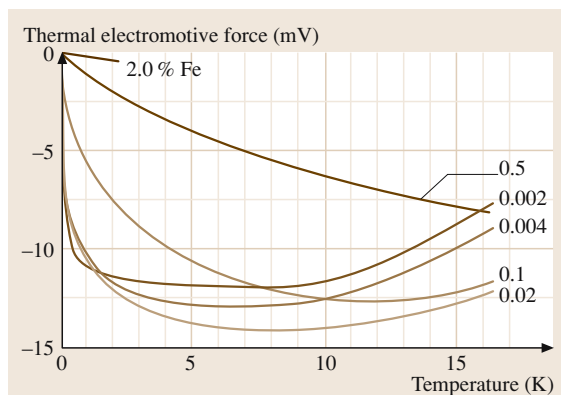


Fig. 3.1-240 Thermal electromotive force of Au–Fe alloys [1.218, p. 58]

Table 3.1-180 Absolute thermoelectric power of gold [1.216, p. 94]

| Temperature (°C) | -255 | -200 | -160 | -100 | 0 | 100 | 300 | 500 | 700 |
|---|-------|-------|-------|-------|------|------|------|------|------|
| Thermoelectr. power ($\mu\text{V/K}$) | -0.93 | -0.78 | +0.80 | +1.00 | +1.1 | +1.8 | +3.1 | +3.3 | +3.7 |

Table 3.1-181 Thermal electromotive force E of Au and Pt (mV) at different temperatures; reference junction at 0 °C [1.216, p. 159]

| T (°C) | -200 | -100 | -50 | +100 | +200 | +400 | +800 |
|--------------------------------|-------|-------|-------|------|-------|-------|--------|
| $E_{\text{Au},\text{Pt}}$ (mV) | -0.39 | -0.21 | -0.10 | 0.77 | 1.834 | 4.623 | 12.288 |

Table 3.1-182 Thermal electromotive force of Au–Fe and Au–Co-alloys [1.216, p. 100]

| T_1 (K) | T_2 (K) | Au–Co _{2.1} Cu (at.%) | Au–Fe _{0.02} Cu (at.%) |
|-----------|-----------|--------------------------------|---------------------------------|
| 4.2 | 10 | 0.044 | 0.093 |
| | 20 | 0.173 | 0.208 |
| 4.2 | 40 | 0.590 | 0.423 |

Table 3.1-183 Thermocouples for very low temperatures [1.216, p. 97, 99]

- AuFe(0.03 at.% Fe)–chromel from 4.2 to 273 K
- AuCo(2.11 at.% Co)–AuAg (0.37 at.% Ag) or Cu from -240 to 0 °C
- AuFe(0.02 at.% Fe)–Cu from -270 to -230 °C

Magnetic Properties

Figure 3.1-243 [1.217] illustrates the metal's magnetic properties. Gold is diamagnetic. The magnetic susceptibility remains constant from 0 K to the melting point. Alloying of gold with B metals causes only weak variations compared to pure gold. In the range of continuous solid solutions, the molar susceptibilities remain negative, the alloys are diamagnetic. Ni, Pd, and Pt dissolve diamagnetically up to 25 at.%. Cr, Fe, and Mn give rise to paramagnetism. Magnetic transformations are reported

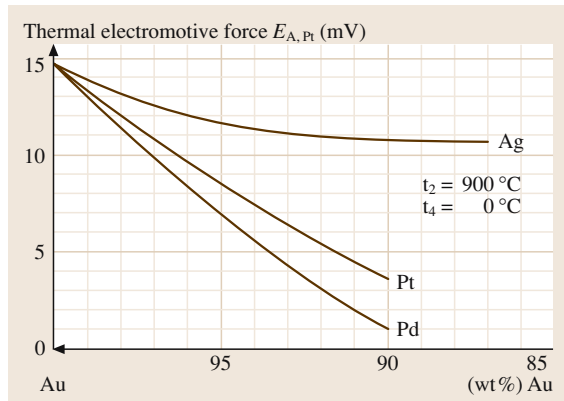


Fig. 3.1-241 Thermal electromotive force of Au alloys [1.216, p. 97]

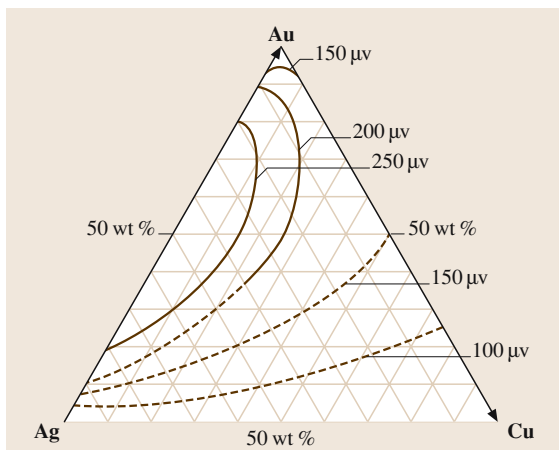


Fig. 3.1-242 Thermal electromotive force of Au–Ag–Cu alloys [1.216, p. 99]

for Au–Co alloys between ≈ 18 and 92 wt% Co at 1122°C and for Au–Ni alloys between ≈ 3 and 95 wt% at $\approx 340^\circ\text{C}$ [1.259].

Thermal Properties

Data for thermal expansion and thermal conductivity of Au and Au alloys are listed in Tables 3.1-145–3.1-149. Table 3.1-184 [1.217] shows the recrystallization temperatures of gold of different purity. After 90% cold work, the hardness decreases by about 50%.

Optical Properties

For the optical properties of colored Au alloys, see Tables 3.1-151, 3.1-152 and Figs. 3.1-244–3.1-247 [1.260–263]. The reflectivity of gold shows a marked decrease at $\approx 550\text{ nm}$ in the visible range with a minimum of $R \approx 0.25$ in the near ultraviolet. Interband transitions occur at $\approx 2.17\text{ eV}$. The reflected light contains all wavelengths above 550 nm, which accounts for the typical gold color.

Table 3.1-184 Recrystallization temperatures of Au 3N, 4N and 5N purity [1.217, p. 210]

| Purity (%) | Decrease of hardness | |
|-------------|------------------------------|-------------------------------|
| | 50% $T_{\text{recryst.}}$ | 100% $T_{\text{recryst.}}$ |
| 99.9 (3N) | 200 | |
| 99.99 (4N) | 160 | 200 |
| 99.999 (5N) | 112 | 149 |

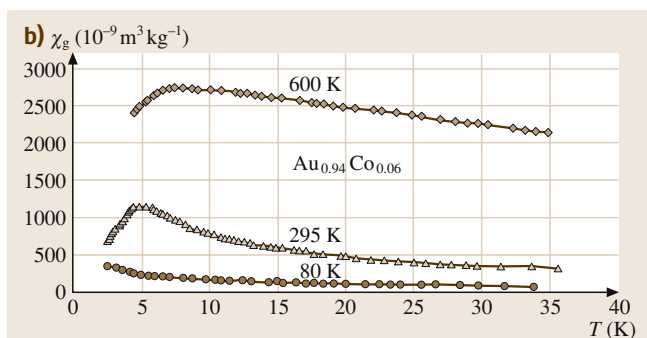
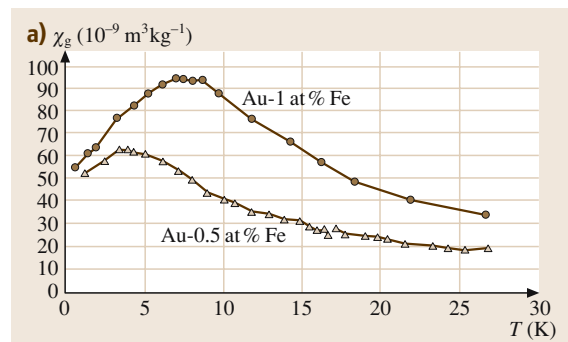


Fig. 3.1-243a,b Magnetic susceptibility of (a) Au–Fe and (b) Au–Co alloys [1.217, p. 169]

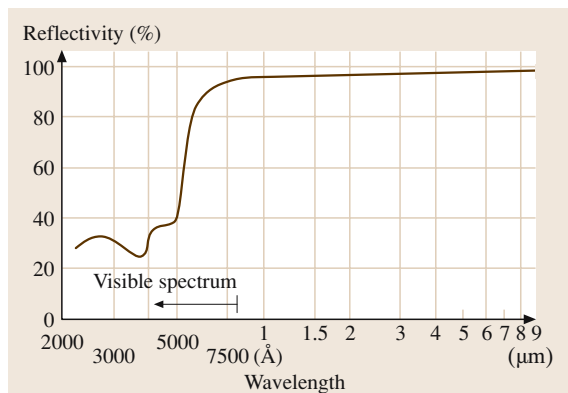


Fig. 3.1-244 Reflectance as a function of wavelength of pure Au [1.260, p. 53]

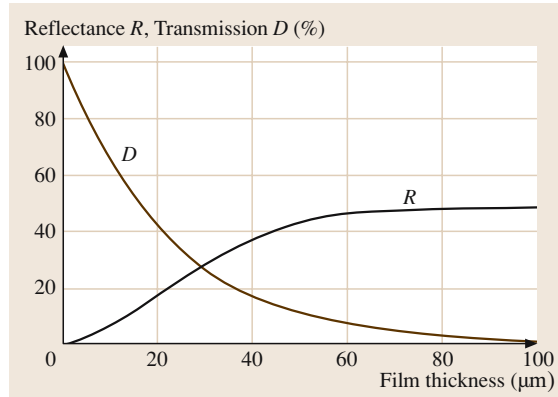


Fig. 3.1-245 Reflectance and transmission of thin Au films at $\lambda = 492 \mu\text{m}$ [1.260]

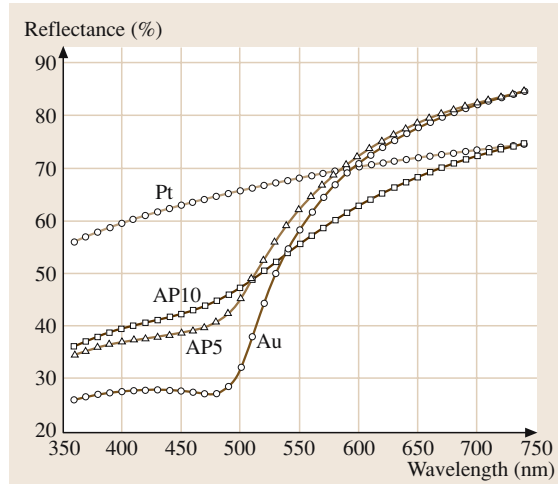


Fig. 3.1-246 Reflectance-wavelength curves for Au–Pt and binary Au–Pt alloys [1.261, p. 130]

Diffusion

Characteristic data are shown on Tables 3.1-153–3.1-156, 3.1-158 and Figs. 3.1-212, and 3.1-248 [1.217, 238].

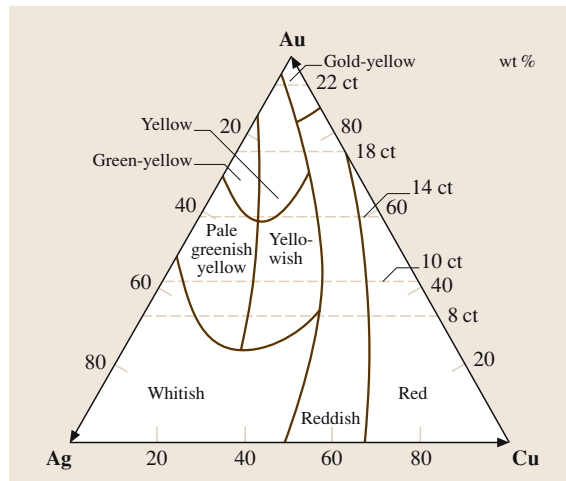


Fig. 3.1-247 Color ranges of Au–Ag–Cu alloys [1.262, p. 37]

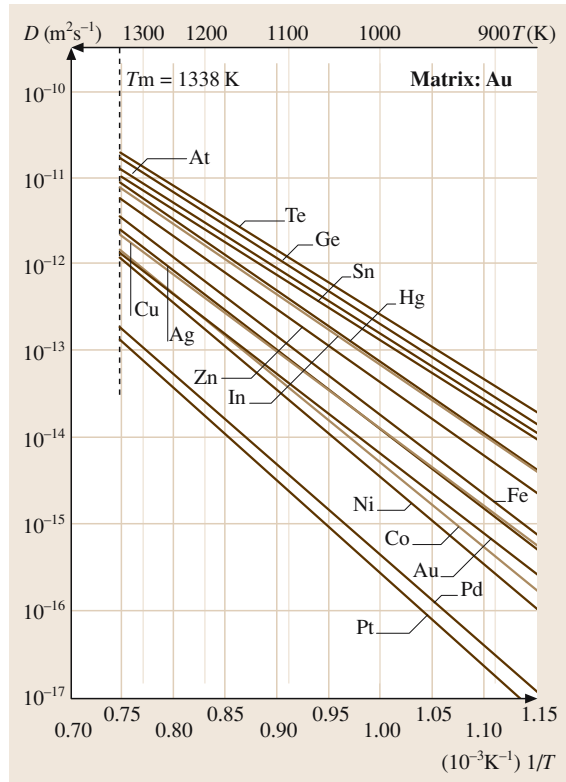


Fig. 3.1-248 Diffusion of impurities in Au [1.238, p. 191]

Chemical Properties

Figures 3.1-249 and 3.1-250 show that gold has the reduction potential of $E_0 = +1.42 \text{ V}$ for Au/Au^{3+} . At room temperature it is resistant against dry and wet atmospheres, H_2O , O_2 , F , I , S , alkali, non-oxidizing acids, and ozone below 100°C . It is dissolved in $3 \text{ HCl} + 1 \text{ HNO}_3$, $\text{HCl} + \text{Cl}_2$ in acid concentration above 6 mol/l , in $\text{NaCN}/\text{H}_2\text{O}/\text{O}_2$, and other oxidizing solutions. Halogens generally attack gold, except for dry fluorine below 300°C . Gold alloys are corrosion-resistant against acids if the base metal content is lower than 50% and also if each base metal present contains more than 50% of noble metal. Detailed information of chemical properties of Au and Au alloys are given in [1.217].

Gold and gold alloys (with Ag, Ir, Pt) and cationic gold (I) phosphines act as selective catalysts in hydrogenation, oxidation, and reduction reactions [1.264–266]. Nanometer-sized Au particles ($\approx 5 \text{ nm}$) in the presence of ceria or a transition-metal oxide have superior catalytic activities [1.267–269, 269].

Special Alloys

Binary Alloys. The material Au–20 wt% Ag is used for low-voltage electrical contacts. Gold–copper alloys form the ordered phases Au_3Cu [60748-60-9], AuCu [12006-51-8], and AuCu_3 [12044-96-1]. Gold–nickel alloys decompose into gold-rich and nickel-rich solid

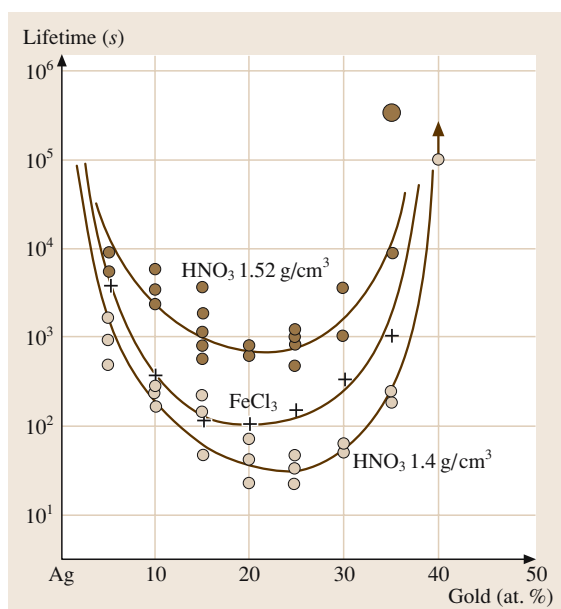


Fig. 3.1-250 Lifetime of Ag–Au solid solutions in HNO_3 and FeCl_3 solution [1.217, p. 197]

solution phases in a miscibility gap below 800°C . The alloy Au–18 wt% Ni is a structural material for turbine blades in jet engines and nuclear and space technology materials.

Alloys of Au–Co(Fe, Ni) with 1–3 wt% Co, Fe, or Ni serve as hard and wear-resistant surface coatings on electrical contacts. The gold-cobalt alloy of Au–5 wt% Co is resistant against silver migration. The gold-platinum alloy of Au–10 wt% Pt is used for electrical contacts working under highly corrosive conditions. The high Pt content alloy Au–30 wt% Pt serves as a material for spinnerets for rayon and as a high-melting platinum solder ($T_{\text{liquidus}} = 1450^\circ\text{C}$, $T_{\text{solidus}} = 1228^\circ\text{C}$), additions $\approx 0.5\%$ of Rh, Ru, or Ir suppress segregation. Gold-Platinum alloys containing 40 to 65 wt% Au harden by quenching from 1100°C and annealing at 500°C to yield strengths up to $\approx 1400 \text{ N/mm}^2$. Au–1 wt% Ti (Figs. 3.1-222, 3.1-231 [1.246, 252, 270, 271]) is of importance for bonding wires, electrical conductors, and as hard high-carat gold alloy for jewelry. Strengthening can be induced by precipitation of the intermetallic compound Au_4Ti and by formation of highly-dispersed Ti oxide on annealing in an oxidizing atmosphere. The alloys Au–12 wt% Ge, Au–3.1 wt% Si, and Au–20 wt% Sn are low melting eutectic solders of high strength, corrosion resistance and stability against temperature cycling,

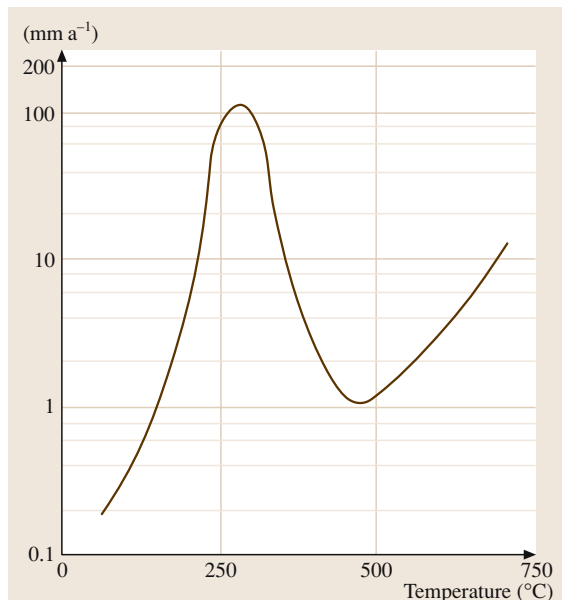


Fig. 3.1-249 Corrosion of gold in dry chlorine gas [1.217, p. 183]

Table 3.1-185 Physical properties of the eutectic alloys Au–20Sn, Au–12Ge, and Au–3Si [1.272, p. 194]

| Composition (wt%) | Melting point (°C) | Young's modulus versus temperature (GPa) | | | | Thermal conductivity (W/m K) | Coefficient of thermal expansion (ppm/°C) |
|-------------------|--------------------|--|-------|--------|--------|------------------------------|---|
| | | –60 °C | 23 °C | 100 °C | 150 °C | | |
| Au–20Sn | 280 | 59.5 | 59.2 | 48.5 | 35.8 | 57.3 | 15.93 ± 0.88 (–50 to 170) |
| Au–12Ge | 356 | 69.8 | 69.3 | 68.2 | 62.7 | 44.4 | 13.35 ± 3.13 (10 to 250) |
| Au–3Si | 363 | 77.0 | 83.0 | 82.8 | 83.0 | 27.2 | 12.33 ± 0.86 (10 to 250) |

used for the hermetic sealing of electronic devices (Table 3.1-185 [1.272]).

Ternary and Higher Alloys. Au–Ag–Cu, Au–Ag–Ni and Au–Ag–Pd alloys are of major importance for jewellery and dentistry (Tables 3.1-186, 3.1-187) [1.250, 251]. The microstructures and thus the mechanical properties are determined by wide miscibility gaps. Additions

Table 3.1-186 Basic compositions (wt%) of gold-based jewellery alloys [1.250, p. 271]

| Jewelry alloys | | | |
|-----------------------|----------|----------|--------------|
| Colored gold fineness | Ag (wt%) | Cu (wt%) | |
| 750 | 0–20 | 5–25 | |
| 585 | 5–35 | 5–35 | |
| 375 | 5–15 | 45–50 | |
| (333) | 5–40 | 25–60 | |
| White gold fineness | Ag (wt%) | Cu (wt%) | Pd(Ni) (wt%) |
| 750 | 0–10 | 0–10 | 10–20 |
| 585 | 0–25 | 5–30 | 5–20 |
| 375 | 0–35 | 5–50 | 5–20 |
| (333) | 0–35 | 10–50 | 5–25 |

Zinc max. 20%. Tin, indium, gallium each max. 4%

of Zn and In serve to adjust the melting ranges. The high-carat Au alloy AuSb0.3Co0.2 can be hardened by cold working and precipitation annealing to 142 HV5 (Fig. 3.1-233) [1.254].

AuAg25Pt5, AuAg26Ni3, and AuCu14Pt9Ag4 are used for electrical contacts working under highly corrosive conditions. AuNi22Cr6 is a hard solder of high mechanical stability [1.231]. Au–Ag–Ge alloys of various compositions are solders applicable under H₂, Ar, or vacuum in melting ranges between 400 and 600 °C. Additions of 0.5–2 wt% Pd, Cd, or Zn improve their ductility [1.273–275].

Table 3.1-187 Basic compositions of noble-metal-based dental alloys [1.251, p. 251]

| Noble metal base | Most common alloying elements |
|--|-------------------------------|
| Crown and bridge alloys | |
| Au | Ag, Cu, Pt, Zn |
| Au–Ag | Pd, Cu, Zn, In |
| Ag–Pd | Cu, In, Au, Zn |
| Porcelain fused to metal alloys | |
| Au | Pt, Pd, In, Sn |
| Au–Pd | Sn, In, Ga, Ag |
| Pd | Cu, Ga, Sn, In |
| Pd–Ag | Sn, In, Zn |

3.1.10.3 Platinum Group Metals and Alloys

Characteristic properties of the platinum-group metals (PGM) Pd, Pt, Rh, Ir, Ru, and Os are their high chemical stability; mechanical strength; thermoelectric and magnetic behavior; and their catalytic activities in heterogeneous and homogeneous chemical reactions, automobile exhaust gas purification, and the stereospecific synthesis of enantiomeric compounds. Their melting temperatures, $T_m(\text{Os}) = 3045^\circ\text{C}$, $T_m(\text{Pd}) = 1554^\circ\text{C}$, hardness, brittleness, and the recrystallization temperatures decrease with increasing nuclear charge, while their thermal expansion and ductility increase.

The catalytic properties of the PGM in the heterogeneous catalysis are based on the moderate values of the heats of adsorption which correspond to the dissociation energies of the reactant molecules. Figure 3.1-251 [1.276] and Table 3.1-188 [1.218] give some values of the heat of adsorption and binding energies between adsorbates and surface atoms on various noble metal single crystals. The heat of adsorption increases for different orientations of the crystal surface planes of the fcc crystals in the order [111] < [100] < [110] (Table 3.1-189 [1.218]). The catalytic activities are element-specific for different re-

Table 3.1-188 Binding energies (kcal/mol) between adsorbates and surface atoms on noble metal single crystals [1.218, p. 267]

| Precious metals | N | O | H | CO | NO |
|-----------------|---------------------------|----|----|-----|----|
| | Binding energy (kcal/mol) | | | | |
| Ru (0001) | | | 61 | 29 | |
| Ir (111) | 127 | 93 | 63 | 34 | 20 |
| Pd (111) | 130 | 87 | 62 | 34 | 31 |
| Pt (111) | 127 | | 57 | 30 | 27 |
| Ag (111) | | 80 | | 6.5 | 25 |

Table 3.1-189 Heat of adsorption of diatomic molecules on different single crystals planes of various transition metals (kcal/mol) [1.218, p. 267]

| Adsorption system | (111) | (100) | (110) |
|--------------------|-------------------------------|-------|-------|
| | Heat of adsorption (kcal/mol) | | |
| O ₂ Pd | 50 | 55 | 80 |
| Co/Ni | 27 | 30 | 30 |
| Co/Pd | 34 | 37 | 40 |
| Co/Pt | 30 | 32 | 32 |
| H ₂ /Pd | 21 | | 24 |
| H ₂ /W | 37 | 33 | 35 |
| N ₂ /Fe | 51 | 53 | 49 |

actions. Reactivity and selectivity of the reactions are presumably controlled by the dimensional fit between adsorbed molecules and catalyst surface, and the alloy composition. A survey of PGM catalyst activities is given in [1.217, 218, 243].

All platinum metals are paramagnetic ($\chi > 0$). The magnetic susceptibilities of palladium and platinum decrease with increasing temperature, the magnetic susceptibilities of rhodium, iridium, ruthenium, and osmium increase with increasing temperature (Fig. 3.1-272 [1.218]).

The platinum group metals occur jointly as alloys and as mineral compounds in placer deposits of varying compositions. Ru and Os are separated from the PGM mix by distillation of their volatile oxides, whereas platinum, iridium, palladium, and rhodium are separated by repeated solution and precipitation as complex PGM chlorides, or by solvent extraction and thermal decomposition to sponge or powder. PGM scrap is recycled by melting with collector metals (lead, iron, or copper) followed by element-specific extraction.

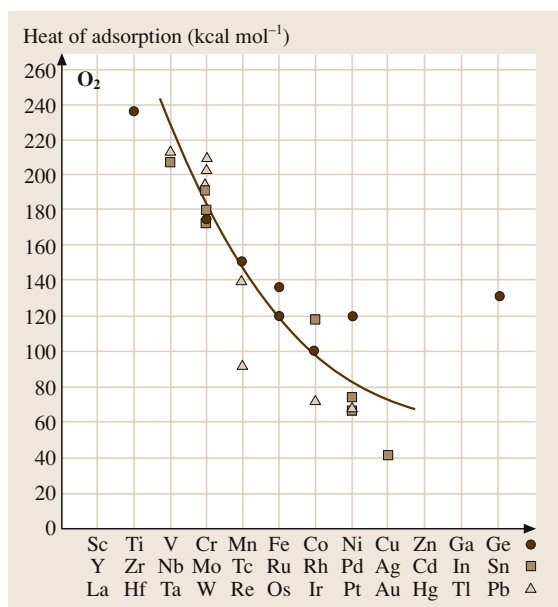


Fig. 3.1-251 Heat of adsorption of molecular oxygen on polycrystalline transition metal surfaces [1.218, p. 265]

Palladium and Palladium Alloys

Applications. Palladium and palladium alloys are important constituents of catalysts of chemical reactions and automobile exhaust gas cleaning, of electrical contacts, capacitors, permanent magnetic alloys, thermocouples, and for the production of high purity hydrogen. The low thermal neutron cross section permits their use in solders and brazes of nuclear structural parts. Classical applications are jewelry and dentistry alloys.

Commercial grades of palladium are sponge and powder in purities of 99.9 wt% to 99.95–99.98 wt% (ASTM (B 589-82)). High purity electronic grade is 99.99 wt%.

Production. Palladium sponge or powder are compacted by pressing and sintering. Melting and alloying is performed in electrical heated furnaces, vacuum arc, or by electron beam melting. Crucible materials are Al_2O_3 and MgO .

Phases and Phase Equilibria. Selected phase diagrams are shown in Figs. 3.1-252–3.1-257 [1.219]. Pd forms continuous solid solutions with all other noble metals and with Co, Cu, Fe, and Ni. Miscibility gaps exist in alloys with C, Co, Ir, Pt, Rh, and ternary Pd–Ag–Cu alloys (Fig. 3.1-257) [1.220]. All platinum-group metals (PGM) lower the γ – α transition temperature in Fe-alloys considerably (Fig. 3.1-343). Thermodynamic data are given in Tables 3.1-190–3.1-194. Numerous intermediate phases exist also in alloys with rare earth metals [1.216, 217, 217, 222]. The solubility of

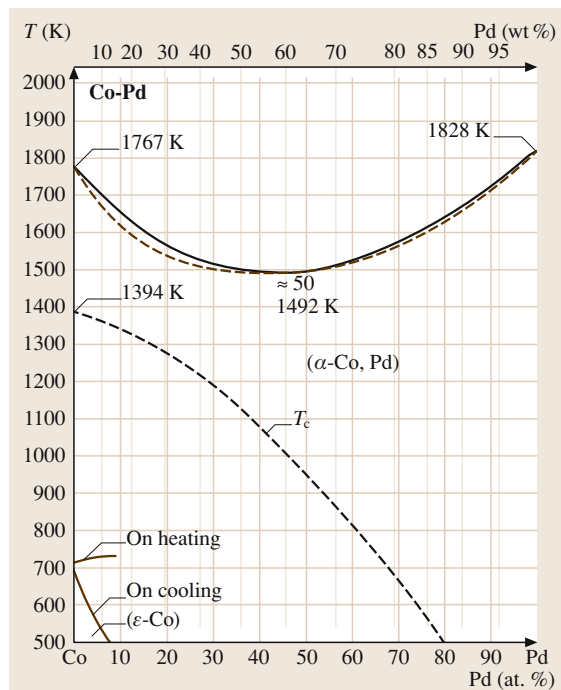


Fig. 3.1-253 Binary phase diagram Pd–Co [1.219]

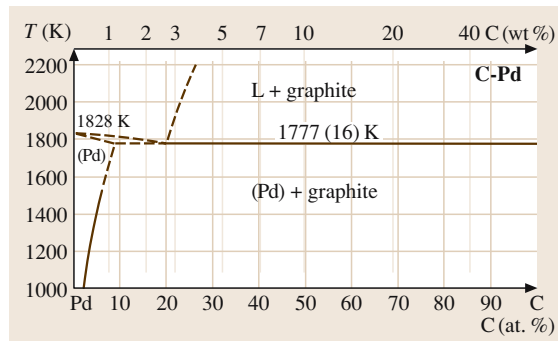


Fig. 3.1-252 Binary phase diagram Pd–C [1.219]

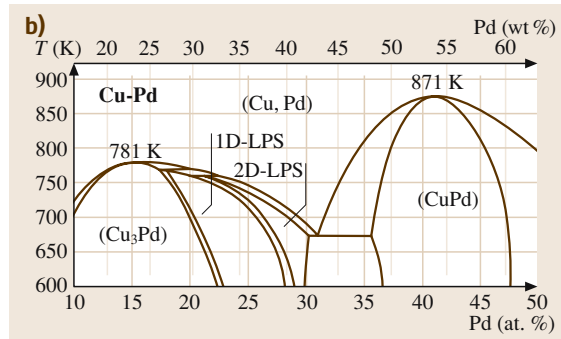
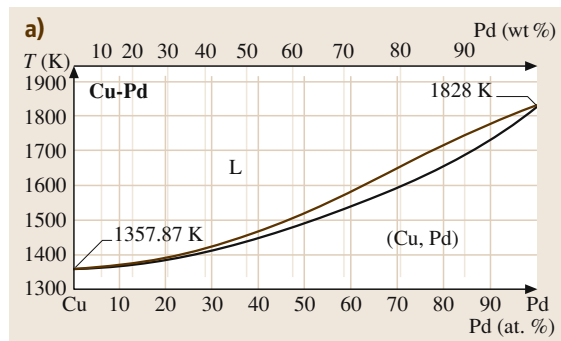


Fig. 3.1-254a,b Binary phase diagrams: Pd–Cu. (a) liquid–solid equilibrium; (b) low temperature (600–900 °C). 1-D LPS = one-dimensional long-period superstructure; 2-D LPS = two-dimensional long-period superstructure [1.219]

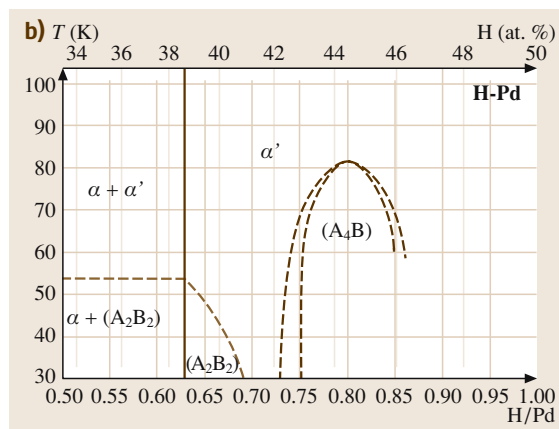
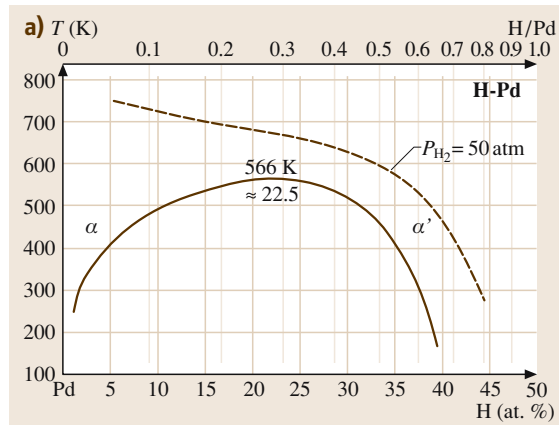


Fig. 3.1-255a,b Binary phase diagrams: Pd–H. (a) Phase diagram; (b) low temperature phase [1.219]

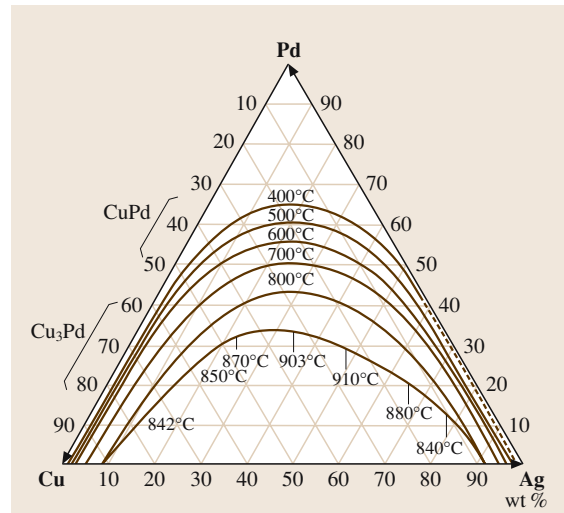


Fig. 3.1-257 Miscibility gap in the Pd–Ag–Cu alloy system [1.220]

Table 3.1-190 Molar heat capacities of solid PGMs [1.222, p. 219]

| Element | $c_p = 4.1868(a + 10^{-3}bT + 10^{-5}T^2)$ J/K | | | |
|---------|--|------|---|-----------|
| | a | b | c | |
| Ir | 5.56 | 1.42 | – | 298–1800 |
| Os | 5.69 | 0.88 | – | 298–1900 |
| Pd | 5.80 | 1.38 | – | 298–1828 |
| Pt | 5.80 | 1.28 | – | 298–2043 |
| Rh | 5.49 | 2.06 | – | 298–1900 |
| Ru | 5.20 | 1.50 | – | 298–1308 |
| Ru | 7.20 | – | – | 1308–1773 |
| Ru | 7.50 | – | – | 1773–1900 |

Table 3.1-191 Latent heat and temperatures of transition of Pd and Pt intermediate compounds [1.222, p. 189]

| Phase | N ₂ | Transition | T _t | L _t |
|--------------------|----------------|----------------|----------------|----------------|
| CuPt | 50 | order-disorder | 800 | 3810 |
| Cu ₃ Pt | 20 | order-disorder | 610 | 1968 |
| Pd ₃ Sb | 25 | order-disorder | 950 | 10 300 |

T_t = transition temperature, L_t = latent heat of transition

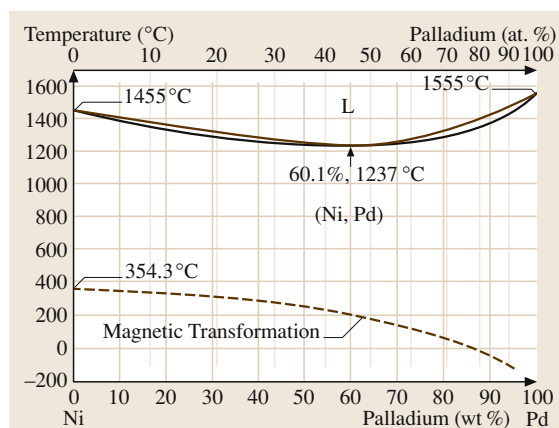


Fig. 3.1-256 Binary phase diagram: Pd–Ni [1.219]

carbon rises from 0.04 wt% at 800 °C to 0.45 wt% at 1400 °C, with the hardness increasing from 80 to 180 HV_{25g} [1.277]. The continuous series of solid solutions of Pd–H-alloys (Fig. 3.1-258) [1.277] splits up below 295 °C into a fcc palladium-rich β phase and an fcc hydrogen-rich phase, forming a miscibil-

Table 3.1-192 Thermodynamic data of Pd [1.217, p. 108]

| T (K) | c_p (J/K mol) | S (J/K mol) | H (J/mol) | G (J/mol) | p (at) |
|--------|-----------------|-------------|-----------|-----------|------------------------|
| 298.15 | 25.99 | 37.823 | 0 | -11.277 | 5.97×10^{-60} |
| 400 | 26.706 | 45.568 | 2.686 | -13.541 | 3.65×10^{-43} |
| 600 | 27.768 | 56.602 | 8.136 | -25.825 | 8.92×10^{-27} |
| 800 | 28.827 | 64.733 | 13.704 | -37.903 | 1.11×10^{-18} |

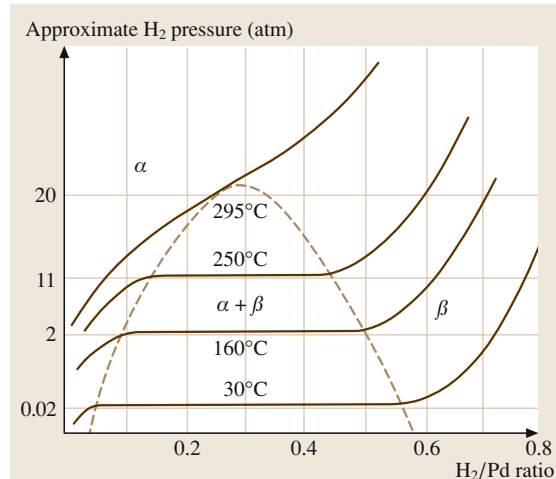
T = Temperature, c_p = specific heat capacity, S = Entropy, H = Enthalpy, G = free Enthalpy, p = partial pressure of the pure elements

Table 3.1-193 Enthalpy of formation H_T of Pd and Pt alloys at temperatures of reaction [1.216, p. 89]

| Base metal | Concentration of alloying metal in at.-% [ETA 89] | | | | | |
|-----------------------------|---|-------------|------------|----------|----------|-------------|
| | Alloy comp. | Temp. (K) | 20 at.-% | 40 at.-% | 60 at.-% | 80 at.-% |
| Enthalpy of formation H_T | | | | | | |
| Pd | Ag | 915 1200 | 283 | 897 | 1290 | 1050 887 |
| Pt | Co | 914 | 1680 | 2580 | 3375 | (90%):1950 |
| | Cu | 1625 | (30%):3110 | | | |
| | Fe | 1123 | -680 | 0 | 1600 | 1800 |

Table 3.1-194 Maximum hydrogen inclusion by platinum-group metals in ml/g (elements) [1.217, p. 616]

| Element | Max H ₂ (ml/g) | Composition |
|---------|---------------------------|---------------------|
| Ru | 123 | RuH _{1.1} |
| Rh | 24 | RhH _{0.2} |
| Pd | 75 | PdH _{0.7} |
| Os | 75 | OsH _{1.2} |
| Ir | 35 | IrH _{0.6} |
| Pt | 2.4 | PtH _{0.04} |

**Fig. 3.1-258** Hydrogen pressure in the Pd–H system [1.278, p. 130]

ity gap which broadens with decreasing temperature. The equilibrium hydrogen-pressure at 295 °C amounts to 19.87 atm with 21 at.-% hydrogen. The α -phase takes hydrogen up to 1300 times of the volume of palladium, corresponding 50 at.-% hydrogen. Further quantities up to 2800 times of the Pd-volume can be loaded by cathodic deposition. The lattice parameters increase with increasing hydrogen content from 3.891 Å to 4.06 Å at 75 at.-% hydrogen. The dissolved hydrogen moves easily and diffuses quickly through thin Pd-membranes. This effect is used for the production of high-purity Pd and for the separation of H isotopes.

Thermal cycling of Pd–H-alloys in the duplex phase causes brittleness due to stresses generated by changes of the lattice dimensions for different quantities of dissolved hydrogen. Palladium-silver alloys with 20–25 wt% silver dissolve higher amounts of hydrogen than pure palladium (Fig. 3.1-259).

For composition and crystal structures, see Tables 3.1-195 and 3.1-196 [1.217, 219, 277]. Primary solid solutions have the fcc structure of Pd. The lattice parameters correspond with few exceptions roughly to Vegard's law. Superlattices occur in alloys with Cu, Fe, Nb, V, in atomic ratios from 1:1, 2:1, and 3:1 (Tables 3.1-123, 3.1-197).

Ordered A₃B-phases of Pd–Mn and Pd–Fe alloys show higher solubility for hydrogen than the disordered phases. In Pd–Mn alloys, hydrogen uptake lowers the temperature of the ordering process.

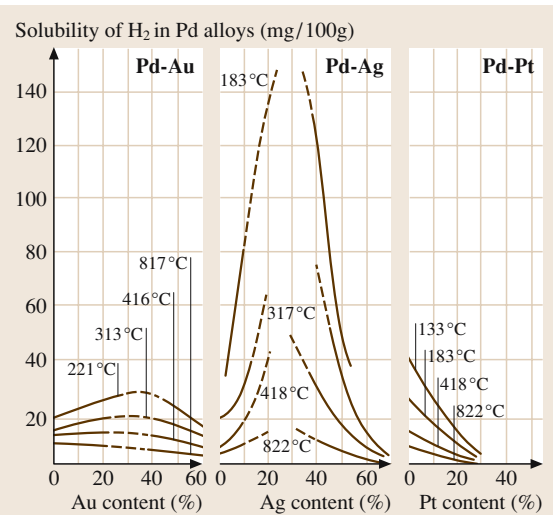


Fig. 3.1-259 Solubility of hydrogen at 1 atm in Pd–Au, Pd–Ag, and Pd–Pt alloys [1.279, p. 44]

Table 3.1-195 Structure and lattice parameters of selected intermediate Pd compounds [1.217, p. 118]

| Phase | Pearson Symbol | a (nm) | b (nm) | c (nm) | c/a | Remarks | Concentration x $A(1-x)B(x)$ |
|-----------|----------------|----------|----------|----------|--------|------------|-----------------------------------|
| C–Pd | cF4 | 0.3735 | | | | | 0.97 |
| Co–Pd | cF4 | 0.3735 | | | | | |
| Cu–Pd | cF4 | 0.377 | | | | HT | 0.5 |
| Cu_3Pd | tP4 | 0.3701 | 0.3666 | 0.9905 | | | |
| Cu_3Pd | tP28 | 0.371 | 2.5655 | 6.9151 | | | 0.19 |
| Fe–Pd | cF4 | 0.38873 | | | | | 0.936 |
| FePd | tP4 | 0.386 | | 0.3731 | 0.9666 | | |
| $FePd_3$ | cP4 | 0.3851 | | | | | |
| H_3Pd_5 | cF* | 0.4018 | | | | | |
| H_4Pd_3 | cP* | 0.2995 | | | | HT > 923 K | |
| H_4Pd_3 | tP4 | 0.2896 | | 0.333 | 1.1499 | | |
| Ni–Pd | cF4 | 0.373 | | | | 298 K | 0.474 |
| Pd_3Zr | hP16 | 0.5612 | | 0.9235 | 1.6456 | | |

HT = high temperature modification

| Ordered structure type | Examples |
|---|--|
| Tetragonal (L1 ₀ -type) | CdPt, CoPt, Cu ₄ Pd, FePd, FePt, MnPt, NiPt |
| Face-centered cubic (L1 ₂ -type) | CoPt ₃ , Cu ₃ Pt, FePd ₃ , FePt ₃ , Fe ₃ Pt, MnPt ₃ , Ni ₃ Pt |
| Body-centered cubic (B2-type) | BePd, CuPd, FeRh, RhSc, RhTi |
| Rhombohedral (L1 ₁ -type) | CuPt (unique) |
| Close-packed hexagonal (DO ₁₉ -type) | Pt ₃ U |

Table 3.1-196 Structures of platinum-group metal oxides [1.219, 277]

| Oxide | Structure type | Unit cell dimensions (Å) | | |
|-----------------------|--------------------------------------|--------------------------|--------|-------|
| | | a | b | c |
| $\alpha\text{-PtO}_2$ | primitive hexagonal | 3.08 | | 4.19 |
| $\beta\text{-PtO}_2$ | primitive orthorhombic | 4.486 | 4.537 | 3.138 |
| Pt_3O_4 | primitive cubic | 5.585 | | |
| PdO | tetragonal | 3.043 | | |
| PdRhO | hexagonal | 5.22 | | 6.0 |
| Rh_2O_3 (LT) | hexagonal (corundum) | 5.108 | | 13.87 |
| Rh_2O_2 | tetragonal (rutile) | 4.4862 | 3.0884 | |
| PdO | tetragonal PdO | 3.03 | | 5.33 |
| PdO ₂ | tetragonal TiO ₂ (rutile) | 4.483 | | 3.101 |

LT = low temperature modification

Table 3.1-197 Superlattice structures of the platinum-group metals [1.280, p. 22]

Mechanical Properties. Characteristic data are shown in Tables 3.1-198–3.1-202 and Figs. 3.1-260–3.1-266 [1.217, 220, 231, 277]. At room temperature Pd is very ductile and can be easily rolled or drawn to form a sheet, foil, and wire. The recrystallization temperatures (Table 3.1-212) depend on purity

grade, degree of cold forming and annealing time. Strengthening is affected by solid solution and by order hardening in alloys, forming superlattice structures. Solid solution hardening is also effected by alloying with rare earth metals in concentrations of 0.1–0.6 at.%.

Table 3.1-198 Modulus of elasticity in crystal directions (GPa) [1.217, p. 214]

| $E(100)$ | $E(110)$ | $E(111)$ |
|----------|----------|----------|
| 65 | 129 | 186 |

Table 3.1-199 Elastic constants of Pd [1.217, p. 216]

| T (°C) | c_{11} | c_{12} | c_{14} |
|----------|----------|----------|----------|
| -273 | 234.1 | 176.1 | 71.2 |
| 7 | 226.2 | 175.2 | 71.5 |

Table 3.1-200 Mechanical properties of Pd (99.9%) at different temperatures (°C) [1.217, p. 215]

| T (°C) | E (GPa) | R_m (MPa) | A (%) | $R_{p0.2}$ (MPa) | HV |
|----------|-----------|-------------|---------|------------------|------|
| 20 | 124 | 190 | 25 | 50 | 50 |
| 250 | 121 | 180 | 16 | 90 | 47 |
| 500 | 117 | 68 | 94 | 50 | 39 |
| 750 | 98 | 28 | 42 | 20 | 17 |

A = Elongation, E = Modul of elasticity,

R_p = Limit of proportionality, HV = Vickers hardness,

R_m = Tensile strength

Table 3.1-201 Tensile strength (MPa) of binary Pd and Pt alloys [1.217, p. 223]

| Alloying element | Weight % of alloying element | | | |
|------------------|------------------------------|------|-------|-----|
| | 2 Pd | 5 Pd | 10 Pd | Pt |
| Ag | 230 | 370 | 270 | 550 |
| Au | 200 | 200 | 220 | 320 |
| Co | 190 | 360 | 210 | — |
| Cu | 240 | 290 | 280 | 400 |
| Fe | 200 | 360 | 230 | — |
| Ni | 190 | 260 | 219 | 450 |
| Pd | — | 170 | — | 190 |
| Pt | 200 | — | 220 | — |
| Rh | 230 | 170 | 290 | 230 |
| Ru | 230 | 250 | 350 | 380 |
| | | | — | 550 |

Table 3.1-202 Mechanical properties of Pd by cold forming as a function of reduction in thickness V in % [1.217, p. 215]

| V (%) | R_m (MPa) | A (%) | HV |
|---------|-------------|---------|------|
| 0 | 220 | 60 | 50 |
| 20 | 250 | 170 | 80 |

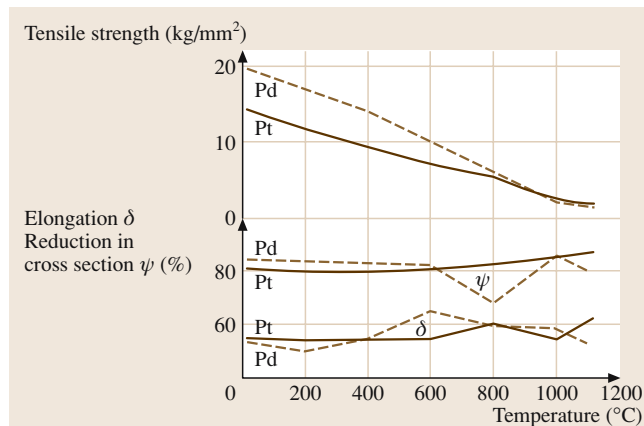


Fig. 3.1-261 Tensile strength of Pd and Pt at different temperatures [1.220, p. 82]

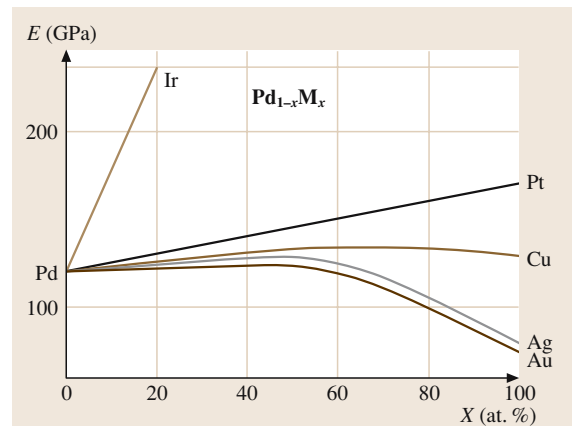


Fig. 3.1-260 Modulus of elasticity of Pd alloys [1.217, p. 216]

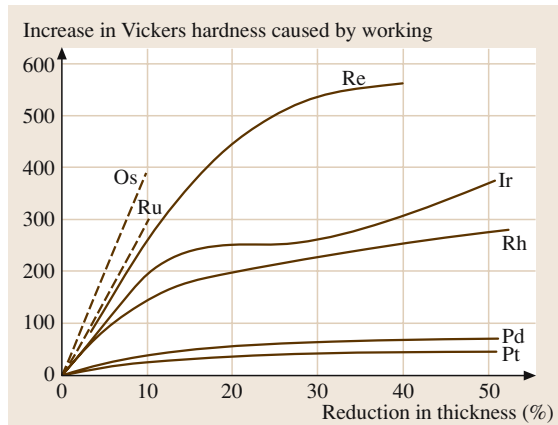


Fig. 3.1-262 Work hardening of the platinum group metals [1.277, p. 93]

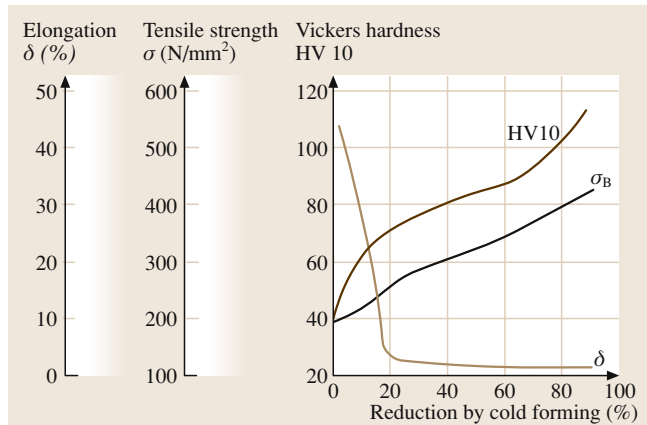


Fig. 3.1-263 Work hardening of Pd (99.99%) (% reduction by cold forming) [1.231, p. 71]

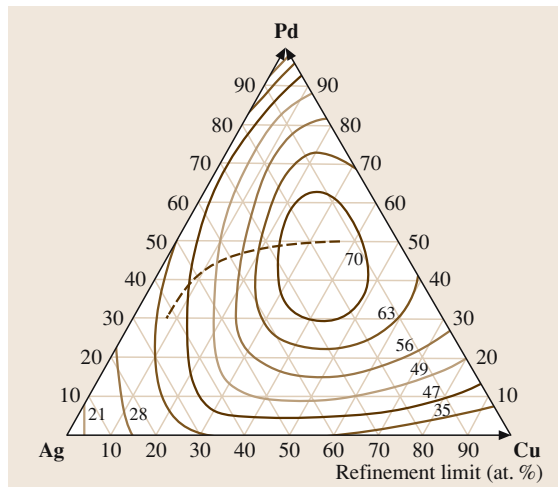


Fig. 3.1-265 Tensile strength of Pd–Ag–Cu alloys. Dashed line: refinement limit [1.220, p. 268]

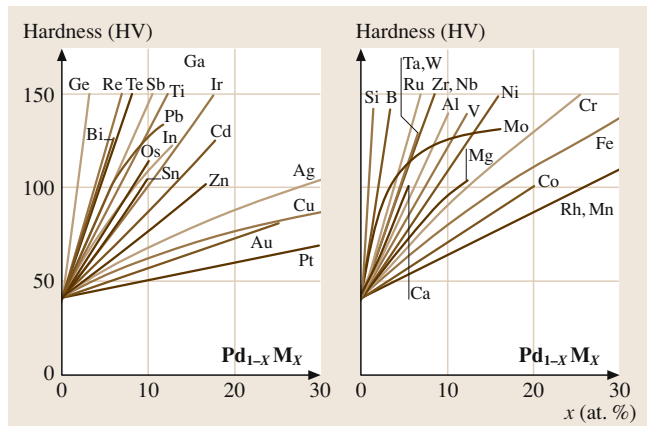


Fig. 3.1-264 Solid solution hardening of Pd by various elements [1.217, p. 217]

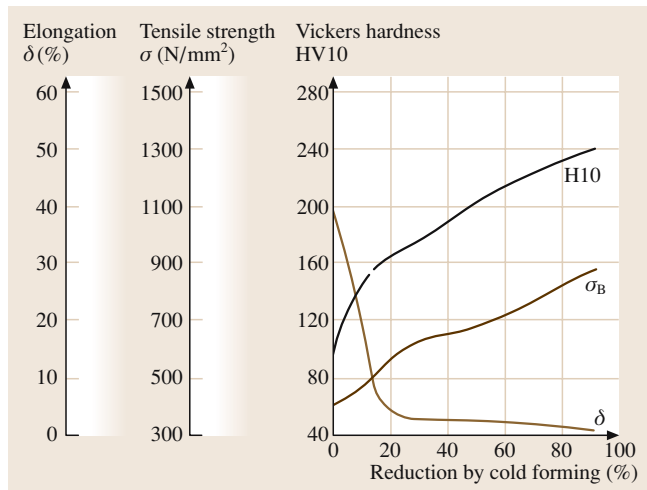


Fig. 3.1-266 Work hardening of PdCu15 alloys (% reduction by cold forming) [1.231, p. 72]

Electrical Properties. In Tables 3.1-203 – 3.1-205 [1.217] and Figs. 3.1-267, 3.1-268 [1.228, 231] characteristic data are shown. Pure Pd shows no superconductivity, PdH and some intermetallic compounds are superconducting at low critical temperatures, e.g., $T_c(\text{Bi}_2\text{Pd}) = 3.7 \text{ K}$.

Table 3.1-203 Residual electrical resistivity ratio (RRR) of pure noble metals [1.217, p. 156]

| 273.2 K/4.2 K | | | | | | | |
|---------------|-----|-----|------|-----|----|------|-----|
| Ru | Rh | Pd | Ag | Os | Ir | Pt | Au |
| 25 000 | 570 | 570 | 2100 | 400 | 85 | 5000 | 300 |

Table 3.1-204 Increase of atomic resistivity of Pd and Pt [1.217, p. 158]

| Basic element | $\Delta\rho/C (\mu\Omega \text{ cm}/\text{at.\%})$ |
|---------------|--|
| Pd | Ag 1.17 Al 2.17 Au 0.65 B 1.43 Bi 5.45 Cd 1.36 Co 2.04 Cr 2.98 Cu 1.35 Fe 2.06 Ga 2.25 Ge 4.13 In 1.96 Ir 7.0 Mn 167 Mo 4.49 Ni 0.72 Pb 3.5 Pt 0.88 Rh 1.67 Ru 3.3 Sn 2.89 V 3.2 Zn 1.73 Zr 2.49 |
| Pt | Ag 2.2 Au 1.3 Be 3 Co 1.7 Cr 6.8 Cu 3 Fe 3.9 In 3.4 Mn 2.95 Mo 6.2 Nb 5.4 Ni 0.9 Os 2.4 Pd 0.6 Rh 1.0 Ru 2.4 Sn 3.9 W 5.7 Zr 4.7 |

Table 3.1-205 Specific electrical resistivity ($\mu\Omega \text{ cm}$) of Pd at different temperatures (K) [1.217, p. 156]

| T (K) | 90 | 175 | 273 | 500 | 800 | 1300 |
|-------|-------|-------|-------|--------|--------|--------|
| | 2.147 | 5.821 | 9.725 | 17.848 | 26.856 | 38.061 |

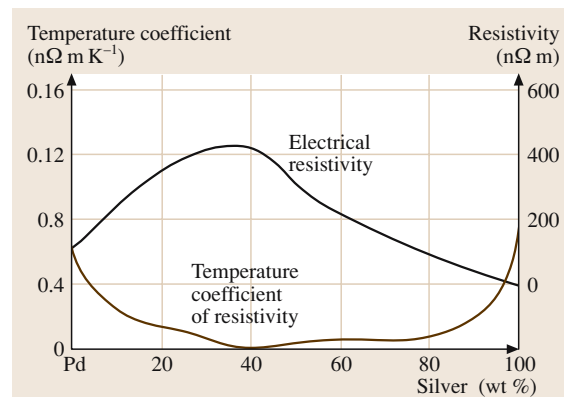


Fig. 3.1-268 Electrical resistivity and temperature coefficient of resistivity of Pd–Ag alloys as a function of Ag content [1.228, p. 702]

Thermoelectric Properties. Tables 3.1-206 – 3.1-209 [1.216, 217] and Figs. 3.1-269, 3.1-270 [1.216, 218] give data of absolute thermoelectric power, thermal electromotive force of pure Pd and Pd alloys at different temperatures. Special alloys for thermocouples with high corrosion resistance are shown in Table 3.1-210 [1.217].

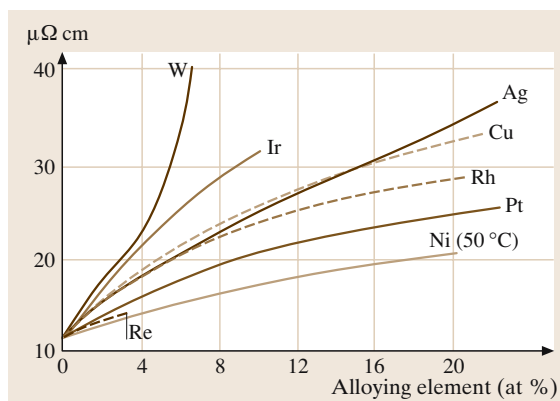


Fig. 3.1-267 Influence of alloying elements on the electrical conductivity of Pd [1.231, p. 67]

| Metal | Absolute thermoelectric power ($\mu\text{V}/\text{grd}$) | | | | | | | | |
|-------|--|-------|-------|-------|------|-------|-------|-------|-------|
| | T (°C) | -255 | -200 | -100 | -20 | 0 | 100 | 300 | 500 |
| Pd | +1.02 | +3.96 | -3.16 | -7.94 | -9.6 | -13.4 | -18.8 | - | -35 |
| Pt | +1.8 | +5.9 | +0.1 | -3.6 | -4.4 | -7.3 | -10.9 | -14.0 | -18.6 |
| Rh | +1.6 | +1.8 | - | +1.7 | - | +1.2 | +0.3 | -0.3 | - |
| Ir | - | - | +1.8 | - | +1.5 | +0.9 | -0.3 | -1.3 | - |
| Ru | - | - | - | - | - | - | -32.5 | -42 | -43 |

Table 3.1-206
Absolute thermoelectric power ($\mu\text{V}/\text{grd}$) of the platinum-group metals at different temperatures [1.216, p. 89]

| Thermal electromotive force $E_{\text{A},\text{Pt}}$ (mV) | | | | | | |
|---|--------|-------|--------|--------|--------|--------|
| T (°C) | Ru | Rh | Ir | Pd | Ag | Au |
| -100 | | -0.32 | -0.35 | 0.48 | -0.21 | -0.21 |
| 0 | 0 | 0 | 0 | 0 | 0 | 0 |
| 100 | 0.684 | 0.70 | 0.660 | 0.570 | 0.740 | 0.770 |
| 300 | 2.673 | 2.68 | 2.522 | -1.990 | 3.050 | 3.127 |
| 600 | 6.485 | 6.77 | 6.201 | -5.030 | 8.410 | 8.115 |
| 900 | 11.229 | 12.04 | 10.943 | -9.720 | 10.943 | 14.615 |
| 1200 | 16.864 | 18.42 | 16.665 | - | - | - |
| 1400 | - | 22.56 | 20.819 | -20.41 | - | - |

Table 3.1-207
Thermal electromotive force $E_{\text{A},\text{Pt}}$ (mV) of the thermocouples of noble metals and pure Pt at different temperatures, reference junction at 0 °C [1.217, p. 159]

| Alloying element | T (°C) | Composition (wt% Ir) | | | | |
|------------------|----------|----------------------|-------|-------|-------|-------|
| | | 10 | 30 | 50 | 70 | 90 |
| Ag | 100 | -1.1 | -2.4 | -3.3 | -0.5 | 0.1 |
| | 1000 | -23.5 | -44.4 | -45.8 | -11.5 | - |
| Au | 100 | -1.0 | -1.7 | -2.7 | -2.7 | 0 |
| | 1000 | -14.5 | -24.1 | -38.5 | -33.5 | 3.0 |
| | 1300 | -22.0 | -34.0 | -52.0 | -48.0 | - |
| Cu | 100 | -1.05 | -1.49 | | | |
| Ir | 100 | 2.01 | 2.02 | | | |
| | 1000 | 22.1 | 26.1 | | | |
| Ni | 100 | -0.80 | -1.47 | -1.75 | -1.75 | -1.65 |
| | 1000 | -9.4 | -9.4 | -10.2 | -11.6 | -11.5 |
| Pt | 100 | 0.32 | 0.83 | 0.75 | 0.53 | 0.22 |
| | 1000 | -2.1 | 7.8 | 9.4 | 7.8 | 4.6 |
| | 1300 | -5.2 | 8.0 | 11.7 | 10.7 | 5.3 |

Table 3.1-208 Thermal electromotive force $E_{\text{A},\text{Pt}}$ (mV) of Pd alloys at different temperatures, reference junction at 0 °C [1.217, p. 160]

Table 3.1-210 Palladium alloys for thermocouples (Th.-C.) of high corrosion resistance [1.217, p. 472]

| T (°C) | Th.-C.1 (mV) | Th.-C.2 (mV) | Th.-C.3 (mV) |
|----------|--------------|--------------|--------------|
| 100 | 3.31 | 4.6 | 3.3 |
| 400 | 15.70 | 21.5 | 15.4 |
| 600 | 24.70 | 34.2 | 24.6 |
| 800 | 33.50 | 46.9 | 33.4 |
| 1000 | 41.65 | 59.6 | 41.3 |

| | | | |
|--------|-----|--------|-------------|
| Th.-C. | 1.: | AuPd40 | Pd38Pt14Au3 |
| Th.-C. | 2.: | AuPd46 | PtIr10 |
| Th.-C. | 3.: | AuPd35 | PtPd12.5 |

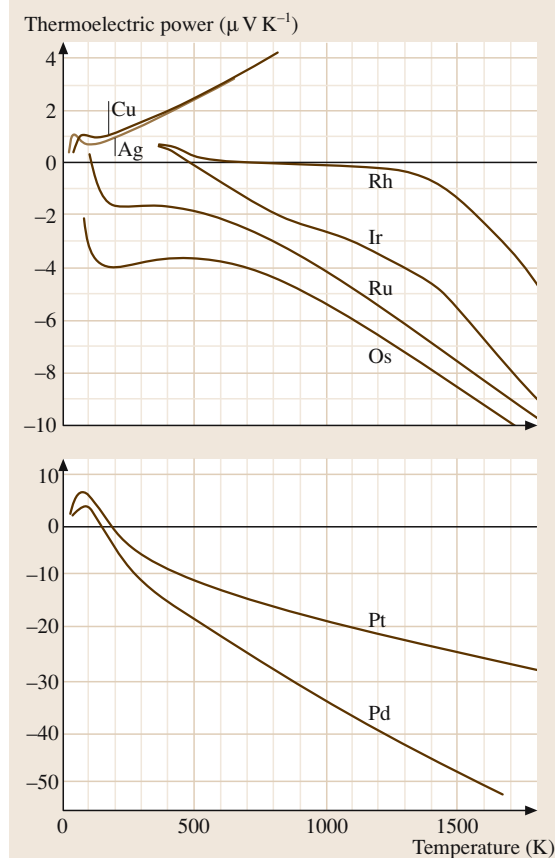


Fig. 3.1-269 Thermoelectric power of the platinum group metals [1.218, p. 58]

Magnetic Properties. All PGMs show magnetostriction in a magnetic field. The reversible change of length is proportional to the square of the applied magnetic field (Table 3.1-211) [1.217, 218]. The paramagnetic susceptibilities of Pd and Pd alloys decrease with increasing

| Metal | S_l |
|------------------------------------|-------|
| Ru | -1.4 |
| Rh | 11 |
| Pd | -39.4 |
| Ir | 3.8 |
| Pt | -32 |
| $\text{Rh}_{0.50}\text{Ir}_{0.50}$ | 9.5 |
| $\text{Rh}_{0.50}\text{Pd}_{0.50}$ | 27 |
| $\text{Ir}_{0.60}\text{Pd}_{0.40}$ | 13.4 |
| $\text{Pd}_{0.67}\text{Pt}_{0.33}$ | -17.4 |
| $\text{Pd}_{0.33}\text{Pt}_{0.67}$ | -79 |

Table 3.1-211
Magnetostriction of platinum-group metal and platinum-group metal alloys, expressed by the factor S_l of proportionality according to $\Delta l/l = S_l H^2$ [1.217, p. 161]

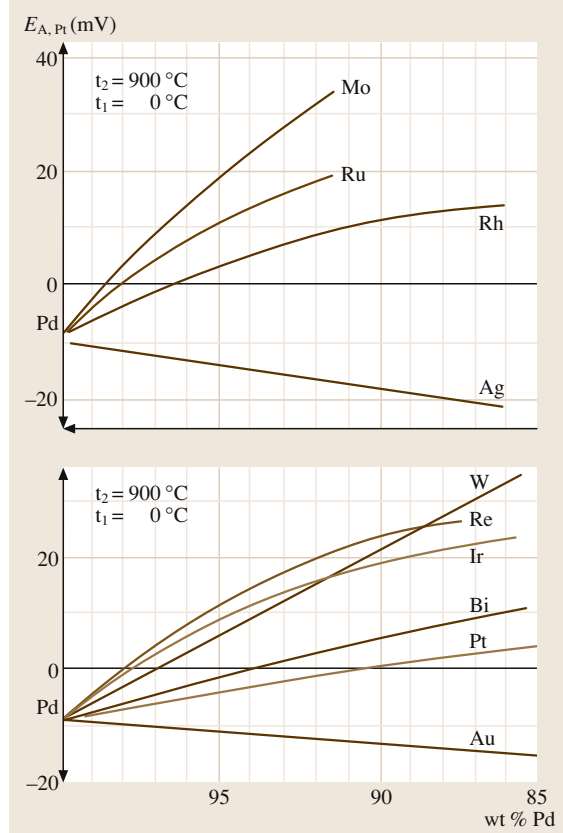


Fig. 3.1-270 Thermal electromotive force of Pd alloys at 900 °C (reference junction at 0 °C) [1.216, p. 97]

temperature (Figs. 3.1-271, 3.1-272) [1.217, 218]. Alloying with 0.05 wt% Rh raises the susceptibility from $88 \times 10^{-10} \text{ m}^3/\text{mol}$ to $160 \times 10^{-10} \text{ m}^3/\text{mol}$. Pd–Cu alloys are diamagnetic up to 50 at.% Pd. The susceptibilities of the ordered phases in this system are higher than those of the disordered solid solution phase. The paramagnetism of Pd decreases by dissolution of H₂ to reach zero at PdH_{0.66} and above. Partial ordering within FePd raises its coercive field from the disordered value of 2 to 260 Oe [1.281, 282].

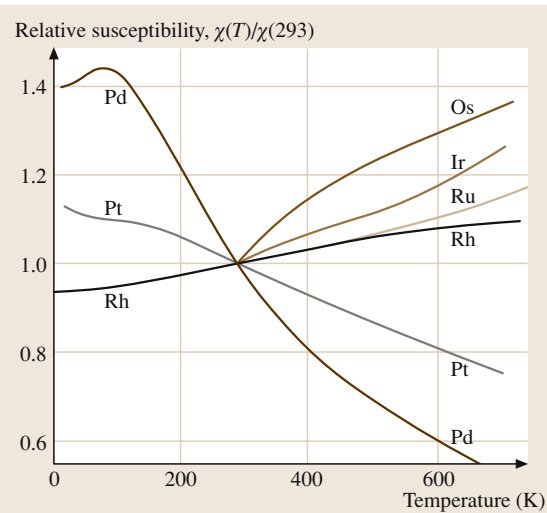


Fig. 3.1-271 Temperature dependence of the magnetic susceptibility of the platinum group metals [1.218, p. 98]

Thermal Properties. Selected data of thermal conductivity and thermal expansion of PGM and PgAg alloys are given in Tables 3.1-212–3.1-215, Fig. 3.1-273. FePd-alloys exhibit around the Fe_3Pd stoichiometry in the disordered state zero coefficient of thermal expansion (Invar effect) [1.281, 282].

Table 3.1-212 Recrystallization temperatures of platinum-group metal (0°C) (Depending on purity, degree of cold forming an annealing time) [1.217, p. 216]

| Metal | Recrys. temperature ($^\circ\text{C}$) |
|-------|--|
| Ir | 1200–1400 |
| Pd | 485–600 |
| Pt | 350–600 |
| Rh | 700–800 |
| Ru | 1200–1300 |

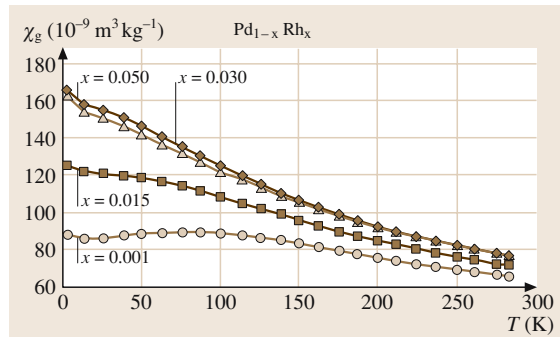


Fig. 3.1-272 Temperature dependence of the magnetic mass susceptibility of $\text{Pd}-\text{Rh}$ alloys [1.217, p. 169]

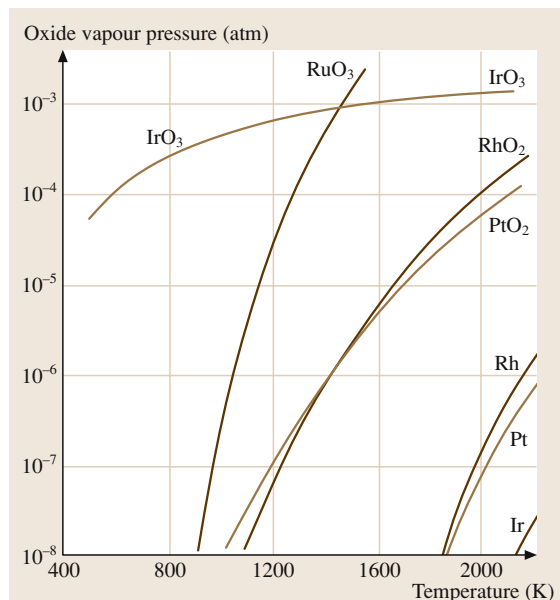


Fig. 3.1-273 Vapor pressures of platinum group metal oxides [1.277, p. 178]

| Temperature ($^\circ\text{C}$) | Thermal conductivity (W/m K) | | | | | | | |
|-------------------------------------|------------------------------|------|-----|-----|-----------------|-----------------|-----------------|----|
| | Pd | Pt | Rh | Ir | Ru ^a | Ru ^b | Ru ^p | Os |
| 100 | 76 | 85.6 | 185 | — | 140 | 180 | 150 | — |
| 273 | 75.6 | 75.0 | 153 | 149 | 110 | 134 | 119 | 88 |
| 600 | 79.0 | 73.0 | 135 | 130 | 95 | 129 | 105 | 85 |
| 800 | 83.0 | 74.8 | 126 | 125 | 87 | 112 | 96 | — |
| 1200 | 88.2 | 83.2 | 118 | 117 | 77 | 101 | 83 | — |

^a vertical to the crystal c axis,

^b parallel to the crystal c axis

^p polycrystalline

Table 3.1-213 Thermal conductivity of platinum-group metal at different temperatures [1.217, p. 153]

Table 3.1-214 Thermal expansion coefficient of the platinum-group metals [1.217, p. 154]

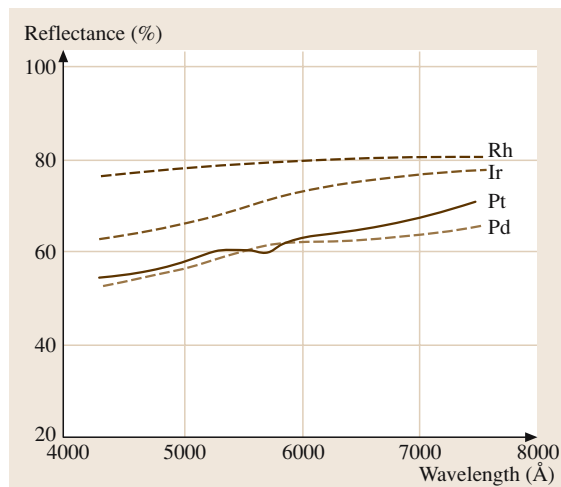
| Temperature (°C) Metal | Thermal expansion coefficients (10^{-6} K^{-1}) | | | | | | | | | |
|---------------------------|---|------|------|-----|-----------------|-----------------|-----------------|-----------------|-----------------|-----------------|
| | Pd | Pt | Rh | Ir | Ru ^a | Ru ^b | Ru ^p | Os ^a | Os ^b | Os ^p |
| 323 | — | — | — | — | 5.9 | 8.8 | 6.9 | 4.0 | 5.8 | 4.8 |
| 373 | 11.9 | 9.1 | 8.5 | 6.7 | — | — | — | — | — | — |
| 423 | | | | | 6.1 | 9.3 | 7.2 | 4.3 | 6.2 | 5.0 |
| 473 | 12.1 | 9.2 | 9.0 | — | — | — | — | — | — | — |
| 623 | | | | | 6.8 | 10.5 | 8.0 | 4.0 | 7.1 | 5.7 |
| 673 | 12.6 | 9.5 | 9.6 | — | — | — | — | — | — | — |
| 723 | | | | | 7.2 | 11.0 | 8.4 | 5.3 | 7.6 | 62 |
| 823 | — | — | 9.6 | — | | 11.7 | 8.8 | 5.8 | 8.3 | 6.9 |
| 1073 | 13.4 | 10.0 | 10.3 | — | — | — | — | — | — | — |

^a vertical to the crystal *c* axis,
^b parallel to the crystal *c* axis
^p polycrystalline

Table 3.1-215 Thermal expansion coefficient of Pd–Ag alloys [1.217, p. 154]

| Temp. range (K) 373–473 | |
|-------------------------|--|
| Pd-content (%) | Thermal expansion coefficient (10^{-6} K^{-1}) |
| 20 | 16.2 |
| 50 | 14.7 |
| 80 | 12.4 |

Optical Properties. In Table 3.1-216 and Fig. 3.1-274 characteristic data are given. The optical reflectance of Pd is increased by alloying with Ru (Fig. 3.1-275).

**Fig. 3.1-274** Optical reflectance of the platinum group metals [1.220, p. 78]**Table 3.1-216** Spectral degree of emission ϵ of the platinum-group metals at different temperatures [1.217, p. 171]

| | Surface | Temperature (°C) | Spectral emission ϵ |
|-----------------|---------|------------------|------------------------------|
| Ru ^b | solid | 1000 | 0.421 |
| | solid | 2000 | 0.314 |
| Os ^b | solid | 1000 | 0.526 |
| | solid | 2000 | 0.383 |
| Rh ^a | solid | < 1966 | 0.29 |
| | liquid | > 1966 | 0.3 |
| Ir ^a | solid | 927–2027 | 0.3 |
| | solid | 2000 | 0.383 |
| Pd ^a | solid | 900–1530 | 0.33 |
| | liquid | 1555 | 0.37 |
| Pt ^a | solid | 1000 | 0.371 |
| | solid | 1400 | 0.421 |
| | liquid | 1800 | 0.38 |

^a 650 nm; ^b 655 nm

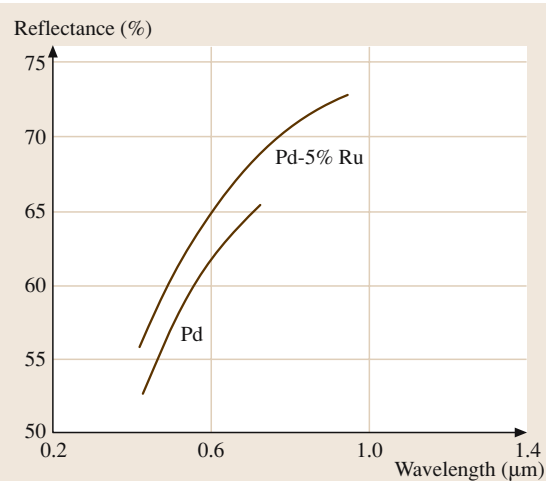


Fig. 3.1-275 Optical reflectance (%) of PdRu5 alloy [1.228, p. 700]

Diffusion. Data for selfdiffusion, diffusion of tracer elements and of hydrogen and oxygen are shown in Tables 3.1-156, 3.1-158, 3.1-217.

Carbon diffuses very rapidly through Pd at elevated temperatures in presence of a concentration gradient on the surface.

Table 3.1-217 Self-diffusion in pure platinum-group metals [1.217, p. 149]

| | Element | D^0 | O | T (K) |
|-------------------|---------|--------------------|-------|------------------|
| Lattice diffusion | Ir(S) | 0.36 | 438.8 | 2092–2664 |
| | Pd(S) | 0.205 | 266.3 | 1323–1773 |
| | Pt | 0.33 | 285.6 | 1598–1837 |
| | Pt(S) | 0.05 | 257.6 | 850–1265 |
| Surface diffusion | Rh(111) | 4×10^{-6} | 174 | 1200–1500 (Vac.) |
| | Pt | 4×10^{-7} | 108 | 1160–1580 (Vac.) |

Chemical Properties. Pd has the reduction potential of $E_0 = 0.951$ for Pd/Pd^{2+} . It is resitant against reducing acids and in oxydizing media above pH 2. Alkali melts attack above $\sim 400^\circ\text{C}$. In oxygen atmosphere between 400 and 800°C are thin PdO -surface layers formed, which dissociate above 800°C . Above 1100°C occur increasing weight losses by evaporation (Fig. 3.1-276).

Catalysis: Pd and Pd alloys are effective catalysts in numerous chemical reactions. In heterogenous catalysis,

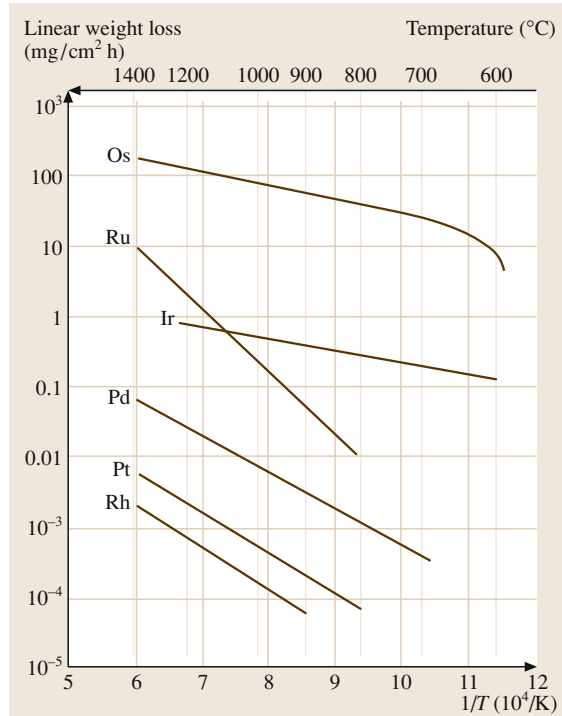


Fig. 3.1-276 Weight losses of the platinum group metals at annealing on air [1.217, p. 183]

PGM are applied in form of wire nets and of powders with high specific surfaces (20 to 1000 m^2/g , “platinum black”, “palladium black”) on carbon or Al_2O_3 supports. Automotive gas cleaning catalysts use of Pd–Pt–Rh alloys in different compositions.

Special Alloys. Tables 3.1-159, 3.1-160, 3.1-218 show typical compositions of Pd containing brazing alloys, Table 3.1-219 Pd containing jewelry alloys. PdAg40 has a very low temperature coefficient of resistivity (0.00003/ $^\circ\text{C}$ between 0 and 100°C , electrical resistivity $42 \mu\text{cm}$). It is used for precision resistance wires (Fig. 3.1-268). Pd60Ni35Cr5 is corrosion resistant against molten salt mixtures up to 700°C , suited for brazing graphit, Mo and W.

Ti–Pd–Ni and Fe–Pd alloys show shape memory effects. Partial replacement of Pd in the alloy Fe30 at.% Pd by > 4 at.% Pt decreases the temperature of the f.c.c./f.c.t. martensite transformation and effects strengthening.

Table 3.1-218 Physical properties of some technical Pd and Pt alloys [1.231, p. 67]

| Material | Density (g/cm ³) | Melting point (interval) (°C) | Electrical conductivity (m/Ω mm ²) | Temperature coefficient of electrical resistance (10 ³ K ⁻¹) | Modulus of elasticity (kN/mm ²) |
|-----------|---------------------------------|----------------------------------|---|--|--|
| Pt(99.9) | 21.45 | 1773 | 9.4 | 3.92 | 16–17 |
| PtIr5 | 21.5 | 1774–1776 | 4.5 | — | 18.5–19.5 |
| PtIr10 | 21.6 | 1780–1785 | 5.6 | 2.0 | ca. 22 |
| PtRu10 | 20.6 | ca. 1800 | 3.0 | 0.83 | ca. 23.5 |
| PtNi8 | 19.2 | 1670–1710 | 3.3 | 1.5 | ca. 18 |
| PtW5 | 21.3 | 1830–1850 | 2.3 | 0.7 | ca. 18.5 |
| Pd(99.99) | 12.0 | 1552 | 9.3 | 3.77 | ca. 12.5 |
| PdCu15 | 11.3 | 1370–1410 | 2.6 | 0.49 | ca. 17.5 |
| FdCu40 | 10.4 | 1200–1230 | 3.0 | 0.28 | ca. 17.5 |
| PdNi5 | 11.8 | 1455–1485 | 5.9 | 2.47 | ca. 17.5 |

Table 3.1-219 Composition and melting temperature range of selected Pd-jewellery alloys [1.217, p. 511]

| Alloy | Melting temperature range (°C) |
|-----------------|--------------------------------|
| Pd95Cu3Ga2 | 1340–1400 |
| Pd95Cu5 | 1400–1460 |
| Pd95Ni5 | 1450–1490 |
| Pd50Ag47.5Cu2.5 | 1200–1280 |

Platinum and Platinum Alloys

Applications. Platinum and platinum alloys are important constituents of catalysts (chemistry, automotive exhaust gas cleaning, fuel cells), sensor materials (thermocouples, resistance thermometers), strong permanent magnet alloys, magnetic and magnetooptical (memory) devices, high temperature and corrosion resistant structural parts, and electrical contacts and connecting elements. Classical applications are jewelry and dentistry alloys.

Commercial grades are sponge and powder in purities varying from minimum 99.9% to 99.95% (ASTM B 561-86). High purity electronic grade is 99.99%.

Production. Platinum sponge or powder are compacted by pressing and sintering. Melting and alloying is done in electrical heated furnaces in Al₂O₃ or MgO crucibles, by vacuum arc and by electron beam melting 99.98%.

Phases and Phase Equilibria. Selected phase diagrams are shown in Figs. 3.1-277–3.1-281 [1.219]. Thermo-dynamic data are given in Tables 3.1-190–3.1-193 and 3.1-220 [1.216, 217, 222]. For compositions and crystal structures, see Tables 3.1-196, 3.1-219, 3.1-222, 3.1-221 [1.217, 219]. Platinum forms continuous solid

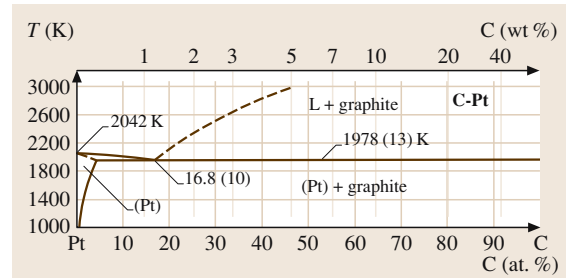
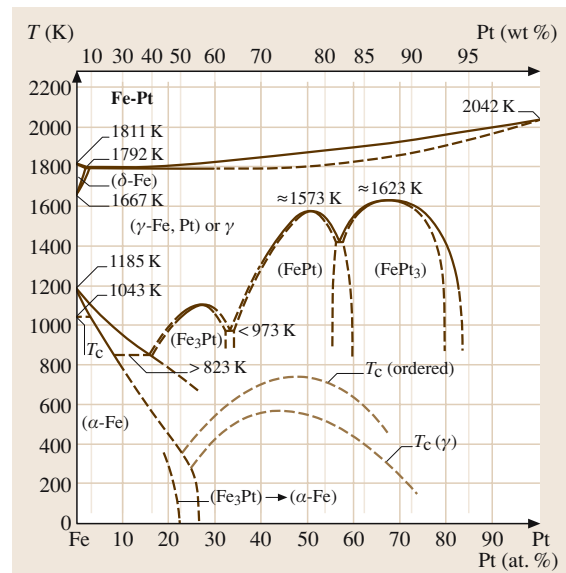
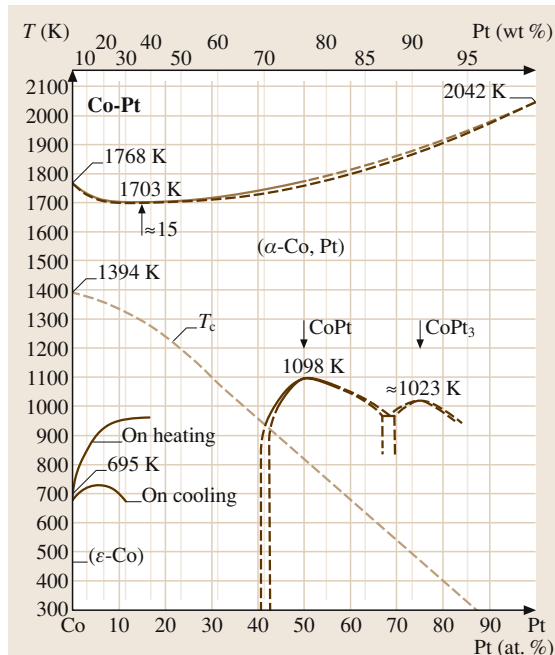
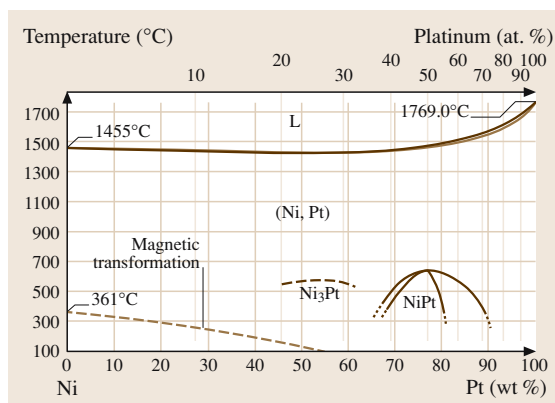
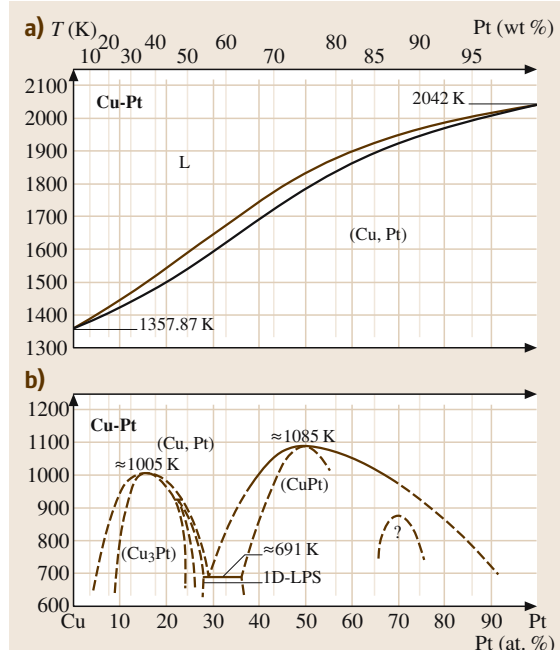
**Fig. 3.1-277** Binary phase diagram Pt–C [1.219]**Fig. 3.1-278** Binary phase diagram Pt–Fe (dash-dotted line: Curie temperature) [1.219]

Table 3.1-220 Thermodynamic data of Pt [1.217, p. 109]

| T (K) | c_p (J/K mol) | S (J/K mol) | H (J/mol) | G (J/mol) | p (at) |
|--------|-----------------|-------------|-----------|-----------|------------------------|
| 298.15 | 25.857 | 41.631 | 0 | 12.412 | 8.26×10^{-92} |
| 400 | 26.451 | 49.314 | 2.664 | -17.961 | 1.30×10^{-66} |
| 800 | 28.593 | 68.313 | 13.677 | -40.973 | 9.75×10^{-30} |
| 1400 | 31.731 | 85.111 | 31.776 | -87.38 | 5.84×10^{-14} |

T = Temperature, c_p = specific heat capacity, S = Entropy, H = Enthalpy, G = free Enthalpy, p = partial pressure of the pure elements

**Fig. 3.1-279** Binary phase diagram Pt–Co [1.219]**Fig. 3.1-281** Binary phase diagram Pt–Ni [1.219]**Fig. 3.1-280a,b** Binary phase diagrams Pt–Cu. (a) Liquid-solid. (b) Solid-solid (1-D LPS = one-dimensional long-period superstructure) [1.219]**Table 3.1-221** Crystal structure and lattice parameters of intermediate phases of Pt oxides [1.219]

| Phase | Structure | Type | a (nm) | b (nm) | c (nm) |
|--------------------------------|--------------|--------------------------------|----------|----------|----------|
| PtO | tetragonal | PtO | 0.304 | | 0.534 |
| Pt ₃ O ₄ | cubic | Pt ₃ O ₄ | 0.6226 | | |
| PtO ₂ | orthorhombic | Fe ₂ O ₃ | 0.4533 | 0.4488 | 0.3138 |
| PtO ₂ | hexagonal | | 0.310 | | 0.435 |

solutions with all other noble metals and with Co, Cu, Fe, and Ni. Miscibility gaps exist with C, Co, Ir, Pt, and Rh. Primary solid solutions have fcc structure and the lattice parameters correspond with few exceptions roughly to Vegard's law. Numerous intermediate phases exist in al-

Table 3.1-222 Structure and lattice parameter of selected intermediate Pt compounds [1.217, p. 119]

| Phase | Pearson Symbol | a (nm) | b (nm) | c (nm) | c/a | Remarks | Concentration x A(1 - x)B(x) |
|--------------------|----------------|--------|--------|--------|--------|---------|---------------------------------------|
| CoPt | tP4 | 0.3806 | 0.3684 | 0.9679 | | | |
| CoPt ₃ | cP4 | 0.3831 | | | | | |
| CuPt | hR32 | 0.7589 | | | | | 0.5 |
| CuPt ₃ | cF4 | 0.3849 | | | | | |
| Cu ₃ Pt | o** | 0.7596 | 0.2745 | 0.777 | | | |
| Cu ₃ Pt | cP4 | 0.3682 | | | | | |
| Fe-Pt | cF4 | 0.376 | | | | | 0.245 |
| FePt | tP4 | 0.3861 | | 0.3788 | 0.9811 | | |
| Fe ₃ Pt | cP4 | 0.3727 | | | | | |
| NiPt | tP4 | 0.3823 | | 0.3589 | 0.9388 | | |
| PtZr | oC8 | 0.3409 | 1.0315 | 0.4277 | | | |
| Pt ₃ Zr | hP16 | 0.5624 | | 0.9213 | 1.6328 | | |

loy systems with rare earth metals. The formation and crystal structures of the intermediate phases have been related to the electron configuration of the alloy components (Engel–Brewer correlation) [1.283, 284]. Phases with superlattice structures are formed with Co, Cu, Fe, Nb, and V in atomic ratios of 1:1, 2:1, and 3:1 (Tables 3.1-123, 3.1-197). The ordered CuPt phase has a long-range ordered rhombohedral structure.

Mechanical Properties. Characteristic data are shown in Tables 3.1-223–3.1-226 [1.217], Figs. 3.1-282–3.1-290 [1.217, 228, 228, 231]. For elastic properties of PGMs at different temperatures, see [1.217]. Strengthening is affected by solid solution hardening, order hardening (Pt–Co, Pt–Cu), and dispersion hardening. Dispersion-strengthened Pt and Pt alloys are remarkably resistant to creep at high temperatures. They are pro-

Table 3.1-223 Elastic constants of Pt [1.217, p. 219]

| c_{11} | c_{12} | c_{44} |
|----------|----------|----------|
| 347 | 173 | 76.5 |

Table 3.1-224 Mechanical properties of Pt (99.9%) at different temperatures (°C) [1.217, p. 220]

| T (°C) | E (GPa) | R_m (MPa) | A (%) | $R_{p0.2}$ (MPa) | HV |
|--------|---------|-------------|-------|------------------|----|
| 20 | 173 | 135 | 41 | 50 | 55 |
| 250 | 169 | 110 | 40 | 40 | 53 |
| 500 | 159 | 78 | 42 | 30 | 50 |
| 750 | 140 | 44 | 46 | 20 | 35 |
| 900 | 126 | 34 | 44 | 17 ^a | 23 |

^a interpolation

A = Elongation, E = Modulus of elasticity, R_p = Limit of proportionality, HV = Vickers hardness, R_m = Tensile strength

Table 3.1-225 Mechanical properties of Pt as function of reduction in thickness (%) by cold rolling [1.217, p. 220]

| Reduction (%) | R_m (MPa) | R_p (MPa) | HV a | b |
|---------------|-------------|-------------|---------|----|
| 0 | 250 | 140 | 50 | 40 |
| 20 | 350 | 310 | 70 | 63 |
| 59 | 400 | 380 | 84 | 73 |

a = Pt > 99.5%, b = Pt > 99.99%

Table 3.1-226 Tensile strength R_m (MPa) and elongation A (%) of binary Pt alloys at different temperatures [1.217, p. 217, 220]

| Alloy compound | Temperature (°C) | | |
|----------------|------------------|--------|--------|
| | 20 | 400 | 600 |
| (wt%) | R_m/A | | |
| Au5 | 340/18 | 290/10 | 250/10 |
| Ir10 | 260/33 | 240/27 | 180/33 |
| Ni5 | 470/26 | 420/26 | 320/25 |
| Pd20Rh5 | 370/30 | 290/18 | 240/23 |
| Rh5 | 225/44 | 150/40 | 120/43 |
| Rh10 | 287/39 | 200/33 | 170/38 |

duced either by co-precipitation with refractory oxides (e.g., 0.16 vol% ZrO₂) or by internal oxidation of alloys with 0.2 wt% Cr or 0.8 wt% Zr. Rh additions improve the solubility for oxygen. TiC powder affects dispersion strengthening in concentrations of 0.04–0.08 wt% (Fig. 3.1-291) [1.277].

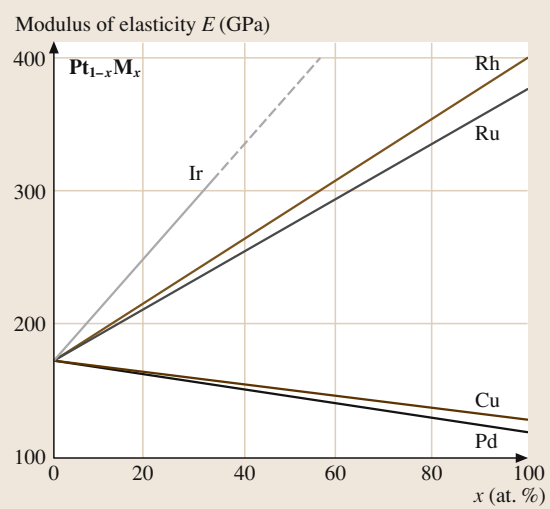


Fig. 3.1-282 Modulus of elasticity of binary Pt alloys [1.217, p. 222]

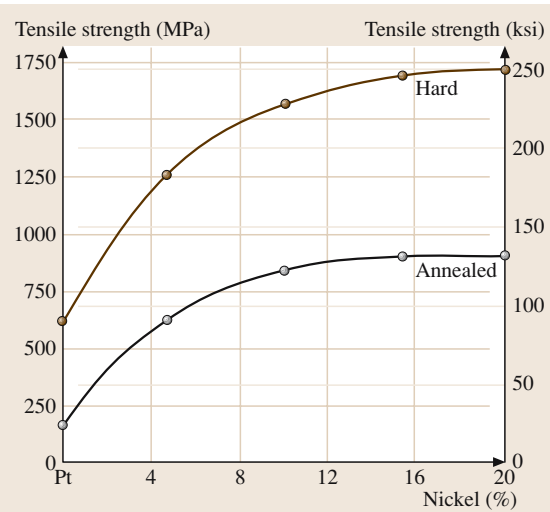


Fig. 3.1-284 Tensile strength of Pt–Ni alloys as a function of Ni content [1.228, p. 695]

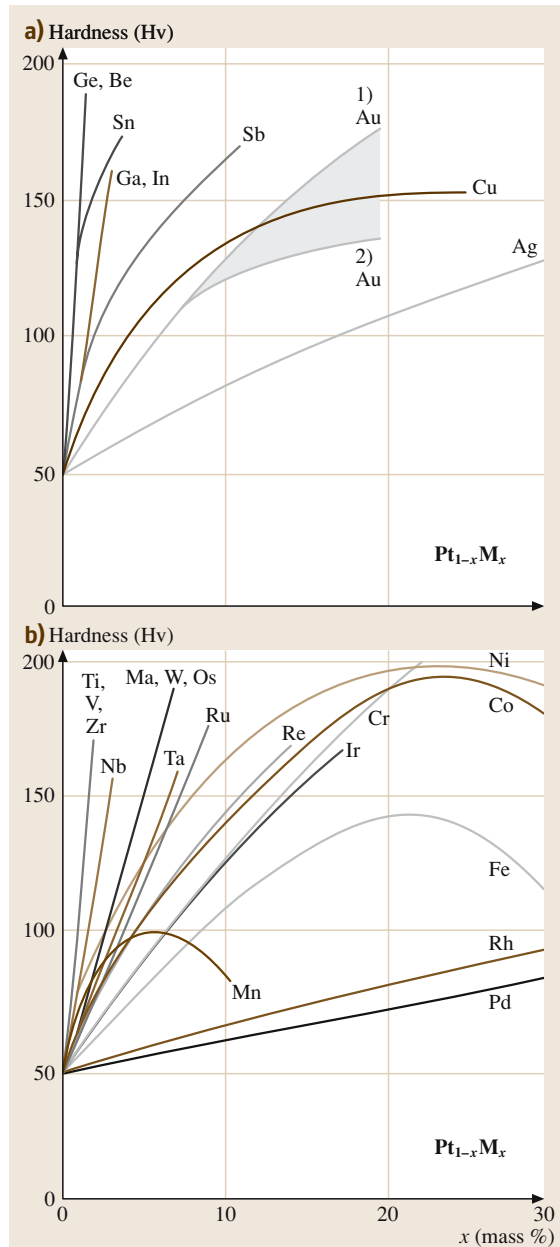


Fig. 3.1-283a,b Solid solution hardening of binary Pt alloys (a) de-alloyed at 900 °C; (b) solution annealed at 1200 °C [1.217, p. 223]

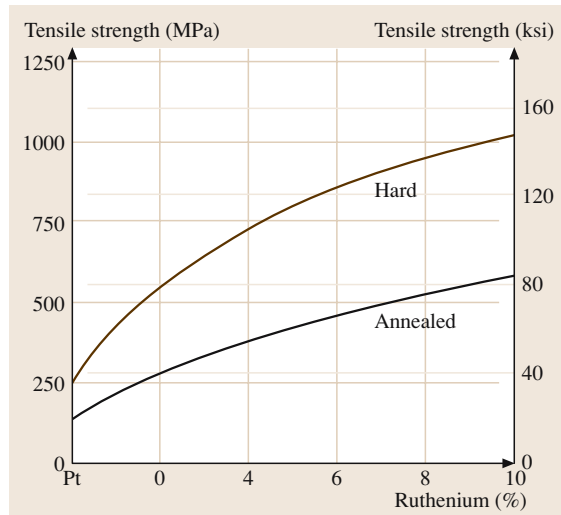


Fig. 3.1-285 Tensile strength of Pt–Ru alloys as a function of Ru content [1.228, p. 694]

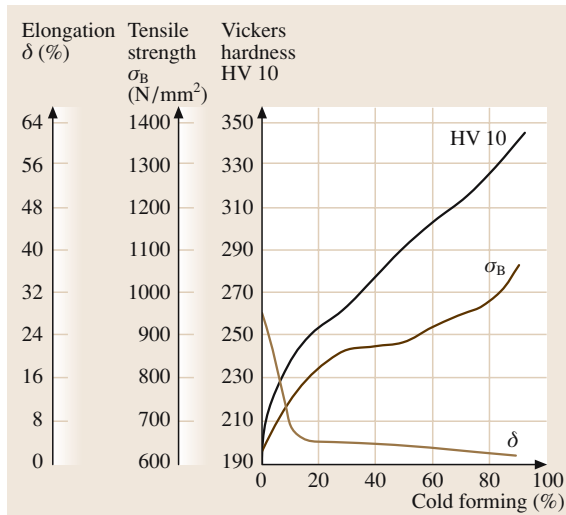


Fig. 3.1-287 Mechanical properties of PtNi8 by cold forming as a function of reduction of cross section [1.231, p. 69]

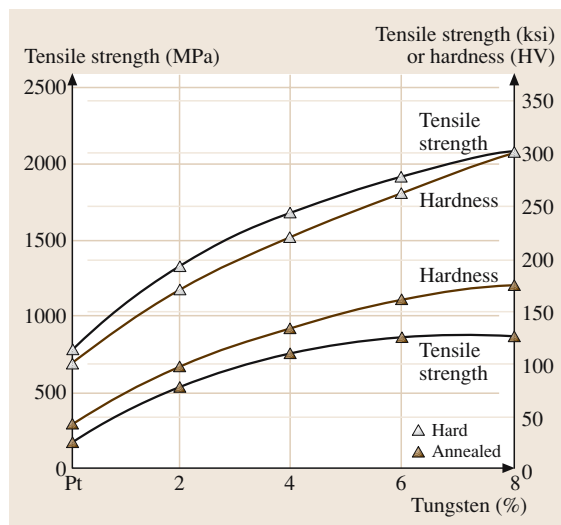


Fig. 3.1-286 Tensile strength of Pt–W alloys as a function of W content [1.228, p. 697]

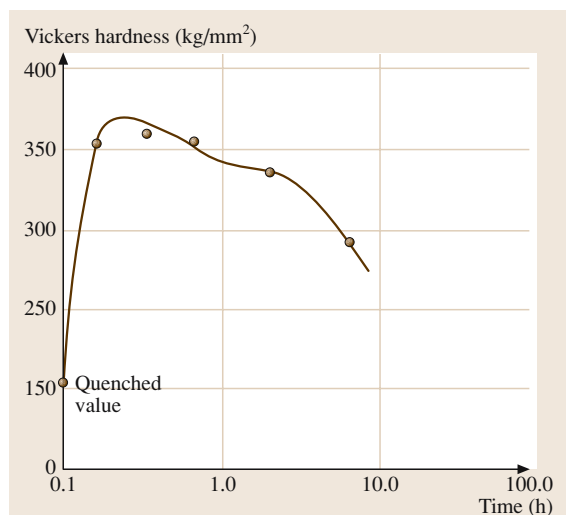


Fig. 3.1-288 Order hardening of stoichiometric CuPt alloy [1.285, p. 49]

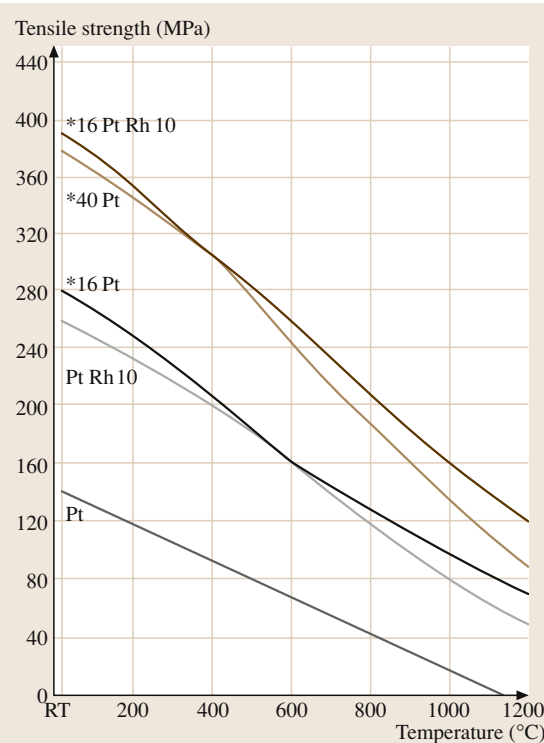


Fig. 3.1-289 Tensile strength of dispersion hardened Pt and PtRh10 (* grain stabilized with 0.16 and 0.40 vol.% ZrO₂, respectively) [1.217, p. 222]

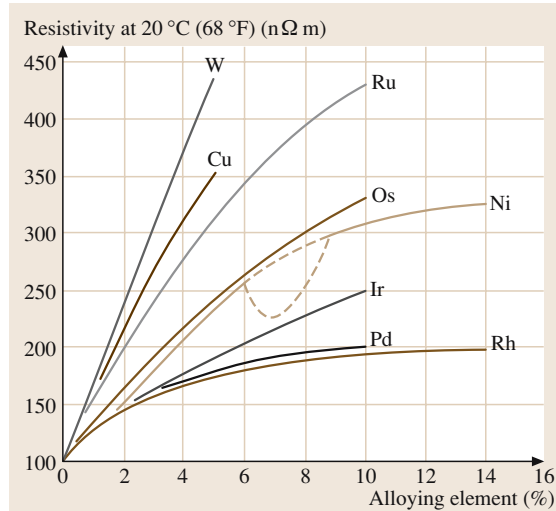


Fig. 3.1-291 Effect of various alloying additions on the electrical resistivity of binary Pt alloys [1.231, p. 67]

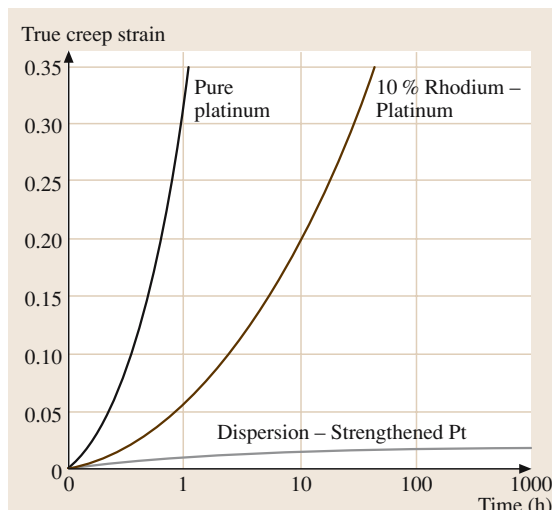


Fig. 3.1-290 Creep curves of TiC-dispersion-strengthened Pt and PtRh wire at 1400 °C in air [1.277]

Electrical Properties. Characteristic data are shown in Tables 3.1-203, 3.1-205, 3.1-227 [1.217], and Figs. 3.1-292–3.1-294 [1.217, 228, 231]. Mo–28 at.% Pt (A15 structure) shows superconductivity at $T_c \approx 4.2\text{--}5.6\text{ K}$ [1.286].

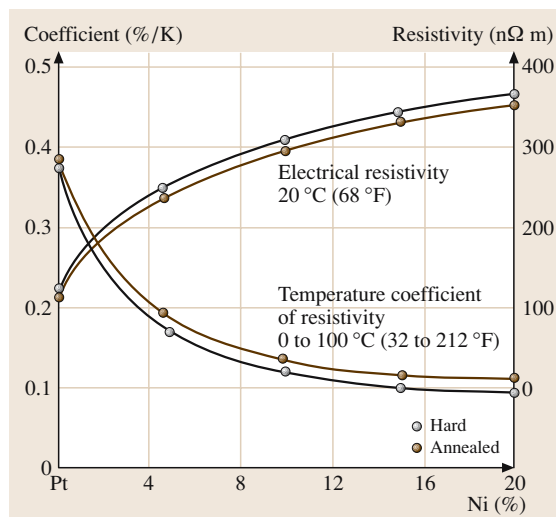
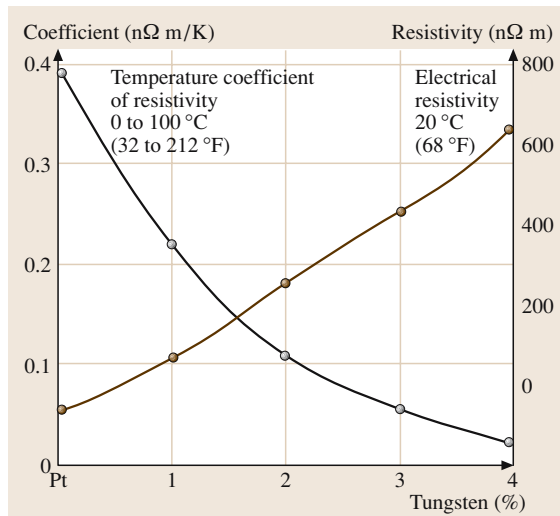


Fig. 3.1-292 Electrical resistivity and temperature coefficient of resistivity (TCR) of Pt–Ni alloys as a function of composition [1.228, p. 696]

Table 3.1-227 Specific electrical resistivity ($\mu\Omega \text{ cm}$) of Pt at temperature (K) [1.217, p. 157]

| $T \text{ (K)}$ | 10 | 50 | 120 | 273 | 673 | 1273 | 1673 |
|-------------------------------|--------|-------|-------|------|-------|-------|-------|
| $\rho \text{ (\mu\Omega cm)}$ | 0.0029 | 0.719 | 3.565 | 9.83 | 24.57 | 37.45 | 53.35 |

**Fig. 3.1-293** Electrical resistivity and temperature coefficient of resistivity (TCR) of Pt–W alloys as a function of composition [1.228, p. 697]

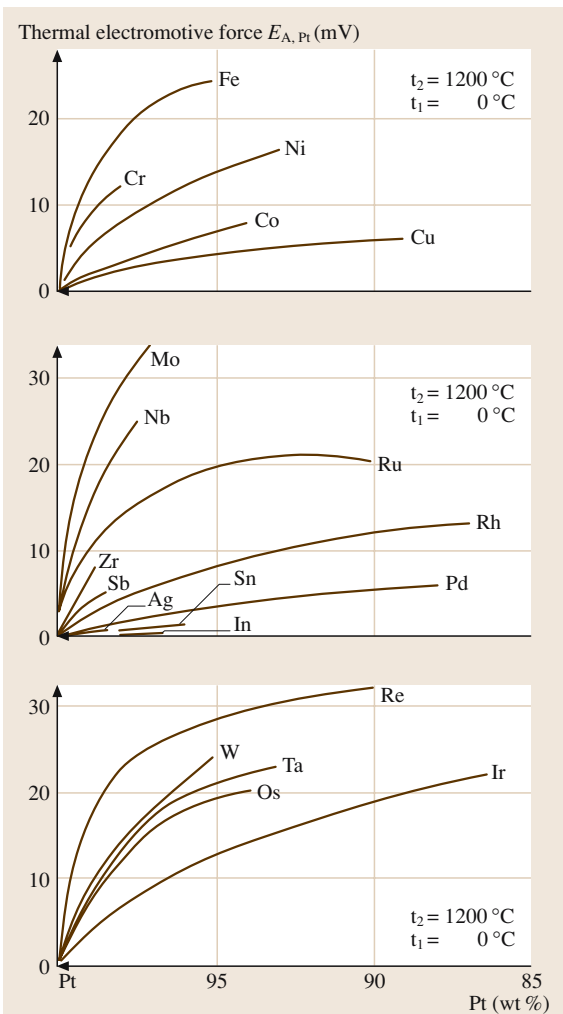
Thermoelectric Properties. Selected values of thermal electromotive force of Pt and Pt alloys are given in Tables 3.1-206, 3.1-207, 3.1-228–3.1-231 [1.216, 217, 222], and Fig. 3.1-295 [1.216]. Thermocouples that are Pt–Rh-based are especially suited for high temperatures (see Fig. 3.1-296).

Table 3.1-228 Pt–Rh thermocouples according IEC 5845 (see Fig. 3.1-296) [1.217, p. 472]

| Class | Alloy | Maximum applicable temperature (°C) |
|---------|----------------|-------------------------------------|
| Type R: | PtRh(87/13)–Pt | 1500–1600 |
| Type S: | PtRh(90/10)–Pt | 1500–1600 |
| Type B: | PtRh(70/30)–Pt | 1750–1800 |

Table 3.1-229 Absolute thermoelectric power of Pt [1.222, p. 1009]

| Temperature (K) | 300 | 400 | 500 | 600 | 700 | 800 | 900 | 1000 | 1100 | 1200 |
|--|-------|-------|-------|--------|--------|--------|--------|--------|--------|--------|
| Thermoelectric power ($\mu\text{V/K}$) | -5.05 | -7.66 | -9.69 | -11.33 | -12.87 | -14.38 | -15.97 | -17.58 | -19.03 | -20.56 |

**Fig. 3.1-294** Thermal electromotive force of binary Pt alloys [1.216, p. 97]

| Alloy const. | T (°C) | Composition (wt% Ir) | | | | | |
|--------------|----------|----------------------|------|------|------|------|------|
| | | 10 | 30 | 40 | 70 | 80 | 90 |
| Ag | 100 | | | | -0.4 | -0.1 | 0.2 |
| | 900 | | | | 6.8 | 4.0 | 4.5 |
| Au | 100 | | | | | 0.8 | 0.4 |
| | 900 | | | | | 11.9 | 13.5 |
| Ir | 100 | 1.3 | 1.2 | | | | |
| | 1000 | 15.7 | 19.1 | 19.4 | | | |
| Rh | 100 | 0.64 | 0.62 | 0.60 | | | |
| | 1000 | 9.57 | 12.3 | 13.3 | | | |
| | 1300 | 13.1 | 17.9 | 19.0 | | | |

Table 3.1-230 Thermal electromotive force of Pt alloys (mV) at different temperatures, reference junction at 0 °C [1.217, p. 160]

Table 3.1-231 Basic values of thermal electromotive force (mV) of common PGM-based thermocouples [1.216, p. 100]

| T_1 (°C) | T_2 (°C) | Pt – Rh10/Pt | Pt – Rh20/Pt – Rh5 | Rh – Ir60 | Pt-el ^b | Pd-or ^c |
|------------|------------|----------------------------|-----------------------------|-----------|--------------------|--------------------|
| 0 | 100 | 0.643 | 0.074 | 0.371 | 3.31 | 4.6 |
| | 500 | 4.221 | 1.447 | 2.562 | 20.20 | 27.9 |
| | 1000 | 9.570 | 4.921 | 5.495 | 41.65 | 59.6 |
| T_1 (K) | T_2 (K) | Au – Co2.1/Cu ^d | Au – Fe0.02/Cu ^d | | | |
| 4.2 | 10 | 0.044 | 0.093 | | | |
| | 20 | 0.173 | 0.208 | | | |
| | 40 | 0.590 | 0.423 | | | |

^b Pt-el = Platinel, Pd83Pt14Au3/AuPd35

^c Pd-or = Pallador, PtIr10/AuPd40

^d at. %

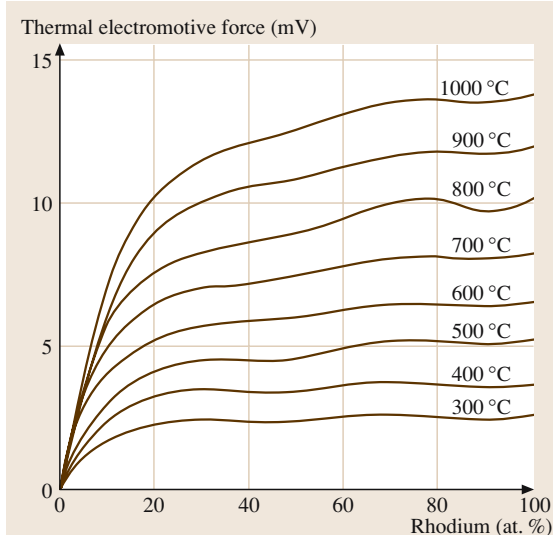


Fig. 3.1-295 Influence of the Rh content on the thermal emf of Pt–Rh alloys against Pt [1.217, p. 473]

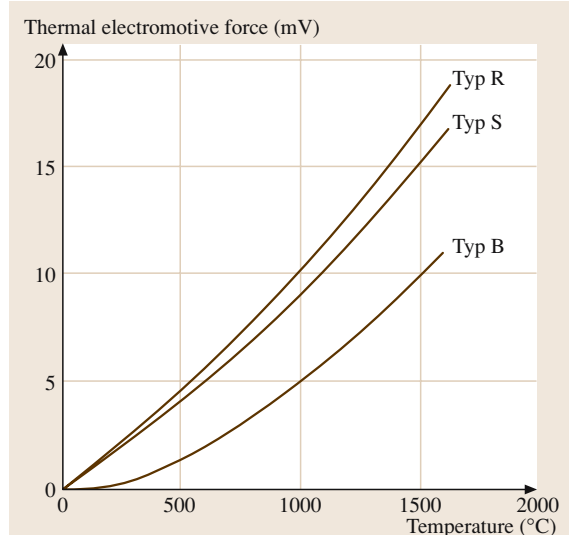


Fig. 3.1-296 Thermal electromotive force of Pt–Rh thermocouples according to IEC 5845 (Type R: PtRh(87/13)–Pt; type S: PtRh(90/10)–Pt; type B: PtRh(70/30)–PtRh(94/6)) [1.217, p. 473]

Magnetic Properties. Selected data are shown in Tables 3.1-211, 3.1-232 [1.217, 222], and Figs. 3.1-297 [1.220] and 3.1-298. The paramagnetic susceptibility of Pt ($25.2 \times 10^{-10} \text{ m}^3 \text{ mol}^{-1}$ at 0 K) rises by alloying with 0.1 at.% Rh to $42.5 \times 10^{-10} \text{ m}^3 \text{ mol}^{-1}$. CoPt is a hard magnetic material ($H_c = 3500\text{--}4700 \text{ Oe}$) but has been replaced by rare-earth transition metal magnetic materials in recent years. Superlattice phases in PtCr-alloys in the composition ranges of 17–65 wt% Cr are ferromagnetic, with the maximum of T_c at ~30 at.% Cr. The superlattice structure in FePt and CoPt with tetragonal crystal symmetry gives rise to high values of magnetic anisotropy. The coercivity of sputtered Pt–Co multilayers is increased by annealing in air, caused by the formation of cobalt oxide at the grain boundaries. The

Table 3.1-232 Characteristic properties of technical permanent magnet alloys [1.222, p. 1053]

| Alloy (wt%) | H_{\max} (kJ/m ³) | H_c (kA/m) | B_r (T) |
|-------------------------|---------------------------------|--------------|-----------|
| Pt77Co23 | 75.0 | 380 | 0.60 |
| Sm34Co66 | 110–160 | 560 | 0.80 |
| Co52Fe35V ₁₃ | 22.4 | 36 | 1.00 |

B = magnetic flux density, H = magnetic field,

B_r = Remanence

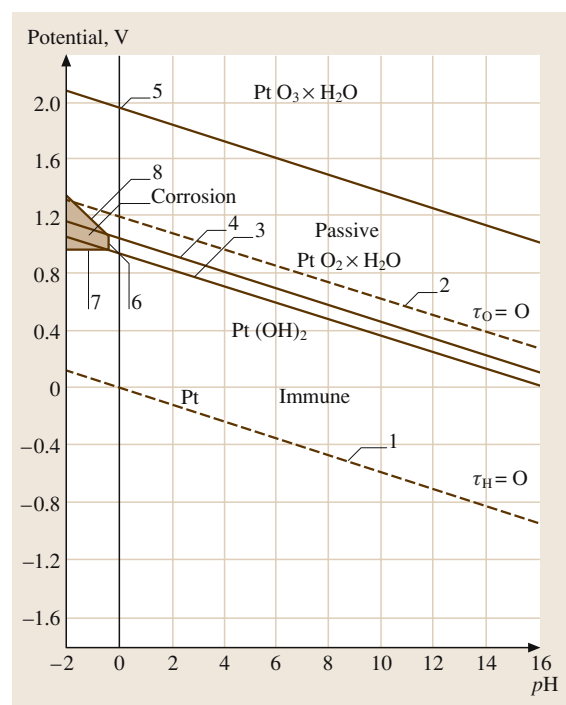


Fig. 3.1-298 Potential pH-diagram of the system Pt/H₂O at 25 °C (see Table 3.1-232) [1.217, p. 201]

oxide layer gives rise to domain pinning and to magnetic isolation of the grains, thus leading to a high perpendicular anisotropy [1.217].

Table 3.1-233 Thermal conductivity λ of Pt–(Au, Rh, Ir) alloys (W/m K) [1.217, p. 153]

| PtAu5 | PtRh5 | PtRh10 | PtRh20 | PtIr5 | PtIr10 |
|-------|-----------------|--------|-----------------|-------|--------|
| 43 | 33 ^a | 30 | 28 ^a | 42 | 31 |

^a = calculated with Wiedemann-Franz' law $\lambda = L\sigma T$, Lorenz number $L = 2.45 \times 10^{-6} \text{ W/K}$ from $\lambda(\text{PtRh10})$ and the specific electrical conductivity of PtRh-alloys

Table 3.1-234 Thermal expansion coefficient α (10^{-6} K^{-1}) of Pt–Rh alloys at different temperature ranges [1.217, p. 155]

| Temperature range (K) Rh-content (wt%) | $\alpha (10^{-6} / \text{K})$ | |
|---|-------------------------------------|--------------------------------------|
| | 273–983 ($10^{-6} / \text{K}$) | 293–1473 ($10^{-6} / \text{K}$) |
| 6 | 10.7 | 11.3 |
| 10 | 10.7 | 11.2 |
| 20 | 10.9 | 11.5 |
| 30 | 10.8 | 11.4 |

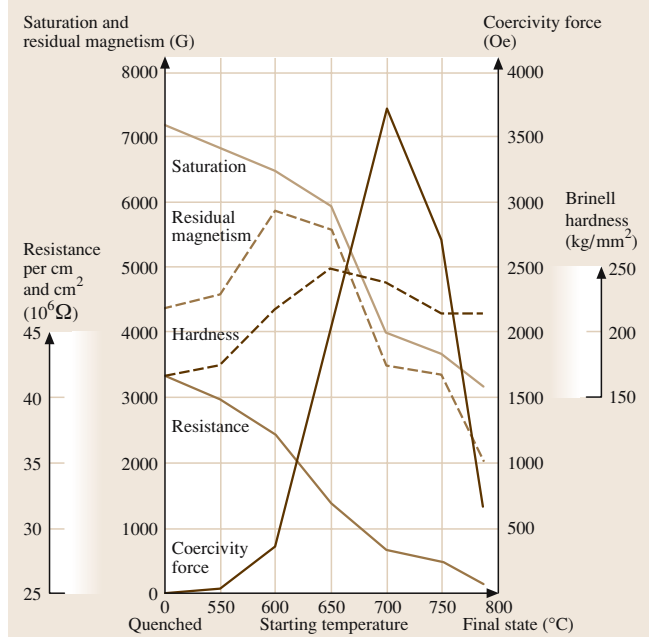


Fig. 3.1-297 Change of magnetic properties of PtCo50 alloy by annealing [1.220, p. 263]

Thermal Properties. Tables 3.1-212–3.1-215, 3.1-233, and 3.1-234 [1.217, 217] provide selected data of thermal conductivity and thermal expansion. In the disordered state the Fe–Pt alloy system exhibits a negative thermal expansion coefficient at room temperature near Fe_3Pt (Invar effect) [1.281, 282].

Optical Properties. Values of the spectral degree of emission and the optical reflectivity are given in Table 3.1-216 [1.217] and Fig. 3.1-275 [1.220].

Diffusion. Data for self-diffusion, diffusion of tracer elements and of hydrogen and oxygen are shown in Tables 3.1-158, 3.1-216, 3.1-217 [1.217].

Chemical Properties. Platinum has the reduction potential of $E_0 = +1.118$ for Pt/Pt^{2+} . It is resistant against reducing acids in all pH ranges, but is attacked by alkali and oxidizing media. Alloying with 30 at.% Rh improves the corrosion resistance against alkali hydroxides. Figure 3.1-298 and Table 3.1-235 [1.217] give the potential pH diagram of the system Pt/H₂O at 25 °C. Dry Chlorine attacks with rising temperature (Fig. 3.1-299 [1.217]). Detailed information about chemical behavior is given in [1.217].

Platinum reacts with ZrC to form Pt_3Zr . It also reacts in the presence of hydrogen with ZrO_2 , Al_2O_3 , and rare earth oxides at temperatures between 1200 and 1500 °C [1.283, 284]. The solubility of oxygen in platinum is very low. Thin coatings of Pt on reactive materials are an effective protection against oxidation. Alloying of Pt with 2 wt% or higher Al improves the oxidation resistance up to 1400 °C by forming protective dense oxide coatings [1.287]. Superalloys that are Pt–Al-based have high compression strength at high temperatures. Third alloying elements (e.g., Ru) stabilize the high-temperature phase down to room temperature and affects solid-solution strengthening [1.288].

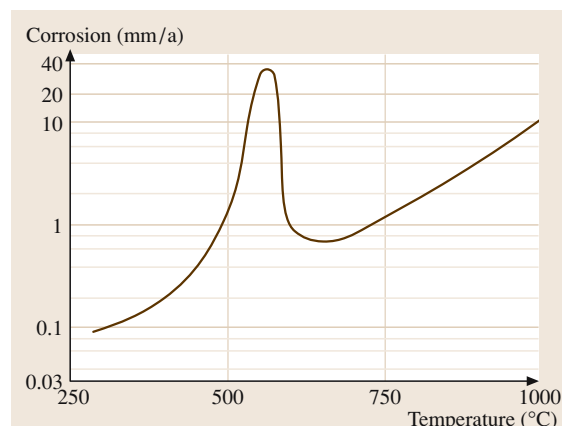


Fig. 3.1-299 Corrosion of Pt in dry Cl_2 gas [1.217, p. 186]

Catalysis. Platinum and Pt alloys are preferably applied in heterogeneous catalysis as wire nets or powders with a high specific surface area ranging from 20 to 1000 m²/g (“platinum black,” “palladium black”) on carbon or Al_2O_3 supports. The catalytic effectiveness is structure-sensitive. Figure 3.1-300 show an example of the catalytic action of Pt for the reaction rate and the product selectivity on different crystal planes [1.218]. Pt–Pd–Rh alloys are the main active constituents of catalytic converters for automobile exhaust gas cleaning.

Special Alloys. Molybdenum clad with Pt serves as glass handling equipment up to 1200 °C. Binary Pt alloys with Cu(4), Co(5), W(5), and Ir(10) at.%; and ternary alloys of Pt–Pd–Cu and Pt–Pd–Co are standard jewelry alloys. Alloys of Pt–Au and Pt–Au–Rh surpass the strength of pure Pt at 1000 °C and resist wetting of molten glass. The materials PtIr₃, PtAu₅ are suitable for laboratory crucibles and electrodes with high mechanical stability.

| Number | Reaction equation | Potential E_0 (V) |
|--------|--|--|
| 1 | $2\text{H}^+ + 2\text{e}^- \rightarrow \text{H}_2$ | 0.000 – 0.0591 $p\text{H}$ |
| 2 | $2\text{H}_2\text{O} \rightarrow \text{O}_2 + 4\text{H}^+ + 4\text{e}^-$ | 1.228 – 0.0591 $p\text{H}$ |
| 3 | $\text{Pt} + 2\text{H}_2\text{O} \rightarrow \text{Pt}(\text{OH})_2 + 2\text{H}^+ + 2\text{e}^-$ | 0.980 – 0.0591 $p\text{H}$ |
| 4 | $\text{Pt}(\text{OH})_2 \rightarrow \text{PtO}_2 + 2\text{H}^+ + 2\text{e}^-$ | 1.045 – 0.0591 $p\text{H}$ |
| 5 | $\text{PtO}_2 + \text{H}_2\text{O} \rightarrow \text{PtO}_3 + 2\text{H}^+ + 2\text{e}^-$ | 2.000 – 0.0591 $p\text{H}$ |
| 6 | $\text{Pt} + \text{H}_2\text{O} \rightarrow \text{PtO} + 2\text{H}^+$ | $\log[\text{Pt}^{++}] = -7.06 - 2p\text{H}$ |
| 7 | $\text{Pt} \rightarrow \text{Pt}^{++} + 2\text{e}^-$ | 1.188 + 0.0259 $\log[\text{Pt}^{++}]$ |
| 8 | $\text{Pt}^{++} + 2\text{H}_2\text{O} \rightarrow \text{PtO}_2 + 4\text{H}^+ + 2\text{e}^-$ | 0.837 – 0.1182 $p\text{H} - 0.0259 \log[\text{Pt}^{++}]$ |

Table 3.1-235 Reaction and potentials corresponding to graphs of Fig. 3.1-298 [1.217, p. 200]

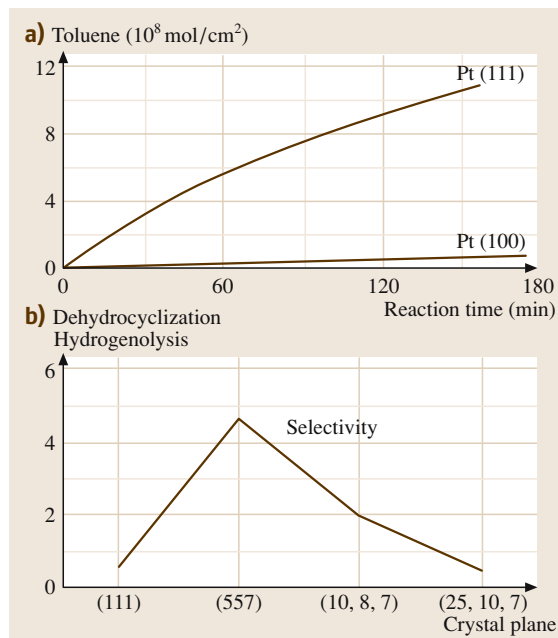


Fig. 3.1-300 (a) Rate of reaction of n-heptane dehydrocyclization to toluol on Pt(111) and Pt(100). **(b)** Variation of selectivity at different crystal planes [1.218, p. 279]

3.1.10.4 Rhodium, Iridium, Rhutenum, Osmium, and their Alloys

Rhodium and Rhodium Alloys

Applications. Rhodium is an essential component of catalysts in numerous chemical reactions and automobile exhaust-gas cleaning. In heterogeneous catalysis it is applied in alloyed form, in homogeneous catalysis as complex organic compounds. Rhodium is an alloy component of corrosion- and wear-resistant tools in the glass industry and a constituent in platinum-group-metal-based thermocouples. Rhodium coatings on silverware and mirrors protect them against corrosion. Commercial grades available are powder, shot, foil, rod, plate, and wires with purity from 98–99.5% (ASTM B 616-78; reappraised 1983).

Production. Rhodium is produced as powder and sponge by chemical reduction or thermal decomposition of the chloro–ammonia complex $(\text{NH}_4)_3[\text{RhCl}_6]$. Bars, rods, and wires are produced by powder compacting and extrusion, while coatings are produced galvanically, by evaporation or by sputtering.

Phases and Phase Equilibria. Selected phase diagrams of Rh are shown in Fig. 3.1-301a–c. Rhodium forms continuous solid solutions with Fe, Co, Ni, Ir, Pd, and Pt. Miscibility gaps exist in alloys with Fe, Co, Ni, Cu, Ag, Au, Pd, Pt, Ru, and Os. Thermodynamic data are given in Table 3.1-236 (see also

Table 3.1-236 Thermodynamic data of Rh [1.217, p. 110]

| T (K) | c_p (J/K mol) | S (J/K mol) | H (J/mol) | G (J/mol) | p (atm.) |
|--------|-----------------|-------------|-----------|-----------|------------------------|
| 298.15 | 24.978 | 31.506 | 0 | -9.393 | 1.43×10^{-89} |
| 400 | 26.044 | 38.993 | 2.598 | -13 | 6.59×10^{-65} |
| 800 | 39.155 | 58.333 | 13.853 | -32.813 | 7.21×10^{-29} |
| 1400 | 35.195 | 76.556 | 33.532 | -73.646 | 1.71×10^{-13} |

T = Temperature, c_p = specific heat capacity, S = Entropy, H = Enthalpy, G = free Enthalpy,

p = partial pressure of the pure elements

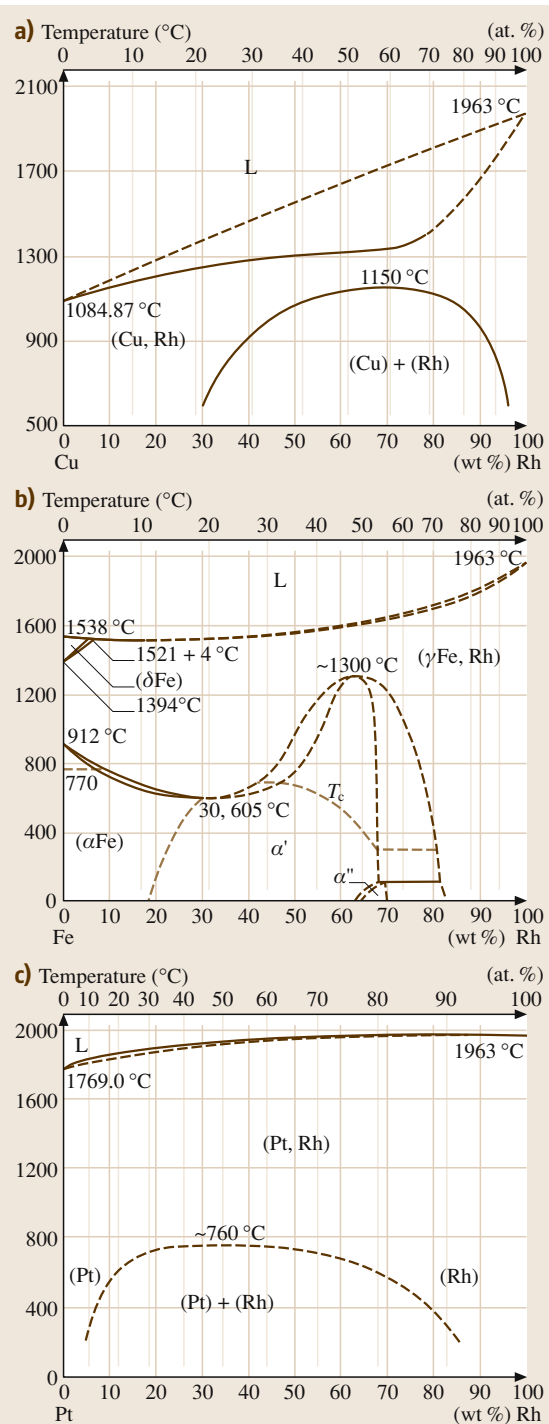


Fig. 3.1-301a–c Phase diagrams of Rh alloys with (a) Cu, (b) Fe, and (c) Pt [1.216, p. 101, 104]

Table 3.1-190) and the maximum hydrogen inclusion is listed in Table 3.1-194.

The compositions and crystal structures of intermediate compounds are shown in Table 3.1-237 (see Table 3.1-197 for superlattice structures).

Mechanical Properties. Characteristic mechanical data of Rh are given in Tables 3.1-238–3.1-241 and Figs. 3.1-302–3.1-307. The modulus of rigidity $G = 153$ GPa; Poisson's ratio is 0.26; the elastic constants are $c_0 = 413$, $c_{12} = 194$, and $c_{44} = 184$.

Rhodium is very hard but can be deformed at temperatures above 200 °C. For strong hardening by deformations, repeated annealing is needed at temperatures higher than 1000 °C. Rh is an effective hardener in Pd and Pt alloys.

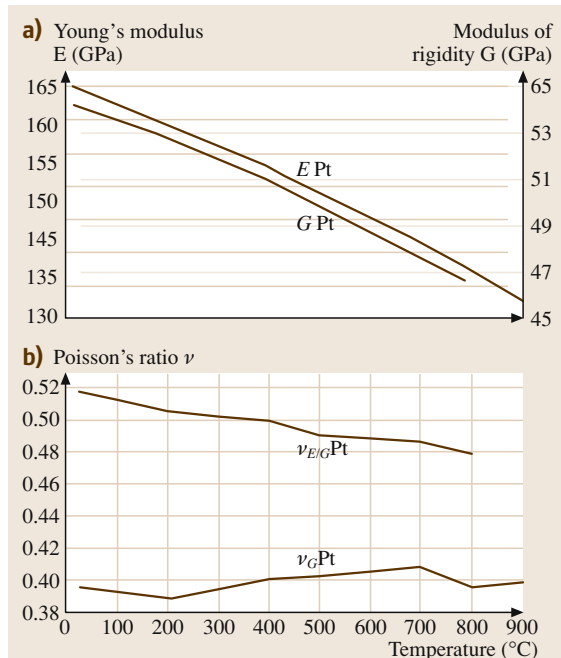


Fig. 3.1-302 (a) Young's modulus E (GPa) and modulus of rigidity G (GPa) of Pt at different temperatures. (b) Poisson's ratio for Pt at different temperatures [1.289, p. 76]

Table 3.1-237 Structure and lattice parameter of selected Rh compounds [1.217, p. 117ff.]

| Phase | Pearson symbol | <i>a</i> (nm) | <i>b</i> (nm) | <i>c</i> (nm) | Concentration x A(1- x)B(x) |
|-------|----------------|---------------|---------------|---------------|--------------------------------------|
| Cu–Rh | cF4 | 0.3727 | | | 0.5 |
| Fe–Rh | cI2 | 0.288885 | | | |
| Fe–Rh | cF4 | 0.374 | | | 0.5 |
| FeRh | cP2 | 0.2998 | | | |
| Fe–Ru | hP2 | 0.258 | | 0.414 | 0.2 |
| Ni–Rh | cF4 | 0.36845 | | | 0.494 |

Table 3.1-238 Mechanical properties of Rh (99%) at different temperatures [1.217, p. 227]

| <i>T</i> (°C) | <i>E</i> (GPa) | <i>R_m</i> (MPa) | <i>A</i> (%) | <i>R_{p0.2}</i> (MPa) | HV |
|---------------|----------------|----------------------------|--------------|-------------------------------|-----------|
| 20 | 386 | 420 | 9 | 70 | 130 |
| 500 | 336 | 370 | 19 | 80 | 91 |
| 700 | 315 | 340 | 16 | 40 | 73 |
| 1000 | — | 120 | 10 | 30 | 52 |

A = elongation of rupture, *E* = modulus of elasticity, *R_p* = limit of proportionality, HV = Vickers hardness, *R_m* = tensile strength

Table 3.1-239 Increase of Rh hardness by cold forming [1.217, p. 227]

| V (%) | HV |
|--------------|-----------|
| 0 | 130 |
| 10 | 275 |
| 30 | 50 |
| 50 | 400 |

Table 3.1-241 Hardness of Rh–Ni alloys at 300 K [1.217, p. 228]

| Alloy | HV 5 |
|--------|-------------|
| RhNi27 | 275 |
| RhNi40 | 220 |
| RhPd20 | 178 |
| RhPt20 | 165 |

Table 3.1-240 Hardness of Pd/Rh and Pt/Rh alloys as a function of composition [1.217, p. 218]

| 2nd metal | HV 5 Content (mass %) | | | | |
|-----------|---------------------------------|-----|-----|-----|-----|
| | 0 | 20 | 40 | 60 | 80 |
| Pd | 130 | 178 | 235 | 229 | 138 |
| Pt | 130 | 165 | 164 | 145 | 123 |

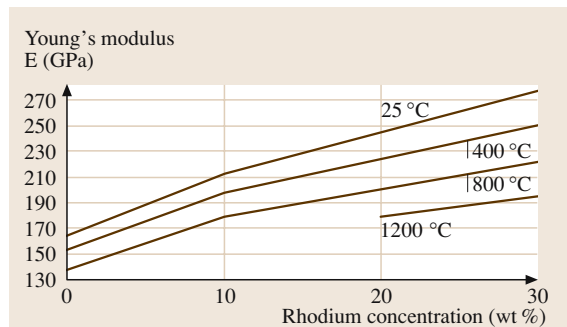
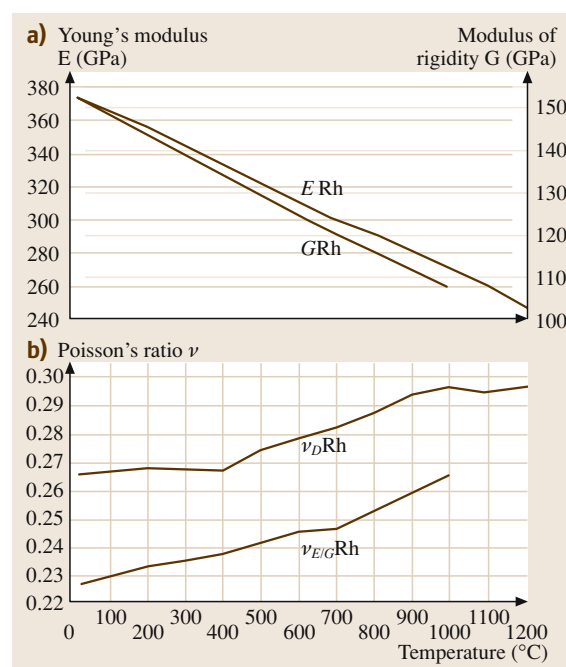
**Fig. 3.1-303** Young's modulus of as cast Pt/Rh-alloys at various temperatures [1.289, p. 80]

Fig. 3.1-305 Vickers hardness of Pt/Rh-10 as a function of reduction (%) and various annealing temperatures [1.218, p. 608]

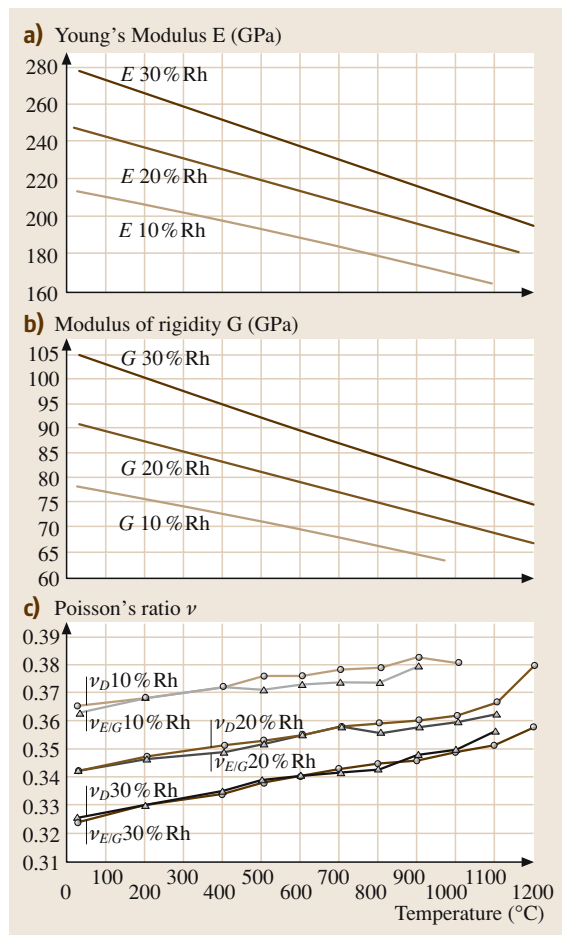
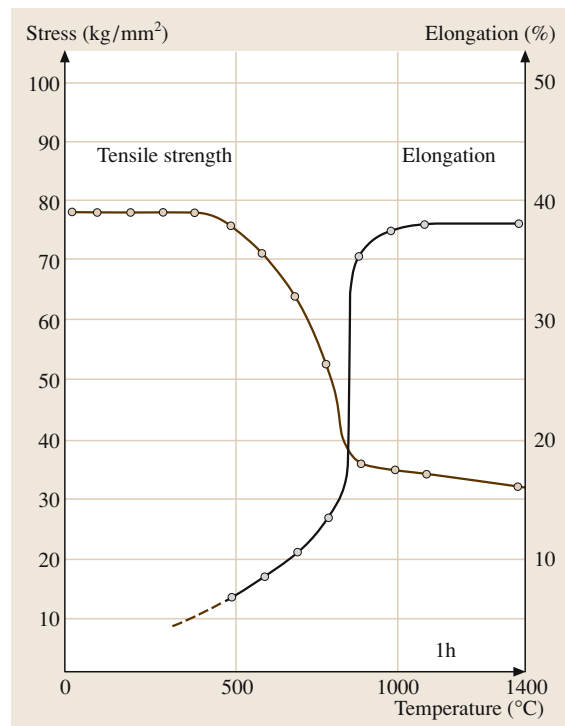
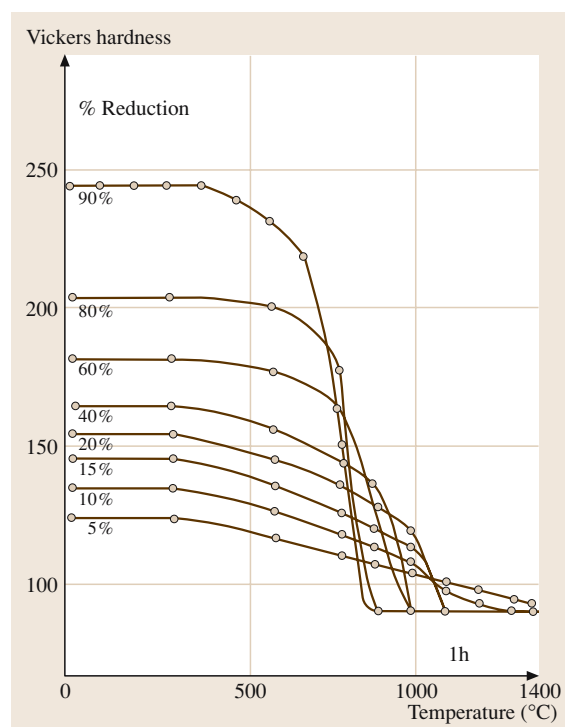


Fig. 3.1-306 (a) Young's modulus E (GPa) of Pt/Rh-10, Pt/Rh-20 and Pt/Rh-30 alloys at different temperatures. (b) Modulus of rigidity G (GPa) of Pt/Rh-10, Pt/Rh-20 and Pt/Rh-30 alloys at different temperatures. (c) Poisson's ratio of Pt/Rh 10, Pt/Rh 20 and Pt/Rh-30 alloys at different temperatures [1.289, p. 79]

◀ **Fig. 3.1-304** (a) Young's modulus E (GPa) and the modulus of rigidity G (GPa) of forged Rh at different temperatures. (b) Poissons ratio for forged Rh at different temperatures [1.289, p. 77]

Fig. 3.1-307 Mechanical properties of Pt/Rh-10 alloy [1.218, p. 609]



Electrical Properties. Characteristic electrical properties are given in Tables 3.1-242 and 3.1-243 (see also Table 3.1-203). Rhodium shows superconductivity below 0.9 K [1.216]. Superconducting Rh alloys are shown in Table 3.1-244. Among the three-element alloys containing precious metals there exists a special group known as magnetic superconductors [1.218]. Figure 3.1-308 shows as example the alloy ErRh₄B₄ with the coexistence of superconductivity and magnetic order changing in the region below the critical temperature of beginning superconductivity [1.218]. Data for light and thermoelectric emission are given in Table 3.1-245 [1.290].

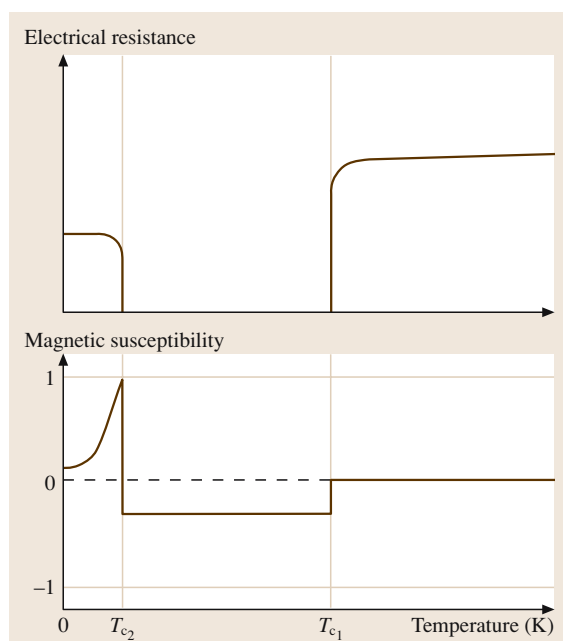


Fig. 3.1-308 Coexistence of superconductivity and magnetic order in ErRh₄B₄ [1.218, p. 637]

Table 3.1-242 Increase of atomic resistivity $\Delta\rho/C$ of Rh [1.217, p. 158]

| Base element | $\Delta\rho/C$ ($\mu\Omega \text{ cm}/\text{at.\%}$) |
|--------------|--|
| Rh | Co 0.34, Cr 4, Fe 0.6, Mn 1.4 |

Table 3.1-243 Specific electric resistivity $\rho_i(T)$ ($\mu\Omega \text{ cm}$) of Rh at temperature T ($\rho_0 = 0.0084$) [1.217, p. 156]

| T (K) | 25 | 70 | 160 | 273 | 500 | 1250 | 1750 |
|-------------|--------|------|------|-----|------|------|------|
| $\rho_i(T)$ | 0.0049 | 0.34 | 2.12 | 4.3 | 9.20 | 26.7 | 40.9 |

Table 3.1-244 Superconducting Pd, Pt, and Rh alloys [1.218, p. 636]

| Pd, Pt Compound | T_c (K) | Rh Compound | T_c (K) |
|----------------------|-----------|----------------------------------|-----------|
| PtNb ₃ | 10.6 | Rh ₂ P | 1.3 |
| Pd _{1.1} Te | 4.07 | Rh ₄ P ₃ | 2.5 |
| PdTe _{1.02} | 2.56 | ErRh ₄ B ₄ | 8.5 |
| PdTe ₂ | 1.69 | | |

Table 3.1-245 Light and thermoelectric emission of Rh, Pd, and Pt [1.220, p. 79]

| Metal | Light-electric constants Wavelength limit (Å) | Work function (V) | Temperature (°C) | Thermoelectric work function (V) |
|-------|--|-------------------|------------------|----------------------------------|
| Rh | 2500 | 4.57 | 20 | 4.58 (at 1550° abs.) |
| | 2700 | — | 240 | |
| Pd | 2490 | 4.96 | RT | 4.99 (at 1550° abs.) |
| Pt | 1962 | 6.30 | RT | 6.37 (at 1550° abs.) |

Thermoelectrical Properties. Tables 3.1-206 and 3.1-207 give data for the absolute thermoelectric power; Tables 3.1-246 and 3.1-247 give the thermal electromotive force of Rh and of Rh/Ir alloys at different temperatures. Rh is also used as a component in Pt-based thermocouples (Tables 3.1-230–3.1-228, Fig. 3.1-295).

Magnetical Properties. Data of the magnetic susceptibility of Rh and Rh alloys are given in Figs. 3.1-271, 3.1-272, and 3.1-309–3.1-312. For magnetostriction data see Table 3.1-211. The superlattice alloy FeRh shows a transition from the antiferro- to the ferromagnetic state near room temperature Fig. 3.1-312 [1.218] where small additions of Pd, Pt, Ir, Ru, or Os enhance this effect.

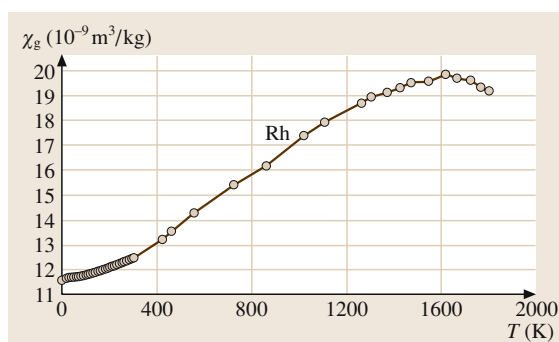


Fig. 3.1-309 Temperature dependence of the mass susceptibility of Rh [1.217, p. 163]

Table 3.1-246 Thermal electromotive force of Rh at different temperatures [1.217, p. 159]

| T (°C) | -200 | -100 | +100 | +400 | +800 | +1000 | +1300 |
|--------------------|-------|-------|-------|-------|--------|--------|--------|
| E _{Rh/Pt} | -0.23 | -0.32 | +0.70 | +3.92 | +10.16 | +14.05 | +20.34 |

Table 3.1-247 Thermal electromotive force of Rh/Ir alloys at different temperatures [1.217, p. 160]

| T (°C) | Composition (wt% Ir) | | | | | |
|--------|----------------------|-------|-------|-------|-------|-------|
| | 10 | 30 | 50 | 70 | 90 | |
| 1000 | | 15.15 | 17.40 | 18.40 | 17.75 | 15.45 |

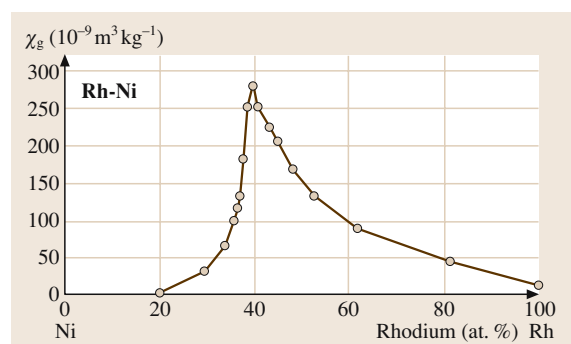


Fig. 3.1-310 Mass susceptibility of Rh–Ni alloys as a function of alloy composition at 4.2 K [1.217, p. 166]

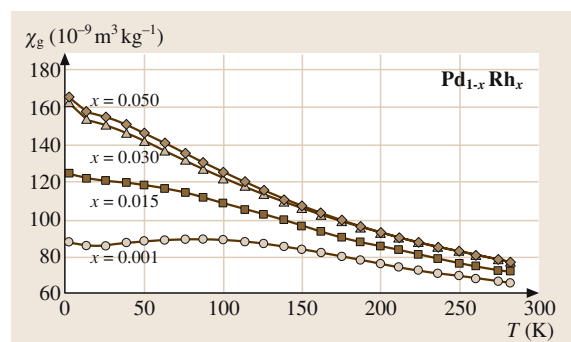


Fig. 3.1-311 Mass susceptibility of Pd–Rh alloys as a function of alloy composition [1.217, p. 169]

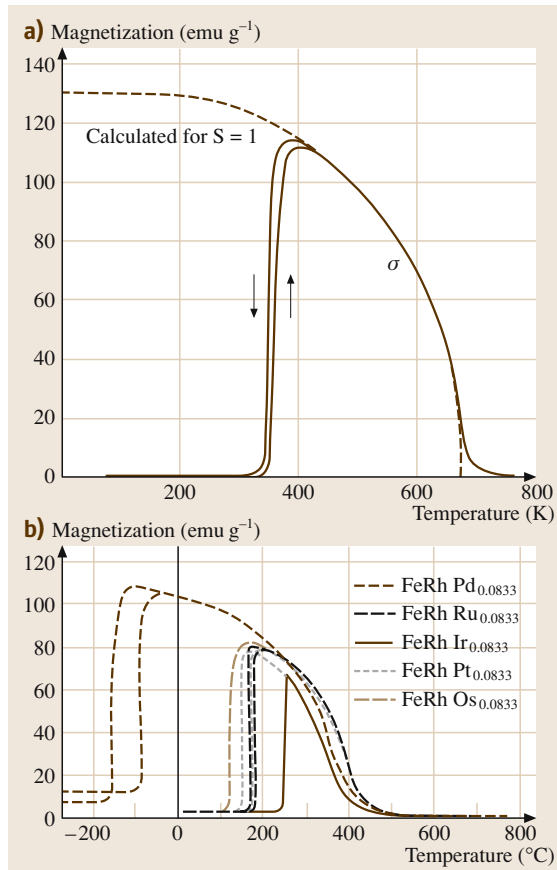


Fig. 3.1-312a,b Metamagnetic behavior of (a) FeRh superlattice alloy [1.218, p. 102]. (b) Variation by addition of small amounts of Pd, Ru, Ir, Pt, Os [1.218, p. 102]

Thermal Properties. Tables 3.1-212–3.1-214 show the recrystallization temperature, thermal conductivity and thermal expansion at different temperatures. Vapor pressure at different temperatures is shown in Fig. 3.1-273.

Optical Properties. Rhodium has the highest optical reflectivity of all platinum-group metals (Fig. 3.1-274), ranging about 20% below the reflectivity of Ag. It is used as hard and corrosion-resistant coating on silver jewelry and for optical reflectors. Data of the spectral emissivity are given in Table 3.1-216.

Diffusion. Data for self-diffusion are given in Table 3.1-217 (see [1.216] for further data).

Chemical Properties. Rhodium is not attacked by acids or alkali even under oxidizing conditions (aqua regia) (Fig. 3.1-313). Sodium hypochlorite attacks in the order of increasing strength: Pt = Rh = Ir = Ru < Pd < Os. Heating in air causes the formation of thin oxide layers above 600°C which decompose above 1100°C (Fig. 3.1-314). Pt alloys with 5–40 wt% Rh are corrosion-resistant against H₂F₂. A detailed survey about these chemical properties is given in [1.216].

Rhodium is the effective component of the three-way Pt/Pd/Rh alloy autocatalyst for the reduction of

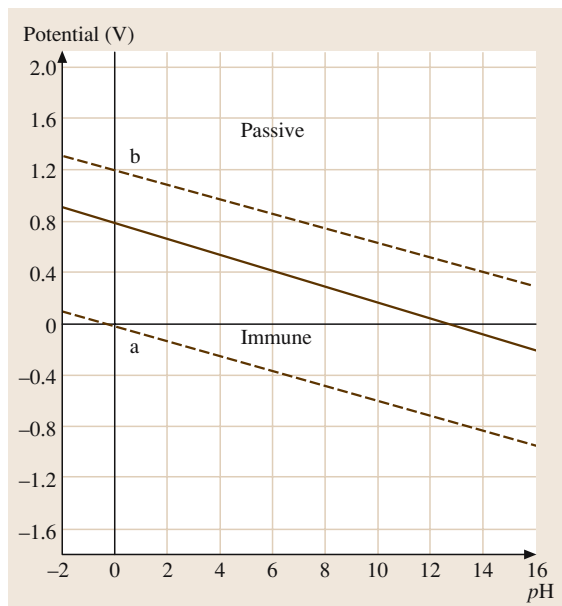


Fig. 3.1-313 Potential pH diagram for the system Rh-H₂O [1.217, p. 202]

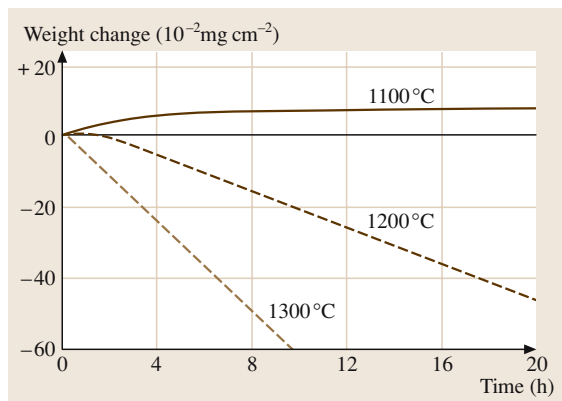


Fig. 3.1-314 Weight change of Rh in oxygen [1.217, p. 185]

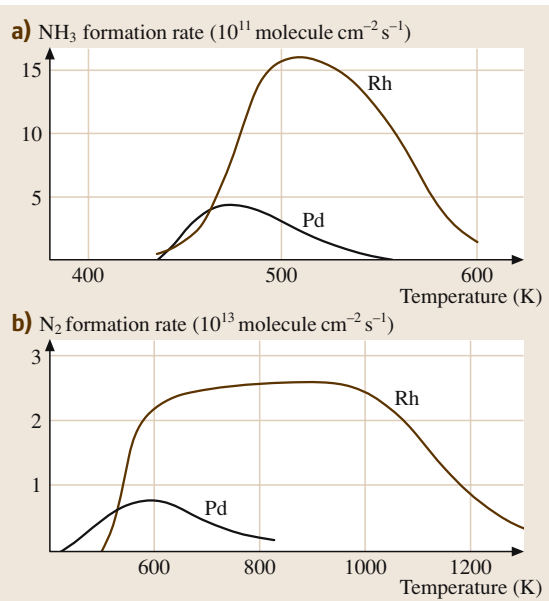


Fig. 3.1-315a,b Product formation rates in $\text{N} = \text{-H}_2$ reactions on Pd- and Rh-catalyst foils. (a) NH_3 formation rates $p(\text{NO}) = 9.4 \times 10^{-5}$ Pa, $p(\text{H}_2) = 4.9 \times 10^{-5}$ Pa. (b) N_2 formation rates $p(\text{NO}) = 1.1 \times 10^{-5}$ Pa, $p(\text{H}_2) = 1.9 \times 10^{-5}$ Pa [1.218, p. 287]

NO_x of exhaustion gases (Figs. 3.1-315a,b). Rh catalysts surpass the group homolog, Co-based catalysts, with lower reaction pressures and temperatures and higher yields [1.216]. Complex organic rhodium compounds on the basis of RhCl (PPH_3) with different substituent ligands are important homogeneous catalysts in the technical production processes for hydrogenation and hydroformylation (“oxo”-processes, e.g., synthesis

of aldehydes and acetic acid). Replacement of PPH_3 by complex chiral phosphane ligands enables the synthesis of asymmetric compounds, e.g., L-DOPA and L-menthol (Fig. 3.1-316a,b) [1.291].

Iridium and Iridium Alloys

Applications. Iridium is used for crucibles to grow high-purity crystals for lasers, medical scanners etc., anodes to prevent corrosion of shipping vessels and under-water structures, coatings of electrodes for the manufacturing of chlorine and caustic soda, as an alloy component of automotive exhaust catalysts, and as alloy component and compounds of chemical process catalysts for the production of acetic acid and complex organic compounds. Iridium is an effective hardener for materials used at high temperature, high wear, and high corrosion conditions (e.g., spark plugs). It is also used as fine-grain forming addition in jewelry and dental gold alloys. Commercial grades available are powder, shot, ingot, and wire in a purity ranging from 98–99.9% (ASTM 671-81, reappraised 1987).

Production. Iridium is produced as powder and sponge by chemical reduction or thermal decomposition of the chloro-ammonia compound $(\text{NH}_4)_2[\text{IrCl}_6]$. Bars, rods, ingot, and wires are produced by compacting of powder followed by extrusion. Coatings are produced galvanically, by evaporation, or by sputtering.

Phases and Phase Equilibria. Figures 3.1-317–3.1-319 [1.216] show the binary phase diagrams of Ir alloys with Pt, Rh, and Ru. Miscibility gaps exist in the solid state also in the alloy systems with Cu, Os, Re, and Ru. Iridium alloyed in Fe lowers the α – λ transition temperature consider-

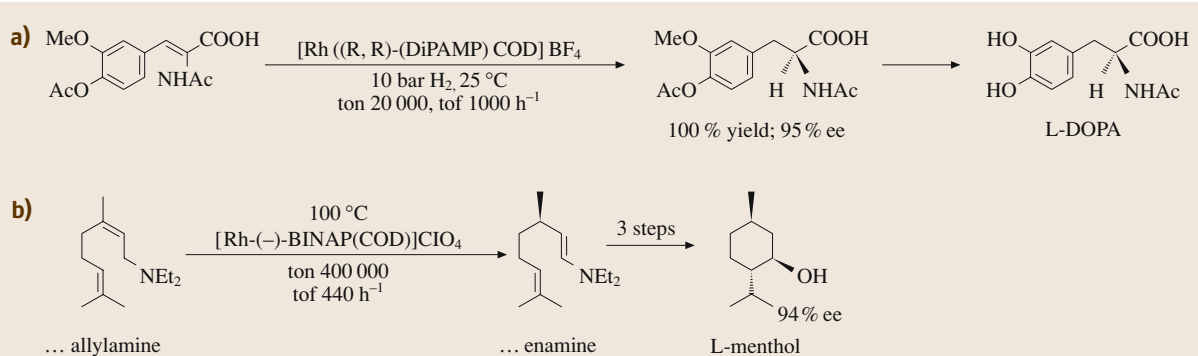


Fig. 3.1-316a,b Examples of organic synthesis of chiral compounds catalysed by complex Rh compounds. (a) L-DOPA. (b) L-menthol [1.291, p. 83]

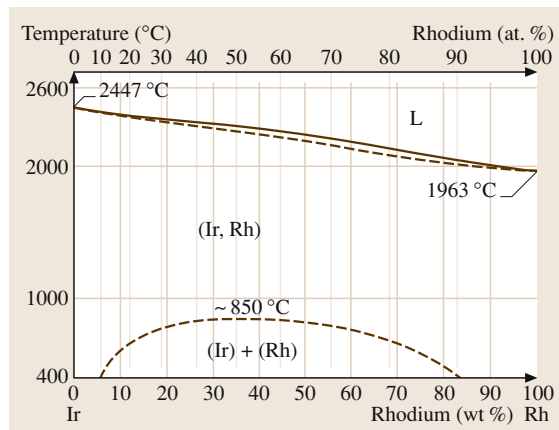
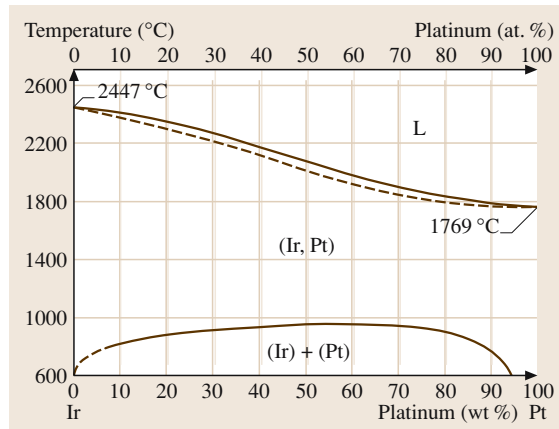


Table 3.1-248 Thermodynamic data of Ir [1.217, p. 109]

| T (K) | c_p (J/K mol) | S (J/K mol) | H (J/mol) | G (J/mol) | p (atm) |
|--------|-----------------|-------------|-----------|-----------|------------------------|
| 298.15 | 24.979 | 35.505 | 0 | -10.586 | |
| 400 | 25.695 | 42.946 | 2.581 | -14.598 | 6.70×10^{-80} |
| 800 | 28.51 | 61.62 | 13.442 | -35.875 | 2.81×10^{-36} |
| 1400 | 32.733 | 78.647 | 31.795 | -78.311 | 1.15×10^{-17} |

T = Temperature, c_p = specific heat capacity, S = Entropy, H = Enthalpy, G = free Enthalpy,
 p = partial pressure of the pure elements

Fig. 3.1-317 Phase diagram of Ir-Pt [1.217, p. 88]

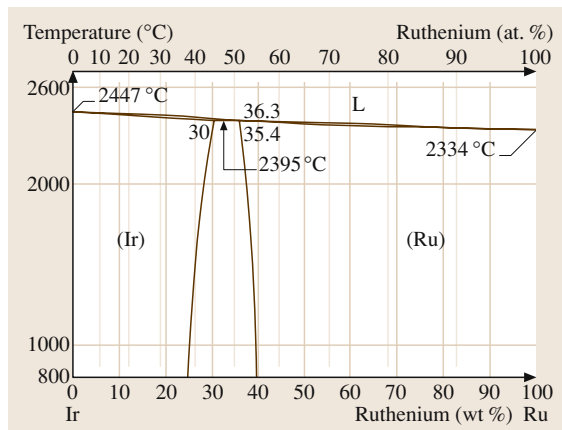


Fig. 3.1-319 Phase diagram of Ir-Ru [1.217, p. 89]

ably (Fig. 3.1-343). Thermodynamic data are given in Table 3.1-248 [1.216].

Structure and lattice parameters of selected intermediate compounds are given in Table 3.1-249 [1.216].

Fig. 3.1-318 Phase diagram of Ir-Rh [1.217, p. 89]

Table 3.1-249 Structure and lattice parameter of intermediate compounds [1.217, p. 117ff.]

| Phase | Pearson symbol | a (nm) | b (nm) | c (nm) | Concentration x A(1 - x)B(x) |
|-------|----------------|----------|----------|----------|---------------------------------------|
| Cu-Ir | cF4 | 0.3629 | | | |
| Ir-Os | hP2 | 0.27361 | | 0.43417 | 0.65 |
| Ir-Os | cF4 | 0.38358 | | | 0.2 |
| Ir-Rh | cF4 | 0.3824 | | | 0.5 |
| Ir-Ru | hP2 | 0.2718 | | 0.4331 | 0.56 |
| Ir-Ru | cF4 | 0.3818 | | | 0.47 |

HT = high temperature modification, LT = low temperature modification

Mechanical Properties. Iridium is extremely hard and can only be deformed at temperatures above 600 °C, with repeated annealing steps at temperatures higher than 1200 °C. The Young's modulus is different for different crystal directions (Table 3.1-250) [1.216], the modulus of rigidity is 214 GPa, and the Poisson's ratio amounts to 0.26.

Characteristic data of mechanical properties of Ir and Pt/Ir alloys are given in Tables 3.1-251–3.1-253 [1.216] and Figs. 3.1-320–3.1-322 [1.289]. Two-phase Ir-based refractory superalloys with fcc and L₁₂ structure of the components (Ir–12Zr and Ir–17Nb, Ir–15Nb–5Ni) have resist temperatures up to 1200 °C and exhibit marked creep resistance (Figs. 3.1-323–3.1-325) [1.292, 293].

Table 3.1-250 Modulus of elasticity in crystal direction [1.217, p. 212]

| $E \langle 110 \rangle$ | $E \langle 111 \rangle$ |
|-------------------------|-------------------------|
| 47.4 GPa | 662 GPa |

Table 3.1-251 Elastic constants of Ir [1.217, p. 212]

$$T = 300 \text{ K} \quad c_{11} = 580 \quad c_{12} = 242 \quad c_{44} = 256$$

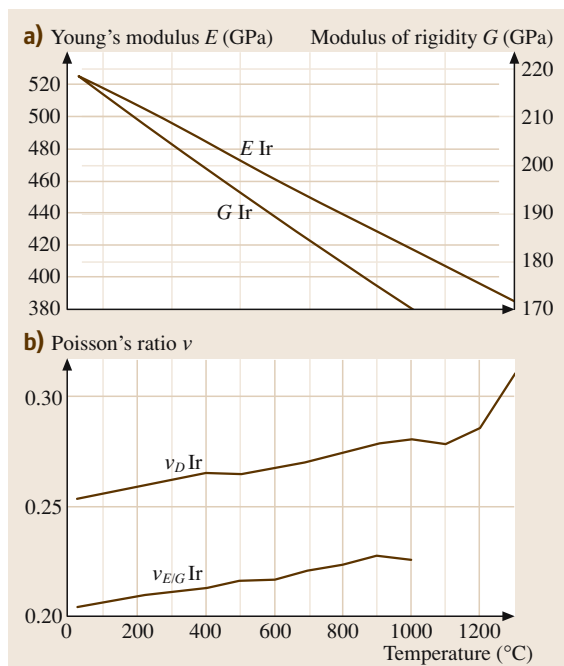


Fig. 3.1-320 (a) Young's modulus of Ir at different temperatures. (b) Poisson's ratio for as cast Ir at different temperatures [1.289]

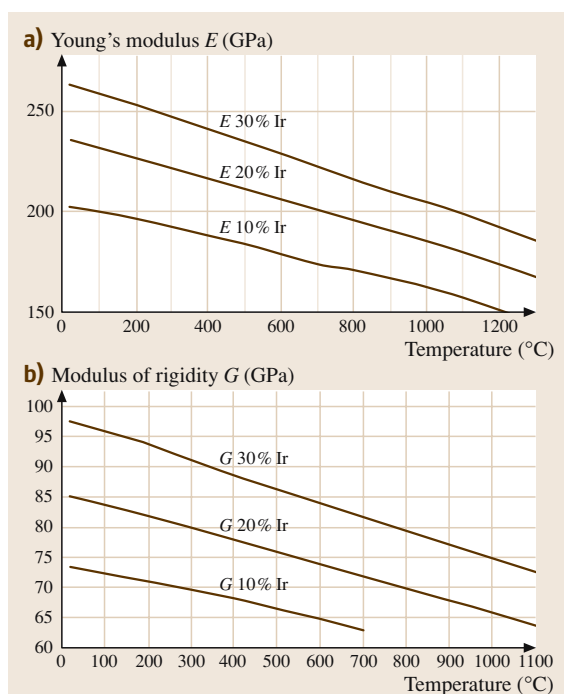


Fig. 3.1-321 (a) Young's modulus of Pt–Ir alloys at different temperatures. (b) Modulus of rigidity of as cast Pt–Ir alloys at different temperatures [1.289]

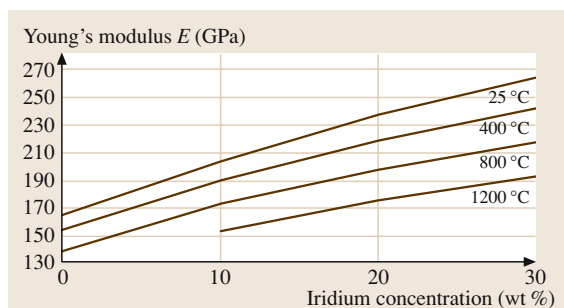


Fig. 3.1-322 Young's modulus of as cast Pt–Ir alloys at different temperatures [1.289]

Table 3.1-252 Mechanical properties of Ir at different temperatures [1.217, p. 213]

| T (°C) | E (GPa) | R_m (MPa) | A (%) | R_{p0.2} (MPa) | HV |
|---------------|----------------|----------------------------|--------------|-------------------------------|-----------|
| 20 | 538 | 623 | 6.8 | 234 | 200 |
| 500 | 488 | 530 | 9 | 12.7 234 | 138 |
| 800 | 456 | 450 | 18 | 51 142 | 112 |
| 1000 | 434 | 331 | — | 80.6 43.4 | 97 |

A = elongation of rupture, *E* = modul of elasticity, *R_p* = limit of proportionality, HV = Vickers hardness, *R_m* = tensile strength

Table 3.1-253 Change of hardness of Ir by degree cold forming V (%) [1.217, p. 312]

| V (%) | HV |
|--------------|-----------|
| 0 | 240 |
| 10 | 425 |
| 20 | 485 |
| 30 | 475 |
| 59 | 590 |

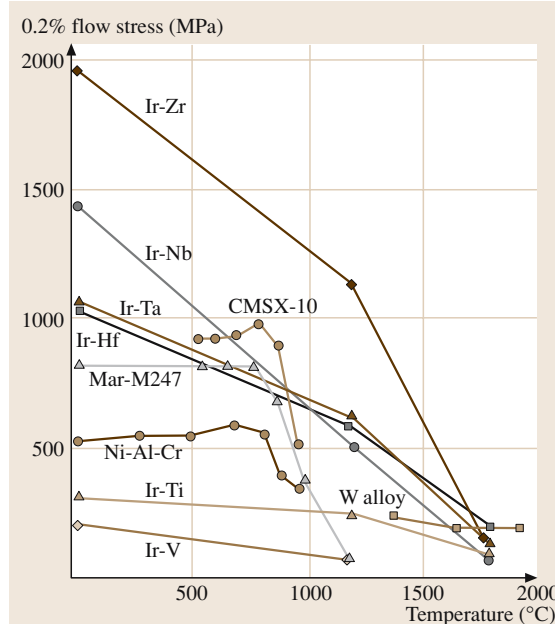
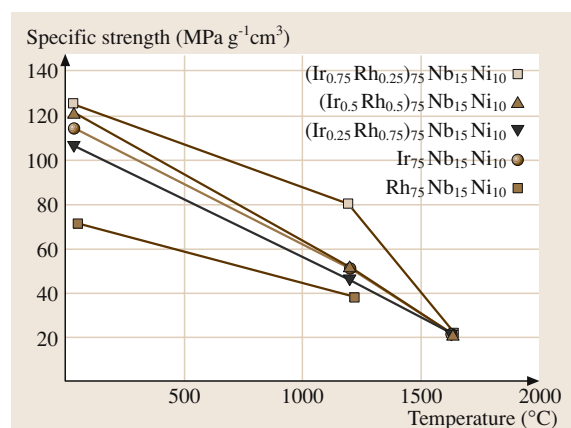
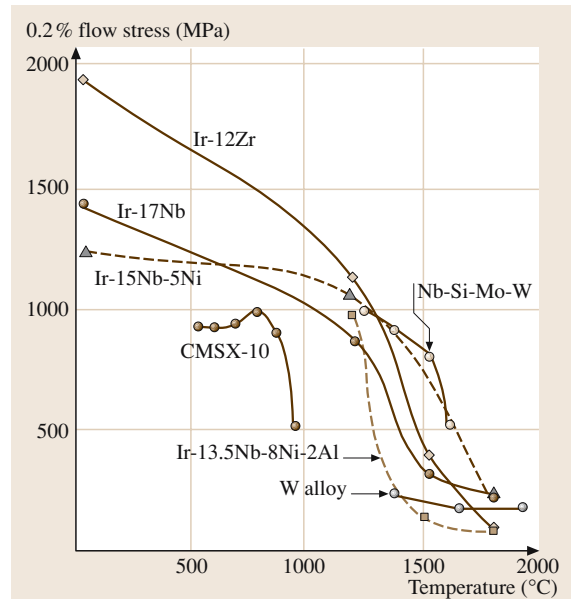
**Fig. 3.1-323** High-temperature compression strength of selected Ir-based alloys [1.292, p. 159]**Fig. 3.1-324** Specific strength of Ir–Rh–Nb alloys [1.293, p. 78]**Fig. 3.1-325** Comparison of compressive strength of Ir alloys versus W and Nb/Mo alloys at various temperatures [1.293, p. 77]

Table 3.1-254 Specific electrical resistivity [$\rho_i(T) = \rho_0 + \rho_i(T)$] of Ir at temperatures T ($\rho_0 = 0.10 \mu\Omega \text{ cm}$) [1.217, p. 157]

| T (K) | 15 | 40 | 140 | 273 | 700 | 1100 | 1500 |
|-------------|--------|------|------|------|-------|-------|-------|
| $\rho_i(T)$ | 0.0013 | 0.10 | 1.96 | 4.65 | 13.90 | 23.20 | 34.02 |

Electrical Properties. The residual resistance ratio (RRR) amounts to 85 (Table 3.1-203). The specific electrical resistivity at different temperatures and the dependence of the atomic resistivity are given in Tables 3.1-254, and 3.1-255 [1.216]. The RRR is listed in Table 3.1-203.

Iridium becomes superconducting below 0.11 K. Some ternary alloys show critical transition temperatures between 3 K and above 8 K (Table 3.1-256) [1.218].

Thermoelectrical Properties. Data for the absolute thermoelectric power and the thermoelectric voltage of Ir, and the thermoelectric voltage of Ir/Rh alloys are shown in Tables 3.1-206–3.1-208, 3.1-257 [1.216] and Fig. 3.1-326 [1.217].

Magnetic Properties. Iridium is paramagnetic. Figures 3.1-271, 3.1-327, 3.1-328 [1.216] show the mass susceptibility of Ir and Pt/Ir alloys at different temperatures. Iridium exhibits magnetostriction according the equation $\Delta l/l = S_l H^2$, with $S_l = +3.8$ (Table 3.1-211).

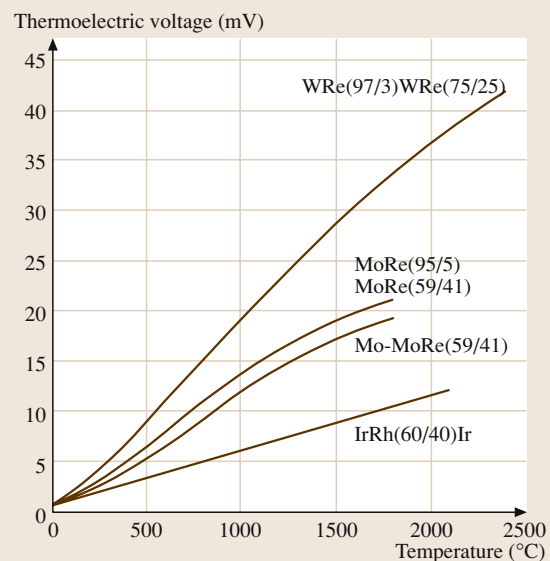


Fig. 3.1-326 Thermoelectric voltage of Ir–Rh alloys compared to Mo–Re and W–Re alloys [1.217, p. 474]

Table 3.1-255 Increase of atomic resistivity [1.217, p. 158]

| Base element | $\Delta\rho/C$ ($\mu\Omega \text{ cm}/\text{at.\%}$) |
|--------------|--|
| Ir | Pt 1.33, Re 2.7, Cr 2, Mo 3.65, W 3, Fe 0.6 |

Table 3.1-256 Superconducting Ir alloys [1.218, p. 636]

| Ir Compound | T_c (K) |
|-------------|-----------|
| IrTe3 | 1.18 |
| Sc5Ir4Si10 | 8.46–8.38 |
| Y5Ir4Si10 | 3.0–2.3 |
| Lu5Ir4Si10 | 3.76–3.72 |

Table 3.1-257 Thermoelectric voltage of Ir at different temperatures [1.216, p. 95]

| T (°C) | -200 | -100 | -50 | +100 | +200 | +400 | +800 |
|--------------------------------|-------|-------|-------|------|-------|-------|-------|
| $E_{\text{Ir},\text{Pt}}$ (mV) | -0.20 | -0.35 | -0.20 | 0.66 | 1.525 | 3.636 | 9.246 |

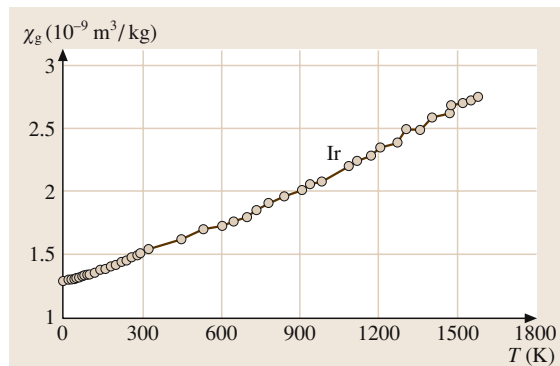


Fig. 3.1-327 Mass susceptibility of Ir at different temperatures [1.217, p. 164]

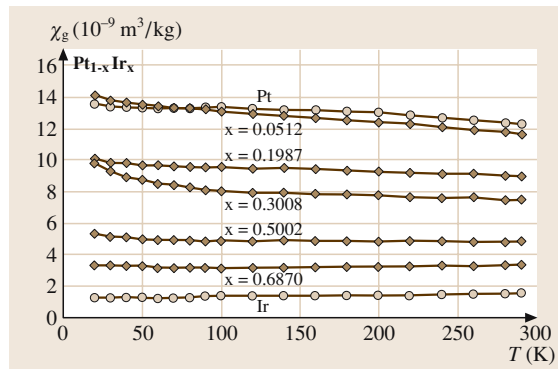


Fig. 3.1-328 Mass susceptibility of Pt–Ir alloys at different temperatures [1.217, p. 68]

Thermal Properties. Tables 3.1-212–3.1-214 give selected data for the recrystallization temperature (varying by purity, degree of cold forming, and annealing time), thermal conductivity, and thermal expansion coefficient.

Optical Properties. The optical reflectivity of Ir is markedly lower than that of Rh increasing in the wavelength range from 0.4 to 0.8 μm (Figs. 3.1-191 and 3.1-274). Data of the spectral emissivity are given in Table 3.1-216.

Diffusion. Table 3.1-217 gives only one value for self diffusion of iridium but further information may be obtained from Landolt–Börnstein [1.238].

Chemical Properties. Iridium is not attacked by acids or alkali even under oxidizing conditions (aqua re-

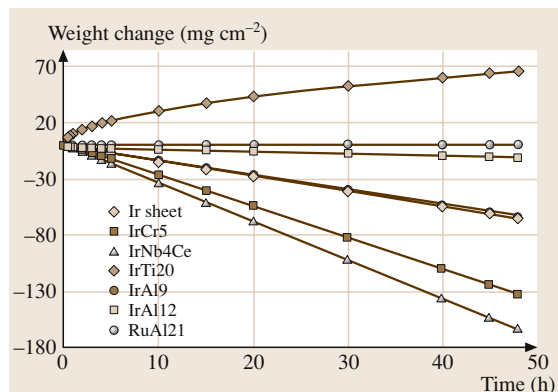


Fig. 3.1-330 Oxidation behavior of various Ir alloys at 1000 °C in air [1.294, p. 100]

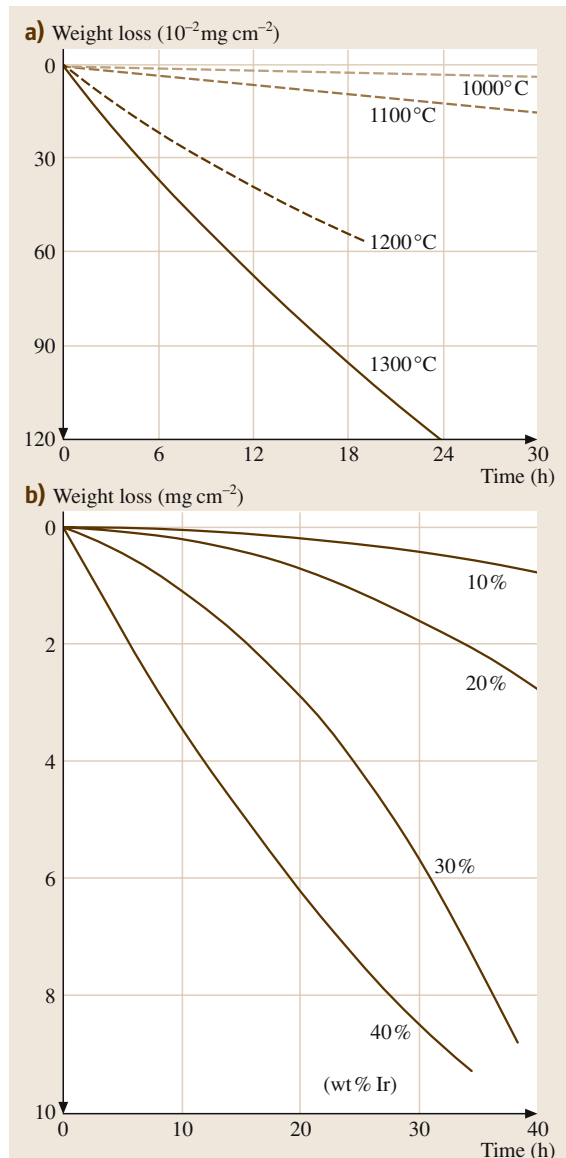


Fig. 3.1-329a,b Evaporation losses. (a) Pt loss in oxygen. (b) Pt–Ir clad loss in oxygen at 900 °C [1.217, p. 184]

gia). It forms volatile oxides in air above 1000 °C but it can be heated up to 2300 °C without danger of catastrophic oxidation. Pt alloys with 1–30 wt% Ir are corrosion-resistant against H_2F_2 . Figures 3.1-329 and 3.1-330 [1.216, 294] show data of the evaporation and oxidation behavior of Ir alloys. A detailed survey on the chemical properties is given in [1.216, 294].

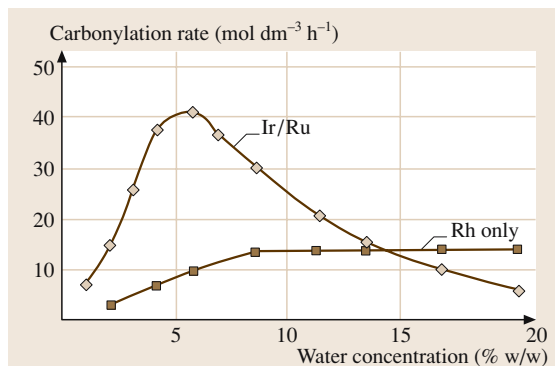


Fig. 3.1-331 Carbonylation rates for Ir–Ru and Rh catalysts in methylacetate reactions [1.295, p. 100]

Metal-organic Ir compounds are effective homogeneous catalysts for organo-chemical reactions such as hydrogenation and carbonylation. The technical production of acetic acid (“Cativa” process). Figure 3.1-331 shows an example for different carbonylation rates of Rh- and Ir/Ru-based catalysts [1.295]. Complex organic Ir catalysts have high stereoselectivity in hydrating cyclic alcohols [1.216].

Ruthenium and Ruthenium Alloys

Applications. Ruthenium is a component of alloys and compounds of chemical process catalysts, and Pt-based catalysts for proton-exchange fuel cells (PEFC). Because of its corrosion resistance, it is used for corrosion-preventing anodes in shipping vessels and under-water structures, pipelines, in geothermal industries, and as coating of electrodes in chlorine and caustic soda production. Ruthenium oxide (RuO_2) and complex Bi/Ba/Pt oxides are materials for electrical resistors. Ruthenium layers on computer hard discs are used for high density data storage improvement of data-storage densities. Ruthenium is an effective hardener of Pd and Pt. Commercial grades available are sponge, powder, grains, and pellets in purity ranging from 99–99.95% (ASTM B 717).

Production. Production of ruthenium starts with chemical reduction of chloro compounds to powder, followed by compacting to pellets. Coatings are produced by galvanic processing, evaporation or sputtering.

Phases and Phase Equilibria. Selected phase diagrams are shown in Figs. 3.1-332–3.1-334, thermodynamic data are listed in Table 3.1-258, and molar heat capacities can be found in Table 3.1-190. Ruthenium alloyed

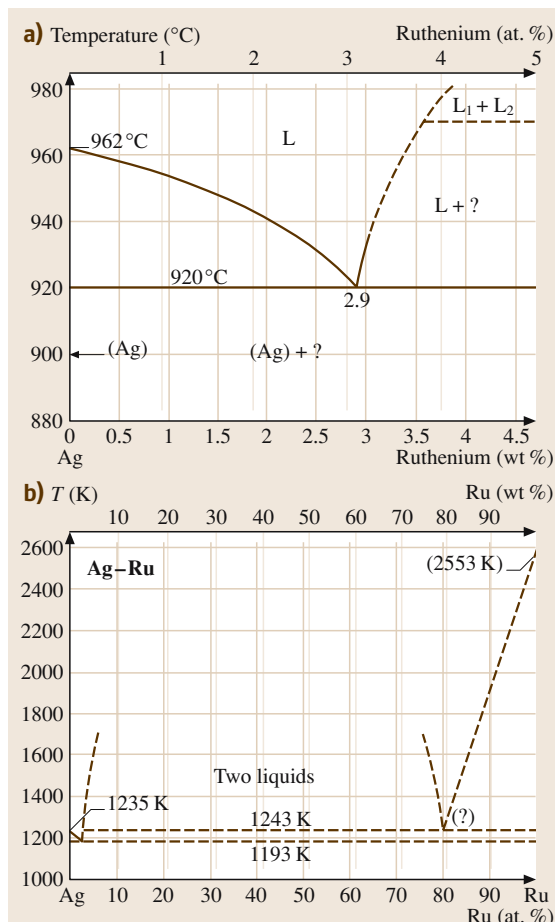


Fig. 3.1-332a,b Phase diagram of Ag–Ru (a) and phase diagram of Ag–Ru in the high-temperature range (b) [1.217, 245]

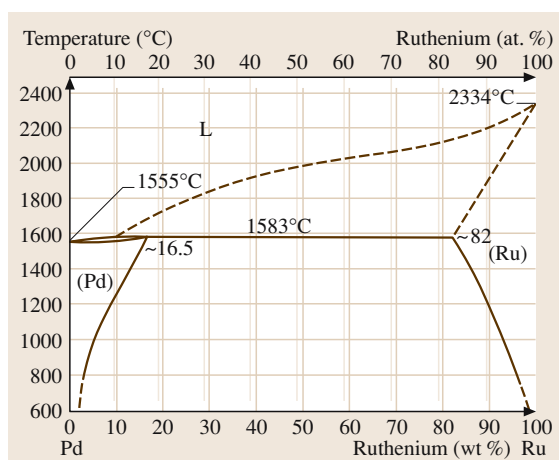
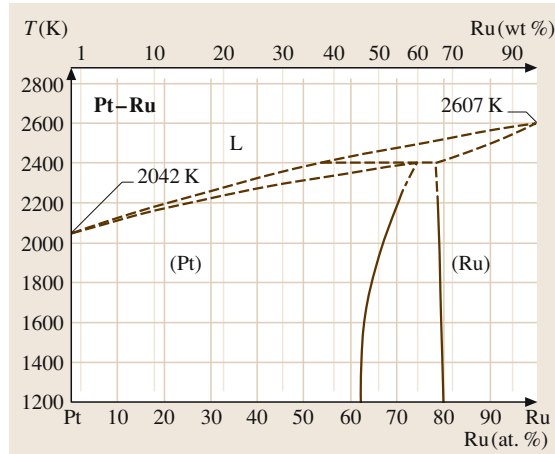


Fig. 3.1-333 Phase diagram of Pd/Ru [1.217]

Table 3.1-258 Thermodynamic data of Ru [1.217, p. 110]

| T (K) | c_p (J/K mol) | S (J/K mol) | H (J/mol) | G (J/mol) | p (at) |
|--------|-----------------|-------------|-----------|-----------|------------------------|
| 298.15 | 23.705 | 28.535 | 0 | -8.508 | |
| 400 | 24.345 | 35.595 | 2.449 | -11.79 | 1.50×10^{-77} |
| 800 | 26.516 | 53.121 | 12.611 | -29.885 | 4.83×10^{-35} |
| 1400 | 30.97 | 69.01 | 29.77 | -66.844 | 7.73×10^{-17} |

T = Temperature, c_p = specific heat capacity, S = Entropy, H = Enthalpy, G = free Enthalpy,
 p = partial pressure of the pure elements

**Fig. 3.1-334** Phase diagram of Pt/Ru [1.245]

to Fe lowers the γ - α transition temperature considerably (Fig. 3.1-343). Table 3.1-259 gives the structure and lattice parameters of intermediate Co and Fe com-

Table 3.1-261 Hardness (HV 5) of Pd/Ru and Pt/Ru alloys at 300 K [1.217, p. 230]

| Alloying metal | HV 5 alloy conc. (wt%) | | | | |
|----------------|------------------------|-----|-----|-----|-----|
| | 0 | 20 | 40 | 60 | 80 |
| Pd | 350 | 412 | 425 | 284 | 243 |
| Pt | 350 | 330 | 446 | 293 | 253 |

pounds. The superlattice structures can be found in Table 3.1-197.

Mechanical Properties. Ruthenium has a Young's modulus of 485 GPa, the Poisson's ratio amounts to 0.29, and the modulus of rigidity is 172 GPa. Characteristic properties of Ru are given in Tables 3.1-260 and 3.1-261. The mechanical properties are marked anisotropic. The hardness of different single crystal faces varies between 100 HV and 250 HV [1.216]. High compression-strength alloys are formed by two-phase Ru-Al intermetallic structures. Figure 3.1-335 gives

Table 3.1-259 Structure and lattice parameter of intermediate compounds [1.217, p. 117ff.]

| Phase | Pearson symbol | a (nm) | b (nm) | c (nm) | Concentration x A(1- x)B(x) |
|-------|----------------|---------|--------|--------|--------------------------------------|
| Co-Ru | hP2 | 0.261 | | 0.4181 | 0.5 |
| Co-Ru | cF4 | 0.3592 | | | 0.2 |
| Fe-Ru | cI2 | 0.2883 | | | 0.06 |
| Fe-Ru | hP2 | 0.258 | | 0.414 | 0.2 |
| Os-Ru | hP2 | 0.27193 | | 0.4394 | 0.5 |

Table 3.1-260 Mechanical properties of Ru at different temperatures [1.217, p. 229], [1.216, p. 31]

| T (°C) | R_m (MPa) | A (%) | $R_{p0.2}$ (MPa) | HV |
|--------|-------------|-------|------------------|----------------------|
| 20 | 500 | 3 | 380 | 250–500 ^a |
| 750 | 300 | 15 | 230 | 160–280 ^b |
| 1000 | 220 (430) | 14 | 190 | 100–200 ^a |

^a at different crystal planes,

^b at 600 °C

A = Elongation of rupture, R_p = Limit of proportionality,

HV = Vickers hardness, R_m = Tensile strength

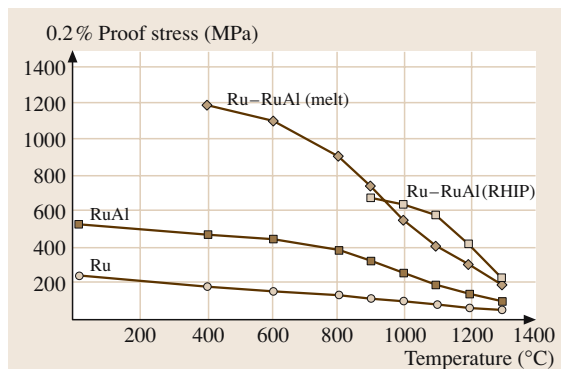


Fig. 3.1-335 High-temperature compression strength of eutectic Ru-70/Al-30 in relation to its constituent phases [1.288, p. 164]

an example of molten and hot isostatic-pressed eutectic Ru (Ru-70/Al-30) in relation to the constituent phases [1.296].

Electrical Properties. The residual resistance ratio (RRR) amounts to 25 000 (Table 3.1-203). Characteristic electrical properties of Ru are given in Tables 3.1-203, 3.1-262, and 3.1-263. The specific electrical resistivity of RuO₂ is $3.5 \times 10^{-5} \Omega \text{ cm}$ ($1 \Omega \text{ cm}$ for PdO for comparison). Together with its low temperature dependence of the coefficient of resistance, Ru is suited for the production of resistors in sintered form or as thick-film layers covering resistors ranging from ≈ 1.5 to $10 \text{ M}\Omega$. Conductive components are either RuO₂, Pb₂Ru₂O₆, or Bi₂Ru₂O₇ together with additions of doping oxides [1.218].

Ruthenium shows superconductivity below 0.47 K [1.218]. Ternary alloys have critical transition temperatures up to 12.7 K (Table 3.1-264).

Thermoelectric Properties. Data of thermoelectric properties of Ru are given in Tables 3.1-206 and 3.1-265.

Table 3.1-262 Specific electrical resistivity $\rho_i(T)$ ($\mu\Omega \text{ cm}$) of Ru at different temperatures ($\rho_0 = 0.016 \mu\Omega \text{ cm}$) $\rho(T) = \rho_0 + \rho_i(T)$ [1.217, p. 156]

| T (K) | 25 | 50 | 100 | 200 | 273 | 300 | 500 |
|-------------|-------|-------|------|------|------|------|------|
| $\rho_i(T)$ | 0.005 | 0.105 | 1.25 | 4.38 | 6.69 | 7.43 | 13.2 |

Table 3.1-265 Thermal electromotive force of Ru at different temperatures [1.217, p. 159]

| T (°C) | +100 | +200 | +300 | +500 | +800 | +1000 | +1200 |
|--------------------|-------|-------|-------|-------|-------|--------|--------|
| $E_{\text{Ru/Pt}}$ | 0.684 | 1.600 | 2.673 | 5.119 | 9.519 | 13.003 | 16.864 |

Magnetic Properties. Figures 3.1-271, 3.1-337, and 3.1-336 present data of the magnetic mass susceptibility of Ru and of Ru/Cr alloy at different temperatures.

Table 3.1-263 Increase of atomic resistivity by alloying ($\Delta\rho/C$ ($\mu\Omega \text{ cm}/\text{at.\%}$)) [1.217, p. 158]

| Base element | $\Delta\rho/C$ ($\mu\Omega \text{ cm}/\text{at.\%}$) |
|--------------|--|
| Ru | Fe 0.21, Re 2, Y 1.5 |
| Os | Y 10 |

Table 3.1-264 Critical transition temperature of superconducting Ru alloys [1.218, p. 636]

| Ru | Composit | T_c (K) |
|------------|----------|-------------|
| TiRuP | | 1.33 |
| ZrRuP | | 12.34–10.56 |
| HrRuP | | 12.70–11.08 |
| TiRuAs | | >0.35 |
| ZrRuAs | | 11.90–1.03 |
| HfRuAs | | 4.93–4.37 |
| Y3Ru4Ge13 | | 1.7–1.4 |
| Lu3Ru4Ge13 | | 2.3–2.2 |

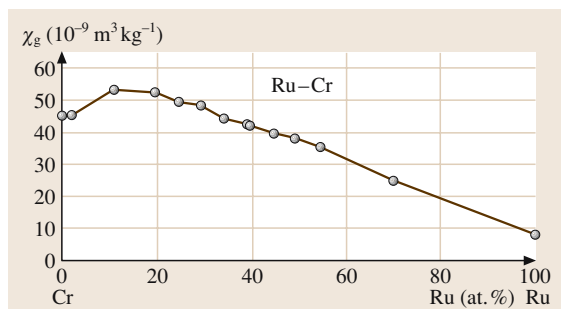


Fig. 3.1-336 Temperature dependence of the mass susceptibility of Ru/Cr alloy [1.217, p. 166]

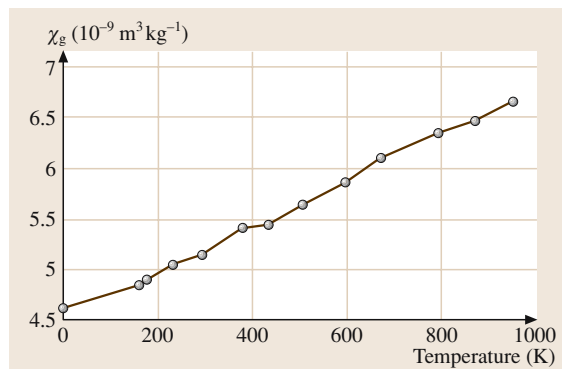


Fig. 3.1-337 Temperature dependence of the mass susceptibility of Ru [1.217, p. 163]

Thermal Properties. Characteristic data of thermal expansion and thermal conductivity are given in Tables 3.1-213 and 3.1-266. Figure 3.1-273 shows the vapor pressure data for Ru.

Optical Properties. The optical reflectivity of Ru is near that of Rh (Fig. 3.1-333). Ruthenium alloyed to Pd enhances the optical reflectivity by 4–5% (Fig. 3.1-275).

Diffusion. Table 3.1-217 gives some values for self diffusion of Ru.

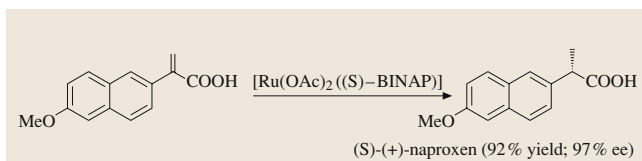


Fig. 3.1-338 Synthesis of (S)-(+)-Naproxen catalysed by Ru-cpxl compound [1.291, p. 83]

Table 3.1-266 Thermal expansion coefficients of Ru and Os at different temperatures [1.217, p. 154]

| Temperature (°C) | (10^{-6} K^{-1}) | | | | | | |
|---------------------|----------------------------|-----------------|-----------------|-----------------|-----------------|-----------------|--|
| | Ru ^a | Ru ^b | Ru ^p | Os ^a | Os ^b | Os ^p | |
| 323 | 5.9 | 8.8 | 6.9 | 4.0 | 5.8 | 4.8 | |
| 423 | 6.1 | 9.3 | 7.2 | 4.3 | 6.2 | 5.0 | |
| 623 | 6.8 | 10.5 | 8.0 | 4.0 | 7.1 | 5.7 | |
| 723 | 7.2 | 11.0 | 8.4 | 5.3 | 7.6 | 6.2 | |
| 823 | 7.6 | 11.7 | 8.8 | 5.8 | 8.3 | 6.9 | |

^a vertical to the crystal *c* axis

^b parallel to the crystal *c* axis

^p polycrystalline

Chemical Properties. Ruthenium is not attacked by acids or alkali even under oxidizing conditions (aqua regia). By heating in air above 800 °C Ru forms the oxides RuO and RuO₂; above 1100 °C Ru forms RuO₃ which vaporizes. Detailed survey about the chemical properties is given in [1.218, 218].

Complex organic Ru compounds are catalysts for the enantioselective hydrogenation of unsaturated carboxylic acids, used in pharmaceutical, agrochemical, flavors and fine chemicals (Fig. 3.1-338) [1.291].

Osmium and Osmium Alloys

Applications. Osmium is used as a component in hard, wear- and corrosion-resistant alloys, as surface coatings of W-based filaments of electric bulbs, cathodes of electron tubes, and thermo-ionic sources. Osmium itself, Os alloys, and Os compounds are strong and selective oxidation catalysts. Commercial grades available are powder in 99.6% and 99.95% purity, OsO₄, and chemical compounds.

Production. The production of Os starts from the mineral osmiridium via soluble compounds and the reduction to metal powder followed by powder-metallurgical compacting.

Phases and Phase Equilibria. Selected phase diagrams are shown in Figs. 3.1-339–3.1-342 [1.216]. Continuous series of solid solution are formed with Re and Ru. Miscibility gaps exist with Ir, Pd and Pt. The solid solubility in the Os–W system are 48.5 at.% for W and ≈ 5 at.% for Os. Osmium alloyed to Fe lowers the γ – α transition temperature considerably (Fig. 3.1-343 [1.297]). Thermodynamic data are given in Table 3.1-267 [1.216] and molar heat capacities in Table 3.1-190. Table 3.1-268 gives structures and lattice parameters of intermediate compounds with Ir, Ru, Pt, and W [1.216].

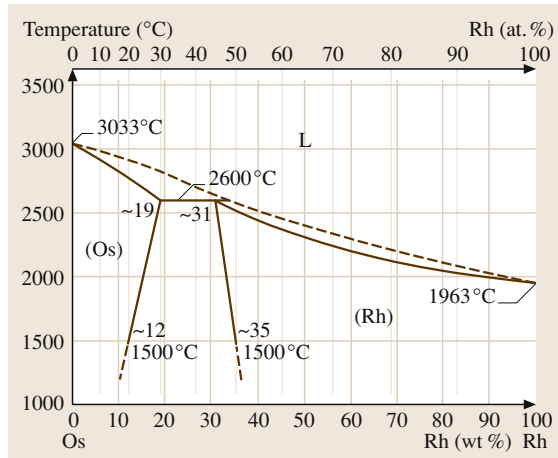
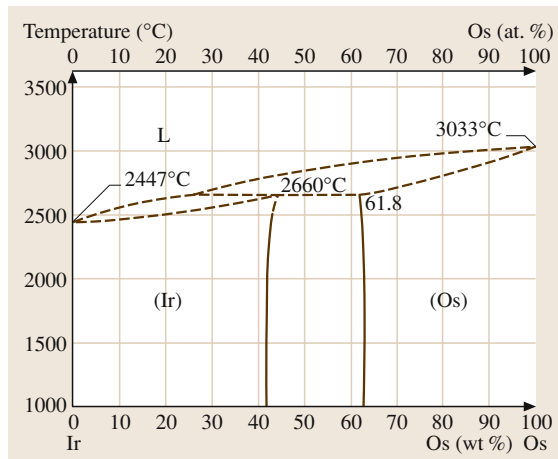


Fig. 3.1-340 Phase diagram of Os–Rh [1.217, p. 90]

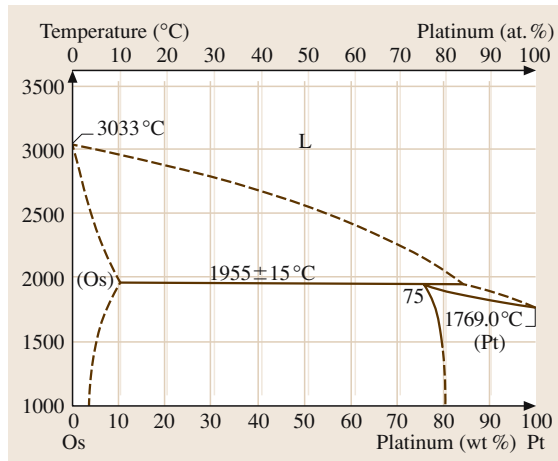


Fig. 3.1-341 Phase diagram of Os–Pt [1.217, p. 90]

Fig. 3.1-339 Phase diagram of Os–Ir [1.217, p. 87]

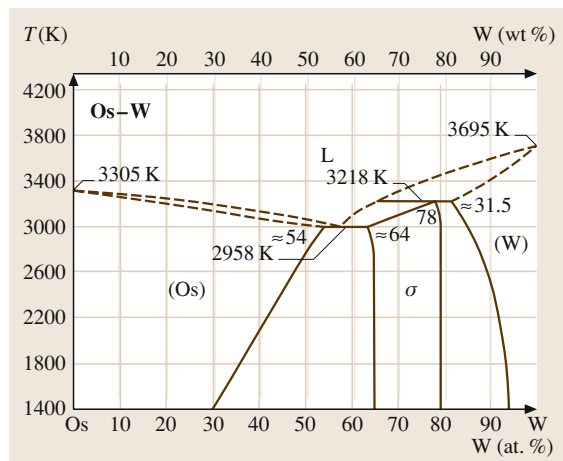


Fig. 3.1-342 Phase diagram of Os–W [1.245]

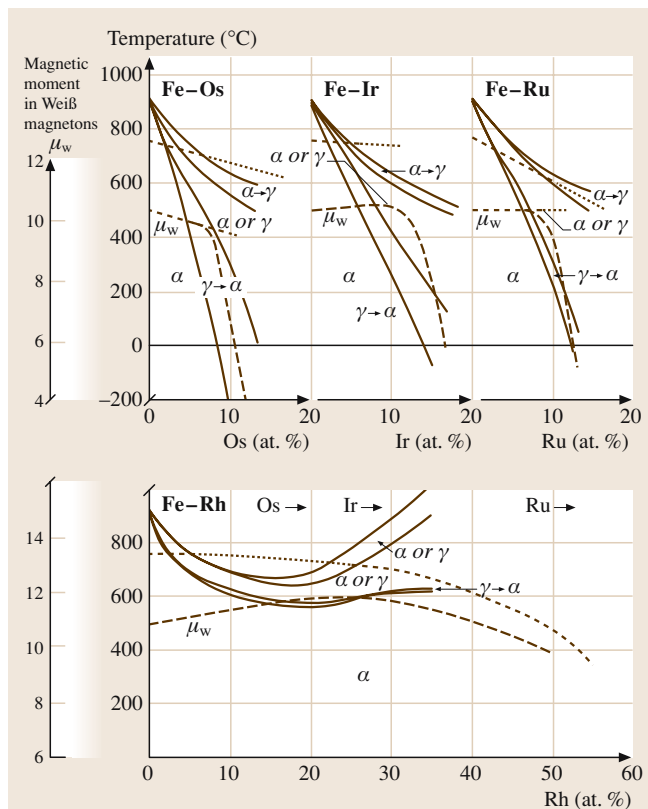


Fig. 3.1-343 Temperature dependence of atomic moments, $\gamma \rightarrow \alpha$ transition and magnetic transition of iron alloys [1.220, p. 259]

Table 3.1-267 Thermodynamic data of Os [1.217, p. 110]

| T (K) | c_p (J/K mol) | S (J/K mol) | H (J/mol) | G (J/mol) | p (at) |
|--------|-----------------|-------------|-----------|-----------|------------------------|
| 298.15 | 24.707 | 32.635 | 0 | -9.73 | |
| 400 | 25.094 | 39.95 | 2.536 | -13.444 | 2.95×10^{-95} |
| 800 | 26.618 | 57.811 | 12.879 | -33.371 | 6.31×10^{-44} |
| 1400 | 28.903 | 73.287 | 29.535 | -73.067 | 5.81×10^{-22} |

T = Temperature, c_p = specific heat capacity, S = Entropy, H = Enthalpy, G = free Enthalpy,
 p = partial pressure of the pure elements

Table 3.1-268 Structure and lattice parameter of selected Os alloy phases [1.217, p. 118]

| Phase | Pearson symbol | a (nm) | c (nm) | Remarks | Concentration x A(1 - x) B(x) |
|--------------------------------|----------------|----------|----------|---------|--|
| Os | hP2 | 0.27353 | 0.43191 | 293 K | |
| Os–Ir | hP2 | 0.27361 | 0.43417 | | 0.35 |
| Os–Ir | cF4 | 0.38358 | | | 0.8 |
| Os–Pt | hP2 | 0.27361 | 0.43247 | | 0.1 |
| Os–Pt | cF4 | 0.39094 | | | 0.8 |
| Os–Ru | hP2 | 0.27193 | 0.4394 | | 0.5 |
| Os ₃ W ₇ | tP30 | 0.9650 | 0.4990 | | 0.78 |

Mechanical Properties. Osmium is very hard and brittle. The hardness is, as in the case of Ru, strongly anisotropic. Characteristic properties for hardness of the element at different temperatures, as well as work hardening and hardness of Os–Pt alloys are given in Tables 3.1-269 and 3.1-270 [1.216, 217] and Fig. 3.1-262. Osmium exhibits a Young's modulus of 570 GPa, a modulus of rigidity of 220 GPa, and the Poisson's ratio is 0.25.

Electrical Properties. The residual electrical resistivity ratio (273.2 K/4.2 K) is 400 [1.216] (Table 3.1-203).

Table 3.1-269 Hardness of Os at different temperatures [1.216]

| T (°C) | HV |
|--------|----------------------|
| 20 | 300–680 ^a |
| 200 | 260–580 ^a |
| 600 | 200–410 ^a |
| 1200 | 130–400 ^a |

^a all values depending on crystal orientation

Table 3.1-270 Hardness of Os–Pt alloys [1.217]

| Pt content (wt %) | HV |
|-------------------|-----|
| 0 | 560 |
| 20 | 578 |
| 40 | 555 |

Table 3.1-271 Specific electrical resistivity $\rho_i(T)$ ($\mu\Omega$ cm) of Os at temperature T [$\rho(T) = \rho_0 + \rho_i(T)$; ($\rho_0 = 0.09 \mu\Omega$ cm²) [1.216]]

| T (K) | ρ_i ($\mu\Omega$ cm) |
|-------|----------------------------|
| 25 | 0.012 |
| 100 | 1.90 |
| 273 | 8.30 |
| 900 | 26.0 |
| 1300 | 38.0 |

At $T < 273$ K; $\rho_0 = 0.8 \mu\Omega$ cm at $T > 273$ K

Table 3.1-271 [1.216] gives the specific electric resistivity of Os at different temperatures. The increase of atomic resistivity is shown in Table 3.1-263. Osmium coatings on W-based dispenser cathodes lower its work function (source Ba–Ca aluminate). It enhances the secondary electron emission (Fig. 3.1-344) and enables the operation at higher current densities in high power klystron and magnetron valves. Osmium shows superconductivity below 0.71 K and Table 3.1-272 gives some examples of superconducting Os alloys [1.218].

Thermoelectric Properties. Figure 3.1-269 shows a comparison of the thermoelectric power of the different noble metals of the platinum group as a function of temperature.

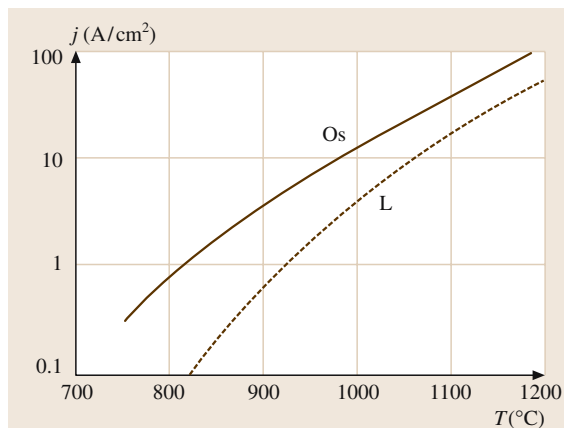


Fig. 3.1-344 Current density as a function of cathodic temperature for a normal cathode (dashed curve) and a cathode with a 5 µm thick Os coating [1.298]

Magnetic Properties. Figures 3.1-271 and 3.1-345–3.1-347 [1.216] give a survey and present selected data of the magnetic mass susceptibility for the element and for Os–Cr alloys. This alloy system exhibits antiferromagnetism in compositions from 0.3 to 2.2 at.% Os in the temperature range on the left-hand side of the bold vertical bars in Fig. 3.1-347. In Fe–Os alloys the temperature of the magnetic transition and the atomic

Table 3.1-272 Superconducting Os-alloys [1.218]

| Os | Compound | T _c (K) |
|--|-----------|--------------------|
| Ce ₃ Os ₄ Ge ₁₃ | 6.1 | |
| Pr ₃ Os ₄ Ge ₁₃ | 16 | |
| Nd ₃ Os ₄ Ge ₁₃ | 1.9 | |
| Eu ₃ Os ₄ Ge ₁₃ | 10.1 | |
| Tb ₃ Os ₄ Ge ₁₃ | 14.1 | |
| Dy ₃ Os ₄ Ge ₁₃ | 2.1 | |
| Er ₃ Os ₄ Ge ₁₃ | 1.9 | |
| ZrOsAs | 8 | |
| HfOsAs | 3.2 | |
| Y ₃ Os ₄ Ge ₁₃ | 3.9–3.7 | |
| Lu ₃ Os ₄ Ge ₁₃ | 3.6–3.1 | |
| Y ₅ Os ₄ Ge ₁₀ | 8.68–8.41 | |
| TiOsP | <1.2 | |
| ZrOsP | 7.44–7.1 | |
| HfOsP | 6.10–4.96 | |

magnetic moment decrease with increasing Os content (see Fig. 3.1-343).

Thermal Properties. Data for the thermal expansion coefficient at different temperatures are given in Table 3.1-266.

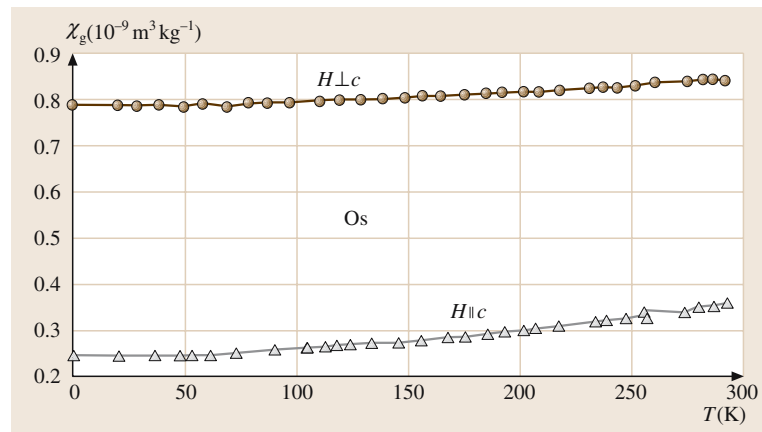


Fig. 3.1-345 Temperature dependence of the mass susceptibility of Os (single crystal) at applied magnet field of 795–700 A/m [1.217, p. 164]

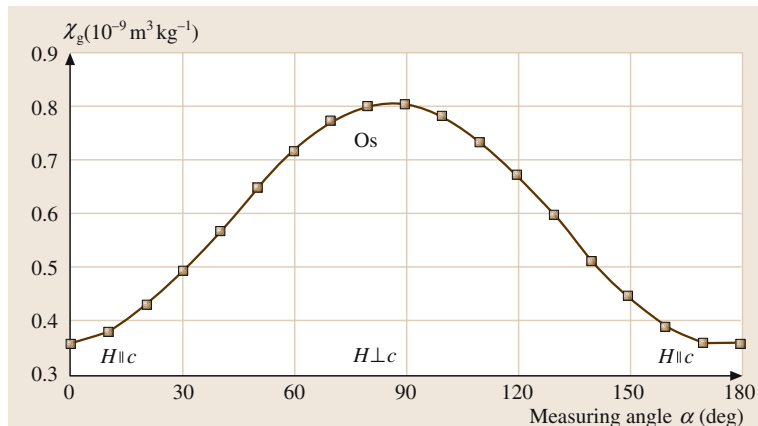


Fig. 3.1-346 Mass susceptibility of an Os single crystal at room temperature as a function of measuring angle [1.217, p. 164]

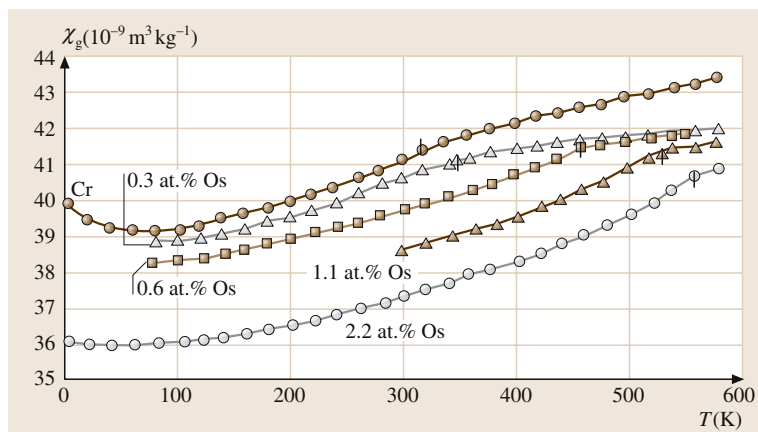


Fig. 3.1-347 Temperature dependence of the mass susceptibility of Os-Cr alloys. Small marks indicate the Neel temperature T_N [1.217, p. 167]

Chemical Properties. Osmium is resistant against HCl but is attacked by HNO_3 and aqua regia. The element oxidizes in powder form readily at room temperature, forming OsO_4 which vaporizes above 130 °C. A detailed survey about chemical properties is given in [1.216]. The oxide OsO_4 serves as a catalyst for the synthesis of asymmetric organic compounds. Figure 3.1-348 shows an example for a ligand-supported chiral dihydroxylation [1.291].

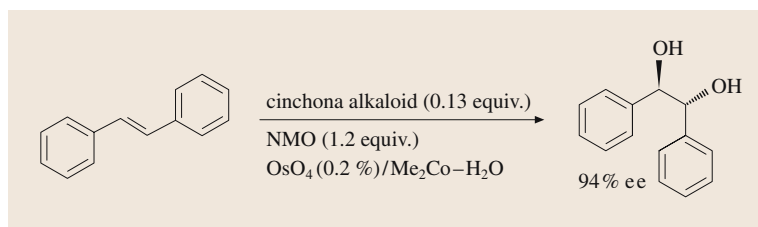


Fig. 3.1-348 Chiral dihydroxylation using OsO_4 as catalyst component [1.291, p. 83]

3.1.11 Lead and Lead Alloys

Lead constitutes only about 12.5 wtppm (weight part per million) of the earth's crust, but concentrated lead ore deposits make it easy to mine. Lead and its alloys are used in a wide range of technical applications because of their low melting point, ease of casting, high density, softness and high formability at room temperature, excellent resistance to corrosion in acidic environments, attractive electrochemical behavior in many chemical environments, chemical stability in air, water and soil, and the high atomic number and stable nuclear structure. Despite their known toxicity, lead and its alloys can be handled safely and it ranks fifth in tonnage consumed (6 Mt/yr), after Fe, Cu, Al, and Zn. The type of data available on different alloys depends to a great extent on the areas of application [1.299].

The most important Pb ore mineral is galena, (87 wt% Pb). The lead ore concentrate is roasted to form Pb oxide. Smelting to reduce the oxide by CO produces Pb. The lead bullion thus obtained contains Sb, As, Te, Sn, Cu, Ni, Co, and Bi besides noble metals, and is

further refined to produce various grades of lead. Commercial grade pure lead is produced by the removal of impurities through selective gas phase oxidation, precipitation from molten lead phase as pure elements, and through the formation of intermetallic compounds with low solubility (removal of Fe, Ni, Co, As, Te, and Sb as oxides; precipitation of Cu as elemental Cu, CuS, and Cu arsenates and antimonides; precipitation of Fe as Fe arsenates and antimonides; precipitation of Ag and Au as intermetallic compounds of Zn with Au and Ag; Bi precipitation through the formation of a compound CaMg₂Bi₂). Electrolytic refining of commercial purity lead is used to obtain lead with purity to levels down to 99.99 to 99.9995 wt%. Zone melting is used to produce ultrapure grades of Pb.

3.1.11.1 Pure Grades of Lead

The commercial grades of pure lead (Table 3.1-273) are used in chemical plants, sound attenuation, roof-

Table 3.1-273 Impurity levels of commercial lead grades [1.299]

| Impurities, additions | Low Bi, low Ag, pure Pb ^{a,d} L50006 | Refined pure Pb ^{b,d} L50021 | Corroding lead ^e L50042 | Pure lead (common lead) ^e L50049 | Chemical lead ^{c,e} L51120 | Copper bearing lead ^e L51121 | Tellurium lead ^e L51123 |
|-------------------------|--|--|---------------------------------------|--|--|--|---------------------------------------|
| (wt%) | max. | max. | | | | | |
| Ag, max. | 0.0010 | 0.0025 | 0.0015 | 0.005 | 0.020 | 0.020 | 0.020 |
| Ag, min. | — | — | — | — | 0.002 | — | — |
| Cu, max. | 0.0010 | 0.0010 | 0.0015 | 0.0015 | 0.080 | 0.080 | 0.080 |
| Cu, min. | — | — | — | — | 0.040 | 0.040 | 0.040 |
| Ag + Cu, max. | — | — | 0.0025 | — | — | — | — |
| SbAs, Sn each | 0.0005 | 0.0005 | — | — | — | — | — |
| As + Sb + Sn, max. | — | — | 0.002 | 0.002 | 0.002 | 0.002 | 0.002 |
| Zn, max. | 0.0005 | 0.0005 | 0.001 | 0.001 | 0.001 | 0.001 | 0.001 |
| Fe, max. | 0.0002 | 0.001 | 0.002 | 0.002 | 0.002 | 0.002 | 0.002 |
| Bi, max. | 0.0015 | 0.025 | 0.050 | 0.050 ^c | 0.005 | 0.025 | 0.025 |
| Te | 0.0001 | 0.0001 | — | — | — | — | 0.035–0.060 |
| Ni, max. | 0.0002 | 0.0002 | — | — | — | — | — |
| Pb (by difference) min. | 99.995 | 99.97 | 99.94 | 99.94 | 99.90 | 99.90 | 99.85 |

^a For chemical applications where low Ag and low Bi contents are required

^b For lead acid battery applications

^c For applications requiring corrosion protection and formability, as per ASTM B29-92

^d As per ASTM B29-92

^e As per ASTM 749-85 (re-approved 1991)

Table 3.1-274 Mechanical properties of pure grades of lead [1.299–301]

| Lead grade | Hardness HB | Yield strength (0.125) (MPa) | Tensile strength (MPa) | Comp. strength (25%) (MPa) | Elongation (%) | Fatigue strength at 10 ⁷ cycles (MPa) | Creep strength (0.2%/yr) (MPa) |
|----------------------------|-------------|------------------------------|------------------------|----------------------------|----------------|--|--------------------------------|
| Pure lead (c) | 4.0 | 5.9 | 13.1 | 15.2 | 45 | 2.7 | |
| Corroding lead, Pb > 99.94 | 3.2–4.5 | 5.5 | 12–13 | | 30 | 3.2 | |
| Refined pure (r) | 3.8 | | 12.1 | | 53 | 3.2 | 1.2 |
| Chemical (c) | 5.2 | 11.3 | 17.9 | 20.0 | 45 | | |
| Chemical (r) | 5.5 | | 19.3 | | 47 | 6.9 | |
| Undesilverized (e) | | | 17.2 | | 50 | | |
| Undesilverized (r) | 4.7 | 8.6 | 16.5 | 17.9 | 51 | 5.0 | 15.8 |

(r) - rolled; (c) - cast; (e) - extruded

ing, flashings and weather stripping, water-proofing, and radiation shielding.

The mechanical properties of pure grades of lead are listed in Table 3.1-274 [1.299–301]. The near ambient temperatures at which lead and its alloys are used correspond to high homologous temperatures ($T/T_M \sim 0.5$ or higher) for lead and therefore significant diffusion can occur. Consequently, the mechanical properties are affected by dynamic and static recovery, recrystallization effects, and creep deformation. Therefore, caution is advised in the use of short-term mechanical properties. The recrystallization temperatures of different lead grades are shown as a function cold work and grain size in Fig. 3.1-349 [1.303]. The lowest reported value of recrystallization temperature for 99.9999 wt% purity lead is $\sim -59^\circ\text{C}$; for lead of not very high purity it is $\sim -33^\circ\text{C}$. The fatigue behavior of 99.99 wt% pure lead in a Haigh push–pull test at a test cycle fre-

quency of 33.67 Hz is presented in the form of S-N (stress to failure versus number of cycles) curves in Fig. 3.1-350 [1.303].

Coefficients of internal friction of relevance to acoustic damping are given in Table 3.1-275 [1.299, 302]. As lead is used in sound attenuation applications, acoustic transmission data of selected single-skin and double-skin partitions with and without lead are given in Table 3.1-276 [1.299]. The sound reduction versus frequency is given in [1.299, 304].

Corrosion rates of lead in H_2SO_4 and HF acids are presented in Figs. 3.1-351 and 3.1-352 [1.301]. Corrosion behavior of chemical lead in some common environments is presented in Table 3.1-277 [1.301]. Corrosion rates of the different lead grades normally fall in the same category.

As lead is extensively used in radiation shielding, the gamma-ray mass-absorption data for lead are presented in Fig. 3.1-353 [1.299, 305].

Table 3.1-275 Experimental values of coefficient of internal friction Q^{-1} . Values in single crystal and polycrystalline lead [1.299, 302] (RT = room temperature)

| Material | Frequency (kHz) | Q^{-1} |
|---------------------------------|-----------------|--|
| Pure polycrystalline lead | 0.016–2 | 0.35×10^{-2} – 4×10^{-2} |
| | 17–28 | 0.2×10^{-2} – 0.8×10^{-2} |
| Single-crystal line lead | 4–64 | 0.2×10^{-2} – 0.7×10^{-2} |
| Single-crystal Pb–0.033 wt% Sn | 30 | 0.11×10^{-2} (max. deformation of 10^{-7} , RT) |
| Single-crystal Pb–0.035 wt% Bi | 30 | 0.22×10^{-3} (max. deformation of 10^{-7} , RT) |
| Single-crystal Pb–0.0092 wt% Cd | 30 | 0.9×10^{-3} (max. deformation of 10^{-7} , RT) |
| Single-crystal Pb–0.0022 wt% In | 4 | 2×10^{-3} (max. deformation of 10^{-7}) |

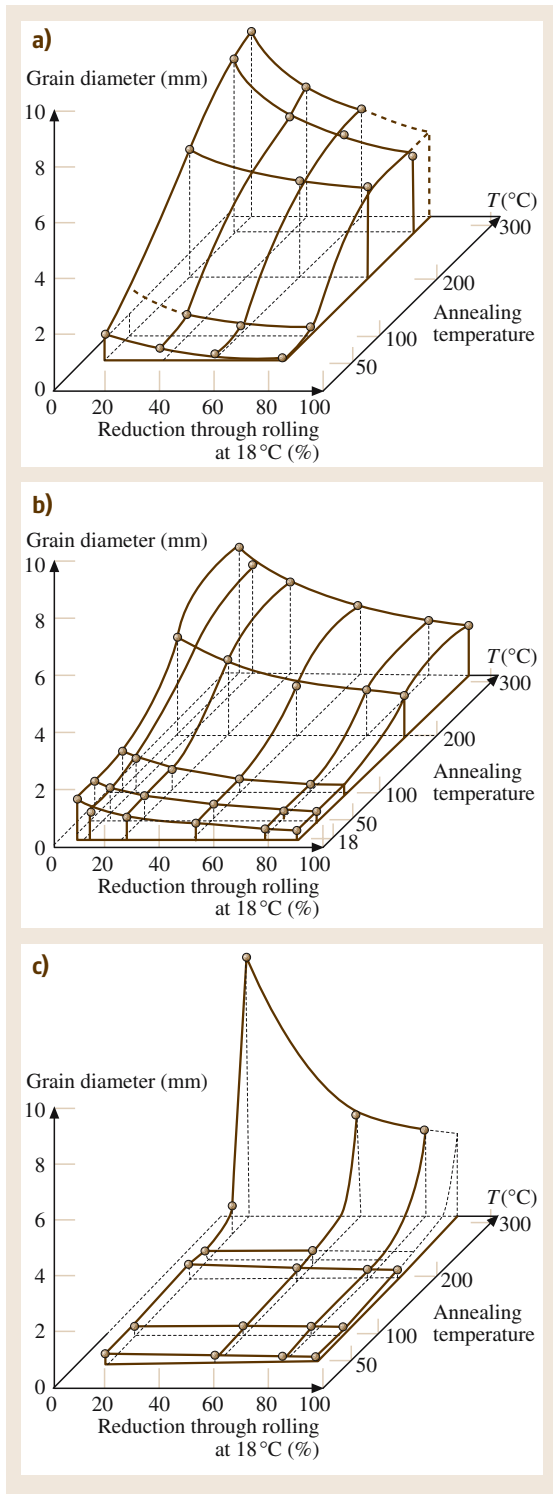


Fig. 3.1-349a–c Recrystallization diagrams: (a) Electrolytic Pb. (b) Parkes Pb. (c) Pattinson Pb [1.303]

Table 3.1-276 Acoustic transmission data of selected single skin and double skin partitions with and without lead [1.299, 304]

| Description of test partition | Thickness (mm) | Surface weight (kg/m ²) | Average SRI (dB) | RW (dB) | STC (dB) |
|---|----------------|-------------------------------------|------------------|---------|----------|
| Single skin – code 1 lead sheet | 0.5 | 5.65 | 22.7 | 25 | 25 |
| Single skin – code 3 lead sheet | 1.52 | 17.16 | 31.8 | 35 | 35 |
| Single skin – 0.5 mm lead equivalent lead impregnated PVC sheet | 2.17 | 7.94 | 27.4 | 30 | 30 |
| Double skin – 12.4 mm Gyproc plasterboard – no infill | 117.76 | 19.04 | 40.2 | 42 | 41 |
| Double skin – code 3 lead sheet bonded to 12.4 mm Gyproc plasterboard – no infill | 121.88 | 52.20 | 51.8 | 52 | 52 |

SRI: sound reduction index; RW: weighted sound reduction; STC: sound transmission classification

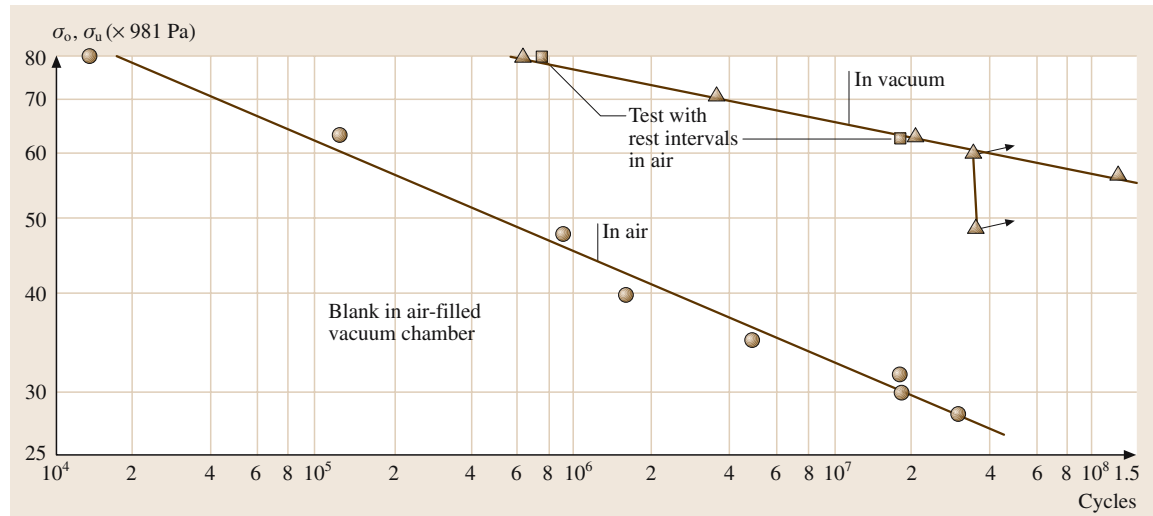


Fig. 3.1-350 S-N (stress vs. number of cycles) curves for Pb in air and vacuum [1.303]

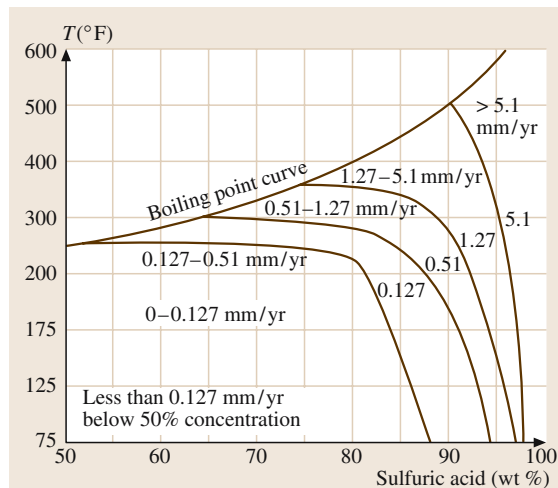


Fig. 3.1-351 Corrosion rates of lead in H_2SO_4 [1.301]

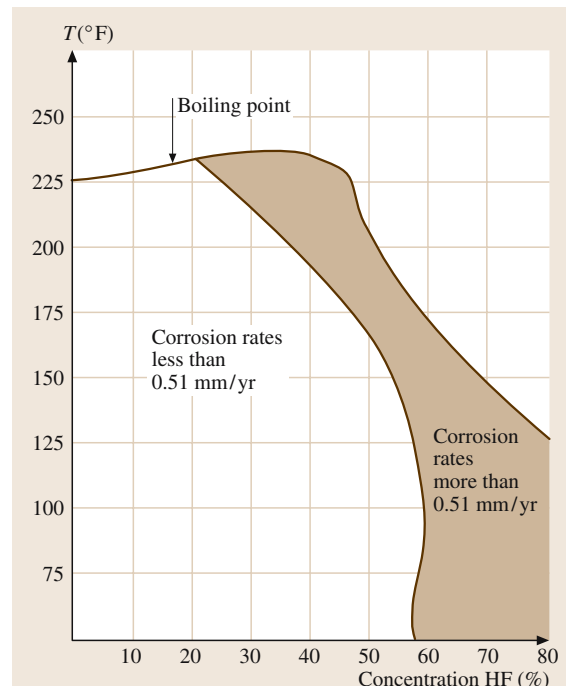


Fig. 3.1-352 Corrosion rates of lead in HF [1.301]

Table 3.1–277 Classifying corrosion behavior of Pb in selected environments [1.301]

| Chemical | Temperature (°C) | Concentration (wt %) | Corrosion class |
|---|------------------|----------------------|-----------------|
| Acetic acid | 24 | Glacial | B |
| Acetone | 24–100 | 10–90 | A |
| Acetylene, dry | 24 | — | A |
| Ammonia | 24–100 | 10–30 | B |
| Ammonium azide | 24 | — | B |
| Ammonium carbonate | 24–100 | 10 | B |
| Ammonium chloride | 24 | 0–10 | B |
| Ammonium hydroxide | 27 | 3.5–40 | A |
| Ammonium nitrate | 20–52 | 10–30 | D |
| Ammonium phosphate | 66 | — | A |
| Ammonium sulfate | 24 | — | B |
| Arsenic acid | 24 | 10 | B |
| Benzene | 24 | — | B |
| Boric acid | 24–149 | 10–100 | B |
| Bromine | 24 | — | B |
| Butane | 24 | — | A |
| Carbon tetrachloride (dry) | BP | 100 | A |
| Chlorine | 38 | — | B |
| Citric acid | 24–79 | 10–30 | B |
| DDT | 24 | — | B |
| Fluorine | 24–100 | — | A |
| Hydrochloric acid | 24 | 0–10 | C |
| Hydrogen chloride (anh HCl) | 24 | 100 | A |
| Mercury | 24 | 100 | D |
| Methanol | 30 | — | B |
| Methyl ethyl ketone | 24–100 | 10–100 | B |
| Phosphoric acid | 24–93 | — | B |
| Sodium carbonate | 24 | 10 | B |
| Sodium chloride | 25 | 0.5–24 | A |
| Sodium hydroxide | 26 | 0–30 | B |
| Sodium nitrate | 24 | 10 | D |
| Sodium sulfate | 24 | 2–20 | A |
| Sulfur dioxide | 24–204 | 90 | B |
| Natural outdoor atmospheres | 24 | — | —A |
| Industrial, natural and domestic waters | 24 | — | —A |
| Soils | 24 | — | —A |

Data mostly correspond to chemical lead. The four corrosion performance categories:

A < 0.051 mm/yr: Negligible corrosion – lead recommended for use;

B < 0.51 mm/yr: Practically resistant – lead recommended for use;

C = 0.51–1.27 mm/yr: Lead may be used where this effect on service life can be tolerated;

D > 1.27 mm/yr: Corrosion rate too high to merit any consideration of lead

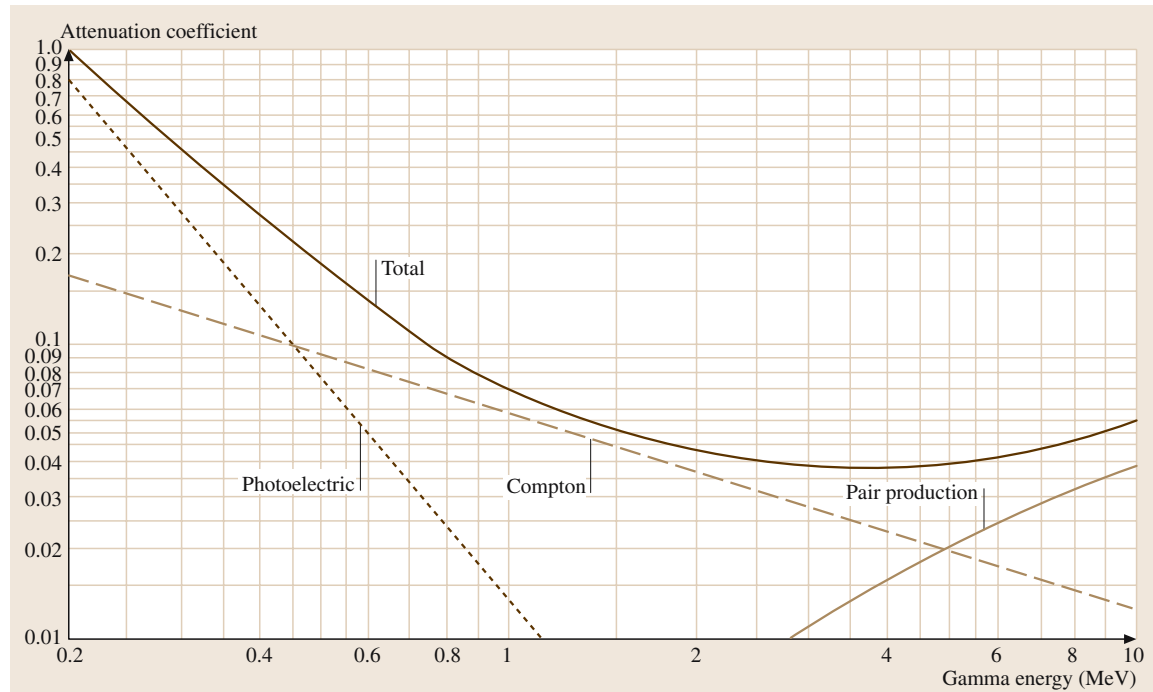


Fig. 3.1-353 Gamma-ray mass-absorption coefficients for lead [1.299, 305]

3.1.11.2 Pb–Sb Alloys

Pb–Sb Binary Alloys

Lead–antimony alloys are widely used for pipe, cable sheathing, collapsible tubes, storage battery grids, anodes, sulfuric acid fittings, and X-ray and gamma ray shielding (in the absence of neutron irradiation). The addition of 1 to 13 wt% Sb to Pb increases tensile strength, fatigue strength, and hardness compared to pure lead (99.99). Lead and Sb form a eutectic system as shown in Fig. 3.1-354 [1.303]. The maximum solubility of Sb in Pb is 3.45 wt% at the eutectic temperature and decreases to 0.3 wt% at 50 °C. Thus considerable age-hardening

can be obtained in these alloys. Small additions of As (0.05–0.1 wt%) dramatically increase the rate of aging and final strength. The microstructure at higher Sb contents consists of proeutectic lead-rich phase surrounded by a network of eutectic phase that contributes to enhanced as-cast and high temperature strength. Shrinkage on solidification varies from 3.85% for Pb to 2.06% for a Pb–16 wt% Sb alloy. These alloys have high corrosion resistance in most environments. They form a protective and impermeable film faster than pure lead and, in some cases, even faster than chemical lead. Table 3.1-278 lists the physical properties of selected Pb–Sb alloys [1.300]. Table 3.1-279 lists the mechanical properties of cast

Table 3.1-278 Physical properties of Pb–Sb alloys [1.300]

| Alloy composition (wt%) | Solidification range (°C) | Coefficient of thermal expansion (10^{-6} K^{-1}) | Specific heat ($\text{J kg}^{-1} \text{ K}^{-1}$) | Thermal conductivity ($\text{W m}^{-1} \text{ K}^{-1}$) | Resistivity ($\text{n}\Omega \text{ m}$) | Density (g cm^{-3}) | Volume change on freezing ^a (%) |
|-------------------------|---------------------------|---|---|---|--|--------------------------------|--|
| Pb–1 Sb | 322–317 | 28.8 | 131 | 33 | | 11.27 | –3.75 |
| Pb–3 Sb | 310–269 | 28.1 | | | | 11.19 | |
| Pb–6 Sb | 285–252 | 27.2 | 135 (solid) | 29 | 253 | 10.88 | –3.11 |
| Pb–9 Sb | 265–252 | 26.4 | 137 (solid) | 27 | 271 | 10.60 | –2.76 |

^a Negative values show contraction

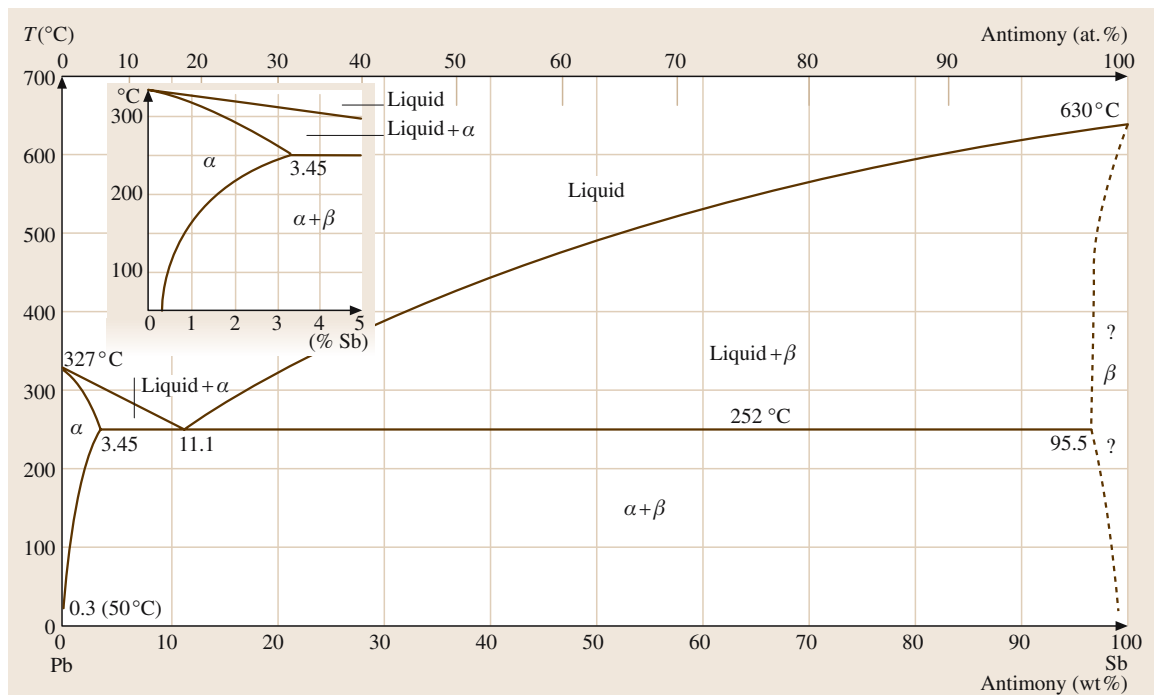


Fig. 3.1–354 Pb–Sb phase diagram [1.303]

Table 3.1–279 Mechanical properties of Pb–Sb alloys [1.299–301, 306]

| Sb content (wt%) | Tensile strength (MPa) | Elongation at fracture (%) | Hardness HB | Yield strength $R_{p0.125}$ (MPa) | Fatigue strength for 2×10^7 cycles (MPa) | Creep strength | Young's modulus (GPa) |
|------------------|------------------------|----------------------------|-------------|-----------------------------------|---|--------------------|-----------------------|
| 1 (a) | 37.9 | 20 | | 19.3 | 7.6 | 190 h at 20.7 MPa | — |
| 1 (c) | 20 | 50 | 7.0 | — | 7.6 | | — |
| 3 (a) | 65.5 | 10 | | 55.2 | — | 630 h at 27.6 MPa | — |
| 3 (c) | 32.43 | 15 | 9.1 | | | | — |
| 6 (a) | 73.8 | 8 | | 71.0 | | 1000 h at 27.6 MPa | |
| 6 (c) | 47 | 24 | 13 | | 17.2 | | 24.15 |
| 6 (r) | 29.6 | 42 | 8.7 | 15.2 | 10.3 | — | — |

(c) cast; (a) cast and stored 30 days at room temperature; (r) rolled

alloys [1.299–301, 306]. Data for one of the rolled alloys are also given to indicate that they exhibit poorer properties.

Pb–Sb-Based Lead Acid Battery Grid Alloys

Lead–acid batteries are the most widely used secondary battery type in current automotive and industrial applications due to the relatively low cost and high availability of the raw materials, room temperature operation, ease of manufacture, long life cycle, versatility, and the ex-

cellent reversibility of the electrochemical system. Lead alloys are used as electrode grids, connectors, and grid posts. The two classes of alloys that are in extensive use are (i) Pb–Sb based ternary and multi-component alloys with As, Sn, Ag, Se, Cu, S, and Cd and (ii) Pb–Ca based ternary alloys and multi-component alloys with Sn, Ag, and Al. In the Pb–Sb based alloys, Sb addition to Pb enhances castability, tensile strength, creep strength, corrosion resistance under battery operating conditions, and resistance to structural changes during deep charge–

discharge cycling. However, Sb migration from Pb–Sb based positive grid alloys to negative electrode results in the reduction of hydrogen over-voltage and consequent decrease in cell voltage. This led to increased degassing and water loss. To minimize this poisoning of negative plates, lower Sb contents (1–3 wt% Sb) are now used in battery grids. The posts and straps use about 3 wt% Sb. Low Sb content promotes the formation of solidification shrinkage porosity and cracking but the cracking tendency is overcome by the use of grain-refining additions of S, Cu, and Se. Arsenic additions to Pb–Sb alloys increase the rate of age-hardening and reduce the time of grid storage required after casting. Arsenic addition also increases the creep resistance which is very beneficial in deep cycling conditions. The addition of tin is used to act synergistically with As and Sb to improve fluidity and castability. It also increases cycle life of deep cycling batteries containing thin plates. Silver additions increases both the corrosion and creep resistance in Pb–Sb alloy grids. Cast Pb–Sb based alloys are typically used in grid alloys as the Pb–Sb based wrought alloys have lower yield strength, tensile strength, and creep strength. The corrosion behavior of wrought alloys is inferior due to the nature of distribution of the PbSb eutectic phase and lower creep resistance. Corrosion of cast Pb–Sb occurs by the attack of Pb–Sb eutectic. It solubilizes some Sb and stresses of corrosion product are accommodated. In rolled alloys the eutectic phase is isolated, which leads to stresses in the grid. The current choice of alloy composition is Pb–1.6Sb–0.2As–0.2Sn–0.2Se. Table 3.1-280

Table 3.1-280 Alloying components of common lead–antimony battery grid alloys [1.300, 307]

| Alloy concentration (wt%) | | | | |
|---------------------------|-----|------|-------|-----|
| Sb | Sn | As | Cu | Se |
| 2.75 | 0.2 | 0.18 | 0.075 | — |
| 2.75 | 0.3 | 0.3 | 0.075 | — |
| 2.9 | 0.3 | 0.15 | 0.04 | — |
| 2.9 | 0.3 | 0.15 | 0.05 | — |
| 1.6 | 0.2 | 0.2 | — | 0.2 |

lists the compositions of common lead–antimony battery grid alloys [1.300, 307].

Lead–antimony alloys containing 0.2 to 1 wt% Sb are used to form barrier sheaths in high voltage cables. Properties of Pb–0.85Sb cable sheathing alloy are presented in the section on cable sheathing alloys. Lead alloys with 6–8 wt% Sb are used to fabricate a wide variety of equipment such as tank linings, pipe and one type of anode used in chromium plating. Alloys with 13 wt% Sb are used to make castings when hardness is of key importance. About 6% of the Pb produced in the world was used in the production of sports and military ammunition due to its high density and low cost. Lead containing up to 8 wt% Sb and 2 wt% As is used.

Pb–Sb–Sn Alloys

These alloys have low melting points, high hardness, and excellent high temperature strength and fluidity. These characteristics together with its applicability for the replication of detail make them suitable as printing types. Table 3.1-281 lists the characteristics of selected type-metal alloys [1.300].

The Pb-rich ternary Pb–Sb–Sn white metal alloys are also used in journal bearings due to the excellent anti-friction (and anti-seizure) characteristics and hardness. These Pb-rich white metal alloys, also referred to as Babbitt alloys, contain 9–15 wt% Sb, 1–20 wt% Sn, and small amounts of Cu and As. Table 3.1-282 lists the physical properties of different bearing alloys [1.299, 300]. The mechanical property data for some of these alloys are presented in Table 3.1-283 [1.299, 308]. Most of the alloys lie in the primary crystallization field of Sb or SbSn of the ternary system. They contain primary crystals of Sb (or SbSn) in a binary (or ternary) eutectic matrix apart from the high-melting Cu-rich phases. Copper contents above 1.5 wt% also increase the hardness. Arsenic addition leads to a fine and uniform structure, improves fatigue strength, and minimizes softening. Arsenic is present in solid solution in Pb, Sb, and Sb-containing phases such as SbSn. The lead–alkali alloys, e.g., Bahnmetall, or the Pb–Sn–alkali alloys, also have a limited significance as bearing metals.

Table 3.1-281 Typical compositions and properties of selected type metals [1.299, 300]

| Alloy | Composition (wt%) | | | Hardness HB | Liquidus temperature (°C) | Solidus temperature (°C) |
|-----------------------|-------------------|----|----|-------------|---------------------------|--------------------------|
| | Pb | Sn | Sb | | | |
| Electrotype – General | 94 | 3 | 3 | 14 | 299 | 245 |
| Linotype – Special | 84 | 5 | 11 | 22 | 246 | 239 |
| Stereotype – Flat | 80 | 6 | 14 | 23 | 256 | 239 |
| Monotype – Ordinary | 78 | 7 | 15 | 24 | 262 | 239 |

Table 3.1-282 Composition and physical properties of selected lead-based white metal bearing alloys [1.299, 300]

| Alloy composition (wt%) | | Freezing range (°C) | Density (g cm ⁻³) | Volume change on freezing ^a (%) | Coefficient of thermal expansion (10 ⁻⁶ K ⁻¹) | Specific heat (J kg ⁻¹ K ⁻¹) | Latent heat of fusion (kJ kg ⁻¹) | Electrical resistivity (nΩ m) | Thermal conductivity (W m ⁻¹ K ⁻¹) |
|-------------------------|---------|---------------------|-------------------------------|--|--|---|--|-------------------------------|---|
| Sb | Sn | | | | | | | | |
| 9.5–10.5 | 5.5–6.5 | 256–240 | 10.50 | −2 | | 150 | 0.9 | 287 | |
| 14–16 | 4.5–5.5 | 272–240 | 9.96 | −2 | 24 | 150 | 0.1 | 282 | |
| 14–16 | 9.3–9.7 | 268–240 | 9.70 | −2.3 | 19.6 | 160 | | 286 | 24 |
| 14.5–17.5 | 0.8–1.2 | 353–247 | 10.10 | −2.5 | | | | | |

^a Negative values show contraction

Table 3.1-283 Composition and mechanical properties of ASTM B23 Pb-based white metal bearing alloys [1.299, 308]

| Alloy no. | Nominal alloy content (wt%) | | | | Yield stress (MPa) | | Elongation at fracture (%) | | Ultimate strength in compression (MPa) | | Hardness HB 500/30 | | Melting range (°C) | Fatigue strength 2 × 10 ⁷ cycles (MPa) |
|-----------|-----------------------------|------|------|---------|--------------------|--------|----------------------------|-------|--|--------|--------------------|--------|--------------------|---|
| | Sb | Sn | Cu | As | 20 °C | 100 °C | 20 °C | 20 °C | 100 °C | 100 °C | 20 °C | 100 °C | | |
| 7 | 15 | 10.0 | <0.5 | 0.45 | 24.5 | 11.0 | 4 | | 107.9 | 42.4 | 22.5 | 10.5 | 240–268 | 28 |
| 8 | 15 | 5.0 | <0.5 | 0.45 | 23.4 | 12.1 | 5 | | 107.6 | 42.4 | 20.0 | 9.5 | 237–272 | 27 |
| 15 | 16 | 1.0 | <0.5 | 0.8–1.4 | | | 2 | | | | 21.0 | 13.0 | 248–281 | 30 |

3.1.11.3 Pb–Sn Alloys

Lead-tin alloys serve as materials for a number of applications as summarized in Table 3.1-284.

The Pb–Sn system (Fig. 3.1-355) shows an extended and strongly temperature-dependent solid solubility of Sn in Pb decreasing from 19.2 wt% at the eutectic temperature to about 1.3 wt% Sn at room temperature. This can lead to significant age-hardening on rapid cooling from the range of the homogeneous α phase. Streaky and granular Sn precipitates lead to hardness increases from about HB = 4 in pure lead to around HB = 12 at the solid solubility limit. In the stable $\alpha + \beta$ range hardness increases less rapidly to about HB = 18 at the eutectic composition.

Pb–Sn-Based Solder Alloys

Lead–tin alloys in the Pb-rich hypoeutectic region are the most widely used of all solders. In the melt, the surface tension increases with Sn content. Table 3.1-285 gives the melting characteristics of some Pb–Sn solders and lists their typical applications. When referring to Pb–Sn solders, the Sn content is customarily given first, for example 40/60 refers to 40 wt% Sn and 60 wt% Pb. Table 3.1-286 summarizes the mechanical and physical properties of different soft solders [1.309]. Further alloying additions are Cd, Bi, Sb, and Ag. Silver is added to increase tensile, creep, fatigue, and shear strengths, and to reduce the dissolution of Ag from Ag alloy coatings. Addition of 5 to 6% in Sn content increases the tensile and creep strengths. Addition

Table 3.1-284 Applications and typical compositions of Pb–Sn materials

| Application | Alloying elements (wt%) | Remarks |
|---------------------------|-------------------------|----------------------------------|
| Sn | Others | |
| Cable sheathing | <0.5 | Sb (0.2), Ca (0.33) or Cd (0.15) |
| Solders | 2–63 | See below |
| Pressure die castings | ~62 (near eutectic) | |
| Organ pipes | (45) 55–74 | |
| Sliding layer on bearings | 10–20 | 5 Cu |
| Type metals | 3–12 | Sb (3–25) |
| Terne steel coatings | 12–20 | Corrosion protection |
| Anodes | 7 | Cr plating |

Table 3.1-285 Melting characteristics and applications of Sn–Pb solders [1.309]

| Solder alloy Sn/Pb | Composition (wt%) | | Temperature (°C) | | | Uses |
|-----------------------|-------------------|----|------------------|----------|-------------|---|
| | Sn | Pb | Solidus | Liquidus | Pasty range | |
| 2/98 | 2 | 98 | 316 | 322 | 10 | Side seams for can manufacture |
| 5/95 | 5 | 95 | 305 | 312 | 13 | For coating and joining metals |
| 10/90 | 10 | 90 | 268 | 302 | 62 | For coating and joining metals |
| 15/85 | 15 | 85 | 227 | 288 | 110 | For coating and joining metals |
| 20/80 | 20 | 80 | 183 | 277 | 170 | For coating and joining metals. For filling dents or seams in automobile bodies |
| 25/75 | 25 | 75 | 183 | 266 | 150 | For machine and torch soldering |
| 30/70 | 30 | 70 | 183 | 255 | 130 | For machine and torch soldering |
| 35/65 | 35 | 65 | 183 | 247 | 116 | General purpose and wiping solder |
| 40/60 | 40 | 60 | 183 | 238 | 99 | Wiping solder for joining lead pipes and cable sheaths. For automobile radiator cores and heating units |
| 45/55 | 45 | 55 | 183 | 227 | 80 | For automobile radiator cores and roofing seams |
| 50/50 | 50 | 50 | 183 | 216 | 60 | For general purpose. Most popular of all |
| 60/40 | 60 | 40 | 183 | 190 | 13 | Primarily used in electronic soldering applications where low soldering temperatures are required |
| 3/37 | 63 | 37 | 183 | 183 | 0 | Lowest melting (Eutectic) solder for electronic applications |

Table 3.1-286 Physical and mechanical property data on Pb–Sn solders [1.309]

| Material (wt%) | Tensile strength (MPa) | Shear strength (MPa) | Density (g cm ⁻³) | Brinell hardness HB | Electrical conductivity (% of σ _{Cu}) | Young's modulus (GPa) | Surface tension (290 °C) (10 ¹¹ N m ⁻¹) |
|-------------------|------------------------------|----------------------------|----------------------------------|------------------------|---|-----------------------------|--|
| Pb | 12.30 | 12.44 | 11.34 | 4.0 | 7.9 | 18.04 | |
| 5/95 Sn/Pb | 28.96 | 20.73 | 11.06 | 9.0 | 8.0 | | |
| 10/90 Sn/Pb | 32.48 | 26.96 | 10.44 | 11.0 | 8.2 | 19.08 | |
| 15/85 Sn/Pb | 34.56 | 30.89 | 10.50 | 11.3 | 8.4 | | |
| 20/80 Sn/Pb | 35.94 | 32.76 | 10.23 | 11.5 | 8.7 | 20.04 | 467 |
| 25/75 Sn/Pb | 37.32 | 36.70 | 10.00 | 11.5 | 8.9 | | |
| 30/70 Sn/Pb | 39.74 | 38.01 | 9.74 | 11.3 | 9.3 | 21.08 | 470 |
| 35/65 Sn/Pb | 41.82 | 38.64 | 9.50 | 11.0 | 9.8 | | |
| 40/60 Sn/Pb | 42.85 | 39.26 | 9.29 | 10.5 | 10.1 | 23.08 | 474 |
| 45/55 Sn/Pb | 42.85 | 39.53 | 9.08 | 10.6 | 10.4 | | |
| 50/50 Sn/Pb | 44.58 | 40.57 | 8.88 | 11.0 | 10.9 | | 476 |
| 60/40 Sn/Pb | 44.23 | 39.40 | 8.51 | 12.0 | 11.3 | 30.07 | |
| 63/37 Sn/Pb | 46.31 | 41.88 | 8.41 | 12.0 | 11.5 | | 490 |
| 62Sn/36Pb/2Ag | 46.31 | 43.20 | 8.42 | 16.0 | 11.6 | 23.57 | |
| 10Sn/88Pb/2Ag | 33.87 | 29.72 | 10.75 | 12.0 | 8.4 | 19.35 | |
| 1Sn/97.5Pb/1.5Ag | 24.88 | 24.88 | 11.28 | 11.0 | 8.8 | | |

of 0.18 wt% Cu causes a further increase. Bismuth-containing solders, the so-called fusible alloys, are used for low temperature soldering and are discussed in the section on fusible alloys. Alloys of Pb–In are primarily used for soldering at low temperatures and where

reduction in gold-scavenging is desired. They are also extremely ductile, making them suitable for use in areas where there is a thermal mismatch. Compositions of other commonly used Pb solders are given in Table 3.1-287 [1.309].

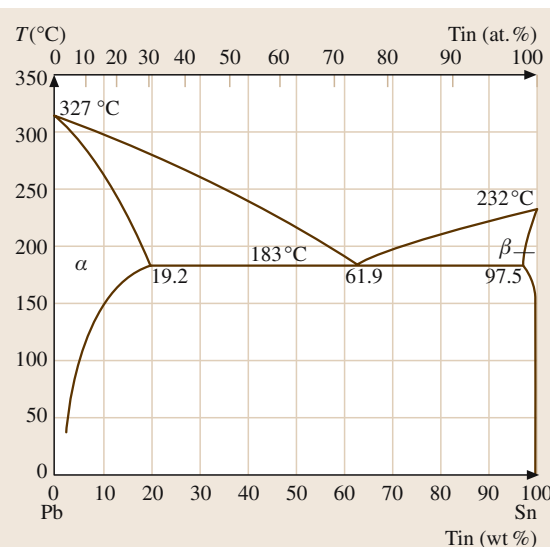


Fig. 3.1-355 The Pb–Sn binary phase diagram [1.303]

3.1.11.4 Pb–Ca Alloys

The Pb–Ca and Pb–Ca–Sn alloys are used in storage battery grid, pipe, wire, cable sheathing, anodes, chemical handling equipment, radiation shielding, and other applications [1.299]. Calcium is also used as a secondary additive in hardened lead-bearing metals. Its solubility in Pb decreases from 0.1 wt% Ca at 328.3 °C to ~ 0.01 wt% Ca at room temperature (Fig. 3.1-356) and pronounced age-hardening can be obtained. A peritectic

Table 3.1-287 Other common Pb-alloy solders [1.309]

| Pb | Sn | Ag | In | Temperature (°C) | | |
|------|----|-----|----|------------------|----------|-------------|
| | | | | Solidus | Liquidus | Pasty range |
| 97.5 | 1 | 1.5 | — | 309 | 309 | Eutectic |
| 36.0 | 62 | 2.0 | — | 179 | 189 | 18 |
| 97.5 | — | 2.5 | — | 304 | 304 | 62 |
| 50 | — | — | 50 | 124 | 209 | 52 |
| 92.5 | — | 2.5 | 5 | 285 | 305 | 36 |

reaction involving liquid Pb–Ca and Pb_3Ca to form the α -Pb–0.1 wt% Ca phase occurs at 328.3 °C [1.303]. At > 0.07 wt% Ca, Pb_3Ca crystallizes directly on solidification. At > 0.1 wt% Ca, the microstructure consists of primary crystals of Pb_3Ca and a Pb matrix with finer Pb_3Ca precipitates. The two-phase structure present at these higher Ca contents leads to grain refinement. Supersaturated solid solutions of Ca in Pb at room temperature can be obtained at high cooling rates upto about 0.13 wt% Pb. The hardness increase observed on aging increases with Ca content. Upon aging, the hardness of a 0.07 wt% Ca alloy at room temperature increases from HB = 4 to HB = 8.25 (10 mm-31.2 kg-120 s) in 6 h. Electrical resistivity drops from 22.63 to $22.25 \times 10^{-6} \Omega \text{ cm}$. Maximum in hardness for quenched alloys occurs at 0.13 wt% Ca and in air-cooled alloys at 0.085 wt% Ca.

Further additions of Li, Ba, and Na increase the hardness. The addition of Sn to Pb–Ca alloys increases the hardness, tensile strength, and stress rupture properties. The hardness decreases as Sb and Bi form

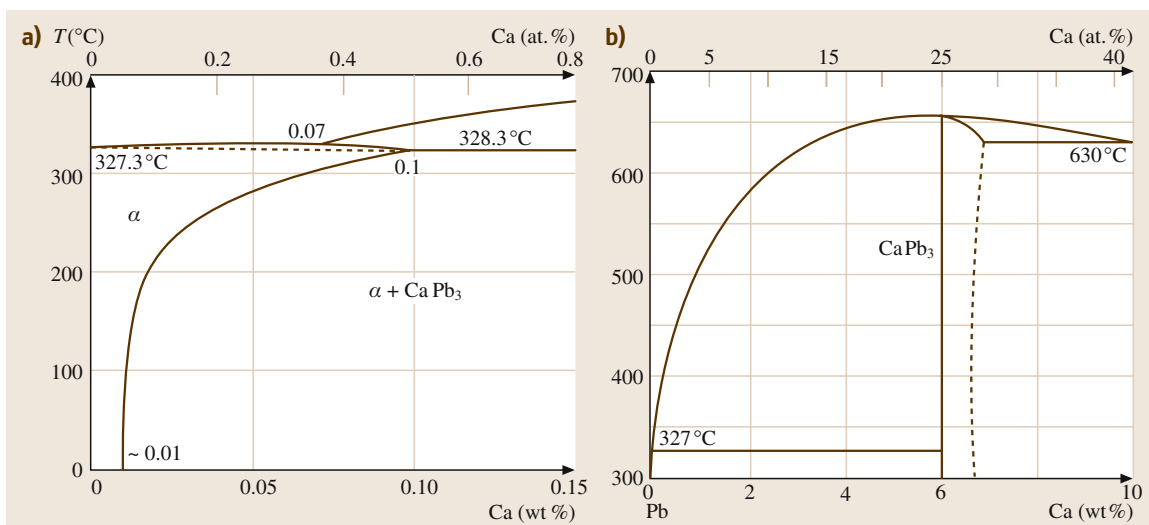


Fig. 3.1-356 Pb-rich portion of the Pb–Ca phase diagram [1.303]

intermetallic compounds with Ca and segregate from the melt. Due to the presence of finely distributed precipitate phase, the age-hardened alloys show a high resistance to recrystallization after room temperature working. The creep rate increases with Ca content, mainly due to the smaller grain size. The mechanical properties of binary Pb–Ca and Pb–Ca–Sn alloys are presented in Table 3.1–288 [1.299, 306]. The fine-grained wrought Pb–Ca and Pb–Ca–Sn alloys possess improved material integrity and also exhibit improved corrosion performance, as they tend to undergo uniform corrosion. The corrosion resistance of these alloys is higher than that of Pb–Sb alloys in many applications.

Pb–Ca–Sn Battery Grid Alloys

Most batteries produced currently use Pb–Ca alloys for grids and connectors and the use of Pb–Sb based alloys is declining [1.307]. The Ca content varies from 0.03 to 0.13 wt%. The narrow freezing range of a few

degrees allows continuous casting and grid production. The mechanical properties in Pb–Ca binary alloys peak at 0.07 wt%. Above 0.06 wt% Ca, cellular precipitation of Pb_3Ca leads to fine grain size. Increasing Ca contents above 0.07 wt% level accelerate corrosion and this is believed to be due to fine grains and primary Pb_3Ca . Addition of Sn dramatically improves the properties by promoting the formation of the more effective and stable Sn_3Ca . The phase relations of Pb rich Pb–Ca–Sn alloys according to [1.310] are shown in Fig. 3.1–357. Tin additions also improve the corrosion resistance and the charge–discharge process by Sn enrichment of the corrosion product layer. Aluminium acts as a deoxidant and prevents drossing loss of Ca. The addition of Sn aids electrochemical properties by preventing passivation of the grid and permitting recharge of batteries from a deeply discharged condition. Additions of Ag to Pb–Ca and Pb–Ca–Sn alloys increase the creep and corrosion resistance. However, Sn and Ag additions are not re-

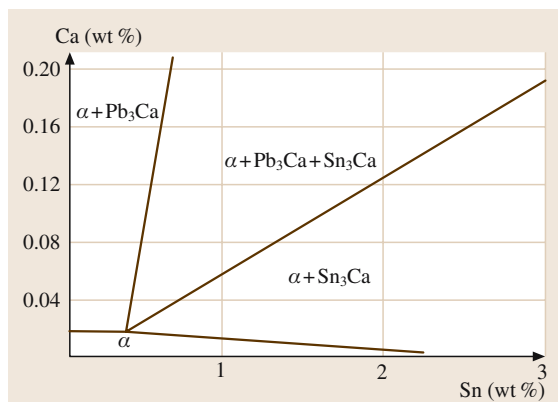
Table 3.1–288 Mechanical properties of Pb–Ca–Sn alloys and corrosion rates in battery environments [1.299, 306]

| Composition (wt%) | | Tensile strength (MPa) | Yield stress ($R_{p0.125}$) (MPa) | Elongation (%) | Creep to failure, at 20.7 MPa (h) | Corrosion rate in battery service (mm yr ⁻¹) |
|----------------------|-----|------------------------------|---|-------------------|---|--|
| Cast | | | | | | |
| 0.025 | | 25.1 | 17.7 | | 1 | 0.279 |
| 0.050 | | 37.2 | 29.0 | | 30 | 0.345 |
| 0.075 | | 46.4 | 35.3 | | 40 | 0.358 |
| 0.100 | | 47.8 | 32.5 | | 10 | 0.411 |
| 0.025 | 0.5 | 25.5 | 19.3 | | 10 | 0.256 |
| 0.050 | 0.5 | 48.2 | 38.5 | | 70 | 0.310 |
| 0.065 | 0.5 | 48.9 | 40.0 | | 200 | 0.325 |
| 0.075 | 0.5 | 50.3 | 40.2 | | 300 | 0.325 |
| 0.100 | 0.5 | 51.7 | 38.7 | | 70 | 0.343 |
| 0.025 | 1.5 | 45.8 | 34.3 | | 30 | 0.246 |
| 0.050 | 1.5 | 55.1 | 46.8 | | 100 | 0.271 |
| 0.075 | 1.5 | 60.1 | 49.2 | | 1000 | 0.297 |
| 0.100 | 1.5 | 57.9 | 43.7 | | 250 | 0.345 |
| Wrought | | | | | | |
| 0.050 | 0.5 | 55.2 | 45.3 | 30 | 10 ^a | |
| 0.07 | 0.5 | 62.1 | 45.0 | 30 | 20 ^a | |
| 0.05 | 1.0 | 61.4 | 52.8 | 25 | 150 ^a | |
| 0.07 | 1.0 | 68.9 | 64.0 | 15 | 400 ^a | |
| 0.050 | 1.5 | 63.8 | 57.4 | 15 | 300 ^a | |
| 0.07 | 1.5 | 71.0 | 65.3 | 14 | 1000 ^a | |

^a At 27.6 MPa

Table 3.1–289 Currently preferred compositions of automotive battery-grid alloys [1.307]

| Manufacturing process; grid type | Composition (wt %) | | | |
|-------------------------------------|--------------------|---------|-------------|-------------|
| | Ca | Sn | Ag | Al |
| Book mold cast; positive | 0.03–0.06 | 0.5–0.9 | 0.010–0.045 | 0.01–0.02 |
| Book mold cast; negative | 0.09–0.13 | 0–0.3 | Trace | 0.015–0.03 |
| Rolled, expanded; positive | 0.06–0.08 | 1.2–1.6 | Trace | 0.003–0.008 |
| Rolled, expanded; negative | 0.06–0.08 | 0–0.5 | Trace | 0.003–0.008 |
| Concast strip, expanded; positive | 0.03–0.06 | 0.4–0.6 | 0.03–0.045 | 0.005–0.010 |
| Concast strip, expanded; negative | 0.07–0.1 | 0–0.2 | Trace | 0.005–0.010 |
| Continuously cast; negative | 0.07–0.1 | 0–0.3 | Trace | 0.005–0.010 |

**Fig. 3.1–357** Suggested phase relations of Pb-rich Pb–Ca–Sn alloys [1.310]

quired in negative grids to provide the corrosion and creep resistance. The Ca content in positive grids is lower than in negative grids to reduce corrosion. Table 3.1–289 presents the compositions of Pb–Ca–Sn alloys currently preferred in lead acid automotive batteries [1.307]. Table 3.1–290 presents mechanical and properties of commonly used Pb–Ca–Sn battery alloys [1.299, 306].

3.1.11.5 Pb–Bi Alloys

Pb–Bi Binary Alloys

Even though the relative difference of atomic radii of Bi (1.56) and Pb (1.75) amounts to about 12%, the solubility of Bi reaches 23.5 wt% at 184 °C and 7.5 wt% at room temperature. While Bi addition has very little influence on mechanical properties, Pb–Bi alloys' excellent wetting properties make them valuable as solders for glass-to-metal joints. Their desirable solidification shrinkage characteristics and casting properties (that provide an ability to reproduce surface details) make them useful in printing and prototyping applications.

The Pb–Bi alloy system exhibits behavior of an eutectic between an hcp intermetallic β phase and the Bi terminal phase at 56.5 wt% Bi and 125 °C. Both Pb and Bi have low cross sections for neutron absorption such that these alloys are attractive in heat transfer applications in nuclear reactor systems [1.299].

Fusible Alloys

Lead forms a number of extremely useful low-melting alloys when combined with Bi, Sn, Cd, or a combination of these metals. The metals In, Sb, and Ag are also

Table 3.1–290 Properties of some of selected Pb–Ca–Sn battery-grid alloys [1.299, 300]

| Alloy composition (wt%) | Liquidus (°C) | Solidus (°C) | Ultimate tensile strength (MPa) | Elongation (%) | Hardness (HR) | Coefficient of thermal expansion (10^{-6} K^{-1}) | Resistivity ($\text{n}\Omega \text{ m}$) |
|----------------------------|------------------|-----------------|---------------------------------------|-------------------|------------------|---|---|
| Pb–0.065Ca–0.7Sn | | 327 | | | | | 219 |
| Pb–0.065Ca–1.3Sn | | 323 | | | | 26.6 | 220 |
| Pb–0.07Ca | | 328 | 36–39 | 35–40 | 70–80 | 30.2 | 218 |
| Pb–0.1Ca–0.3Sn | 338 | 328 | 41–45 | 20–35 | 90–95 | | 219 |
| Pb–0.1Ca–0.5Sn | 336 | 327 | 44.8–51.7 | 25–35 | 85–90 | | 219 |
| Pb–0.1Ca–1Sn | 332 | 325 | 52–55 | 20–35 | 90–95 | | 212 |

added in some of the alloys. Some of these alloys melt at a temperature lower than the boiling point of water, and those containing appreciable amounts of Bi (> 55 wt%) expand slightly upon solidification.

The melting point of the Pb–Sn–Cd ternary eutectic is only 145 °C. By the addition of Zn, a quaternary eutectic can be obtained with a melting point of 138 °C at a composition of Pb–16.7 wt% Cd–52.45 wt% Sn–2.25 wt% Zn. A further effective decrease in the melting point is obtained by additions of Bi to Pb–Cd–Sn alloys. The quaternary Bi–Pb–Cd–Sn eutectic has a melting point of about 70 °C and a composition of Pb–50 wt% Bi–12.5 wt% Cd–12.5 wt% Sn (Wood's metal). The phases of the quaternary eutectic are solid solutions corresponding to the Pb, Sn, and Cd phases, as well as and the β -phase of the Pb–Bi system. The quaternary Pb–Bi–Sn–Cd eutectic alloy is brittle when cast, and becomes ductile on storage for two to three hours. The melting point of the quaternary eutectic alloy can be further lowered to 47 °C by additions of In. Addition of Hg instead of In could also lower the melting point of Pb–Bi–Sn–Ca eutectic but is not used due to its high vapor pressure

and toxicity. In addition to the above quaternary eutectic alloys, alloys of the ternary-Pb–Bi–Sn system are also of great technical importance. One of these alloys is the Newton-metal (Pb–50 wt% Bi–20 wt% Sn) that has approximately the ternary eutectic composition. The melting temperature of this eutectic alloy is 90 °C. Another important alloy is Rose's metal, with a composition Pb–50 wt% Bi–25 wt% Sn and a melting temperature of 100 °C. Table 3.1-291 presents the compositions and properties of selected fusible alloys [1.299, 300].

Low melting alloys are employed in safety devices such as sprinkler systems and boiler plugs, as special solders where high temperatures cannot be used, hermetic seals for molds, patterns, punches and dies, for anchoring punches in punch plates, and for bending tubing (Table 3.1-292).

3.1.11.6 Pb–Ag Alloys

The addition of Ag to Pb in the range of 0.01–0.1 wt% provides high resistance to recrystallization, grain refinement, and high creep strength. Eutectic Pb–Ag

Table 3.1-291 Compositions and properties of selected fusible alloys [1.299, 300]

| Alloy composition ^a (wt%) | Liquidus (°C) | Solidus (°C) | Volume change on freezing (vol. %) ^b | Density (g cm ⁻³) | Conductivity (% of IACS) | Coefficient of thermal expansion (10 ⁻⁶ K ⁻¹) | Specific heat (J kg ⁻¹ K ⁻¹) | Latent heat of fusion (kJ kg ⁻¹) | Thermal conductivity (W m ⁻¹ K ⁻¹) |
|---|------------------|-----------------|--|----------------------------------|-----------------------------|---|--|---|--|
| Pb–42Bi–11Sn–9Cd | 88 | 70 | 2 | 9.45 | 4 | 24 | 168 | 23 | 21 |
| Pb–42.9Bi–5.1Cd–7.9Sn–4Hg–18.3In | 43 | 38 | | | | | | | |
| Pb–44.7Bi–5.3Cd–8.3Sn–9.1In ASTM Alloy 117 | 47 | 47 | 1.4 | 8.85 | 4.5 | | 147 | 14 | |
| Pb–48Bi–14.5Sn–9Sb | 227 | 103 | 1.5 | 9.50 | 3 | 22 | 189 | | |
| Pb–49Bi–21In–12Sn ASTM Alloy 136 | 58 | 58 | 1.5 | 8.60 | 3 | | 134.4 | | 21 |
| Pb–50Bi–9.3Sn–6.2Cd | 70 | 78 | | | | | | | |
| Pb–50Bi–10Cd–13.3Sn ASTM Alloy 158 | 70 | 70 | 1.7 | 9.40 | 4 | 22 | 168 | 32 | |
| Pb–51.7Bi–8.1Cd | 92 | 92 | | 10.25 | | | | | |
| Pb–52.5Bi–15.5Sn ASTM Alloy 203 | 96 | 96 | | 9.71 | | | | | |
| Pb–55Bi ASTM Alloy 255 | 124 | 124 | 1.5 | 10.30 | 3 | | 126 | 16 | 16.8 |

^a Alloys may contain small amounts of Ag, Cu, Sb and Zn

^b Positive values indicate expansion on freezing

Table 3.1-292 Typical applications of some common fusible alloys [1.299, 300]

| Alloy | Melting temperature (°C) | Typical applications |
|-----------------------------------|--------------------------|--|
| ASTM 117 | 47 | Dental models, part anchoring, and lens chucking |
| ASTM 158 (Woods metal) | 70 | Bushings and locators in jigs and fixtures, lens chucking, reentrant tooling, founding cores and patterns, light sheet-metal embossing dies, tube bending, and Wood's metal-sprinkler heads |
| ASTM 255 | 124 | Inserts in wood, plastics, bolt anchors, founding cores and patterns, embossing dies, press-form blocks, duplicating plaster patterns, tube bending, and hobbyist pans |
| ASTM 281 | 138 | Locator members in tools and fixtures, electroforming cores, dies for lost-wax patterns, plastic casting molds, prosthetic development work, encapsulating avionic components, spray metalizing, and pantograph tracer molds |
| Pb–48 wt% Bi–14.5 wt% Sn–9 wt% Sb | 103–217 | Punch and die assemblies, small bearings, anchoring for machinery, tooling, forming blocks, and stripper plates in stamping dies |

alloys containing about 2.5 wt% Ag are used as soft solders of high melting point. The alloy Pb–0.1 wt% Ag is used as a precoat to metallurgically bond lead to steel. Alloys of Pb–0.8–1 wt% Ag are used as insoluble anodes for electrowinning of metals from leach solutions and for electrogalvanizing. The alloys Pb–6 wt% Sb–1 wt% Ag, Pb–1 wt% Ag, Pb–2 wt% Ag, and Pb–1 wt% Ag–1 wt% Sn are used as anodes for cathodic protection.

3.1.11.7 Pb–Cu, Pb–Te, and Pb–Cu–Te Alloys

Maximum solubility in Pb is very low for both Cu (< 0.007%) and Te (< 0.005%). Copper contents of less than 0.1% provide considerable grain refinement and structural stability at high temperature. Pb–Cu alloys are used in cable sheathing and chemical applications. A Te content of 0.01% refines and stabilizes the grain size and increases the work-hardening in Pb–Te alloys. Significant age-hardening is also obtained from supersaturated solid solutions containing up to 0.1 wt% Te. The optimal Te content is 0.04–0.05% with Cu addition of 0.06%. Alloys of Pb–Te have very high fatigue strengths and are used in cable sheathing, radiation shielding, and steam-heating coil applications.

3.1.11.8 Pb–As Alloys

The alloy Pb–0.85 wt% As has very low volume shrinkage on solidification and pore free castings obtained

with this alloy are used in radiation protection applications. Arsenic is added in Pb–Sb alloys to accelerate age hardening. It is also used in Pb cable sheathing alloys to enhance the bending and creep resistance.

3.1.11.9 Lead Cable Sheathing Alloys

Lead alloys are used as cable sheath in the construction of electrical cables for communication and high voltage transmission. The cable sheath serves as an impermeable barrier to prevent access of moisture to the insulated core, a containment of the oil or gas in oil- or gasfilled cables, and a ground to the power cables under short circuit conditions. The sheaths need to be easily applied in long lengths and should have good creep resistance, fatigue resistance, corrosion resistance, and microstructural stability. Table 3.1-293 lists some of cable sheathing alloys and their typical applications.

3.1.11.10 Other Lead Alloys

Alloys of Pb–Li are attractive in some nuclear shielding applications due to their ability to thermalize neutrons. Lead containing more than 0.5 wt% In wets glass, and Pb–In alloys with up to 5 wt% In can be used for soldering glass over a narrow temperature range. Additions over 25 wt% of In are made to Pb–Sn solders to increase their alkali resistance. An addition of 1–2 wt% In in Pb–Ag solders increases their strength. Indium is also used in multi-component fusible alloy systems.

Table 3.1-293 Compositions of commonly-used cable sheathing alloys [1.299]

| Alloy name | Nominal composition (wt%) | Fatigue strength (MPa) at 10 ⁷ cycles 37–50 Hz | Applications |
|------------|-------------------------------|---|---|
| Alloy B | Pb-0.8-0.95 Sb | 9.6 | Solid type cables and telecommunication cables subjected to severe vibrations |
| Alloy 1/2B | Pb-0.5 Sb | 7.5 | Solid type cables and telecommunication cables subjected to severe vibrations |
| Alloy C | Pb-0.35–0.45 Sn-0.12–0.18 Cd | 5.4 | Power cables in ships. Acceptable for most types of cables |
| Alloy 1/2C | Pb-0.18–0.22% Sb-0.06–0.09 Cd | 4.2 0.07% ^a | Oil-filled and submarine power cables. Power cables subjected to severe vibrations in service. Acceptable for most types of reinforced cables |
| Alloy E | Pb-0.35–0.45 Sn-0.15–0.25 Sb | 6.3 | Solid type power cables, telecommunication cables, and reinforced gas or oil pressurized power cables under moderate vibrations |
| Pb–Cu | Pb-0.06 Cu | 3.34 | Gas or oil pressurized power cables |
| Cu–Te | Pb-0.06 Cu-0.045 Te | 6.9 | Cables subjected to high vibrations and oil-filled cables |
| F3 | Pb-0.15 As-0.15 Sn-0.1% Bi | 6.1 | PILC cables, submarine cables, power cables subjected to severe bending or vibration conditions |
| Pb–Ca–Sn | Pb-0.033 Ca-0.38 Sn | 0.11% ^a | High-voltage DC and AC submarine cables |

^a Reversible strain for 10⁷ cycle at 30 Hz in reversible cantilever bending

References

- 1.1 E. G. Emley: *Principles of Magnesium Technology* (Pergamon, New York 1966)
- 1.2 IMA: *Annual Report* (Int. Magnesium Association, Washington, DC 2001)
- 1.3 M. M. Avedesian, H. Baker: *Magnesium and Magnesium Alloys*, ASM Specialty Handbook (ASM, Metals Park 1999)
- 1.4 I. J. Polmear: *Light Metals, Metallurgy of the Light Metals* (Wiley, New York 1995)
- 1.5 G. Neite: Structure and properties of nonferrous alloys. In: *Materials Science and Technologie*, Vol. 8, ed. by K. H. Matucha (Verlag Chemie, Weinheim 1996)
- 1.6 C. S. Roberts: *Magnesium and Its Alloys* (Wiley, Chichester 1960)
- 1.7 C. Kammer: *Magnesium Taschenbuch* (Aluminium Verlag, Düsseldorf 2000)
- 1.8 G. L. Song, A. Atrens: Corrosion mechanisms of magnesium alloys, *Adv. Eng. Mater.* **1** (1999)
- 1.9 C. Kammer: *Aluminium Handbook 1, Fundamentals and Materials* (Aluminium Verlag, Düsseldorf 2002)
- 1.10 J. R. Davis (Ed.): *Aluminium and Aluminium Alloys*, ASM Specialty Handbook (ASM, Metals Park 1993)
- 1.11 H. W. L. Phillips: *Equilibrium Diagrams of Aluminium Alloy System* (The Aluminium Development Association, London 1961)
- 1.12 J. Thonstad, P. Fellner, G. M. Haarberg, J. Hives, H. Kvande, A. Sterten: *Aluminium Electrolysis – Fundamentals of the Hall-Héroult Process*, 3rd edn. (Aluminium Verlag, Düsseldorf 2001)
- 1.13 International Aluminium Institute (AIA, London 2003), www.world-aluminium.org and www.world-aluminium.org
- 1.14 E. Nachtigall, H. Landerl: The treatment of the conductor alloy E-AlMgSi, *Aluminium Ranshofen Mitteilungen* **2**, 40–43 (in German) (1955)
- 1.15 E. Nachtigall, G. Lang: Electrical conductivity of aluminium castings, *Mitt. Verein. Metallwerke Ranshofen-Berndorf*, 16–19 (in German) (1965)
- 1.16 L. F. Mondolfo: *Aluminium Alloys – Structure and Properties* (Butterworths, London 1976)
- 1.17 C. Kammer: Thermomechanical treatment of Al strip casting. Ph.D. Thesis (TU Bergakademie Freiberg, Freiberg 1989) (in German)
- 1.18 E. Schürmann, I. K. Geissler: Solid-state phase equilibria in the Al and Mg rich areas of the Al-Mg-Li system, *Giessereiforschung* **32**, 163–174 (in German) (1981)
- 1.19 A. Dons: AlFeSi-Particles in industrially cast aluminium alloys, *Z. Metallkunde* **76**, 609–612 (1985)

- 1.20 A. Cziraki, B. Fogarassy, I. Szábo: Structure of high purity Al-Fe-Si-cast with different cooling rates, *Cryst. Res. Technol. Berlin* **20**, 279–281 (1985)
- 1.21 H. Westengen: Structure inhomogenities in direct chill cast sheet ingots of commercial pure aluminium, *Z. Metallkunde* **73**, 360–368 (1982)
- 1.22 H. P. Godard, W. B. Jepson, M. R. Bothwell, R. L. Kane: *The Corrosion of Light Metals* (Wiley, New York 1967)
- 1.23 K. R. Van Horn: *Aluminium. Bd. 1, Properties, Physical Metallurgy and Phase Diagrams* (ASM, Metals Park 1967)
- 1.24 D. Altenpohl: *Aluminium and Aluminium-Alloys* (Springer, Berlin, Heidelberg 1965 (in German))
- 1.25 U. Hielscher, H. Arbenz, H. Diekmann: Properties of AISI-casting alloys with low iron content, *Giesserei* **53**, 125–133 (in German) (1966)
- 1.26 U. Hielscher: Ductile aluminium-silicon casting alloys for safety components in cars, *Schweiz. Alum. Rundsch.* **29**, 13–15 (in German) (1979)
- 1.27 U. Hielscher, R. Klos: A new low iron diecasting alloy, *Aluminium* **71**, 676–685 (in German) (1995)
- 1.28 W. Jung-König, U. Zwicker: Behaviour of light metal alloys on heating, *Aluminium* **34**, 337–345 (in German) (1958)
- 1.29 H. Vosskühler: Aluminium-Gusslegierungen hoher Dauerstandfestigkeit mit Magnesium und Silicium, *Aluminium* **31**, 219–222 (1955)
- 1.30 K. Wellinger, E. Keil, G. Maier: Strength of aluminium and its alloys up to 300 °C, *Aluminium* **34**, 458–463 (in German) (1958)
- 1.31 K. Wellinger, E. Keil et al.: On the mechanical properties of aluminium and aluminium alloys at elevated temperatures, *Aluminium* **39**, 372–377 (in German) (1963)
- 1.32 E. Richter, E. Hanitzsch: Elastic modulus and other physical properties of aluminium-base materials. Part 1., *Aluminium* **70**, 570–574 (in German) (1994)
- 1.33 D. Lenz, G. M. Renouard: Definition of cold rolled tempers by means of flow curves and energy of deformation, *Aluminium* **46**, 694–699 (in German) (1970)
- 1.34 A. Odok, G. Thym: The technical and economic advantages of continuous strip casting, *Aluminium Engl. Suppl.* **50**, E9–E11 (English transl.) (1974)
- 1.35 C. Kammer, M. Krünnacker et al.: Thermomechanical treatment of continuously cast and rolled Al99.5 alloy, *Neue Hütte* **35**, 418–421 (in German) (1990)
- 1.36 C. Kammer, M. Krünnacker et al.: Comparison of the strengthening effects in strip cast Al99.5, AlMn1 and AlMn1Fe1, *Metall* **45**, 135–138 (in German) (1991)
- 1.37 J. Althoff: Properties and uses of a new heat-resistant Al-Mn alloy, *Metall* **31**, 263–267 (in German) (1977)
- 1.38 J. Althoff: Examples of the application-orientated development of high-strength aluminium manganese alloys, *Aluminium Engl. Suppl.* **56**, E37–E39 (English transl.) (1982)
- 1.39 P. Brenner, H. Kostron: Treatment of AlMgSi-alloys, *Z. Metallkunde* **31**, 89–97 (1939)
- 1.40 I. Novikov: *Theory of Heat Treatment of Metals*, 1st edn. (Metalurgija, Moscow 1978)
- 1.41 Y. Takeuchi: Effect of plastic deformation on the natural ageing of AlCuMg1, AlCuMg2 and AlZn-MgCu0.5, *Aluminium* **47**, 665–670 (in German) (1971)
- 1.42 K. Lücke, P. Stüwe: On the theory of impurity controlled grain boundary motion, *Acta Met.* **19**, 1067–1099 (1971)
- 1.43 H. Warlimont: Effect of segregation and precipitation on the recrystallisation and grain size of non-ferrous metals, *Freiberg. Forschungsh. B* **200**, 31–57 (in German) (1979)
- 1.44 D. B. Goel, P. Furrer, H. Warlimont: Precipitation behaviour of AlMnCuFe-alloys, *Aluminium* **50**, 511–516 (in German) (1974)
- 1.45 E. Nes, S. Slevolden: Casting and annealing structures in strip cast alloy, *Aluminium* **55**, 319–324 (1979)
- 1.46 E. Nes, J. D. Embury: The influence of a fine particle dispersion on the recrystallisation behaviour of a two phase aluminium alloy, *Z. Metallkunde* **66**, 589–593 (1975)
- 1.47 E. Nes, S. Slevolden: The concept of a grain size diagramm in the analysis of the recrystallisation behaviour of AlMn-alloys, *Aluminium* **52**, 560–563 (1976)
- 1.48 E. Nes: The effect of a fine particle dispersion on heterogeneous recrystallisation, *Acta Met.* **24**, 391–398 (1976)
- 1.49 C. Kammer, M. Krünnacker et al.: Thermomechanical treatment of strip cast AlMn1Fe1 alloy, *Metall* **43**, 1162–1168 (in German) (1993)
- 1.50 W. Huppertz: The fundamentals of corrosion protection of aluminium alloys used as structural materials. Part 1, *Metall* **49**, 505–509 (in German) (1995)
- 1.51 K. H. Matucha: Structure and properties of nonferrous alloys. In: *Materials Science and Technology*, Vol. 8, ed. by R. W. Cahn, P. Haasen, E. J. Kramer (VCH, Weinheim 1996)
- 1.52 J. R. Davis (Ed.): *Heat-Resistant Materials*, ASM Specialty Handbook (ASM, Metals Park 1997)
- 1.53 H. Sibum, G. Volker, O. Roidl, H. U. Wolf: Titanium and titanium alloys. In: *Ullmann's Encyclopedia of Industrial Chemistry*, Vol. A27 (VCH, Weinheim 1996) pp. 95–122
- 1.54 J. L. Murray: *Phase Diagrams of Binary Titanium Alloys* (ASM, Metals Park 1990)
- 1.55 D. F. Williams: Medical and dental materials. In: *Materials Science and Technology*, Vol. 14, ed. by R. W. Cahn, P. Haasen, E. J. Kramer (VCH, Weinheim 1992)
- 1.56 S. Steiner: *Properties and Selection: Irons, Steels and High Performance Alloys*, Metals Handbook, Vol. 1, 8th edn. (ASM, Metals Park 1961)

- 1.57 G. Sauthoff: *Intermetallic Materials*, Landolt-Börnstein, New Series **VIII/2**, ed. by P. Beiss, R. Ruthardt, H. Warlimont (Springer, Berlin, Heidelberg 2002)
- 1.58 T. K. Roy, R. Balasubramanian, A. Ghosh: Metall. Mater. Trans. Trans. A **27**, 3993–4003 (1996)
- 1.59 Y. W. Kim: JOM-J. Min. Met. Mater. Soc. **46** (1994)
- 1.60 N.S. Stoloff, V.K. Sikka: *Pysical Metallurgy and Processing of Intermetallic Compounds*, 1st edn. (Chapman & Hall, London 1996)
- 1.61 Y. W. Kim, R. Wagner, M. Yamaguchi: Gamma titanium aluminides, Proc. ISGTA'95 (TMS, Warrendale 1995)
- 1.62 R. Darolia, J.J. Lewandowski, C.T. Liu, P.L. Martin, D.B. Miracle, M.V. Nanthal: Structural intermetallics, Proc. First Intl. Symp. (TMS, Warrendale 1993)
- 1.63 K. Otsuka, C.M. Wayman (Eds.): *Shape Memory Materials* (Cambridge University Press, Cambridge 1998)
- 1.64 K. Otsuka, T. Kakeshita (Guest Eds.): Science and technology of shape-memory alloys: New developments, Mater. Res. Soc. Bull. **27**, 91–129 (2002)
- 1.65 H. Horikawa: , Proc. 1st Europ. Conf. on Shape Memory and Superelastic Technologies, Antwerp 1999) 256
- 1.66 A.E. Pelton, S.M. Russell, J. DiCello: The physical metallurgy of nitinol for medical applications, JOM-J. Min. Met. Mater. Soc. **55**, 33–37 (2003)
- 1.67 W. Chang: Zirconium products: Technical data sheet (Allegheny Technologies Inc. Pittsburgh, PA), www.alleghenytechnologies.com/wahchang
- 1.68 C. Lemaignan, A.T. Motta: Zirconium alloys in nuclear applications. In: *Materials Science and Technology*, Vol. 10B/II, ed. by B.R.T. Frost (VCH, Weinheim 1994)
- 1.69 A. Inoue, T. Zhang, T. Masumoto: Production of amorphous cylinder and sheet of La₅₅Al₂₅Ni₂₀ alloy by a metallic mold casting method, JIM **31**, 425 (1990)
- 1.70 A. Peker, W.L. Johnson: Appl. Phys. Lett. **63**, 2342 (1993)
- 1.71 W.L. Johnson: Fundamental aspects of bulk metallic glass formation in multicomponent alloys, Mater. Sci. Forum **225–227**, 35 (1996)
- 1.72 A. Inoue: *Bulk Amorphous Alloys* (Trans Tech, Uetikon-Zurich 1998)
- 1.73 A. Takeuchi, A. Inoue: Mater. Sci. Eng. A **304–306**, 446 (2001)
- 1.74 T. Wada, T. Zhang, A. Inoue: Mater. Trans. **43**, 2843 (2002)
- 1.75 C.C. Hays, J. Schroers, U. Geyer, S. Bossuyt, N. Stein, W.L. Johnson: Glass forming ability in the Zr-Nb-Ni-Cu-Al bulk metallic glasses. In: *Metastable, Mechanically Alloyed and Nanocrystalline Materials*, ed. by H. Eckert, H. Schlörb, L. Schultz (Trans Tech, Uetikon-Zurich 1995)
- 1.76 G. He, W. Löser, J. Eckert, L. Schultz: Mater. Sci. Eng. A **352**, 179 (2003)
- 1.77 J. E. Truman: Stainless steels. In: *Constitution and Properties of Steels*, Materials Science and Technology, Vol. 7, ed. by F.B. Pickering (VCH, Weinheim 1992) p. 527
- 1.78 W. Dahl (Ed.): *Eigenschaften und Anwendungen von Stählen* (Institut für Eisenhüttenkunde IEHK, RWTH Aachen, Aachen 1993) p. 727 in German
- 1.79 J.R. Davis (Ed.): *Stainless Steels*, ASM Specialty Handbook (ASM, Metals Park 1994)
- 1.80 J.R. Davis (Ed.): *Carbon and Alloy Steels*, ASM Specialty Handbook (ASM, Metals Park 1996)
- 1.81 J.E. Bringas (Ed.): *Handbook of Comparative World Steel Standards* (ASTM, West Conshohocken 2001)
- 1.82 B. Predel (Ed.): *Phase Equilibria, Crystallographic and Thermodynamic Data of Binary Alloys*, Landolt-Börnstein, New Series **IV/5** (Springer, Berlin, Heidelberg 1991–1998)
- 1.83 J.L. Lee, H.K.D.H. Bhadeshia: Mater. Sci. Eng. A **171**, 223–230 (1993)
- 1.84 G. Vander Voort: *Atlas of Time Temperature Diagrams*, Vol. 1, 2 (ASM, Materials Park 1991)
- 1.85 H. Schneider: Investment casting of high-hot strength 12% chrome steel, Foundry Trade J. **108**, 562 (1960)
- 1.86 K. Yagi, G. Merkling, H. Irie, H. Warlimont (Eds.): *Creep Properties of Heat Resistant Steels and Superalloys*, Landolt-Börnstein, New Series **VIII** (Springer, Berlin, Heidelberg 2004)
- 1.87 VDEh (Ed.): *Stahl-Eisen-Werkstoffblatt (SEW)* no. 470, Feb. 1976 (Verlag Stahleisen GmbH, Düsseldorf 1976)
- 1.88 J.R. Davis (Ed.): *Tool Materials*, ASM Specialty Handbook (ASM, Metals Park 1995)
- 1.89 J.R. Davis (Ed.): *Cast Irons*, ASM Specialty Handbook (ASM, Metals Park 1996)
- 1.90 W. Betteridge: *Cobalt and Its Alloys* (Ellis Horwood, New York 1982)
- 1.91 J.R. Davis (Ed.): *Nickel, Cobalt and Their Alloys*, ASM Specialty Handbook (The Materials Information Society, Materials Park 2000)
- 1.92 W. Gudat, O. Rader (Eds.): *Electronic Structure of Solids. Photoemission Spectra and Related Data. Magnetic Transition Metals*, Landolt-Börnstein, New Series **III/23** (Springer, Berlin, Heidelberg 1999)
- 1.93 B. Predel: *Phase Equilibria*, Landolt-Börnstein, New Series **IV/5** (Springer, Berlin, Heidelberg 1991–1998)
- 1.94 J.R. Davis (Ed.): *Tool Materials*, ASM Specialty Handbook (The Materials Information Society, Materials Park 1995)
- 1.95 P. Beiss, R. Ruthardt, H. Warlimont (Eds.): *Powder Metallurgy Data*, Landolt-Börnstein, New Series **VIII/2** (Springer, Berlin, Heidelberg 2002)
- 1.96 J.R. Davis (Ed.): *Nickel, Cobalt and Their Alloys*, ASM Specialty Handbook (ASM International, Materials Park 2000)
- 1.97 J.R. Davis (Ed.): *Heat-Resistant Materials*, ASM Specialty Handbook (ASM International, Materials Park 1997)

- 1.98 J. C. Fuggle, U. Hillebrecht, R. Zeller, Z. Zolonierek, P. Bennet, C. Freiburg: Phys. Rev. B **27**, 719 (1982)
- 1.99 W. Gudat, O. Rader (Eds.): *Electronic Structure of Solids. Photoemission Spectra and Related Data. Magnetic Transition Metals*, Landolt-Börnstein, New Series **III/23** (Springer, Berlin, Heidelberg 1999)
- 1.100 B. Predel: *Phase Equilibria, Crystallographic and Thermodynamic Data of Binary Alloys*, Landolt-Börnstein, New Series **IV/5** (Springer, Berlin, Heidelberg 1991–1998)
- 1.101 K. Yagi, G. Merckling, H. Irie, H. Warlimont (Eds.): *Creep Properties of Heat Resistant Steels and Superalloys*, Landolt-Börnstein, New Series **VIII** (Springer, Berlin, Heidelberg 2004)
- 1.102 G. Joseph, K.J.A. Kundig: *Copper, Its Trade, Manufacture, Use, and Environmental Status* (ASM International, Materials Park 1998)
- 1.103 Wieland-Werke AG: *Wieland-Kupferwerkstoffe* (Ulm, Germany 1999)
- 1.104 J. R. Davis (Ed.): *Copper and Copper Alloys*, ASM Specialty Handbook (ASM, Metals Park 2001)
- 1.105 H. Warlimont, L. Delay: *Martensitic Transformations in Copper-, Silver-, and Gold-Based Alloys* (Pergamon, Oxford 1974)
- 1.106 B. Predel: *Cr-Cs-Cu-Zr*, Landolt-Börnstein, New Series **IV/5** (Springer, Berlin, Heidelberg 1991–1998)
- 1.107 J. B. Conway, B. N. Flagella: *Creep Rupture Data for the Refractory Metals to High Temperatures* (Gordon Breach, New York 1971)
- 1.108 R. Kieffer, G. Jangg, P. Ettmayer: *Sondermetalle* (Springer, Vienna 1971) in German
- 1.109 American Society for Metals: *Properties and Selection: Nonferrous Alloys and Pure Metals*, Metals Handbook, Vol. 2, 9th edn. (American Society for Metals, Metals Park 1979)
- 1.110 W. C. Hagel, J. A. Shields, S. M. Tuominen: Processing and production of molybdenum and tungsten alloys, Proc. Symp. on Refractory Technology for Space Nuclear Power Applications, CONF-8308130 (Oak Ridge National Laboratory 1983) 98
- 1.111 K. H. Miska, M. Semchyshen, E. P. Whelan (Eds.): *Physical Metallurgy and Technology of Molybdenum and its Alloys* (AMAX, Michigan 1985)
- 1.112 J. Wadsworth, T. G. Nieh, J. J. Stephens: Recent advances in aerospace refractory metal alloys, Inter. Mater. Rev. **33**(3), 131 (1988)
- 1.113 E. Pink, I. Gaal: Mechanical properties and deformation mechanisms of non-sag tungsten wires. In: *The Metallurgy of Doped, Non-Sag Tungsten*, ed. by E. Pink, L. Bartha (Elsevier, New York 1989) p. 209
- 1.114 T. G. Nieh, J. Wadsworth: Recent advances and developments in refractory alloys, Mat. Res. Soc. Symp. Proc. **322**, 315 (1994), ISBN: 1-55899-221-9
- 1.115 E. Pink, R. Eck: Refractory metals and their alloys. In: *Materials Science and Technology – A Comprehensive Treatment*, Vol. 8, ed. by R. W. Cahn, P. Haasen, E. J. Kramer (VCH Verlag, Weinheim 1997) p. 589
- 1.116 E. Lassner, W. D. Schubert: *Tungsten: Properties, chemistry, technology of the element, alloys, and chemical compounds* (Kluwer/Plenum, New York 1999)
- 1.117 G. Leichtfried: *Handbook of Extractive Metallurgy* (Wiley-VCH, Weinheim 1997) p. 1371
- 1.118 G. Leichtfried: *Powder Metallurgy Data*, Landolt-Börnstein, New Series **VIII/2A** (Springer, Berlin, Heidelberg, New York 2002)
- 1.119 G. Leichtfried: Molybdenum lanthanum oxide: Special material properties by dispersoid refining during deformation. In: *Advances in Powder Metallurgy and Particulate Materials*, Vol. 9 (MPIF, Princeton 1992) p. 123
- 1.120 D. M. Moon, R. C. Koo: Mechanism and kinetics of bubble formation in doped W, Metall. Trans. **2**, 2125 (1971)
- 1.121 H. G. Sell, D. F. Stein, R. Stickler, A. Joshi, E. Berkey: The identification of bubble forming impurities in doped tungsten, J. Inst. Met. **100**, 275 (1972)
- 1.122 P. Makarov, K. Povarova: Principles of the alloying of tungsten and development of the manufacturing technology for the tungsten alloys, Proc. 15th Plansee Seminar, Vol. 3 (Plansee AG, Reutte 2001) p. 464
- 1.123 G. A. Geach, J. E. Hughes: The alloy of rhenium with molybdenum or with tungsten and having good high temperature properties, Proc. 2nd Plansee Seminar (Plansee AG, Reutte 1955) p. 245
- 1.124 R. I. Jaffee, C. T. Sims, J. J. Harwood: The effect of rhenium on the fabricability and ductility of molybdenum and tungsten, Proc. 3rd Plansee Seminar (Plansee AG, Reutte 1958) p. 380
- 1.125 J. G. Booth, R. I. Jaffee, E. I. Salkovitz: The mechanisms of the rhenium-alloying effect in group VI-A metals, Proc. 5th Plansee Seminar (Plansee AG, Reutte 1964) p. 547
- 1.126 Plansee Aktiengesellschaft: Material Data Base, Reutte (2000)
- 1.127 H. Borchers, E. Schmidt (Eds.): *Stoffwerte und Verhalten von metallischen Werkstoffen*, Landolt-Börnstein **IV/2b**, 6th edn. (Springer, Berlin, Heidelberg 1964)
- 1.128 T. E. Tietz, J. W. Wilson: *Behavior and Properties of Refractory Metals* (Stanford Univ. Press, Stanford 1965) p. 325
- 1.129 Plansee Aktiengesellschaft: Tungsten Brochure, Reutte (1997)
- 1.130 C. Cagran, C. Brunner, A. Seifter, G. Pottlacher: Liquid-phase behaviour of normal spectral emissivity at 684.5 nm of some selected metals, High Temp.-High Press. **34**, 669 (2002)
- 1.131 Dechema-Werkstoff-Tabelle: *Oxidierende Heißgase* (Dechema, Frankfurt 1981)
- 1.132 A. Schintlmeister, H.-P. Martinz, P. Wilhartitz, F. P. Netzer: Low-temperature oxidation of industrial molybdenum surfaces, Powder Metallurgy

- World Congress & Exhibition, Granada 1998 (EPMA 1998) 526
- 1.133 G. Leichtfried: Powder metallurgical components for light sources, Habilitation Thesis (Montanuniversität, Leoben 2003)
- 1.134 E. Fromm, E. Gebhardt: *Gase und Kohlenstoff in Metallen* (Springer, Berlin, Heidelberg 1976) p. 747 in German
- 1.135 R. Speiser, G. R. St. Pierre: Proc. AGARD (Advisory Group for Aerospace Research and Development) Conf. on refractory metals, Oslo 1963
- 1.136 J. Disam, H.-P. Martinz, M. Sulik: European Patent Specification EP798402
- 1.137 C. A. Krier: *Coatings for the Protection of Refractory Metals from Oxidation*, Defense Metals Information Center Report 162 (Battelle Memorial Institute, Columbus 1961)
- 1.138 W. Knabl: Oxidationschutz von Refraktärmetallen auf der Basis von Silizid- und Aluminidschichten. Ph.D. Thesis (Montanuniversität, Leoben 1995) in German
- 1.139 H.-P. Martinz, M. Sulik: Oxidation protection of refractory metals in the glass industry, Glastechnische Berichte, Glas Sci. Technol. **73**(C2) (2000)
- 1.140 C. Stickler: Mikroplastizität und zyklisches Spannungs-Dehnungsverhalten von Ta und Mo bei Temperaturen unter $0.2 T_m$. Ph.D. Thesis (University of Vienna, Vienna 1998) in German
- 1.141 F. Benesovsky: *Pulvermetallurgie und Sinterwerkstoffe* (Plansee AG, Reutte 1982) p. 95, in German
- 1.142 E. Pink, H. Kärle: Zum Rekristallisationsverhalten von Sintertantal, Planseeberichte für Pulvermetallurgie **16**, 105 (1968) in German
- 1.143 G. Leichtfried, G. Thurner, R. Weirather: Molybdenum alloys for glass-to-metal seals, Proc. 14th Plansee Seminar, Vol. 4 (Plansee AG, Reutte 1997) p. 26
- 1.144 H. H. R. Jansen: The recrystallization texture of non-sag wire. In: *The Metallurgy of Doped, Non-Sag Tungsten*, ed. by E. Pink, L. Bartha (Elsevier, New York 1989) p. 203
- 1.145 D. B. Snow: The recrystallization of non-sag tungsten wire. In: *The Metallurgy of Doped, Non-Sag Tungsten* (Elsevier, New York 1989) p. 189
- 1.146 V. I. Trefilov, Y. V. Milman: Physical basis of thermomechanical treatment of refractory metals, Proc. 12th Plansee Seminar, Vol. 1 (Plansee AG, Reutte 1989) p. 107
- 1.147 E. Parteder, W. Knabl, R. Stickler, G. Leichtfried: Bruchzähigkeit und Porenverteilung von Molybdän Stabmaterial in Abhängigkeit des Reckgrades und des Rekristallisationsgrades, Proc. 14th Plansee Seminar, Vol. 1 (Plansee AG, Reutte 1997) p. 984, in German
- 1.148 E. Parteder, H. Riedel, R. Kopp: Densification of sintered molybdenum during hot upsetting: Experiments and modeling, Mat. Sci. Eng. A **264**, 17 (1999)
- 1.149 E. Parteder: Ein Modell zur Simulation von Umformprozessen pulvemetallurgisch hergestellter hochschmelzender Metalle. Ph.D. Thesis (RWTH, Aachen 2000) in German
- 1.150 E. Parteder, H. Riedel: Simulating of hot forming processes of refractory metals using porous metal plasticity models, Proc. 15th Plansee Seminar, Vol. 3 (Plansee AG, Reutte 2001) p. 60
- 1.151 B. P. Bewlay, C. L. Briant: Discussion of "Evidence for the Existence of Potassium Bubbles in AKS-Doped Tungsten Wire" and Reply, Met. Trans. A **22A**, 2153 (1991)
- 1.152 C. L. Briant: The effect of thermomechanical processing on the microstructure of tungsten rod, Proc. 13th Plansee Seminar, Vol. 1 (Plansee AG, Reutte 1993) p. 321
- 1.153 J. L. Walter, C. L. Briant: Tungsten wire for incandescent lamps, J. Mat. Res. **5**, 2004 (1990)
- 1.154 G. L. Krasko: Effect of impurities on the electronic structure of grain boundaries and intergranular cohesion in tungsten, Proc. 13th Plansee Seminar, Vol. 1 (Plansee AG, Reutte 1993) p. 27
- 1.155 A. Kumar, B. L. Eyre: Grain boundary segregation and intergranular fracture in molybdenum, Proc. R. Soc. London A **370**, 431 (1980)
- 1.156 St. M. Cardonne: Tantalum and its alloys, Advanced Mat. & Processes **9**, 16 (1992)
- 1.157 P. Wilhartzit, G. Leichtfried, H. P. Martinz, H. Hutter, A. Virág, M. Grasserbauer: Applications of 3D-SIMS for the development of refractory metal products, Proc. 2nd Europ. Conf. on Advanced Materials and Processes, ed. by T. W. Clyne, P. J. Withers, London 1992) 323
- 1.158 J. Femböck, R. Stickler, A. Vinckier: The effect of strain rate and heating rate on the tensile behavior of W and W-Th₂O between room temperature and 1400 °C, Proc. 11th Plansee Seminar, Vol. 1 (Plansee AG, Reutte 1985) p. 361
- 1.159 D. L. Chen, B. Weiss, R. Stickler, M. Witwer, G. Leichtfried, H. Hödl: Fracture toughness of high melting point materials, Proc. 13th Plansee Seminar, Vol. 1 (Plansee AG, Reutte 1993) p. 621
- 1.160 E. S. Meiren, D. A. Thomas: Effect of grain boundaries on the bending ductility of tungsten, Metall. Trans. **23B**, 937 (1965)
- 1.161 P. F. Browning, C. L. Briant, B. A. Knudsen: Dependence of material properties on processing history during wire drawing of commercially doped tungsten lamp wire, Proc. 13th Plansee Seminar, Vol. 1 (Plansee AG, Reutte 1993) p. 336
- 1.162 P. K. Wright: High temperature creep behavior of doped tungsten wire, Metall. Trans. **9**, 955 (July 1978)
- 1.163 J. Neges, B. Ortner, G. Leichtfried, H. P. Stüwe: On the 45° embrittlement of tungsten sheets, Mat. Sci. Eng. A **196**, 129 (1995)
- 1.164 Y. V. Milman: unpublished results

- 1.165** A. Seeger: The temperature dependence of the critical shear stress and of work hardening of metal crystals, *Philos. Mag.* **7**, 771 (1954)
- 1.166** J. W. Christian: Plastic deformation of bcc metals, Proc. International Conference on the Strength of Materials (ICSM-2), Asilomar (ASTM, Philadelphia 1970) 31
- 1.167** H. Mughrabi: unpublished results
- 1.168** H. Ullmaier: Design properties of tantalum or everything you always wanted to know about tantalum but were afraid to ask, ESS (European Spallation Source) report ISSN 1433-559X, 03-131-T (2003)
- 1.169** W. Rinnerthaler, F. Benesovsky: Untersuchungen über das Mikrodehnungsverhalten von Molybdän, *Planseeberichte für Pulvermetallurgie* **21**, 253 (1973) in German
- 1.170** C. Stickler, D. L. Chen, B. Weiss, R. Stickler: Time dependent microplastic deformation of Mo and Ta at low temperatures, Proc. 14th Plansee Seminar, Vol.1 (Plansee AG, Reutte 1997) p.1004
- 1.171** K. J. Bowman, R. Gibala: Cyclic deformation of W single crystals, *Scripta Met.* **20**, 1451 (1986)
- 1.172** M. A. Meyers, Y.-J. Chen, F. D. S. Marquis, J. B. Isaacs: High strain rate behavior of Ta, The Univ. of Cal., Inst. for Mechanics and Materials, Report **94-25** (1994)
- 1.173** C. C. Wojcik: Thermomechanical processing and properties of niobium alloys, Proc. of the Internat. Symposium Niobium 2001 (Niobium 2001 Limited, Orlando 2001) 163
- 1.174** H. Mughrabi, K. Herz, X. Stark: Cyclic deformation and fatigue behavior of α -Fe mono- and polycrystals, *Int. J. Fracture* **17**, 193 (1981)
- 1.175** M. Werner: Temperature and strain rate dependence of the flow stress of Ta single crystals in cyclic deformation, *Revue de Physique Appliquee* **23**, 672 (1988)
- 1.176** J. Femböck, K. Pfaffinger, B. Weiss, R. Stickler: Verhalten von Mo-Werkstoffen unter zyklischer Beanspruchung, Proc. 10th Plansee Seminar, Vol.2 (Plansee AG, Reutte 1981) p. 27
- 1.177** K. Pfaffinger, J. Femböck: Versuchsplanung und statistische Auswertung von Schwingfestigkeitsdaten von Mo-Werkstoffen, Proc. 10th Plansee Seminar, Vol. 2 (Plansee AG, Reutte 1981) p. 233
- 1.178** K. Mecke, C. Holste, W. F. Terentjev: Dislocation arrangement in cyclically deformed Mo, *Krist. Tech.* **15**, 83 (1980)
- 1.179** S. Kong, B. Weiss, R. Stickler, M. Witwer, H. Hödl: Cyclic stress strain behavior of high melting point metals, Proc. 13th Plansee Seminar, Vol.1 (Plansee AG, Reutte 1993) p. 720
- 1.180** D. R. Helebrand, R. I. Stephens: Cyclic yield behavior of Ta, *J. Mater. Sci.* **7**, 530 (1972)
- 1.181** C. Stickler, W. Knabl, R. Stickler, B. Weiss: Cyclic behavior of Ta at low temperatures under low stresses and strain rates, Proc. 15th Plansee Seminar, Vol. 3 (Plansee AG, Reutte 2001) p. 34
- 1.182** J. M. Meiniger, J. C. Gibeling: LCF of Nb and Nb-1Zr alloys, *Met. Trans.* **23A**, 3077 (1992)
- 1.183** H. J. Shi, L. S. Niu, C. Korn, G. Pluvineage: High temperature fatigue behavior of Mo-TZM alloy under mechanical and thermomechanical cyclic load, *J. Nuclear Mat.* **278**, 328 (2000)
- 1.184** R. F. Brodrick: LCF-data of P/M-W between 1650 and 3300 °C, Proc. ASTM **64**, 505 (1965)
- 1.185** S. S. Manson: *Thermal Stress and Low Cycle Fatigue* (McGraw-Hill, New York 1981) p. 187
- 1.186** R. E. Schmunk, G. E. Korth, M. Ulrickson: Tensile and LCF measurements on cross rolled tungsten, *J. Nuclear Mat.* **103**, 943 (1981)
- 1.187** T. Kimishima, M. Sukekawa, K. Owada, M. Shimizu: Fatigue data of Mo, 9th Symp. on Engineering Problems of Fusion Research 1981 (IEEE, New York 1981) 255
- 1.188** H. Nishi, T. Oku, T. Kodeira: Influence of microstructural change caused by cyclic strain on the LCF strength of sintered Mo, *Fusion-Engineering-Design* **9**, 123 (1989)
- 1.189** Z. M. Sun, Z. G. Wang, H. Hödl, R. Stickler, B. Weiss: Low cycle fatigue and creep behavior of recrystallized Mo near room temperature, *Materialwissenschaft und Werkstofftechnik* **26**, 483 (1995)
- 1.190** M. Papakyriacou, H. Mayer, C. Pypen, H. Plenk, S. Stanzi-Tschegg: Influence of loading frequency on high cycle fatigue properties of bcc and hcp metals, *Mat. Sci. Eng. A* **A308**, 143 (2001)
- 1.191** H. A. Calderon, G. Kostorz: Microstructure and plasticity of two molybdenum-base alloys (TZM), *Mat. Sci. Eng. A* **A160**, 189 (1993)
- 1.192** C. W. Marschall, F. C. Holden: Fracture toughness of refractory metals and alloys. In: *High Temperature Refractory Metals*, ed. by L. Richardson (Gordon Breach, New York 1964) p. 129
- 1.193** M. Rödig, H. Derz, G. Pott, B. Werner: Fracture mechanics investigations of TZM and Mo5Re, Proc. 14th Plansee Seminar, Vol.1 (Plansee AG, Reutte 1997) p. 781
- 1.194** D. Padhi, J. J. Lewandowski: Effects of test temperature and grain size on the charpy impact toughness and dynamic toughness (KID) of polycrystalline niobium, *Met. Mat. Trans. A* **34**, 967 (2003)
- 1.195** J. A. Shields, P. Lipetzky, A. J. Mueller: Fracture toughness of 6.4 mm arc cast Mo and TZM Plate at RT and 300 °C, Proc. 15th Plansee Seminar, Vol. 4 (Plansee AG, Reutte 2001) p. 187
- 1.196** J. X. Zhang, L. Liu, M. L. Zhou, Y. C. Hu, T. Y. Zuo: Fracture toughness of sintered Mo-La₂O₃, *Internat. J. Refract. Met. Hard Mat.* **17**, 405 (1999)
- 1.197** D. L. Chen, B. Weiss, R. Stickler: The effective fatigue threshold: Significance of the loading cycle below the crack opening load, *Internat. J. Fatigue* **16**, 485 (1994)
- 1.198** J. Riedle: Bruchwiderstand in Wolfram-Einkristallen: Einfluß der kristallographischen Orientierung, der Temperatur und der Lastrate. In: *Fortschrittsberichte VDI*, Reihe 18, Mechanik/Bruchmechanik, Vol. 184 (VDI, Düsseldorf 1995) in German

- 1.199 R. Pippan: *Bruchzähigkeitsuntersuchungen an W Proben* (Erich Schmid Institut, Leoben 1999) Report in German
- 1.200 Y. Mutoh, K. Ichikawa, K. Nagata, M. Takeuchi: Effect of Re addition on fracture toughness of W at elevated temperatures, *J. Mat. Sci.* **30**, 770 (1995)
- 1.201 A. Fathulla, B. Weiss, R. Stickler: Short fatigue cracks in technical P/M-Mo alloys. In: *The Behavior of Short Fatigue Cracks, Mechanical Engineering Publications*, Vol. 1 (EGF Pub., Suffolk 1986) p. 115
- 1.202 R. Grill, H. Clemens, P. Rödhammer, A. Voitcek: P/M processing, characterization and application of Ta-10W, Proc. 14th Plansee Seminar, Vol. 4 (Plansee AG, Reutte 1997) p. 211
- 1.203 R. Heidenreich, R. Schäfer, H. Clemens, M. Witwer: Mechanical properties of high-temperature fasteners from refractory alloys, Proc. 13th Plansee Seminar, Vol. 1 (Plansee AG, Reutte 1993) p. 664
- 1.204 A. Fathulla, B. Weiss, R. Stickler, J. Femböck: The initiation and growth of short cracks in pm-Mo, Proc. 11th Plansee Seminar, Vol. 1 (Plansee AG, Reutte 1985) p. 45
- 1.205 H. Kitagawa, S. Takahashi: Applicability of fracture mechanics to very small cracks or the cracks in the early stage, Proc. second international conference on mechanical behavior of materials (ASM, Metals Park 1976) 627
- 1.206 B. Weiss, R. Stickler: Methods for predicting the fatigue strength of P/M-materials, Proc. International Powder Metallurgy Conf. PM'88, Orlando 1988, 3
- 1.207 B. Weiss, R. Stickler, A. F. Blom: A model for the description of the influence of small 3-dimensional defects on the HCF limit, Proc. Conf.: Short Fatigue Cracks, Sheffield 1990 (Mechanical Engineering Publications Limited, Suffolk 1992) 423
- 1.208 G. Leichtfried: Die Entwicklung von kriechfesten Molybdän - Seltenerdioxid - Werkstoffen für Hochtemperaturanwendungen. Ph.D. Thesis (Montanuniversität, Leoben 1997) in German
- 1.209 D. M. Moon, R. Stickler: Creep behavior of fine wires of P/M pure, doped and thoriated tungsten, High Temp. High Press. **3**, 503 (1971)
- 1.210 J. W. Pugh: On the short time creep rupture properties of lamp wire, *Metall. Trans.* **4**, 533 (1973)
- 1.211 J. H. Schröder, E. Arzt: Weak beam studies of dislocation/dispersoid interaction in an ODS superalloy, *Scripta Met.* **19**, 1129 (1985)
- 1.212 J. Rössler, E. Arzt: Kinetics of dislocation climb over hard particles – Climb without attractive particle-dislocation interaction, *Acta Met.* **36**, 1043 (1988)
- 1.213 J. Rössler, E. Arzt: A new model-based creep equation for dispersion strengthened materials, *Acta Met. Mat.* **38**(4), 671 (1990)
- 1.214 G. Zilberstein, J. Selverian: Creep deformation of non-sag tungsten in argon doped with low oxygen concentrations, Proc. 13th Plansee Seminar, Vol. 1 (Plansee AG, Reutte 1993) p. 132
- 1.215 G. Zilberstein: Creep properties of non-sag tungsten recrystallized in stagnant oxygen-doped argon, *Int. J. Refract. Met. Hard Mat.* **16**, 71 (1998)
- 1.216 Degussa AG (Ed.): *Edelmetall-Taschenbuch* (Degussa, Frankfurt 1967)
- 1.217 Degussa AG (Ed.): *Edelmetall-Taschenbuch*, 2nd edn. (Hüthig, Heidelberg 1995)
- 1.218 L.S. Benner, T. Suzuki, K. Meguro, S. Tanaka (Eds.): *Precious Metals, Science, Technology* (Int. Precious Metals Institute, Allentown 1991)
- 1.219 B. Predel (Ed.): *Phase Equilibria, Crystallographic, Thermodynamic Data of Binary Alloys*, Landolt-Börnstein, New Series **IV/5** (Springer, Berlin, Heidelberg 1991-1998)
- 1.220 E. Raub: *Die Edelmetalle und ihre Legierungen* (Springer, Berlin, Heidelberg 1940)
- 1.221 P.J. Spencer, K. Hack: *Swiss Materials* **2**, 69–73 (1990)
- 1.222 C.J. Smithells, E.A. Brandes: *Metals Reference Book*, 5th edn. (Butterworth, London 1977)
- 1.223 P. Villars, L. D. Calvert: *Pearson's Handbook of Crystallographic Data for Intermetallic Phases*, Vol. 2, 3 (American Society for Metals, Metals Park 1985)
- 1.224 Landolt-Börnstein: *Technik*, Landolt-Börnstein, New Series **IV/4**, 6th edn. (Springer, Berlin, Heidelberg 1967)
- 1.225 W. Hume-Rothery, G.V. Raynor: *The Structure of Metals and Alloys* (Institute of Metals, London 1956)
- 1.226 Gmelin: *Handbuch der anorganischen Chemie*, Syst. Nr. 61 (Springer, Berlin, Heidelberg 1970–1975)
- 1.227 V. Behrens, K.H. Schröder: *Werkstoffe für elektrische Kontakte und ihre Anwendungen*, Kontakt u. Studium, Vol. 366 (Expert, Ehningen 1992)
- 1.228 W. H. Cubberly, H. Baker, D. Benjamin (Eds.): *Metals Handbook*, Vol. 2, 9th edn. (American Society for Metals, Metals Park 1979) pp. 671–678
- 1.229 E. M. Savitskii, A. Prince: *Handbook of Precious Metals* (Hemisphere, New York 1989) pp. 117–128
- 1.230 K.-H. Hellwege, A. M. Hellwege (Eds.): *Elastics, Piezoelectric, Pyroelectric, Electrooptic Constants, Nonlinear Dielectric Susceptibilities of Crystals*, Landolt-Börnstein, New Series **III/18** (Springer, Berlin, Heidelberg 1984) p. 66
- 1.231 Doduco: *Datenbuch, Handbuch für Techniker*, 2. Aufl. (Doduco, Pforzheim 1977)
- 1.232 H. Spengler: *Metall* **18**, 36 (1964)
- 1.233 K.-H. Hellwege, J. L. Olsen: *Metals – Electronic Transport Phenomena*, Landolt-Börnstein, New Series **III/15** (Springer, Berlin, Heidelberg 1982) p. 167
- 1.234 D. D. Pollock: *Trans. Metall. Soc. AIME* **230**, 753 (1964)
- 1.235 H. Flükiger, W. Klose (Eds.): *Superconductors Acta Na*, Landolt-Börnstein, New Series **III/21** (Springer, Berlin, Heidelberg 1990)
- 1.236 Chr. Raub: *Z. Metallkde.* **55**, 195 (1964)
- 1.237 R. E. Hummel: *Optische Eigenschaften von Metallen und Legierungen* (Springer, Berlin, Heidelberg pp. 158,178

- 1.238 H. Mehrer (Ed.): *Diffusion in Solid Metals and Alloys*, Landolt-Börnstein, New Series III/26 (Springer, Berlin, Heidelberg 1990)
- 1.239 G. Schlamp: *Mater. Sci. Technol.* **8**, 471–587 (1996)
- 1.240 D. Lee: *Modern Chlor-Alkali Technology*, Vol. 2, ed. by C. Jackson (Horwood, Chichester 1983)
- 1.241 S. U. Falk, A. J. Salkind: *Alkaline Storage Batteries* (Wiley, New York 1971)
- 1.242 A. Fleischer, J. J. Lander: *Zinc-Silver-Oxide Batteries* (Wiley, New York 1971)
- 1.243 H. Renner: *Ullmann's Encyclopedia of Industrial Chemistry* (Wiley-VCH, Weinheim 2002)
- 1.244 D. Z. Stöckel: *Z. Werkstofftechnik* **10**, 238 (1979)
- 1.245 B. Predel: *Phase Equilibria, Crystallophic and Thermodynamik Data of Binary Alloys*, Landolt-Börnstein, New Series IV/5 (Springer, Berlin, Heidelberg 1991–1998)
- 1.246 H. Renner: *Ullmann's Encyclopedia of Industrial Chemistry*, 6th edn. (Wiley-VCH, Weinheim 2001)
- 1.247 R. Forro: *Gold Bull.* **36**(2), 39–58 (2003)
- 1.248 N. Yuantao: *Gold Bull.* **34**(3), 77–87 (2001)
- 1.249 H. Ahlborn, G. Wassermann: *Z. Metallkde.* **55**, 685 (1964)
- 1.250 E. Drost, J. H. Hausselt: *Interdisc. Sci. Rev.* **17**, 271–280 (1992)
- 1.251 B. Kempf, J. Hausselt: *Interdisc. Sci. Rev.* **17**, 251–260 (1992)
- 1.252 G. Humston: *Gold Bull.* **26**, 139 (1993)
- 1.253 C. J. Raub D. Ott: *Z. Metallkde.* **25**(4), 629 (1992)
- 1.254 M. Du Toit, E. van der Lingen, L. Glaner, R. Süss: *Gold Bulletin*, quarterly reviews, Vol. 35, ed. by C. Corti, D. Thompson (World gold council, London 2002) p. 49
- 1.255 Gmelin: *Gmelin Handbuch der anorganischen Chemie*, Vol. 62 (Springer, Berlin, Heidelberg 1970–1975) p. 619
- 1.256 H. R. Khan, Ch. R. Raub: *Gold Bulletin*, quarterly reviews, Vol. 8, ed. by C. Corti, D. Thompson (World gold council, London 1975) pp. 114–118
- 1.257 H. R. Khan: *Gold Bulletin*, quarterly reviews, Vol. 17, ed. by C. Corti, D. Thompson (World gold council, London 1984) pp. 94–100
- 1.258 J. Kopp: *Gold Bulletin*, quarterly reviews, Vol. 9, ed. by C. Corti, D. Thompson (World gold council, London 1976) p. 55
- 1.259 M. Hansen, K. Anderko: *Constitution of Binary Alloys*, 2nd edn. (McGraw-Hill, New York 1958) pp. 195, 221
- 1.260 E. Raub: *Die Edelmetalle und ihre Legierungen*, Reine angewandte Metallkunde, Vol. 5, ed. by W. Köster (Springer, Berlin, Heidelberg 1955) Chap. II, A5, pp. 53, 54
- 1.261 T. Shiraishi, K. Hisatsune, Y. Tanaka, E. Miura, Y. Takuma: *Gold Bull.* **34**, 130 (2001)
- 1.262 W. S. Rapson, T. Groenewald: *Gold Usage* (Academic Press, New York 1978) p. 37
- 1.263 D. Compton et al.: *Gold Bulletin*, quarterly reviews, Vol. 10, ed. by C. Corti, D. Thompson (World gold council, London 1977) p. 51
- 1.264 G. C. Bond: *Gold Bulletin*, quarterly reviews, Vol. 34, ed. by C. Corti, D. Thompson (World gold council, London 2001) p. 117
- 1.265 A. St. K. Hashmi: *Gold Bulletin*, quarterly reviews, Vol. 36, ed. by C. Corti, D. Thompson (World gold council, London 2003) p. 3
- 1.266 M. Gupta, A. K. Tripathi: *Gold Bulletin*, quarterly reviews, Vol. 34, ed. by C. Corti, D. Thompson (World gold council, London 2001) p. 120
- 1.267 C. Corti, R. J. Holliday, D. T. Thompson: *Gold Bulletin*, quarterly reviews, Vol. 35 (World gold council, London 2002) p. 111
- 1.268 R. Grisel, K. J. Weststrate, A. Gluhoi, B. E. Nieuwenhuys: *Gold Bull.* **35**, 39–45 (2002)
- 1.269 H. Knosp, R. J. Holliday, Ch. W. Corti: *Gold in dentistry*, Vol. 36 (2003) pp. 93–102
- 1.270 G. Gafner: *Gold Bulletin*, quarterly reviews, Vol. 22, ed. by C. Corti, D. Thompson (World gold council, London 1989) p. 112
- 1.271 G. Humston, D. M. Jacobson: *Gold Bulletin*, quarterly reviews, Vol. 25, ed. by C. Corti, D. Thompson (World gold council, London 1992) p. 139
- 1.272 D. R. Olsen, H. M. Berg: , Proc. 27th Electronic Components Conf. (IEEE, Piscataway 1977)
- 1.273 G. Zwingmann: *Z. Metall.* **34**(18), 726 (1964)
- 1.274 G. Petzow, G. Effenberg: *Ternary Alloys* (Verlag Chemie, Weinheim 1988)
- 1.275 W. Müller: *Metallische Lotwerkstoffe* (DVS, Düsseldorf 1990)
- 1.276 K. Toyoshima, Somorjai: *Cat. Rev. Sci. Eng.* **19** (1979)
- 1.277 A. S. Darling: , Review 175 (Institute of Metals, London 1973)
- 1.278 J. B. Hunter: *Platinum Met. Rev.* **4**(4), 130 (1960)
- 1.279 A. G. Knapton: *Platinum Met. Rev.* **21**(2), 44 (1977)
- 1.280 R. S. Irani: *Metals Rev.* **17**, 22 (1973)
- 1.281 A. Kussmann, G. Von Rittberg: *Ann. Phys.* **7**, 173 (1950)
- 1.282 A. Kussmann, K. Jesson: *J. Phys. Soc. Jpn.* **17**, 272 (1962)
- 1.283 A. S. Darling: *Platinum Met. Rev.* **11**, 138 (1967)
- 1.284 A. S. Darling: *Platinum Met. Rev.* **13**, 53 (1969)
- 1.285 R. S. Irani, R. W. Cahn: *Met. Rev.* **16**, 49 (1972)
- 1.286 H. Ocken, J. H. N. Van Vucht: *J. Less-Comm. Met.* **15**, 196–199 (1968)
- 1.287 I. Gurappa: *Platinum Met. Rev.* **45**(3), 124 (2001)
- 1.288 I. Wolff, P. J. Hill: *Platinum Met. Rev.* **44**(4), 161 (2000)
- 1.289 J. Merker, D. Lupton, M. Töpfer, H. Knake: *Platinum Met. Rev.* **45**, 76–80 (2001)
- 1.290 G. Borelius et al.: *Proc. K. Acad. Wet.* **33**, 17 (1930)
- 1.291 Th. J. Colacot: *Platinum Met. Rev.* **46**(2), 83 (2002)
- 1.292 I. M. Wolff, P. J. Hill: *Platinum Met. Rev.* **44**(4), 159 (2000)
- 1.293 Y. Yamabe-Mitarai, Y. F. Gu, H. Harada: *Platinum Met. Rev.* **46**(2), 77, 78 (2002)
- 1.294 M. Graff, B. Kempf, J. Breme: *Metall* **53**, 616–621 (1999)
- 1.295 J. H. Jones: *Platinum Met. Rev.* **44**(3), 100 (2000)

- 1.296 I. M. Wolff, P. J. Hill: *Platinum Met. Rev.* **44**(4), 164 (2000)
- 1.297 M. Fallot: *Ann. Phys. (Paris)* **10**, 29 (1938)
- 1.298 Philips AG: *Philips Techn. Rev.* , 73 (1966)
- 1.299 S. Guruswamy: *Engineering Properties and Applications of Lead Alloys* (Dekker, New York 2000) pp.1–635
- 1.300 Lead Industries Association: *Properties of Lead and Lead Alloys*, Booklet No. 5M (Lead Industries Association, New York 1983) pp.12–83
- 1.301 Lead Industries Association: *Lead for Corrosion Resistant Applications – A Guide* (Lead Industries Association, New York 1974)
- 1.302 G. Baralis, I. Tangerini: A study of some dynamic properties of lead and its alloys, Proc. 3rd Intl. Lead Conference, Venice, ed. by European Lead Development Committee and Lead Development Association (Pergamon, London 1968) 309–319
- 1.303 W. Hofmann: *Lead and Lead Alloys* (Springer, Berlin, Heidelberg 1970)
- 1.304 G. Kerry, P. Lord: *Project Report LM-375*, International Lead Zinc Research Organization (ILZRO) (University Salford, Salford 1990)
- 1.305 Lead Industries Association: *Lead Shielding for the Nuclear Industry* (Lead Industries Association, New York 1985)
- 1.306 R. D. Prengaman: Wrought lead–calcium–tin alloys for tubular lead/acid battery grids, *J. Power Sources* **53**, 207–214 (1995)
- 1.307 A. Siegmund, R. D. Prengaman: Grid alloys for automobile batteries in the new millennium, *J. Metals* **53**, 38 (2001)
- 1.308 ASTM: *Standard Specification for White Metal Bearing Alloys*, ASTM B23 (American Society for Testing Materials, West Conshohocken 1996)
- 1.309 Lead Industries Association: *Solders and Soldering – A Primer* (Lead Industries Association, Sparta 1996)
- 1.310 P. Adeva, G. Caruana, M. Aballe, M. Torralba: The lead-rich corner of the Pb–Ca–Sn phase diagram, *Mater. Sci. Eng.* **54**, 229–236 (1982)